008418

PROCEEDINGS OF THE TWENTY FIRST ANNUAL CONFERENCE ON FOSSIL ENERGY MATERIALS

April 30 - May 2, 2007

Prepared by
R. R. Judkins
Compiled by
LaRonda Mack

OAK RIDGE NATIONAL LABORATORY
MANAGED BY
UT-BATTELLE, LLC
FOR THE
U.S. DEPARTMENT OF ENERGY
UNDER CONTRACT DE-AC05-00OR22725

12/31/1941 – 10/19/2007

In memory of

Dr. Roddie Reagan Judkins

Fossil Energy Program Director

Oak Ridge National Laboratory

Dr. Roddie Judkins, long-time Director of the Fossil Energy Program at the Oak Ridge National Laboratory and the driving force behind this conference, passed away on October 19th 2007. As many of you know, he struggled for many years with a debilitating illness, yet throughout he maintained the optimistic, ebullient demeanor for which he was well known, and which was in full evidence at this conference. Although he was small in physical stature, he cast a long shadow. His illness did not diminish the tremendous effort he expended in promotion of the Fossil Energy Program. It was a privilege to have known him and to have worked closely with him; he was an inspiration to us all, and we will miss him greatly. (Ian Wright – Interim Director)

008418

PROCEEDINGS OF THE TWENTY FIRST ANNUAL CONFERENCE ON FOSSIL ENERGY MATERIALS

April 30 – May 2, 2007
Knoxville, Tennessee

Compiled by
L.S. Mack

Date Published: December 2007

Prepared by
OAK RIDGE NATIONAL LABORATORY
P.O. Box 2008
Oak Ridge, Tennessee 37831-6285
Managed by
UT-Battelle, LLC
for the
U.S. DEPARTMENT OF ENERGY
Under contract DE-AC05-00OR22725

CONTENTS

SESSION 3 – COATINGS AND PROTECTION OF MATERIALS

SESSION 4 – FUNCTIONAL MATERIALS

SESSION 5 – BREAKTHROUGH CONCEPTS

PREFACE

The 21st Annual Conference on Fossil Energy Materials was held in Knoxville, Tennessee, on April 30 through May 2, 2007. The meeting was sponsored by the U.S. Department of Energy's (DOE) Office of Fossil Energy through the ARM Program (Advanced Research Materials).

The objective of the ARM Program is to conduct research and development on materials for longer-term fossil energy applications, as well as for generic needs of various fossil fuel technologies. The management of the program has been decentralized to the DOE Oak Ridge Operations Office and Oak Ridge National Laboratory (ORNL). The research is performed by staff members at ORNL and by researchers at other national laboratories, universities, and in private industry. The work is divided into the following categories: (1) New Alloys: Properties and Performance, (2) Coatings and Protection of Materials, (3) Functional Materials, and (4) Breakthrough Concepts.

These proceedings were produced primarily from electronic files provided by the authors. They have been neither externally refereed nor extensively edited. However, most of the papers have already undergone technical review within the individual organizations before submission to the Program Office. The proceedings are available on the ORNL Fossil Energy Program home page at http://www.ornl.gov/fossil.

The successful completion of the conference and publication of the proceedings has required help from several people. The organizers wish to thank Angela Beach of the ORNL Conference Office for her help in the many arrangements and the numerous staff and support personnel associated with the conference. Finally we express our sincere appreciation to the authors whose efforts are the very basis of the conference.

CONFERENCE CHAIRMEN

ORNL
Roddie R. Judkins
Ian G. Wright

DOE
Pat Rawls
Robert R. Romanosky Jr.

Conference Coordinators
LaRonda Mack
Pam Stanley
Regina Pride

SESSION 1

NEW ALLOYS

ADVANCED PRESSURE BOUNDARY MATERIALS

Michael Santella
Oak Ridge National Laboratory, 1 Bethel Valley Road, Oak Ridge, Tennessee, 37831-6096
Email: santellaml@ornl.gov; Telephone: 865-574-4805

John Shingledecker
Oak Ridge National Laboratory, 1 Bethel Valley Road, Oak Ridge, Tennessee, 37831-6155
Email: shingledecjp@ornl.gov; Telephone: 865-574-5108

ABSTRACT

Synchrotron diffraction experiments were conducted to examine the real-time transformation behaviour of an experimental 9Cr-3W-3Co-NbV steel with high B and low N (N130B), and the commercial P92 steel under simulated weld heat-affected zone thermal cycles. When heated to peak temperatures near 1100°C, both steels rapidly transformed from ferrite to 100% austenite. During cooling, both transformed to martensite near 400°C. Both steels also retained untransformed austenite: 1.7% in N130B and 5.8% in P92. When N130B was heated to about 60°C above its A_3 of 847°C about 56% of the original ferrite never transformed to austenite. During cooling an additional 21% of ferrite and 23% of martensite formed. It retained no austenite. When P92 was heated to just above its A_3 of 889°C about 15% of its original ferrite never transformed to austenite. During cooling an additional 22% of ferrite and 60% of martensite formed. This steel retained about 2.3% of austenite. Metallographic examinations indicated that the $M_{23}C_6$ in N130B was much more stable than that in P92 for heating to the lower peak temperatures. Analysis using equilibrium thermodynamics suggested that the more stable $M_{23}C_6$ in N130B could raise its apparent A_3 by sequestering C. This could cause the ferrite-austenite transformation to appear sluggish. Thermodynamic analysis also indicated that the $M_{23}C_6$ in N130B contained about 3.9 at% B compared to about 0.08 at% B in that of P92. In contrast, the Mo and W content of the $M_{23}C_6$ was predicted to be higher in P92.

INTRODUCTION

Much of the high strength of the 9 wt% Cr steels being developed for power generation applications is related to their low temperature (< 1000°C) phase transformation behaviour. The Cr, added primarily for oxidation/corrosion resistance, has the important side effect of increasing hardenability, i.e., the ease with which martensite can form in the alloys [1]. The result of alloying and processing is that martensitic steels are produced after normalizing treatments consisting of a high temperature solution treatment followed by air cooling. The as-normalized martensitic structure is composed of fine laths, typically < 1 μm wide x many microns long. The laths contain dense dislocation tangles generated by the plastic accommodation of strain during the austenite-to-martensite transformation [1]. Finally, the martensitic microstructures are tempered to develop the desired mechanical properties.

Tempering tends to promote both recovery of the dislocation substructure and precipitation of particles based on $M_{23}C_6$ and M(C,N) [2,3,4,5]. Ideally, tempering causes the dislocation substructure to recover into a subgrain structure. The $M_{23}C_6$ particles tend to precipitate on prior austenite grain boundaries and subgrain boundaries pinning them [3,4]. The M(C,N) particles also precipitate on boundaries, but they may be uniformly distributed throughout the matrix as well [4]. The M(C,N) particles pin dislocations and impede their motion. The remarkable strength properties of these martensitic steels derive finally from the combination of dislocation hardening, particle hardening, and solid solution hardening [4].

The fact that martensitic steels respond to tempering with microstructure-property changes has disadvantages as well. One source of concern originates with the localized heating that accompanies welding. Welding produces gradients in the unmelted base metal where temperatures decrease from the melting point (near 1500°C) to the ambient welding temperature (up to 200-300°C) over distances of a few millimetres. This heat-affected zone (HAZ) experiences highly dynamic microstructure changes, one consequence of which is that a small region of relatively weak material typically forms between the weld deposit and the unaffected base metal [6]. The weakened HAZ regions tend to be failure initiation sites whenever welds are loaded transversely at low stresses (< 100 MPa) and high temperatures (< 650°C). This is the type of behaviour referred to as Type IV failure [7,8].

There are considerable economic and environmental benefits in understanding, controlling, and eliminating the causes of Type IV failure in martensitic steels because it limits their potential advantages in power generation systems [9]. Recent studies indicate that B additions coupled with control of N levels can suppress the Type IV failure mechanism in welded 9Cr steels [10,11,12]. Several mechanisms were suggested as possible explanations for this behaviour, but the reasons for it are still unclear. With this in mind the present work was done to investigate the austenite-ferrite transformation behaviour in more detail. Synchrotron diffraction experiments were used determine ferrite and austenite phase fractions of a commercial 9Cr steel (P92) and a Type-IV-resistant 9Cr-3W-3Co-NbV steel with high B and low N (N130B) during simulated weld thermal cycles.

EXPERIMENTAL DETAILS

The chemical compositions of the two 9Cr steels that were used are given in Table 1. The alloys were supplied in normalized-and-tempered (N+T) condition: 1 h @ 1080°C + 1 h @ 800°C for the boron-steel N130B and 2 h @ 1070°C + 2 h @ 780°C for the P92 steel. Specimens with dimensions of 1 mm x 4.8 mm x 112 mm were used where the diffracting surfaces were metallographically polished.

Table 1 Chemical compositions

	Element (wt%)										
ID	C	Si	Mn	Cr	W	Mo	Co	Nb	V	N	B
N130B	0.077	0.30	0.49	8.97	2.87	---	2.91	0.046	0.18	0.0015	0.013
P92	0.09	0.16	0.47	8.72	1.87	0.45	---	0.06	0.21	0.050	0.002

Full details about the synchrotron experiments including data analysis procedures are available from previous reports and from Elmer et al [13].

To select peak temperatures for the diffraction experiments, the HAZ temperatures were calculated using a 3D Rosenthal analysis and then compared to the A_1 and A_3 temperatures estimated from equilibrium thermodynamics calculations using the Thermo-Calc software and a Thermotech database [14]. The calculated A_1 and A_3 temperatures are given in Table 2.

Because of the limitation of data collection at 3 s intervals, the heating rates were adjusted to reach the peak temperatures in 9 s so that a few diffraction patterns were captured during heating. The 3 s dwell was added to capture at least one diffraction pattern at the peak temperatures. Ultimately, there were some discrepancies between the programmed and actual peak temperatures as shown in Table 3.

Microstructures of the heat treated specimens were examined optically and by scanning electron microscopy.

Table 2. A_1 and A_3 transformation temperatures estimated from equilibrium thermodynamics calculations

	Temperature (°C)	
Steel	A_1	A_3
N130B	817	847
P92	824	889

Table 3. Comparison of programmed and actual peak temperatures

	Peak temperature (°C)	
Experiment	Programmed	Actual
N130B-1	843	911
N130B-4	1100	1122
P92-1	843	896
P92-4	1100	1088

RESULTS

Specimens of both steels that were heated to the highest simulated HAZ peak temperatures rapidly transformed from ferrite to austenite and were completely austenitized. As expected, on cooling, austenite was retained well below the respective A_1s until the M_Ss were reached in the vicinity of 400°C. Diffraction was continued until the specimens were below 40°C. At that point both steels retained small amounts of austenite, about 1.7% for N130B and about 5.8% for P92. Overall, the transformation behaviour agreed with conventional expectations about what will happen in weld HAZs.

The results for specimens that were heated to the lowest peak temperatures are shown in Figure 1. As indicated, the peak temperature for the N130B was 911°C, a temperature about 60°C higher than the calculated A_3. The peak temperature for the P92 specimen was 896°C which is just at its calculated A_3. In both steels, relative to welding, these temperatures would be considered representative of the fine-grained HAZ region. For these thermal history conditions there is a significant difference in the transformation behaviour of the two steels, and overall it was more complicated than expected.

For the N130B, Figure 1 indicates that the maximum amount of austenite formed was 44%. This means that 56% of the original ferrite (tempered martensite) never transformed to austenite. During cooling, before the M_S was reached the amount of ferrite increased another 21%. The ferrite grows because it is the stable phase below A_1, and because there is no nucleation barrier to its formation. When the M_S was finally reached the remaining austenite transformed to martensite. This transformation sequence resulted in a microstructure composed of 56% of the original ferrite, 21% of newly grown ferrite, and 23% of martensite. No retained austenite was detected in this specimen.

In contrast, Figure 1 shows that the P92 transformed to about 85% austenite for the indicated thermal cycle. About 15% of the original ferrite never transformed. During cooling between the peak temperature and M_S the amount of ferrite further increased by about 22%. Eventually, the austenite transformed to about 60.4% martensite. About 2.3% of austenite was retained in the microstructure.

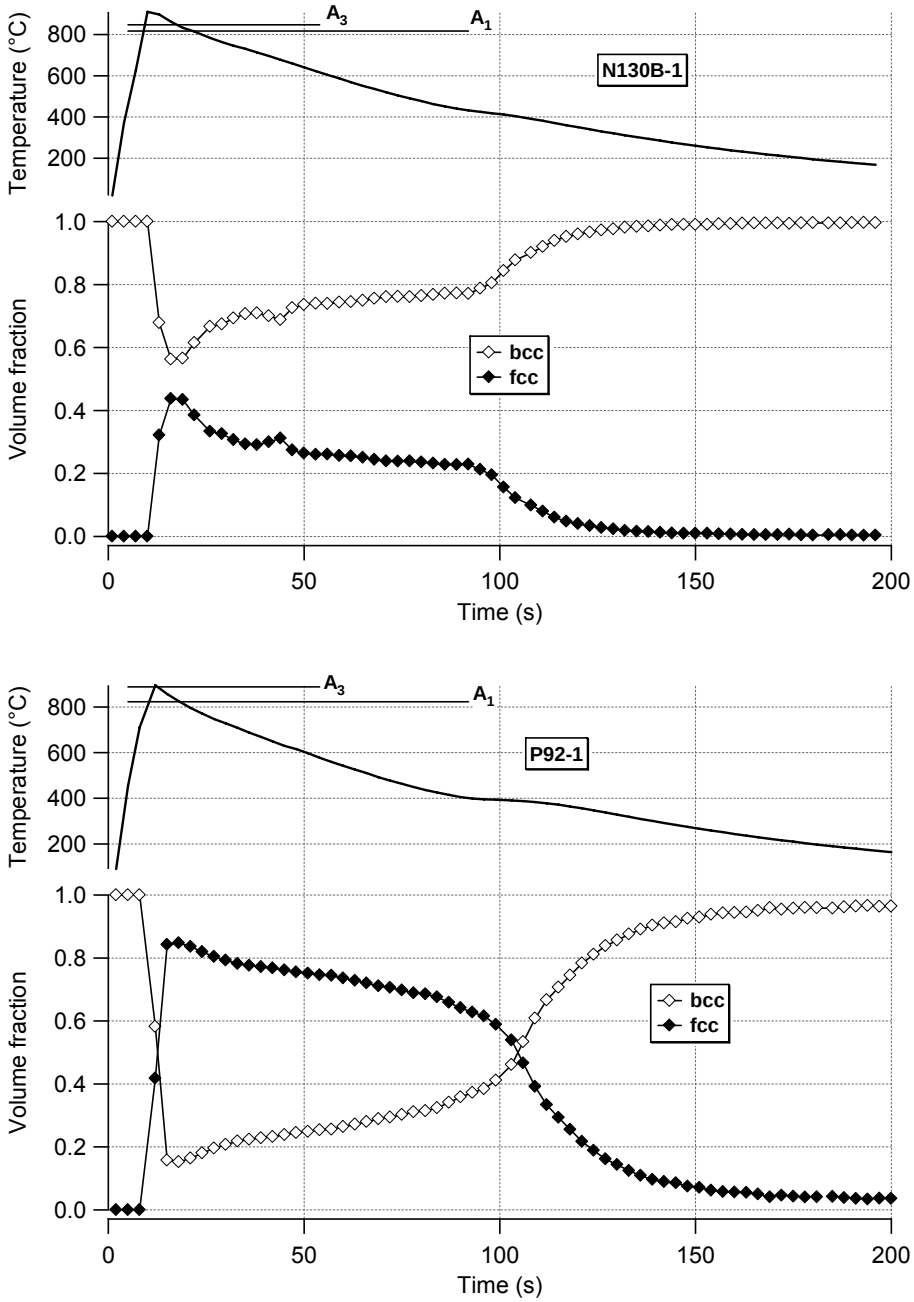

Figure 1 Plots of temperature and corresponding bcc and fcc phase fractions with time for (top) N130B with peak temperature of 911°C, and (bottom) P92 with peak temperature of 896°C

The original microstructures of both alloys were characteristic of the N+T condition in these types of steels. Subgrain boundaries and prior austenite grain boundaries were clearly delineated by carbide precipitation. Consistent with other observations [10,11,12], the prior austenite grain size of the N130B steel was somewhat larger than that of the P92.

The effects on the microstructures of N130B and P92 of heating through the thermal histories shown in Figure 1 are illustrated by the optical micrographs of Figure 2. Many carbide particles are still visible

along subgrain boundaries and prior austenite grain boundaries in N130B. The original tempered martensite structure appears largely preserved and many of the original prior austenite grain boundaries are clearly visible. There are also regions, like the one outlined in Figure 2, near some prior austenite grain boundaries where carbide dissolution is apparent, and where it appears that the original tempered martensite structure was replaced by new martensite. In the P92, prior austenite grain boundaries are still faintly visible and these appear decorated by carbides. However, the original subgrain structure is no longer visible, and there is no clear indication that carbides are present except on the austenite grain boundaries. The general structure appears martensitic, but small grains that appear to be ferrite are also present.

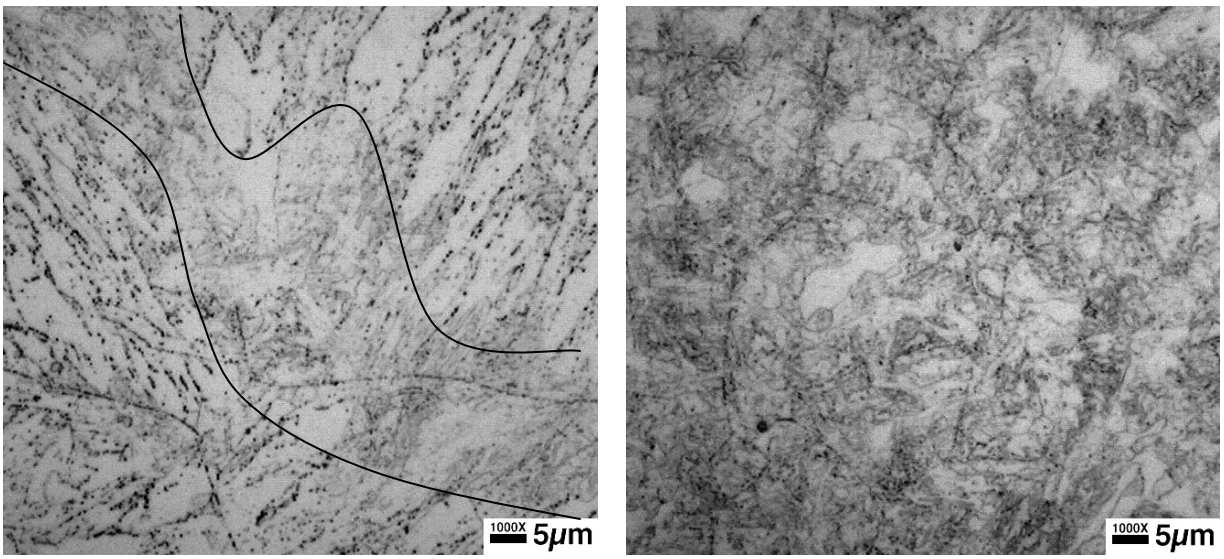

Figure 2 Optical micrographs showing the microstructures of (top) N130B and (bottom) P92 after heating through the respective thermal cycles shown in Figure 1

More details of these last two structures are shown in the secondary electron SEM images presented in Figure 3. Carbide particles are clearly evident in N130B. They are widely distributed through the microstructure except for the grain extending from the lower left corner of the micrograph. This feature appears to be a ferrite grain. Carbide particles are also evident in the P92 specimen, especially outlining the prior austenite grain boundaries. Otherwise, there are few carbides distributed throughout the microstructure. Grains showing little internal structure are visible and these presumably are ferrite. The bulk of the microstructure appears composed of martensite containing few visible carbides.

Vickers indentation with a 200 g load was used to measure the hardness of the specimens from Figure 2. The measured values were 2.57 GPa for N130B, and 4.02 GPa for P92. These hardnesses are consistent with interpretation of the diffraction data and metallography.

DISCUSSION

Figure 1 clearly shows there is a fundamental difference in the transformation behaviours of the experimental N130B steel and the commercial P92 steel for peak temperatures near their respective A_3s. These diffraction data confirm that the transformation of the original tempered martensite structure to the equilibrium austenite phase is much more sluggish in N130B than in P92. This occurs even though the

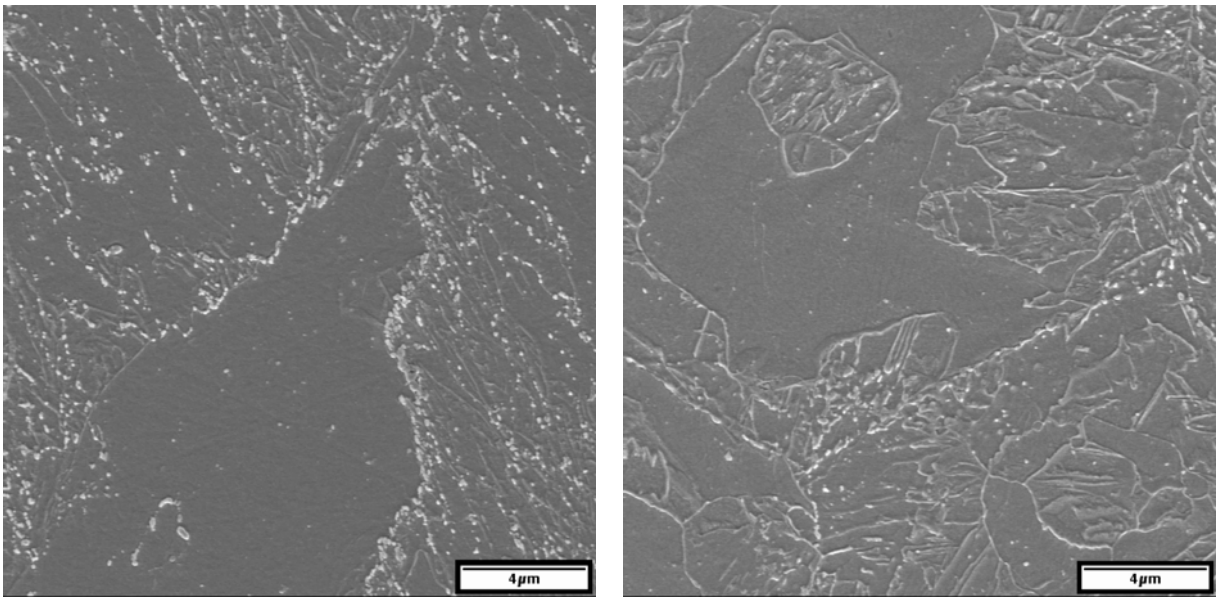

Figure 3 SEM micrographs showing the microstructures of (left) N130B and (right) P92 after heating through the respective thermal cycles shown in Figure 1

N130B is heated about 60°C above its calculated A_3 while the P92 is heated just to its A_3. Kobayashi et al [15] observed a similar effect using electrical resistivity measurements to follow transformations in two 9Cr steels of identical composition except that one contained 0.0098 wt% B. The starting condition of the steels was solution treated and quenched so that the progress of carbide precipitation during continuous heating (10°C/min) was also captured. Azuma et al [16] observed metallographically that 0.009 wt% B retarded the transformation of ferrite to austenite in 12Cr steels. They also observed that carbide dissolution was retarded in the B-containing alloy. The work of Kondo et al [10,11] indicates that austenite nucleation in a weld HAZ of the N130B steel is reduced compared to that in P92. The diffraction data are consistent with these studies relative to the effect of B on the transformation rate of ferrite to austenite.

The microstructures shown in Figure 2 and Figure 3 suggest that the carbide precipitates in N130B were much more stable than those of P92 for heating to temperatures near their A_3. The bulk of these visible particles are undoubtedly $M_{23}C_6$. Equilibrium thermodynamics calculations [14] indicate that both alloys will contain about the same total amount of $M_{23}C_6$, 1.7 vol% in N130B and 1.8 vol% in P92, and that the solution temperatures are 839°C in N130B and 858°C in P92. The compositions (at%) of the $M_{23}C_6$ particles in the N130B and P92 were also calculated at their respective tempering temperatures and they are given in Table 4. The $M_{23}C_6$ in both steels is predicted to contain similar levels of Fe, Cr, Mn, and V. One possibly significant difference is that $M_{23}C_6$ in N130B is expected to contain 3.9 at% B while that of P92 is much lower, 0.08 at%. Another difference is that $M_{23}C_6$ in P92 contains a much high amount of the refractory metal elements Mo and W compared to N130B. This information suggests that B may be more potent at stabilizing $M_{23}C_6$ against dissolution and coarsening than Mo and W.

Table 4 Calculated compositions of $M_{23}C_6$ carbides in N130B at 800°C and P92 at 780°C

	Composition, at%								
Alloy	Fe	Cr	Co	Mn	Mo	V	W	B	C
N130B	23.3	53.1	0.3	0.6	---	0.6	1.4	3.9	16.8
P92	21.6	50.8	---	0.8	3.5	0.6	2.1	0.08	20.6

The stability of the $M_{23}C_6$ carbides can also impact the ferrite-austenite transformation behaviour by removing C from solution. This would have the effect of artificially reducing the carbon concentration in N130B and increasing its A_3 relative to that expected based on bulk C concentration. The predicted sensitivity of A_3 to carbon concentration in a N130B base alloy is shown in Figure 4. Reducing the bulk/matrix C concentration clearly increases A_3.

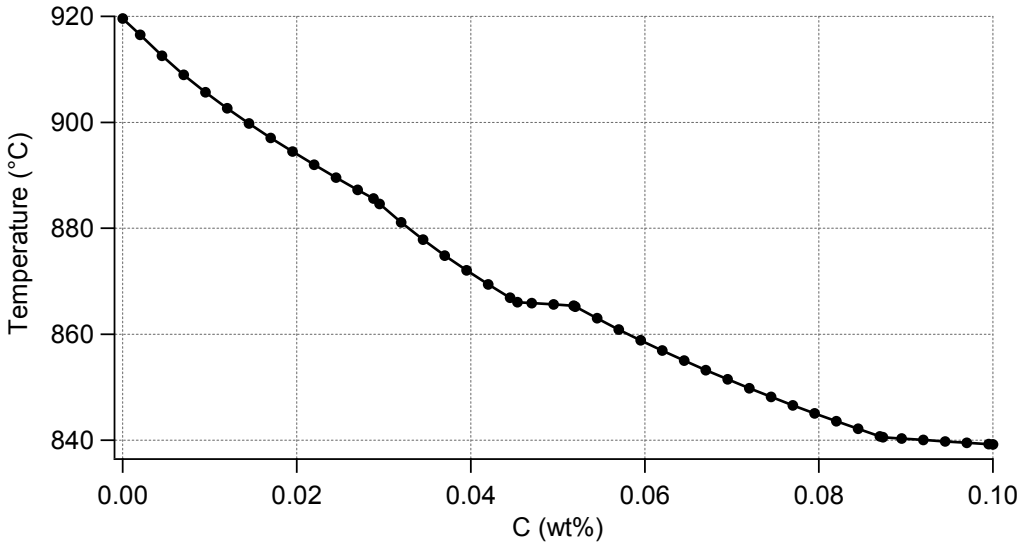

Figure 4 Calculated dependence of A_3 with C concentration in a base alloy of N130B composition

Taken all together, these data and analysis indicate that the stability against dissolution of $M_{23}C_6$ for short-time high-temperature exposures characteristic of fine-grained HAZs is increased in N130B by its elevated B concentration compared to P92. In addition, $M_{23}C_6$ that is more stable under these heating conditions would have the effect of increasing the apparent A_3 of N130B as the diffraction data confirm. An apparent increase of A_3 would make the ferrite-austenite transformation appear sluggish or difficult to complete for temperatures in the vicinity of the true A_3.

Whether the difference of transformation behaviour between N130B and P92 when heated through conditions characteristic of fine-grained HAZs is relevant to the resistance of high-B 9Cr steel to Type IV failure remains to be discovered. The hardness of the N130B microstructure in Figure 2, 2.57 GPa, is much lower that that of P92, 4.02 GPa. Based on this it might be expected that the regions of P92 weld HAZs characterized by peak temperatures in this vicinity would have better creep strength than those of N130B. Other detailed analysis of weld HAZ microstructures clearly indicates that the opposite is true [10,11,12]. The N130B structure shown in Figure 2 could certainly develop significant creep strength based on its still large fraction of small subgrains decorated with carbides. The possibility also exists of additional $M_{23}C_6$ precipitation from what was dissolved during the HAZ thermal cycle. Both of these could be sources of strengthening [4]. In contrast, P92 would have a much higher potential for $M_{23}C_6$ precipitation during subsequent tempering and creep testing because more of the initial distribution is dissolved. In addition, because P92 formed so much more new martensite as shown in Figure 1 it is likely to have a greater potential for dislocation hardening. The microstructures shown in Figure 2 and Figure 3 also suggest that the newly-formed prior austenite grain size of P92 is relatively small, even compared to the prior austenite grain size in its N+T condition. The prior austenite grain structure of N130B is much more non-uniform by comparison, and at least some of its original large austenite grain structure appears preserved.

Kondo et al [11] suggested that grain refinement in the fine-grained HAZ was avoided because B suppressed the nucleation of new austenite during heating. However, their work confirms that austenite nucleation was only suppressed at subgrain boundaries and not at the prior austenite boundaries. The thermodynamic calculations indicate that the equilibrium B concentration of ferrite in N130B at its 800°C tempering temperature is about 0.0001 wt%, and in P92 at its 780°C tempering temperature it is 0.00001 wt%. These B concentrations are well below those that are generally needed to influence nucleation of ferrite from austenite in carbon steels [17]. It is still feasible that the difference of prior austenite grain structure influences the suppression of Type IV failure in high B 9Cr steels like the N130B. However, it is also feasible that the thermodynamic and kinetic stability of carbides ultimately control their creep behaviour.

CONCLUSIONS

Synchrotron diffraction was used to follow the ferrite-austenite transformation in two 9Cr steels, an experimental 9Cr-3W-3Co-NbV steel with high B and low N (N130B) and the commercial alloy P92. Diffraction data were collected as the steels were heated through simulated weld heat-affected zone thermal cycles.

When heated to peak temperatures near 1100°C, both steels rapidly transformed from ferrite to 100% austenite. During cooling, both also transformed to martensite near 400°C. Both steels also retained untransformed austenite: 1.7% in N130B and 5.8% in P92.

Transformation behaviour near their respective A_3s was more complicated. When the N130B was heated to about 60°C above its A_3 of 847°C about 56% of the original ferrite never transformed to austenite. During cooling an additional 21% of ferrite and 23% of martensite formed. It retained no austenite. When the P92 was heated to just above its A_3 of 889°C. About 15% of the original ferrite never transformed to austenite. During its cooling an additional 22% of ferrite and 60% of martensite formed. This steel retained about 2.3% austenite.

Metallographic examinations indicated that the $M_{23}C_6$ in N130B was much more stable than that in P92 for heating to the lower peak temperatures. Analysis using equilibrium thermodynamics suggested that the more stable $M_{23}C_6$ in N130B could raise its apparent A_3 by sequestering C. Thermodynamic analysis also indicated that the $M_{23}C_6$ in N130B contained about 3.9 at% B compared to about 0.08 at% B in that of P92. In contrast, the Mo and W content of the $M_{23}C_6$ was predicted to be higher in P92.

ACKNOWLEDGEMENT

This research was sponsored by the Office of Fossil Energy, Advanced Research Materials Program, (DOE/FE AA 15 10 10 0) U.S. Department of Energy under Contract DE-AC05-00OR22725 with UT-Battelle, LLC. The APS is supported by the U.S. DOE, Basic Energy Sciences, Office of Science under contract No. W-31-109-Eng-38. Access to the SEM was through the SHaRE User Facility which is http://www.ornl.gov/bes/BES/microscopy/microsco.htm supported by the Division of Scientific User Facilities, Basic Energy Science Program, Office of Science, U.S. DOE. The technical assistance of S. S. Babu, J. W. Elmer, and T. A. Palmer were invaluable for conducting the experiments and analyzing the diffraction data.

REFERENCES

[1] H. K. D. H. Bhadeshia, "Design of Creep-resistant Steels," ISIJ International, 41 (2001), no. 6, pp.626-640

[2] J. M. Vitek and R.L. Klueh, "Precipitation Reactions during the Heat Treatment of Ferritic Steels," Metallurgical Transactions, 14A (1983), pp. 1047-1055

[3] W. B. Jones, C. R. Hills, and D. H. Polonis, "Microstructural Evolution of Modified 9Cr-1Mo Steel," Metallurgical Transaction, 22A (1991), pp. 1049-1058

[4] K. Maruyama, K. Sawada, and J. Koike, "Strengthening Mechanisms of Creep Resistant Tempered Martensitic Steel," ISIJ International, 41 (2001), pp. 641-653

[5] J. Hald, "Microstructure and Long-Term Creep Properties of 9-12% Cr Steels," pp. 20-30 in proceedings of 2005 ECCC Creep Conference

[6] C. R. Brinkman, V. K. Sikka, J. A. Horak, and M. L. Santella, "Long-Term Creep Rupture Behavior of Modified 9Cr-1Mo Steel Base and Weldment Behavior," ORNL/TM-10504, Oak Ridge National Laboratory, Oak Ridge, Tennessee, 1987

[7] F. V. Ellis and R. Viswanathan, "Review of Type IV Cracking," pp. 59-76 in PVP-Vol. 380, Fitness-for-Service Evaluations in Petroleum and Fossil Power Plants, ASME 1998

[8] J. A. Francis, W. Mazur, and H. K. D. H. Bhadeshia, "Type IV cracking in ferritic power plant steels," Materials Science and Technology, 22 (2006), pp. 1387-1395

[9] C. J. Middleton, J. M. Brear, R. Munson, and R. Viswanathan, "An Assessment of the Risk of Type IV Cracking in Welds to Header, Pipework, and Turbine Components Constructed from the Advanced Ferritic 9% and 12% Chromium Steels," pp. 69-78 in Proceedings of the 3rd Conference on Advances in Materials Technology for Fossil Power Plants, The Institute of Materials, London, 2001

[10] M. Kondo, M. Tabuchi, S. Tsukamoto, F. Yin, and F. Abe, "Suppression of Type IV Failure in High-B Low-N 9Cr-3W-3Co-NbV Steel Welded Joint," pp. 987-998 in Proceedings of the 4th Conference on Advances in Materials Technology for Fossil Power Plants

[11] M. Kondo, M. Tabuchi, S. Tsukamoto, F. Yin, and F. Abe, "Suppressing type IV failure via modification of heat affected zone microstructures using high boron content in 9Cr heat resistant steel welded joints," Science and Technology of Welding and Joining, 11 (2006), no. 2, pp. 216-223

[12] S. K. Albert, M. Kondo, M. Tabuchi, F. Yin, K. Sowada, and, F. Abe, "Improving the Creep Properties of 9Cr-3W-3Co-NbV Steels and their Weld Joints by the Addition of Boron," Metallurgical Transactions, 36A (2005), pp. 333-343

[13] J. W. Elmer, T. A. Palmer, S. S. Babu, and E. D. Specht, "In situ observations of lattice expansion and transformation rates of α and β phases in Ti-6Al-4V," Materials Science and Engineering A 391 (2005), pp. 104-113

[14] N. Saunders, "Fe-DATA, version 6, a database for thermodynamic calculations for Fe alloys," Thermotech Ltd., Surrey Technology Centre, The Surrey Research Park, Guilford, Surrey GU2 7YG, U.K.

[15] S. Kobayashi, K. Toshimori, K. Nakai, Y. Ohmori, H. Asahi, and T. Muraki, "Effects of Boron Addition on Tempering Processes in an Fe-9Cr-0.1C Alloy Martensite," ISIJ International, 42 (2002), Supplement, pp. S72-S76

[16] T. Azuma, D. Miki, and Y. Tanaka, "Effect of Boron on Microstructural Change during Creep Deformation in 12% Cr Heat Resistant Steel," pp. 177-186 in Proceedings of the 3rd Conference on Advances in Materials Technology for Fossil Power Plants, The Institute of Materials, London, 2001

[17] B. M. Kapadia, "Prediction of the Boron Hardenability Effect in Steel – A Comprehensive Review," pp. 448-480 in Hardenability Concepts with Applications to Steel, the Metallurgical Society of AIME, AIME, Warrendale, Pennsylvania, 1978

CORROSION PERFORMANCE OF STRUCTURAL ALLOYS FOR OXY-FUEL COMBUSTION SYSTEMS

K. Natesan and D. L. Rink
Argonne National Laboratory, 9700 South Cass Avenue, Argonne, IL 60439
E-mail: natesan@anl.gov; Telephone: (630) 252-5103; Fax: (630) 252-8681

ABSTRACT

The U.S. Department of Energy (DOE) Office of Fossil Energy is intensely promoting research and development of oxyfuel combustion systems that employ oxygen, instead of air, for burning the fuel. The resulting flue gas primarily consists of H_2O and CO_2 that facilitates sequestration of CO_2, thereby leading to reduction in CO_2 emissions. Also, as the oxidant is bereft of N_2, NO_x emissions are minimized to a great extent from the exhaust gas. Studies at NETL have indicated that oxy-fuel combustion can increase efficiency in the power plants from the current 30-35% to 50-60%. However, the presence of H_2O/CO_2 and trace constituents like nitrogen and sulfur in the environment at the operating temperatures and pressures can have adverse effects on the corrosion and mechanical properties of structural alloys. Thus, there is a critical need to evaluate the response of structural and turbine materials in simulated H_2O/CO_2 environments in an effort to select materials that have adequate high temperature mechanical properties and environmental performance.

During the past year, a program was initiated to evaluate the corrosion performance of structural alloys in CO_2 and CO_2-steam environments at elevated temperatures. Materials selected for the study include intermediate-chromium ferritic steels, Fe-Cr-Ni heat-resistant alloys, and nickel-based superalloys. Coupon specimens of several of the alloys were exposed to pure CO_2 at temperatures between 650 and 850°C for times up to 1450 h. The corrosion tests in CO_2-50% steam environment was conducted at temperatures between 650 and 850°C for times up to 1250 h. The steam for the experiment was generated by pumping distilled water and converting it to steam in the preheat portion of the furnace, ahead of the specimen exposure location. Preliminary results will be presented on weight change, scale thickness, internal penetration, and microstructural characteristics of corrosion products.

BACKGROUND

An increase in carbon dioxide gas in the atmosphere is identified as one of the major causes for the global climate change and one of the source of carbon dioxide is the exhaust from fossil fuel fired combustion power plants. The energy production, in particular electricity generation, is expected to increase due to population increase and per capita increase in energy consumption. To meet the energy needs, fossil fuels (coal, oil, and gas) will play a major part in production even with a projected increase in alternate renewable sources. However, to minimize the carbon dioxide emission, the current systems emphasize capture from power plants and subsequent sequestartion. The oxy-fuel combustion systems can enable recycling of the carbon dioxide to the compressor, use of novel gas turbines, and advance reuse.

The U.S. department of Energy Office of Fossil Energy is supporting the development of combustion systems replacing air with nearly pure oxygen with a goal to achieving a near zero-emission coal-based power system. For this purpose turbines and combustor technologies that use pure oxygen in fuel combustion are being developed. The major advantage of combustion under pure oxygen is the potential for separation and capture of CO_2 and for achieving power system efficiencies in the range of 50 to 60%.

Clean Energy Systems, Inc. (CES) has developed zero-emission fossil-fueled power generation technology, integrating proven aerospace technology into conventional power systems. The core of CES' process involves replacing conventional steam boilers and exhaust gas cleaning systems with "gas generator" technology adapted from rocket engines. The gas generator burns a combination of gaseous oxygen and any gaseous fuel composed primarily of the elements carbon, hydrogen, and oxygen (C-H-O), including natural gas, landfill gas, or syngas from coal, refinery residues or biomass. The combustion is performed at essentially stoichiometric conditions in the presence of recycled water to produce a mixed gas of steam and carbon dioxide (CO_2) at high temperature and pressure.

The first generation zero-emission power projects are also considering use of the effluent from oxy-fuel combustion in a gas turbine to generate electricity. For example, in the ongoing Zero Emission Norwegian Gas (ZENG) Project in Norway plans to identify the requirements to modify a gas turbine to work on the steam/Co2 mixture. Specifically, the study examines capability of turbines that could support a 200 MWe plant using the oxy-fuel combustion system.

The objective of this work is to evaluate the oxidation and corrosion performance of structural and gas turbine alloys in CO_2 and steam/CO_2 environments over a wide temperature range. Further, the goal is to establish the kinetics of scaling and internal penetration, if any, and develop correlations for long term performance of the alloys. Eventually, the influence of the exposure environment on the mechanical properties, especially creep, fatigue, and creep fatigue, of the candidate alloys needs evaluation.

EXPERIMENTAL PROCEDURE

MATERIALS

The compositions of the Fe-base alloys selected for the study are listed in Table 1. Numerous alloys, both ASME coded and uncoded, were selected for corrosion evaluation. The alloys included advanced ferritic steel modified 9Cr-1Mo, The included austenitic Fe-alloys were Type 304 and 330 stainless steel and Alloy 800H. In addition, several high-Ni alloys (333, 617, 625, 602CA, 230, 693, 740, and 718) were included in the study, especially for application at temperatures above 700°C. MA956 is a Fe-Cr alloy produced by powder metallurgy route via high-energy ball milling and subsequent extrusion.

OXIDATION/CORROSION EXPERIMENTS

Two different experimental systems were used for the oxidation in CO_2 and in steam-CO_2 environments. The experiments in CO2 were conducted in a three-zone, resistance-heated furnace that contained 35-mm O.D. quartz reaction tube, which was closed at the bottom (se

Table 1. Nominal composition (in wt.%) of alloys selected for corrosion study

Material	C	Cr	Ni	Mn	Si	Mo	Fe	Other
Modified 9Cr	0.10	9	0.8	0.5	0.4	1.0	Bal	Nb 0.08, V 0.20, N 0.06
304	0.08	18.0	8.0	1.6	0.6	-	Bal	
800H	0.08	20.1	31.7	1.0	0.2	0.3	Bal	Al 0.4, Ti 0.3
330	0.05	10.0	35.0	1.5	1.25	-	Bal	
333	0.05	25.0	45.0	-	1.0	3.0	18.0	Co 3.0, W 3.0
617	0.08	21.6	53.6	0.1	0.1	9.5	0.9	Co 12.5, Al 1.2, Ti 0.3
625	0.05	21.5	Bal	0.3	0.3	9.0	2.5	Nb 3.7, Al 0.2, Ti 0.2
602CA	0.19	25.1	62.6	0.1	0.1	-	9.3	Al 2.3, Ti 0.13, Zr 0.19, Y 0.09
230	0.11	21.7	60.4	0.5	0.4	1.4	1.2	W 14, Al 0.3, La 0.015
693	0.02	28.8	Bal	0.2	0.04	0.13	5.8	Al 3.3, Nb 0.67, Ti 0.4, Zr 0.03
740	0.07	25.0	Bal	0.3	0.5	0.5	1.0	Co 20.0, Ti 2.0, Al 0.8,, Nb+Ta 2.0
718	-	19.0	52.0	-	-	3.0	19.0	Nb 5.0, Al 0.5, Ti 0.9, B 0.002
MA956	-	20.0	-	-	-	-	Bal	Al 4.5, Ti 0.5, Y_2O_3 0.6

Figure 1. Photograph of experimental set up for oxidation tests in a CO_2 environment

Fig.1). The alloy samples were polished with 600-grit SiC abrasive paper and rinsed with ethyl alcohol. The specimens were attached to a 5-mm O.D. thermocouple well located in the center of each reaction tube. Carbon dioxide gas entered through a 5-mm O.D. quartz tube attached to the inside of the reaction tube, passed through the sample section, and exited at the top. The temperature in the vicinity of the samples was controlled to within ~1°C. The dimensions and weight of the test coupons were determined before and after exposure to the gas environment.

A tubular resistance-heated furnace (see Fig. 2) was used to expose coupon specimens of the alloys to flowing mixture of steam and CO_2. The system consists of a furnace with a constant temperature zone of ≈20 cm and a reaction chamber made of high-purity alumina. The steam for the experiment was generated by pumping distilled water and converting it to steam in the preheat portion of the furnace, ahead of the specimen exposure location. The exhaust steam from the chamber was condensed in a steam condenser. The flow rate was 6 cc/h of water. A mass balance on the water flow showed that almost all the input water was collected as the effluent, indicating that the steam consumption was negligible during the oxidation of specimens. Argon gas was used to disperse the steam in the reaction chamber.

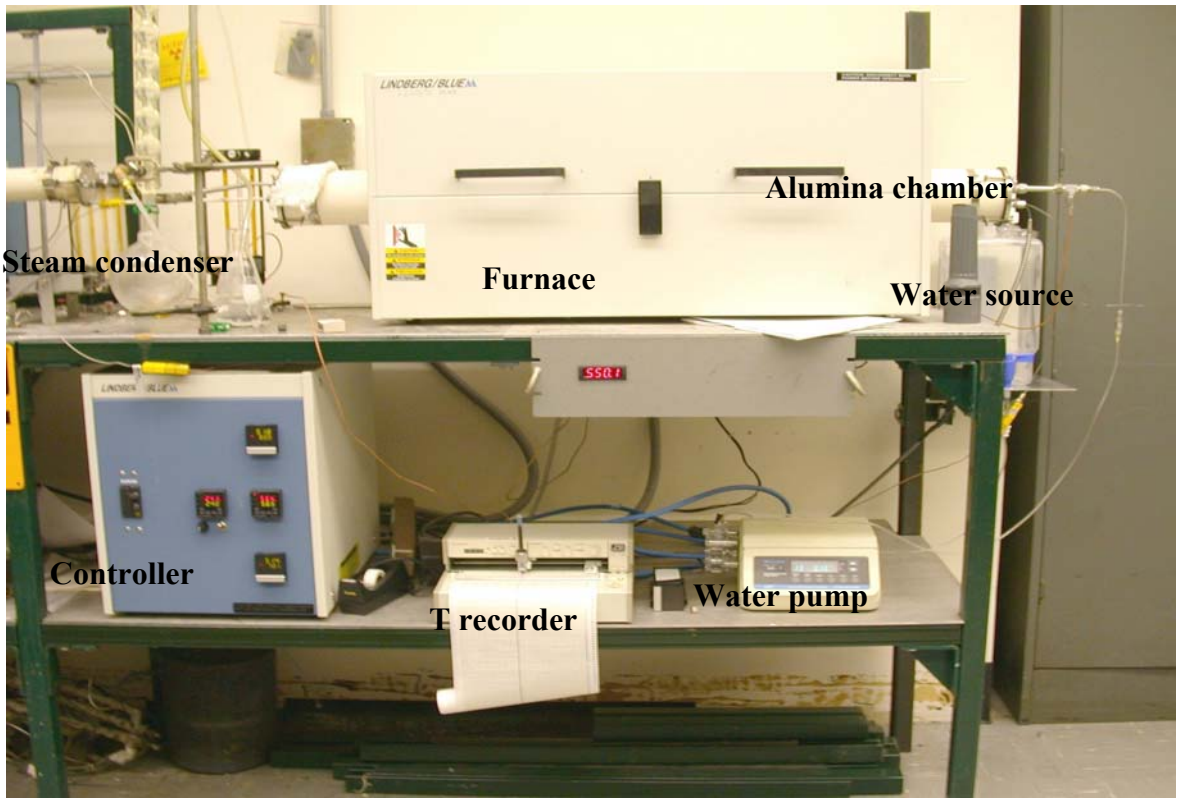

Figure 2. Test facility used for oxidation of alloys in steam/CO_2 environments.

Upon completion of the exposures, the specimen surfaces were analyzed using a scanning electron microscope equipped with an energy dispersive X-ray analyzer. In addition to weight change in specimens, microscopy of the cross sections of the exposed specimens was used to establish the internal penetration, if any, into the substrate of the various specimens.

RESULTS AND DISCUSSION

OXIDATION PERFORMANCE

Specimens were exposed to pure carbon dioxide gas for 1452 h at temperatures of 650, 750, and 850°C. The specimens were retrieved periodically to measure the weight change and re-exposed

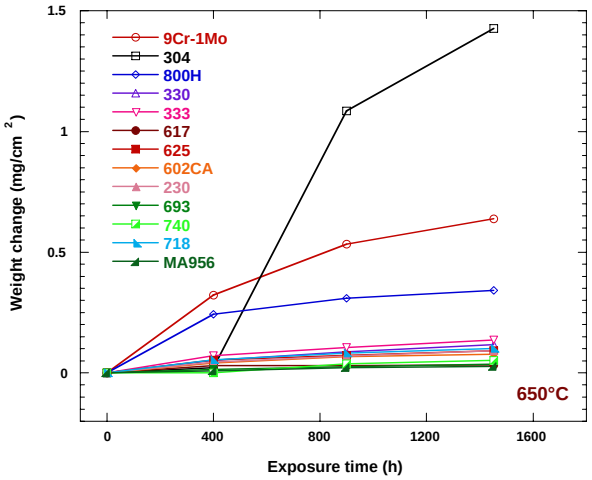

Figure 3. Weight change for alloys after exposure in CO_2 at 650°C.

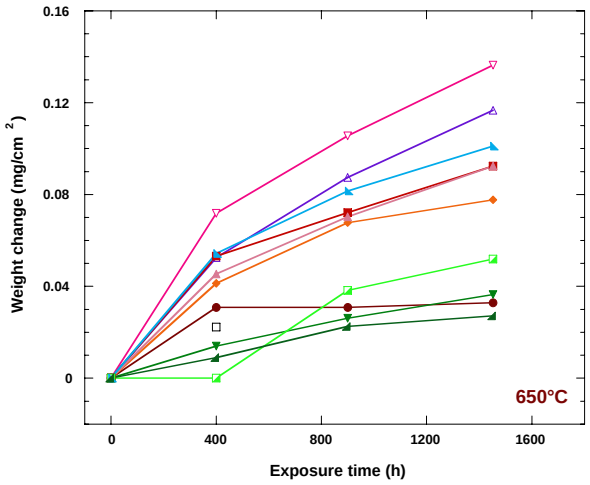

Figure 4. Magnified view of the data in Fig. 3.

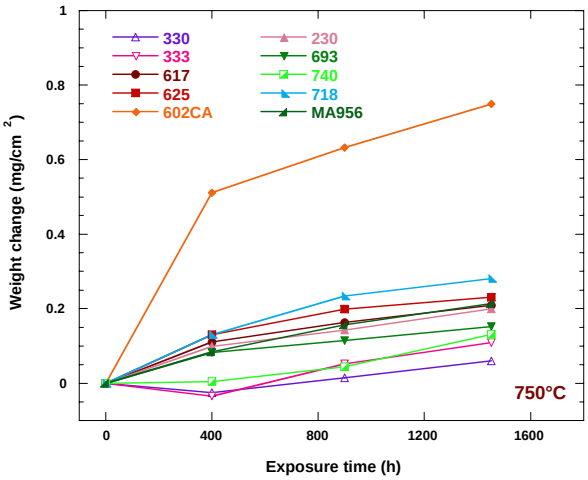

Figure 5. Weight change for alloys after exposure in CO_2 at 750°C.

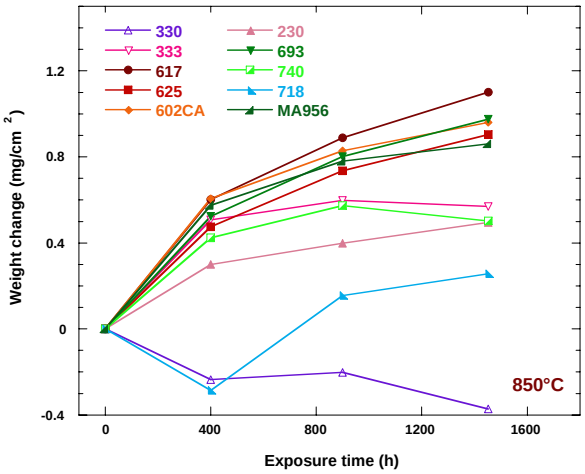

Figure 6. Weight change for alloys after exposure in CO_2 at 850°C.

for longer time. Figure 3 shows the weight change data for several alloys after exposure at 650°C. Figure 4 shows a magnified view of the data in Fig. 3 to differentiate the oxidation performance of alloys that are bunched together in Fig. 3. Figures 5 and 6 show the weight change data for alloys that were tested at 750 and 850°C. The data indicate a increase in weight change by factors of 2-3 and 7-10 at exposure temperatures of 750 and 850°C when compared with those observed at 650°C.

Specimens were also exposed to 50% steam-50% carbon dioxide environment for 1865 h at 650°C and for 2760 h at 750°C. The test at 850°C is currently in progress. The specimens in these tests were also retrieved periodically to measure the weight change and re-exposed for longer time. Figure 7 shows the weight change data for several alloys after exposure at 650°C. Figure 8 shows a magnified view of the data in Fig. 7. Figure 9 shows the weight change data

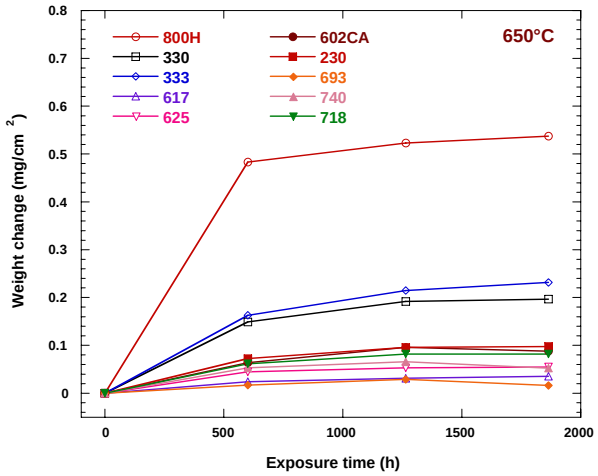

Figure 7. Weight change for alloys after exposure in 50% steam-50% CO_2 at 650°C.

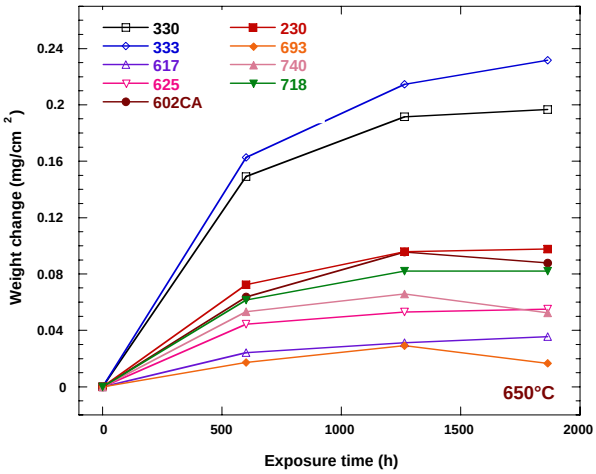

Figure 8. Magnified view of the data in Fig. 7.

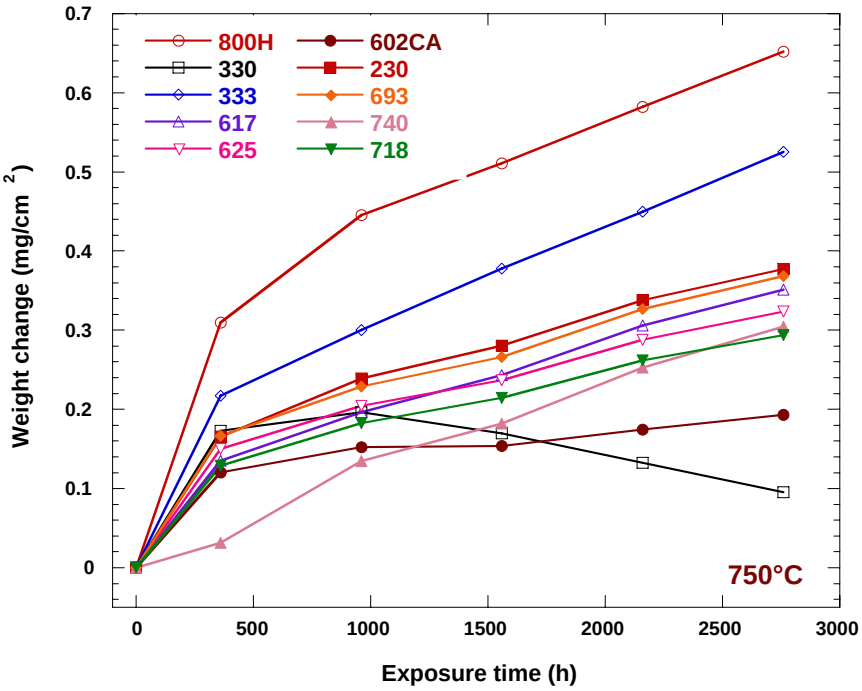

Figure 9. Weight change for alloys after exposure in 50% steam-50% CO_2 at 750°C.

for the alloys tested at 750°C in steam-CO_2 environment. The data indicate that the weight change is about a factor of three greater at 750°C when compared with those at 650°C.

Figure 10 shows a comparison of weight change data obtained in pure CO2 and in 50% steam-50% CO2 environments at 750°C. Preliminary indications are that the initial oxidation rate in steam-CO2 mixture is somewhat faster than in pure CO_2. Additional tests are in progress and the entire database will be used to compare the oxidation performance of the alloys as a function of temperature, steam content, and alloy chemistry.

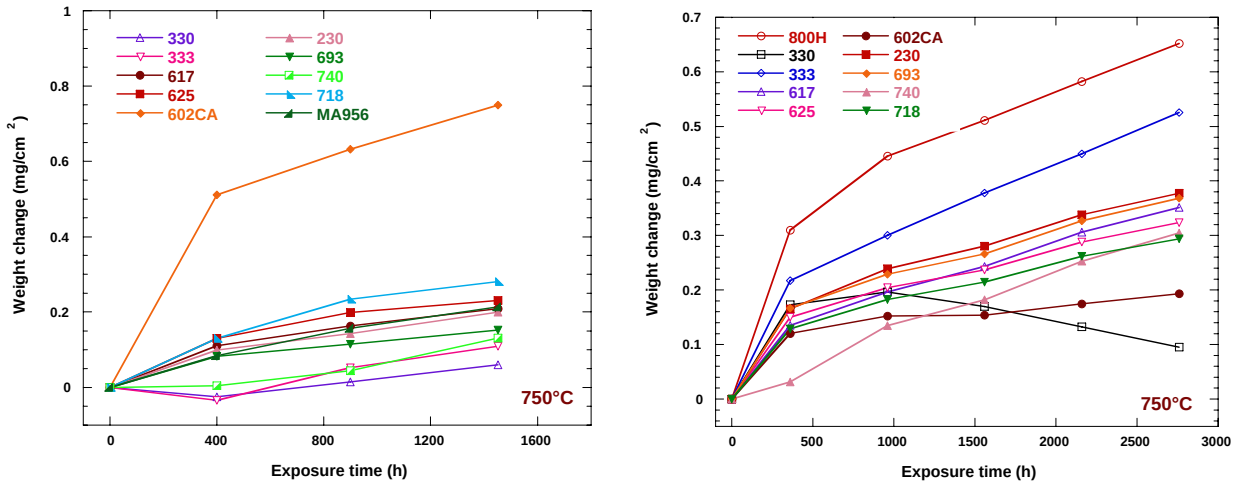

Figure 10. Weight change for alloys after exposure in (left) pure CO_2 and (right) 50% steam-50% CO_2 environments at 750°C.

MICROSTRUCTURAL OBSERVATIONS

Extensive analysis is in progress to evaluate the microstructural characteristics of the scales and internal penetration, if any, of the alloys after exposure in CO_2 and in steam-CO_2 environments.

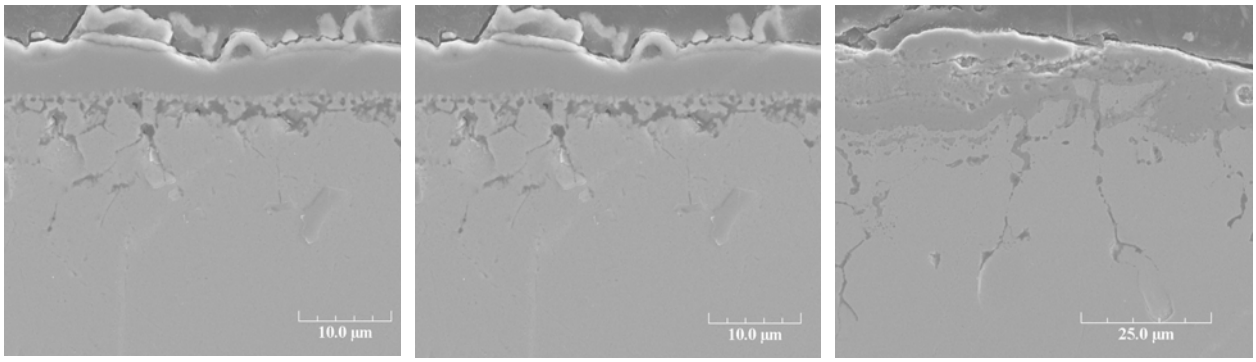

(a) (b) (c)

Figure 11. SEM photomicrographs of Ally 800H (un-etched) after exposure 1452-h exposure in CO2 gas at (a) 650, (b) 750, and (c) 850°C.

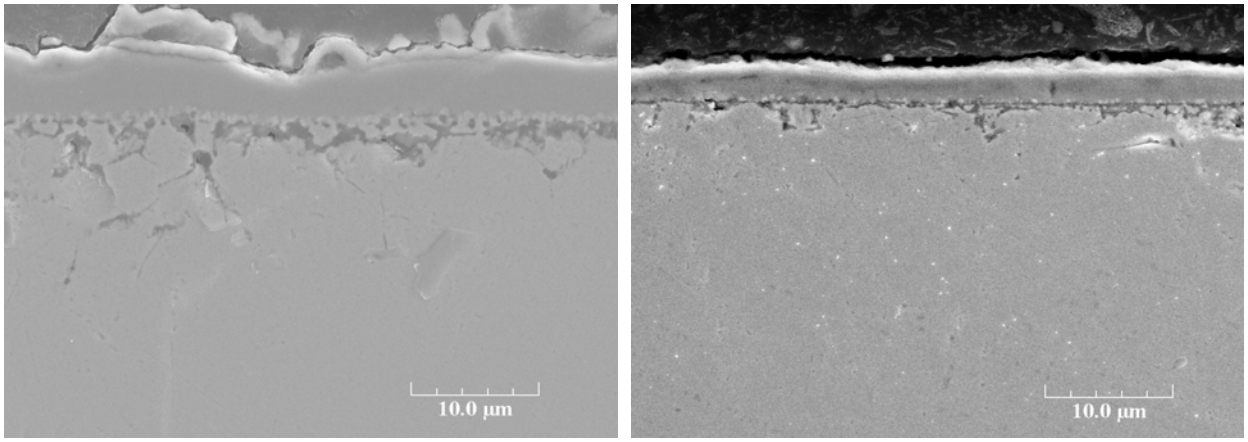

(a) (b)

Figure 12. Scanning electron photomicrographs of cross sections of Alloy 800H (un-etched) after exposure at 750°C in (a) pure CO_2 for 1452 h and (b) 50% steam-50% CO_2 for 960 h.

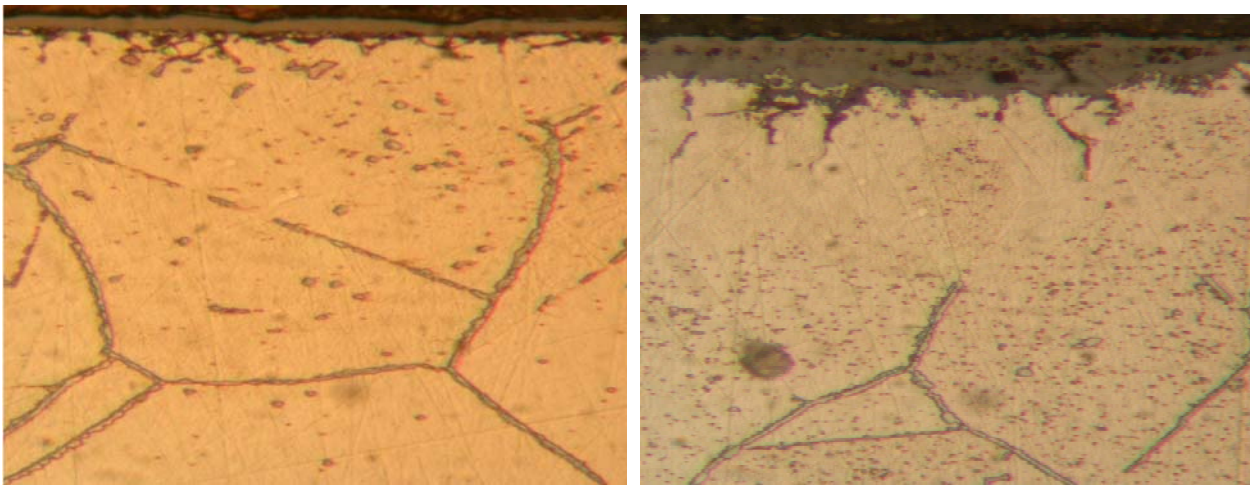

(a) (b)

Figure 13. SEM photomicrographs of Ally 800H (un-etched) after exposure 1452-h exposure in CO_2 gas at (a) 750, and (b) 850°C.

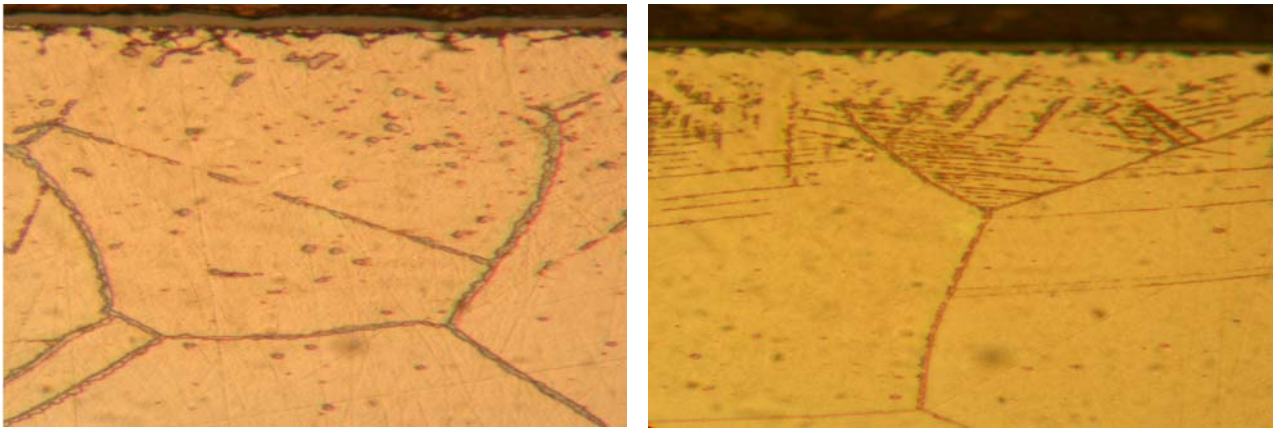

(a) (b)

Figure 14. SEM photomicrographs of Ally 800H (etched) after exposure at 750°C in (a) CO_2 gas for 1452 h and (b) 50% steam-50% CO_2 mixture for 960 h.

We next address the thermodynamic aspects of metal corrosion in a bioxidant situation, such as an oxygen/carbon environment. The following surface reactions are possible on a divalent metal A:

$$A + 1/2\ O_2 = AO, \tag{21}$$

$$A + C = AC, \tag{22}$$

where AO and AC are the oxide and carbide reaction products, respectively. Under equilibrium conditions, the partial pressures of oxygen and activity of carbon are defined by the relations

$$(a_O)_{eq} = pO_2^{1/2} = \exp(\Delta G_{AO}/RT), \tag{23}$$

$$(a_C)_{eq} = \exp(\Delta G_{AC}/RT), \tag{24}$$

where ΔG_{AO} and ΔG_{AC} are the standard free energies of formation of the oxide and carbide, respectively, at temperature T. From Eqs. (23) and (24), one should be able to deduce the conditions for oxidation or carburization; however, a further reaction must be considered, namely

$$AC + 1/2\ O_2 = AO + C, \tag{25}$$

with the equilibrium condition

$$(a_C/a_O)_{eq} = \exp[(\Delta G_{AC} - \Delta G_{AO})/RT]\ a_{AC}/a_{AO}. \tag{26}$$

If we assume unit activity for the phases AC and AO, Eq. (26) is reduced to

$$(a_C/a_O)_{eq} = \exp[(\Delta G_{AC} - \Delta G_{AO})/RT]. \tag{27}$$

Examination of Eqs. (23), (24), and (27) permits the identification of various situations that limit the type of surface corrosion products that can be formed, as follows:

(i) if $(a_O)_{gas} > (a_O)_{eq}$ and $(a_C)_{gas} < (a_C)_{eq}$, (28)

then AO is the only stable surface phase;

(ii) if $(a_O)_{gas} < (a_O)_{eq}$ and $(a_C)_{gas} > (a_C)_{eq}$, (29)

then AC is the only stable surface phase; and

(iii) if $(a_O)_{gas} > (a_O)_{eq}$ and $(a_C)_{gas} > (a_C)_{eq}$, (30)

then both AO and AC should be stable and form as surface products. However, reference to Eq. (25) indicates that only one phase will form, depending on which of the following conditions prevails:

(a) $$(a_C/a_O)_{gas} > (a_C/a_O)_{eq}, \quad (31)$$

(b) $$(a_C/a_O)_{gas} < (a_C/a_O)_{eq}. \quad (32)$$

Condition (a) will cause Eq. (25) to proceed to the left, and AC will be the stable phase where the metal is in contact with the gas phase. In condition (b), AO will be the stable phase, and Eq. (25) will proceed to the right.

A convenient way of representing the possible corrosion products as a function of gas chemistry is to construct thermochemical diagrams that depict the stability ranges of various condensed phases as functions of the thermodynamic activities of the two components of the reactive gas. Figure 3.3 shows a thermochemical stability diagram for the Cr–C–O system developed for a temperature of 982°C. In the construction of this diagram, the thermodynamic activities of the metal and corrosion–product phases are assigned a value of unity. In multicomponent alloys, the activities of constituent elements will be less than unity and should be accounted for in the analysis. Further, in gas/solid reactions that involve multicomponent alloys, a more complex corrosion product (i.e., more complex than a binary compound) can result that would decrease the thermodynamic activities of the specific phase in the mixture.

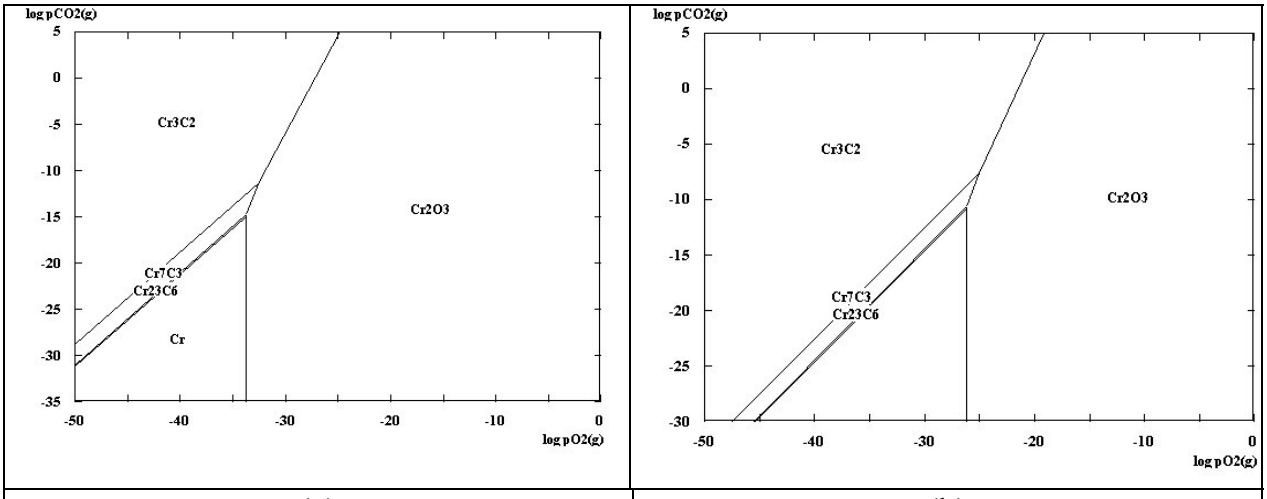

(a) (b)

Figure 12. Scanning electron photomicrographs of cross sections of Alloy 800H (un-etched) after exposure at 750°C in (a) pure CO_2 for 1452 h and (b) 50% steam-50% CO_2 for 960 h.

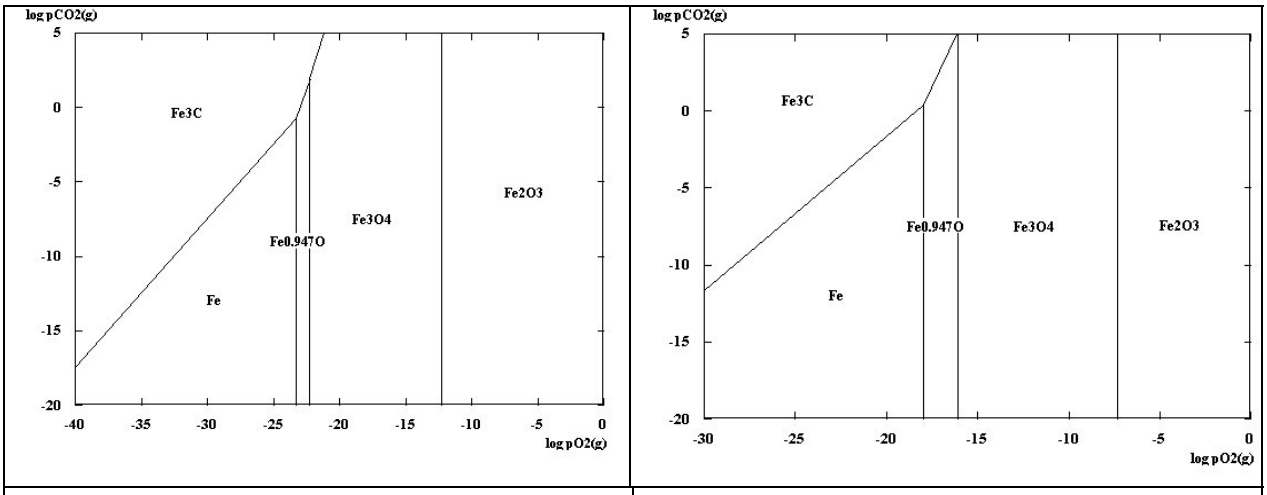

(a) (b)

Figure 12. Scanning electron photomicrographs of cross sections of Alloy 800H (un-etched) after exposure at 750°C in (a) pure CO_2 for 1452 h and (b) 50% steam-50% CO_2 for 960 h.

We have initiated a study to evaluate the oxidation performance of structural alloys in CO_2 and CO_2-steam environments at temperatures up to 1000°C

We will incorporate additional gas-turbine alloys as they become available

The preliminary results indicate that the oxide scales that develop on the alloys are not that protective and internal carburization of the substrate can occur

The internal carbon diffusion accompanied by carbide precipitation can be modeled to predict the long term performance of the alloys

The carburization, even though looks subtle, can have significant degrading effect on the mechanical properties such as, creep rupture, fatigue, and creep fatigue

ACKNOWLEDGEMENTS

This work was supported by the U.S. Department of Energy, Office of Fossil Energy, Advanced Research Materials Program, Work Breakdown Structure Element ANL–4, under Contract DE-AC02-06CH11357.

REFERENCES

R. E. Anderson, S. E. Doyle, and K. L. Pronske, "Demonstration and Commercialization of Zero-Emission Power Plants," 29th International Technical Conference on Coal Utilization & Fuel Systems, April 18-22, 2004, Clearwater, FL.

SOLID STATE JOINING OF OXIDE DISPERSION STRENGTHENED ALLOY TUBES

Bimal K. Kad[1], Ian Wright[2], and Rod Judkins[2]
[1]University of California - San Diego, La Jolla, CA 92093
[2]Oak Ridge National Laboratory, Oak Ridge, TN 37830

ABSTRACT

Oxide dispersion strengthened (ODS) Fe_3Al and Fe-Cr-Al based (MA956) alloys are currently being developed for heat-exchanger tubes for eventual use at operating temperatures of up to 1100^{o}C in the power generation industry. The development challenge is to produce thin walled tubes, employing powder extrusion methodologies, with a) adequate strength for service at operating temperatures to b) mitigate hoop creep failures. The latter is attempted by enhancing the as-processed grain size via secondary recrystallization. While these mechanical property challenges are being steadily achieved, there is now a forward looking effort to explore joining methods essential to fabricating component systems and assemblies. The challenge is to preserve the dispersion microstructure, responsible for the high temperature strength, during subsequent joining operations which precludes all melting driven welding techniques. We report here on parametric studies of non-fusion based inertia welding of MA956 tubes in butt-joint configurations. Detailed examinations of the weld microstructure, observations of the grain size, micro-hardness and the nature of the solid state interface between the mating surfaces suggest that high quality welds are feasible for a variety of welding conditions. The desired high temperature performance is explored via creep testing. The results obtained are discussed in terms of the process variables employed, the resulting heat affected zone (HAZ) width and the joint microstructures obtained. A high performance joint is facilitated at high weld pressures resulting in a narrow HAZ width.

Research Sponsored by the U.S. Department of Energy, Office of Fossil Energy, Advanced Research Materials Program, under contract DE-ACOR-96OR22464 with UT-Batelle subcontract to the University of California-San Diego.

INTRODUCTION

Oxide dispersion strengthened (ODS) ferritic FeCrAl (MA956, PM2000, ODM751) and the intermetallic Fe_3Al-based alloys are promising materials for high temperature, high pressure, tubing applications, due to their superior corrosion resistance in oxidizing, oxidizing/ sulphidizing, sulphidizing, and oxidizing/chlorinating environments[1-4]. Such high temperature corroding environments are nominally present in the coal or gas fired boilers and turbines in use in the power generation industry. The target applications for ODS alloys in the power generation industry are thin walled (0.1" thick) tubes, about 1 to 3 inches in diameter, intended to sustain internal pressures (P) of up to 1000psi at temperatures of 1000-1100^{o}C. Within the framework of this intended target application, the candidate dispersion strengthened alloys must strive to deliver a combination of high mechanical strength at temperature, as well as prolonged creep-life (hoop creep in particular) in service.

This material migration to ODS alloys for high temperature service poses significant fabrication challenges. These materials are not readily welded via conventional means or the welds perform poorly. Early work on Fe_3Al, FeCrAl family of ODS alloys provides the outlook that they cannot be subjected to a fusion based joining process. The density disparity between the matrix and the dispersoid precludes any melt based joining, as the lighter oxide dispersion so critical to the high temperature creep performance will simply float away. Thus, solid-state joining methodologies that preserve the dispersion microstructure are inherently more suitable and attractive. Thus, process design and validation of appropriate solid-state joining methodologies represent a critical developmental and design challenge that must be overcome in order to exploit and deploy ODS alloys. Solid-state welding procedures like a) Inertia welding b) Magnetic Pulse welding c) Flash welding and d) Braze/Diffusion welding are the norm in this developmental regime. Recent work has addressed inertia and friction welding of ODS Fe_3Al & MA956 alloys[5-9] with significant promise of developing meaningful joining solutions for component fabrication. While recent in-house work has focused on a) Inertia, b) Magnetic Pulse and c) Flash welding techniques, Figure 1, this current report details parametric studies on inertia welding on account of being deemed a commercially viable and mature technique for eventual fabrication tasks. Processing details of joints and ensuing creep performance are evaluated.

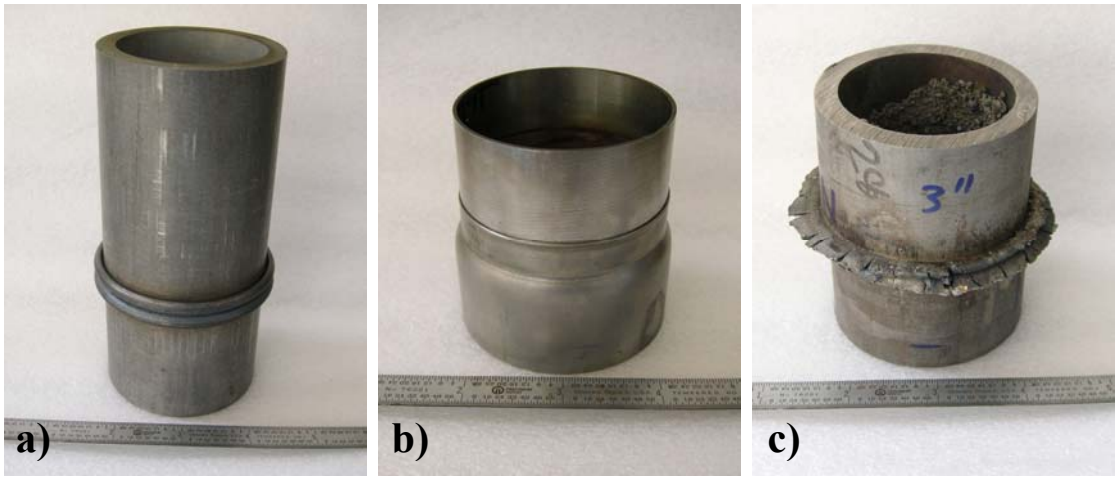

Figure 1a) Inertia welded butt joint (UCSD), b) pulse welded lap joint (UCSD) c) flash-upset butt joint (EWI) in 2"ID ODS-MA956 alloy tubes. The joints are robust but exhibit process dependent creep performance variances.

EXPERIMENTAL DETAILS

Materials: All materials for this study were provided by Special Metals Corporation in the form of nominal 2-1'2"OD, ¼" wall thick MA956 tubing in the un-recrystallized fine-grained state. Short sections were cut for inertia welding trials and the joints were recrystallized for 1-hour at 1375°C to produce the coarse grained microstructure necessary for maximum creep performance.

Welding Equipment: Figure 2 shows the sequence of welding operation to produce robust joints in MA956 tubing. All joints were fabricated using either the Caterpillar model 150B, 180B inertia welding machines. Initial trials were attempted on model 150B followed by a production style configuration adopted for the 180B model which provide for better joint concentricity. The intended mating pieces are suitably clamped in the head chuck (spinning piece) and the tailstock (stationery) piece. The head stock moves to the starting position (separated by 1/8" from the tail stock piece) and rotates to the desired RPM. Upon achieving the prescribed flywheel RPM (fixed kinetic energy), the drive mechanism disengages and a fixed weld force is applied which brings the parts in contact. Frictional heat causes mating surfaces to soften and plastically deform to form a full circumferential through wall-thickness joint. When rotation stops, the parts are held for a few seconds during which the weld cools while still held firmly in the collets. The entire weld process takes up to 60 seconds. Process variables such as friction force, rotational speed and upset displacement are monitored for evaluation of overall joint performance.

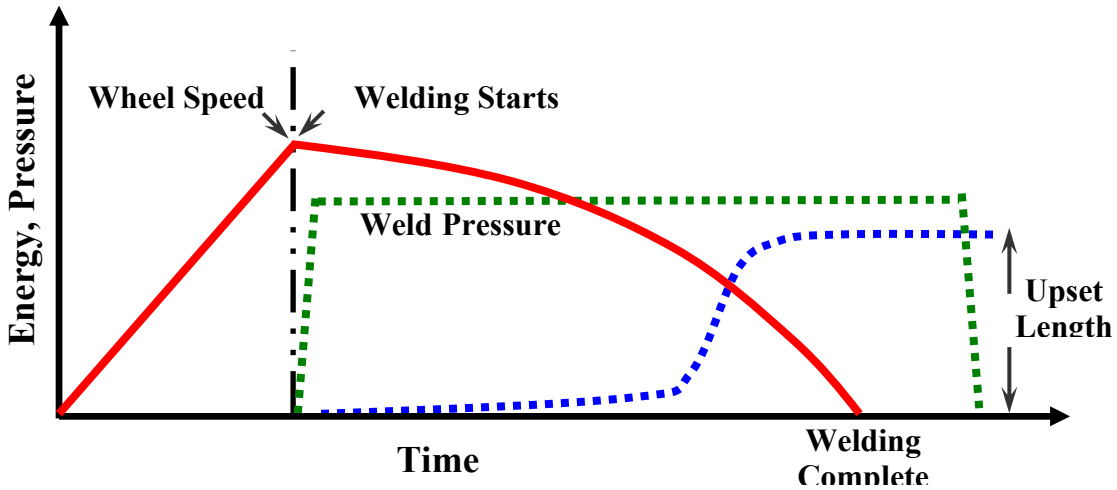

Figure 2. Schematic sequence of events in Single Stage Inertia Welding used for MA956 Joints.

Mechanical Testing: Creep test coupons are spark machined from the joint sections, Figure 3. Creep tests coupons are flat dog-bone shaped samples 0.125" wide and 0.040" nominal thickness where the width and the thickness correspond respectively to the tube circumference and the wall thickness. For a tube wall thickness of 0.25" versus the actual test specimen thickness of 0.04" multiple samples can be sliced from a single spark cut slug thereby providing ample test efficiencies.

Figure 3. Creep specimens cut from the MA956 joints.

MATERIALS CHARACTERIZATION

Figure 4(b) shows the optical micrograph of polished and etched longitudinal section microstructure of a typical inertia welded joint. The initial tubes have their grains elongation along the tube axis. However in the as-welded configuration the macroscopic grain flow rotates the grain elongation from being parallel to the tube axis to perpendicular near the bond line, Figure 4(c). Heat localization at the mating surfaces results in dynamic recrystallization in a narrow region of the bond line where the grains can be resolved at the resolution of an optical microscope, Figure 4(a). The joints were subsequently recrytsallized as this is the default treatment for high creep performance. TEM images of the recrystallized HAZ region present a slightly different picture, Figure 4(d). The most significant difference is that the bent grains are fragmented and reorganized into small grains with only a slight aspect ratio parallel to the bond line. Any grain shape anisotropy is mitigated and the microstructure can be approximated as isotropic across the bond line in the Heat Affected Zone.

Considerable effort has been expended to control the HAZ width and the grain microstructure in the joints produced. As a consequence joints have been produced with HAZ widths in the rage of 0.1mm – 3.0mm principally altering the weld pressure during fabrication, see Figure 2. Creep testing of this entire array of samples continues till date. Looking ahead to the next section, we note that the general trend of reducing the HAZ width produces impressive gains in the over all creep performance

Creep Properties: The geometrical considerations for creep testing of joints are an important issue as illustrated here. The baseline hoop creep data is extracted from 2-1/2"OD tubes that were subsequently flattened and samples cut in the transverse orientation. However, for the joint sections, transverse samples are not feasible as the processed joint width is considerably narrower than the 0.125" specimen width and any sample cross-section will contain the base material as well. The issue is further exacerbated as the tube joint will need to be flattened to extract the transverse specimen. Thus an alternate strategy of extracting

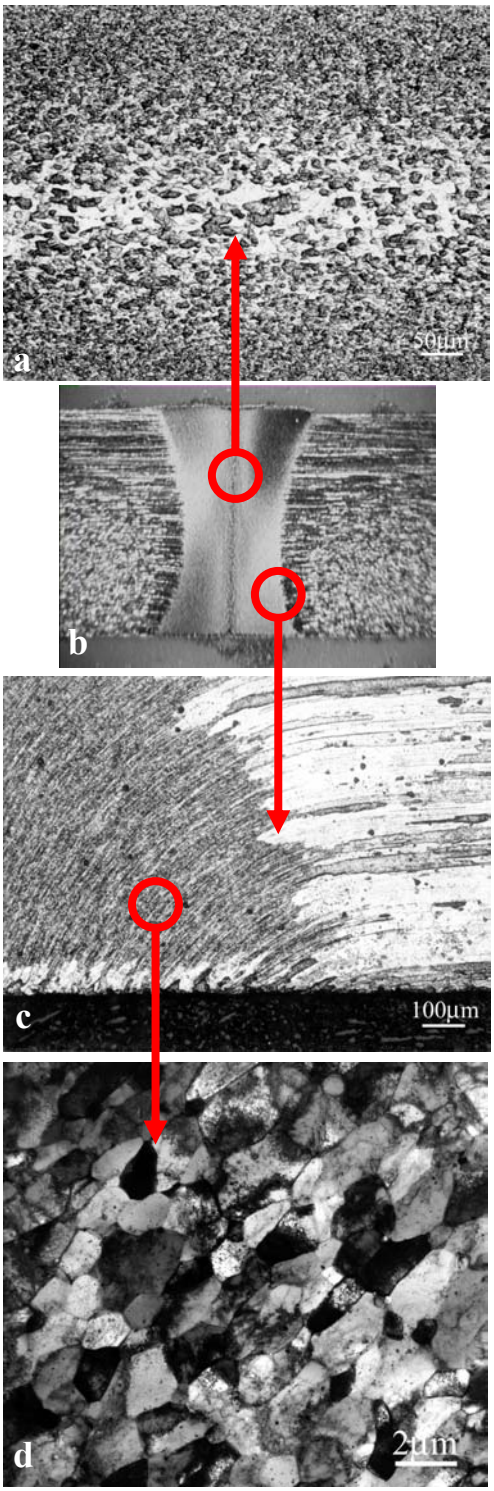

Figure 4. Weld HAZ microstructure (b) with coarse grains at the bond centerline (a). Macroscopic flow in welding causes grain rotation parallel to bond centerline (c) with (d) grain fragmenting upon recrystallization.

longitudinal specimens ensures the joint section comprises the entire gage cross-section. We like to point out that sample orientation is a particular issue in MA956 tubes on account of the grain shape anisotropy where grains are extended along the longitudinal direction. However, the joint microstructure reveals that the recrystallized grain microstructure in the joint is fairly isotropic, see Figure 4(d), and the particular orientation of the volume of material comprising the joint region during testing is not critical. Thus, the joint creep performance can be evaluated in the longitudinal sample geometry where the base material in the gage length is loaded elastically and the bulk of the creep, as surmised from the tensile tests, occurs in the small volume of the joint region in the gage length.

Table 1 lists the creep test results for several series (IW#7-9) of inertia welds produced using variations in energy input and weld pressure conditions. Sample IW#8 with the largest HAZ yields poor LMP performance when compared to the as-received and recrystallized base material. This performance is incrementally improved as the HAZ is reduced to 1-1.5mm (as in IW#7), However, significant creep enhancements are achieved for joints where the HAZ is as narrow as 100-200μm, see Figure 5. This joint feature is fully reproducible in subsequent joints.

Table 1: Creep testing of Inertia Welded Joints in MA956 Tube Materials

Test	HAZ width	Test Temp	Stress	Creep rate/day	LMP
MA956, HT1375^{o}C, 1hr, Air	**NA**	**900^{o}C**	**2Ksi**		**45.00**
IW#8, HT1375^{o}C, 1hr, Air	**2.5–3.0mm**	**800^{o}C**	**2Ksi**	**4.6x10^{-3}**	**42.72**
IW#8, HT1375^{o}C, 1hr, Air	**2.5–3.0mm**	**900^{o}C**	**2Ksi**		**43.04**
IW#7, HT1375^{o}C, 1hr, Air	**1.0–1.5mm**	**800^{o}C**	**2Ksi**		**43.59**
IW#7, HT1375^{o}C, 1hr, Air	**1.0–1.5mm**	**800^{o}C**	**2Ksi**		**43.87**
IW#7, HT1375^{o}C, 1hr, Air	**1.0–1.5mm**	**850^{o}C**	**2Ksi**	**4.0x10^{-4}**	**44.50**
IW#7, HT1375^{o}C, 1hr, Air	**1.0–1.5mm**	**850^{o}C**	**2Ksi**		**44.12**
IW#7, HT1400^{o}C, 1hr, Air	**1.0–1.5mm**	**850^{o}C**	**2Ksi**		**44.22**
IW#7, HT1375^{o}C, 1hr, Air	**1.0–1.5mm**	**900^{o}C**	**2Ksi**		**43.72**
IW#7, HT1375^{o}C, 1hr, Air	**1.0–1.5mm**	**900^{o}C**	**2Ksi**		**44.29**
IW#7, HT1375^{o}C, 1hr, Air	**1.0–1.5mm**	**900^{o}C**	**2Ksi**		**44.52**
IW#9, HT1375^{o}C, 1hr, Air	**0.1–0.2mm**	**850^{o}C**	**2Ksi**	**1.0x10^{-4}**	**47.20**
IW#9, HT1375^{o}C, 1hr, Air	**0.1–0.2mm**	**900^{o}C**	**2Ksi**		**47.71**
IW#9, HT1375^{o}C, 1hr, Air	**0.1–0.2mm**	**900^{o}C**	**2Ksi**	**1.6x10^{-4}**	**48.60**
IW#9, HT1375^{o}C, 1hr, Air	**0.1–0.2mm**	**950^{o}C**	**2Ksi**	**4.0x10^{-4}**	**48.47**

At the outset the results seem to indicate the importance of processing parameters in dictating overall creep response as indicated by observed creep rate and overall Larsen-miller parameter (LMP). For example, Table 1 shows that for reduced HAZ, a lower overall creep strain rate is possible even for testing at higher temperatures. What is clearly promising is that robust quality joints are possible with creep performance approaching and exceeding the base material performance. This suggests that the base material microstucture may not optimum which is perhaps being favorably altered during the high weld pressure processing. We surmise that the dynamic hot working

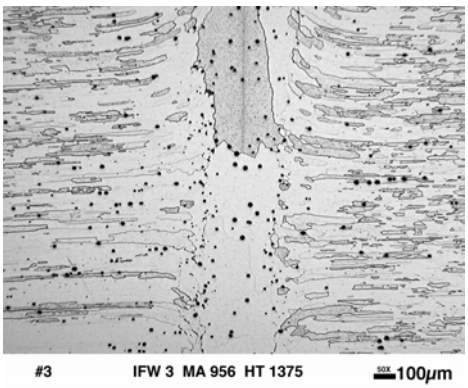

Figure 5. Narrow HAZ width joints produced at large weld pressures.

induced during inertia welding may aid the subsequent secondary recrystallization to produce large grain size in the HAZ. This is consistent with the observed HAZ grain structure of Figure 5, and needs to be confirmed via further TEM study. In keeping with the general trend of reducing the joint HAZ width subsequent joints are produced, via a combination of energy input and weld pressure process parameters to closely mimic the HAZ microstructure of Figure 5. These tests continue till date. Threshold performance has been systematically improved. For equivalent tests at 900^{o}C, the base material LMP is about 45 compared to the IW#9 joint with LMP of 47.71 and 48.60. Thus, the notion of improving joint creep performance via manipulating the factors that dictate HAZ width has significant merit as been demonstrated here.

SUMMARY AND CONCLUSIONS

Inertia welding of ODS MA956 tubes has been successfully attempted. The butt joint configuration is a viable joint intended for heat exchanger fabrication employing MA956 tubes. Results show that robust joints can be produced over a wide range of processing parameters. However, the process needs to be optimized specifically to improve the overall creep performance of the joint and consequently the fabricated component. Significant improvements have been demonstrated via manipulating the process parameters of energy input and weld pressure that dictate the thermal excursion in the heat affected zone as well as the overall deformation history in the vicinity of the bonding interface. Our results till date suggest that the scale of the HAZ region has an effect on the ensuing creep performance and efforts to manipulate process parameters to mitigate HAZ width have significant merit for overall creep enhancement of the fabricated joint. A narrow HAZ is key to improving the joint creep response.

REFERENCES

1 C. Capdevila and H.K. Bhadeshia, 'Manufacturing and Microstructural Evolution of Mechanically Alloyed Oxide Dispersion Strengthened Superalloys', *Advanced Engineering Materials*, 2001, **3**(9), 647.

2. R.F. Singer and E. Arzt, *High Temperature Alloys for Gas Turbine and Other Applications*, D. Reidel Publishing Co., Liege, 1986.

3. F. Starr, 'Emerging Power Technologies and Oxide Scale Spallation', *Mater. High. Temp*., 1995, **13**(4), 185-192.

4 B.A. Pint and I.G. Wright, 'Long Term High Temperature Oxidation Behavior of ODS Ferritics', *Journal of Nuclear Materials*, 2002, **307-311**, 763-768.

5. I.A. Bucklow, S.B. Dunkerton, P.L. Threadgill, 'Investigation into the Joining of Creep Resistant Oxide Dispersion Strengthened Alloys', TWI Members Report 570/1996.

6. C.Y. Kang, T.H. North, D.D. Perovic, 'Microstructural Features of Friction Welded MA956 Material' *Met. Mater. Trans A*, 1996, **27A** (12) 4019–4029.

7. K. Shinozaki, C.Y. Kang, Y.C. Kim, M. Aritoshi, T.H. North, Y. Nakao, 'The Metallurgical and Mechanical Properties of ODS Alloy MA956 Friction Welds' *Welding J. Res. Suppl*. August 1997, 289–299.

8. B.J. Inkson and P.L. Threadgill, 'Friction Welding of FeAl40 Grade 3 ODS Alloy' *Mater. Sci. Eng*. 1998, **A258**, 313–318.

9. T.H. North, Friction Joining of Particle Reinforced Composites. *Proc. 6th Int. Symp*., JWS, Nagoya, 1996, 673-682.

APPLICATIONS FOR DISPERSION-STRENGTHENED ALLOYS IN THERMAL POWER SYSTEMS

John P. Hurley
University of North Dakota Energy & Environmental Research Center
15 North 23rd Street, Stop 9018, Grand Forks, ND 58202-9018
E-Mail: jhurley@undeerc.org; Telephone: (701) 777-5159; Fax: (701) 777-5181

ABSTRACT

Dispersing small quantities of ceramic particles along the grain boundaries of an alloy can substantially increase its resistance to creep at high temperatures. This creep resistance, if matched with corrosion resistance, makes these alloys particularly suited for the highest-temperature applications within thermal power systems. The University of North Dakota Energy & Environmental Research Center (EERC) is working with Oak Ridge National Laboratory to determine corrosion resistance and methods of joining oxide dispersion-strengthened (ODS) alloys in laboratory, pilot-scale, and commercial-scale tests. The EERC has previously demonstrated a very high-temperature heat exchanger (HTHX) that could be used to produce pressurized air at up to 1090°C for an indirectly fired combined-cycle (IFCC) power plant. An IFCC using this type of heat exchanger has the potential to reach efficiencies of 45% when firing coal and over 50% when a natural gas-fired duct burner is used to additionally heat the gas entering the turbine, efficiencies similar to those of an integrated gasification combined cycle, but with operation almost identical to those of current pulverized coal-fired boilers. IFCCs have the added benefit of minimizing water usage by dramatically reducing the amount of cooling and makeup water as compared to a typical pulverized coal (pc) plant because only half as much steam is produced. Because of its high efficiency, an IFCC system is the most appropriate power concept for employing oxygen-enriched combustion in order to make carbon dioxide removal more economical. After water condensation, only carbon dioxide is left in the gas stream, which can then be used industrially or sequestered, leaving near-zero emissions. If the system is cofired with coal and biomass, sequestration of the carbon dioxide would create a net reduction of its concentration in the atmosphere.

In addition to their use in IFCC systems, heat exchangers made of corrosion-resistant dispersion-strengthened alloys can be used in many types of thermal power systems. In advanced gasification systems they can be used to preheat steam to high temperatures for steam gasification of coal in order to produce the highest possible hydrogen concentration in the syngas. This is especially important in a FutureGen scenario where the hydrogen is to be separated from the syngas for use as a transportation fuel. In addition to power generation systems, there are many scenarios for the use of HTHXs to increase the efficiency of many industrial thermal systems. One such case is the recuperation of heat from the flue gas of an aluminum melter. In 2006 and 2007, rings of MA754, MA956, HR160, and 304 stainless were exposed in an aluminum melter at the Superior Aluminum Alloys plant in New Haven, Indiana. Analyses showed that the MA956 or other alumina scale-forming dispersion-strengthened alloys may be suitable for use in heat exchangers in these systems at up to approximately 1100°C.

THE NEED FOR HIGHER TEMPERATURES IN POWER GENERATION

The electricity generating capacity in the United States is projected to grow by 250,000 MW by 2030.[1] Initially, the greatest growth will occur in natural gas-fired power systems, but will then shift back to coal-fired systems so that one-half of the net growth will be in coal-fired systems by 2020, and all of the net growth will be coal-fired from 2020 to 2030. To fuel these plants, coal production is expected to grow from 1125 million tons in 2004 to 1355 million tons in 2020, and 1703 million tons in 2030, 96% of which will be for electric power generation. Yet this growth occurs at a time of increased public concern over the emission of greenhouse gases, particularly CO_2. Since coal utilization creates more CO_2 per unit of power produced than any other form of fuel, the growth in coal firing will be accompanied by increased pressure from the public, boardrooms, and lawmakers to convert the coal as efficiently as possible.

In thermal power systems, the need for greater efficiency will require the use of higher-temperature materials for construction because the quality of the heat produced is more important than quantity in determining efficiency. That is, the heat in a small volume of gas at a high temperature is more efficiently converted to kinetic energy in a turbine than if the same amount of energy were present in a larger volume of gas at a lower temperature. This means that the heat exchangers used to contain the working fluid, the turbine blades against which the fluid pushes, and the materials from which they are made will ultimately limit the efficiency of a power system. Without employing higher-temperature materials than at present, the efficiencies of the energy conversion systems cannot grow substantially.

COAL COMBUSTION SYSTEMS

The greatest research efforts in advanced coal combustion technologies are currently pursuing ultrasupercritical steam technology. By pushing toward 760°C steam and 35 MPa pressure, energy conversion efficiencies over 45% can be reached. Up to 675°C high-chromium austenitic steels appear workable, but above that temperature nickel-based alloys are suggested,[2] although some new austenitic alumina scale-forming dispersion-strengthened steels are under development that may also reach 750°C with both creep and oxidation resistance.[3]

To reach even higher efficiencies, a different type of energy cycle is required than just the standard Rankine steam cycle. One such type of coal combustion system was researched extensively in the 1990s and early 2000s by the U.S. Department of Energy (DOE). The indirectly fired combined cycle (IFCC) power plant was developed under the High Performance Power System, or HiPPS Program. An indirectly fired combined-cycle plant uses, essentially, a coal-fired boiler where a fraction of the boiling water heat exchanger pipes near the hottest part of the flame are replaced with pipes carrying 1 MPa air being heated to as much as 1100°C. This hot air is sent to a gas turbine where it offsets over two-thirds of the natural gas normally burned in the turbine. Figure 1 is a schematic of such a system which is, essentially, a natural gas-fired combined-cycle power plant in which much of the heating of the gas turbine comes through the combustion of coal. The waste heat from the turbine and the coal combustion system is used to produce steam, perhaps

ultrasupercritical, to turn a steam turbine. The Brayton (gas turbine) cycle which make one-half of the electricity in the IFCC is inherently more efficient than a Rankine (steam) cycle because there is no loss of the heat of vaporization of the water in the Brayton cycle. Therefore, an IFCC system will always be more efficient than a system based solely on the Rankine cycle.[4,5]

IFCCs have the added benefit of minimizing water usage by dramatically reducing the amount of cooling and makeup water, since only half as much steam is produced as in a typical steam plant. The high efficiency of an IFCC system also makes it suitable for oxygen-blown combustion in order to make carbon sequestration more economical. In that case, flue gas is recirculated and pure oxygen added to the stream to burn the coal, leaving a gas stream comprising mostly CO_2 and steam. After water condensation, only carbon dioxide is left in the gas stream, which can then be used industrially or sequestered, leaving near-zero emissions. If the system is cofired with coal and biomass, sequestration of the carbon dioxide would create a net reduction of its concentration in the atmosphere. Oxygen firing also prevents the formation of thermal NO_x. In addition, by staging combustion of the coal, the volume of flue gas would be dramatically reduced, shrinking the overall size and capital cost of the system.

Although IFCC systems have many potential benefits, materials requirements for the high-temperature air heater and turbines are stringent. Pressures for the air heaters are much lower than those for ultrasupercritical systems, so the need for creep resistance is much reduced and austenitic steels are not automatically required. However, temperatures of as much as 1200°C require materials exceptionally resistant to oxidation or corrosion by the products of coal combustion. Ferritic oxide

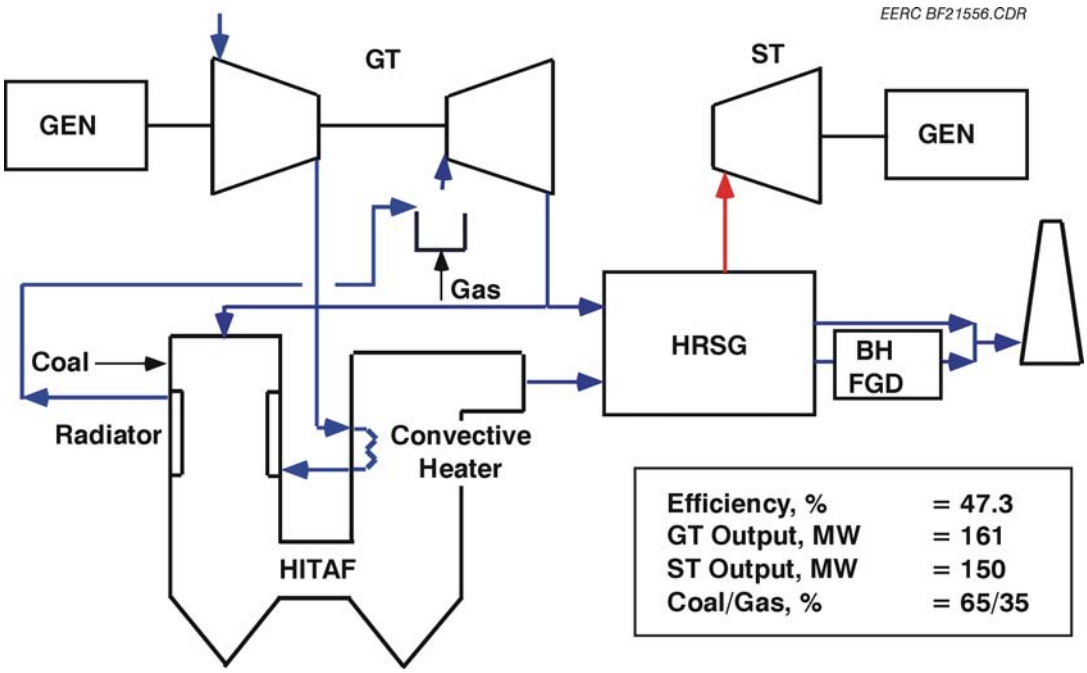

Figure 1. The United Technologies Research Center High-Performance Power System concept.

dispersion-strengthened (ODS) alloys are excellent candidates for this type of environment.[6–9] The presence of small stable oxides (often yttria [Y_2O_3]) helps to prevent dislocation motion and preserve the high-temperature strength of these materials. Grain boundary sliding and Herring–Nabarro diffusional creep are both retarded by the elongated grain structure typical of ODS alloys. Iron-based ODS alloys such as MA956 have excellent corrosion resistance at high temperatures if they contain approximately 4.5% aluminum or more. The aluminum forms a protective oxide layer that can resist even direct contact with flowing slag, as long as the surface is cooled below the solidus temperature of the slag.[7]

COAL GASIFICATION SYSTEMS

Research on the IFCC concept was largely stopped in the early 2000s when DOE decided to focus instead on the FutureGen power system concept.[10] Based on coal gasification, FutureGen plants can reach similar efficiencies as IFCCs, but have the added benefit of being able to separate hydrogen from the syngas during offpeak hours for use in the transportation sector. As shown in Figure 2, taken from Sondreal et al.,[11] the hydrogen concentration in the syngas produced in atmospheric-pressure oxygen-blown coal gasifiers is increased at lower temperatures. However, in order to fire the syngas in a turbine, it has to be produced at high pressures. The figure shows that in high-pressure gasification, temperatures of over 900°C are required to produce the highest hydrogen

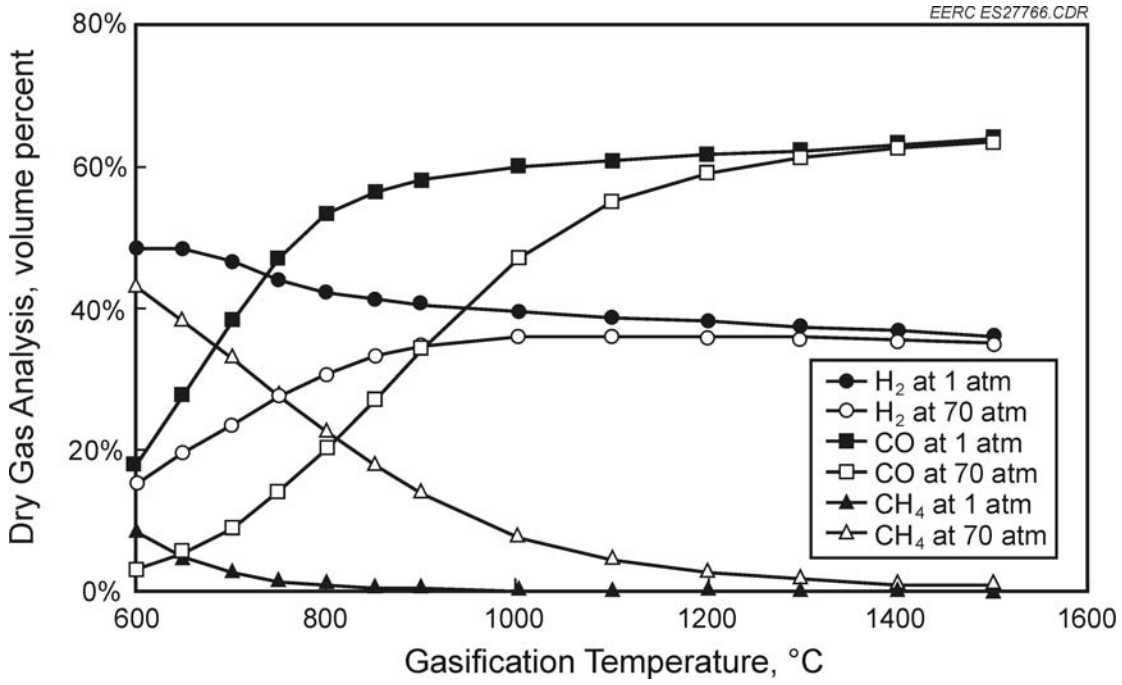

Figure 2. The effects of temperature and pressure on syngas compositions produced from oxygen-blown coal gasification.

concentrations. To increase them even further, the steam gasification reaction must be emphasized in the gasifier:

$$H_2O + C \rightarrow CO + H_2 \qquad \text{[Eq. 1]}$$

However, the steam gasification reaction is endothermic, requiring 56,490 Btu per mole of carbon consumed. To produce the heat required, more carbon can be burned in the gasifier by firing with higher oxygen concentrations, but then more carbon dioxide is produced rather than the preferred carbon monoxide. Another option is to inject superheated steam into the system. In this case, a very high temperature heat exchanger (HTHX) carrying the steam can be placed within the combustion zone of the gasifier to heat the steam and then inject it into the reducing zone where the steam and other endothermic reactions take place, reducing the need for added oxygen combustion and increasing the overall hydrogen content of the syngas. The HTHX would most likely be made from alumina-forming ODS alloys.

EXPOSURE IN AN ALUMINUM REMELTER

In addition to power generation systems, there are many scenarios for the use of HTHXs to increase the efficiency of many industrial thermal systems. One such case is the recuperation of heat from the flue gas of an aluminum melter such as that shown in Figure 3. In 2006 and 2007, rings of MA754, MA956, HR160, and 304 stainless were exposed in an aluminum melter at the Superior Aluminum Alloys plant in New Haven, Indiana. The rings were placed at the flue gas exit from the aluminum bath as shown in Figure 4a. Figure 4b shows a close-up of the rings composed of three identical sets of four. From the left to the right, the four rings in each set are 304 stainless, MA754 (NiCr ODS), MA956 (FeCrAl ODS), and HR150 (NiCoCr nonODS). They are supported on alumina rods carried on mullite refractory blocks. The gases to which the samples were exposed were the products of natural gas combustion with 1% excess air and vapors of the aluminum fluxes containing Na, K, Cl, F, and O, as well as alloying agents Cu, Mn, Mg, Zn, Si, and S. They were exposed for 5 ½ months at temperatures which were 85% of the time between 1200° and 1290°C, the rest of the time below that range.

At the end of the exposure, the samples were found in a rubble pile formed when the supports and additional refractory from above had collapsed onto the samples. The stainless steel was completely disintegrated (unrecoverable), and the HR160 was badly warped and corroded. Figure 5 shows a cross section of an MA956 ring showing suspected catastrophic corrosion through the formation of a liquid phase. The rings lost up to 25% of their mass during the exposure. Initial scanning electron

Figure 3. A typical aluminum melter.

Figure 4. The placement of the samples in the melter: a) from the position of the aluminum bath looking out into the flue section, b) close-up of the samples showing three identical sets of four metal types.

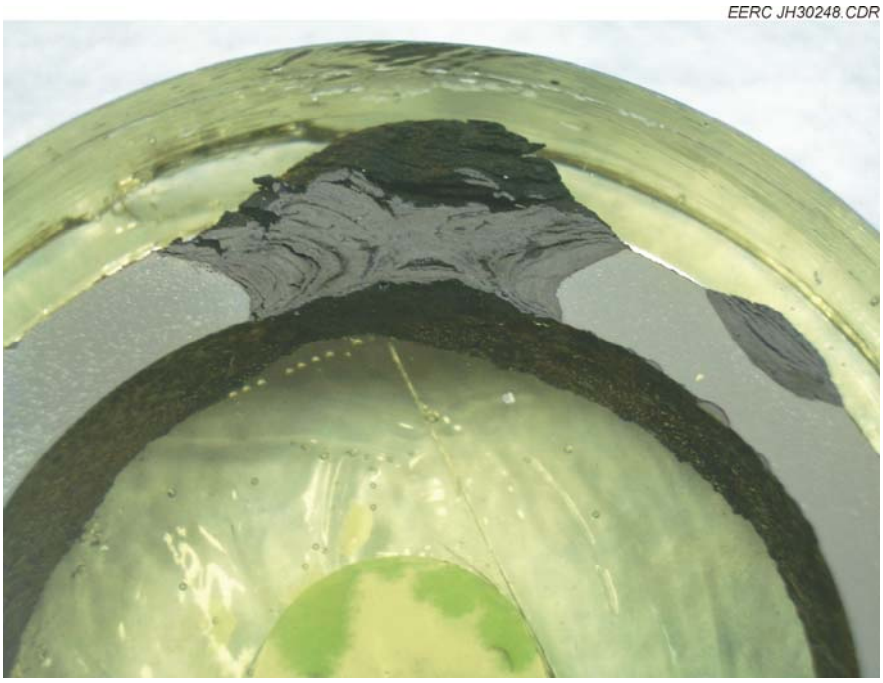

Figure 5. Polished cross section of an MA956 ring showing probable catastrophic corrosion.

microscopy (SEM) analyses howed no unusual concentrations of fluxing elements in the corroded areas, but did show substantial increases in aluminum near the heavily corroded regions, indicating that they were possibly splashed with liquid aluminum that may have dissolved the oxide scale leading to rapid catastrophic corrosion. However, further SEM analyses will be performed to determine the specific cause of the heavy corrosion.

Figure 6 shows a cross section of an MA754 ring. In contrast to the MA956, there was no catastrophic corrosion, but the samples were badly oxidized with a 15% loss of weight, mostly through vaporization of the chromia scale. Initial SEM analyses showed substantial void space development through 20% of the metal thickness. In general, it appears that neither the MA956 or MA754 formed any adverse reaction products with the aluminum fluxing agents. However, they may have been splashed with aluminum metal, and otherwise were simply exposed to temperatures that exceeded the ability of their oxide scales to protect them, so that there was substantial oxidation and vaporization of the oxides produced. However, more detailed SEM analyses are planned to better determine the loss mechanisms and whether they could be used in such systems, but at somewhat lower temperatures.

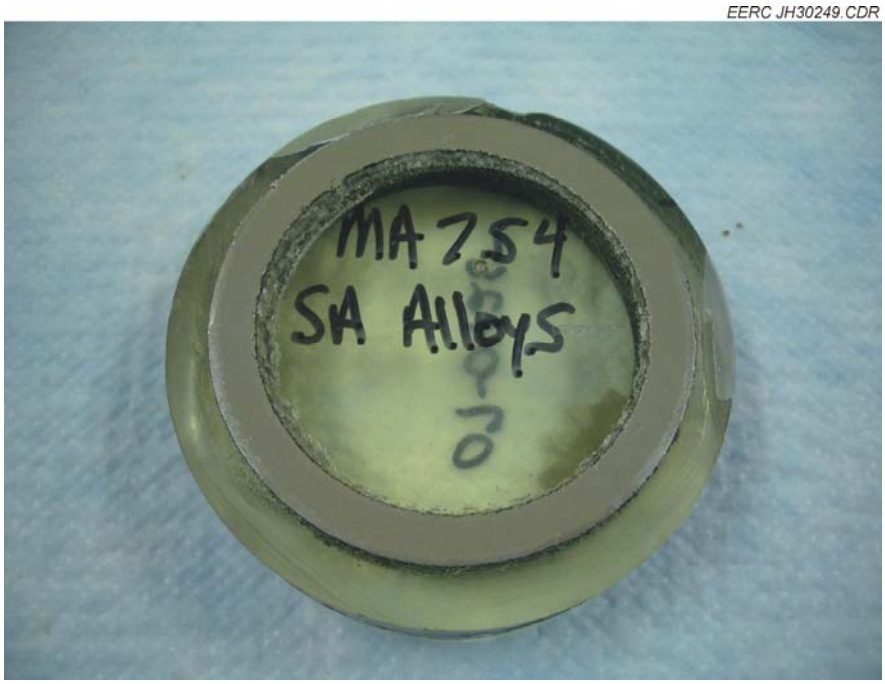

Figure 6. Polished cross section of an MA754 ring.

SUMMARY

In order to increase the efficiencies of advanced thermal energy systems, whether combustion or gasification for electric power generation or industrial systems such as aluminum melters, higher-working fluid temperatures must be reached. To reach the highest temperatures, especially over 1000°C, EERC experience shows that creep and corrosion-resistant dispersion-strengthened alloys are usually the best suited for these applications. However, careful testing in both simulated and actual systems for long durations is necessary in order to best define the temperature windows in which these materials are best used.

ACKNOWLEDGMENTS

Funding for this work was provided by the DOE Advanced Research Materials Program, DOE–United Technologies Research Center High-Performance Power System Program, DOE–EERC Fossil Energy and National Center for Hydrogen Technology Cooperative Agreements, the North Dakota Industrial Commission, and Xcel Energy.

REFERENCES

1. Energy Information Administration. *International Energy Outlook 2006*; DOE/EIA-0484(2006), June 2006.

2. Viswanathan, R.; Coleman, K.; Shingledecker, J.; Sarver, J.; Stanko, G.; Borden, M.; Mohn, W.; Goodstine, S.; Perrin, I. *Boiler Materials for Ultrasupercritical Coal Power Plants*; Final Summary Report for U.S. Department of Energy; DE-FG26-01NT41175; Energy Industries of Ohio, 2007.

3. Yamamoto, Y.; Brady, M.P.; Lu, Z.P.; Maziasz, P.J.; Liu, C.T.; Pint, B.A.; More, K.L.; Meyer, H.M.; Payzant, E.A. Creep-Resistant, Al_2O_3-Forming Austenitic Stainless Steels. *Science* **2007**, *316* 433–436.

4. United Technologies Research Center. *Combustion 2000 Phase II Final Technical Report*; DE-AC22-95PC95144, 2001.

5. Robson, F.L.; Ruby, J.D.; Nawaz, M.; Seery, D.J.; Jones, M.L.; Hurley, J.P. Application of High-Performance Power Systems (HiPPS) in Vision 21 Power Plants. In *Proceedings of the 2002 American Power Conference*; Chicago, IL, 2002.

6. Wright, I.G.; Stringer, J. Materials Issues for High-Temperature Components in Indirectly Fired Cycles. In *Proceedings of the International Gas Turbine and Aeroengine Congress and Exhibition*; Orlando, FL, 1997.

7. Hurley, J.P.; Weber, G.F.; Jones, M.L. Tests of High-Temperature Heat Exchangers for Indirectly Fired Combined Cycles. In *Proceedings of the 20th Annual International Pittsburgh Coal Conference*; Pittsburgh, PA, 2003.

8. Turker, M.; Hughes, T.A. Oxidation Behavior of Three Commercial ODS Alloys at 1200°C. *Oxidation of Metals* **1995** *44*, 505–525.

9. Whittenberger, J.D. Elevated Temperature Mechanical Properties of the Iron Base Oxide Dispersion Strengthened MA 956 Bar. Metallurgical Transactions A **1981**, *12A*, 845–851.

10. www.fossil.energy.gov/programs/powersystems/futuregen (accessed 2007).

11. Sondreal, E.A.; Swanson, M.L.; Benson, S.A.; Holmes, M.J.; Jensen, M.D. A Review of Gasification Technology for Coproduction of Power, Synfuels, and Hydrogen from Low-Rank Coals. In *Proceedings of the Symposium on Western Fuels: 20th International Conference on Lignite, Brown, and Subbituminous Coals*; Denver, CO, Oct 24–26, 2006.

STEAM TURBINE MATERIALS AND CORROSION

Gordon R. Holcomb
NETL-Albany, 1450 Queen Ave SW, Albany, OR 97321
Email: Gordon.Holcomb@netl.doe.gov; Voice: (541) 967-5874; Fax: (541)-967-5914

David E. Alman
NETL-Albany, 1450 Queen Ave SW, Albany, OR 97321
Email: David.Alman@netl.doe.gov; Voice: (541) 967-5885; Fax: (541)-967-5845

Őmer N. Doğan
NETL-Albany, 1450 Queen Ave SW, Albany, OR 97321
Email: Omer.Dogan@netl.doe.gov; Voice: (541) 967-5858; Fax: (541)-967-5845

James C. Rawers
NETL-Albany, 1450 Queen Ave SW, Albany, OR 97321
Email: James.Rawers@netl.doe.gov; Voice: (541) 967-5882; Fax: (541)-967-5845

Karol K. Schrems
NETL-Albany, 1450 Queen Ave SW, Albany, OR 97321
Email: Karol.Schrems@netl.doe.gov; Voice: (541) 967-5804; Fax: (541)-967-5845

Malgorzata Ziomek-Moroz
NETL-Albany, 1450 Queen Ave SW, Albany, OR 97321
Email: Margaret.Ziomek-Moroz@netl.doe.gov; Voice: (541) 967-5943; Fax: (541)-967-5914

ABSTRACT

Ultra-supercritical (USC) power plants offer the promise of higher efficiencies and lower emissions. Current goals of the U.S. Department of Energy's Advanced Power Systems Initiatives include power generation from coal at 60% efficiency, which would require steam temperatures of up to 760°C. This project examines the steamside oxidation of candidate alloys for use in USC systems, with emphasis placed on applications in high- and intermediate-pressure turbines. As part of this research a concern has arisen about the possibility of high chromia evaporation rates of protective scales in the turbine. A model to calculate chromia evaporation rates is presented.

INTRODUCTION

Current goals of the U.S. Department of Energy's Advanced Power Systems Initiatives include power generation from coal at 60% efficiency, which would require steam conditions of up to 760°C and 35MPa, so called ultra-supercritical (USC) steam conditions. This is in comparison to conventional sub-critical steam plants which operate at about 37% efficiency (steam at 540°C-14.5 MPa) and advanced plants that are currently just being introduced into the market that operate at 40 to 45% efficiency (steam at 600°C-28MPa). The importance of increased efficiency is because it is estimated that for each 1% raise in plant efficiency will eliminate approximately 1,000,000 tons of CO_2 over the lifetime of an 800MW coal fired plant.[1] The overarching limitation to achieving the DOE goal is a lack of cost effective metallic

materials that can perform at these temperatures and pressures.[2] Improving alloy resistance to high temperature corrosion is one key in developing new, efficient and clean coal-fired ultra-supercritical (USC) steam plants.[2]

For the USC application, both turbine and boiler materials will operate at higher temperatures and pressures than in conventional plants. However, the development of creep strength in alloys is often obtained at the expense of corrosion and oxidation resistance. Therefore, the strategies to confer corrosion resistance may be needed if ever increasing cycle temperatures are to be achieved in advanced plants. To identify or develop alloys and strategies that can meet these performance requirements, it is critical to understand the degradation mechanisms that will occur during operation.

A critical aspect of materials usage in USC steam turbines is oxidation behavior. Oxidation can result in several adverse conditions: general section loss from material thinning, deep and localized section loss from internal oxidation along grain boundaries, dimensional changes that are critical in airfoils, and downstream erosion from oxide spallation. Evaporation of protective chromia scales may also be an issue at the higher temperatures and pressures of USC steam turbines. In addition, oxidation may modify creep behavior (beyond mere section loss) by its near-surface effects on grain boundary morphologies and precipitation strengthening.

PROJECT OBJECTIVES

The objective of this research is to understand materials degradation in USC steam environments and to identify and/or develop viable materials for use in USC steam turbines. A variety of materials-based approaches are used that can be broadly categorized into steam oxidation, surface treatments, and alloy development. The steam oxidation portion of this research is presented here.

There are two basic objectives of the steam oxidation research. The first is to characterize candidate commercial alloys (primarily nickel-base superalloys) as to their steam oxidation resistance. An important consideration in this was to compliment, and not to duplicate, other DOE-sponsored research in this arena—namely the USC boiler consortium effort in atmospheric pressure steam.

The second objective is to develop steam oxidation models for use in USC steam turbine environments. Thus far modeling has focused on chromia evaporation. Future plans include the development of models to address geometric effects on oxide spallation, and high temperature creep and oxidation interactions.

OXIDATION BEHAVIOR OF CANDIDATE ALLOYS

The oxidation behavior is examined of candidate alloys for use in USC steam turbines. Alloys include the most promising alloys identified by the USC boiler and turbine consortiums, the UK-US Collaboration on Energy Research & Development in the Field of Fossil Energy Technology, the Electric Power Research Institute (EPRI),[3] and in use in the Scholven Unit F demonstration.[4] These are listed in Table 1. The USC turbine consortium alloys (Udimet 720, Haynes 282, and Nimonic 105) were recently obtained from GE-Energy (Schenectady, NY) and added to the study.

Table 1. Candidate alloys for use in advanced steam turbines.

Alloy	Class	USC Boiler	EPRI Turbine Candidate	Scholven Unit F Turbine	UK-US	USC Turbine
T92	Fe Ferritic	X			RR	
SAVE12 9.5Cr	Fe Ferritic	X			X	
SAVE12 10.5Cr	Fe Ferritic	X			X	
TP347HFG	Fe Austenitic	X			RR	
HR6W	High Ni & Cr	X				
Haynes 230	Ni Superalloy	X			X	
Haynes 282	Ni Superalloy					X
Inconel 617	Ni Superalloy	X		X	X	
Inconel 625	Ni Superalloy			X	X	
Inconel 718	Ni Superalloy		X		X	
Inconel 740	Ni Superalloy	X			RR	
Nimonic 90	Ni Superalloy		X		X	
Nimonic 105	Ni Superalloy					X
Udimet 720Li	Ni Superalloy					X

Current tests are at ambient pressures and include furnace exposures, thermogravimetric analysis (TGA), and cyclic oxidation. These test procedures were earlier described in detail.[5] In brief, furnace exposures were for up to 2000 hr in air with 3% water vapor with 100 hour temperature cycles and slow heating and cooling rates. TGA tests were for 300 hr in Ar with 35% water vapor. Cyclic oxidation tests were for up to 2000 cycles in air with 40% water vapor with hourly temperature cycles with rapid heating and cooling rates. Progress in the testing plan is shown in Table 2.

Table 2. Percentage of completed tests for each alloy at each temperature.

Alloy	Cyclic				Furnace				TGA			
°C	650	700	760	800	650	700	760	800	650	700	760	800
T92	0%	0%	100%		100%	36%	100%	71%	0%	0%	0%	0%
Save12 9.5 Cr	41%	0%	100%		100%	54%	100%	36%	0%	0%	75%	100%
Save12 10.5 Cr	41%	0%	100%		100%	54%	100%	36%	0%	0%	75%	100%
TP347HFG	0%	0%	100%	0%	100%	36%	100%	71%	0%	0%	0%	0%
HR6W	0%	0%	100%	0%	100%	36%	100%	71%				50%
Haynes 230	0%	0%	100%	0%	100%	41%	100%	36%				100%
Inconel 617	0%	0%	100%	0%	100%	36%	100%	36%				100%
Inconel 625	0%	0%	100%	0%	100%	71%	100%	71%				50%
Inconel 718	0%	0%	100%	0%	100%	0%	100%	36%				0%
Inconel 740	0%	0%	100%	0%	100%	54%	100%	36%				25%
Nimonic 90	0%	0%	100%	0%	100%	36%	100%	36%				0%

As examples of the kinetics and microstructures found, representative results from cyclic oxidation tests are shown in Figs. 1-4 at 760°C for Inconel 740, Haynes 230, Inconel 718, and Nimonic 90. Of note are the decreases in mass with time for Haynes 230, Inconel 718, and to a lesser extent, Inconel 740. No spalling was observed, so this decrease indicates evaporative losses. Scale thickness with time is a competition between scale growth from oxidation and scale loss from evaporation. Nimonic 90, with its higher oxidation rate and thicker scale did not yet show the gradual decrease in mass with time that indicates a steady state scale thickness has been reached. The microstructures shown in Figs. 1-4 show that internal oxidation of aluminum has occurred beneath the oxide scale and predominantly along grain boundaries.

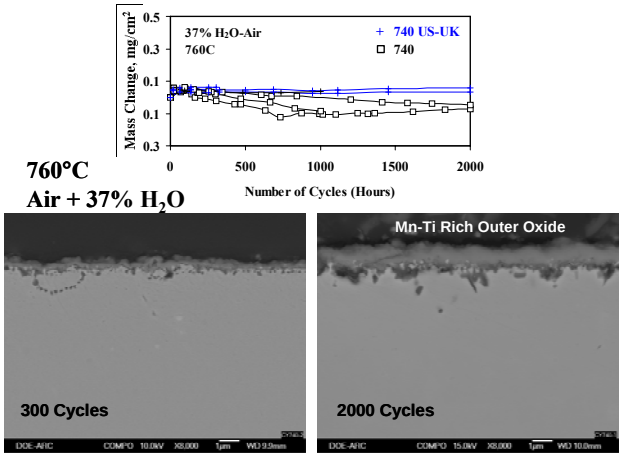

Fig. 1. Cyclic oxidation of Inconel 740 at 760°C.

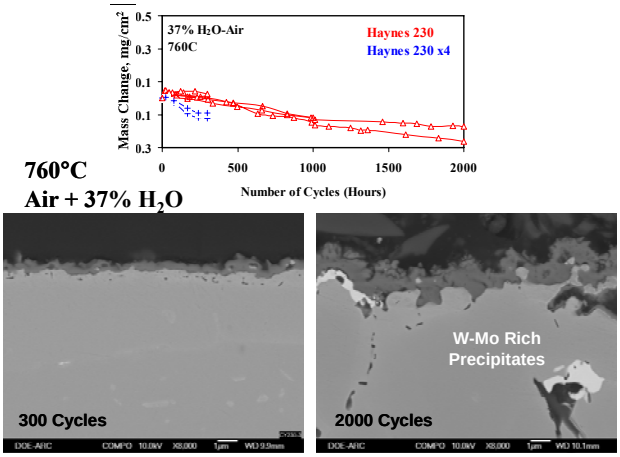

Fig. 2. Cyclic oxidation of Haynes 230 at 760°C.

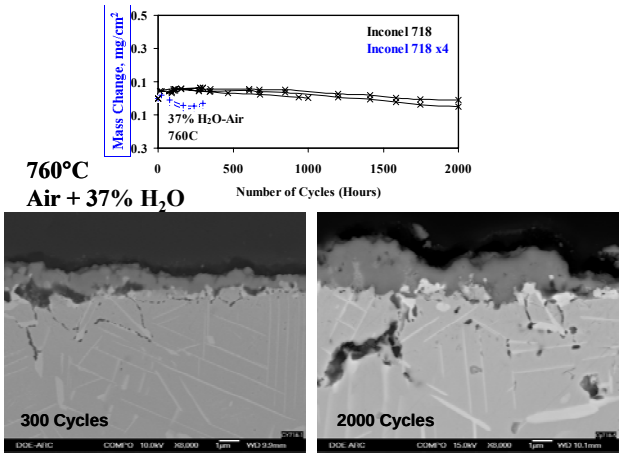

Fig. 3. Cyclic oxidation of Inconel 718 at 760°C.

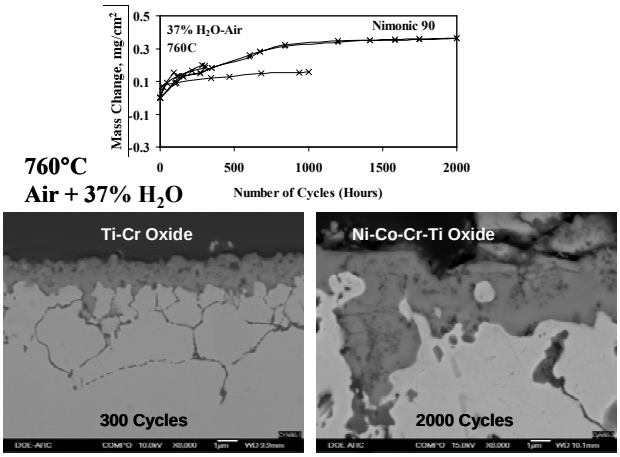

Fig. 4. Cyclic oxidation of Nimonic 90 at 760°C.

In contrast with cyclic tests, furnace exposures show mass increases with time. Chromia evaporation is suppressed in these furnace exposures due to 1) the samples being in crucibles and thus less exposed to the flowing gas, and 2) a much lower water vapor partial pressure.

CHROMIA EVAPORATION MODEL

The oxidation of alloys protected by the formation of Cr_2O_3 (chromia formers) can undergo scale loss due to reactive evaporation of chromium containing gas species. Water vapor increases the evaporation loss by allowing the formation of $CrO_2(OH)_2(g)$, which has a higher vapor pressure than $CrO_3(g)$. $CrO_3(g)$ is the predominate Cr gas specie in dry air or oxygen. The reaction is given by Eq. (1).

$$\tfrac{1}{2}Cr_2O_3(s) + H_2O(g) + \tfrac{3}{4}O_2(g) \rightarrow CrO_2(OH)_2(g) \qquad (1)$$

Evaporation can change the overall oxidation kinetics from parabolic behavior to linear kinetics or even to breakaway oxidation. Linear kinetics can arise after scale growth from oxidation, which decreases with increasing scale thickness, matches the scale loss from reactive evaporation. The change in scale thickness, x, with time, t can be described in terms of the parabolic rate constant, k_p, and the linear reactive evaporation rate, k_e, as:

$$\frac{dx}{dt} = \frac{k_p}{x} - k_e \tag{2}$$

At long times or high reactive evaporation rates, a limiting scale thickness, x_L, arises that is given by:

$$x_L = \frac{k_p}{k_e} \tag{3}$$

The approach used to determine evaporation rates was to assume that volatility is limited by the transport of $CrO_2(OH)_2(g)$ through a boundary layer in the gas phase. For flat plate geometry with laminar flow, the evaporation rate can be calculated by:[6-7]

$$k_e\left(\frac{kg}{m^2 s}\right) = 0.664\, Re^{0.5} Sc^{0.343} \frac{D_{AB}\rho}{L} \tag{4}$$

Where Re and Sc are the dimensionless Reynolds and Schmidt numbers, D_{AB} is the gaseous diffusion coefficient between the Cr gas specie and the solvent gas (m^2/s), ρ is the density (kg/m^3) of the evaporative specie in the gas, and L is the length (m) in the flow direction of the flat plate. Equation 4 is valid for Sc numbers between 0.6 and 50.[6] Assuming ideal gas behavior and a reaction described by Eq. (1), this can be expanded to:

$$k_e\left(\frac{kg}{m^2 s}\right) = 0.664\, Re^{0.5} Sc^{0.343} \frac{D_{AB} M_i P_T}{LRT} P_{H_2O} P_{O_2}^{3/4} \exp\left(-\frac{\Delta G}{RT}\right) \tag{5}$$

Where M_i is the molecular mass of $CrO_2(OH)_2(g)$, P_T is the total pressure, ΔG is the Gibbs energy of Eq. (1), and P_{H2O} and P_{O2} are partial pressures of H_2O and O_2. In a similar fashion for turbulent flow ($Re > 5\times10^5$):

$$k_e\left(\frac{kg}{m^2 s}\right) = 0.0592\, Re^{4/5} Sc^{1/3} \frac{D_{AB} M_i P_T}{LRT} P_{H_2O} P_{O_2}^{3/4} \exp\left(-\frac{\Delta G}{RT}\right) \tag{6}$$

The right-hand sides of Eqs. (5-6) are essentially the partial pressure of $CrO_2(OH)_2(g)$, which depends on ΔG. Figure 5 shows the dependence of $P_{CrO2(OH)2}$ from T, P_T, and three literature sources for ΔG.[8-10] The P_{O2} dependence lowers $P_{CrO2(OH)2}$ going from moist air to oxygenated steam, while increasing the total pressure lowers ΔG and increases $P_{CrO2(OH)2}$.

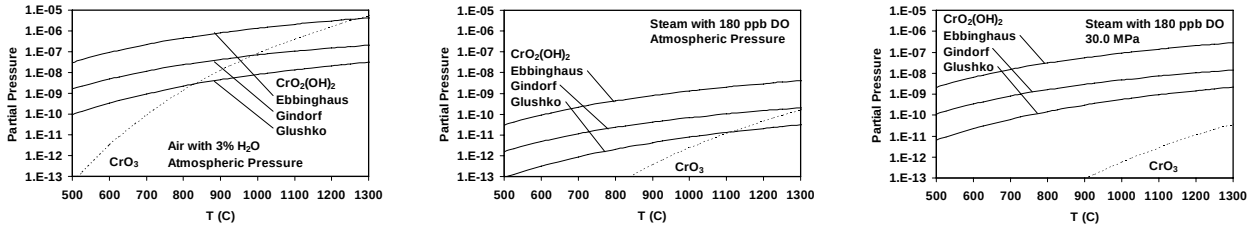

a) b) c)

Fig. 5. Partial pressures over pure Cr_2O_3 for a) 3% H_2O in air at atmospheric pressure, b) steam with 180 ppb dissolved oxygen (DO) at atmospheric pressure, and c) steam with 180 ppb DO at 30.0 MPa. The three curves for $CrO_2(OH)_2(g)$ arise from three literature sources for ΔG.[8-10]

The cyclic oxidation tests were done with gas flowing parallel to the flat sample surface, and so can be described by Eq. (5). Figure 6 shows mass change results from Haynes 230 at 760°C for two different gas velocities compared with predicted evaporation mass loss. The agreement is excellent using the Gindorf[10] values for ΔG.

The model was applied to steam turbine conditions using Eq. (6). Some predictions are shown in Fig. 7 for supercritical steam with 180 ppb dissolved oxygen (DO). These predicted rates are quite large compared to the experimental tests at atmospheric pressure and low gas velocities. The highest value in Fig. 7 (for 760°C and 34.5 MPa) of 3.84×10^{-7} kg/m^2/s corresponds to about 0.6 mm per year of metal loss (assumes a metal density of 9 g/cm^3 and a conversion to a Cr basis). This is a large value for metal loss for a component expected to operate many years, and it may be larger if the scale losses enough Cr to become non-protective. Current state-of-the-art steam turbines operate at approximately 600°C and 30 MPa, and would have a predicted evaporation rate of about 8×10^{-8} kg/m^2/s. Typical subcritical steam power plants operate at 538°C and 16.5 MPa, and would have a predicted evaporation rate of about 2×10^{-8} kg/m^2/s. These later two cases should have lower evaporation rates in practice because the ferritic-martensitic steels used usually form Fe-Cr spinel outer scales instead of chromia scales. This lowers the activity of chromia in the scale, which lowers the partial pressure of $CrO_2(OH)_2$(g) and thus lower the evaporation rate.

Another factor that would lower the predicted evaporation rate for USC conditions is that the gas is assumed to be free of already existing $CrO_2(OH)_2$(g). But the superheater, with a steam velocity of 10-25 m/s, undoubtedly undergoes significant evaporative attack that would partially saturate the gas entering the turbine. This could shift the most damaging attack from the turbine to the superheater.

Laboratory corrosion tests generally seek to mimic the process environment as closely as possible. In cases where this is difficult, then one seeks to establish conditions where the corrosion mechanisms are the same. For steam turbines, laboratory tests with the same combination of temperature, pressure, gas velocities, and steam chemistry are extremely difficult and expensive. Therefore tests sacrifice one or more of the conditions—usually pressure or gas velocity. For examining the effects of Cr-evaporation as a corrosion mechanism, laboratory tests may be best served with much higher oxygen partial pressures so as to increase the evaporation rate. In Fig. 8 the advanced steam turbine points are from the 760°C data Fig. 6. The representative laboratory curves are as a function of the partial pressure of O_2 in Air+H_2O and O_2+H_2O atmospheres. The laboratory curves were all calculated at atmospheric pressure, v = 0.02 m/s and L = 0.02 m. The right-hand-side of the laboratory curves drop sharply as P_{H2O} approaches zero. The right-hand-side end points of the laboratory curves are limits—reactive evaporation in drier O_2 or drier air would switch at that point from $CrO_2(OH)_2$(g) being the dominate gas specie to CrO_3(g), and would not drop further with less H_2O.

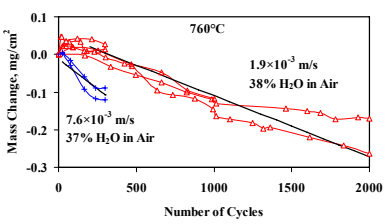

Fig. 6. Cyclic oxidation of Haynes 230 at 760°C. Straight solid lines are the predicted slopes from reactive evaporation of Cr_2O_3(s) using the Gindorf[10] data for $CrO_2(OH)_2$(g).

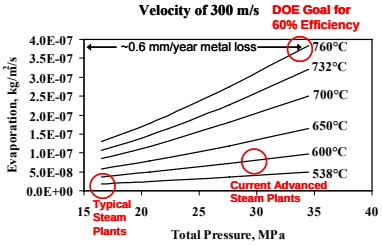

Fig. 7. Predicted evaporation rates in steam with 180 ppb DO, 300 m/s flow rate, and a characteristic length of 0.05 m.

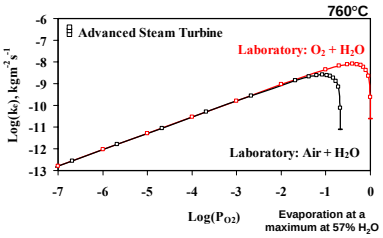

Fig. 8. Predicted evaporation rates at 760°C for USC turbines (180 ppb DO, P_T of 20.7, 27.5 and 34.5 MPa, v = 300 m/s) compared with atmospheric pressure laboratory tests.

NEAR TERM FUTURE WORK

From the start of this project, a goal has been to examine the effects of pressure on steam oxidation. Procurement of the main component required for USC steam exposures, the autoclave, took over three years of solicitations, cancellations, and renegotiations. The autoclave arrived in December of 2006 and is currently being brought on-line. It is of Haynes 230 construction and is dual rated for temperatures and pressures of up to either 4500 psi at 1400°F (310 bar at 760°C) or 5000 psi at 1375°F (345 bar at 746°C). Some photographs of it are in Fig. 9. A schematic of the entire setup is in Fig. 10. Comparisons between field and autoclave exposures to supercritical steam are planned.

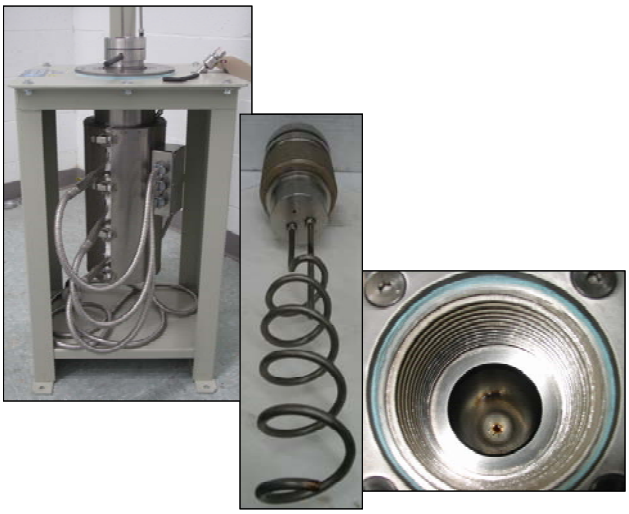

Fig. 9. The Haynes 230 autoclave dual rated for temperatures and pressures of up to either 310 bar at 760°C or 345 bar at 746°C.

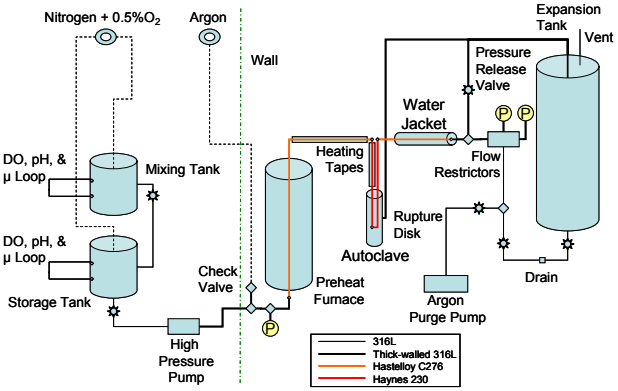

Fig. 10. Schematic of the USC exposure apparatus.

Also planned are studies on the geometric effects on oxide spallation by examining the oxidation of wires of differing diameters, and on interactions between oxidation and creep behavior.

SUMMARY

Steam oxidation behavior is directly linked to implementing USC steam power generation for improved efficiencies and reduced CO_2 emissions. Two basic objectives of the steam oxidation research were presented. The first was to characterize candidate commercial alloys (primarily nickel-base superalloys) as to their steam oxidation resistance. Beyond simple scale formation, the primary degradation mechanisms were shown to be internal oxidation and chromia evaporation. The second objective was to develop steam oxidation models for use in USC steam turbine environments. A model was shown for chromia evaporation and predictions were made as far as extending the model to USC conditions.

REFERENCES

1. R. Swanekamp, Power, 146 (4), 2002, pp. 32-40.
2. R. Viswanathan, J. F. Henry, J. Tanzosh, G. Stanko, J. Shingledecker, B. Vitalis, R. Purgert, Journal of Materials Engineering and Performance, 14, 2005, pp. 281-292.
3. R. Viswanathan and W. Bakker, Journal of Materials Engineering and Performance, 10, 2001, pp. 96-101.
4. "Materials Development in the European AD700 Program," Materials & Components in Fossil Energy Applications, No. 162, Spring/Summer 2005, U.S. Department of Energy.
5. G. R. Holcomb and M. Ziomek-Moroz, "Steam Turbine Materials and Corrosion," Proceedings of the 20th Annual Conference on Fossil Energy Materials, Knoxville, TN, June 12-14, 2006 (U.S. Department of Energy, Office of Fossil Energy, Advanced Research Materials).
6. D. R. Gaskell, An Introduction to Transport Phenomena, New York (NY): Macmillan Publishing, 1992, pp. 78-89 (chapter 2) and 569-578 (chapter 11).
7. G. H. Geiger, D. R. Poirier, Transport Phenomena in Metallurgy, Reading (MA): Addison-Wesley Publishing, 1973, pp. 7-13 (chapter 1), 463-467 (chapter 13) and 529-537 (chapter 15).
8. Glusko Thermocenter of the Russian Academy of Sciences—Izhorskaya 13/19, 127412, Moscow Russia: IVTAN Association; 1994.
9. B. B. Ebbinghaus, Combustion and Flame, Vol. 93, 1993, pp. 119-137.
10. C. Gindorf, K. Hilpert. L. Singheiser, "Determination of Chromium Vaporization Rates of Different Interconnect Alloys by Transpiration Experiments. H. Yokokawa, S. C. Singhal, editors, in Solid Oxide Fuel Cells (SOFC VII), Proceedings Vol. 2001-16, Pennington (NJ): Electrochemical Society, 2001, pp. 793-802.

SESSION 2

POSTERS

DEVELOPMENT OF INORGANIC MEMBRANES FOR HYDROGEN SEPARATION

Brian. L. Bischoff
Oak Ridge National Laboratory, P.O. Box 2008, Oak Ridge, TN 37831-6044
E-mail: bischoffbl@ornl.gov; Telephone: (865) 241-3172; Fax: (865) 576-3502

K. Dale Adcock
Oak Ridge National Laboratory, P.O. Box 2008, Oak Ridge, TN 37831-6044
E-mail: adcockkd@ornl.gov; Telephone: (865) 574-239; Fax: (865) 576-3502

Lawrence E. Powell
Oak Ridge National Laboratory, P.O. Box 2008, Oak Ridge, TN 37831-6044
E-mail: powellle@ornl.gov; Telephone: (865) 574-9415; Fax: (865) 576-3502

T. Gordon Sutton
Oak Ridge National Laboratory, P.O. Box 2008, Oak Ridge, TN 37831-6044
E-mail: suttontg1@ornl.gov; Telephone: (865) 574-8758; Fax: (865) 576-3502

Curtis J. Miller
Oak Ridge National Laboratory, P.O. Box 2008, Oak Ridge, TN 37831-6044
E-mail: millercj@ornl.gov; Telephone: (865) 574-3781; Fax: (865) 576-3502

ABSTRACT

The purpose of this work is to improve the method of fabricating tubular metal supported microporous inorganic membranes. Earlier work focused on the original development of inorganic membranes for the purification of hydrogen. These membranes are now being scaled up for demonstration in a coal gasification plant for the separation of hydrogen from coal-derived synthesis gas for a project funded by the Office of Fossil Energy's Gasification and Coal Fuels programs [1]. This project is part of FutureGen, an initiative to build the world's first integrated sequestration and hydrogen production research power plant. Although previous work in the Advanced Research Materials Program project led to development of a tubular metal supported microporous membrane which was approved by the Department of Energy for testing, the membranes generally have lower than desired selectivities for hydrogen over other gases common in synthesis gas including carbon dioxide. The work on this project over three years will lead to general improvements in fabrication techniques that will result in membranes having higher separation factors and higher fluxes. Scanning electron microscopy and profilometry data will be presented to show qualitatively and quantitatively the surface roughness of the support tubes. We will discuss how the roughness affects membrane quality and methods to improve the quality of the support tube surface.

INTRODUCTION

The purpose of this work is to improve the method of fabricating tubular metal supported microporous inorganic membranes. Earlier work focused on the original development of these membranes which are now being scaled up for demonstration in a coal gasification plant for the separation of hydrogen from coal-derived synthesis gas for a project funded by the Office of Fossil Energy's Gasification and Coal Fuels programs. Although previous work lead to development of a tubular metal supported microporous membrane based on ORNL technology which was approved by the Department of Energy for testing, the membranes generally have lower than desired selectivities for hydrogen over other gases including carbon dioxide. The work on this project over three years will lead to general improvements in fabrication techniques that will lead to membranes having higher separation factors and higher fluxes.

EXPERIMENTAL

Previous work has shown that high selectivities for helium or hydrogen over carbon dioxide can be achieved and that the permeance of helium and hydrogen increases with increasing temperature. At 250°C, the ideal separation factor for a ceramic supported membrane was 48.3. As a result of the lower temperature required for the separation of hydrogen in the Integrated Gasification Combined Cycle (IGCC) concept plant, a switch was made to metallic supports. Metallic supports are more robust when compared to ceramic supports and can be sealed into membrane modules more easily by welding or brazing. A transmission micrograph of a stainless steel support membrane is shown in Figure 1. The dark area is the stainless steel type 316L support tube which has a thickness of approximately 500 μm and a pore-size of approximately 5 μm. The layer directly on top of the support tube is an intermediate layer (gray in color) having a pore-size of 7 nm with an average thickness of 2-3 μm. The top separative layer (white) is approximately 0.5 μm thick and has a pore-size less than 1 nm. These membranes made using metallic supports have had somewhat lower selectivities and data has also shown that membranes produced using supports made from water atomized metal powers had lower selectivities than membranes produced using supports made from gas atomized powder. It is believed that these lower selectivities are due to imperfections in the support tube that result in pin-holes or over-sized pores in the subsequently applied membrane layers. Scanning electron micrographs (SEM), at a 60° to the surface, of supports made from water atomized stainless steel powder and gas atomized stainless steel powder are shown in Figures 2 and 3. Figure 2 shows the roughness of the surface from the irregularly shaped particles made by water atomization while Figure 3 shows a smoother surface from the spherical particles made by gas atomization. While Figure 3 shows a smoother surface, there are still some surface irregularities due to the larger particles protruding from the surface. Since the intermediate layer is only approximately 2-3 micrometers thick, the intermediate layer would have a difficult time smoothing out the surface of a support tube made from water atomized powder. This layer is now the support structure for the very thin nanoporous separative layer. Without a smooth intermediate layer, it would be difficult to fabricate membranes having no leaks in the separative layer. Therefore, much of our effort to date has been quantifying the smoothness of the support surface as a function of tube forming properties and correlating these properties to the performance data of completed membranes.

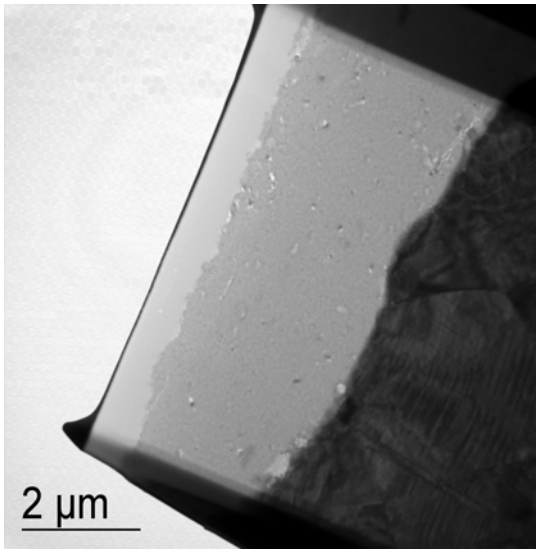

Figure 2 Transmission micrograph showing the support tube (dark), intermediate aluminum oxide layer (gray), nanoporous separative layer (almost white), and sputtered metal layer added to aid in sectioning.

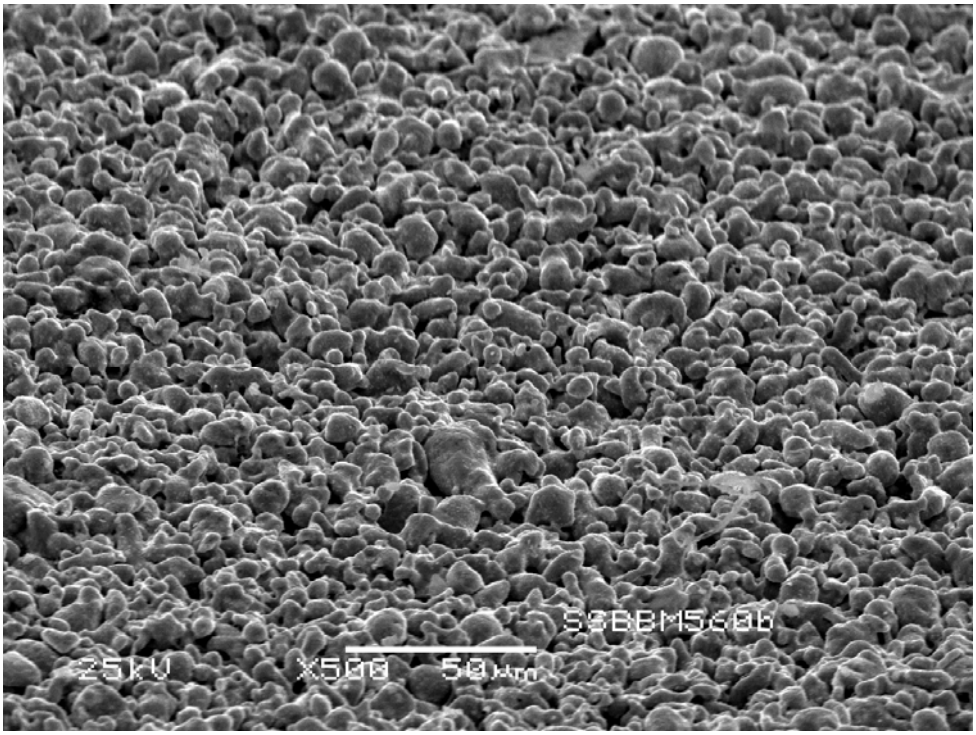

Figure 1 SEM of inside surface of support tube made from water atomized powder taken at 60°.

Profilometry of the surface of the support tubes has been initiated using a software product called MeX from Alicona Imaging. This software works with SEM images taken at various tilt angles to evaluate the roughness of the surface along an axis. This analysis is being used to correlate measured surface roughness with membrane properties and powder properties

used to make the supports. Figure 4 shows how the software can use colors to illustrate the height of particles and the depths of the valleys. While the image of the support made from water-atomized powder contains bright pinks and purples (indicating particles protruding high above the surface and orange/yellow areas, (indicating deep valleys), the image of the support made from gas-atomized powder contains mostly light blues and greens indicating a more uniform surface. Figures 5 and 6 show an analysis along an arbitrary line drawn across the samples. Although placement of the line is very subjective, this analysis shows that the peak-to-valley distances are greater in the supports made from water-atomized powder.

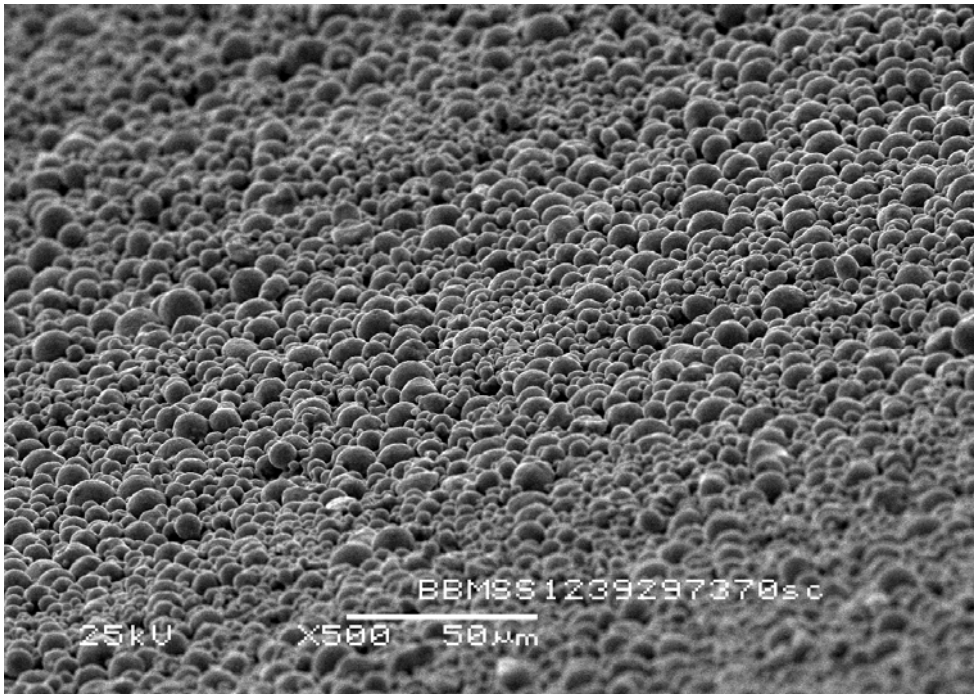

Figure 3 SEM of inside surface of support tube made from gas atomized powder taken at 60°.

Performance

Membranes fabricated using supports made from gas atomized powder were tested at the National Energy Technology Laboratory (NETL) in Pittsburgh, PA as part of a project to scale up ORNL's hydrogen separation membranes. The selectivities for hydrogen over carbon dioxide were usually found to be less than 5 at temperatures below 200°C but increased to as high as 48 when the temperature was increased to 300-450°C. Results for one of the membranes are shown in Figure 7. The large increase in selectivity is mostly due to a large increase in the permeance of hydrogen as the temperature is increased.

FUTURE WORK

Samples of gas atomized powder in varying particle size have been procured. Also, a sample of a gas atomized stainless steel powder having a narrower particle size distribution than our earlier as-received powders has been procured. This powder is essentially the same as the powder used to fabricate the tubes shown in Figure 3 with the largest particles removed

leaving particles mostly less than 10 micrometers in diameter. When these tubes are formed, we will evaluate the supports for surface roughness, apply membrane layers and measure for the quality of membrane layer, mainly leak rate.

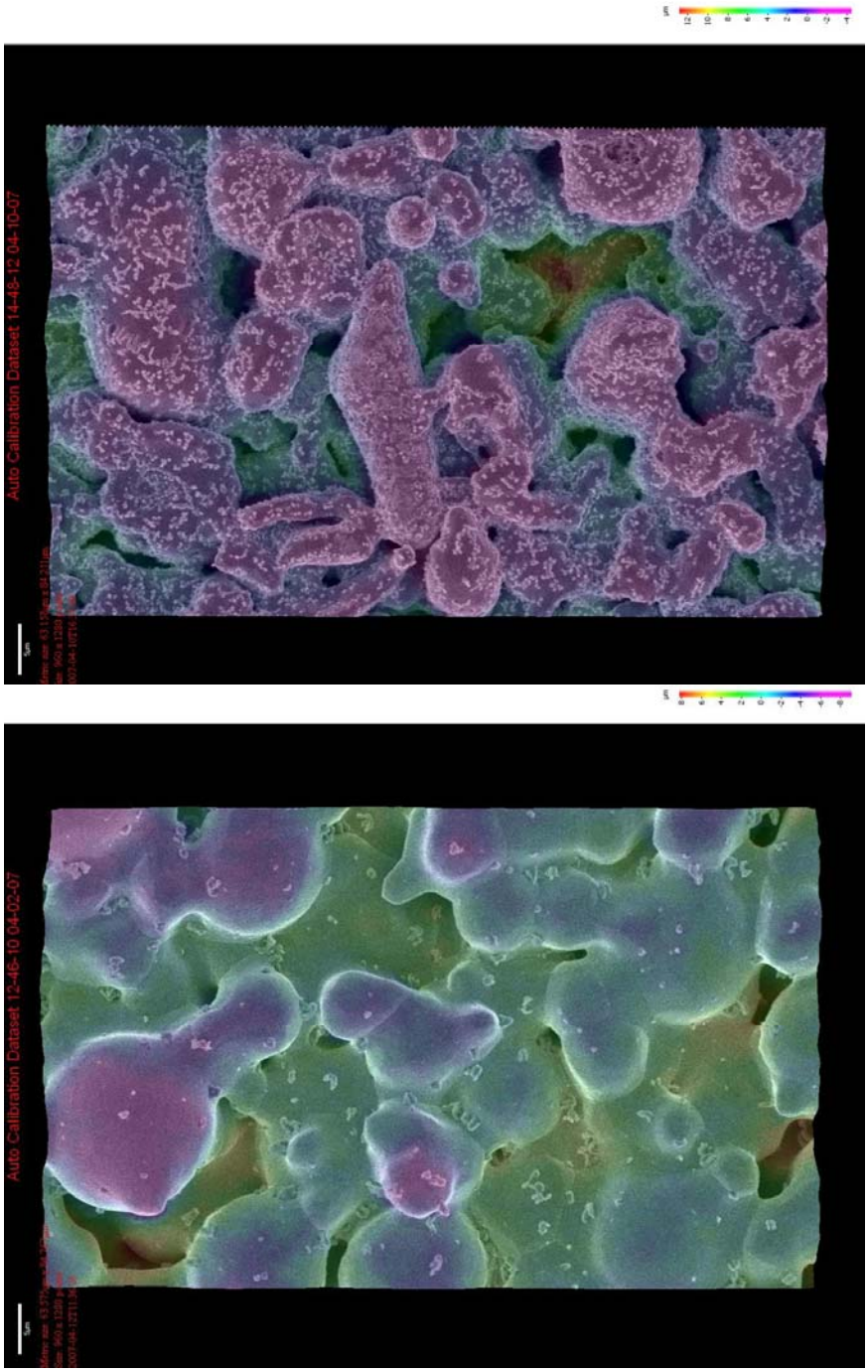

Figure 4. Colors help identify peaks and valleys of support. Contrast in colors for support made from water atomized powder (upper) shows larger peak-to-valley distances than support made from gas-atomized powder (lower).

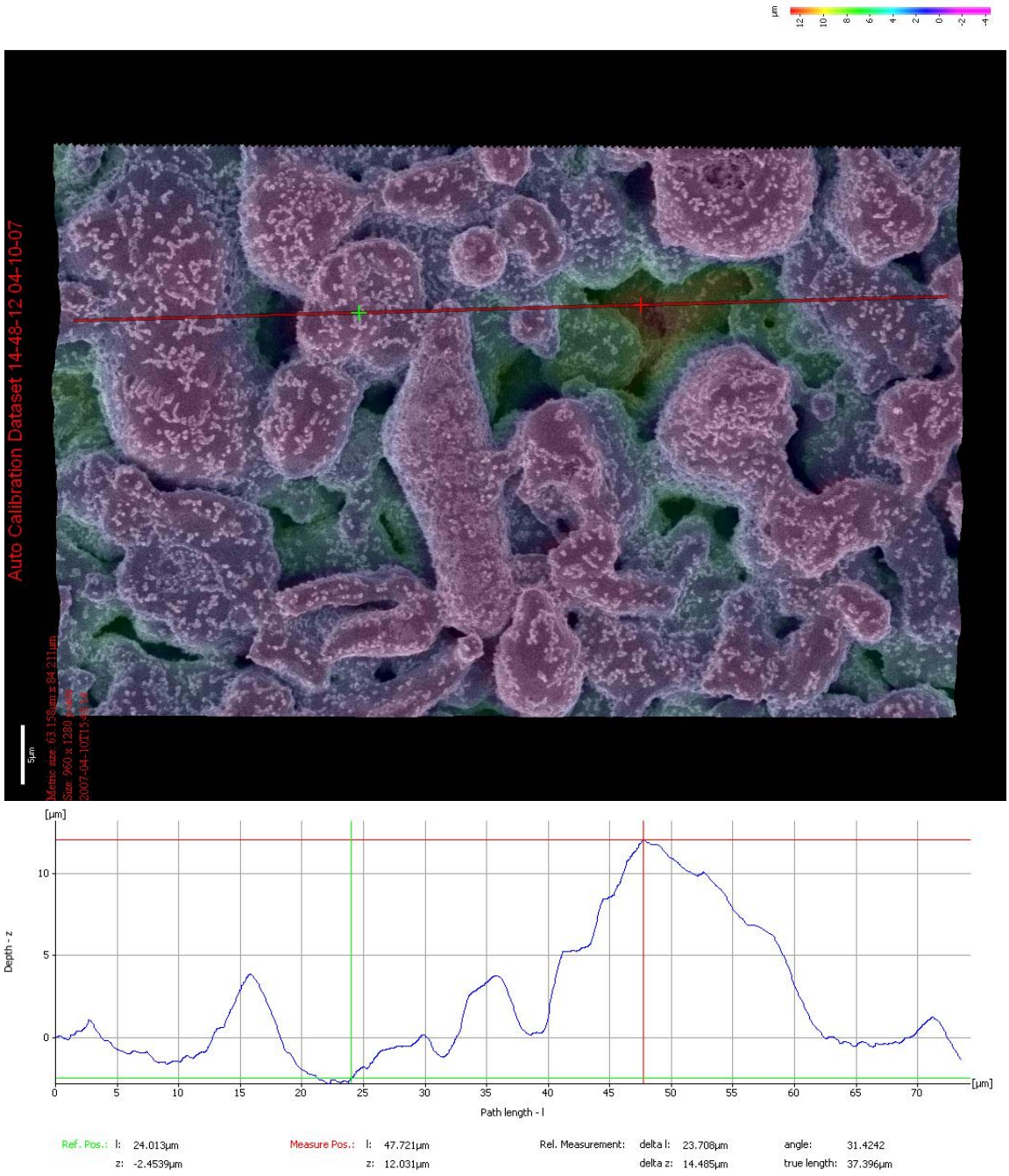

Figure 5 Linear analysis of surface made from water-atomized powder shows large peak-to-valley transitions.

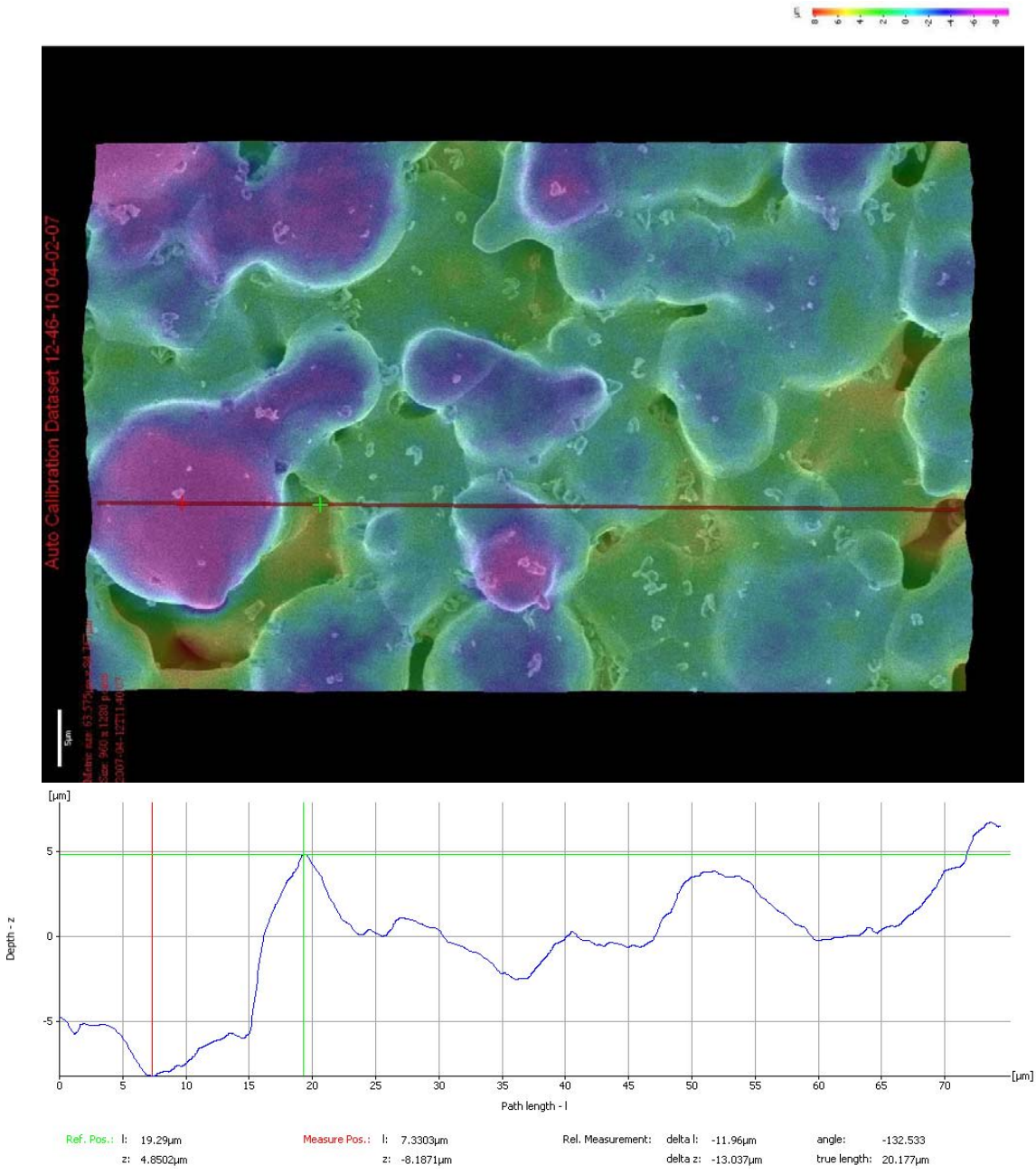

Figure 6 Linear analysis shows smaller peak-to-valley transitions in supports made from gas-atomized powder.

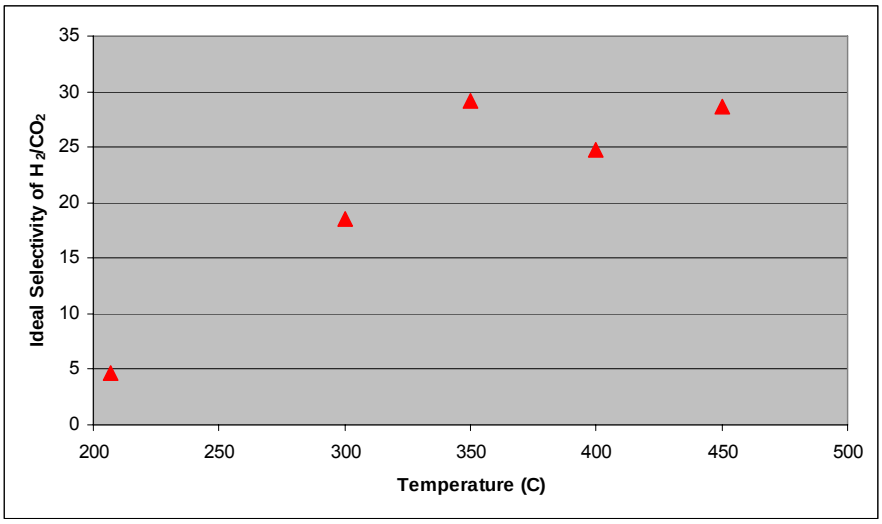

Figure 7 Pure gas selectivity (ratio of pure gas permeances) of hydrogen over carbon dioxide measured at NETL as part of Scale-up Project

REFERENCES

1. Judkins, R.R.; Bischoff, B.L., "Scale-Up of Microporous Inorganic Hydrogen-Separation Membranes," *Proceedings 22nd Annual International Pittsburgh Coal Conference, Sept. 12-15, 2005*.

PILOT FACILITY FOR THE PRODUCTION OF SILICON CARBIDE FIBRILS

Richard D. Nixdorf
ReMaxCo Technologies, Inc
1010 Commerce Park Drive, Suite I
Oak Ridge, TN 37830
Tele: (865) 482-7552
nixdorfr@indceramicsolns.com

ABSTRACT

This project was delayed for over one year due to an unfortunate accident by a freight shipper, when the 4,500 pound Fibrils synthesis reactor was dropped from a loading dock. The unit suffered significant damage, a six month insurance company dispute and a six month repair activity. The repaired Fibrils Synthesis Reactor has now been moved to a materials development company in Alfred, NY, near Alfred University. The unit will be operated under the supervision of a Ph.D. level ceramic scientist. The reactant gas control system has been installed and tested. The electrical, vacuum and the microwave systems have been activated and tested. Initial microwave Fibrils synthesis experimental runs have been conducted. The results of those first experiments will be reported. The U.S. Patent has been filed on the process. The experimental plan for the remainder of 2007 will be discussed, as well as, the future plans for 2008. The focus of the 2007 work is providing adequate Fibril quantities to Fossil Energy companies to allow initial evaluation of the product to resolve severe materials problems. A secondary benefit of this project is the interest that is coming from other advanced materials areas. The presentation will discuss these applications in aerospace, commercial aircraft engines, defense activities, and commercial steel production.

INTRODUCTION

This research was sponsored by the U.S. Department of Energy, Fossil Energy Advanced Research Materials Program. The U.S. Department of Energy projects using the Silicon Carbide Fibrils as a primary structural component for fiber reinforced silicon carbide composite heat exchanger tubes that would be fabricated by chemical vapor infiltration.

The VLS silicon carbide fibrils are grown when gaseous reactants are dissolved into a liquid catalyst and precipitated on to the growing fibril to form a perfect single crystal structure. ReMaxCo Technologies has access to a commercial ceramic fiber papermaking process. When SiC fibril development work produces adequate quantities, silicon carbide fibril paper will be produced and rolled into the required geometric shapes for the heat exchanger tube, joints and elbows. These shapes will be treated with a bindering process capable of liquid and pressure impermeability at high temperatures in a corrosive environment.

The major limitations of the previous “state of the art” fibril growth were the high temperatures required (1600oC to 1700oC), the slow fibril growth rate (~0.17 mm/hr), and the large quantity of excess of expensive methyl trichlorosilane gas, which is wasted1. The commercial process is complicated by the processing of large quantities of hydrogen gas at high temperatures and the generation of corrosive hydrochloric acid2. This current work continues a proof-of-concept, microwave based, VLS process development completed in 1999 by ReMaxCo. The catalyst was heated to the experimental temperature (1200oC to 1300oC) while a mixture of MTS and hydrogen were introduced into an aluminum oxide ceramic container. The MTS is dissociated and the carbon and silicon components are dissolved into the catalyst. The catalyst saturates and precipitates silicon carbide onto the surface of the growing fibril. These experiments yielded fibril growth rates of 0.75 mm/hr. That was an improvement of approximately 4.4 times faster than the best graphite furnace runs3. Volume scale up of the process was demonstrated.

The current project moves the commercial process development to a pilot scale commercial reactor that will lead to sufficient quantities of fibrils to allow expanded work by Oak Ridge National Laboratory and combustion chamber component suppliers to develop heat exchanger tubes, robust combustion chamber tiles and hot gas filters.

A semi-continuous, microwave heated, vacuum reactor was previously designed, fabricated and tested in earlier experiments. The major obstacles that had to be overcome during this current project was the questionable performance of the reactor. The original design of the reactor focused the microwaves in such a manner that they missed the catalyst/fibrils growth zone. The microwaves did react with the insulation and the reactor was heated by coupling with the insulation. Modifications were made to the reactor to focus the microwaves on the catalyst. SiC Fibrils were produced using both MTS and Starfire SP4000 (a commercial silcon carbide organic precursor material) as feed-gas precursors. Both precursors produced fibrils at temperatures of less than 1000oC. The new Starfire SP4000 produced fibrils as low as 800oC, without the use of hydrogen and without producing the hazardous hydrochloric acid.

TECHNOLOGY APPROACH

The previous low-productivity, semi-continuous, microwave heated, vacuum reactor is shown in Figures 1.

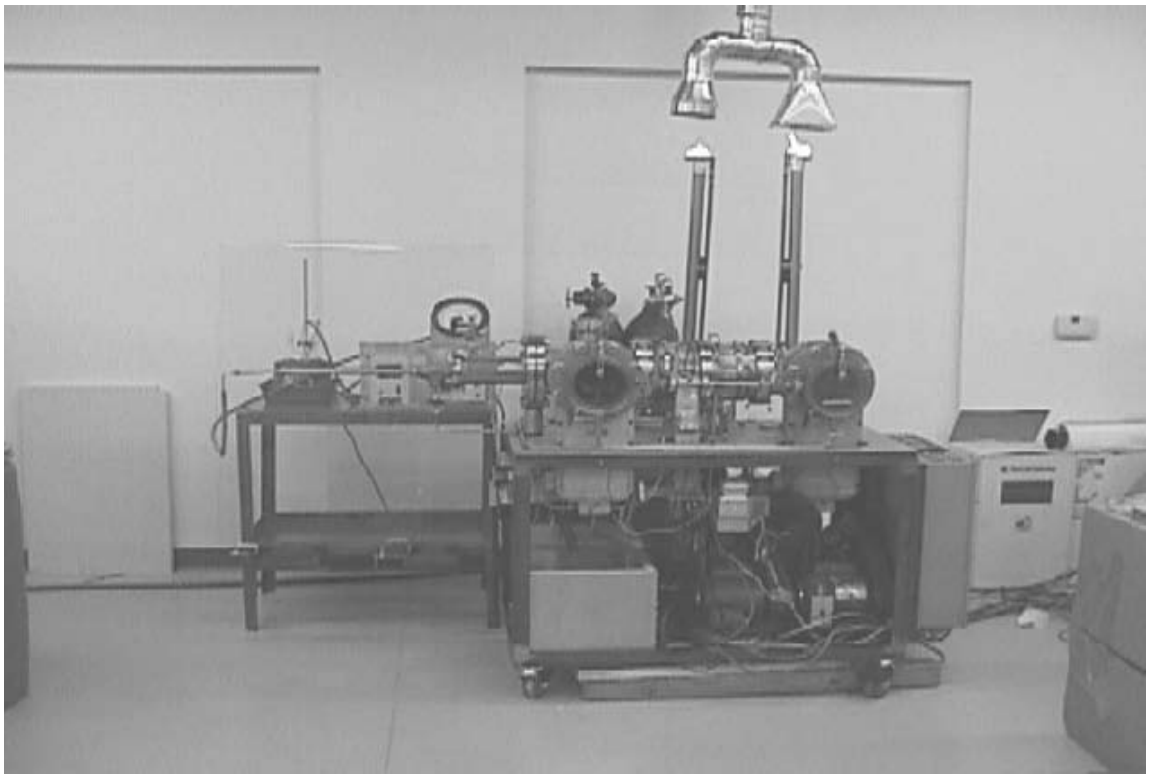

Figure 1. Fibril microwave reactor in operation

The boundary conditions for the experiments were determined by running a computer thermodynamic analysis on the raw materials system. The results are shown in Figure 2.

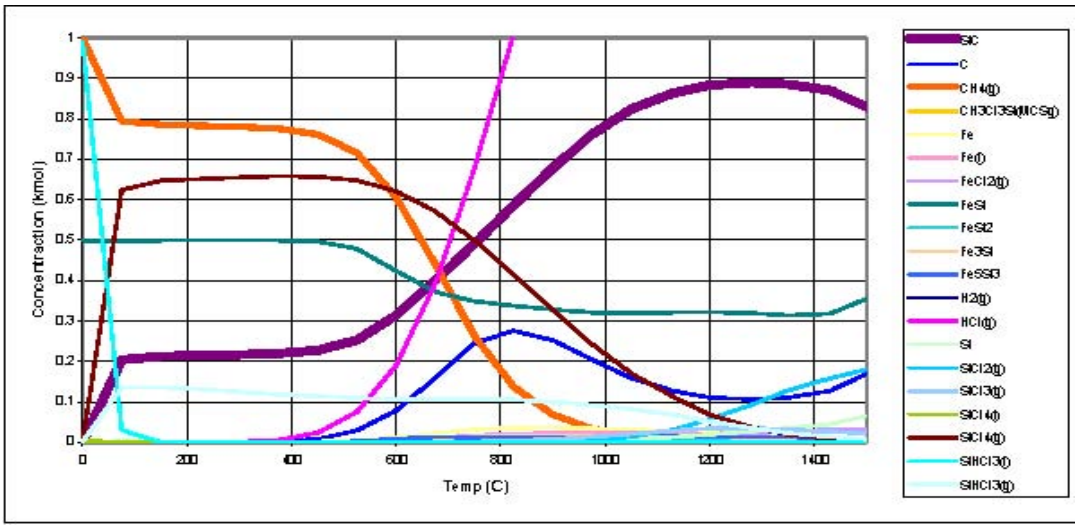

Figure 2. Thermodynamic analysis showing optimum temperature range for growing silicon carbide fibrils

Cylindrical aluminum oxide reaction boats were coated, on the inner surface, with a catalyst and placed into the reactor under a light vacuum. Several catalyst options were tested including ferrous silicon, iron powder and several mixtures thereof. A series of reaction boats traveled, one at a time, through the reactor. Each boat is first preheated with resistance heaters to 850o C to 900o C, measured by a Type K thermocouple. Each reaction boat was then moved, in turn, to the microwave heated section. The catalyst is heated to the required temperature of 1200oC to 1300oC, measured by a Mikron M90-Q Infrared Pyrometer while a mixture of MTS (methyl trichlorosilane) and hydrogen were introduced into the catalyst-coated area of the boat. The MTS forms the carbon and silicon components, which dissolve into the catalyst to grow the Fibrils.

Once the furnace was debugged and running consistently, process optimization experiments were conducted to achieve fibril growth and define operating parameters. The operating results from these experiments were used to design a second-generation microwave reactor to solve the problems that became apparent in operating the current reactor. There was also a group of experiments to identify a less hazardous raw material gas than the methyl trichlorosilane.

EXPERIMENTAL PROCEDURES

A number of runs were made to debug the microwave reactor and the reaction gas feed system. The MTS reaction gas is generated by bubbling hydrogen through liquid MTS in a steel container. The steel container was replaced with a transparent, heated glass bubbler to allow the operator to view the hydrogen flow through MTS liquid and control the vapor pressure of the M TS gas (Figures 3 and 4).

Figure 3. Metal bubbler

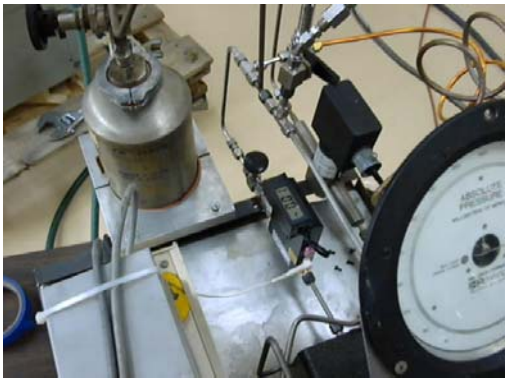

Figure 4. Glass bubbler

Silicon Carbide Fibrils Reaction Vessel Runs

The fibril catalyst seed paint was prepared using metallurgical grade –325 mesh ferrous silicon mixed in a dispersant paint purchased from YZP Corporation in a 1:1 ratio. The paint was applied in a 0.1-millimeter thick coating to the interior diameter of a 7.6 centimeter diameter x 7.6 centimeter long high-density aluminum oxide cylinder. When the paint dried, the boats were loaded in the vacuum chamber of the microwave reactor. A boat that exhibits some Fibril growth is shown in Figure 5

Figure 5. Ceramic boat with microwave grown Fibrils

The microwave reactor was evacuated by vacuum pumps to approximately 30 mTorr, and then flushed with nitrogen gas at a pressure of 150 Torr. After the nitrogen flush, the furnace was backfilled with hydrogen gas to a pressure of 150 Torr and maintained at less than 180 Torr throughout the microwave fibril growth run. The preheat zone resistance heaters were stabilized at 800oC and held there throughout the run. Each one of the two 2-KW microwave sources was stabilized at 1.8-KW. Hydrogen flow was run through the MTS bubbler at a rate of 0.13 liters/minute for a period of one to three hours. Figure 6 shows the reaction zone during microwave assisted silicon carbide fibril growth.

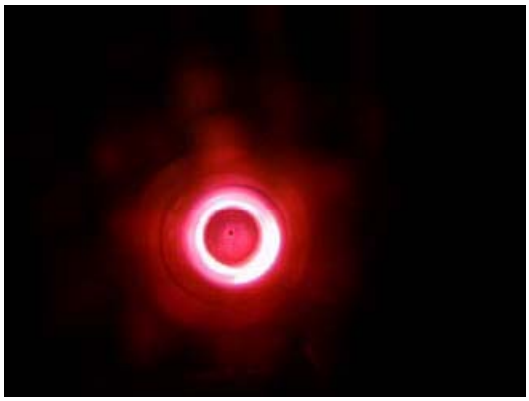

Figure 6. Fibril growth in the microwave field. Glowing annulus is the catalyst layer reacting to the microwave energy

Additional optimization testing was conducted replacing ferrous silicon with iron particles, then a mixture of 50% ferrous silicon and 50% iron by weight. In addition, the procedure described above was tested replacing the MTS liquid with a SP4000, a polysilymethylene CVD silicon carbide precursor produced by Starfire Systems. The SP4000 can be reacted in nitrogen gas rather than the more dangerous hydrogen required by the MTS liquid and gas.

Typical Run Sheet:

5/8/02

Reactant Gas	SP4000
Atmosphere	Hydrogen
Catalyst	Fe
Fibrils Observed	Yes

A nitrogen purge was used during start up.
14:45 Hydrogen was turned on

Time	MZ1 (kW)	MZ2 (kW)	GZ1 (C)	GZ2 (C)	Press. (Torr)	Main Flow (lpm)	Bubbler Flow (lpm)	Temp. (C)
15:00	1.80	1.80	530	484	175	0.52	0.08	NR
15:04	Some glow appeared in spots							
15:07	MZ1 and MZ2 power adjusted to prevent arcing. GZ set pts to 600C							
15:18	GZ set points to 700C							
15:20	GZ set points to 800C							
15:30	1.80	1.80	NR	NR	NR	0.52	0.13	NR
16:30	1.90	1.90	801	734	165	0.52	0.13	854
16:45	2.00	2.00	801	735	160	0.52	0.13	904
17:00	2.00	2.00	802	738	185	0.51	0.13	909
17:40	2.00	2.00	802	744	175	0.51	0.13	922
17:50	2.00	2.00	800	742	180	0.51	0.13	921
18:00	2.00	2.00	800	745	160	0.51	0.13	924
18:10	2.00	2.00	800	745	170	0.51	0.13	924
18:30	2.00	2.00	800	743	175	0.51	0.13	920
19:00	2.00	2.00	800	745	165	0.51	0.12	921

RESULTS

The only fibril growth in the initial microwave field configuration happened after being in the microwave growth chamber for approximately three hours. The microwave intensity was measured in the fibril growth area and found to be zero. The furnace was rebuilt to focus more of the microwave field in the fibril growth zone. This improved the fibril growth quality and time. The fibrils grown in this sequence are shown in Figures 7, 8, 9, and 10. The fibril quality is good, but the fibril yield was very low. They are 2 to 5 micrometer diameter in size.

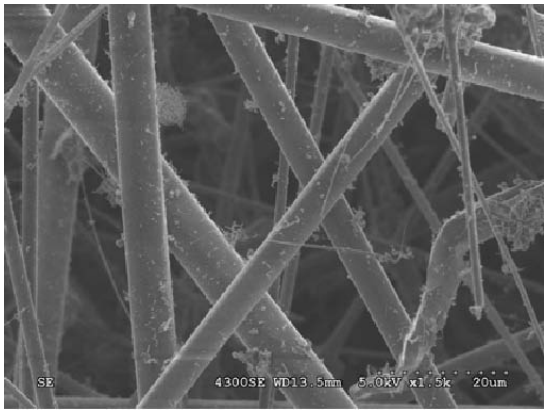

Figure 7. Fibril growth on the boat by digital camera

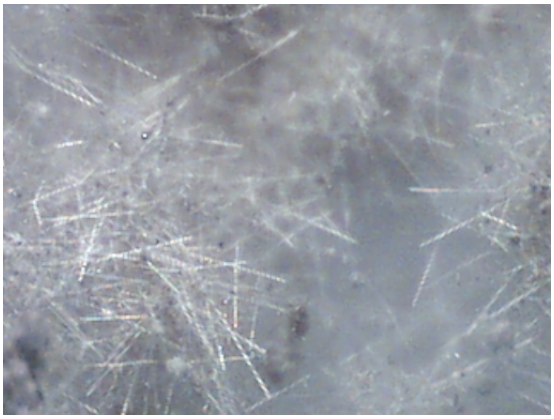

Figure 8. Electron microscopy of same Fibril product

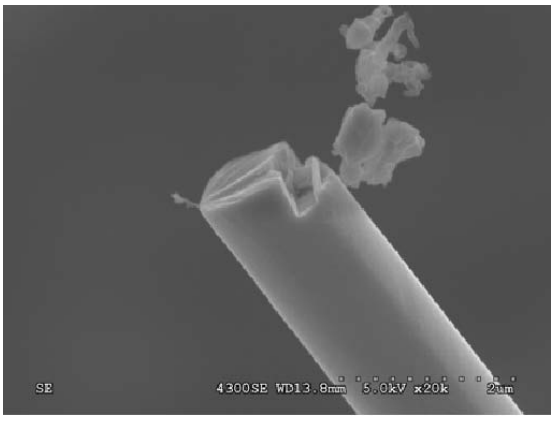

Figure 9. Electron microscopy shows perfect single crystal growth

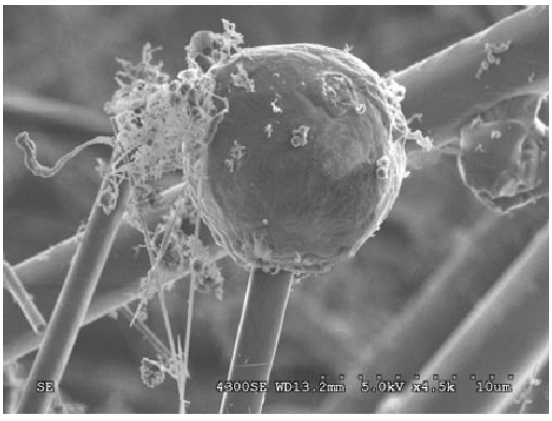

Figure 10. Fibril growth balls indicate true VLS growth process

There are a number of issues with the fibril reactor that need to be improved and will be implemented in the next phase of this work. The microwave field uniformity was poor and can be significantly improved. The catalyst paint tended to flake off the tops and sides of the round ceramic boats. Flat ceramic plates will be more efficient. Finally, the MTS gas feed mechanism had very little mass flow control and an irregular feed pattern to the fibril growth zone. A more accurate mass flow controller and a manifold-mixer are needed for the reaction gas distribution.

One of the problems with scaling the fibril development to a large-scale commercial process is the generation of significant quantities of hydrochloric acid in the off-gas stream. This acid destroys the vacuum system and the exhaust ducts. Silicon carbide fibrils were produced using the SP4000 in nitrogen. An unexpected advantage, beyond the elimination of acid in the off-gas, was the fact that fibrils grew at 850oC. The MTS reaction required a temperature of 1200oC to 1300oC. Fibrils grown in the SP4000 experiments are shown in Figures 11, 12, 13 and 14. They are 5 to 15 micrometers in diameter. Melt growth balls in Figure 13 were observed with the fibrils indicating that they were VLS growth products.

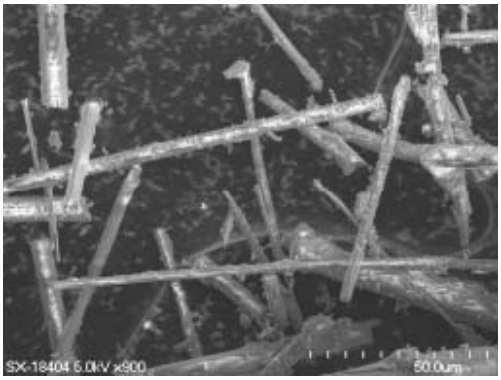

Figure 11. Scanning electron microscopy of SP4000 Fibrils

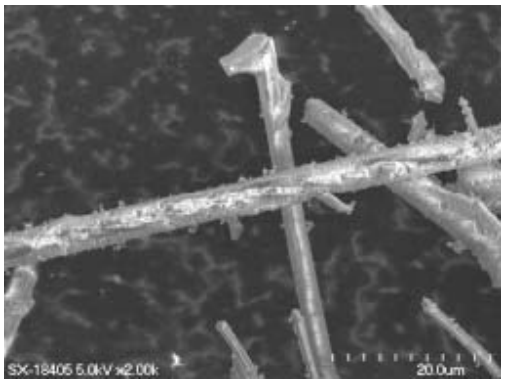

Figure 12. 2,000X magnification showing Fibril size

Figure 13. Melt growth balls indicating vapor-liquid-solid

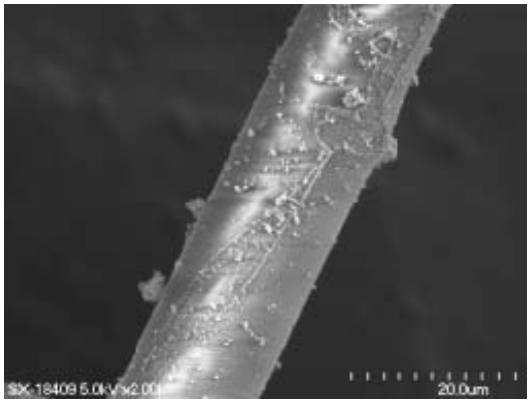

Figure 14. Fibril from growth ball

CONCLUSIONS ON THE FIRST GENERATION PILOT REACTOR

These experiments demonstrated that silicon carbide fibrils could be produced at temperatures as low as 850oC, as compared to the 1700oC in the previous graphite furnaces. The fibril growth rate has been increased by a factor of four over previous technologies. The microwaves exhibited a significant effect on lowering the fibril reaction temperature and accelerating the fibril growth process. The SP4000 silicon carbide precursor provides a reaction without hazardous off-gas products, with a projected future volume cost of $600/liter (kilogram).

A commercial process is feasible by overcoming the equipment engineering problems encountered on this project. Those include a uniform microwave field, good control and uniform distribution of reactant gases, and the use of flat ceramic reaction boats. These improvements will get the commercial process

closer to the $300 per pound project goal.

With these improvements in place, one can improve on previous technology to accomplish:

1 Lower energy consumption
2 Higher growth rates
3 Reduced reactant gas waste
4 Lower cost raw materials
5 Consistent quality fibrils product

SECOND GENERATION FIBRIL REACTOR

Introduction

The First Generation Fibril Reactor exhibited inflexible problems with microwave field distribution and control, as well as, non-uniform reactant gas feed control and distribution. A Second Generation Fibril Reactor has been designed and fabricated to overcome these principal issues. Solutions were insured by employing the design services of experienced experts in the fields of chemical vapor deposition gas distribution (MS&E Resources) and microwave field control (RF Technologies). The total system design was coordinated by an experienced furnace designer and fabricator.

Reactor Configuration

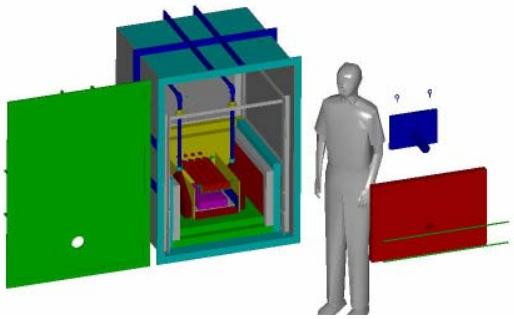

Figure 15. Reactor assembly

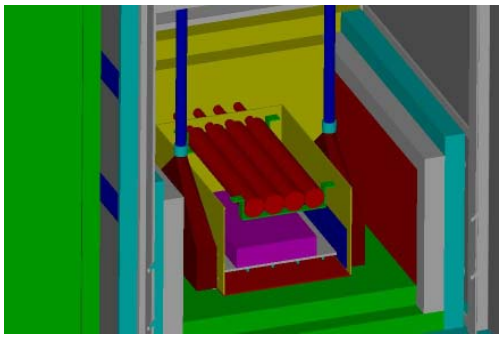

Figure 16. Fibril Growth Area

Figure 15 shows the entire reactor assembly inside the vacuum chamber. Figure 16 shows the fibril growth zone. The round tubes above the flat plat are the microwave applicators (red), designed to produce a uniform and controllable microwave field on the aluminum oxide flat plate (purple) containing the fibril seed crystals. The reactant gases are feed through the triangular gas plenums (burgundy) across the seeded growth plates. Electrical heating elements are located in the wall or the reaction chamber to maintain the chamber at a uniform 800oC. The microwave energy boosts this temperature at the seed crystal surface to 1,000oC to assure that the reactant gases only react with the seed crystals to prevent reactant gas waste and silicon carbide growth on the reaction chamber walls.

Reactor Fabrication

Figure 17. Fabricated Second Generation Fibrils Reactor

Figure 17 shows the Second Generation Fibrils reactor, as fabricated. The left view is the full unit. The middle view is the microwave units and the microwave coaxial feed system. And the right view is the fibrils growth chamber, with fibril boats coated with seed crystals.

FUTURE WORK

The Second Generation Fibrils Pilot Reactor, incorporating all of the improvements described above, should be capable of producing 200 grams of fibrils per day. This reactor started in May 2007, tested, process optimized, then operated to supply sample quantities to various researchers in the Fossil Energy Materials Program and in commercial applications. Samples should be ready for shipment to customers by August 2007. Success in testing and demand for volume product will lead to the design of a continuous reactor capable of commercial volumes of silicon carbide fibrils.

ACKNOWLEDGEMENTS

The author acknowledges the support of the U.S. Department of Energy's (DOE) Fossil Energy through the Advanced Research Materials Program under the project direction of Dr. Roddie R. Judkins for the funding of this work. Gratitude is expressed to Oak Ridge National Laboratory's High Temperature Materials Laboratory for the electron microscopy work of Larry Allard and Larry Walker and to Microwave Materials Technology for microwave equipment engineering and fabrication.

REFERENCES

1. P.D. Shalek, et all, "Scale-Up and Optimization of the VLS Growth Process for Beta-SiC Whiskers for the Period of April 1982 – September 1989", DARPA Final Report, DOE/OAR&TD Topical Report, LA-12119, November 1991.

2. R.W. Ohnsorg, W.E. Hollar, Jr., and S.K. Lau, "Engineering Scale Development of Vapor-Liquid-Solid (VLS) Process for the Production of Silicon Carbide Fibrils" Phase II Report, ORNL/Sub/90-SD861/02, April 1995.

3. R.D. Nixdorf, "Development of a Commercial Process for the Production of Silicon Carbide Fibrils", Phase I Final Report, ORNL/Sub/98-SU604/01,

ACTIVATED CARBON COMPOSITES FOR AIR SEPARATION

Frederick S. Baker
Oak Ridge National Laboratory, Bethel Valley Road, P. O. Box 2008, Oak Ridge, TN 37831-6087
E-mail: bakerfs@ornl.gov; Telephone: (865) 241-1127; Fax: (865) 576-8424

Cristian I. Contescu
Oak Ridge National Laboratory, Bethel Valley Road, P. O. Box 2008, Oak Ridge, TN 37831-6087
E-mail: contescuci@ornl.gov; Telephone: (865) 241-3318; Fax: (865) 576-8424

Costas Tsouris
Oak Ridge National Laboratory, Bethel Valley Road, P. O. Box 2008, Oak Ridge, TN 37831-6087
E-mail: tsourisc@ornl.gov; Telephone: (865) 241-3246; Fax: (865) 241-4289

Joanna McFarlane
Oak Ridge National Laboratory, Bethel Valley Road, P. O. Box 2008, Oak Ridge, TN 37831-6087
E-mail: burchelltd@ornl.gov; Telephone: (865) 576-8595; Fax: (865) 576-8424

ABSTRACT

Large-scale application of oxygen-blown coal gasification, currently the most effective and efficient approach for production of hydrogen from coal is still in need of a cost-effective means of enriching O_2 concentration in air. This project is focused on the development of activated carbon composites for the production of an oxygen-enriched air stream suitable for coal gasification. The method proposed exploits the molecular sieving properties of porous materials, including activated carbon. The potential to separate O_2 and N_2 from air is based on the different diffusion rates of the two molecules in the composite, which has been previously demonstrated. In addition, it has been recently discovered that the peculiar magnetic properties of O_2 molecules induce sizable magnetodesorption effects at equilibrium in a static system at room temperature and under moderate magnetic field intensity. The effects were attributed to a transition in the magnetic state of O_2 molecules; i.e., from paramagnetic in the gas phase to a non-magnetic state when confined in the micropores of the adsorbent. This effect was observed only when the carbon adsorbent was pre-loaded with super-paramagnetic nanoparticles of Fe_3O_4, and was explained attributed to the local enhancement of magnetic field caused by magnetite particles supported on the microporous adsorbent.

In continuation of the development of composite materials for air separation based on molecular sieving properties and magnetic fields effects, several molecular sieve materials were tested in a flow system, and the effects of temperature, flow conditions, and magnetic fields were investigated. New carbon materials adsorbents, with and without pre-loaded super-paramagnetic nanoparticles of Fe_3O_4 were synthesized; all materials were packed in chromatographic type columns which were placed between the poles of a high intensity, water-cooled, magnet (4 Tesla). In order to verify the existence of magnetodesorption effect, separation tests were conducted by injecting controlled volumes of air in a flow of inert gas, while the magnetic field was switched on and off. Gas composition downstream the column was analyzed by gas chromatography and by mass spectrometry. Under the conditions employed, the tests confirmed that N_2 – O_2 separation occurred at various degrees, depending on material's intrinsic properties, temperature and flow rate. The effect of magnetic fields, reported previously for static conditions, was not confirmed in the flow system. The best separation was obtained for zeolite 13X at sub-ambient temperatures. Future directions for the project include evaluation of a combined system, comprising carbon and zeolite molecular sieves, and testing the effect of stronger magnetic fields produced by cryogenic magnets.

INTRODUCTION

Carbon fiber composite molecular sieves (CFCMS) have been developed at Oak Ridge National Laboratory (ORNL) as a novel class of adsorbent which combines tailored gas adsorption properties, good gas permeability, and electrical conductivity.[1-3] The structure of CFCMS comprises carbon fibers (about 10 μm in diameter) bonded at their contact points by a continuous carbon skeleton that is electrically conductive. The combination of open structure, microporosity, and electrical conductivity allows the material to be used in a regenerative, electrical swing adsorption (ESA) system.[4-6] This is the analog of pressure swing adsorption (PSA) where regeneration of the adsorbent is facilitated by resistive heating of the carbon monolith.

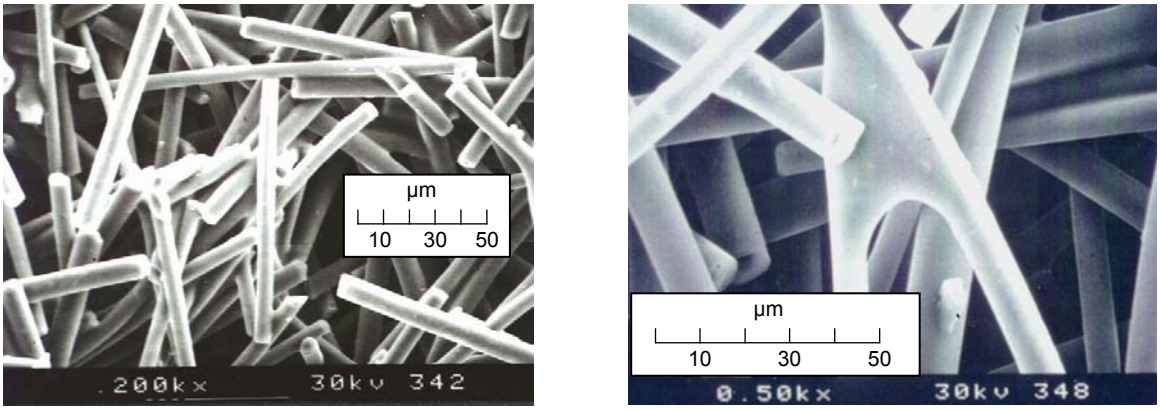

Figure 1 - SEM images showing the structure of CFCMS material

Preliminary work demonstrated that CFCMS material has the potential for separating O_2 and N_2 in air. [7] Further findings also indicated that the efficiency of separation could be increased by better tailoring the pore size distribution to very narrow micropore sizes (< 2 nm). Based on characterization of a series of CFCMS samples, it was found that O_2 was more rapidly adsorbed on the carbon fiber than N_2, and with higher equilibrium uptakes, provided the fiber contained a high proportion of very narrow micropores. The conclusion was that CFCMS activated under certain conditions is able to separate O_2 and N_2 from air based on kinetic effects, i.e. the difference in diffusion rates of the two molecules in the network of narrow micropores in the carbon fiber structure. Since O_2 molecules are only slightly smaller in size than N_2 molecules (their kinetic diameters are 3.62 nm and 3.80 nm), achieving selectivity requires a carbon molecular sieve with very narrow and well controlled pore size distribution in the critical range of 3-5 nm. Although controlling the pore size of carbon materials is achievable, the almost perfect separation selectivity offered by zeolites under favorable conditions is hard to match.

Addition of a magnetic field was also investigated in an attempt to further enhance the potential of molecular sieving effects. On theoretical grounds it was hypothesized that adsorption of O_2 should be influenced by magnetic fields whenever adsorption is accompanied by a transition between paramagnetic and diamagnetic states. Although the literature on magnetic field effects on adsorption and desorption is scarce, several examples show that the occurrence of magneto-adsorption-desorption effects strongly depends on the nature of solids and gases, temperature, and the intensity of magnetic fields. [8-12] An appropriate combination of these factors could lead to a separation process based on selective adsorption from a mixture of gases. In this context it has been reported that separation of O_2 and N_2 in high magnetic fields is in principle plausible in a steady magnetic field through adsorption of paramagnetic O_2 molecules into micropores of porous ferromagnetic solids. [13]

In order to verify this theoretical prediction, a series of measurements of O_2 adsorption isotherms was carried out in static, equilibrium conditions.[14] In preliminary tests it was found that the amount of O_2 adsorbed at equilibrium was lower (by about 6% at 0.1 MPa) in presence of a weak magnetic field (0.8 Tesla) than in absence of the magnetic field. Although small, this magnetodesorption effect was sizable and observed repeatedly at room temperature for activated carbon fibers loaded with 10 wt % of superparamagnetic magnetite nanoparticles (Fe_3O_4, average size 16 nm). The results of these preliminary tests motivated continuation of the project for additional verification and confirmation of the effect at higher magnetic field intensities and in dynamic conditions; in the new series of tests reported here, a flow system, rather than static, was used to better simulate the conditions of air separation for practical applications. Tests for air separation in absence of a magnetic field were also carried out.

DISCUSSION OF CURRENT ACTIVITIES

MATERIAL PREPARATION AND CHARACTERIZATION

Carbon Fiber Composite Molecular Sieves (CFCMS)

A series of CFCMS composites were used as support for loading a dispersed magnetic phase, magnetite. The CFCMS materials were selected based on their microporous structure and BET surface area values.[15] The surface and porosity properties were characterized by adsorption of N_2 at 77 K and by adsorption of CO_2 at 273 K.[16] All adsorption measurements were made using the Autosorb 1 instrument (Quantachrome). Adsorption data were further processed to calculate the pore size distribution of porosity and surface areas using the density functional theory (DFT) in the non-local density approximation. [16-19] The DFT software available from Quantachrome was used for calculations. Figures 1 and 2 show the results of pore size distribution in form of cumulative and differential plots. The results obtained from N_2 adsorption at 77 K (lowest accessible pores ~ 10 Å) and CO_2 adsorption at 273 K (pores between 3 and 12 Å) are overlapped in both plots.

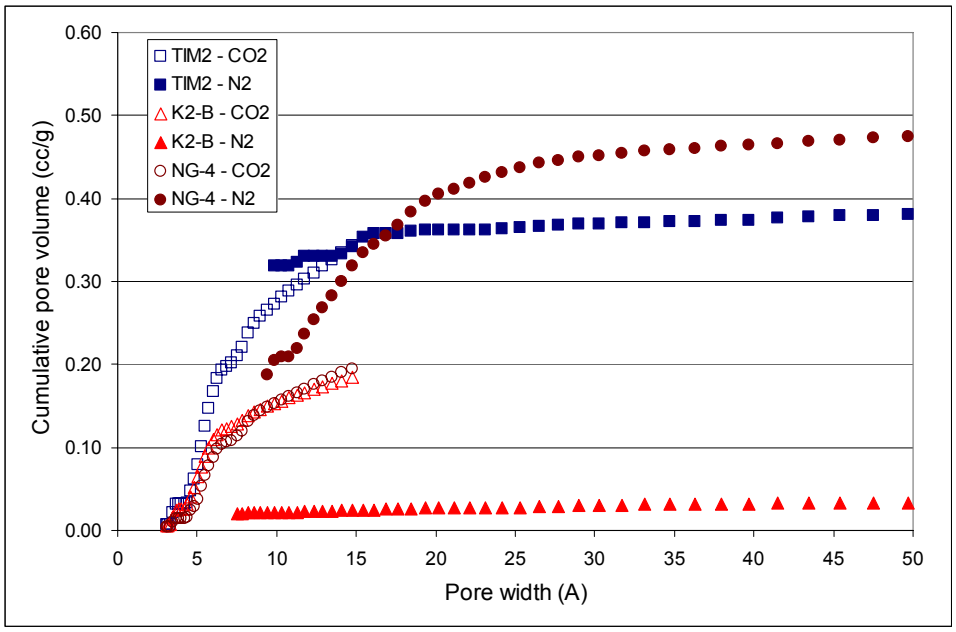

Figure 1: Cumulative pore volume distribution as a function of pore widths. Data calculated by DFT method from N_2 adsorption and CO_2 adsorption are plotted on a common scale.

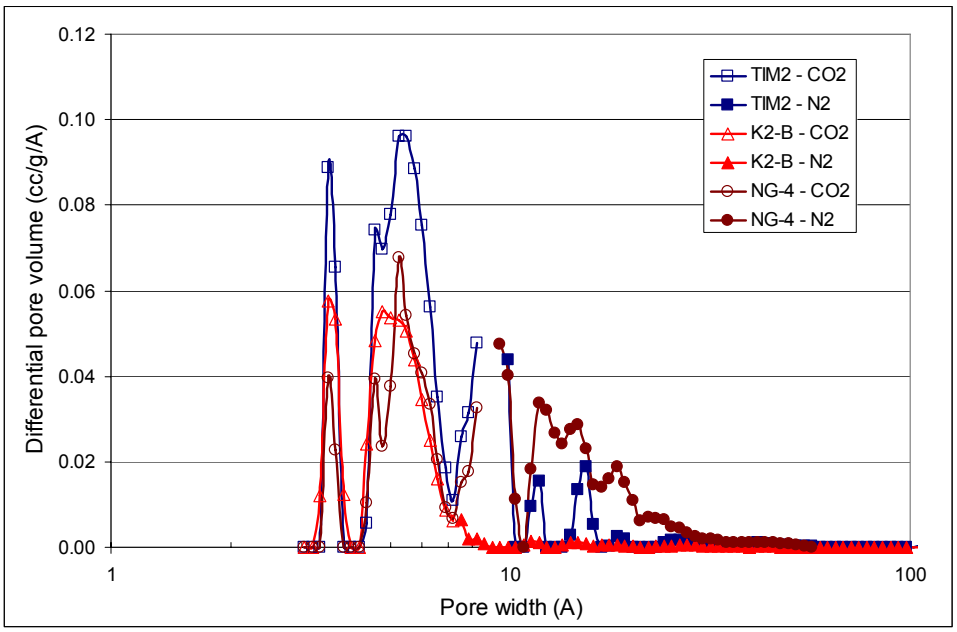

Figure 2: Differential distribution of pore volume as a function of pore width. Data calculated by DFT method from N_2 adsorption and CO_2 adsorption are plotted on a common logarithmic scale.

The results presented in Table 1 include the surface area values calculated from N_2 adsorption data using the BET equation, and from the N_2 and CO_2 adsorption data using the DFT method; the pore volume calculated from N_2 and CO_2 adsorption data using the DFT method; and the average pore width calculated from the same adsorption data using the DFT method. Comparing the results reveals several differences between the three samples:

- Sample NG-4 has a relatively large surface area based on BET result (1123 m^2/g) and DFT result from N_2 adsorption (923 m^2/g). In contrast, CO_2 adsorption reveals lower surface area (600 m^2/g), suggesting blockage of pore entrance by bulky oxidized surface groups, that may have been formed during the activation process.
- Sample TIM-2 has a slightly lower BET surface area (964 m^2/g) and the DFT results for N_2 adsorption (960 m^2/g) and CO_2 adsorption (1090 m^2/g) are not much different. For this sample, both molecular probes used as adsorbate (N_2 and CO_2) give essentially the same pore volume (0.34 – 0.39 cc/g), which is a strong indication that the material is largely microporous. Indeed, the average pore width calculated by DFT method is 9.8 Å (based on N_2 adsorption) or 5.2 Å (based on CO_2 adsorption).
- Sample K2-B has a very small surface area value based on N_2 adsorption data (73 m^2/g from BET equation; 85 m^2/g from DFT method). This contrasts with the large surface area measured by CO_2 adsorption (640 m^2/g based on DFT method), and is a strong evidence that the material contains very narrow micropores that cannot be accessed by N_2 at 77 K, but are accessible to CO_2 at 273 K. With an average pore width of 7.5 Å (based on N_2 adsorption) or 3.5 Å (based on CO_2 adsorption), the K2-B material is expected to have the most pronounced molecular sieving properties.

Distribution of porosity by pore width is different for the three materials. While all carbons have narrow micropores between 5 and 7 Å (Fig. 2), the corresponding volume is larger for sample TIM-2 than for

samples K2-B and NG-4. In addition, samples TIM-2 and NG-4 have large micropores in the range of 7 – 20 Å; this range of micropores is missing from sample K2-B.

Table 1 Surface area and porosity characteristics of base CFCMS materials selected for tests

	Surface area			Pore volume		Average pore width	
CFCMS	BET N2	DFT N2	DFT CO2	DFT N2	DFT CO2	DFT N2	DFT CO2
	m2/g	m2/g	m2/g	cc/g	cc/g	A	A
NG 4	1123	923	600	0.476	0.195	9.4	5.2
TIM 2	964	960	1090	0.394	0.344	9.8	5.2
K2-B	73	85	640	0.035	0.185	7.5	3.5

Magnetite-loaded CFCMS

As explained in the Introduction, previous results have shown that moderate intensity magnetic fields affect the adsorption of O_2 at equilibrium (at room temperature and maximum 0.1 MPa) on magnetite-loaded microporous activated carbon composites (CFCMS). [14] The effect was explained [20] on thermodynamic grounds after Ozeki and Sato [13] assuming that the magnetic state of O_2 confined in narrow micropores of activated carbon changes from paramagnetic (for free O_2) into random magnetism (for O_2 clusters confined. The decrease of magnetization manifested in presence of an applied magnetic field is expected to induce an increase in pressure (i.e., desorption) of O_2. The effect is too weak to be observed on pure microporus adsorbents (such as CFCMS), but was observed in static conditions with magnetite-doped CFCMS, because of the local enhancement of magnetic fields in nanopores induced by superparamagnetic Fe_3O_4 nanoparticles. [14]

In order to verify the occurrence of this effect in dynamic conditions, a series materials loaded with Fe_3O_4 were synthesized. The carbon supports selected were two granular mesoporous carbons derived from wood (WV A-1500 and SA-30, both from MeadWestvaco) and the CFCMS sample NG-4. The cold precipitation method used previously [21] was employed for loading magnetite on these carbons. The method consists essentially in precipitation of Fe_3O_4 from aqueous solutions containing $Fe(NO_3)_3$ and $FeSO_4$ in the stoichimetric ratio Fe^{III} : Fe^{II} = 2:1 necesary for formation of the mixed oxide $Fe^{III}{}_2O_3.Fe^{II}O$. The precipitation agent is concentrated ammonia solution and the precipitation occurs at pH 10-11. No heating is necessary. In contrast with the ceramic method for synthesis of magnetite, which involves high temperature processes and results in a highly sintered product, the cold synthesis method preserves the nanosized colloidal particles of magnetite.

It was found that the above procedure can be used with the CFCMS sample NG-4, yielding uniformly loaded carbon particles (about 1 – 1.5 mm in size) and a clear residual solution that contained only traces of iron salts. The Fe-NG-4 sample (10 % Fe_3O_4) was obtained by this method. X-ray analysis showed the presence of a Fe_3O_4 phase with small average crystallite size. However, the precipitation method described above could not be used with the wood-derived mesoporous carbons because of their high phosphorus content. It was found that these carbons have been activated with phosphoric acid, and the residual phosphorus on their surface perturbed the precipitation reactions leading to formation of Fe_3O_4 in presence of ammonia as described above. Rather than leading to homogeneous deposits of magnetite on carbon, preferential complexation of Fe^{III} by surface phosphorus caused deposition of Fe_2O_3 (non magnetic) and precipitation of ferrous hydroxide in the aqueous phase.

Zeolite

A granular sample of zeolite X13 was also used for air separation tests in the flow system. Before packing in a chromatographic-type column, zeolite beads (1.5 - 2 mm) were pretreated at 140 ^{o}C for dehydration.

Experimental setup

All adsorbents in form of granules (1-2 mm) were packed in chromatography-type columns (copper tube, 50 cm long, ¼ inch diameter) which were rolled into a 3-coils spiral (5 cm diameter) that was placed flat between the poles of a water-cooled electromagnet (Applied Magnetics Lan, model 2V1). The maximum field intensity between the magnet poles was 1.5 Tesla.

Before packing in chromatography-type columns, all adsorbents were pre-dried overnight at 140 ^{o}C. After packing in the column all adsorbents were conditioned overnight in a flow of He (50 cc/min) at 150 – 200 ^{o}C. After conditioning the adsorbent, the flow of He was adjusted to the desired value for air separation tests (15 – 30 cc/min). The tests were performed by injecting controlled volumes of air through a septum upstream of the adsorbent column, and analyzing the composition of the gas exiting from the column.

In a first series of tests the gas composition analysis was performed with a Hewlett Packard 5890 series II gas chromatograph (GC) equipped with thermal conductivity (TC) detector. The chromatograph was operated by Agilent ChemStation software for GC systems. It was found that the difference between thermal conductivities of oxygen and nitrogen is not large enough to afford separate identification of the components in a mixture using the TC detector. To correct that, the GC analysis of gas composition downstream the adsorbent column was replaced later by analysis by mass spectroscopy. A Vacuum Technology Inc. mass spectrometer (MS) was used, which was operated by the manufacturer's software (VTI). The instrument was connected through a flow controlling valve and capillary tube to a derivation of the main gas line downstream the adsorbent column. This latter setup was proven more efficient for separate detection of oxygen and nitrogen concentration breaking through the column after air injection, even though the two components were poorly separated on the column.

AIR SEPARATION BASED ON MOLECULAR SIEVING EFFECTS

Carbon fiber composite molecular sieves (CFCMS)

Figures 3 shows examples of mass spectrometer signals for N_2 (blue line) and O_2 (red line) recorded after the breakthrough of air following an injection of 5 cc in a flow of He (30 cc/min) through a 50 cm long column filled with CFCMS TIM-2. The tests were done a various temperatures and at constant flow rate, which was vented out at atmospheric pressure. The pressure shown on this plot (in the range of 10^{-5} Torr) is the actual pressure in the mass spectrometer chamber.

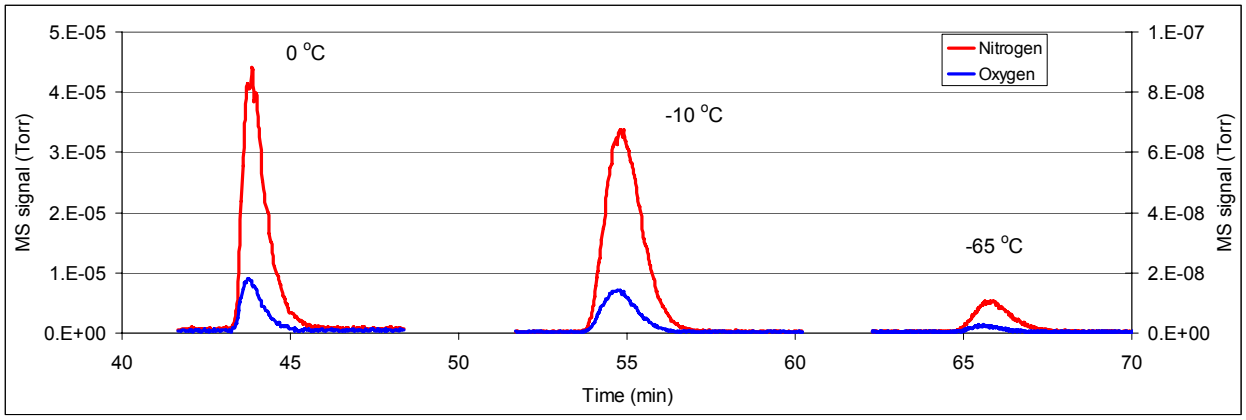

Figure 3: Example of breakthrough nitrogen and oxygen mass spectrometer signals measured for sample TIM-2 after injection of 5 mL air at various temperatures. Flow rate of He carrier was 30 cc/min.

The result of Fig. 3 shows that the peaks corresponding to N_2 and O_2 exiting the column were overlapped. The area under each peak corresponds to the concentration of that component in the mixture and reflects the air composition (roughly 21 vol % O_2; 79 vol % N_2, traces of Ar, CO_2 H_2O etc). In order to better evaluate the effectiveness of N_2 – O_2 separation, the mass signals for N_2 and O_2 were normalized to the peak maximum of each component; the results for four different temperatures are shown in Fig. 4.

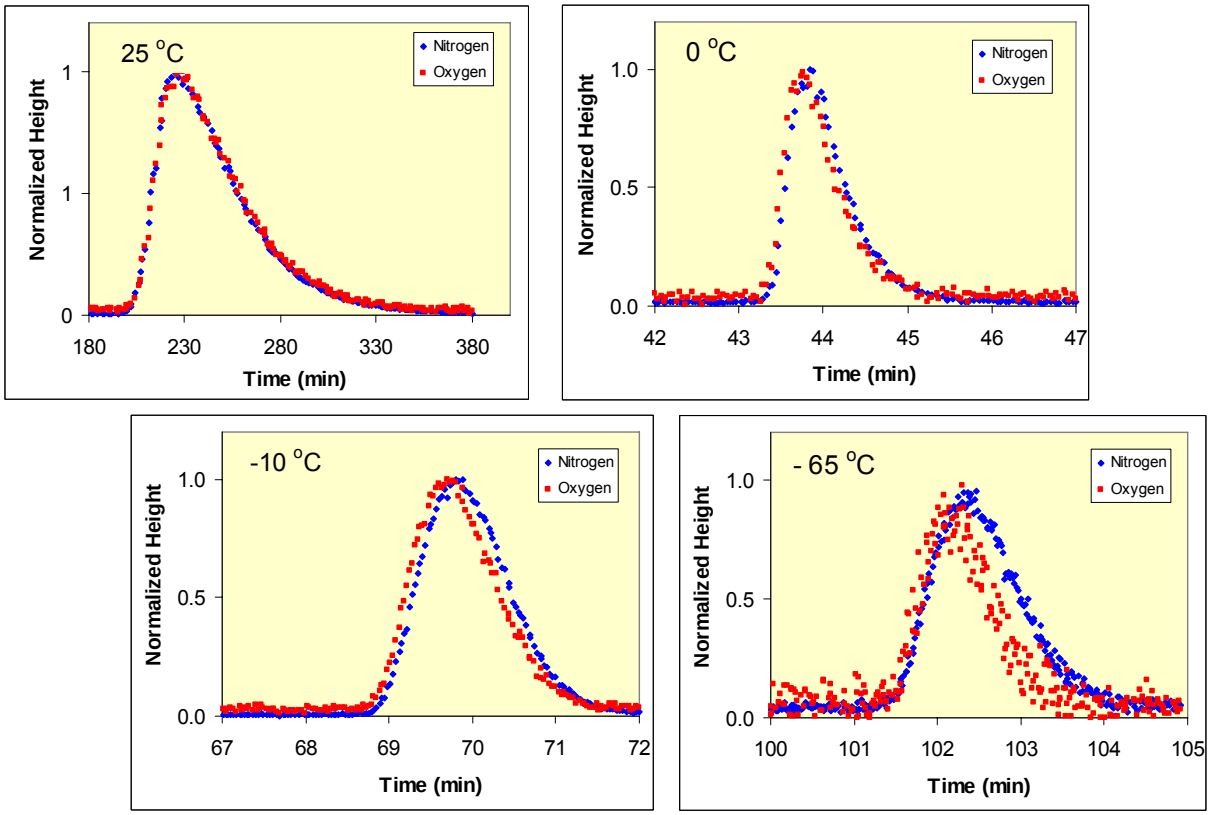

Figure 4: Normalized mass spectrometer signals for N_2 (blue) and O_2 (red) breaking through a 50 cm column packed with CFCMS TIM-2 material after injection of air at various temperatures. The flow rate of carrier gas (He) was 30 cc/min.

This test result shows that (1) separation of $N_2 - O_2$ is possible, with the N_2 peak being delayed with respect to the O_2 peak; (2) the delay of N_2 peak increases as the temperature is lowered below room temperature; (3) the efficiency of separation was not high enough in the test conditions selected, but could be improved by adjusting the flow rate, length of column, and the size of injection.

Figure 5 shows the results of a similar test with the CFCMS material K2-B.

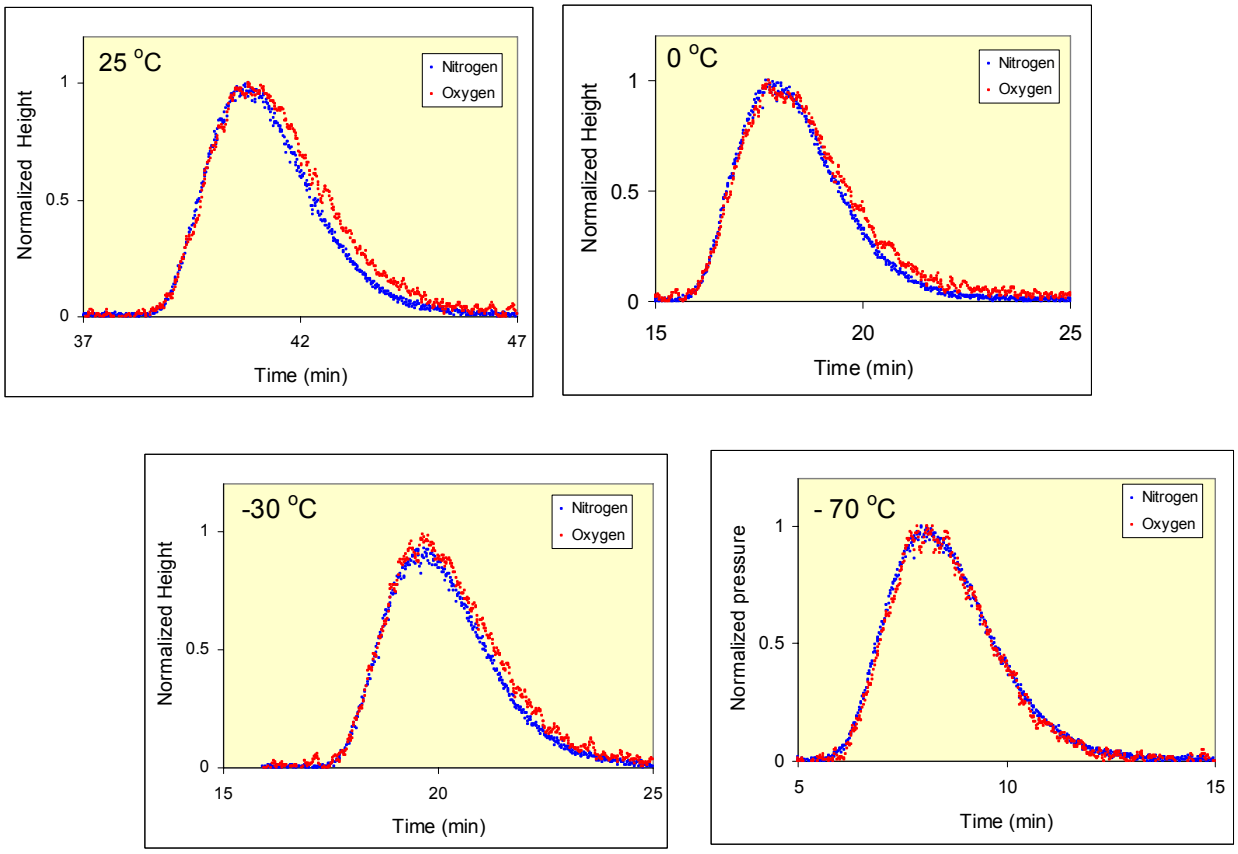

Figure 5: Normalized mass spectrometer signals for N_2 (blue) and O_2 (red) breaking through a 50 cm column packed with CFCMS K2-B material after injection of air at various temperatures. The flow rate of He was 15 cc/min.

A common trend observed by comparing the two sets of results is that lowering the temperature induces a gradual delay of the nitrogen peak with respect to the oxygen peak. The effect of temperature is greater for the TIM-2 material CFCMS sample for which the N_2 peak is delayed more at lower temperatures. As shown in Fig. 2, TIM-2 has the largest volume of micropores in the 5 – 7 Å range (which is the range of pore widths efficient for molecular sieving separation of O_2 and N_2); larger micropores and small mesopores are also present. For this material there is little separation at room temperature, but separation is enhanced at lower temperatures. In contrast, although separation occurs even at room temperature on the CFCMS K2-B material, lowering the temperature causes the overlap of the two peaks. This material has a very narrow porosity distribution, with narrow micropores distributed in the 5 – 7 Å range (but with lower pore volume in this range); larger micropores and mesopores are absent. The results of Table 1 also show that the access of N_2 to the internal porosity is more restricted on this material. The combination of

these factors determine the occurrence of $N_2 - O_2$ separation at room temperature on the K2-B sample, which is taught to be caused by its narrow pore distribution. The reason why separation selectivity is gradually lost at low temperatures (Fig. 5) is probably blockage of narrowest pores by selective adsorption of gas molecules at low temperature.

Zeolite

Zeolite 13X, with internal channel openings between 7.5 - 9 Å, is an industry standard for air separation and gas purification based on molecular sieving. [22,23] A sample of zeolite 13X (beads, 1.5-2 mm) was used in this project as a reference material. A temperature effect similar to that shown in Fig. 3 for CFCMS, though more clearly defined, was observed for this zeolite (Fig. 6). Although the column length used in this test was shorter (30 cm), air separation was more efficient, and improved greatly with lowering the temperature. However, common trend, also observed with CFCMS materials, was seen: lowering the temperature causes a delay of the nitrogen peak with respect to the oxygen one. This observation shows that the separation mechanism is the same for all three materials, i.e. it is based on kinetic separation during diffusion in narrow nanopores.

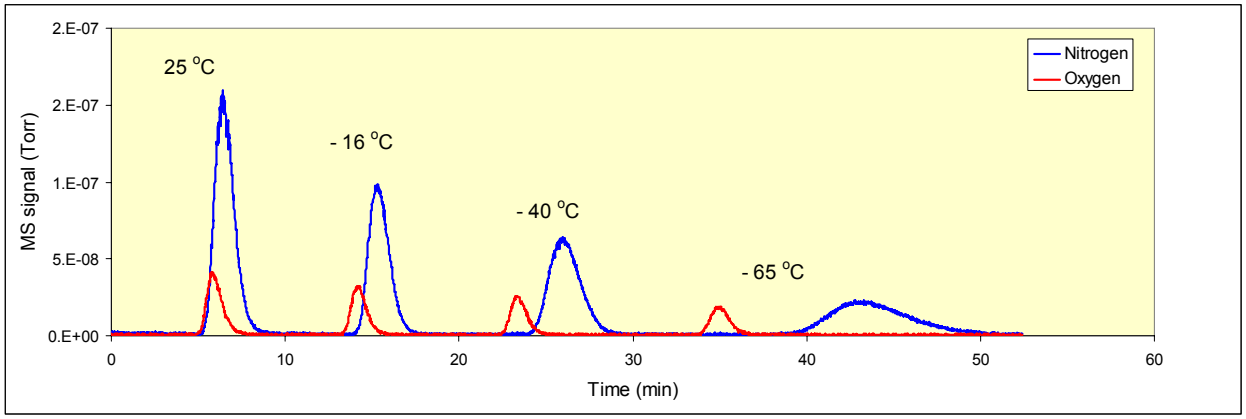

Figure 6: Mass spectrometer signals showing breakthrough of N_2 (blue) and O_2 (red) on zeolite 13X after injection of 5 mL air at various temperatures on. Flow rate of He carrier was 30 cc/min.

INFLUENCE OF MAGNETIC FIELDS ON DYNAMIC AIR SEPARATION

All tests on effects of magnetic fields on dynamic air separation were carried out using gas chromatographic (GC) analysis; the instrument was equipped with a thermoconductivity detector and the carrier gas was He. Various materials, packed in chromatography-type columns as described above, were investigated in dynamic conditions; this included CFCMS samples TIM-2 and K2-B, magnetite-loaded CFCMS (Fe-NG-4), and zeolite X13 for reference. The flow conditions and the size of air injection were varied in an attempt to improve the separation. All tests were done at room temperature and atmospheric pressure.

When carbon materials (pure or loaded with Fe_3O_4) were used, the delay of the N_2 peak was not large enough as to afford separate detection of O_2 and N_2 peaks using the TC detector of the GC system. However, when a zeolite packed column was used, the nitrogen peak was delayed more compared with the oxygen one, and two distinct peaks were clearly identified by the TC detector (Fig. 7). For this system, several tests were done in an attempt to detect magnetic field effects. The zeolite column was placed between the poles of the water-cooled magnet, and identical air injections were done repeatedly with the magnetic field switched on and off. No differences were observed in the breakthrough times or the

magnitude of the two peaks (Fig. 7). Based on this result (and on many others, not reported here) the effect of magnetic fields on dynamic air separation on zeolite 13X was not confirmed.

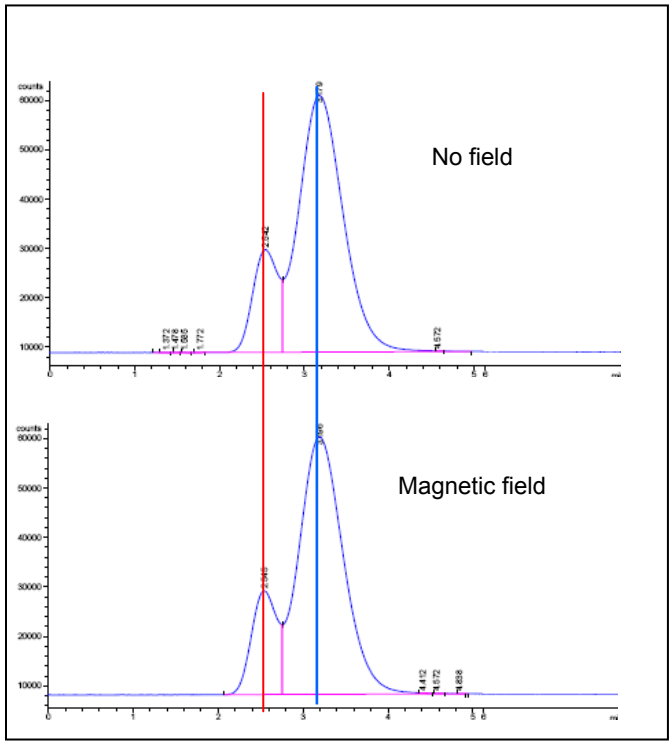

Figure 7: Example of air separation on zeolite 13X at room temperature (red – oxygen; blue – nitrogen). The flow rate of he carrier was 30 cc/min and the injection size was 0.1 cc. No detectable differences were seen between the cases with and without magnetic field (1.5 Tesla) applied.

CONCLUSIONS

The findings reported here confirm that CFCMS materials have the potential for separating O_2 and N_2 from air on the basis of the different diffusion rates of the two molecules in the composite. The results show that in dynamic conditions, nitrogen diffusion through the extended pore system of microporous adsorbents is slower than that of oxygen, and become seven slower as the temperature is lowered. Carbon fiber molecular sieves have potential for N_2 - O_2 separation, provided better tailored porosity is developed, with pore widths comparable to molecular dimensions. This depends on identifying and demonstrating alternative techniques of activation, and using new carbon precursors (such as lignine) that are known to produce extensive networks of uniformly narrow micropores. The effect of magnetic fields on air separation was not confirmed at room temperature for zeolite 13X and for Fe_3O_4-loaded CFCMS in dynamic conditions. At this moment it is unclear whether this conclusion can be generalized, given the fact that this finding in dynamic conditions contradicts previous results obtained in static (equilibrium) conditions. These data require more sophisticated measurements, using much higher intensity magnetic fields, to verify the preliminary results and determine whether magnetic fields can be exploited for separation of O_2 and N_2 from air. Furthermore, as current results show, efficient air separation is achievable on zeolite. There is a large potential for further development by combining air separation on zeolite with second-stage purification or oxygen enrichment on carbon molecular sieves, notably CFCMS, to exploit the electrical swing adsorption capability of these materials.

ACKNOWLEDGEMENTS

Research sponsored by Office of Fossil Energy, U.S. Department of Energy, National Energy Technology Laboratory, under the Fossil Energy Advanced Research Materials Program, contract number DE-AC05-00OR22725 with UT-Battelle, LLC.

REFERENCES

1. Burchell, T. D., Judkins, R. R., Rogers, M. R., and Williams, A. M., A Novel Process for the Separation of Carbon Dioxide and Hydrogen Sulfide for Gas Mixtures, *CARBON*, **35** (1997) 1279-1294.
2. Burchell, T. D., Weaver, C. E., Chilcoat, B. R., Derbyshire, F., and Jagtoyen, M., Activated Carbon Fiber Composite Material and Method of Making, U.S. Patent 6,030,698 (February 29, 2000) Assigned to Lockheed Martin Energy Research Corporation.
3. Burchell, T. D., Weaver, C. E., Chilcoat, B. R., Derbyshire, F., and Jagtoyen, M., Activated Carbon Fiber Composite Material and Method of Making, U.S. Patent 6,258,300 (July 10, 2001) Assigned to UT-Battelle, LLC.
4. Burchell, T. D., and Judkins, R. R., A Novel Carbon Fiber Based Material and Separation Technology*, Energy Conservation and Managemen*t, **38** Supplement, S99-S10 (1997).
5. Wilson, K. A., Burchell, T. D., and Judkins, R. R., Carbon Fiber Composite Molecular Sieve Electrically Regenerable Air Filter Media, U. S. Patent 5,827,355, (October 27, 1998), Assigned to Lockheed Martin Energy Research Corporation.
6. Judkins, R. R., and Burchell, T. D., Gas Separation Device Based on Electrical Swing Adsorption, U. S. Patent 5,972,077 (October 26, 1999) Assigned to Lockheed Martin Energy Research Corporation.
7. Burchell, T. D., Omatete, O., Gallego, N. C., and Baker, F. S., Novel Activated Carbon Composites for Air Separation, *Proceedings of the 18th Annual Conference on Fossil Energy Materials*, Knoxville, TN, June 2-4, 2004.
8. Kaneko, K., Fukuzaki, N., and Ozeki, S., The Concentrated NO Dimer in Micropores Above Room Temperature, *J. Chem. Phys*., **87** (1987) 776-777.
9. Takaishi, Y., Dimers of Oxygen Molecules in the Pores of Ca_6A Zeolite, *J. Chem. Soc. Faraday Trans*., **93** (1997) 1257-1260.
10. Yamamoto, I., Yamaguchi, M., Goto, T., and Miura, S., Chemical Equilibrium of the Ferromagnetic LaCo-H_5 System in Strong Magnetic Fields, *J. Alloys Compounds*, **231** (1995) 205-207.
11. Ozeki, S., Wakai, C., and Ono, S., Is Magnetic Effect on Water Possible?, *J. Phys. Chem*., **95** (1991) 10557-10559
12. Miyamoto, J., Matsubara, Y., Kurashima, H, Tazaki, T., and Ozeki, S., Magnetic Field Effects on Physical Adsorption Equilibrium Between Solids and Gases of Organic Molecules and Oxygen, *Nippon Kinzoku Gakkaishi*, **61** (1997) 1300-1305.
13. Ozeki, S., and Sato, H., Magnetic Interactions in Adsorption at Solid Surfaces, in *Encyclopedia of Surface and Colloid Science*, Marcel Dekker, New York, pp. 3120-3131 (2002).
14. Baker, F. S., Contescu, C. I., Tsouris, C., and Burchell, T. D., Activated CarbonComposites for Air Separation, *Proceedings of the 20th Annual Conference on Fossil Energy Materials*, Knoxville, TN, June 12-14, 2006.
15. Brunauer, S., Emmett, P. H., and Teller, E., Adsorption of Gases in Multimolecular Layers, *J. Am. Chem. Soc*., **60** (1938) 309-319.
16. Gregg, S. J., and Sing, K. S. W., "*Adsorption, Surface Area and Porosity*", 2nd Edition, Academic Press, London (1982).
17. Lastoskie, C., Gubbins, K. E., and Quirke, N., Pore Size Distribution Analysis of Microporous Carbons: A Density Functional Theory Approach, *J. Phys. Chem*., **97** (1993) 4786-479.

18. Jagiello, J., and Thommes, M., Comparison of DFT Characterization Methods Based on N_2, Ar, CO_2, and H_2 Adsorption Applied to Carbons with Various Pore Size Distributions, *CARBON*, **42** (2004) 1227-1232.
19. Rodriquez-Reinoso, F. and Linares-Solano, A., Microporous Structure of Activated Carbons as Revealed by Adsorption Methods, in "*Chemistry and Physics of Carbon"*, Edited by P. A. Thrower, Volume 21, pp. 1-146, Marcel Dekker, New York (1988).
20. Baker, F. S., Contescu, C. I., Tsouris, C., Gallego, N. C., and Burchell, T. D., Carbon Fiber Composite Molecular Sieve for Air Separation, *Extended Abstracts, Carbon 2006 International Conference,* Aberdeen, Scotland, July 16-21, 2006.
21. Spacu, P., Brezeanu, M., Patron. L., Contescu, A., and Crisan, D., Coordination Compounds as Raw Materials for Mixed Oxides, *Thermochimica Acta*, **178** (1991) 231-239.
22. Jee, J.-G., Lee, J.-S., and Lee, C.-H., Air Separation by a Small Scale Two-Bed Medical O_2 Pressure Swing Adsorption, *Ind. Eng. Chem. Res.* **40** (2001) 3647-3658.
23. Jee, J.-G., Lee, S.-J., Moon, H.-M., and Lee, C.-H., Adsorption Dynamics of Air on Zeolite 13X and CMS Beds for Separation and Purification, *Adsorption* **11** (2005) 415-420.

ENABLING THE PRACTICAL APPLICATION OF OXIDE DISPERSION-STRENGTHENED FERRITIC STEELS

I.G. Wright
Oak Ridge National Laboratory, 1 Bethel Valley Road, MS 6156, Oak Ridge, TN 37831
E-mail: wrightig@ornl.gov; telephone: 865-574-4451; Fax: 865-241-0215

B.A. Pint
Oak Ridge National Laboratory, 1 Bethel Valley Road, MS 6156, Oak Ridge, TN 37831
E-mail: pintba@ornl.gov; telephone: 865-576-2897; Fax: 865-241-0215

E.G. Dyadko
MER Corporation, 7960 S. Kolb Rd., Tucson, AZ 85706
E-mail: edyadko@mercorp.com; telephone: 520-574-1980 x142; Fax: 520-574-1983

N.S. Bornstein
Consultant, 43 Richmond Lane, W. Hartford, CT 06117
E-mail: normanbornstein@sbcglobal.net; telephone: 860-408-1432

G.J. Tatlock
University of Liverpool, Brownlow Hill, Liverpool L69 3GH, England
E-mail: g.j.tatlock@liverpool.ac.uk; telephone: 011-44-151-794-5367; Fax: 011-44-151-794-4675

ABSTRACT

Effort has continued to evaluate joints made in oxide dispersion-strengthened (ODS) FeCrAl by (i) pulsed plasma-assisted diffusion (PPAD) bonding, and (ii) transient liquid phase (TLP) bonding. Creep tests of PPAD-bonded butt joints in air at 1000°C, using small, shoulder-loaded, dog bone-shaped specimens and an incrementally-loaded test technique, indicated that failure occurred at loads of up to 82% of that required to fail the parent alloy in the same test. For high creep-strength ferritic steels joined by conventional welding methods, failure at loads of 50-80% that required to fail the parent alloy ('strength reduction factors') are considered to be acceptable. The failures apparently did not initiate along the joints; the observed mode of failure of the joined specimens was the same as observed for monolithic specimens of this alloy, by crack-initiated transgranular brittle fracture, followed by ductile overload failure. The progress of TLP bonding has been slower, with the major effort focused on understanding the behavior of the transient liquid phase and its interaction with the alloy microstructure during the various stages of bonding. Creep testing using the same procedures also has been used to evaluate changes resulting from torsional deformation of ODS-FeCrAl tubes in an attempt to modify their microstructures and increase their hoop strength. Interpretation of the results so far has not shown a clear trend, largely due to difficulties in measuring the effective angle of twist in the specimen gauge lengths. Other issues that have been addressed are the refinement of an approach for prediction of the oxidation-limited service lifetime of alumina scale-forming ODS alloys, and alternative routes for ODS alloy powder processing. Analysis of alloy specimens oxidized to failure (in some cases involving exposures for many thousands of hours) over a range of temperatures has provided an improved basis for calculating the values of parameters required in the lifing model (minimum Al content for protective behavior; initiation point for scale spallation); a quantitative description of the influence of specimen shape remains to be addressed.

INTRODUCTION

ODS alloys have distinct advantages over conventional high-temperature alloys in that they exhibit creep strength at significantly higher temperatures, and have exceptional inherent resistance to high-temperature oxidation in terms of rate of scale growth and scale adherence due to the formation of α-Al_2O_3 scales [1]. Because of these properties, ODS alloys provide an alternative choice for the lower end of the temperature range usually attributed to ceramics. There is currently a resurgence of industrial interest in ODS alloys for applications ranging from high-temperature heat exchangers for indirect preheating of steam or H_2 for gasification of coal, and for heat recuperation in fossil fuel-fired metal smelters and melters, to use as a replacement for refractories used for containment of molten metal in the production of H_2 from coal [2]. There is also renewed interest in the use of ODS alloys for airfoils for use at the higher temperatures anticipated in gas turbines burning syngas with variable quantities of H_2 [3].

The barriers that have prevented the broad application of ODS alloys still are centered around cost (since ODS alloy production involves a powder metallurgical route), and the fact that they cannot be joined by conventional fusion welding (since the fine dispersion of oxides typically agglomerates in the fusion zone, leaving a joint which may be an order of magnitude lower in high-temperature creep strength than the monolithic alloy [4-6]). Other joining methods involving brazing or diffusion bonding have been demonstrated with some success [5,7-10], particularly with B-containing brazing alloys. A common difficulty was obtaining grain growth across the bond, and no creep data have been reported to indicate that extent of strength reduction. Three methods which do not involve the addition of an extra filler material recently have shown promise: friction stir welding [11,12]; solid-state diffusion bonding (joints in alloy PM2000 exhibited 70% of the room-temperature shear strength of the parent alloy [13]); and pulsed plasma-assisted diffusion bonding [14]. Progress in transient liquid-phase (TLP) bonding and pulsed plasma-assisted diffusion (PPAD) bonding are reported.

Since ODS-FeCrAl alloys form very thin, protective alumina scales that are uniform in thickness with negligible internal attack, it is difficult to estimate service lifetime from readily-measurable parameters such as section thinning. Because of the very well-controlled oxidation behavior, and since the Al concentration gradient in the alloy is essentially flat (in many cases) until very near the end of life, a relatively straightforward basis for predicting the oxidation-limited lifetimes of these alloys is possible by equating the oxidation lifetime to the rate of consumption of the available Al to form the alumina scale [15,16]. Progress in measuring some of these parameters is reported.

RESULTS AND DISCUSSION

JOINING

Transient Liquid-Phase (TLP) Bonding

Further characterization of the TLP bonds described earlier [17] was made to determine the effects of heat treatment on homogenizing the composition in the vicinity of the bonds, and on the microstructure of the alloy. A specimen cut from a block of unrecrystallized alloy PM2000 (condition KKL4) that had been bonded using the original TLP foil, was subjected to the standard recrystallization anneal for alloy PM2000 (1h at 1380°C). The appearance of the bond, shown in Fig. 1a, indicates some porosity (or incomplete bonding) near the edges of the specimen whereas, near the center of the specimen, the bond line was demarcated by a change in alloy grain structure (Figs. 1 b and c), and any associated porosity was very fine. The backscattered electron (BSE) image of a similar section of the bond from examination in a scanning electron microscope (SEM), shown in Fig. 1d, indicates that some alloy grain growth had occurred in the immediate vicinity of the bond line, extending approximately 100 μm into the alloy, but that secondary recrystallization of the bulk of the alloy had not proceeded to produce the desired large grain structure. A particularly notable feature was that the bright-appearing (element X-rich) precipitates

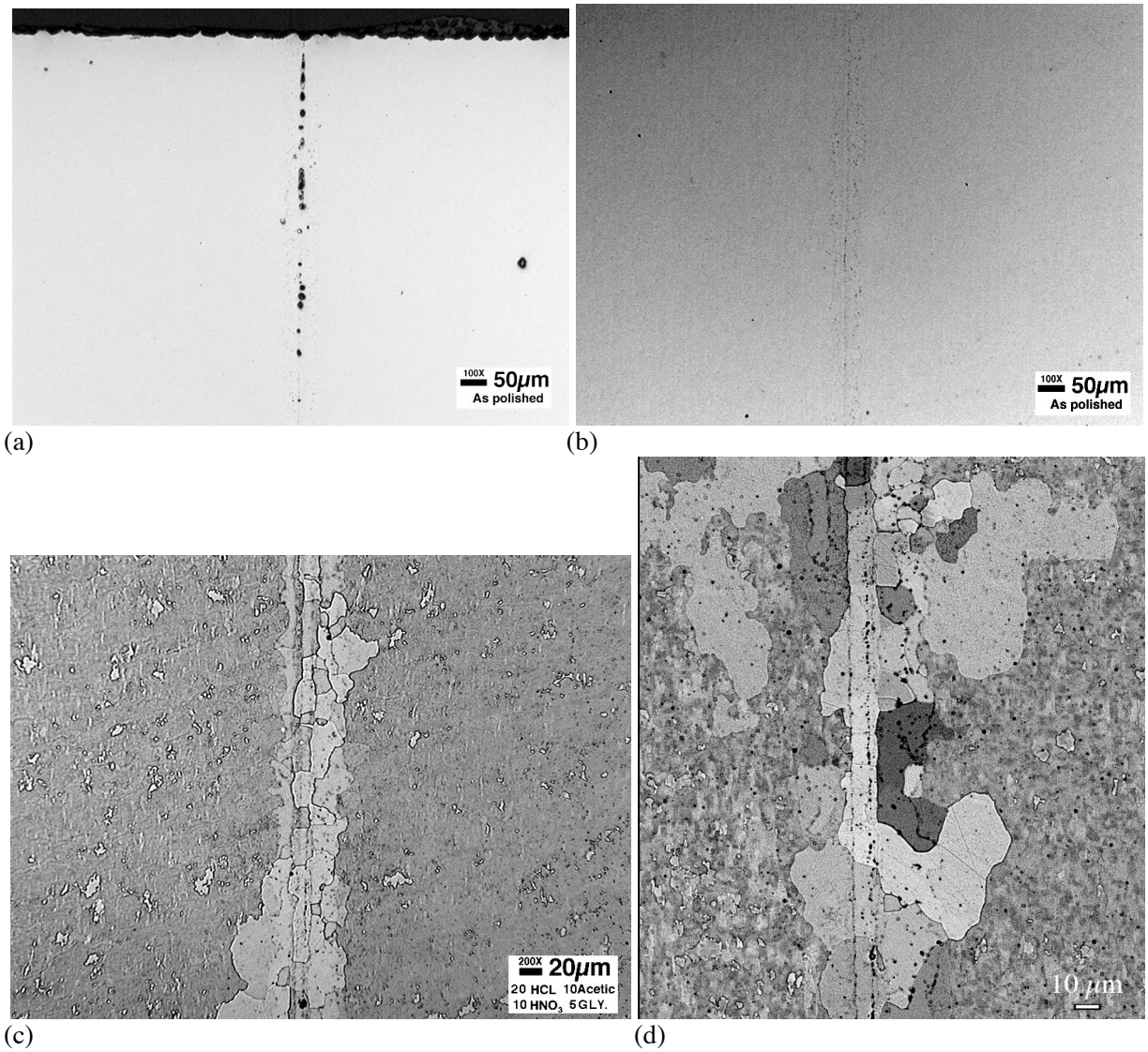

(a) (b)

(c) (d)

Figure 1. Joint made in unrecrystallized alloy PM2000 using the original TLP foil, after a recrystallization anneal for 1 h at 1380°C a), (b), optical images of unetched cross sections; (c) optical image of an etched cross section; (d) SEM BSE image of a cross section.

associated with yttrium-aluminum garnet (YAG) particles, reported earlier after joining and after annealing for 4h at 1000°C [17], were absent, indicating that their presence was an artifact of the point in the processing at which the joints had been examined.

Figure 2 illustrates concentration profiles [made using an electron probe microanalyzer (EPMA)] from the bond line into the alloy for the major elements of interest. Note that, until intellectual property issues concerning the composition of the TLP phase are resolved, its key elements will be denoted 'X' and 'Z.' Two such line scans were made, and both showed a uniform reduction in concentration of elements X and Z over 450 and 650 μm, respectively, confirming increased diffusion away from the bond (these data are summarized in Table I). The distances over which diffusion occurred were much greater than the depth to which recrystallization was observed near the joint; in both line scans, changes were apparent over a distance of approximately 100 μm either side of the bond line. The alloy Al concentration adjacent to the bond decreased by a maximum of approximately 1 at% (Fig. 2a), and there was a corresponding increase in Fe concentration (not shown), but such variations were within the range of variations observed periodically throughout the bulk of the alloy, and so are probably not meaningful. Overall, the observed

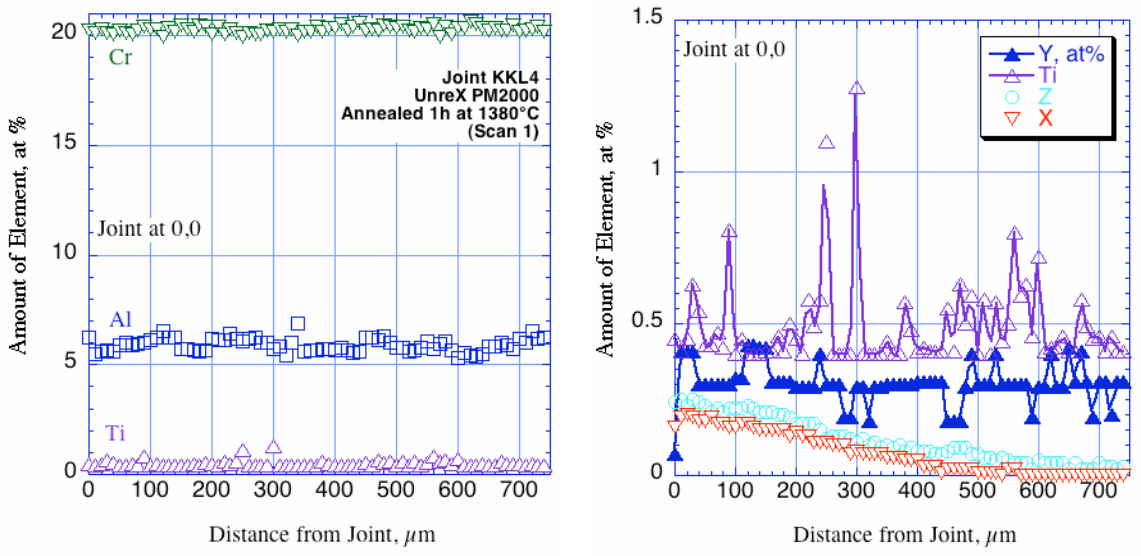

(a) (b)

Figure 2. EPMA concentration profiles through TLP joint made in unrecrystallized alloy PM2000 using the original TLP foil, after a recrystallization anneal for 1 h at 1380°C (a), (b) major and minor elements, Scan 1.

Table I. Depth of Diffusion of TLP Elements

Condition	Conc. At Joint, at%		Diffusion Depth, μm	
	X	Z	X	Z
PM2000, KKL4, Original TLP Foil				
As Joined	0.3 (2.0)*	2.5	170	80
4h at 1000°C	≈1.0 (5.2)*	1.2	270	150
1h at 1380°C	0.15	0.24	450	650
PM2000, KKL6, Original TLP Foil				
As Joined	0.4 (71)*	2.1	90	50
4h at 1000°C	1.1 (1.25)*	0.8	150	150
1h at 1380°C	—	—	—	—
PM2000, KKL4, Sputter-Deposited TLP				
As Joined+2h at 1000°C	0.23	0	>30	-0-
+1h at 1380°C	0.18	0.01	530	-0-

*X-rich precipitates

recrystallization behavior suggests simply that the heat treatment associated with the original TLP bonding (1h at 800°C, followed by 1h at 1000°C) was sufficient to allow recovery of the alloy to occur, leaving insufficient strain in the alloy to drive recrystallization

The cross sections shown in Fig. 3 are from a bond (butt weld) made using 14 mm diam. rods of unrecrystallized alloy PM2000 (condition KKL4), in which the TLP phase was applied by sputtering from the TLP foil used in the earlier bonding. This route was used as a means of introducing less TLP phase into the alloy surface, and facilitating post-bonding homogenization. The alloy is shown after experiencing heat treatments of 1h at 900°C followed by 2h at 1100°C in Ar-4vol%H_2, all under compressive loading, followed by furnace cooling. Unetched, the bond line exhibited what appeared to be a string of small pores (Fig. 3a); SEM images suggested that these features may have been metallographic artifacts (Figs. 3c,d). The overall grain size of the nominally unrecrystallized alloy appeared to be larger

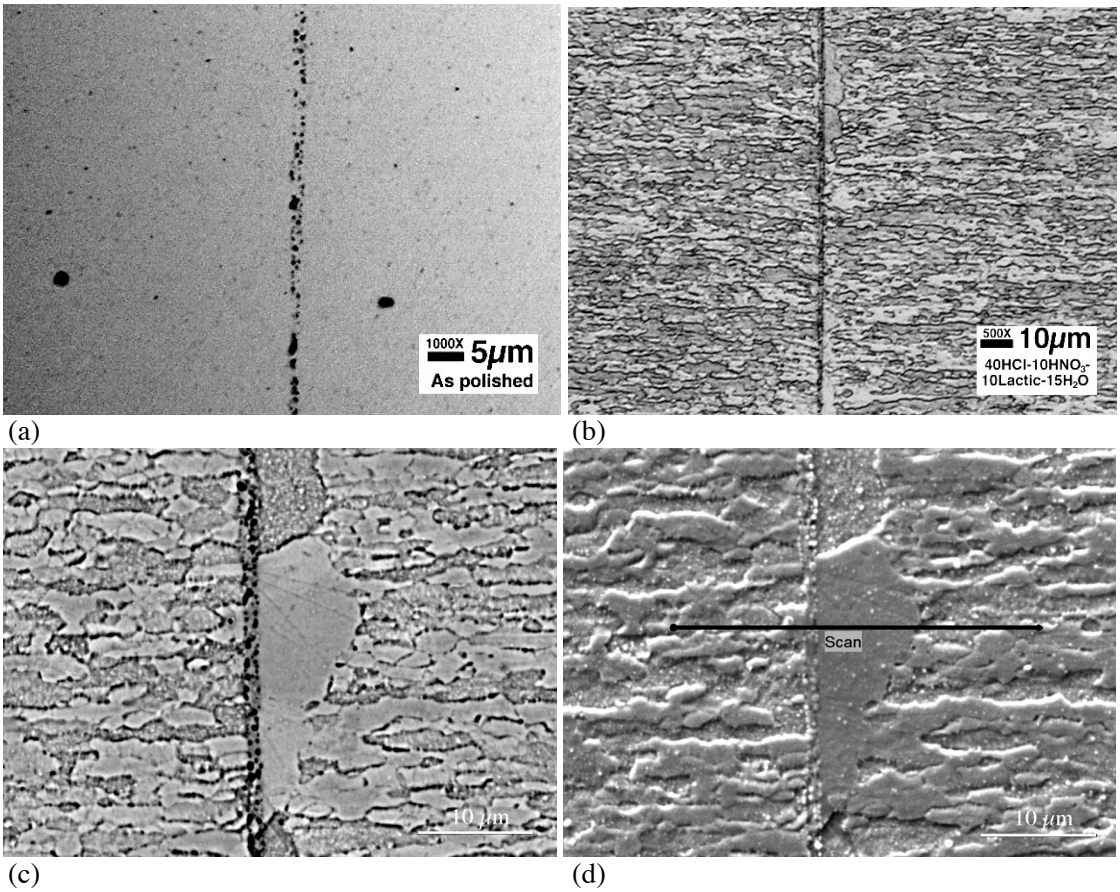

Figure 3. Cross sections of PM2000 (KKL4) after joining and interdiffusion (1h at 900°C plus 2h at 1100°C in Ar-4H_2, furnace cool); optical micrographs of unetched (a) and etched (b) cross sections; (c) SEM BSE image; (d) SEM SE image showing location of line scan.

than expected (though full secondary recrystallization had not occurred) and, in a few areas, there were some larger grains associated with the bond line (Figs. 3b-d), similar in appearance to (but smaller than) those seen earlier (Fig. 1c,d). The concentration profiles shown in Fig. 4 are typical of three such profiles that were measured. Surprisingly, the concentration profile for TLP element X was flat; the measured

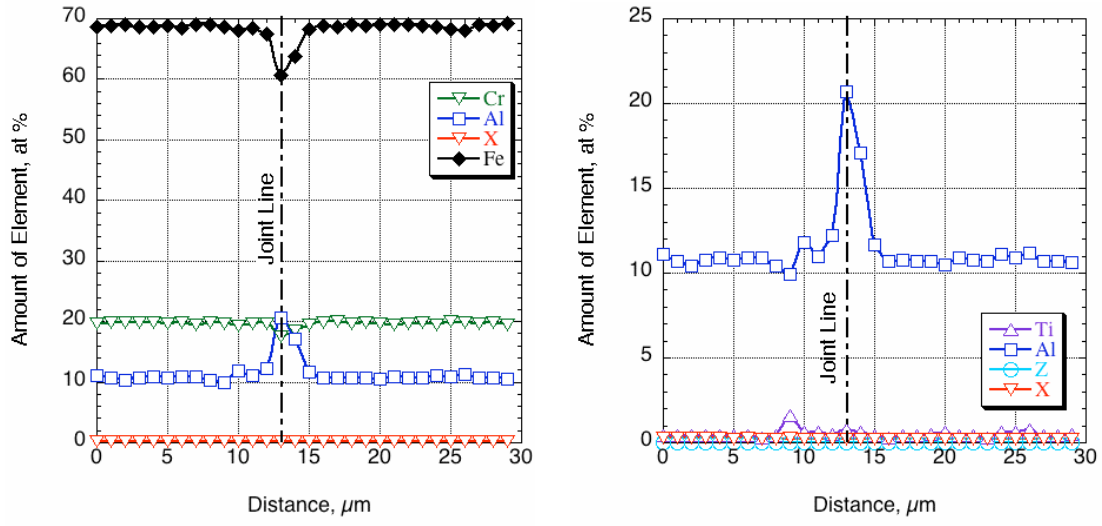

Figure 4. Concentration profiles for (a) major elements; and (b) minor elements along Scan 1.

level was 0.23-0.28 at%, which is directly comparable to those measured for bonds made using the TLP foil, but there were no areas of excess element X in the form of large precipitates. The measured level of TLP element Z was essentially zero, suggesting that the composition of the TLP alloy had been changed as a result of the sputtering process. The other notable feature of these concentration profiles was the presence of an Al peak along the bond line, reaching 21 at%, in places (Fig. 4b). On average, the measured composition of the bond line was: 63.0Fe-18.0Cr-18.0Al-0.67Ti-0.23X, while the bulk alloy was: 68.8Fe-19.8Cr-10.7Al-0.37Ti-0.28X (in at%), indicating an enrichment in Al and Ti, and a decrease in Fe and Cr at the bond line. Previously, precipitates consisting of mixtures of Al_2O_3 and TiC have been found along bond lines in this alloy (by transmission electron microscopy [18]), presumably formed by reactions during bonding; no TEM nor analyses for O or C were made on this specimen. These concentration profiles did not extend sufficient distance to determine the depth to which element X had penetrated into the alloy.

Figure 5 shows micrographs of an additional specimen of this bond that was subjected to the standard recrystallization anneal for alloy PM2000 (1h at 1380°C). Unetched, the bond line appeared to contain fewer voids or second phase particles than that shown in Fig. 3a. The etched cross section in Fig. 5c indicates a string of small, recrystallized grains extending up to 30 μm either side of the bond line, similar to those shown in Fig. 1, while the structure of the bulk of the alloy could not be determined using current

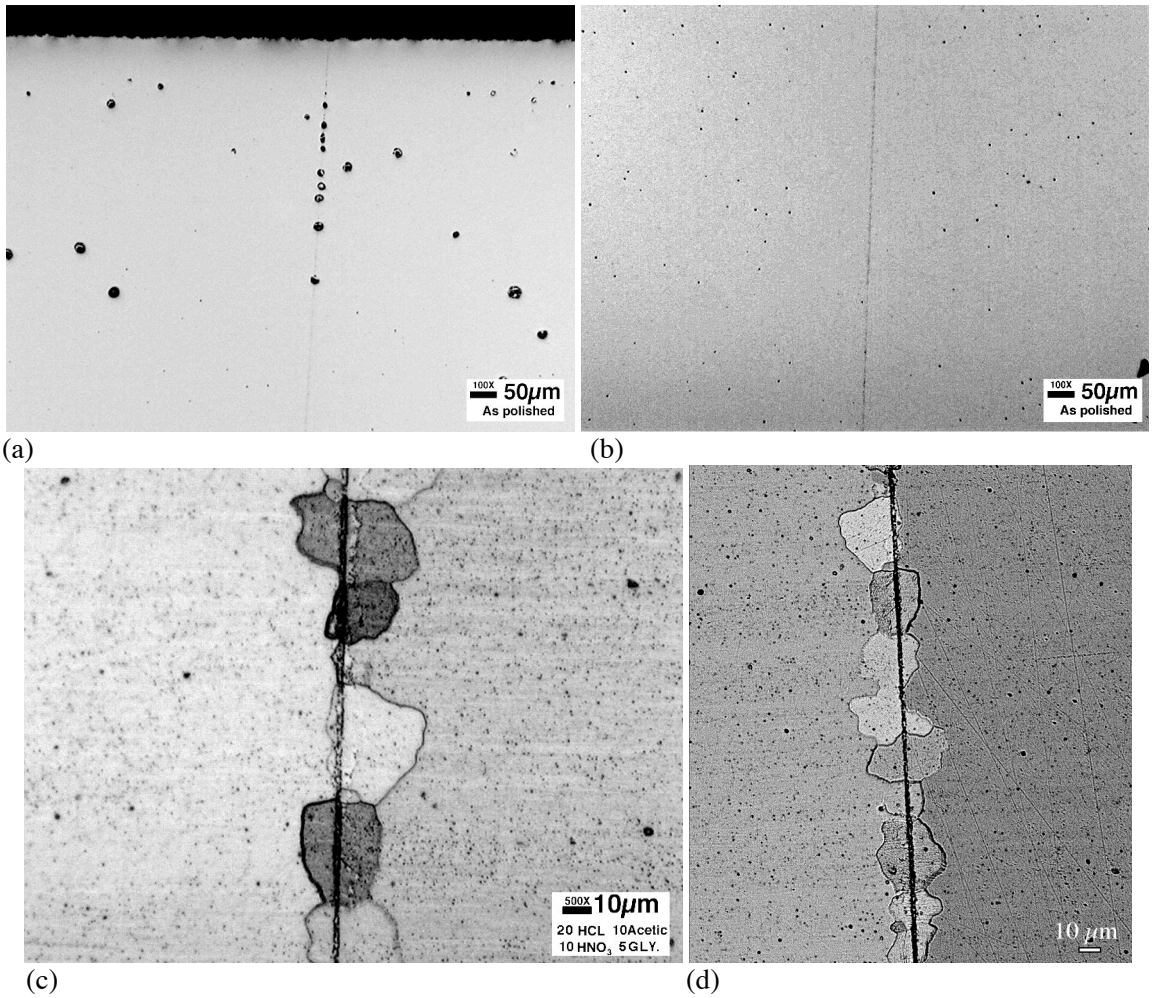

Figure 5. Cross section of TLP joint after joining + interdiffusion + recrystallization anneal (1h at 900°C/2h at 1100°C plus 1h at 1380°C in Ar-4H_2, furnace cool). (a),(b) optical micrographs of unetched joint; (c) optical micrographs of etched joint; (d) SEM SE image of cross section.

etching techniques; no grain boundaries were revealed, but it was considered unlikely that the alloy had fully recrystallized. There appeared to be separate large grains either side of the bond line. The EPMA concentration profiles through the joint, shown in Fig. 6, indicate that the concentration of element X decreases from 0.18 at% at the bond line to 0.01at% over 530 μm, which is very similar to the profile measured on the specimen bonded using the TLP foil, as summarized in Table I. Figure 6b also indicates the continuing presence of Al and Ti enrichments at the bond line, with significant depletions of Al in a zone up to 10 μm either side of the bond line. Those depletions coincided with enrichments in Ti, Cr, or Fe, but there was no consistent pattern. While this bond appears to be metallurgically sound, the disruption in grain structure across the bond would be expected to degrade its creep strength. One possible route for promoting secondary recrystallization though the bond may be to introduce some level of cold work into the alloy by rolling, immediately after bonding.

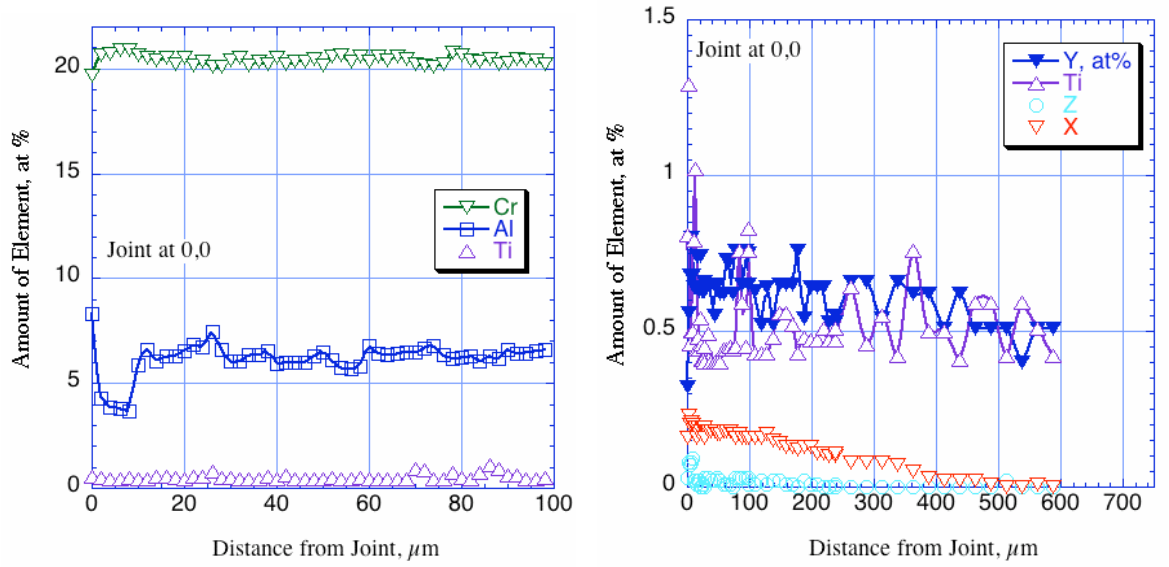

(a) (b)

Figure 6. EPMA concentration profiles on one side of a TLP joint (a) major elements, Scan 1; (b) minor elements, Scan 2.

Since application to the surfaces to be bonded by sputtering resulted in the apparent loss of one of the constituents of the TLP, it was anticipated that the melting temperature of the TLP would be higher than desired. In a further attempt to provide the desired TLP composition in a form of a foil, a new batch of TLP has been processed, using revised procedures to eliminate the use of lubricants that may leave a residue in the foil. In addition, a new compression platform has been built for use on an Instron machine to provide better control of specimen assembly and testing. This platform is shown schematically in Fig. 7. Compromises inherent in using this approach (instead of the controlled atmosphere, hot-pressing equipment used earlier) is that the joining occurs in air, with the attendant issues of oxide filming of the surfaces to be joined, and temperature limitations that (at present) preclude joining and secondary recrystallization in one step.

Pulsed Plasma-Assisted Diffusion Bonding

The compression rig used for PPAD bonding by MER Corp. [19] is shown schematically in Fig. 8. The conditions used for bonding were 9V, 1200A, 62Hz, 70% duty cycle at a constant temperature. Joining was carried out in an Ar atmosphere. The temperature range used in the experiments was from 1170-1380°C, the latter conditions intended to promote secondary recrystallization following bonding. The bond and associated alloy microstructure were examined by metallography and, where secondary recrystallization had not been accomplished during bonding, specimens were given a further heat treatment (1h at 1380°C in air), but no further strain was applied to the specimens. The joining process

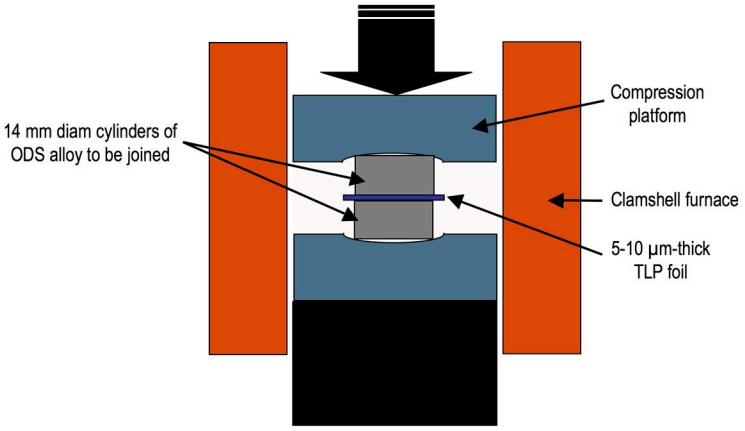

Figure 7. Revised compression platform for TLP bonding

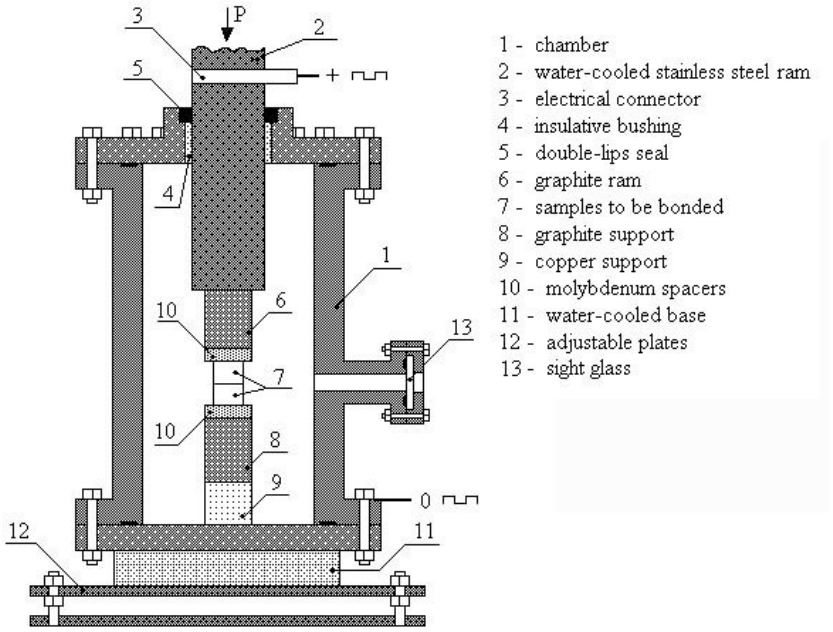

Figure 8. Schematic diagram of rig used for pulsed plasma assisted diffusion bonding of unsupported work pieces.

cycle involved the application of a compressive force of 5 to 12.5MPa perpendicular to the joint while the samples were heated. Micro-plasma discharges between the two halves of the joint resulted in local redistribution of material in the vicinity of the interface, and disruption of any surface oxide layer present on the faces being joined.

The specimens used for making butt joints by PPAD bonding were 19 mm diameter rods of as-extruded PM2000, which was used in the fine-grained condition (Plansee specification KKL4), with no secondary recrystallization. The mating faces were ground to a 1200 grit (U.S.) finish, and ultrasonically cleaned sequentially in acetone and ethanol before joining. Optical micrographs of cross-sections across various joints are shown in Fig. 9. During secondary recrystallization, grain growth occurred through the original interface, which was still delineated as a fine line, as shown in the micrographs, and in more detail in Fig. 10a. These bonds were further examined by transmission electron microscopy (TEM)[20]. Figure 10b is a bright-field TEM micrograph of a sample cut across the bonded interface, which runs down the center of

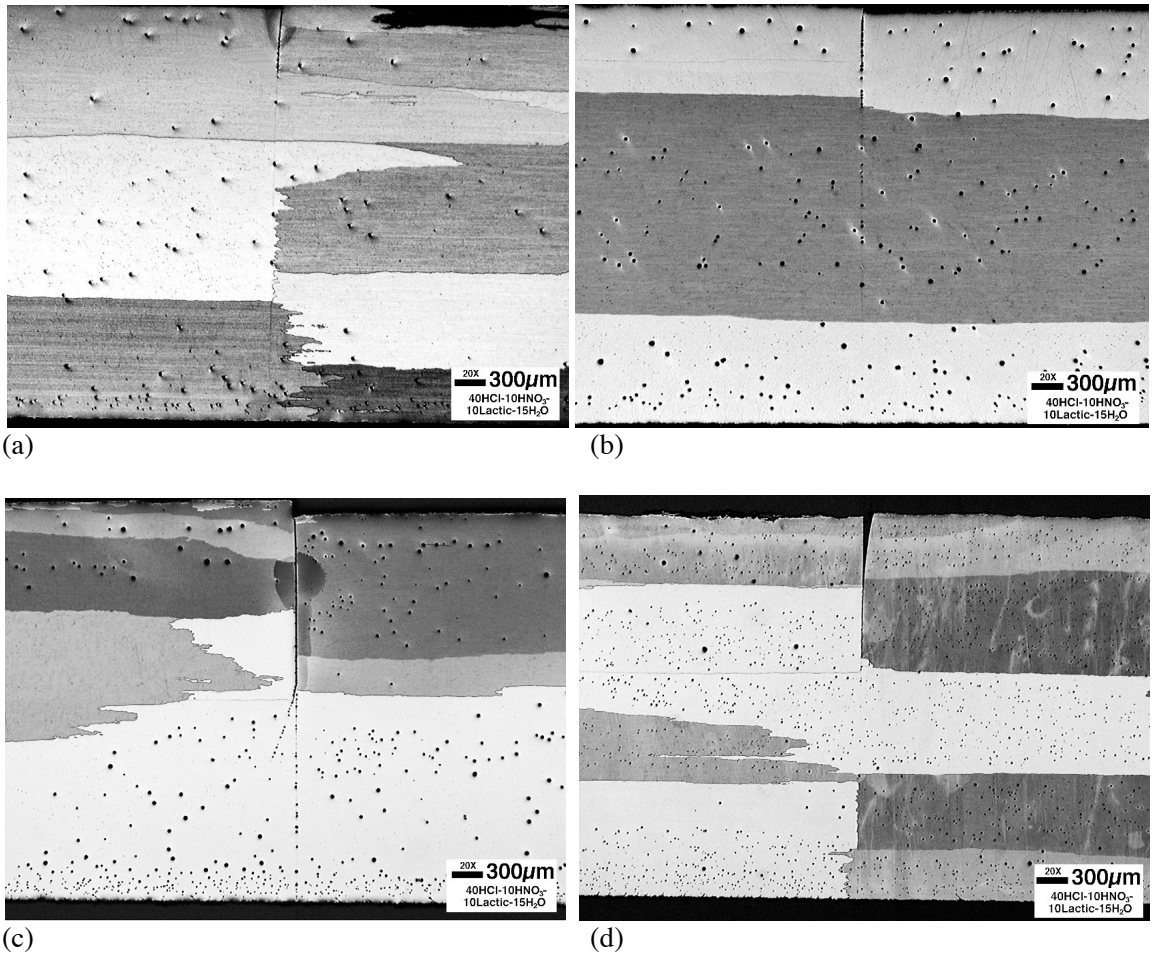

Figure 9. Optical micrographs of etched cross-sections through PPAD-bonded joints. The load to cause failure in the creep test was (a) 77.3 MPa; (b) 76 MPa; (c) 46.7 MPa; and (d) 36.1 MPa.

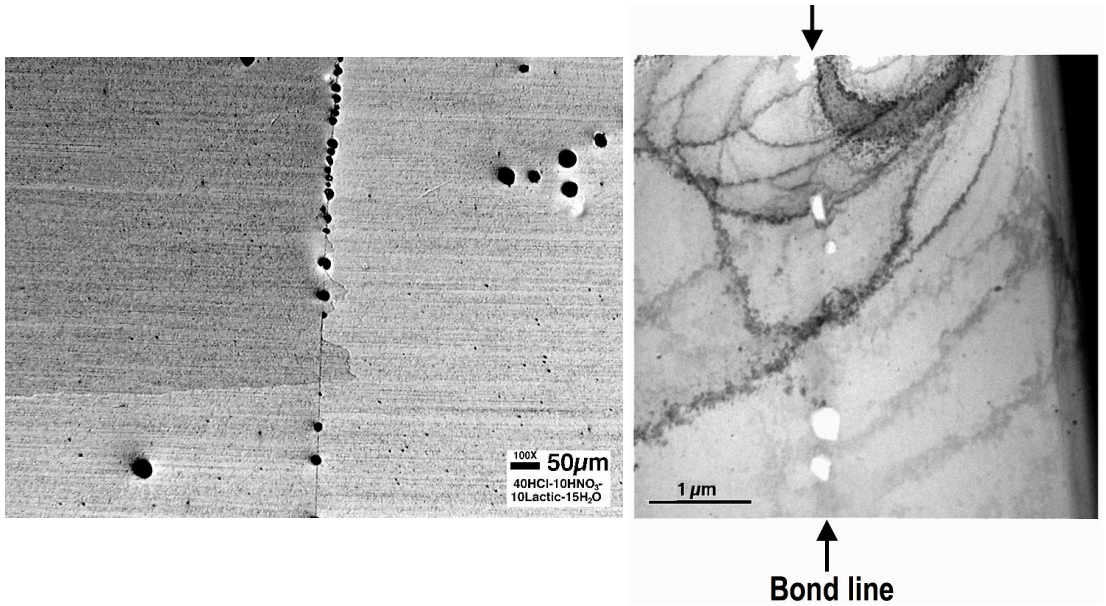

Figure 10. (a) Optical micrograph, and (b) corresponding bright field TEM image of the original bond line, showing that the line of apparent porosity is actually a line of bright alumina particles.

the micrograph. The original interface is marked by a string of white-appearing particles, which would explain the contrast seen in the optical images. The dark bands crossing the micrograph (Fig. 10b) are artifacts (bend contours) caused by changes in the electron diffraction conditions that occur as the TEM sample distorts under its own weight. However, the continuity of these contours across the interface indicates that the alloy grain spanning the interface is a single crystal. The slight darkening along the line of the interface was due to thickness variations across the sample: the sample was slightly thicker at the interface than in the surrounding area, since the hard oxide particles at the interface thinned more slowly than the matrix, but also shielded the adjacent region from the ion beam. The particles along the interface had a separation of between 0.5 and 2 μm and a typical size of about 0.2 μm. The variation in spacing of the particles may influence the ease with which the grain boundaries move through the interface during recrystallization, hence explaining some of the serrations along the boundaries seen in Figs. 9 and 10.

The particles found along the interface were examined by energy-dispersive X-ray analysis, and all gave similar spectra that corresponded to almost pure aluminum oxide. In some cases a small Y signal was observed, most likely due to the presence of small Y-rich particles in the vicinity of the alumina. The fine dispersion of Y or yttrium-aluminum oxide particles found throughout the sample were in the size range of 20-30nm, and larger alumina or carbide particles occasionally were present. Since the distribution of the non-interfacial particles in the alloy was similar in both the region near the interface and well away from it, their distribution did not appear to have been affected by the bonding process. Overall, the microstructure shown in Fig. 10 clearly demonstrates that PPAD bonding has produced a sound joint in alloy PM2000.

The strength of the joints so produced was measured in an incrementally-loaded creep test at 1000°C in air. Miniature shoulder-loaded, dog bone-shaped creep specimens were cut from the butt-joined cylinders by electro-discharge machining; Fig. 11 indicates how the specimens were oriented and their dimensions.

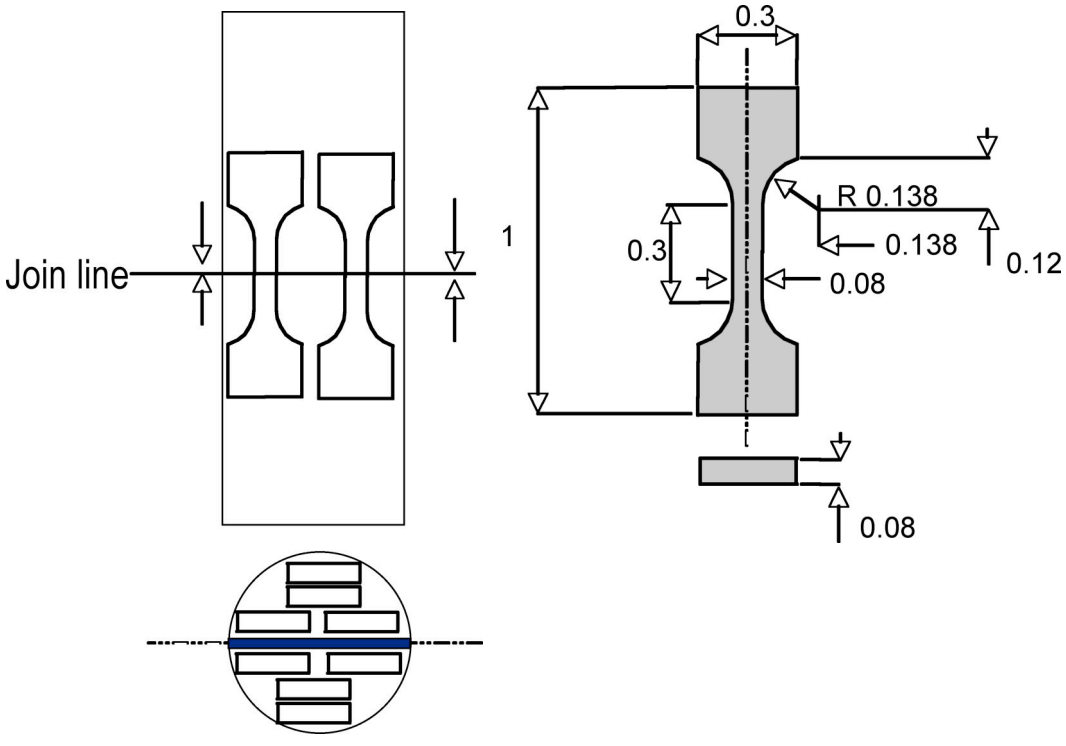

Figure 11. Miniature creep specimens used in the incrementally-loaded creep test, showing (a) orientation of specimens cut from butt-joined cylinders; and (b) specimen dimensions (in inches).

The creep tests used dead weight loading, which was increased in increments of 5 MPa, typically once per day, until obvious creep was observed, or failure occurred. Figure 12a summarizes the loads at failure as a function of PPAD processing temperature, and Fig. 12b compares the loads at failure with those for recrystallized monolithic specimens made from the same bar stock. The best joints exhibited joint strength factors (JSFs) of 82%. For high creep-strength ferritic steels joined by conventional welding methods, typical JSF values are 50-80%, and for weldable high-temperature Ni-base alloys, values of approximately 80% are considered acceptable [21,22].

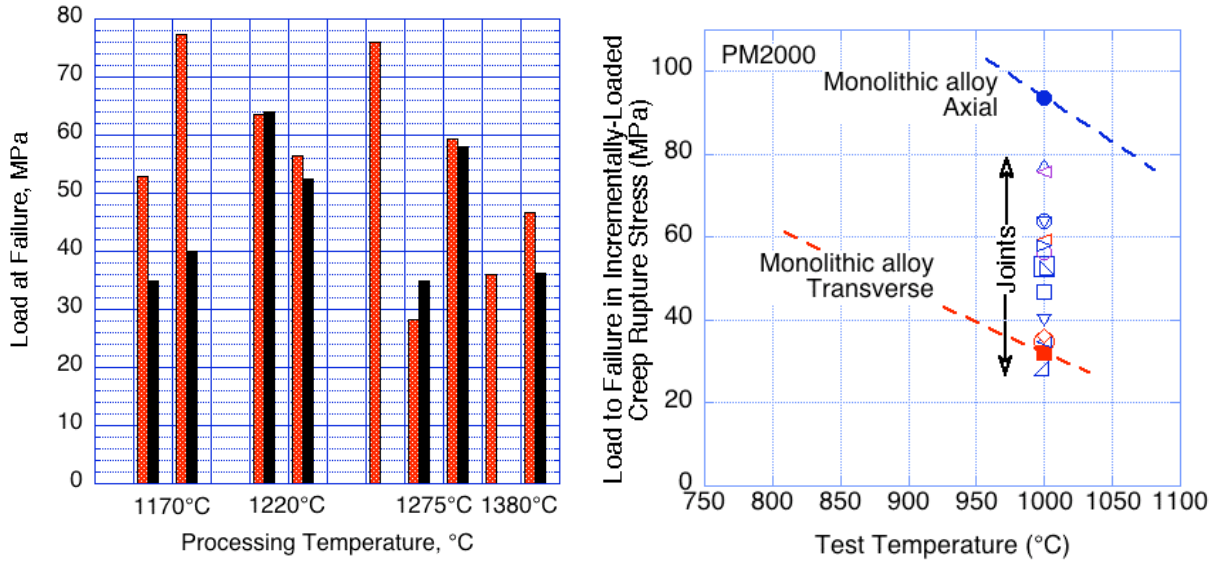

(a) (b)

Figure 12. Summary of the creep strengths of butt joints in PM2000 made by PPAD bonding (a) bar chart showing results for duplicate specimens as a function of processing temperature; (b) comparison with the axial and transverse creep strengths for monolithic specimens from the same starting material.

The failures in these joints apparently did not initiate along the bond line, but often in the vicinity of a grain boundary, as shown in Fig. 13. The observed mode of failure was by crack-initiated transgranular brittle fracture, followed by ductile overload failure, which is typical for this alloy [23,24]. Because of the large grain size in these miniature specimens, the gauge of the specimen shown was essentially two grains wide. Typically, cracking initiated in one grain, causing the other to fail by overloading. There was a limited amount of porosity present in the samples, and this did not increase noticeably during the testing.

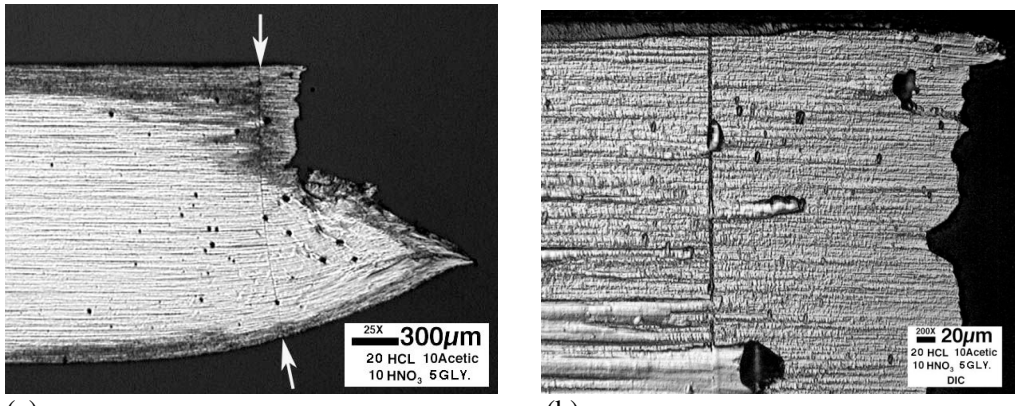

(a) (b)

Figure 13. Heavily-etched cross sections of failed butt joints, illustrating that failure did not occur in the bond line (a) classic brittle/ductile failure, with the bond line shown by arrows; and (b) enlarged view of the top part of the fracture surface shown in (a).

OXIDATION-LIMITED SERVICE LIFETIME

Key parameters needed for analytical modeling to predict the oxidation-limited service lifetime of ODS-FeCrAl alloys are accurate values for the oxidation rate (as a function of temperature and environment), the initial Al reservoir of the alloy [Al content (C_B) and volume of the part subject to oxidation ($\underline{V}$)], and the minimum residual Al content at which protective scale formation is no longer supported (C_{B^*}).

Oxidation-limited lifetime data have been generated for relevant ODS alloys, as well as other FeCrAlY-type compositions made by conventional processing; the alloys tested are listed in Table II. Specimens of each alloy with different thicknesses (and shapes) were exposed to provide a range of initial Al reservoir, and run in laboratory air at temperatures from 1000 to 1300°C until failure occurred. Examples of the lifetimes observed for alloys Inconel MA956 and 956HT are shown in Fig. 14 (each data point represents a specimen run to failure), plotted against the parameter component volume/surface area (V/A). Note that, at 1100°C, lives up to 23kh were observed, and that exposures at 1000°C have not yet reached times to

Table II. Nominal Compositions of Ferritic ODS Alloys of Interest (atomic percent).

Alloy	Fe	Cr	Al	Mo	W	Ti	Si	Y	Zr	O	C	S*	N*
INCO MA 956	Bal	20.05	8.77	0	0.01	0.40	0.13	0.24	0	0.65	0.06	41	608
	Bal	19.39	8.40	0	0	0.39	—	0.30	—	0.66	0.04	180	—
INCO MA956HT	Bal	21.45	11.01	0.01	—	0.43	0.09	0.22	0	0.69	0.13	80	1059
	Bal	21.72	10.66	0.01	0	0.43	0.11	0.23	0	0.68	0.17	71	1064
PM2000	Bal	18.91	9.82	0.01	0.01	0.49	0.07	0.22	0	0.81	0.04	34	104
	Bal	20.02	10.62	0	0	0.44	0.04	0.23	0	0.74	0.03	50	211
Dour Alloy ODM 751	Bal	16.13	9.62	0.82	0	0.61	0.07	0.24	0	1.58	0.03	93	893
	Bal	16.36	7.57	0.85	0	0.65	0.11	0.24	0	1.62	0.03	82	918
ODS-Fe_3Al (PMWY1)	Bal	2.39	25.93	—	—	0.01	0.07	0.20	0	0.96	0.24	33	3300
ODS-Fe_3Al (PMWY2)	Bal	2.13	27.07	—	—	0	0.05	0.21	0	0.62	0.16	30	3480
ODS-Fe_3Al (PMWY3)	Bal	2.14	27.29	—	—	0	0.07	0.22	0	0.43	0.12	24	150
Kanthal APM	Bal	20.37	10.65	—	—	0.03	0.43	0	0.06	0.17	0.13	16	—
Kanthal APMT**	Bal	21.33	9.74	1.55	0	0.02	1.11	0.15	0.06	0.17	0.13	0	1512
	Bal	21.43	9.3	1.51	0	0.02	0.88	0.13	0.06	0.17	0.16	0	1979

*ppma
**+0.07Hf

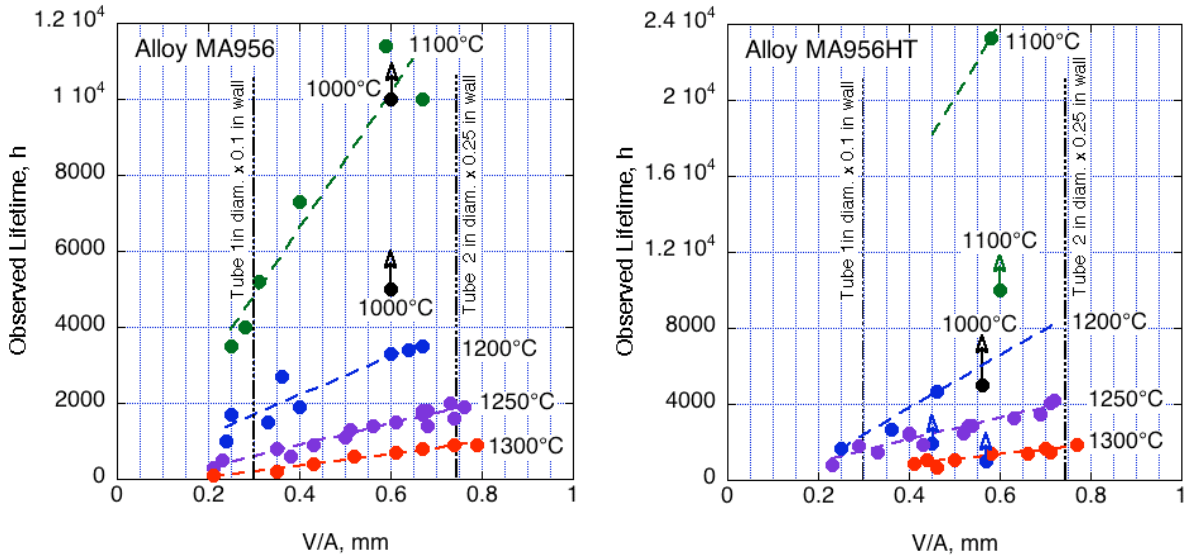

(a) (b)

Figure 14. Summary of cyclic oxidation exposures in air, run to failure at each of four temperatures, for (a) alloy MA956; and (b) alloy MA956HT.

produce failures. The value of *V/A* for a tube of 1 in diam. and 0.1 in wall thickness is 0.3, and 0.75 for a tube of 2 in diam. and 0.25 in wall thickness. The oxidation lifetime for MA956HT was found to be significantly longer than for MA956. While the major nominal difference is the increased Al level (C_B) in MA956HT, the measured oxidation kinetics for MA956HT were, in fact, slower than for MA956, while the extent of scale spallation was similar. Thus, the longer lifetime was not only the result of a larger reservoir of Al, but also because of a lower rate of Al consumption.

For a given value of *V/A*, algorithms for lifetime as a function of temperature can be obtained from plots such as that shown in Fig. 15. However, this approach does not provide flexibility for including effects of changes in *V/A*, oxidation rate, and variations in C_{B^*}, for which new data are needed for each new condition considered. Instead, a simple model [25] based on earlier work [15,16] was used to relate service life (time to breakaway, t_b) to the quantity (Al available for oxidation) / (oxidation rate). The input parameters needed are those that describe the oxidation kinetics of each alloy (Arrhenius data for calculating the temperature-dependence of the oxidation rate); and Al reservoir data (initial mass fraction of Al in the alloy, C_{Bo}; mass fraction of Al in the alloy at which a protective Al_2O_3 can no longer form, C_{B^*}; and the densities of the alloy and alumina). Using this approach, calculation of the oxidation-limited lifetime requires simply input of alloy temperature, and the area and volume of alloy exposed.

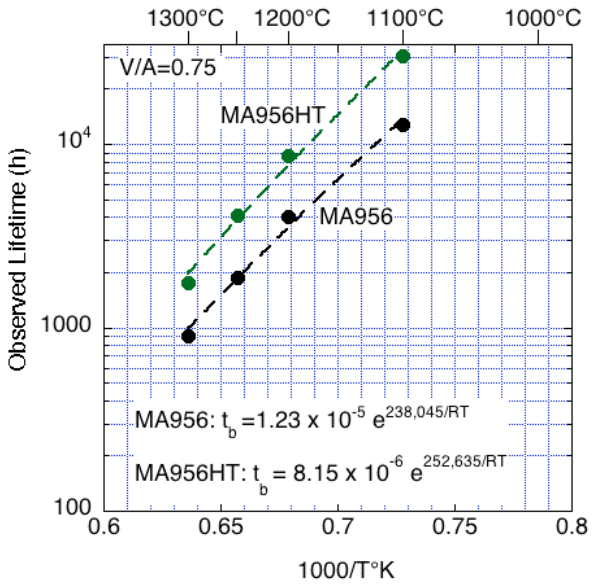

Figure 15. Temperature-dependence of oxidation-limited lifetimes for alloys MA956 and MA956HT (in the algorithms shown, t_b is in hours; T is in °K, and R = 8.314 $Jmole^{-1}K^{-1}$).

Efforts have continued to measure values of oxidation kinetics and C_{B^*} by means of specimens exposed until oxidation failure occurred. During the course of these measurements, it became clear that the basic assumption made in the model—that the Al concentration gradient through the specimen remains flat—is not always valid, and that local scale spallation can result in Al concentration gradients, and an increased rate of consumption of Al [26]. Geometrical/shape factors appear to be important, with the shape most subject to scale spallation being the parallelepiped used for standard oxidation specimens. As a result, data were collected from concentration profiles measured at the center of standard specimens (which typically did not fail first), and at the ends (which were most susceptible to spallation). Data from such measurements are summarized for alloys Inconel MA956 and 956HT in Figs. 16 and 17; the data for both alloys were essentially indistinguishable, so that the overall trends deduced reflect all of the data.

From these plots, the point at which the alumina scale was no longer protective was taken to be that at which Cr started to be oxidized, that is, the Al concentration corresponding to the point where the Cr concentration profile started to decrease. The overall result was that the deduced value of C_{B^*} ranged from ≈ 0.2 at% at the specimen centers (no spallation), to 0.5at% at the specimen ends for the standard

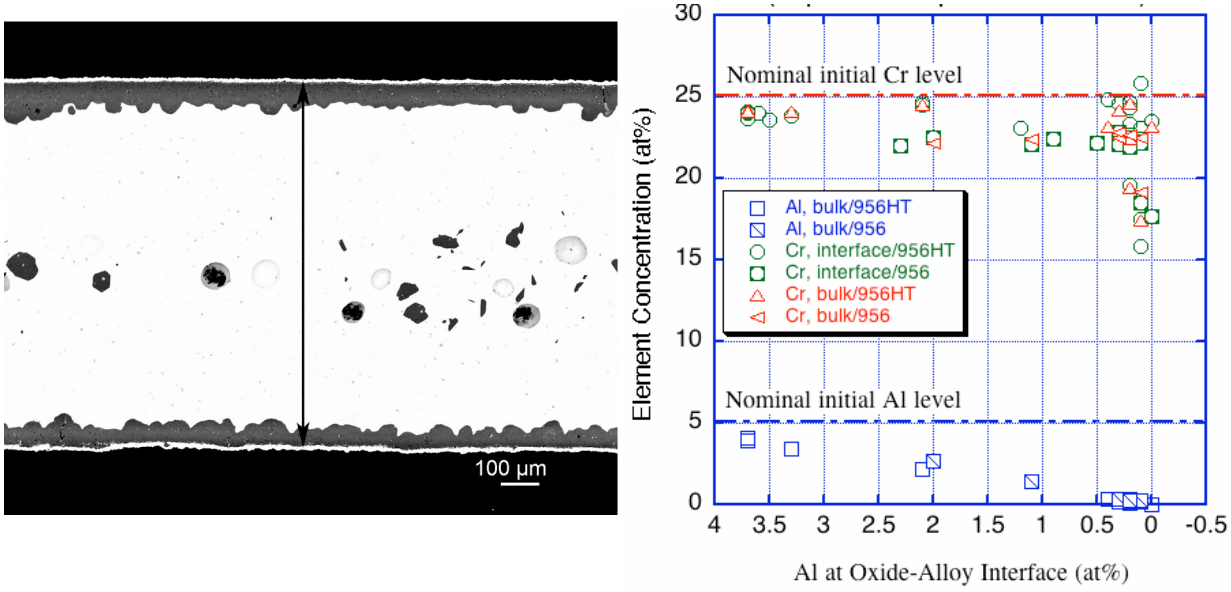

(a) (b)

Figure 16. Measurement of minimum Al for protective behavior (C_{B^*}) for MA956 and MA956HT (a) cross section of the center of a specimen of MA956 oxidized to failure at 1200°C; and (b) plot of corresponding Al and Cr concentrations measured at the metal-oxide interface in the central region of multiple specimens oxidized to failure at 1200°C.

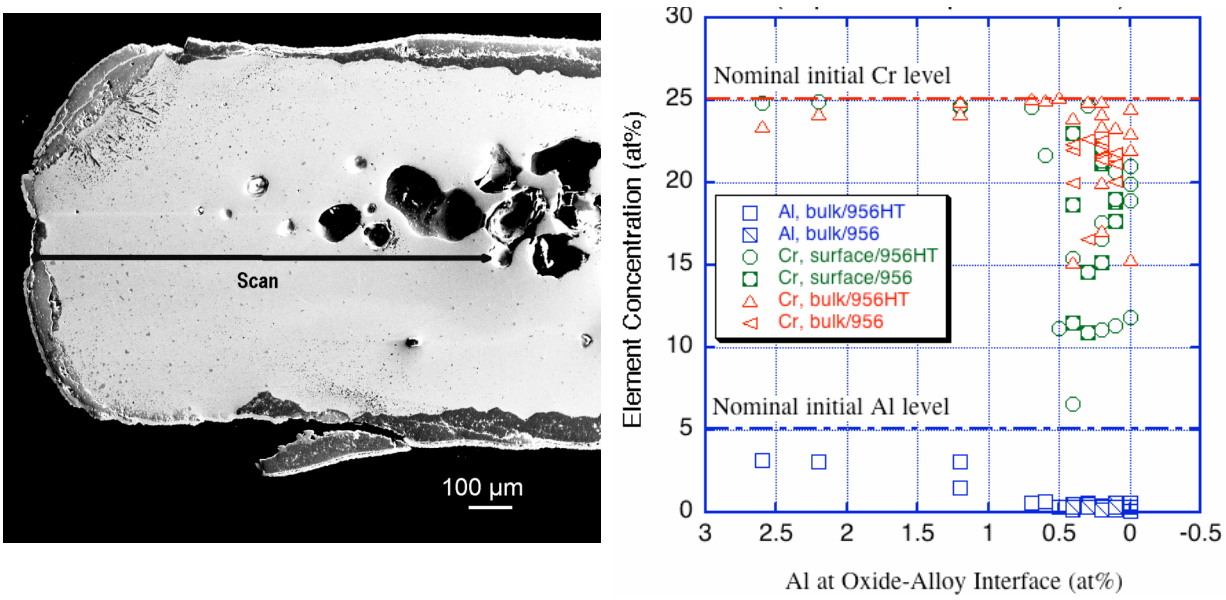

(a) (b)

Figure 17. Measurement of minimum Al for protective behavior (C_{B^*}) for MA956 (a) cross section of the end of a specimen of MA956 and MA956HT oxidized to failure at 1200°C; and (b) plot of corresponding Al and Cr concentrations measured at the metal-oxide interface at the ends of multiple specimens oxidized to failure at 1200°C.

parallelepiped oxidation specimen. When used in the simple two-stage model for MA956 [26], the value of 0.5at% gave an excellent fit to the observed lifetimes shown in Fig. 14a (which were generated using standard specimens). However, the same value of C_{B^*} underestimated the observed lifetimes for MA956HT (Fig. 14b) which were generated using disc-shaped specimens, whereas a value of 0.2 at% provided a closer fit, suggesting that there was some contribution to Al loss by scale spallation from the disc specimens, but not as much as from the parallelepipeds.

SUMMARY

Two techniques for joining ODS alloys have shown good promise. Transient liquid-phase diffusion bonding, using a thin foil of low-melting TLP alloy, produces what appear to be clean joints. The initial, unexpected, microstructural features can be explained by considerations of the local concentration and transport of the TLP phases away from the joint with time and temperature. Heat treatments have resulted in acceptable dispersion of the TLP constituents after joining. A continuing issue is that it appears that the thermal histories associated with the TLP processing routes used so far have diminished the driving force for post-joining, secondary recrystallization of the alloy to form the desired large aspect-ratio grain structure. Re-evaluation of the processing steps in the TLP joining process for compatibility with a secondary recrystallization step is the next goal.

Interaction with MER Corporation has determined the appropriate processing parameters to produce very promising butt joints by pulsed plasma-assisted diffusion bonding. When secondary recrystallization after bonding resulted in grain growth through the bond line, joint strengths up to 82% of the bulk parent alloy were measured in creep tests in air at 1000°C. This technique is ready for demonstration on appropriate components (tubes), and the next step should be to measure standard creep data using exemplar joints in specimens taken from bonded tubes.

The completion of some of the long-term oxidation lifetime tests of ODS-FeCrAl alloys has produced not only data against which the predictions of the analytical model can be compared, but also values of a key parameter needed by the oxidation lifetime model. As the exposures of full sets of specimens of a given alloy complete testing, it will be possible to reevaluate the overall oxidation kinetics for use with the new parameter values in a refined version of the model. While it is considered that the assumptions embodied in the model are satisfactory for application to oxides grown on tubes, edge/end effects and specimen shape (which are more important for components made from plate or sheet) have been noted to give rise to Al concentration gradients that can significantly reduce oxidation lifetime. The effects of environments other than air on oxidation lifetime also need to be considered, since constituents such as water vapor or CO_2 in the environment could modify the mode and/or rate of oxide growth.

ACKNOWLEDGMENTS

This research was sponsored by the Fossil Energy Advanced Research Materials (ARM) Program, U.S. Department of Energy, under contract DE-AC05-96OR22464 with UT-Battelle LLC. The authors thank the director of the ARM program, Robert Romanosky, of the National Energy Technology Laboratory, and Roddie Judkins, Director of the Fossil Energy program at ORNL, for their continued enthusiasm and support. We also thank Hu Longmire for developing metallographic preparation skills for ODS-FeCrAl alloys; Larry Walker for electron microprobe analysis expertise; Dorothy Coffey for her skill with focused ion-beam milling to produce the TEM samples; John Shingledecker and Ralph Martin for advice and assistance with creep testing; and Jim Keiser for reviewing the manuscript.

REFERENCES

1. See, for instance, I.G. Wright, B.A. Pint, and Z.P. Lu, "Overview of ODS alloy development," Proc. 19th Annual Conference on Fossil Energy Materials, Knoxville, Tennessee, 9th-11th May 2005.
2. J.P. Hurley, "Applications for Dispersion-Strengthened Alloys in Thermal Power Systems," Proc. 21st Annual Conference on Fossil Energy Materials, Knoxville, Tennessee, 30th April–2nd May 2007.
3. Private communication, D. Arrell (Siemens Power Generation, Inc.) to I.G. Wright (ORNL), May 2007.
4. See, for instance, "Incoloy® alloy MA956," Special Metals Corporation Technical Bulletin No. SMC-008 (2004).

5. H.D. Hedrich, H.D. Mayer, G. Haufler, M. Kopf, and N. Reheis, "Joining of ODS Superalloys," pp. 789-798 in *Proc. Conf. on Materials for Advanced Power Engineering,* D. Coutsouradis, J.H. Davidson, J. Ewald, P. Greenfield, T. Khan, M. Malik, D.B. Meadowcroft, V. Regis, R.B. Scarlin, F. Schubert, and D.V. Thornton, Eds., Kluwer Academic Publishers, Dordrecht (1994).
6. M.A. Harper, *Development of ODS Heat Exchanger Tubing*, Special Metals Corporation, Huntington, KY, April 2003.
7. M.G. McKimpson and D. O'Donnell, "Joining ODS materials for high-temperature applications," *JOM,* 46, (7), 49-51 (1994).
8. T.I. Kahn and E.R Wallach, "Transient liquid-phase diffusion bonding and associated recrystallization phenomenon when joining ODS ferritic superalloys," *J. Mater, Sci*., 31 (11), 2937-2943 (1996).
9. W.F. Gale and D.A. Butts, "Transient Liquid Phase Bonding," *Sci. and Techn. of Welding and Joining*, 9 (4), 283-300 (2004).
10. V.G. Krishnardula, N.I. Sofrijon, W.F. Gale, and J.W. Fergus, "Transient Liquid-Phase Bonding of Ferritic Oxide Dispersion-Strengthened Alloys," *Met. Mat. Trans. A*, 37, 407-500 (2006).
11. C.Y. Kang, T.H. North, and D.D. Petrovic, "Microstructural features of friction-welded MA 956 superalloy material," *Met. Mat. Trans. A*, 27, 4019-4029 (1996)
12. P.D. Sketchley, P.L. Threadgill, and I.G. Wright, "Rotary friction welding of an Fe_3Al-based ODS alloy," *Mat. Sci. & Eng. A-Structural Materials Properties, Microstructures, and Processing*, Special Issue, 329, 756-762 (2002).
13. V.G. Krishnardula, R. Aluru, N.I. Sofyan, J.W. Fergus, W.F. Gale, "Solid-State Diffusion Bonding of MA956 and PM2000," pp. 885-888 in *Trends in Welding Research,* Proc. 7th Intl. Conf., S.A. David, T. DebRoy, J.C. Lippold, H.B. Smartt, and J.M. Vitek, Eds., ASM (2005).
14. K. Nishimoto, K. Saida, and R. Tsuduki, "Effect of pulsed electric-current on densification behavior of bonded interlayer of oxide dispersion-strengthened superalloys," pp. 747-755 in *Joint. J. Japan Institute of Metals*, 65, No. 8 (2001).
15. W. J. Quadakkers and K. Bongartz, "The prediction of breakaway oxidation for alumina-forming ODS alloys using oxidation diagrams," *Werkstoffe und Korrosion*, 45, 232-41 (1994).
16. M. J. Bennett, H. Romary and J. B. Price, "The Oxidation Behavior of Alumina-Forming Oxide Dispersion-Strengthened Ferritic Alloys at 1200-1400°C," pp. 95-103 in *Heat-Resistant Materials*, K. Natesan and D. J. Tillack, eds. (ASM, Materials Park, Ohio, 1991).
17. I.G. Wright, N.S. Bornstein, E.G. Dyadko, and S.N. Dryepondt, "Enabling The Practical Application Of Oxide Dispersion-Strengthened Ferritic Steels," Proc. 20th Annual Conference on Fossil Energy Materials, Knoxville, Tennessee, 24th-26th April 2006.
18. I.G. Wright, B.A. Pint, C.G. McKamey, "ODS alloy development," Proc. 17th Annual Conference on Fossil Energy Materials, Knoxville, Tennessee, 22nd-24th April 2003.
19. E.G. Dyadko, "Novel Joining Technique for Oxide Dispersion-Strengthened Iron Aluminide Alloys," Final Report on Contract No. DE-FG03-00ER83041 December, 23, 2006.
20. G.J. Tatlock, E.G. Dyadko, S.N. Dryepondt, and I.G. Wright, "Pulsed Plasma-Assisted Diffusion Bonding of ODS-FeCrAl Alloys," *Met. Mat. Trans. A*, 38A, 1663-5 (2007).
21. See, for instance, J. Schubert, A. Klenk, and K. Maile, "Determination of weld strength factors for the creep rupture strength of welded joints," pp. 792-805 in *Creep & Fracture in High-Temperature Components-Design & Life Assessment Issues*, I.A. Shibli, S.R. Holdsworth, and G. Merkling, Eds., DES*tech* Publications, Inc. (2005).
22. J. P. Shingledecker and I. G. Wright, "Evaluation of the materials technology required for a 760ºC power steam boiler," pp. 107-119 in *Materials for Advanced Power Engineering 2006*, J. Lecomte-Beckers, M. Carton, F. Schubert, and P. J. Ennis, Eds., Schriften des Forschungszentrums Jülich (2006).
23. W.H. Weigert, R.J. Henricks, "Tensile and creep-rupture behavior of two advanced, oxide dispersion-strengthened sheet alloys," pp. 575-584 in *Superalloys 1980*, J.K. Tien, S.T. Wlodek, H. Morrow, M. Gell, and G. R. Maurier, Eds., ASM (1980).
24. J.D. Whittenberger, "Tensile and creep properties of the experimental oxide dispersion-strengthened iron-base sheet alloy MA956 at 1365K," *Met. Trans. A*, 9A, 101-110 (1978).

25. I.G. Wright, B.A. Pint, L.M. Hall, and P.F. Tortorelli, "Oxidation lifetimes: experimental results and modeling," paper presented at the European Federation of Corrosion Workshop on *Lifetime Modeling of High-Temperature Corrosion Processes*," Frankfurt am Main, Germany, February 2001.
26. I.G. Wright, C.G. McKamey, and B.A. Pint, "ODS alloy development," Proc. 16th Annual Conference on Fossil Energy Materials, Baltimore, Maryland, 22nd-24th April 2002.

CONTROL OF DEFECTS AND MICROSTRUCTURE IN ODS ALLOYS

Gordon J Tatlock
University of Liverpool, Department of Engineering, George Holt Bldg., Ashton Street, Liverpool L69 3GH, UK
E-mail: tatlock@liv.ac.uk; Telephone: + 44 151 794 5367; Fax: +44 151 794 4675

Hameed Al-Badairy†
Saudi Aramco, Research and Development Centre, P.O. Box 62, Dhahran 31311, Saudi Arabia
E-mail:hameed.badairy@aramco.com; Telephone: + 966 3 8724066

Chun-Liang Chen
University of Liverpool, Department of Engineering, George Holt Bldg., Ashton Street, Liverpool L69 3GH, UK
E-mail: chen@liv.ac.uk; Telephone: + 44 151 794 5394; Fax: +44 151 794 4675

Andy R Jones
University of Liverpool, 3 Brownlow St., Liverpool L69 3GL, UK
E-mail: andy.jones@liv.ac.uk; Telephone: + 44 151 794 8026; Fax: +44 151 794 8370

ABSTRACT

High-temperature heat exchangers for application in gasifier fuel gas cooling or high efficiency indirectly fired cycles, require development of metal alloys for tubing capable of service at temperatures in excess of 1100^{0}C (~2000^{0}F). And similar, future operational requirements characterize the demands on materials for advanced combustor cans for application in combined cycle gas turbines. Amongst candidate alloys available for high temperature service, commercial FeCrAl-based mechanically alloyed (MA) Oxide Dispersion Strengthened (ODS) materials such as PM2000 (and MA956), have a composition and microstructure designed to impart creep strength and oxidation resistance in components operating at temperatures from ~1050ºC to 1200ºC and above. Despite the potential benefits offered by these FeCrAl-based ODS alloys they currently suffer from a number of performance shortfalls, notably in biaxial creep performance and the performance of joints. In the latter instance, joining techniques that involve fusion techniques can cause agglomeration and loss of the dispersion of fine-scale oxide particles introduced during the mechanical alloying process. This usually leads to disruption in the beneficial grain structures introduced by subsequent secondary recrystallisation annealing, resulting in a substantial reduction in high temperature creep performance in the joint region.

The current work reports studies made on the application of friction stir welding as a solid state technique for autogenous joining of PM2000 ODS alloy sheet; in particular, the influence of the joining process on the initial microstructure of the alloy and the microstructures that developed during subsequent heat treatment. Microstructures throughout the joint region were compared, examining the influence of the friction stir technique on oxide particles and grain structures alike. Separate studies are also reported on the influence of surface finish on the 1100ºC oxidation behaviour of PM2000 alloy sheet and initial results on evolution of microstructure in PM2000 alloy plate hot-spun to produce combustor can geometry components.

INTRODUCTION

The ODS FeCrAl alloys have significant potential for application in components for use in demanding high temperature environments such as power generation plant[1,2,3], where a combination of excellent high temperature creep strength under biaxial loading conditions and oxidation resistance in combustion gases is required[4]. The ODS base alloys can be supplied in various product forms ready for incorporation in components and can be provided with final heat treatments that will generate release condition creep resistant coarse grained microstructures[5] and a

protective alpha alumina oxide layer[6]. However incorporation of components in fabricated structures usually involves joining technologies and those which involve fusion techniques generally produce unacceptable, irreversible microstructural change and property degradation in these alloys. Hence, there is considerable interest in finding approaches to the design and fabrication of components in these materials which either involve minimal or zero-fusion joining techniques or, by additional processing, can minimise the number of joints required. Thus, friction stir welding[7], which is a solid state joining technique, offers potential for introducing seam welds in ODS sheet or plate, while established techniques such as metal spinning[8] has the potential to shape a combustor can in one step from ODS alloy plate, obviating the need for any seam welds. The influence of both techniques on ODS alloy parent microstructures is being explored as part of current studies[9, 10] and results are reported in following sections. On a similar theme, of the way processing can influence performance, preliminary results are also presented which indicate the influence that surface finish can have on the oxidation behaviour of PM2000 alloy.

EXPERIMENTAL

The PM2000 alloy used in the current work was supplied free issue in several product forms and conditions by Siemens Industrial Turbomachinery Ltd. Alloy sheet (as-rolled) nominally 2mm in thickness was supplied direct by Siemens in the as-friction stir welded condition, where subcontract joining (50mm/min threaded tool speed) had been performed by TWI. Combustor cans, manufactured on subcontract elsewhere, by hot metal spinning of nominally 10mm thick PM2000 flat alloy plate, were also supplied by Siemens for metallurgical examination.
Separately, samples of 2mm thick PM2000 alloy sheet subject to high temperature annealing (2000h/1100ºC) in simulated combustion gases were supplied for metallographic examination by Cranfield University, UK.
Standard metallographic techniques reported elsewhere[9] were used to prepare samples for imaging using low voltage Scanning Electron Microscopy (SEM) channelling contrast, Electron BackScatter Diffraction (EBSD) analysis and Transmission Electron Microscopy (TEM) examination.

RESULTS AND DISCUSSION

FRICTION STIR WELDING

A typical SEM channelling contrast image of a transverse section through 2mm thick friction stir welded PM2000 sheet in the welded and secondary recrystallised (SR) annealed (1h/1380ºC) condition is shown in Fig.1.

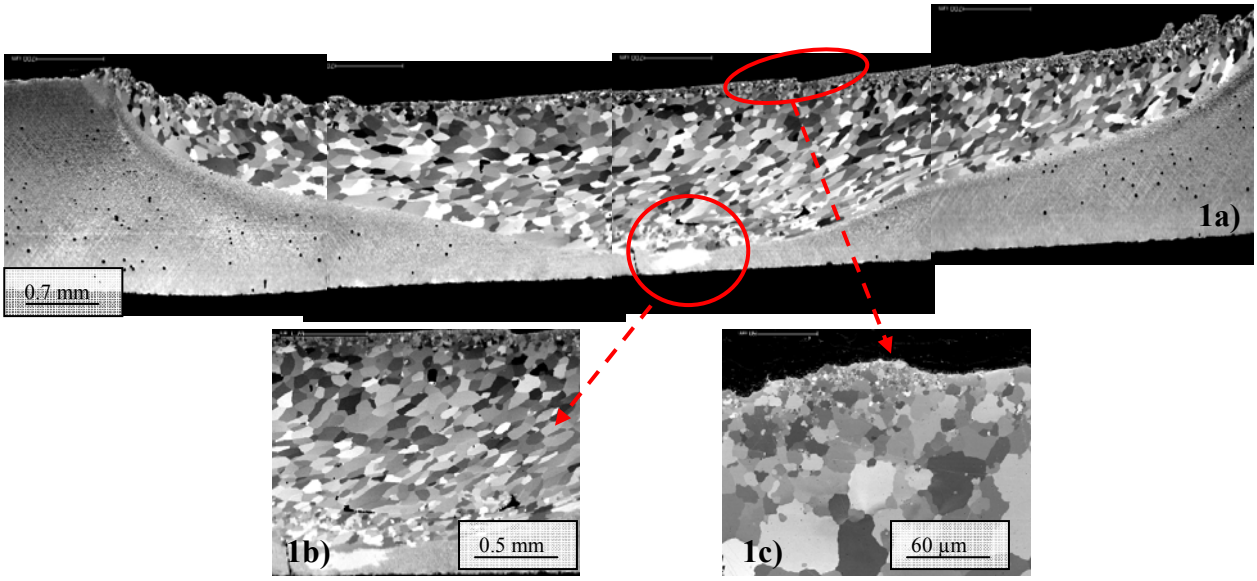

Figure 1. a) Channelling contrast image of SR friction stir weld in PM2000, showing the weld and HAZ. b) a large recrystallised grain grown into parent plate in the weld root c) fine grained region on weld cap.

The image reveals a large, relatively equiaxed grain structure in the weld itself, a Heat Affected Zone (HAZ), and parent plate that has remained in a fine-grained condition despite receiving the standard (1h/1380ºC) release SR anneal for these materials. Also, there is some evidence of an apparent tendency for 'layering' of grain structures in the weld nugget itself, consistent with the cylindrical sheets of material that are extruded during each rotation of the threaded tool which deposits material from the 'front' to the back' of the weld during the friction stir joining process. The large recrystallised grain seen in the root of the weld (Fig. 1b) has grown into parent sheet outside the weld zone, suggestion that the pattern of deformation in the weld root region enabled progress of secondary recrystallisation beyond the weld zone itself. In contrast, in the rest of the parent sheet, there appears to have been no further secondary recrystallisation, either by independent nucleation in the PM2000 sheet, or by intrusion of growing grains nucleated originally in the weld zone. Recrystallisation at the surface of the friction stir weld tended to be characterised by a layer of much finer grains (Fig. 1c). It is thought this could have arisen due to the cooling rate at the weld surface during joining, prior to the recrystallisation anneal. It is also worth noting that despite the fact that the parent material did not undergo secondary recrystallisation during post weld annealing, there is clear evidence (Fig. 1a) of the sort of porosity that evolves in these materials after high temperature annealing. It is suspected that the reason the PM2000 sheet failed to undergo secondary recrystallisation was that it was supplied in a processed condition which had allowed some recovery, thereby reducing the remaining level of stored energy below that which would enable nucleation of secondary recrystallisation to occur.
EBSD was used to investigate the grain orientation and the grain boundary geometries in the weld samples. Figure 2a shows an orientation map of the friction stir weld region after secondary recrystallisation, which demonstrates

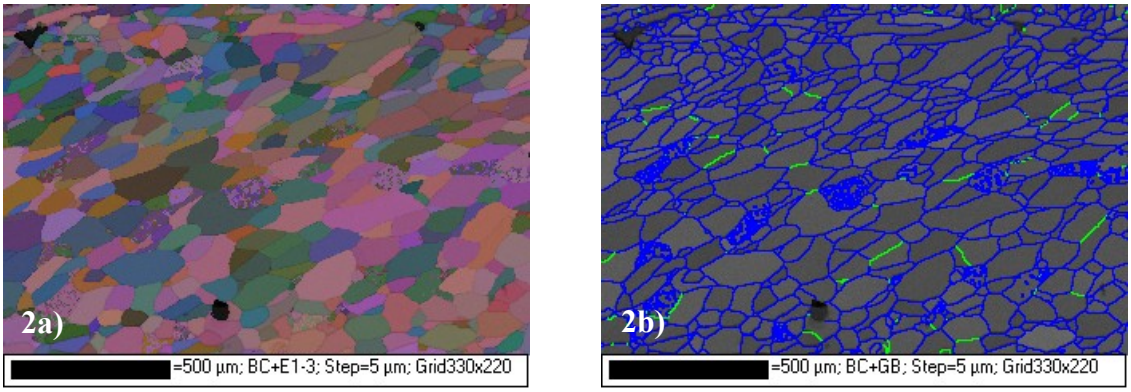

Figure 2: a) EBSD grain orientation (colour map) and b) grain boundary angle maps (blue = high angle (>10^0) boundary; green = low angle boundary) from the FSW region.

that grains were oriented randomly in this region. Overall there was no evidence of any preferred orientation in the secondary recrystallised grain structures that formed in the weld zone after annealing (1h/1380ºC). Fig. 2b shows the grain boundary misorientation map for the same region as shown in Fig. 2a. High angle grain boundaries (defined here as those with a misorientation >10 degrees) are highlighted in blue and can be seen to comprise the majority of boundaries in the weld after recrystallization. Similar EBSD analysis of regions away from the weld zone in annealed sheet suggested that the majority of the microstructure comprised elongated grains which consisted of numerous sub-grains with an irregular morphology, confirming that in the non-FSW region of the PM2000 sheet only recovery had taken place.
TEM observations provided further details of the grain structures, deformation behaviour, and particle size distributions in the various sample regions (FSW and non-FSW regions, before and after the recrystallisation treatment). Figure 3a shows the microstructure of the non-FSW region before recrystallisation treatment. It reveals a fine grain/sub-grain structure elongated and aligned with the working direction in the plane of the sheet and containing large numbers of fine-scale Yttrium Aluminium Garnet (YAG) particles. The material is in a fine grained condition characteristic of the microstructure in these alloys following consolidation and working, and contains a high density of sub-grain boundaries and a residual density of free dislocations within the sub-grain interiors. Additionally, the fine YAG particles tended to be aligned along the grain boundaries in the working direction in the plane of the sheet. There was also clear evidence of Zener pinning of dislocations at particles in the microstructure. Figure 3b shows the microstructure of the non-FSW region after the secondary recrystallisation anneal. The

elongated sub-grain structures remained and, together with the particles, showed slight evidence of coarsening, while the residual dislocation density within the sub-grains was reduced by recovery processes.

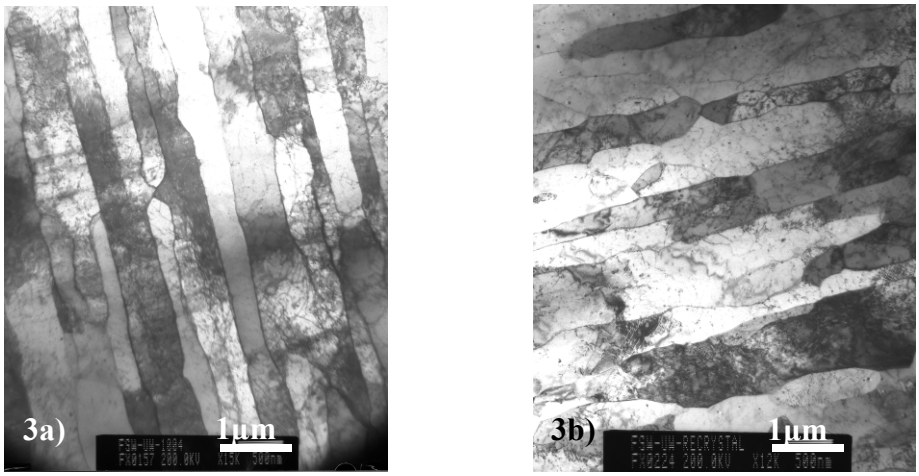

Figure 3: TEM micrographs of the non-FSW region a) before and b) after the SR (1h/1380ºC) anneal

On the other hand, Fig. 4a shows the microstructure of the FSW region before the recrystallisation treatment. A fine, equiaxed grain/sub-grain structure exists with a relatively low dislocation density present within sub-grain interiors. It was noted that the YAG particle array had been re-distributed into a more random arrangement in the matrix, with

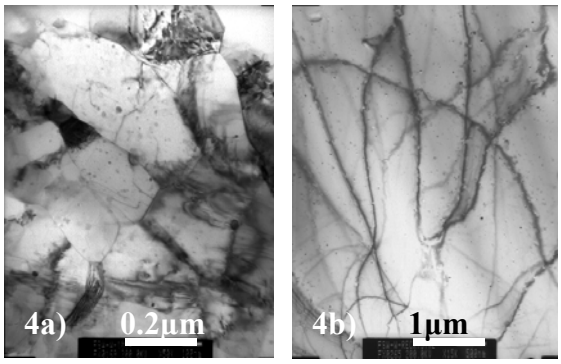

Figure 4: TEM micrographs of the FSW region a) before and b) after the SR (1h/1380ºC) anneal

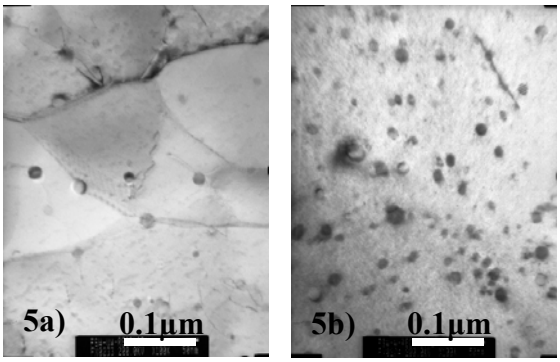

Figure 5: YAG particles in a) non-FSW and b) FSW regions following an SR (1h/1380ºC) anneal

no significant evidence for any remaining alignment of YAG particles or of aligned, coincident grain boundaries. This suggests that the FSW process had had significant effect on the particle distribution in the PM2000 and that the temperature rise accompanying the process had also led to significant re-arrangement of the dislocation/sub-grain structures. The microstructure of the FSW region after recrystallisation is shown in Fig. 4b. Unlike the parent sheet, the FSW region was, essentially, dislocation free, having undergone recrystallisation to a relatively coarse grain size, confirming that FSW imparted sufficient additional stored energy as well as microstructural change to enable nucleation of SR in the weld region. In addition, Figs 5a and 5b show that the size distribution of the YAG particles remains similar in the weld zone to that in the parent PM2000 sheet after SR, with perhaps a slight coarsening in both regions compared to the as-received condition.

EFFECTS OF SURFACE ROUGHNESS ON OXIDATION OF PM2000

The microstructures of three PM2000 sheet samples with three different surface roughness conditions (A5-as received (Ra (mean roughness) of 4.8µm, Rt (maximum roughness) of 45.3µm), G5-coarse ground (Ra of 4.7µm, Rt

of 24.9µm) and D5-fine ground (Ra of 0.4µm, Rt of 4.4µm) were investigated after cyclic oxidation in combustion gases for 2000hours at 1100ºC. Figure 5a shows the SEM image of the oxide scale layer in the as-received sample. The oxide scale grew over the irregular geometry of the parent metal surface. Numerous cracks, fractures, voids, and spallation were found. This implies that large stresses are generated by the oxidation process. These are growth stresses, which arise due to the finite size of specimens and the resultant curvature, and thermal stresses, which arise from differential thermal expansion or contraction between the matrix and scale. A columnar grain structure was observed in the oxide scale. Figure 5b shows a micrograph of the oxide scale layer on the coarse ground specimen. Oxide spallation of the scale was clear on both sides of the specimen, particularly on the uneven surface regions, where large stresses could be generated. However, the microstructure of the scale showed fewer cracks, fractures and voids and, in general, the scale grew relatively evenly over the matrix. In contrast, the oxide scale on the fine ground specimen was tightly adherent and had a fine microstructure, as shown in Fig. 5c. An extremely uniform scale without cracks, fractures and voids was found to have grown over the flat surface of the matrix, with a columnar grain structure clearly visible in the scale. Overall, the morphologies of the oxide scales were found to be strongly affected by the parent alloy surface quality, with increased roughness leading to increasing levels of defects (cracks, fracture, and spallation). However, the thickness of the oxide scale was found to be largely independent of surface quality, except where spallation had occurred.

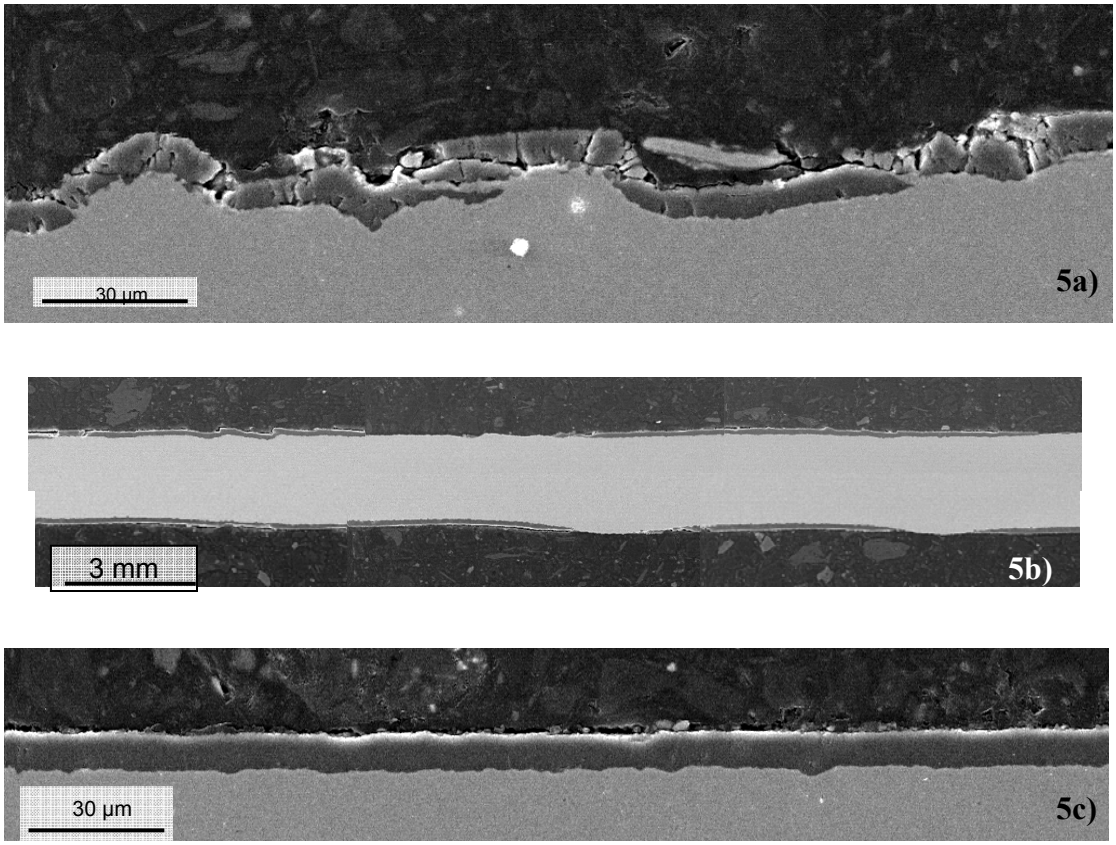

Figure 5: SEM images of oxide scale on a) as-received b) coarse ground and c) fine ground PM2000 alloy sheet subject to cyclic oxidation in combustion gases for 2000hours at 1100ºC.

For comparison, Fig. 6 shows results from Cranfield University[11] of change in mass in annealed specimens of the three different surface finishes. It illustrates that mass change in the as-received specimen exhibits a significant drop after 1000 hours; however, the curves of the coarse and fine ground specimens increase with exposure times. This is likely to have been due to numerous instances of spallation during the early stages of exposure, followed by re-oxidation and subsequent re-spallation, leading to overall loss of mass on the samples with the as-received finish. Analysis of the microstructure shows evidence of re-oxidation, as illustrated, for example, in Figure 5a. On the other hand, there is no evidence to show that re-oxidation took place on the coarse and fine ground specimens. The fine

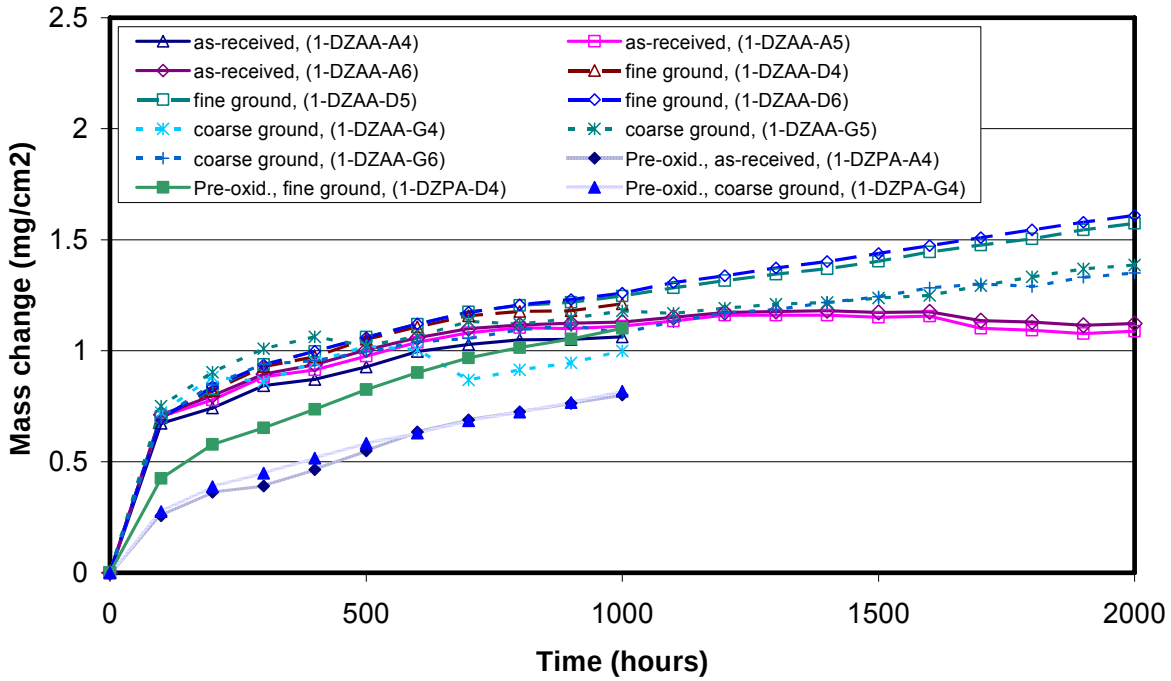

Figure 6: 'Isothermal' exposure of P2000 in combustion gas at 1100°C showing the effects of surface finish and pre-oxidation.[11]

ground specimens exhibited larger change (gain) in net mass than the coarse ground PM2000 samples, due to the occurrence of limited oxide scale spallation on the annealed, course ground sample.

HOT SPUN PM2000 COMBUSTOR CANS

Figure 7a is a transverse section which shows the microstructure near the inner surface of an SR PM2000 can produced from a 10mm thick alloy precursor plate by hot spinning (gas burner preheat). Large grains and numerous small voids were observed in this region (Fig 7b). While no evidence was found for large grains near the outer surface of the hot spun can, a thin layer of smaller recrystallised grains was observed, Fig. 7c. This suggests that the complex pattern of deformation introduced during the hot spinning process leads to significant heterogeneities in recrystallisation behaviour across the thickness of the can wall. This microstructural variability is consistent with the sort of deformation complexities that would be anticipated as a result of shape change introduced using, essentially, a single-sided industrial working process. These results are similar in terms of the level of microstructural change,

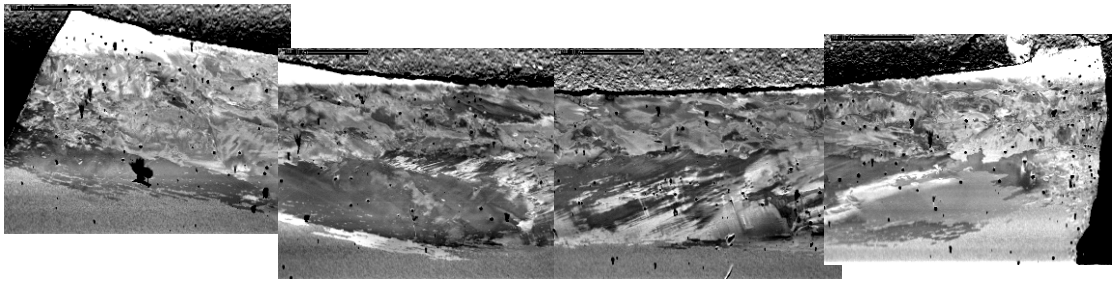

Figure 7a: SEM image showing the microstructure of a transverse section through a PM2000 spun can near the inner wall (10mm thickness).

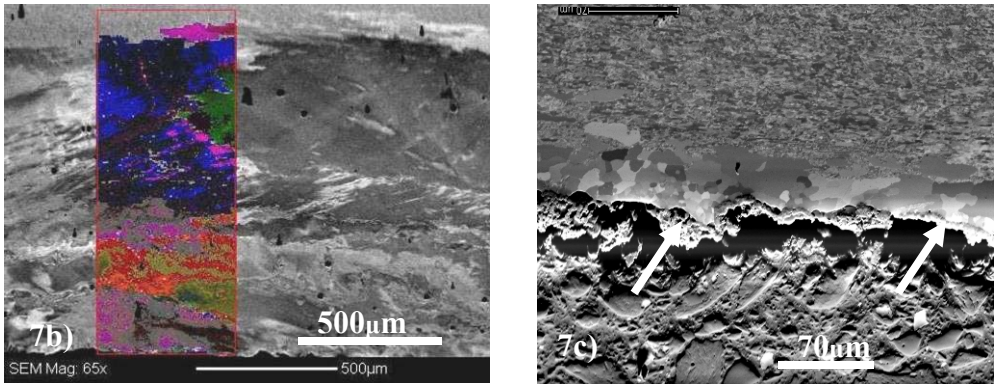

Figure 7 continued: b) EBSD detail from Fig 7a illustrating local grain structures c) fine grained regions adjacent to the outer wall regions (arrowed) of the spun can.

following deformation and recrystallisation, to those seen in PM2000 subject to industrial flow forming, another complex industrial deformation process.[4, 5]

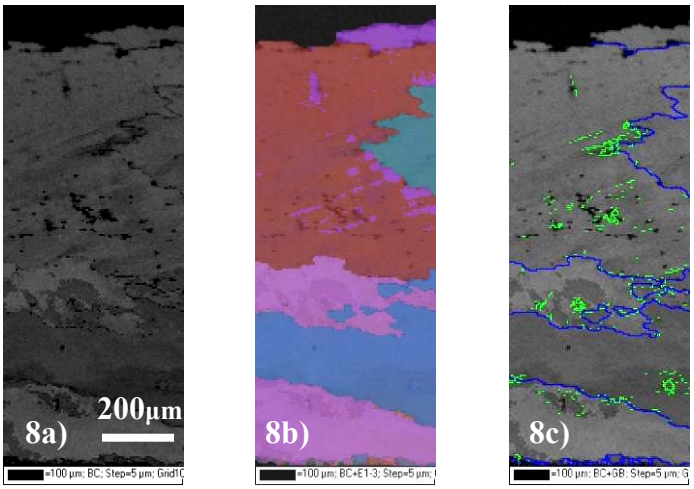

Figure 8: a) SEM image of microstructure near spun can inner wall b) corresponding EBSD image showing grain orientation contrast c) EBSD of same area showing high angle (>10^0, blue), and low angle (<10^0, green) boundaries

EBSD data showing grain orientation and grain boundary misorientation in the region near the spun can inner wall are shown in Fig. 8 and confirm the presence of large recrystallised grains with high angle grain boundaries, together with the presence of a small number of low angle grain boundaries. The results (Fig. 8b) provided no indication of any strong texture effects in this region.

CONCLUSIONS

The microstructures developed in friction stir welds in PM2000 sheet and in can spun from PM2000 plate have been examined and an assessment made of the influence of surface finish on the morphology of oxidation in the same alloy. Conclusions of this work are:

(i) friction stir welding appears to hold promise as a technique for solid state joining of ODS materials such as alloy PM2000 in sheet or plate form;

(ii) there appears to be no loss or coarsening of the distribution of YAG particles in the friction stir weld zone. In fact, the joining process homogenizes the spatial distribution of oxide particles in the weld, removing stringers present in parent sheet and encouraging subsequent formation of equiaxed secondary recrystallised grain structures;

(iii) parent sheet in friction stir weld samples resisted secondary recrystallisation on annealing (1h/1180^{0}C) following joining, suggesting the alloy had been subject to an earlier recovery anneal; however, there was some evidence of growth of recrystallised grains across the weld interface, suggesting that, in the right samples, it might be possible to achieve more extensive recrystallisation through the joint and, therefore, improved final properties;

(iv) Surface finish affects the degree of oxide spallation and, hence, mass change that occurs during high temperature oxidation of PM2000 alloy in combustion gases. Fine ground samples provide the most adherent oxide scale;

(v) Recrystallisation in samples of PM2000 alloy processed from plate into can by metal spinning produces microstructures which vary across the wall of the can. This behaviour is very similar to the sort of recrystallisation observed in flow formed PM2000 and reflects the complex patterns of deformation that arise in these industrial processing methods.

ACKNOWLEDGEMENTS

The authors are grateful for funding from the Advanced Research Materials (ARM) Programme, U.S. Department of Energy, Office of Fossil Energy under contract DE-AC05-96OR22464 managed by U.T.–Battelle, LLC. The authors also acknowledge Siemens Industrial Turbomachinery Ltd., UK and Cranfield University, UK who supplied the friction stir welded PM2000 alloy sheet and spun can, and PM2000 alloy oxidation samples, respectively. The authors also appreciate the access to facilities and support of Professor D.J.Prior and Mr D Atkinson in the SEM-EBSD studies.

REFERENCES

1. J.S. Benjamin, '*Dispersion strengthened superalloys by Mechanical Alloying'*, Metall. Trans., vol. 1, 2943–51, 1970.
2. J. Ritherdon, A. R. Jones, U. Müller, and I. G. Wright, *'Improving the high-temperature performance in ODS alloys for application in advanced power plant,'* 927-938 in Parsons 2003: Engineering Issues in Turbine Machinery, Power Plant and Renewables, Eds. A. Strang, et al., for the Institute of Materials, Minerals, and Mining, 2003.
3. I.G. Wright, B.A. Pint, and Z.P. Lu, *'Overview of ODS alloy development,'* Presented at the 19th Annual Conference on Fossil Energy Materials, Knoxville, Tennessee, May 9th-11th, 2005.
4. F Starr, A R White and B Kazimierzak, *Proc. Conf. 'Materials for Advanced Power Engineering'*, Liege, Eds Coutsouradis et al., Kluwer, Academic Pub.,1393, 1994
5. R. Timmins and E. Arzt *`Diffusion creep in a coarse grained ODS superalloy. under transverse loading'*, Scripta Metall., 22, 1353-1356, 1988.
6. W. J. Quadakkers, *'Growth mechanisms of oxide scales on ODS alloys in the temperature range 1000-1100°C'* Werkstoffe und Korrosion 41, 659-668, 1990
7. W. M. Thomas, D. G. Staines, I. M. Norris, R. Frias, *'Friction Stir Welding – Tools and Developments'*, Doc IIW-1639-03, Welding in the World, Vol. 47, n° 11/12, 10-17, 2003
8. E. Quigley and J. Monaghan**, '***Metal forming: an analysis of spinning processes'*, Journal of Materials Processing Technology, 103(1), 114-119, 2000.
9. J. Ritherdon and A.R. Jones, *'Reduction in Defect Content in ODS Alloys'* Proc. 19th Annual Conf. on Fossil Energy Materials, Knoxville, Tennessee, May 9-11, 2005, Eds. Judkins et al., ORNL, 2005.
10. A.R.Jones , Ö. Selsil and S. E. Burns 'Reduction in Defect Content in ODS Alloys, Proc.20th Annual Conf. on Fossil Energy Materials, June 12-14 2006, Ed. R.R. Judkins, Oak Ridge National Laboratory, Tennessee, USA, 39, 2006
11. N.J.Simms and J.E.Oakey, Cranfield University, UK, private communication.

CONCEPTS FOR SMART PROTECTIVE HIGH-TEMPERATURE COATINGS

P.F. Tortorelli
Oak Ridge National Laboratory, Oak Ridge, TN 37831-6156
tortorellipf@ornl.gov ; Tel: (865) 574-5119; FAX (865) 241-0215

M.P. Brady
Oak Ridge National Laboratory, Oak Ridge, TN 37831-6115
bradymp@ornl.gov; Tel: (865) 574-5153; FAX (865) 241-0215

I.G. Wright
Oak Ridge National Laboratory, Oak Ridge, TN 37831-6156
wrightig@ornl.gov; Tel: (865) 574-4451; FAX (865) 241-0215

ABSTRACT

Design of smart protective coatings is envisioned as a means to overcome materials barriers imposed by the environments associated with advanced fossil energy systems. To this end, short-term sulfidation behavior over a range of temperature was studied for baseline stainless steels and an iron aluminide as a step toward addressing corrosion resistance at lower sulfur activities and temperatures in terms of the implications for alloy/coating design for such conditions. The superior sulfidation resistance of an iron aluminide in a H_2-H_2S-H_2O gas mixture (relative to steels), previously established by extensive studies at 800°C, appeared to be maintained at lower temperatures (400 and 600°C).

INTRODUCTION

All fossil fuel-derived processes contain reactive species such as sulfur, water vapor, oxygen, carbon, etc. Consequently, high-temperature degradation of many alloys or ceramics limits performance or materials lifetimes in fossil, particularly coal-based, systems such that efficiency, emission, and/or economic requirements are not realized. Therefore, resistance to this degradation is a critical material barrier to the operation of advanced fossil energy systems. Achievement of high-temperature corrosion resistance for a particular material is predicated on the formation of stable, protective (slowly reacting, mechanically sound, adherent) surface products. Factors affecting the establishment and stability of such layers have been studied for many years, yet the selection or development of materials to withstand the harsh operating conditions of advanced fossil-fuel-based technologies is still an imposing technical challenge given multiple reactive species, high temperatures and pressures, and variations in operating conditions. Consequently, to seek solutions that have the most far-ranging impact on this difficult, wide-ranging problem, new approaches to corrosion resistance in multiple or changing high-temperature environments (such as the smart corrosion-resistant coatings proposed by Nicholls[1]) are needed.

The long-range aim of this work is to assess the feasibility of different material and design approaches to smart protective coatings by exploring new alloying and microstructural routes to improved high-temperature environmental resistance of metallic materials. As such, this work supports the overarching goal of the Department of Energy's Fossil Energy Advanced Research (AR) Materials Program to provide a materials technology base to assure the success of coal-based fuels and advanced power generation systems. This specific project is motivated by needs for materials with improved high-temperature environmental resistance that could be used as protective coatings under the harsh conditions encountered in advanced fossil systems. The focus is on coating concepts because coatings offer possibilities for corrosion protection under aggressive (and changing) environmental conditions while the substrate provides strength or other desired properties. The project's goal is not to develop coatings per se. Rather, it is to examine concepts that can then be translated into coatings by further developmental efforts if promising high-temperature corrosion results are found for a particular composition/microstructure combination and possible synthesis routes can be identified. This approach can hopefully lead to concepts for "smart" coatings or materials that have the ability to sense and respond appropriately to a particular set or series of environmental conditions in order to provide high-temperature corrosion protection.

The current effort is focused on concept definition and exploratory experimentation aimed at proof-of-principle. (The most successful concepts can transition to a more comprehensive project within the AR Materials Program or graduate to a technology development project.) The strategies previously explored in this work involved cooperative or in-place oxidation or sulfidation reactions of multiphase alloys.[2-4] Alloy systems based on Mo-Si-B and TiAlCr(-X) compositions (X = Nb, Ta, or both) were investigated. More recently, the project has focused on lower, more realistic sulfidation temperatures relative to previous work in simulated coal syngas mixtures (H_2-H_2S-H_2O) which primarily involved investigations of behavior at 800°C. The present experiments allow exploration and understanding of how compositions and structures react in various ways determined by not only the nature of the reactive species but also by temperature and partial pressure so as to define routes to establishing effective protective barrier layers can form under different environmental conditions.

The present set of lower-temperature experiments involved conventional types 410, 430, 446, and 316L stainless steel formed by powder metallurgy (P/M) techniques as well as a P/M iron-aluminide. Iron aluminide was included as a benchmark for excellent high-temperature sulfidation resistance, at 700- 800°C.[5,6] Results from these exposures are used to (1) directly address whether the superior sulfidation resistance of iron aluminide is maintained at lower temperatures and sulfur pressures and (2) form a basis for exploring more advanced alloy systems (as was previously done with Mo-Si-B and Ti-Al-CR-X, see above).

RESULTS AND DISCUSSION

Table 1 shows the nominal compositions of the alloys used in this study. Specimens were exposed to 79%H_2-5.5%H_2S-1.5%H_2O-Ar (vol%) at 400, 600, and 800°C. During most of the exposures to this mixed gas, specimen mass was continually monitored using a Cahn micorobalance. Post-exposure characterization of selected specimens was by scanning electron micoscopy and x-ray diffration.

The partial pressures of oxygen and sulfur for 79%H_2-5.5%H_2S-1.5%H_2O-Ar at 400, 600, and 800°C are shown in Table 2. These pressures are calculated using equilibrium thermodynamics, which yield fairly accurate values at higher temperatures, but may be unrealistic at lower temperatures, where kinetic limitations may produce nonequilibrium conditions. At equilibrium, alumina would be expected to form on the iron aluminide under all three exposure conditions; this previously has been experimentally observed at 800°C in this mixed gas[7] and accounts for its sulfidation resistance. However, given possible kinetic limitations and nonequilibrium gas compositions at lower temperatures, it is therefore important to conduct experimental screening to determine whether iron aluminide still has better sulfidation resistance relative to conventional stainless steels under these conditions.

Table 1. Nominal Compositions of Alloys Used in This Study

Type	**Wt%**				
	Fe	**Cr**	**Ni**	**C**	**Other**
316L	65	17	12	0.03	2Mo, 2Mn, 1Si
410	86	12		0.1	<1Mn
430	83	16		0.1	<1Mn, <1Si
446	75	25	<0.2	<0.2	<1Si
FeAlCr	82	2			16Al

Table 2. Temperatures and Calculated Partial Pressures for 79%H_2-5.5%H_2S-1.5%H_2O-Ar

Temp. (°C)	**P_{O_2} (atm)**	**P_{S_2} (atm)**
400	10^{-37}	10^{-11}
600	10^{-28}	10^{-8}
800	10^{-22}	10^{-6}

Significant reactions of the steels were observed at all temperatures. X-ray diffraction revealed that the principal corrosion products were iron and chromium sulfides. Type 316L stainless steel showed the extent of sulfidation. For example, after only a 1-h exposure at 800°C, a type 316L stainless steel specimen showed a relative mass gain of 13% in contrast to ~22% in 3 h for types 430 and 446 and 1.4% for the iron aluminide after 72 h. (Relative, rather than specific, mass changes are reported because the P/M materials were not fully dense.) The high susceptibility of a Ni-containing austenitic stainless steel in this specific environment at 800°C was first reported by DeVan[7] for a model type 310 steel. This is presumably due to the presence of the Ni, which readily forms sulfide (which should be molten at 800°C), although the in-plan diffraction analyses did not detect such at any of the exposure temperatures. The more extensive sulfidation of type 316L relative to the ferritic steels was also observed at the lower exposure temperatures, as shown by the mass change data in Figs. 1 (1 h, 600°C) and 2 (72 h, 400°C).

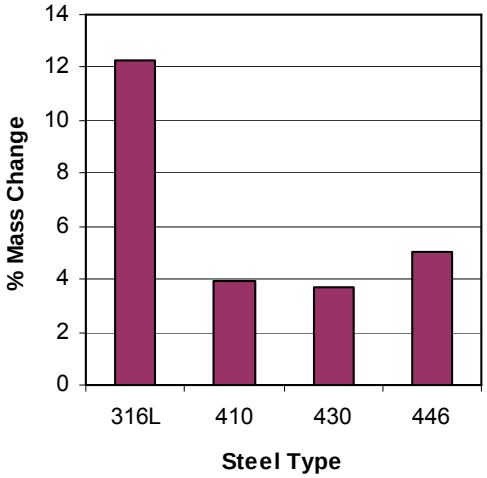

Fig. 1. Mass change for 1-h exposures to 79%H_2-5.5%H_2S-1.5%H_2O-Ar at 600°C

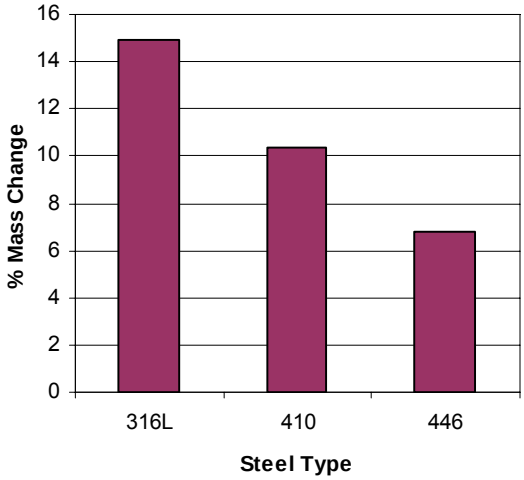

Fig. 2. Mass change for 72-h exposures to 79%H_2-5.5%H_2S-1.5%H_2O-Ar at 400°C

Gravimetric results as a function of time for the type 446 steel are presented in Fig.3, which shows the expected increase in the extent of sulfidation with exposure temperature (and increasing sulfur partial pressure, see Table 2). Representative micrographs of the type 446 steel corresponding to each exposure temperature are also shown in Fig. 3. At 800°C, relatively thick, blocky sulfides were observed., much like what was observed under the same exposure conditions for Fe-Al alloys when their protective alumina surface layer failed to provide protection (due to inadequate levels of aluminum either generally or locally).[8] Present data are insufficient to definitively conclude that one ferritic steel is more sulfidation resistant than the others, but there was some indication that the higher-Cr type 446 stainless steel sulfidized less that types 410 and 430, although at a much greater rate than iron aluminide – see Fig. 4. This is consistent with general trends that higher chromium alloys are more sulfidation resistant.[9]

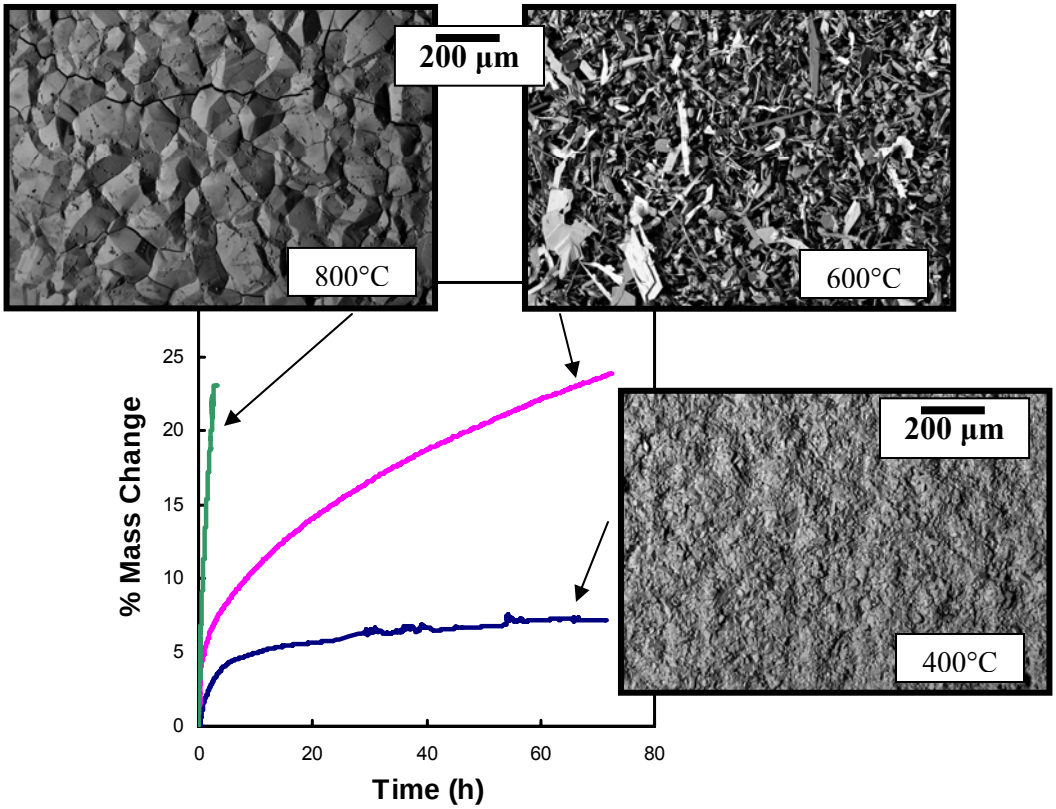

Fig. 3. Type 446 stainless steel exposed to 79%H_2-5.5%H_2S-1.5%H_2O-Ar

While it is possible that an iron aluminide would actually sulfidize to a much greater extent at lower temperatures if a protective alumina couldn't form, the present data do not yield evidence for this. The mass changes at all three temperatures were much lower than the steels (see, for example, Fig. 4) and, at 400°C, it was difficult to obtain a good measurement of mass change. X-ray diffraction of the exposed surfaces did not reveal any reaction products. Therefore, even though kinetics to form alumina at these lower temperatures are presumably sluggish, there must be a protective effect of the native, pre-existing oxide or there is still sufficient near-surface mobility to establish a barrier layer. Other work with iron aluminides in an actual syngas environment at approximately 400-450°C showed that preoxidation at 800°C was critical to assure longer-term corrosion resistnace,[10] but the much greater complexity of that environment makes the relevance of these observations to the present case problematical.

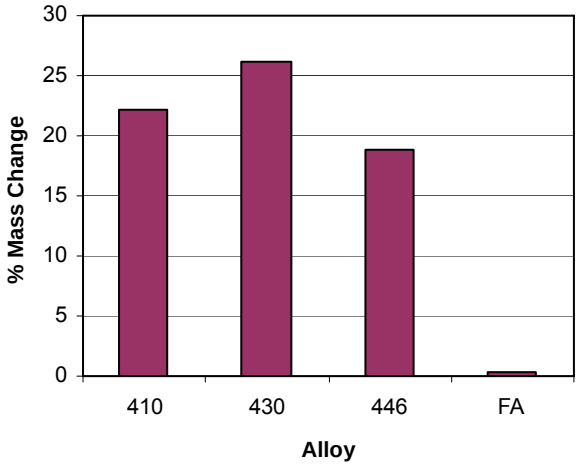

Fig. 4. Mass change for 27-h (type 410) or 72-h exposures (types 430, 446 and iron aluminide, FA) to 79%H_2-5.5%H_2S-1.5%H_2O-Ar at 600°C

SUMMARY

For type 316L and 400-series steels exposed to a simulated syngas (79%H_2-5.5%H_2S-1.5%H_2O-Ar, vol%), significant sulfidation was observed at 400, 600, and 800°C with formation of iron and chromium sulfides. Relatively little differences in sulfidation resistance were found between the 300-series and the 400-series steels at 400°C, but 316L was substantially more susceptible at 600 and 800°C. An iron aluminide composition showed superior sulfidation resistance at 800°C (as shown previously) as well as at lower temperatures where alumina growth is sluggish: almost negligible mass changes were found in short-term exposures (up to 72 h) at all temperatures and no reaction products were detected by conventional x-ray diffraction.

ACKNOWLEDGEMENTS

Research sponsored by the Office of Fossil Energy Advanced Research Materials Program, U. S. Department of Energy, under contract DE-AC05-00OR22725 with UT-Battelle, LLC.

REFERENCES

1. J.R. Nicholls, *JOM* 52 (2000)

2. F. Gesmundo and B. Gleeson, *Oxid. Met.* 44 (1995) 211.

3. M. P. Brady, B. Gleeson and I. G. Wright, *JOM* 52 (2000) 16.

4. P.F. Tortorelli, M.P. Brady, and I.G. Wright, *Proc 19th Annual Conf. Fossil Energy Materials.,* R.R. Judkins and L.S. Mack (compilers), U.S. Department of Energy, 2006; http://www.ms.ornl.gov/FEM/pdf/Proceedings20Fossil06.pdf

5. J.H. DeVan and P.F. Tortorelli, *Mater. at High Temp.* 11 (1993) 30.

6. K. Natesan and P.F. Tortorelli, pp. 265-80 in Nickel and Iron Aluminides: Processing, Properties, and Applications, S. C. Deevi, V. K. Sikka, P. J. Maziasz and R. W. Cahn (eds.), ASM International, Materials Park, OH, 1997.

7. J. H. DeVan, pp. 107-15 in Oxidation of Intermetallics, T. Grobstein and J. Doychak (eds.), TMS, Warrendale, PA, 1989.

8. P.F. Tortorelli, J.H. DeVan, G.M. Goodwin, and M. Howell, pp. 203-212 in Elevated Temperature Coatings: Science and Technology I, N. B. Dahotre, J. M. Hampikian, and J. J. Stiglich (eds.), The Minerals, Metals, and Materials Society, Warrendale, PA, 1995.

9. P. Kofstad, High Temperature Corrosion, Elsevier, 1988.

10. C.G. McKamey, P.F. Tortorelli, E. Lara-Curzio, D. McCleary, J. Sawyer, and R.R. Judkins, paper 4.03 in *Proc. Fifth Int'l. Symp. on Gas Cleaning at High Temperature*, September 2002, http://www.netl.doe.gov/publications/proceedings/02/GasCleaning/4.03paper.pdf.

CHARACTERIZATION AND OXIDATION BEHAVIOR OF SILICIDE COATING ON MULTIPHASES MO-Si-B ALLOYS

Matthew J. Kramer
225 Wilhelm Hall, Ames Laboratory and Department of Materials Science and Engineering,
Iowa State University, Ames, IA 50011 USA
Email: mjkramer@ameslab.gov; Telephone: (515) 294-0726; Fax: (515) 294-4291
Zhihong Tang and Mufit Akinc
2220 Hoover Hall, Ames Laboratory and Department of Materials Science and Engineering,
Iowa State University, Ames, IA 50011
Email: makinc@iastate.edu; Telephone: (515) 294-0738; Fax: (515) 294-5444

ABSTRACT

Mo_{ss}-based Mo-Si-B multiphase alloys possess improved fracture toughness compared to its single-phase silicide counterparts ($MoSi_2$, Mo_5Si_3 or T2) without sacrificing high temperature strength, but they degrade rapidly in an oxidizing environment at elevated temperature. In the present study, $MoSi_2$ coating was applied to protect Mo_{ss}-based alloy from high temperature oxidation via pack cementation. Boron-modified $MoSi_2$ coating was also produced in an attempt to enhance the oxidation resistance of $MoSi_2$ coating via co-deposition of B and Si, using a two-step process. Isothermal and cyclic oxidation tests on coated Mo-4.3Si-1.1B alloy were performed at 1100ºC and 1600ºC, respectively up to 200 hours. The $MoSi_2$ coating provide enough protection from oxidation in both static and cyclic condition at 1100ºC, while it degraded after ten hours by forming T1 ($Mo_5Si_3B_x$) phase at 1600ºC via inter-diffusion between coating and substrate. The coating lifetime of $MoSi_2$ was limited by the Si depletion by diffusing into substrate. The Additions of boron into $MoSi_2$ did not enhance the oxidation resistance as boride phases (MoB or Mo_2B_5) do not slow the diffusion of Si to substrate to stabilize $MoSi_2$ or Mo_5Si_3.

INTRODUCATION

Molybdenum borosilicides have been investigated as a candidate material capable of service temperatures much higher than 1100ºC. Two specific alloy systems have received considerable interests from the scientific community for high temperature applications. The first one, which was pioneered by Akinc and his co-workers[1], consists of three intermetallics alloys, Mo_5Si_3, the T2 phase Mo_5SiB_2 and the A15 phase Mo_3Si. They exhibit excellent oxidation resistance and creep strength up to 1600ºC. The boron addition is critical for providing the observed oxidation resistance due to formation of low viscosity borosilicate glass layer that flows and seals the porous scale. However, these alloys also have low fracture toughness, and the thermal expansion anisotropy of the T1 phase make these alloys susceptible to thermal stress induced microcracking[2]. These deficiencies in mechanical behavior can be improved by moving towards the Mo-rich portion of the systems [3-8]. The second alloys, incorporates the bcc-Mo phase to impart some ductility and fracture toughness to a three-phase microstructure containing Mo_3Si and Mo_5SiB_2 (T2) along with Mo_{ss}. The Mo_{ss} phase can improve the room and high temperature fracture toughness significantly depending on its volume fraction and its distribution [6, 7]. However it presents a challenge in achieving adequate oxidation resistance as $Mo_5Si_3B_x$–based alloys do. The oxidation resistant phase of these alloys is believed to be T2 phase (Mo_5SiB_2) yet, its high boron content results in a borosilicate glass with a much low viscosity than that formed with the T1 phase ($Mo_5Si_3B_x$) leading to excessive volatility of MoO_3 through the scale, contributing to unacceptable metal recession rates above about 1300°C [9, 10]. Schneibel et al. [11] explored designing a bcc-Mo containing composite to balance acceptable oxidation resistance with adequate mechanical behavior with limited success.

An emerging consensus is to protect the Mo_{ss}-based alloys with an oxidation resistant coating [12, 13]. One approach for developing an oxidation resistant coating is to deposit a silicon-rich phase, such as the $MoSi_2$ or T1-based alloy, onto the surface of the component. The halide activated pack cementation (HAPC) process has been successfully employed to deposit $MoSi_2$ onto a two-phase T2/Mo(ss) eutectic alloy by Ito et al.[13], and Mo-3Si-1B alloy by Sakidja et al. [12]. Although the steady-state oxidation rate of the coated alloy was nearly equal to that of $MoSi_2$ for up to 50 hours at 1300°-1500°C, the $MoSi_2$ layer was partially transformed to T1 phase, and the long term effect of this microstructural change on the oxidation resistance of the coating was not investigated. The present

work investigates the feasibility of using the HAPC process to form oxidation resistant diffusion coatings on the Mo_{ss}-based Mo-4.3Si-1.1B (wt.%) alloy. Coating process development, oxidation performance and interdiffusion behavior of the coated alloy will be discussed.

EXPERIMENTAL

The nominal composition of the substrate alloy selected for this study is Mo-4.3 wt.%Si-1.1wt.%B (all compositions are in weight percent unless stated otherwise). These ternary alloys contain Mo_3Si, Mo_5SiB_2 (T2) and α-Mo (Mo solid solution), and were fabricated by either drop-casting or sintering powder compacts. Both drop-cast and sintered alloys were cut into small coupons and polished with 600-grit SiC paper, then ultrasonically cleaned in acetone and ethanol. The halide-activated pack cementation process was employed to deposit silicon and/or boron onto the substrate samples. The components in pack cementation include: the masteralloy (i.e. a powder of the element or elements to be deposited on the surface of the parts, such as Si and/or B), a halide activator (e.g. NaF), and an inert filler powder (e.g. Al_2O_3). Three kinds of pack cementation processes were employed in this study: i) Si deposition only, ii) co-deposition of Si and B, and iii) two-step boronizing and siliconizing. The deposition process was carried out at 900ºC or 1000ºC for 12-48 hours in flowing Ar atmosphere.

Isothermal oxidation tests on coated samples were conducted in a tube furnace in flowing dry air at 1100ºC or 1600ºC up to 400 hours. Thermal cycling exposure was also carried out in air at 1100ºC. The thermal cycle consists of heating to 1100ºC at 20ºC/min, holding for 24 hours and cooling in 5 min to room temperature. Mass change was continuously recorded after every cycle. The as-deposited, annealed and oxidized samples were examined by X-ray diffraction (XRD, Scintag XDS 2000, Cupertino, CA) to identify the phases formed. Microstructural features of the surface and cross-section of the samples were examined by scanning electron microscopy using backscattered electron imaging (SEM/BSE, JEOL, JSM 6100, Peabody, MA) and energy dispersive spectroscopy (EDS, Oxford Instruments, Valley, CA).

RESULTS AND DISCUSSION

Silicide Coating

Fig.2a shows a typical cross-section of the silicide coating formed on sintered alloy 3 (Mo-4.3Si-1.1B) coupon after 48 hours pack cementation at 1000ºC in an Si pack. The EDS and XRD analysis confirmed that the coating was $MoSi_2$ with the $C11_b$ structure. A uniform coating layer about 40μm in thickness formed on the substrate. At least 10 measurements were taken and the average thickness of $MoSi_2$ layer was determined. Growth of $MoSi_2$ layer was found to be parabolic with respect to deposition time with a corresponding rate constant of $8\times10^{-11}cm^2/s$ at 1000ºC. This value compares very well with the intrinsic parabolic growth rate constant of $MoSi_2$ obtained from Si/Mo diffusion couple (3.91×10^{-10} cm^2/s) [14]. The inward-diffusion of silicon is thought to be the rate-controlling step. None of the Mo_5Si_3, Mo_3Si or T2 (Mo_5SiB_2) phases were detected between the $MoSi_2$ layer and the substrate. This result is in agreement with the kinetic studies of Mo/Si diffusion couple as well, [14] that the intrinsic growth rates of Mo_5Si_3 and Mo_3Si are slower than that of $MoSi_2$ about two or three orders of magnitude at 1000ºC. It should be noted the $MoSi_2$ coating of the as-deposited alloy was always cracked at the corners and edges of the substrate, and the perpendicular microcracks were extending to the surface were also observed (see Fig2a).

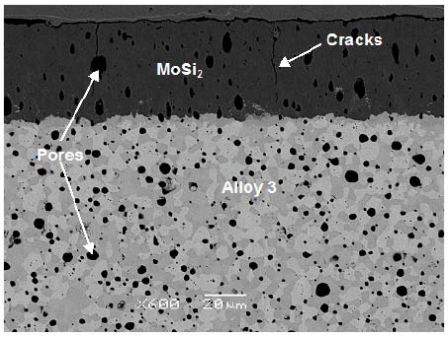

(a)

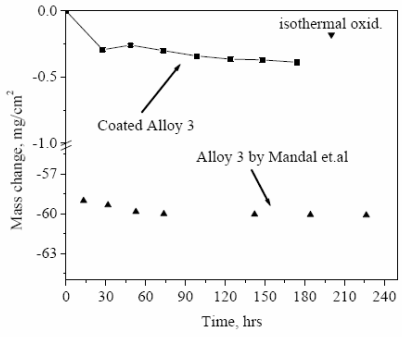

(b)

Figure 1 a. Micrographs of silicide coating growing on sintered Mo-4.3Si-1.1B alloy by a NaF activated pack; b. Mass change of a pack cemented alloy after isothermal and cyclic oxidation at 1100ºC in dry air

The oxidation behavior of the coating was assessed by measuring the weight change as a function of exposure time. Fig.2b show that the weight gain data at 1100ºC for pack cemented alloy. For comparison, the mass change of uncoated Mo-4.3Si-1.1B alloy reported by Mandal et. Al [15] at 1100ºC was also included in this plot. Only a slight weight loss of about 0.2 mg/cm^2 was observed after oxidation at 1100ºC for 200 hrs. Even after 8 cycles (total 192 hours), weight loss was less than 0.5 mg/cm^2, suggesting that the micorcracks formed by pack cementation process was sealed by silica glass and had no obvious detrimental effect on the oxidation behavior of $MoSi_2$ coating during exposure to air at 1100ºC. For comparison, Mandal et. al.[15] reported the uncoated Mo-4.3%Si-1.1%B alloy suffered a significant weight loss of more than –60 mg/cm^2 at 1100ºC for 200 hrs, suggesting a loss of volatile MoO_3. Clearly, $MoSi_2$ coating significantly suppressed the rapid oxidation of alloy 3. The cross-section of oxidized alloy is shown in Fig.3a. No significant oxidation was observed in the coating or substrate. Only a thin silica glass formed at the surface. A very thin Mo_5Si_3 layer was observed between the silica scale and $MoSi_2$ coating due to selective oxidation of Si. In addition, a Mo_5Si_3 layer below the $MoSi_2$ coating less than 20μm thick was observed as a result of interdiffusion between coating and substrate.

Oxidation in air at 1600ºC for two hours results in a small weight loss of about -0.1 mg/cm^2, but significant changes in the microstructure (see Fig.3b). The microstructure of the coating depicts three layers: i) an outer layer about 25μm in thickness comprising mixed $MoSi_2$/T1 phases, ii) an intermediate layer about 50μm in thickness containing single T1 phase, and iii) a 10μm thick interlayer consisting of MoB and T2 phases. The cracks that penetrated through the outer $MoSi_2$ layer were arrested at the intermediate T1 layer and sealed by the silica glass.

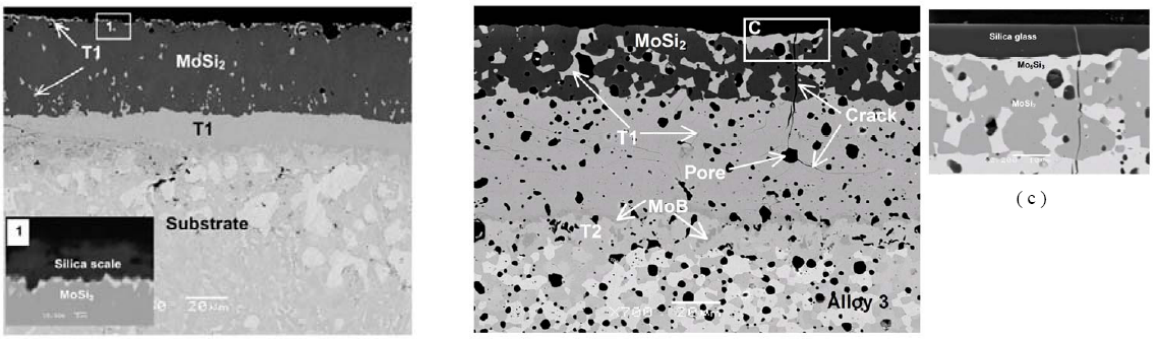

Figure 2 Micrographs showing cross-section of silicide coating growing on sintered Mo-4.3Si-1.1B alloy by a NaF-activated pack after isothermal oxidization in dry air: (a) at 1100ºC for 200hrs, (b) at 1600ºC for 2 hours.

Although the transformation rate from $MoSi_2$ to T1 layer was not experimentally determined, annealing of the sample in Ar confirmed that the transformation of a $MoSi_2$ coating, is less than 12hrs at 1600ºC. Once $MoSi_2$ layer is completely transformed to T1, the coating oxidized rapidly since the T1 and MoB/T2 multilayer structure do not form a protective silica layer. In fact, the coated alloy was completely oxidized after exposure to air at 1600ºC for 50 hours.

Borosilicide Coating

The rapid loss of the $MoSi_2$ coating is a result of preferential silicon diffusion into substrate which leads to the growth of T1 layer. Since the oxidation behavior of T1-based phase is strongly dependent on boron content, undoped T1 (i.e., Mo_5Si_3) exhibits catastrophic mass loss above 1000ºC due to formation of a porous oxide scale. A small amount of boron added to Mo_5Si_3 results in a non-porous, protective scale. The B addition allows viscous flow to close submicron scale porosity. Meyer and Akinc [16] studied the isothermal oxidation of several B-doped Mo_5Si_3 alloys around Mo_5Si_3 phase field at 1450ºC and concluded that a minimum boron content is somewhere between 0.14 wt.% and 0.91 wt.% required in order to form a protective scale on Mo_5Si_3-based materials. This boron level is definitely exceeds the solubility of B in Mo_5Si_3. Indeed, the oxidation resistant Mo_5Si_3-based alloys studied to date were always multiphase containing at least a small amount of $MoSi_2$, T2 or MoB phases. Therefore, the boron-modified silicide diffusion coatings were developed via pack cementation in order to address the poor

oxidation behavior of T1 interlayer. Two approaches were employed: co-deposition of B and Si onto alloy 3 and sequential deposition of B followed by Si.

Co-Deposition Of B And Si

The SEM micrograph in Fig.4a shows the cross-section of a multilayered borosilicide coating formed on sintered Mo-4.3Si-1.1B alloy after 48 hours co-deposition of Si and B in a pack with Si/B=9 (#3) at 1000ºC. Instead of single $MoSi_2$ layer observed in silicon only coating, the co-deposited coating consists of three layers: i) an 20µm thick $MoSi_2$ outer layer, ii) a 30µm thick intermediate layer consisting of MoB needles and particles in a $MoSi_2$ matrix. The presence of MoB was confirmed by XRD by carefully polishing away the top $MoSi_2$ layer, iii) a 10µm thick inner layer containing mostly T2 (Mo_5SiB_2) phase with dispersed MoB particles. Thus, MoB phase was successfully incorporated into the coating by incorporating B in the pack mixture. The distribution of boron in the coating suggested that diffusion of B in $MoSi_2$ layer is much faster than Si.

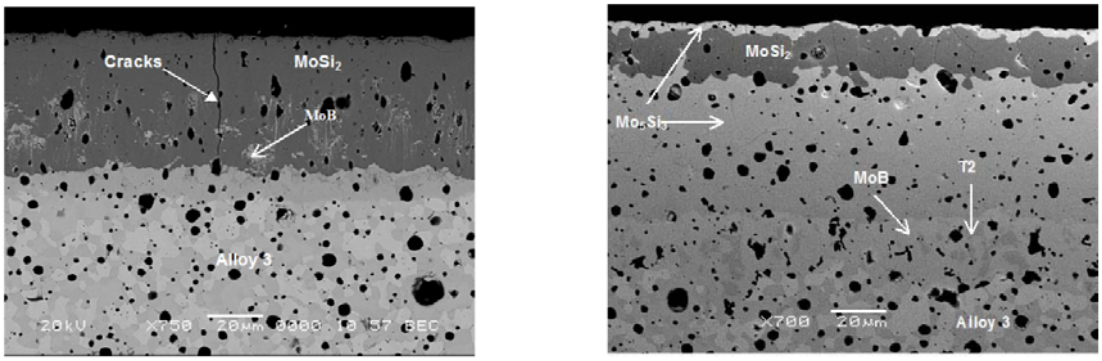

(a) (b)

Figure 3 SEM micrographs of B-modified silicide coating on sintered Mo-4.3Si-1.1B alloy produced by co-deposition of B and Si: (a) as-deposited, (b) after isothermal oxidation in dry air at 1600ºC for 2 hours.

Both short-time and long-time isothermal oxidation tests were run on the co-deposited samples. A weight loss of less than –0.1 mg/cm^2 was observed after oxidation at 1600ºC for two hours in air, while the sample is totally oxidized after 50 hrs exposure. Fig.4.b shows back-scattered electron (BSE) images of co-deposited alloy after short-time oxidation. No obvious oxygen attack into substrate through cracks was observed, which indicated that cracks were sealed by borosilicate glass and were not the cause of the long-time oxidation failure. The $MoSi_2$ coating was partially transformed into T1 phase and an interlayer consisting of MoB particles-dispersed T2 matrix with was observed. The interlayer has the same phase constitutions (T2+MoB) as that in Si only coating. It is thicker (25µm vs. 15µm) perhaps in part due to the incorporation of boride phases into $MoSi_2$ coating. According the Mo-Si-B ternary phase diagram, MoB is can co-exist with $MoSi_2$ and Mo_5Si_3 phases. However, careful XRD and SEM analysis after removing the top layer showed no evidence of MoB phase in either $MoSi_2$ or Mo_5Si_3 phases, suggesting that MoB must have reacted with Si to form T1 as silicon diffuses into the substrate, as will be discussed later. The $MoSi_2$ layer was completely transformed into T1 phase after annealing at 1600ºC for twelve hours. It is presumed that poor oxidation resistance of Mo_5Si_3 layer formed by interdiffusion between the coating and substrate is responsible for the degradation.

Two-Step B+Si Coating

Fig.5 shows the micrographs of Mo-4.3Si-1.1B alloy after boronizing. A complex two-layer diffusion microstructure was developed: a ~10µm thick outer Mo_2B_5 layer with dispersed MoB particles, a ~30µm thick network of T2 and MoB mixed inner layer. Apparently, MoB in T2/MoB inner layer formed from reaction of B with Mo phase in the substrate, and T2 evolved from reaction of B with Mo_3Si. Closer examination of the interface between the coating/substrate by SEM/EDS revealed fine T2 particles, which were formed within the $MoSi_3$ phase near the interface. Dark spots observed in the inner T2 layer were identified as $MoSi_2$ phase by EDS. The formation of $MoSi_2$ could occur if Si content exceeds the solubility limit in T2 phases as B reacts with Mo_3Si to form T2.

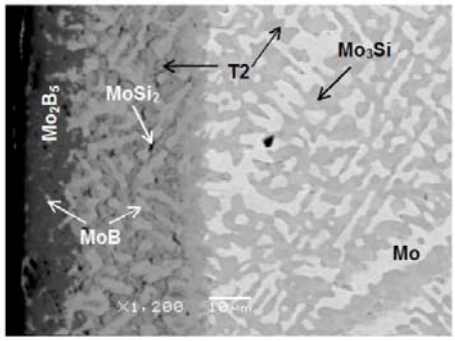

Figure 4 SEM micrographs of cast Mo-4.3Si-1.1B alloy pack cemented in a B pack

Fig.6a shows the cross-sectional microstructure of as-prepared and annealed two-step coating (B+Si). After two step pack cementation (boronizing and siliconizing), Mo_2B_5 top layer formed is totally converted into $MoSi_2$ and a ~12μm thick $MoSi_2$ layer is formed. A 40μm thick T2+MoB intermediate layer is observed between $MoSi_2$ and substrate. The thickness of this intermediate layer is similar to that of B-packed alloy 3 (Fig.5). It implies that when Mo_2B_5/MoB transformed into $MoSi_2$ by Si cementation followed by B diffuse through $MoSi_2$ since the solubility of boron in $MoSi_2$ is negligible.

After annealing at 1400ºC for 24 hours, the $MoSi_2$ phase is completely transformed into T1, and the T2 fraction in the T2/MoB layer increased. Unlike the as-packed coating in which the T2/MoB interlayer consists of MoB matrix with interconnected T2 phase, the interlayer in the annealed coating consists of T2 matrix with isolated MoB grains. Some Mo_5Si_3 particles were also observed in the T2 phases.

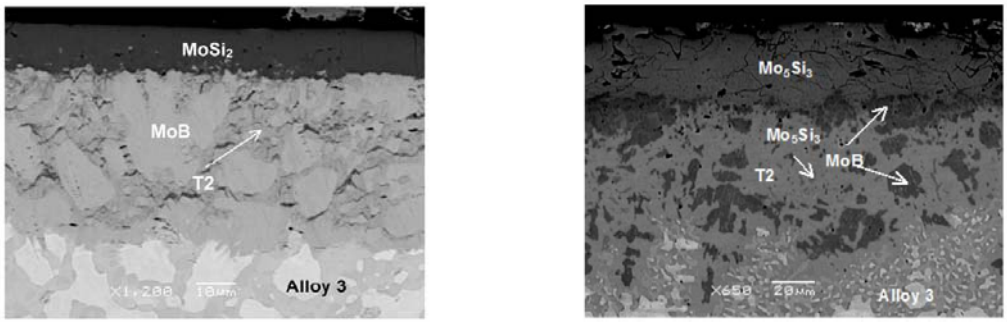

(a) (b)

Figure 5 SEM micrographs of cast Mo-4.3Si-1.1B alloy by boronizing in a B pack (#2) followed by siliconizing in a Si pack(#1): (a) as packed coating, (b) annealed at 1400ºC for 24 hours

Evaluation Of Silicide And Borosilicide Coating

The excellent high temperature strength and oxidation resistance qualify $MoSi_2$ as protective coating for Mo-based alloys. Similar studies by Ito et al.[13, 17] on Mo-9Si-18B (at.%) alloy and Sakidja et al.[12] on Mo-14.2Si-9.6B at.% alloy revealed. Two significant challenges for future high temperature application still remain: i) thermal stresses generated by coefficient of thermal expansion (CTE) mismatch at the coating-substrate or coating-oxide interface, and the large CTE anisotropy of T1 may induce cracks during process. Although these cracks may be sealed by silica (or borosilicate) glass at high temperature, it may still cause degradation of coating under thermal cycling, ii) the rapid diffusion of Si from $MoSi_2$ coating results in the formation of the T1 phase which does not provide oxidation protection for the substrate.

Thermal Stress

$MoSi_2$ is goes through ductile-to-brittle transition at approximately 1000ºC. Thermal stress resulting from the CTE mismatch between the $MoSi_2$ coating and substrate can cause cracks in the coating if they reach or exceed a critical value, i.e., the strength of $MoSi_2$. Since the tensile strength of $MoSi_2$ is much lower than its compressive strength (275 MPa vs. more than 1378 MPa)[18], tensile stresses are particularly damaging and will promote transverse microcracking in the coating, as observed in this study.

Using the bulk CTE as and ΔT=975ºC (cooling the sample to room temperature from 1000ºC), the thermal stresses developed in the $MoSi_2$ coating are 1041, 709 and 520MPa with substrates Mo, Mo_3Si and Mo_5SiB_2, respectively. These stresses definitely exceed the tensile strength of $MoSi_2$ (275MPa). As shown Fig.2a and Fig.4a, the transverse microcracking was observed in the as-packed $MoSi_2$ coating no matter how slowly they were cooled. Fortunately, the present oxidation experiments showed that no significant oxidation through cracks (Δm<-1mg/cm^2) occurred since the silicate glass formed by oxidation may have sealed them. Similar results were also reported by Ito et.al.[13]. They indicated the presence of microcracks in the as-deposited $MoSi_2$ coating on T2/Mo_{ss} substrate; however, steady-state weight gain with mass gain of less than 2mg/cm^2 was observed after 50 hours oxidation at 1500ºC. It

should be noted that the $MoSi_2$ were not completely transformed into T1 phases after 50 hours exposure in Ito's experiments, which provide the reservoir of Si for the formation of continuous silicate glass.

Thermodynamic Stability

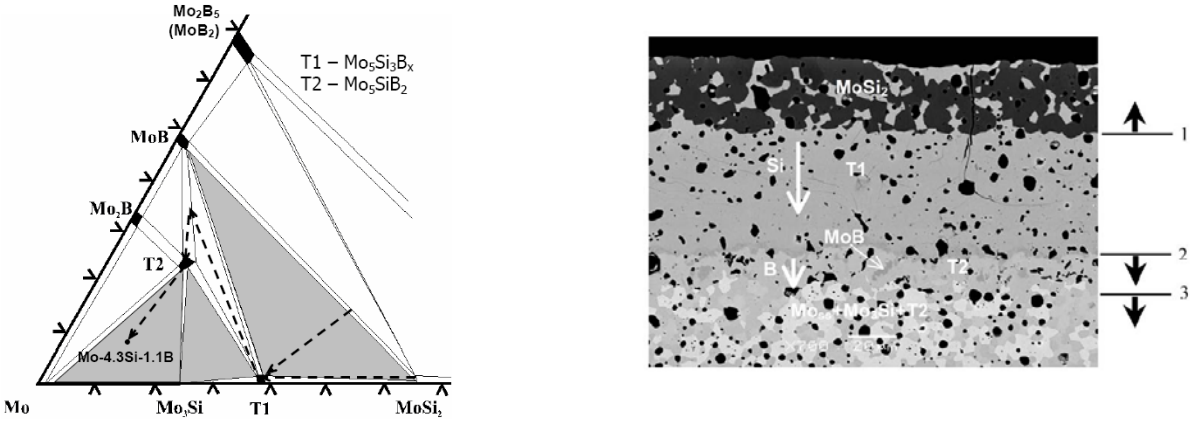

Figure 6 Schematic description of diffusion path showing reaction between $MoSi_2$ coating and three-phase (Mo+Mo_3Si+T2) substrate ,

From the microstructural features, the diffusion paths for silicide and boron-modified silicide coatings on multiphase alloy 3 can be drawn on Mo-Si-B ternary phase diagram (Fig.7). A diffusion zone with Mo_5Si_3 (T1) and MoB+T2 two-phase layer was observed in both cases whether the coating contains boride phases or not. The diffusion reaction can be described as followed: $MoSi_2$ decomposes into T1 ($Mo_5Si_3B_x$) and Si by Equation (1) as in $MoSi_2$/Mo and $MoSi_2$/T2 diffusion couple. The interface 1 shifts toward $MoSi_2$ phase and the Si atoms diffuse through T1 to interface 2, at which additional T1 phase is formed by the following reactions:

$$5MoSi_2 \rightarrow Mo_5Si_3 + 7Si_{Mo_5Si_3} \qquad (1)$$

The interface 1 shifts toward $MoSi_2$ phase and the Si atoms diffuse through T1 to interface 2, at which additional T1 phase is formed by the following reactions:

$$3Si + 5MoB \rightarrow Mo_5Si_3B_x + (5-x)B \qquad (2)$$

$$2Si + Mo_5SiB_2 \rightarrow Mo_5Si_3B_x + (2-x)B \qquad (3)$$

Since solubility of boron in T1 phase is negligible, the excess boron atoms must diffuse toward interface 3 to form boron-rich phases such as: T2 and MoB since B has limited solubility in T2 phase. Therefore, the lifetime of silicide coating is limited by the growth rate of T1 layer, i.e. conversion of $MoSi_2$ into T1.

In B/Si co-deposition coating, the diffusion path did not change even though the composition of the coating moved up to the B-rich side along the tie line between MoB and $MoSi_2$ in the ternary Mo-Si-B phase diagram. MoB did not stabilize the $MoSi_2$ phase; rather it reacted with Si to form T1 phase and release B atoms. The excess B diffuses to coating/substrate interface to form borides by reacting with Mo and Mo_3Si.

For the $MoSi_2$-based coating, the lifetime is limited by the growth rate of T1 layer. Fig.8 shows the apparent growth rate of Mo_5Si_3 layer for $MoSi_2$/Mo diffusion couple. The data represents the intrinsic growth rate of Mo_5Si_3 layer. Although there is some scatter in the data in part due to difference in sample preparation, the values are on the same order magnitude. The apparent growth rates of Mo_5Si_3 layer in the $MoSi_2$/T2 diffusion couple and $MoSi_2$ coating on T2+Mo_{ss} are also included. The growth rates of Mo_5Si_3 in ternary Mo-Si-B system are slightly lower than that of $MoSi_2$/Mo diffusion couple presumably due to the existence of T1+MoB two-phase layer. The lifetime of $MoSi_2$ coating on three-phase Mo-Si-B alloy can be estimated by considering conversion rate of $MoSi_2$ to T1. Fig.9 shows that estimated lifetime as a function of exposure temperature assuming that the initial thickness of $MoSi_2$ layer is 100μm. The maximum and minimum lifetimes are calculated based highest and lowest data in growth rate of Mo_5Si_3 layer in Fig.8a. The coating can last more than 1000 hours with service temperature below 1300ºC, while it will lose protection less than hundred hours above 1500ºC due to rapid interdiffusion.

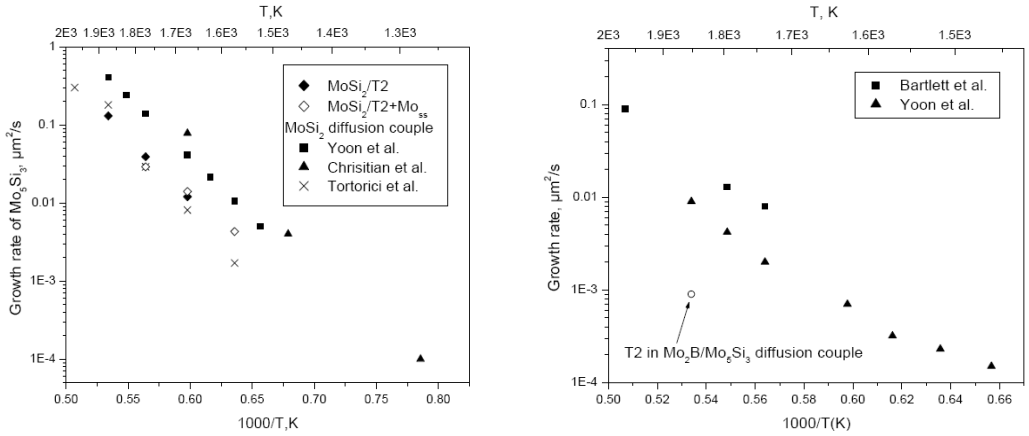

(a) (b)

Figure 7 Arrhenius plot of parabolic growth rate as a function of the reciprocal temperature for a) Mo_5Si_3 and b) Mo_3Si.

Strategies Of Extending Lifetime Coating

$MoSi_2$-based coating was impaired above 1300ºC by the formation of poor oxidation resistant Mo_5Si_3 interlayer due to rapid interdiffusion. No alloy has been identified as a diffusion barrier for $MoSi_2$/Mo couple. Addition of refractory alloying elements such as W and Nb can slow the growth rate of $(Mo,M)_5Si_3$ significantly[19], but not enough to last for several hundred hours above 1500ºC. Thus new coating design strategy needs to be considered. Thom et al.[20, 21] reported that Mo-13.4Si-2.6B (T1+MoB+$MoSi_2$) and Mo-9.9Si-1.4B (T1+T2+Mo_3Si) alloys possess excellent oxidation resistance up to 1600ºC. Thus, if the coating composition was shifted to Mo-rich regions, such as T1+T2+Mo_3Si three phase region, the Si diffusion inward will result in the formation of Mo_3Si or T2 interlayer instead of T1 according to Mo-Si-B ternary phase diagram. The intrinsic growth rate of Mo_3Si phase is about at least one order of magnitude lower than that of Mo_5Si_3 at the temperature of 1000-1700ºC as shown in Fig.8, And this can reduce the depletion rate of Si from silicide coating, therefore extend the lifetime of coating.

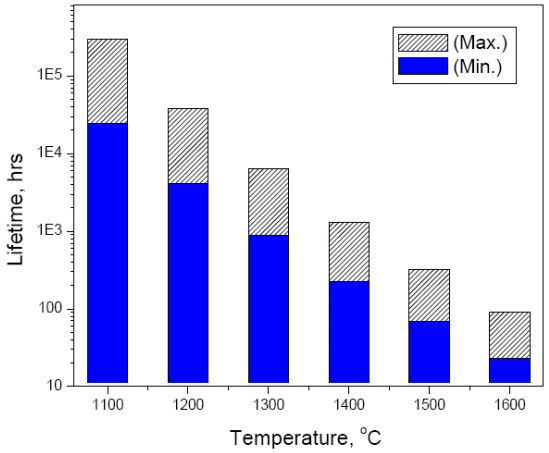

Figure 9. Estimated lifetime of $MoSi_2$-based coating on three-phase (Mo_{ss}+Mo_3Si+T2) alloy

SUMMARY

$MoSi_2$-based silicide diffusion coating was successfully deposited onto Mo_{ss}-based multiphase Mo-Si-B alloy via pack cementation, the coating process, oxidation behavior and interdiffusion behavior were investigated, and the results obtained are summarized as follows:

1. In the pack siliconizing coating, a $MoSi_2$ layer was developed on the three phase substrate (Mo+Mo_3Si+Mo_5SiB_2). After annealing or exposure to air at high temperature, $MoSi_2$ was transformed to T1 phase, which possesses poor oxidation resistance at elevated temperature.
2. Boride phases (MoB and Mo_2B_5) were successfully added to $MoSi_2$ coating either by co-deposition of B and Si or by a two-step process, and the concentrations of boride phases can be controlled by adjusting the Si/B ratio in the pack mixture. However, those boride phases cannot be stabilized with either $MoSi_2$ or Mo_5Si_3 phases after exposure to high temperature. MoB phase was consumed by the formation of Mo_5Si_3 as silicon diffuse downward and the expelled boron diffused downward into substrate to form new borides. As a result, a diffusion zone with Mo_5Si_3/(T2+MoB) layers formed.

3. Both silicide and boron-silicide coating can prevent the oxidation of Mo-4.3Si-1.1B alloy at 1100ºC in both static and cyclic conditions and estimated to be lasted for thousand of hours, while the coating lost their protection at 1600ºC due to rapid interdiffusion between $MoSi_2$ and substrate, which leads to formation of poorly oxidation resistant T1 phase. The lifetime of $MoSi_2$-based coating is limited by Si depletion through the formation of T1 phase.
4. New coating design approach was proposed based on the diffusion data. T1-based Mo-Si-B coating will reduce the Si depletion rate from the surface by formation of slow growing Mo_3Si or T2 layer without sacrificing the oxidation resistance of the coating, therefore extending the coating lifetime above 1500ºC.

ACKNOWLEDGEMENTS

"This manuscript has been authored, in whole or in part, under Contract No. DE-AC02-07CH11358 with the U.S. Department of Energy. The United States Government retains and the publisher, by accepting the article for publication, acknowledges that the United States Government retains a non-exclusive, paid-up, irrevocable, world-wide license to publish or reproduce the published form of this manuscript, or allow others to do so, for United States Government purposes.

REFERENCES

[1] M. Akinc, M. K. Meyer, M. J. Kramer, A. J. Thom, J. J. Huebsch, B. Cook, Materials Science & Engineering, A: Structural Materials: Properties, Microstructure and Processing A261 (1999) 16-23.
[2] H. L. Zhao, M. J. Kramer, M. Akinc, Intermetallics 12 (2004) 493-498.
[3] D. M. Dimiduk, J. H. Perepezko, MRS Bulletin 28 (2003) 639-645.
[4] R. Sakidja, S. Kim, J. S. Park, J. H. Perepezko, Materials Research Society Symposium Proceedings 753 (2003) 59-64.
[5] J. H. Perepezko, R. Sakidja, S. Kim, Z. Dong, J. S. Park, Structural Intermetallics 2001, Proceedings of the International Symposium on Structural Intermetallics, 3rd, Jackson Hole, WY, United States, Sept. 23-27, 2001 (2001) 505-514.
[6] J. H. Schneibel, P. F. Tortorelli, M. J. Kramer, A. J. Thom, J. J. Kruzic, R. O. Ritchie, Materials Research Society Symposium Proceedings 753 (2003) 53-58.
[7] J. H. Schneibel, R. O. Ritchie, J. J. Kruzic, P. F. Tortorelli, Metallurgical and Materials Transactions A: Physical Metallurgy and Materials Science 36A (2005) 525-531.
[8] J. H. Schneibel, M. J. Kramer, O. Unal, R. N. Wright, Intermetallics 9 (2001) 25-31.
[9] M. G. Mendiratta, T. A. Parthasarathy, D. M. Dimiduk, Intermetallics 10 (2002) 225-232.
[10] T. A. Parthasarathy, M. G. Mendiratta, D. M. Dimiduk, Acta Materialia 50 (2002) 1857-1868.
[11] J. J. Kruzic, J. H. Schneibel, R. O. Ritchie, Scripta Materialia 50 (2003) 459-464.
[12] R. Sakidja, J. S. Park, J. Hamann, J. H. Perepezko, Scripta Materialia 53 (2005) 723-728.
[13] K. Ito, T. Murakami, K. Adachi, M. Yamaguchi, Intermetallics 11 (2003) 763-772.
[14] J.-K. Yoon, J.-Y. Byun, G.-H. Kim, J.-S. Kim, C.-S. Choi, Thin solid films 405 (2002) 170-178.
[15] P. Mandal, A. J. Thom, M. J. Kramer, V. Behrani, M. Akinc, Materials Science & Engineering, A: Structural Materials: Properties, Microstructure and Processing A371 (2004) 335-342.
[16] M. K. Meyer, M. Akinc, Journal of the American Ceramic Society 79 (1996) 2763-2766.
[17] K. Ito, T. Hayashi, M. Yokobayashi, T. Murakami, H. Numakura, Metallurgical and Materials Transactions A: Physical Metallurgy and Materials Science 36A (2005) 627-636.
[18] T. A. Kircher, E. L. Courtright, Materials Science & Engineering, A: Structural Materials: Properties, Microstructure and Processing 155 (1992) 67-74.
[19] P. I. Glushko, V. I. Zmii, N. A. Semenov, B. M. Shirokov, Powder Metallurgy and Metal Ceramics (Translation of Poroshkovaya Metallurgiya (Kiev)) 42 (2003) 154-157.
[20] A. J. Thom, E. Summers, M. Akinc, Intermetallics 10 (2002) 555-570.
[21] A. J. Thom, M. J. Kramer, P. Mandal, M. Akinc, Scripta Materialia 53 (2005) 915-919.

SESSION 3

COATINGS AND PROTECTION OF MATERIALS

LONG-TERM PERFORMANCE OF ALUMINIDE COATINGS ON Fe-BASE ALLOYS

Bruce A. Pint
Oak Ridge National Laboratory, P.O. Box 2008, Oak Ridge, TN 37831-6156
E-mail: pintba@ornl.gov; Telephone: (865) 576-2897; Fax: (865) 241-0215

Ying Zhang
Department of Mechanical Engineering, Tennessee Technological University, P.O.Box 5014, Cookeville, TN 38505-0001
E-mail: yzhang@tntech.edu; Telephone: (931) 372-3265; Fax: (931) 372-6340

Sebastien Dryepondt
Oak Ridge National Laboratory, P.O. Box 2008, Oak Ridge, TN 37831-6156
E-mail: dryepondtsn@ornl.gov; Telephone: (865) 576-2894; Fax: (865) 241-0215

L. R. Walker
Oak Ridge National Laboratory, P.O. Box 2008, Oak Ridge, TN 37831-6064
E-mail: walkerlr@ornl.gov; Telephone: (865) 574-5339; Fax: (865) 576-5413

Ian G. Wright
Oak Ridge National Laboratory, P.O. Box 2008, Oak Ridge, TN 37831-6156
E-mail: wrightig@ornl.gov; Telephone: (865) 574-4451; Fax: (865) 241-0215

ABSTRACT

Aluminide coatings made by chemical vapor deposition on representative ferritic (Fe-9Cr-1Mo) and austenitic (Type 304L) substrates were evaluated after exposure in humid air at 650°-800°C. A humid air environment was used to identify coating failure during exposure, as uncoated substrates experience rapid oxidation at these temperatures. One goal of this work was to demonstrate the potential benefits and problems with alumina-forming coatings. The higher exposure temperatures were selected to accelerate the degradation of the coating by interdiffusion with the substrate. These results support development of a coating lifetime model. The critical Al content of the coating at which failure occurs is a key parameter needed to complete the model, and a coating failure after ~10kh at 700°C provides some information. Another goal of the work was to examine the effect of the coating on the substrate creep properties. Creep rates are reported at 650°C with and without coatings and with various heat treatments.

INTRODUCTION

Enriching the surface of high-performance alloys with Al to improve their environmental resistance by forming a protective external alumina scale has been studied for many years.[1-12] Alumina-forming coatings are used at higher temperatures (>900°C), where the slow growth rate of an alumina scale and its stability in the presence of water vapor[13] are superior to coatings that form chromia or silica-rich scales. Chromia-forming coatings are more widely employed at lower temperatures for Fe-base alloys in environments such as steam. However, with a goal of ultra-supercritical (USC) steam coal-fired power plants,[14] the higher temperatures will increase the H_2O-accelerated volatility of chromia and silica scales[13] and require more stable alumina scales formed by Al-rich coatings.

For USC-type applications, several research groups are developing aluminide coatings compatible with the heat treatment schedule of ferritic-martensitic steels (e.g. Fe-9Cr)[10,11] and on methods for coating large

components such as weld-overlay.[15] Another objective is to clearly define the inherent benefits and problems with aluminide coatings on Fe-base ferritic (e.g. Fe-9Cr-1Mo, T91) and austenitic (e.g. Fe-18Cr-8Ni, 304L) substrates to justify their usage and improve their durability.[16-19] An aluminide coating lifetime model is being developed, based on long-term interdiffusion studies.[16] One long-term performance problem with aluminide coatings may be associated with degradation due to the coefficient of thermal expansion (CTE) mismatch between aluminides and these substrates[17,18] and the loss of strength due to the interdiffusion of Al into the substrate.[19] As part of this work, long-term oxidation studies were conducted at 650°-800°C on model aluminide coatings made in a controlled, laboratory-scale chemical vapor deposition (CVD) process.[20] An environment of air + 10vol.% water vapor was used as a low cost (compared to steam) method for determining coating performance. Unlike dry air, many Fe-base alloys are rapidly oxidized in wet air when not coated,[17,18,21] thereby providing an indication when the coating is no longer effective. One of the limitations of the lifetime model[16] has been estimating the critical Al content for coating failure, C_b. Some information was available from Fe-Al-Cr alloys[22,23] but a recent coating failure at 700°C has provided a more relevant indication of C_b. A summary of the first series of creep experiments also is included with recommendations for future work.

EXPERIMENTAL PROCEDURE

Substrates (~1.5mm thick) coated were commercial T91 (Fe-9.3 at.%Cr-0.56Mo-0.46Mn-0.26V-0.55Si-0.15Ni-0.46C-0.22N-0.005S), P92 (Fe-9.9at.%Cr-0.55%W-0.30Mo-0.46Mn-0.26V-0.32Si-0.12Ni-0.51C-0.23N-0.009S) and commercial type 304L stainless steel (Fe-19.7 at%Cr-7.9Ni-1.81Mn-0.15Mo-0.76Si-0.32N-0.09C-0.006S). The laboratory-scale CVD reactor and coating process for low-activity (thin coatings formed after 6h at 900°C with ~5 µm Al-rich outer layer and ~50 µm total thickness including the interdiffusion zone) and high-activity (thick coatings formed after 4h at 1050°C with ~20-40 µm outer layer and ~150-275 µm total thickness on T91) as well as the as-coated microstructure are described elsewhere.[16-18,24] (Typical as-deposited Al profiles for these coatings are shown in Figures 4 and 9.) For comparison, similar coatings were made by a laboratory-scale pack cementation process[25] which is more relevant to commercial coating processes. Coated specimens were exposed with the as-coated surface finish and were cleaned in acetone and methanol prior to exposure. Mass changes (±0.01mg/cm^2) were measured using a Mettler Toledo model AG245 balance. Cyclic oxidation exposures were conducted with a 100h cycle time with specimens in an alumina boat with faces parallel to the gas stream. Distilled water was atomized into the flowing gas stream (850 ml/min) through an alumina tube (e.g. gas velocity of 1.7 cm/s at 700°C) and was calibrated to 10±1 vol.% based on the amount of water injected. Creep tests were performed at 650°C in laboratory air on 25mm long dog bone specimens with a gage section of 2 x 2 mm, a 600grit finish and loads of 100-140MPa. The load was calculated based on the entire gage including any applied coating and selected to lead to rupture in <1 kh. Corrosion and creep specimens were examined by field emission gun, scanning electron microscopy (SEM) equipped with energy dispersive x-ray analysis (EDXA), and by electron probe microanalysis (EPMA) using wavelength dispersive x-ray analysis. Coated specimens were examined in plan view every 2 kh by SEM. Copper plating was used prior to sectioning.

RESULTS AND DISCUSSION

650°C OXIDATION RESULTS

Figure 1 shows typical behavior of coated and uncoated specimens at 650°C in air + 10% water vapor. After an incubation period, uncoated T91(Fe-9wt.%Cr-1Mo) and P92(Fe-9wt.%Cr-2W) specimens

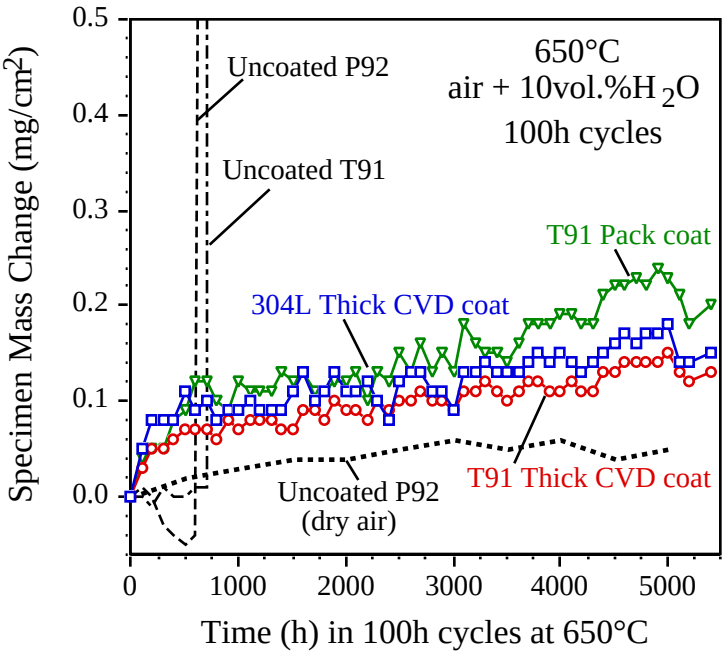

Figure 1. Specimen mass changes during 100h cycles for thick CVD coated 304L and T91 (Fe-9Cr-1Mo) and uncoated T91 and P92 (Fe-9Cr-2W) alloys at 650°C in air + 10% water vapor.

underwent accelerated oxidation with the formation of a thick Fe-rich oxide. In dry air at 650°C, a low mass gain was observed, Figure 1. Specimens with a thick coating made by CVD or pack cementation did not exhibit accelerated attack after >5 kh of exposure. However, minimal interdiffusion is expected at this temperature[16,19] and coating lifetimes can be extensive (>41 kh for slurry coatings in steam[11]).

700°C OXIDATION RESULTS

To accelerate failure due to interdiffusion of Al with the substrate (thereby lowering the surface Al content), exposures also were conducted at 700° and 800°C. (These temperatures exceed any realistic service condition but are necessary to induce coating failure.) Figure 2 shows the mass gain behavior at 700°C. The aluminized coatings showed low mass gains typical of alumina-forming coatings.[17,18] The exception was the thin CVD coating on T91, which exhibited a very high mass gain after ~10 kh and was stopped after 11 kh (110, 100-h cycles). Iron oxide nodules were observed on the specimen surface in SEM plan view. Figure 3 shows EPMA results from a polished cross-section of coated T91 after exposure. Areas of thin Al-rich surface oxide are still evident but Fe-rich oxide nodules penetrate up to ~50µm into the substrate, Figure 3e. The duplex Fe-rich oxide layer with outward (primarily FeO) and inward-growing (Fe and Cr spinel) layers is typical for Fe-base alloys at this temperature in humid air and steam.[17,22,23] The other feature of note was the fine dispersion of AlN particles (Figs 3b and 3f) beneath the original coating layer. These particles are typical in N-containing substrates[10,11,26] and may be detrimental to substrate strength as N was preferentially removed from the substrate.

Residual Al profiles were measured by EPMAin areas where oxide nodules had not formed on the surface, Figure 4. A typical low activity Al profile (dashed line) made by the same process is shown for reference. The starting peak Al content was ~18 at% and was reduced to ~3.5at% after 11 kh. The maximum Al diffusion depth increased from ~50 µm to ~195µm. In each of the three post-exposure profiles, there are peak points in the profile that correspond to the AlN precipitates. Some Al was lost due to oxide formation, but >50% (based on the area under the Al curve) of the Al reduction at the coating surface was due to

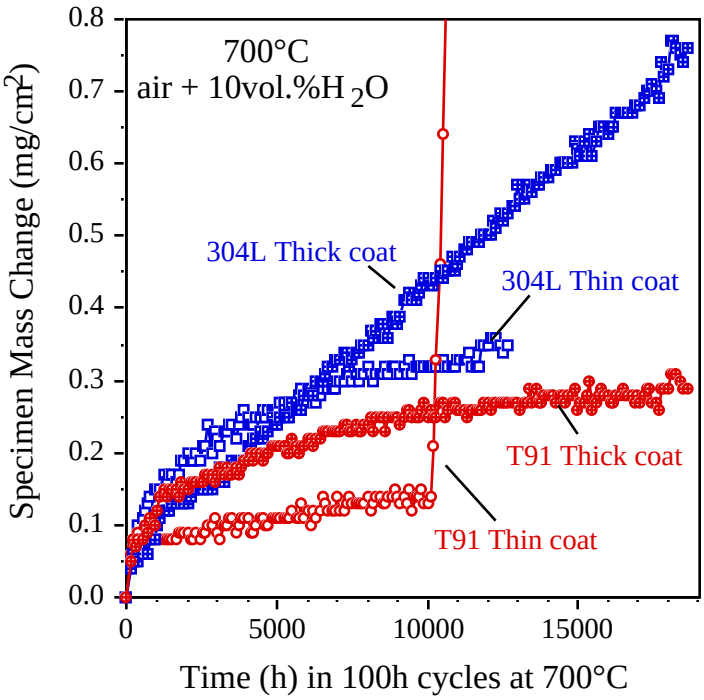

Figure 2. Specimen mass changes during 100h cycles at 700°C in air+10%H_2O. Results are shown for uncoated and coated specimens with different coating thicknesses.

interdiffusion with the substrate. (Amore accurate analysis will require further characterization of the AlN volume fraction to accurately account for Al in these precipitates.) The apparent C_b value of 3.5at% is significantly lower than the 20%Al needed for sulfidation resistance[17,28,29] but somewhat higher than observed for Fe-13Cr+Al alloys, where only ~2.1at.% Al was needed for resistance to water vapor at

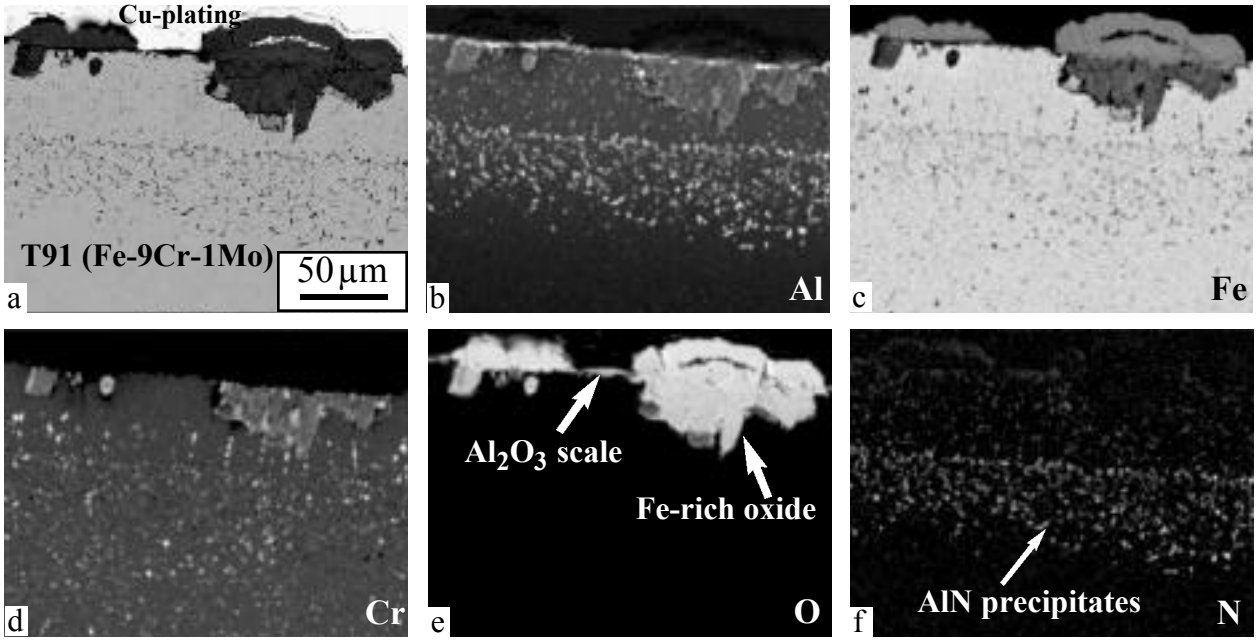

Figure 3. Polished section of CVD thin coating on T91 after 11kh at 700°C in humid air. (a) secondary electron image and EPMA x-ray maps of (b) Al, (c) Fe, (d) Cr, (e) O and (f) N.

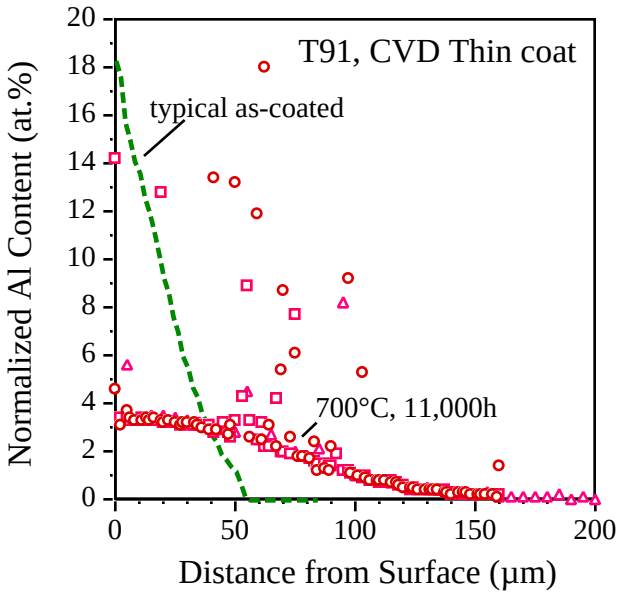

Figure 4. Normalized Al content by EPMA as a function of depth for as-deposited CVD thin coat on T91 (dashed line) and after 11 kh at 700°C.

680°C.[23] However, the higher alloy Cr content (13%) would be expected to lower C_b,[22] as would the lower temperature and water vapor content (<2.5%) in the prior work.[23] The effect of Cr content also may explain why the thin coating on 304L has not failed after 12 kh at 700°C, Figure 2. The 304L substrate and coating contain ~19at,%Cr and this should improve the selective oxidation of Al by a third element effect,[27] and likely reduce C_b.

This newly-measured value of C_b can now be entered into the lifetime model[16] to predict oxidation behavior as a function of temperature and starting Al content. Initial calculations indicate that the thick coating would have a lifetime of >550 kh at 700°C. Of course, the result also must consider that Al would diffuse to >2mm into the tube wall and compromise the substrate creep strength.[19]

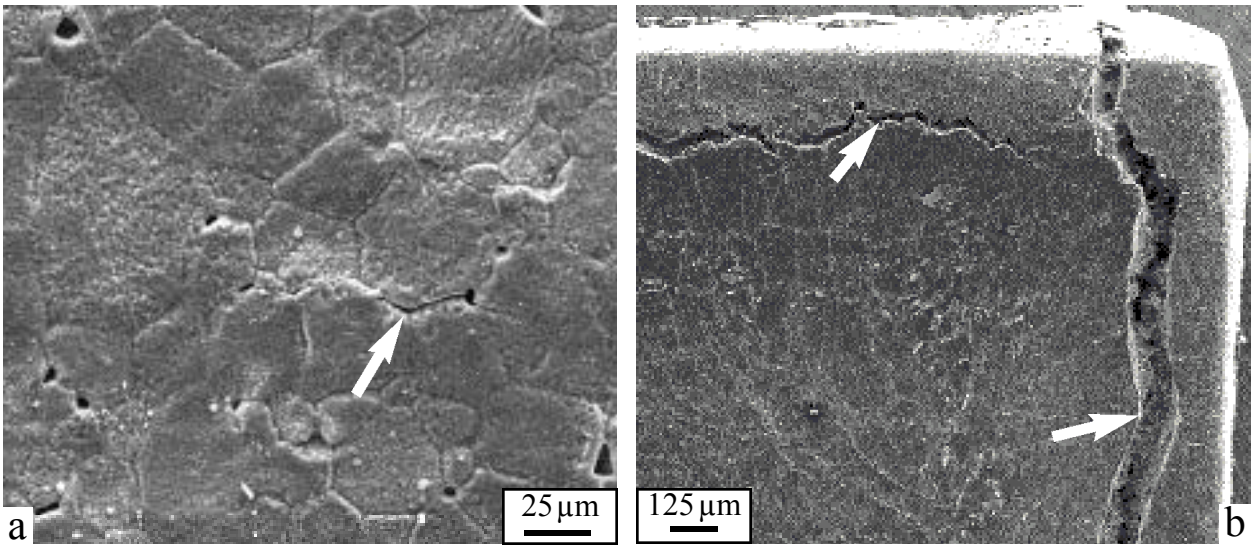

Figure 5. SEM secondary electron plan-view images of coated specimens exposed for 180, 100-h cycles at 700°C in humid air; (a) T91 and (b) 304L. Arrows point to cracks in the coating.

For the thick coatings at 700°C, Figure 2, the T91 substrate showed nearly parabolic behavior after ~19kh. For the 304L substrate, the mass gain was higher than for the thin coating with almost linear kinetics. This difference is attributed to more severe cracking on the specimen face, and particularly the specimen edge, compared to coated T91, Figure 5. The damage at the edge of the coated 304L specimen is similar to that observed during 1h cycles.[18] Thick coated T91 showed no macroscopic cracking at the edges but did show fine cracks in the face, arrow in Figure 5a. One important difference between the two substrates is that on T91 the ~160µm thick interdiffusion zone is also ferritic, so the only CTE mismatch is between the ~40µm Al-rich (Fe_3Al) outer layer and the substrate (~20 and ~13 ppm/K at 700°C, respectively).[17] On 304L, Al interdiffusion resulted in a ferritic layer as well as the intermetallic, $(Fe,Ni)_3Al$ outer layer, resulting in three layers with three different CTEs.[17,18] The increased cracking observed on the coated 304L specimen led to additional oxidation hence the higher rate of mass gain. The lower mass gain for both of the thinner coatings, Figure 2, is likely due to a reduction in the mismatch strain energy with the thinner coating layers, and thus reduced cracking. When the thin coating failed on T91, there was no indication of cracks in the coating, only nodule formation typical of accelerated attack due to the presence of water vapor.

800°C RESULTS

Figure 6 shows mass gains for thick coatings exposed at 800°C. As at 700°C, the coatings on T91 tended to show lower mass gains than those on 304L substrates. The exposure of coated 304L was stopped after 6kh. A similar thick coating on T91 also was exposed for 6kh. This specimen showed a higher mass gain than the nominally similar coated T91 specimen that has been exposed >14kh, Figure 6. (This may be related to scale spallation observed on the latter or excessive oxidation on the former.) Figure 7 shows cross-sections of the coated specimens after 6kh. The coated 304L substrate showed significant deformation compared to the ferritic substrate. As discussed earlier, this was attributed to the CTE mismatch of the thicker ferritic interdiffusion layer with the austenitic substrate. The higher mass gain for the coated 304Lspecimen was attributed to complete oxidation of the outer layer in some locations, arrows in Figure 7a. An oxide layer formed on the surface and at the interface between the inner and outer layer, Figure 8. In some cases, the outer layer appeared to have been cracked but the cracking did not continue into the inner layer, as after exposure in 1h cycles.[18] Residual Al profiles in the coating are shown in Figure 9a. The outer layer appeared to be a mixture of ~45Ni-37Al-12Fe and ~Fe-14Cr-3Al phases. The

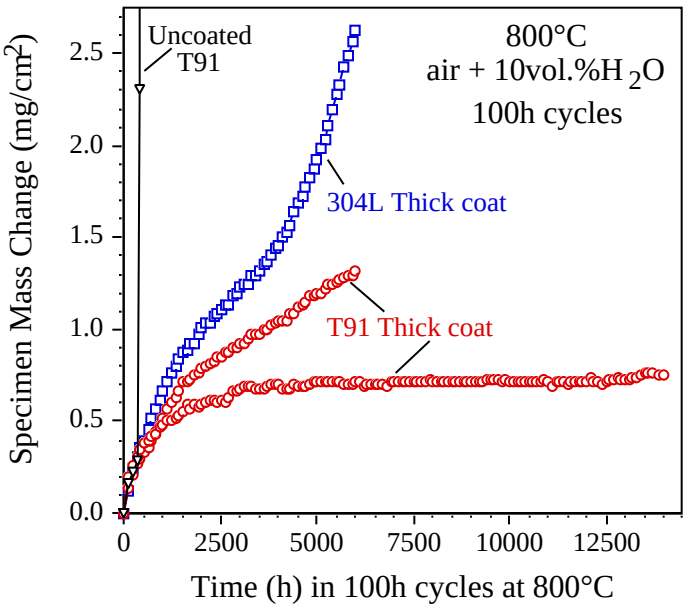

Figure 6. Specimen mass changes during 100h cycles at 800°C in air+10%H_2O.

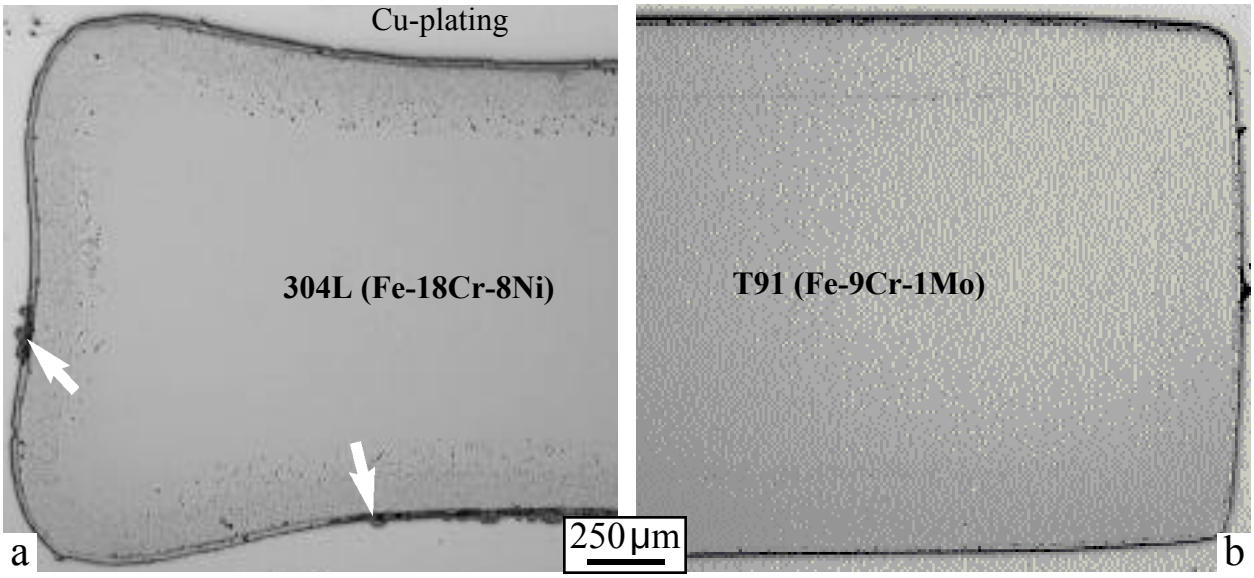

Figure 7. Light microscopy of polished sections of CVD thick coatings after 6kh at 800°C in humid air. (a) 304L substrate and (b) T91 substrate.

NiAl phase is darker gray in Figure 8b. The matrix of the inner layer contained only 4.5%Al (Figure 9a) as well as some Al-rich NiAl particles, Figure 8. The inner layer had increased in depth to ~260µm compared to the starting thickness of ~140µm, Figure 9a. The slower Al diffusivity and Al-induced phase transformation (of the austenitic substrate to ferrite)[3] reduced the starting coating Al content compared to T91 (Figure 9b), limited interdiffusion to some degree and made a more abrupt diffusion profile than in T91, Figures 4 and 9b.

A higher magnification of the coating on T91 after 6kh showed similar degradation of the outer layer, Figure 10. Some oxide had formed at the interface with the inner layer, which may explain the higher mass gain compared to the other coated T91 specimen, Figure 6. Because of the cracks and internal oxidation, the Al profile (Figure 9b) indicated that the outer layer is depleted in Al compared to the inner layer, which still contains ~8% Al. Based on the previous diffusion tests, where the Al content had dropped from 26% to 12% at the surface after 2kh at 800°C, this observation is consistent with the model prediction.[16] The residual Al profile extends to the center of the 1.5mm thick specimen, Figure 9b. Based on these

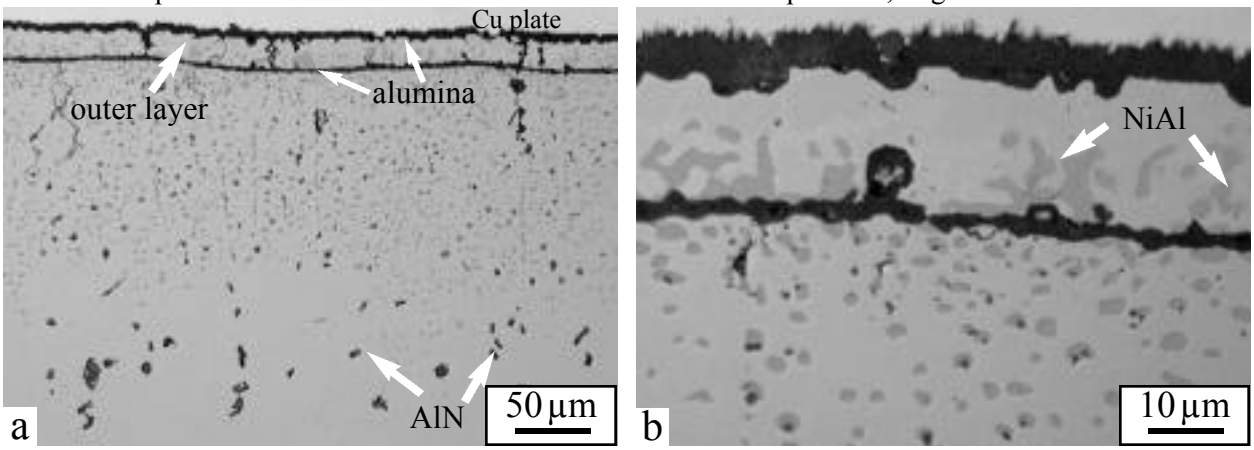

Figure 8. Light microscopy of polished section of CVD thick coating on 304Lsubstrate after 6kh at 800°C in humid air; oxide formed at the interface between the inner (ferritic, low Al) and outer (intermetallic, high Al) coating layers. (b) The darker gray phase in the coating is β-NiAl.

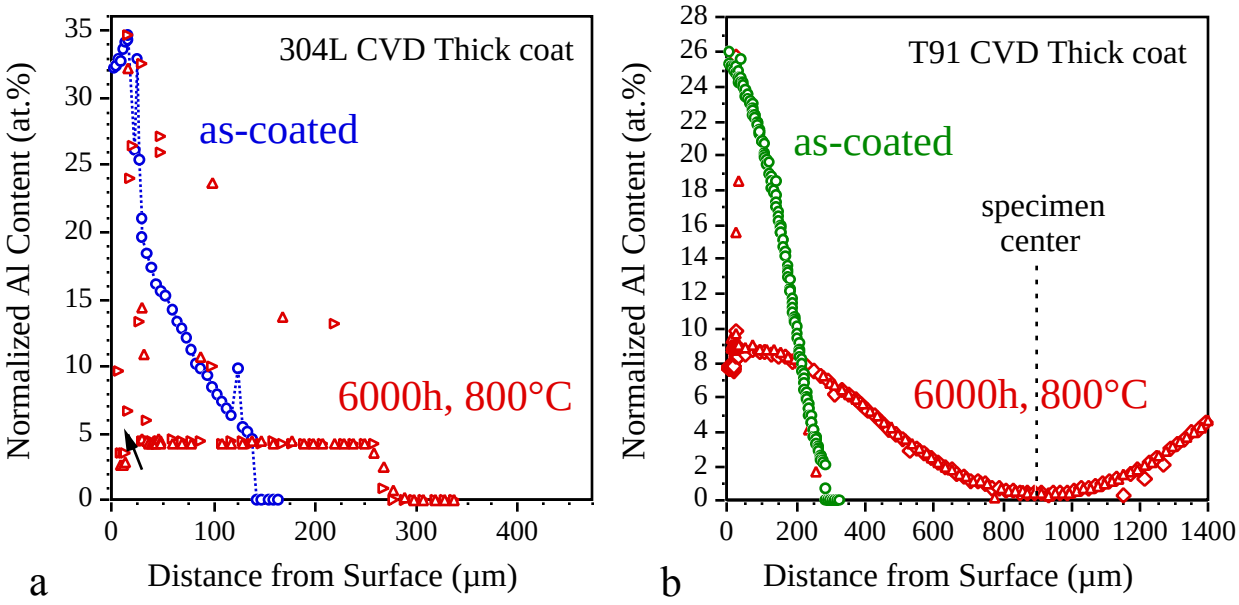

Figure 9. Normalized Al content by EPMA as a function of depth for CVD thick coatings on (a) 304L and (b) T91, as-coated and after 6kh at 800°C.

observations, it is unlikely that the other coated T91 specimen will experience accelerated oxidation (i.e. coating Al content below C_b) in the near future, although the outer layer may experience breakaway oxidation similar to the 304L specimen.

650°C Creep Testing

Figures 11 and 12 summarize the steady-state creep rates from P92 specimens cut from a pipe with various coatings and heat treatments. Some coating studies have maintained the coating temperature at ≤700°C in order to avoid disrupting the ferritic-martensitic (FM) microstructure.[10,11] However, these coatings tend to form high-Al, brittle phases such as Fe_2Al_5. Steels like P92 are typically given a two stage heat treatment of austenization for ~1h at 1050°C (designated HT) followed by quenching in air and then tempering for ~2h at 750°C (designated LT). The creep rates for uncoated P92 in Figure 11a show that an HT heat treatment followed by slow cooling, similar to a pack or CVD coating process, did not adversely affect the creep rate compared to as-received, fully heat-treated P92. However, the HT exposure did

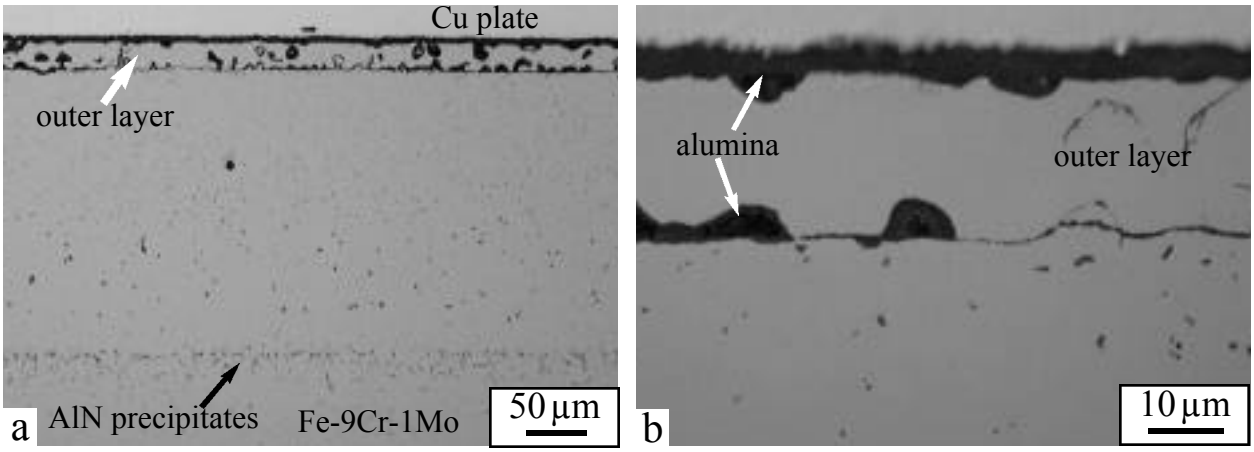

Figure 10. Light microscopy of polished section of CVD thick coating on T91 after 6kh at 800°C in humid air.

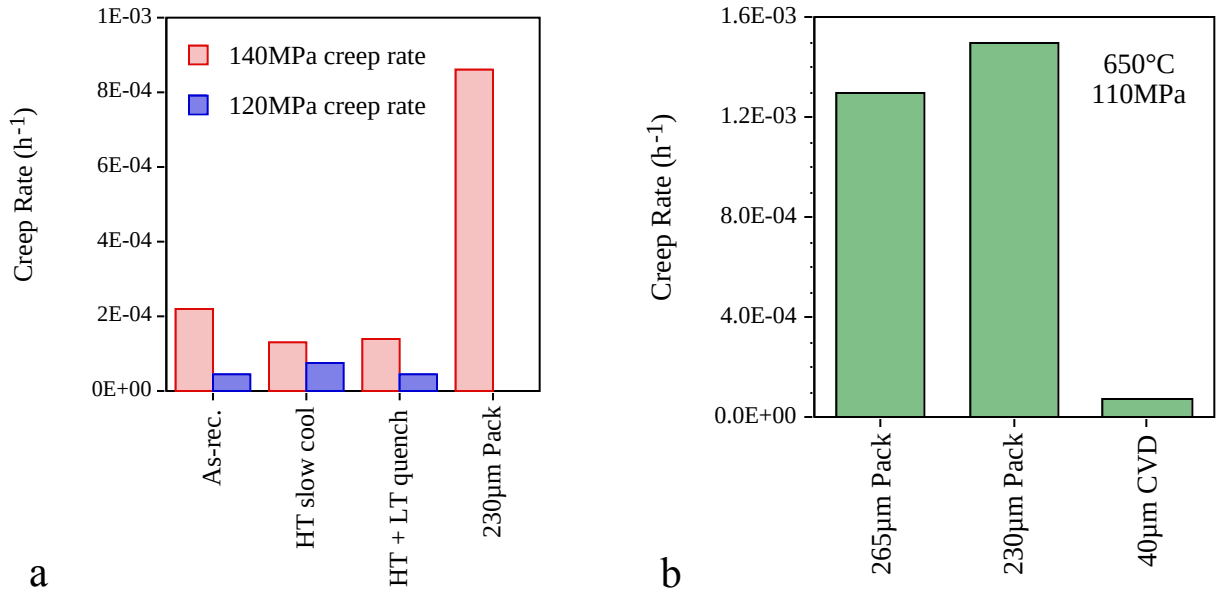

Figure 11. Steady-state creep rates for P92 specimens with and without aluminide coatings and various heat treatments (HT: 1h, 1050°C; LT: 2h,750°C) tested at 110-140 MPa at 650°C in laboratory air.

coarsen the microstructure which may reduce the fracture toughness. A P92 specimen given a HT anneal and subsequent LT anneal followed by quenching also showed a similar creep rate, Figure 11a.

The effect of aluminizing also is shown in Figure 11. A typical ~230µm thick pack coating had a significant negative effect on the creep rate. The effect could be modeled by assuming that the coated area of the gage had no creep strength and only the unaffected substrate supported the applied load.[19] With only a 2x2mm gage, a second series of thin pack and CVD coatings were made for testing with significantly lower creep rates compared to the thicker coatings, Figure 11b and 12. A combination of alternating creep (~200h) and corrosion (5, 100-h cycles at 650°C in wet air) exposures also were

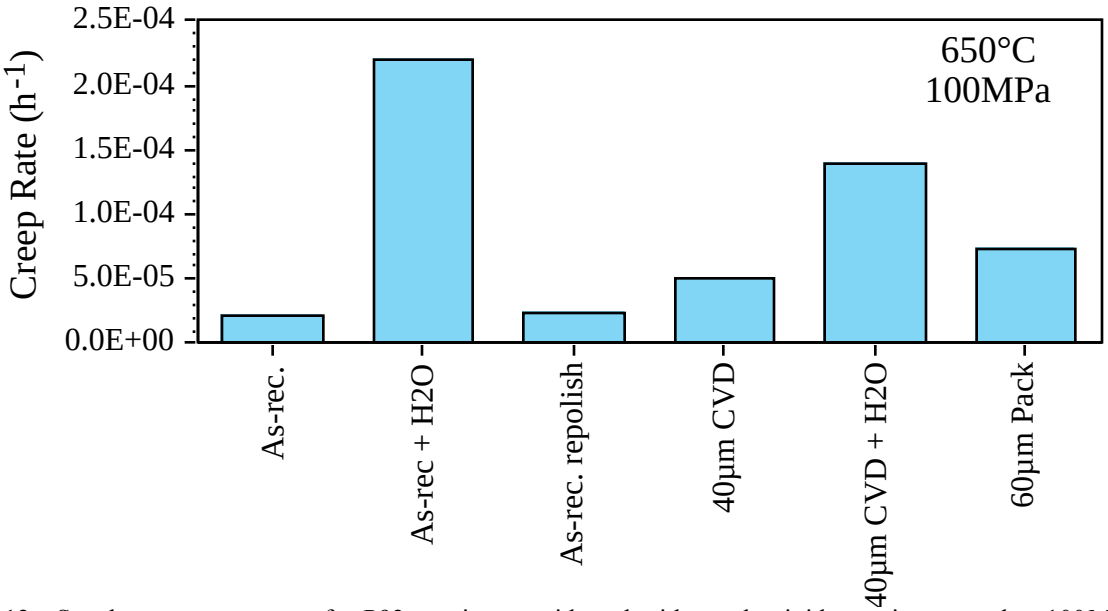

Figure 12. Steady-state creep rates for P92 specimens with and without aluminide coatings tested at 100 MPa at 650°C in laboratory air. Some specimens were tested after exposure for 500h at 650°C in wet air (+ H_2O).

performed.[30] The goal of this work was to quantify the effect on the creep rate of a thick Fe-rich oxide forming on uncoated P92 and consuming substrate. However, a significant difference was noted between specimens that were first creep tested and then exposed to water vapor and specimens that were exposed to water vapor first (+H_2O in Figure 12). The prior exposure in water vapor increased the creep rate of both coated and uncoated specimens. Also, the creep rate of the uncoated specimens did not increase during further corrosion exposures in wet air when the oxide continued to grow and consume the gage section. The unexpected results suggested that the thick oxide layer may be load bearing. In order to avoid these complications, future creep testing should be conducted in wet air or steam environments to observe the effect of environment on mechanical properties.

SUMMARY

Long-term oxidation performance of coated ferritic (T91) and Fe-base austenitic (304L) substrates were conducted in humid air at 650°-800°C. The higher temperatures were used to accelerate the Al interdiffusion to create coating failures. Using 100h exposure cycles, none of the thicker coatings showed accelerated attack of the substrate at the higher temperatures. A thinner coating on T91 failed after ~10,000h at 700°C, allowing rapid oxidation of the substrate when only ~3.5at.%Al remained in the coating. This result established a minimum Al content for modeling coating lifetime. In general, aluminide coatings on 304L substrates showed higher mass gains and more degradation than similar coatings on T91 substrates. This difference is attributed to the Al-induced phase transformation from austenite to ferrite in the interdiffusion zone, causing more severe CTE mismatch problems. Creep testing of coated and uncoated P92 specimens was conducted at 650°C to evaluate the effect of heat treatments and coating on the substrate steady-state creep properties.

ACKNOWLEDGMENTS

The author would like to thank G. Garner J. Moser, K. Cooley and H. Longmire for assistance with the experimental work. B. Armstrong, S. J. Pawel and P. F. Tortorelli provided helpful comments on the manuscript. The research was sponsored by the U.S. Department of Energy, Fossil Energy Advanced Research Materials Program and work at the SHaRE User Facility by the Division of Scientific User Facilities, under contract DE-AC05-00OR22725 with UT-Battelle, LLC.

REFERENCES

1. N. R. Lindblad, *Oxid. Met*., 1 (1969) 143.
2. J. L. Smialek and C. E. Lowell, *J. Electrochem. Soc.*, 121 (1974) 800.
3. N. V. Bangaru and R. C. Krutenat, *J. Vac. Sci. Tech. B*, 2 (1984) 806.
4. G. W. Goward, *Mater. Sci. Tech.*, 2 (1986) 194.
5. D. M. Miller, S. C. Kung, S. D. Scarberry and R. A. Rapp, *Oxid. Met.*, 29 (1988) 239.
6. B. M. Warnes and D.C. Punola, *Surf. Coat. Tech.*, 94-95 (1997) 1.
7. M. Zheng and R. A. Rapp, *Oxid. Met.*, 49 (1998) 19.
8. B. A. Pint, I. G. Wright, W. Y. Lee, Y. Zhang, K. Prüßner and K. B. Alexander, *Mater. Sci. Eng.*, A245 (1998) 201.
9. K. Bouhanek, O. A. Adesanya, F. H. Stott, P. Skeldon, D. G. Lees and G. C. Wood, *Mater. Sci. Forum*, 369-372 (2001) 615.
10. V. Rohr and M. Schütze, *Mater. Sci. Forum*, 461-464 (2004) 401.
11. A. Agüero, R. Muelas, M. Gutiérrez, R. Van Vulpen, S. Osgerby and J. P. Banks, *Surf. Coat. Tech.*,

201 (2007) 6253.
12. V. Deodeshmukh, N. Mu, B. Li and B. Gleeson, *Surf. Coat.Tech.*, 201 (2006) 2836
13. E. J. Opila, *Mater. Sci. Forum*, 461-464 (2004) 765
14. R. Viswanathan and W. Bakker, *J. Mater. Eng. Performance*, 10 (1) (2001) 81
15 S. W. Banovic, J. N. Du Pont and A. R. Marder, *Mater. High Temp.*, 16 (1999) 195
16. Y. Zhang, A. P. Liu and B. A. Pint, *Mater. Corr.*, in press (2007)
17. B. A. Pint, Y. Zhang, P. F. Tortorelli, J. A. Haynes and I. G. Wright, *Mater. High Temp.*, 18 (2001) 185
18. Y. Zhang, B. A. Pint, G. W. Garner, K. M. Cooley and J. A. Haynes, *Surf. Coat. Tech.*, 188-189 (2004) 35
19. S. Dryepondt, Y. Zhang and B. A. Pint, *Surf. Coat.Tech.*, 201 (2006) 3880
20. W. Y. Lee, Y. Zhang, I. G. Wright, B. A. Pint and P. K. Liaw, *Met. Trans.*, 29A (1998) 833
21. B. A. Pint, R. Peraldi and P. J. Maziasz, *Mater. Sci. Forum*, 461-464 (2004) 815
22. B. A. Pint and I. G. Wright, *Mater. Sci. Forum*, 461-464 (2004) 799
23. I. Kvernes, M. Olivera and P. Kofstad, *Corr. Sci.*, 17 (1977) 237
24. Y. Zhang, B. A. Pint, K. M. Cooley and J. A. Haynes, in preparation
25. Y. Zhang, Y. Q. Wang and B. A. Pint, NACE Paper 07-468, Houston, TX, presented at NACE Corrosion 2007, Nashville, TN, March 2007
26. Y. Zhang, B. A. Pint, K. M. Cooley and J. A. Haynes, *Surf. Coat.Tech.*, 200 (2005) 1231
27. F. H. Stott, G. C. Wood and J. Stringer, *Oxid. Met.*, 44 (1995) 113.
28. P. F. Tortorelli and J. H. DeVan, *Mat. Sci. and Eng.*, A153 (1992) 573.
29. P. F. Tortorelli and K. Natesan, *Mater. Sci. Eng.*, A258 (1998) 115.
30. S. Dryepondt, Y. Zhang and B. A. Pint, NACE Paper 07-471, Houston, TX, presented at NACE Corrosion 2007, Nashville, TN, March 2007

IMPROVING THE WELDABILITY OF FECRAL WELD OVERLAY COATINGS

J.N. DuPont, J.R. Regina, and K. Adams
Lehigh University, Bethlehem, PA 18015

ABSTRACT

Fe-Cr-Al weld claddings are currently being considered as corrosion resistant coatings for boiler tubes in coal fired power plants. Although these alloys could potentially be good coating candidates due to their excellent high-temperature corrosion resistance, they are susceptible to cracking due to hydrogen embrittlement at elevated aluminum concentrations. The current study investigated the hydrogen cracking susceptibility of Fe-Cr-Al weld overlay claddings deposited by the gas tungsten arc and gas metal arc processes. The cracking susceptibility of these alloys is a strong function of the Al and Cr content of weld overlay. Additions of Cr to the overlay will decrease the amount of Al that can be accommodated before cracking occurs. Less Al and Cr could be tolerated in gas metal arc welds compared to gas tungsten arc welds. The hydrogen cracking susceptibility was not linked exclusively to the formation of the inherently brittle intermetallic compounds (Fe_3Al and FeAl) as observed from previous results on Fe-Al weld overlays. The presence of $(Fe,Cr)_xC_y$ and $(Fe,Al)_3C$ type carbides was found to improve the cracking resistance to the point where crack-free welds could be obtained on some of the overlays that contained the brittle intermetallic phases. This improvement in cracking resistance is attributed to the hydrogen trapping potential of the carbide phases. Research currently being conducted to exploit the beneficial effect of carbides for reducing cracking susceptibility is described.

INTRODUCTION

Fe-Cr-Al based alloys are good candidates for corrosion resistant weld overlay coatings because they exhibit excellent oxidation and sulfidation resistance in a wide range of high-temperature environments. These alloys rely on both aluminum and chromium additions for increased corrosion protection, and it has been shown that the corrosion resistance of these alloys in simulated low NOx environments improved with an increase in the aluminum and chromium concentrations. Recent studies have indicated that Fe-Cr-Al based alloys require approximately 7.5 - 10% wt% aluminum and chromium additions up to ~ 5 wt% to remain protective in a wide variety of low NOx type atmospheres[1,2]. Unfortunately, these alloys are also susceptible to cracking due to environmental embrittlement from hydrogen. Previous work has shown that Fe-Al weld overlays produced with both the GTAW and GMAW processes were subject to cracking when the aluminum concentration in the weld deposit was greater than approximately 8-11%Al [3], and this Al range represents the composition over which the intermetallics begin to form. Thus, the objective of this research is to establish the range of weldable FeCrAl compositions and develop methods for improving the cracking resistance of the coatings so that they can be exploited for corrosion protection in coal fired power plants.

EXPERIMENTAL PROCEDURE

Gas tungsten arc (GTAW) and gas metal arc (GMAW) weld overlays were deposited onto A285C carbon steel (0.16 wt% C). For the GTA welds, a dual wire feeder system was utilized with commercially pure 1100 aluminum and 430 ferritic stainless steel filler metals. A smaller matrix of welds was prepared on a low carbon experimental substrate (0.017 wt% C). Welds with a wide range of aluminum and chromium concentrations were prepared by independently varying the feed rates of the two filler metal wires. Welds were produced with a travel speed of 2mm/s and energy input of approximately 1210J/mm. The filler metal wire feed speeds were independently varied from 0 – 74mm/s to adjust the aluminum and chromium contents of the weld deposits. The GMA welds were prepared with a composite wire that had a solid Al core and a steel outer sheath with Cr powder additions. The cracking behavior of the weld deposits was investigated using a non-destructive dye-penetration technique. Weld overlay compositions were determined using electron probe microanalysis (EPMA). Phase identification was conducted using X-Ray Diffraction (XRD) on a Bruker AXS General Area Detector Diffraction System using Co Kα x-rays. Weld samples were removed in cross-section, mounted, and polished to 0.01μm SiO_2 finish for light optical microscopy (LOM). Measurements of the particle area fraction and number of particles per unit area of weld were made using a LECO© quantitative image analysis (QIA) system interfaced with a light optical microscope. Identification of fine scale carbides was performed by removing the carbide precipitates from the matrix using a

carbide extraction technique. Samples were also prepared with an FeCrAl matrix and various quantities of TiC as hydrogen trapping sites. These alloys were prepared with an arc button melting process using virgin materials.

RESULTS AND DISCUSSION

GTA WELDS

Figure 1 shows the cracking susceptibility of the weld overlays as a function of aluminum and chromium concentration prepared with the GTAW process. The XRD phase identification results are shown in Figure 2. There were four microstructural regimes observed in the weld overlay coatings: ferrite with $(Fe,Al)_3C$ carbides, ferrite with $(Cr,Fe)_xC_y$ carbides, Fe_3Al/FeAl with $(Fe,Al)_3C$ carbides, and Fe_3Al/FeAl with $(Cr,Fe)_xC_y$ carbides. The weldability boundary from Figure 1 is superimposed on the phase ID results for reference, and the approximate location of the order/disorder transformation boundary that indicates the formation of Fe_3Al/FeAl intermetallic phases is also shown. It was not possible to distinguish between the Fe_3Al and FeAl intermetallic phases, so they are collectively grouped as Fe_3Al/FeAl here. The phase fields containing Fe_3Al/FeAl phases may have also contained ferrite, but due to the peak overlap between these phases it could only be determined that the intermetallic phases were present within the weld metal as a result of the super lattice reflections. Thus, the order/disorder transformation boundary describes the composition range where ferrite phase begins to transform to the ordered intermetallic phases. Chromium additions appeared to moderately stabilize the ferrite phase, as increasing the chromium content of the weld caused the intermetallic transformation to occur at higher aluminum concentrations. According to the binary Fe-Al phase diagram, a two-phase region of ferrite + Fe_3Al has been reported to exist between approximately 11wt%Al – 13wt%Al. From the reported phase diagrams, the actual order/disorder transformation may have occurred over a range of aluminum concentrations, where the onset of the ordered transformation began at approximately 11wt%Al and may not have completely transformed to the ordered intermetallic Fe_3Al phase until approximately 13wt%Al (for binary Fe-Al welds). The $(Fe,Al)_3C$ carbides form in the weld overlays containing less than 4wt%Cr, whereas welds containing above approximately 4wt%Cr contained the $(Cr,Fe)_xC_y$ type carbides. Research conducted to date has shown that the hydrogen cracking susceptibility of Fe-Al type alloys is linked exclusively to the presence of the brittle Fe_3Al and FeAl intermetallic phases [3,4]. However, the combined weldability and phase ID results shown in Figure 2 indicate that the cracking susceptibility of these weld overlays can not be linked solely to the presence of the intermetallic phases. Crack-free welds could be deposited on some compositions that exhibited the intermetallic phases, while cracking was observed on some of the alloys that did not exhibit any of the ordered intermetallic phases. These results indicate that the addition of chromium and the presence of second phase particles has a strong influence on the cracking susceptibility of these alloys.

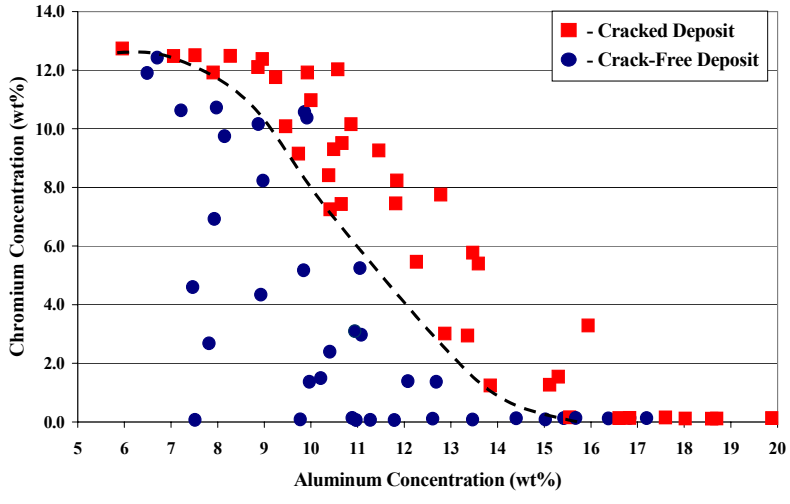

Figure 1. Cracking susceptibility of the weld overlays as a function of aluminum and chromium concentration prepared with the GTAW process.

Recent research has demonstrated particles such as carbides, oxides, and nitrides can act as hydrogen trapping sites[5]. Permanent hydrogen trapping sites can reduce the overall amount of diffusible hydrogen available to embrittle the metal, and can therefore reduce the cracking susceptibility of the alloy. The effectiveness of microstructural features to trap hydrogen depends largely on the type of feature. For example, oxide inclusions are more effective trapping sites than dislocations, while carbides are even more effective than oxides at trapping free hydrogen. Although the size and number

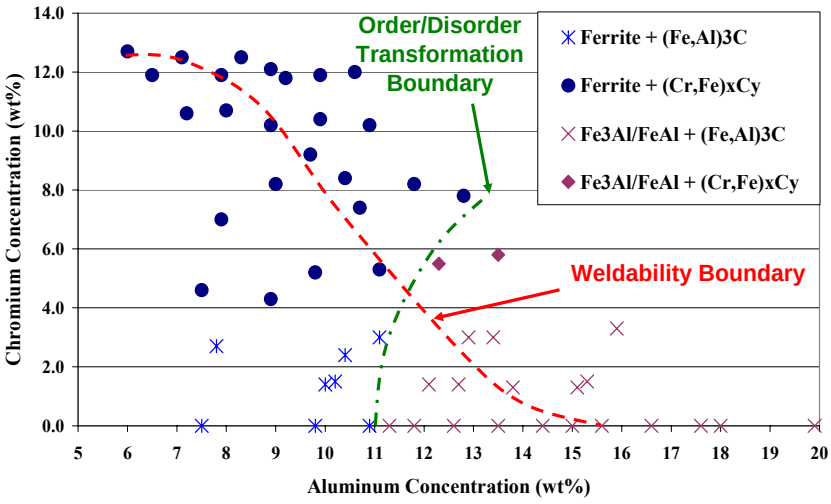

Figure 2. X-Ray diffraction phase identification results of the weld overlays. The weldability boundary from Figure 1 is superimposed on the results.

of particles within the welds are expected to effect the amount of trapped hydrogen, the amount of particle surface area within the weld should provide a more direct indication on the effectiveness of the particles to trap hydrogen. This is based on the idea that hydrogen trapping sites rely on the segregation of hydrogen to the particle/matrix interface, rather than hydrogen incorporation into the actual carbide or oxide [5]. Figure 3 shows that the particle surface area per unit volume of weld metal increases as the volume percent of particles increases, which is expected. More importantly, the results indicate that the cracked and crack-free welds can be separated based on their particle surface area. For the current welding conditions, welds containing particle/matrix interfacial areas less than approximately 80 mm^2/mm^3 were susceptible to hydrogen cracking. Welds containing between approximately 80 mm^2/mm^3 and 100 mm^2/mm^3 particle surface area values appeared to undergo a transition between cracked and crack-free welds. Weld overlays containing particle surface areas greater than approximately 100 mm^2/mm^3 were found to be immune to hydrogen cracking. This correlation between the amount of particle surface area and the susceptibility of the welds to hydrogen cracking indicates that the size and distribution of particles within the weld has a significant effect on the hydrogen cracking behavior of the Fe-Cr-Al weld overlay claddings. It should be noted that the amount of surface area required to prevent cracking is expected to depend on the particle type, amount of hydrogen available, and residual stress. Thus, the results presented here are not intended to provide a general value required to prevent cracking, but to demonstrate the important role of particles in reducing the cracking susceptibility of these alloys. These results are described in more detail in Reference 6.

The results described above suggest that the carbon content of the weld should influence the amount of carbides in the weld and the corresponding resistance to hydrogen cracking. The cracking results of welds made on the low carbon substrates shown in Figure 4 confirm this expected trend. The weldability limit for the high carbon substrate is provided with these results for comparison. There is a rather distinct compositional boundary between welds that were cracked and crack-free for each substrate. These results show that a reduction in carbon content associated with the lower carbon substrate significantly decreases the range of weldable compositions. The difference in

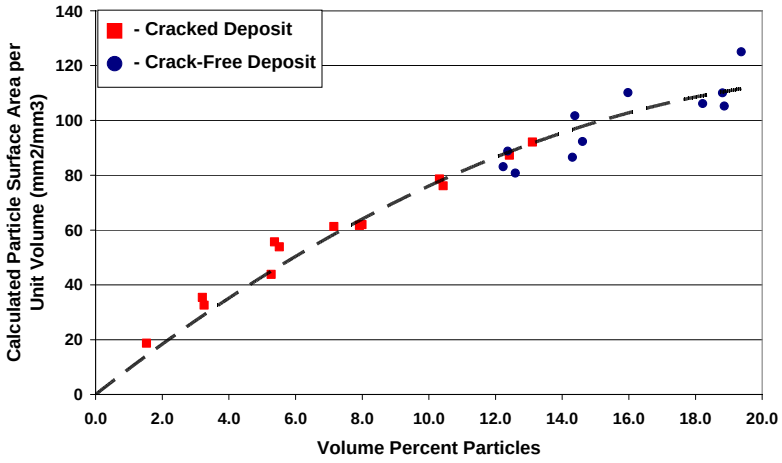

Figure 3. Calculated particle surface area per unit volume of weld metal as a function of volume percent particles for welds containing the $(Fe,Cr)_xC_y$ type carbides.

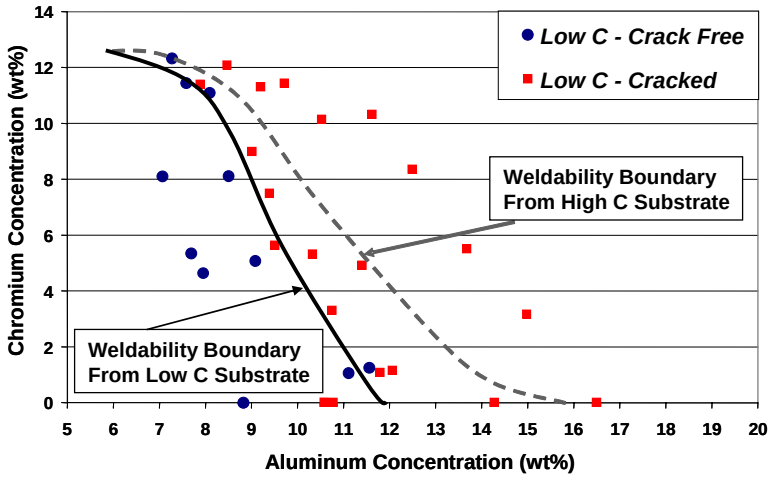

Figure 4. Weldability results of low C steel substrates.

cracking behavior between the low and high carbon welds is most significant at the lower chromium levels where the intermetallic phases form. Volume fraction measurements made on select samples confirmed that the amount of carbides in welds made on the low carbon substrate was much lower than those made on the high carbon substrate. For example, a 10.2Al-5.3Cr overlay made on the low carbon substrate contained only ~1 volume percent of particles and cracked, whereas a 9.8Al-5.2Cr overlay (i.e, similar Al and Cr) on the higher carbon steel plate contained ~15 volume percent particles and was crack-free.

GMA WELDS

Figure 5 shows typical weldability results for the GMA welds. The weldability boundary for the GTA welds is superimposed for reference. These results show that weld overlays prepared with the GMAW process can not tolerate as much Al and Cr before cracking occurs compared to the GTA weld overlays. GMA welds prepared under a wide range of conditions with different shielding gases and wire compositions showed similar results. This difference is attributed to the higher of amount of hydrogen generally present with the GMAW process, which may be due to hydrogen pick up in the arc by the fine metal droplets transferred across the arc. Since GMAW is the preferred process for industrial applications due to the higher deposition rate, these results indicate that the weldability of these alloys needs to be improved so that higher Al and Cr concentrations can be accommodated for adequate corrosion resistance.

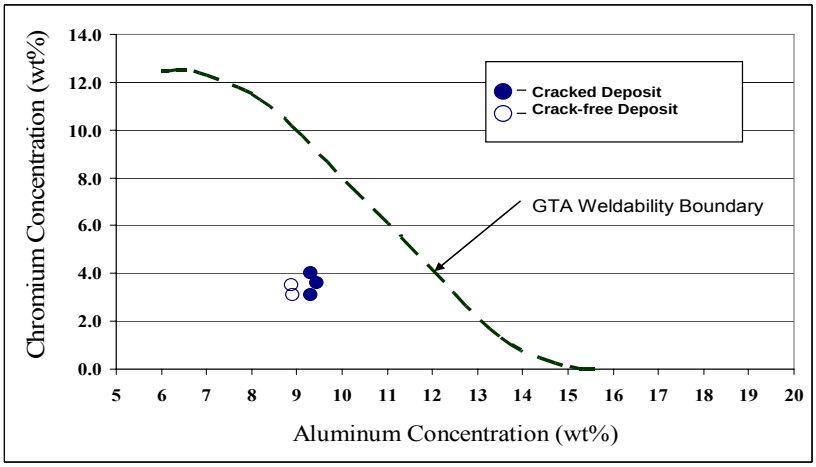

Figure 5. Weldability results for the GMAW process.

PRELIMINARY RESULTS ON TiC ADDITIONS

The GTA weldability results demonstrated that carbide particles can serve as effect hydrogen trapping sites for improving the cracking resistance, while the GMA results indicate that improvement in cracking resistance is needed in order to apply these alloys with the GMA process that is preferred by industry. Research conducted to date on the addition of hydrogen trap sites has shown that TiC is one of the most effective hydrogen trap sites due to its high binding energy[5]. The addition of TiC is also convenient for this system because TiC forms during solidification by a monovariant eutectic reaction during solidification. Thus, work has been initiated on a systematic study for controlled additions of TiC to these alloys for improved weldability. The amount of TiC that forms will depend on the amount of Ti and C, the solute redistribution behavior of Ti and C during solidification, and the

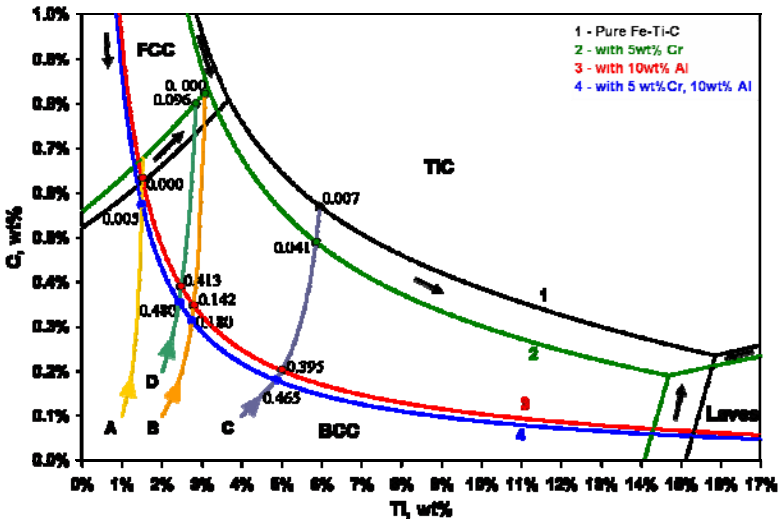

Figure 6. Liquidus projections and calculated primary solidification paths for various Fe-Cr-Al-Ti-C alloys. Numbers indicate calculated values of eutectic constituent.

position of the monovariant eutectic lines on the appropriate liquidus projection [7]. A preliminary matrix of 16 alloys (Table 1) was prepared using arc button melting with systematic variations in Al, Cr, Ti, and C. The appropriate liquidus projections for the Fe-Ti-C, Fe-5Cr-Ti-C, Fe-10Al-Ti-C, and Fe-10Al-5Cr-Ti-C systems were calculated using Thermo-Calc. The 10Al and 5Cr levels are used here because these alloy levels have been shown to provide good corrosion resistance in a wide range of environments. The 10Al and 5Cr concentrations were added individually to the Fe-Ti-C system to observe the effect of TiC formation.

The calculated liquidus projections, primary solidification paths, and amount of α-bcc / TiC eutectic that are expected to form during solidification are shown in Figure 6. The solute redistribution behavior was determined to be consistent with equilibrium solidification using Clyne and Kurz model[8]. The solidification paths and resultant amount of TiC-containing eutectic that forms was calculated using a solute redistribution model recently published[7]. The results indicate that the addition of 5wt% Cr to the Fe-Ti-C system, as in alloy system 2, caused the α/TiC mono-variant line to decrease to lower titanium and carbon concentrations, the α/γ-fcc mono-variant line increased to greater carbon concentrations, and the α/Laves mono-variant line decreased to lower titanium concentrations. The addition of 10wt% Al to the Fe-Ti-C system, as in alloy system 3, caused the α/TiC mono-variant line to decrease to much lower titanium and carbon concentrations than in alloy system 2, the α/γ mono-variant line increased to much greater carbon concentrations and is off the scale of the figure, and the α/Laves mono-variant line was not observed in the calculations which were conducted up to 20wt% Ti. The addition of 10wt% Al and 5wt% Cr to the Fe-Ti-C system, as in alloy system 4, caused the α/TiC boundary to decrease to even lower titanium and carbon concentrations than in alloy system 3, the α/γ boundary increases to even greater carbon concentrations and is again off the scale of the figure, and the α/Laves boundary was again not observed in the calculations performed up to 20wt% Ti. For each alloy system, the primary solidification path ends once it intersects the mono-variant eutectic line in its respective alloy system. The total fraction of eutectic that is expected to form for each alloy that intersects the mono-variant line is given next to the small dots in Figure 6. The fraction of eutectic that is expected to form provides an indication of how much TiC will form. The total fraction of eutectic that forms directly after primary solidification is equivalent to the fraction of liquid that remains when the primary solidification path intersects a mono-variant eutectic line. As 5wt% Cr is added to the Fe-Ti-C system, as in alloy C in system 2, the α/TiC monovariant line shifts to slightly lower Ti and C compositions. Thus, for identical Ti and C nominal compositions in the Fe-Ti-C and Fe–5Cr–Ti–C systems, the calculated primary solidification paths is truncated. This leads to a larger calculated fraction of liquid remaining when the solidification path intersects the mono-variant eutectic line and it would be expected that a higher volume fraction of monovariant eutectic α/TiC constituent will form. The same rational holds for the addition of 10wt% Al and 10wt%Al – 5wt%Cr to the Fe-Ti-C system, which both respectively further suppress the α/TiC monovariant line to lower Ti and C compositions. Alternatively, for a nominal composition increase of either or both Ti and C, the fraction of liquid present when the primary solidification path intersects the α/TiC mono-variant eutectic lines increases, which translates to an increasing amount of eutectic that should form. It appears that alloys B and D in system 2 come close to the triple point between fcc, bcc, and TiC phase fields. This may or may not occur depending on whether alloys actually solidify under absolute equilibrium conditions or if the positions of the calculated liquidus lines are completely accurate. The amount of TiC will also increase with additions of Ti and C, which is intuitively expected.

Figure 7 compares preliminary results of the microstructures of Alloys 2B and 2D. The microstructures contain a α/TiC eutectic constituent in an α matrix. As expected, alloys from the "D" series exhibit significantly higher amounts of the α/TiC eutectic constituent due to the higher Ti and C additions. Work is in progress to quantify the amount of eutectic constituent in each alloy in order to validate the modeling results. This will provide a framework for controlling the amount of TiC in the alloy. Once this is accomplished, hydrogen desorption and weldability tests will be conducted to determine the effectiveness of the TiC additions for improving weldability.

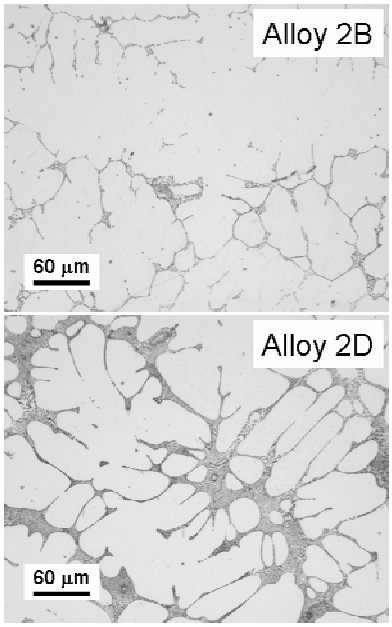

Figure 7. Microstructures of Alloys 2B and 2D.

Table 1: Compositions (wt %) of experimental Fe-Al-Cr-Ti-C alloys.

Alloy #	Fe	Al (wt%)	Cr (wt%)	Ti (wt%)	C (wt%)
1A	Balance	-	-	1	0.1
1B	Balance	-	-	2	0.1
1C	Balance	-	-	4	0.1
1D	Balance	-	-	2	0.2
2A	Balance	-	5	1	0.1
2B	Balance	-	5	2	0.1
2C	Balance	-	5	4	0.1
2D	Balance	-	5	2	0.2
3A	Balance	10	-	1	0.1
3B	Balance	10	-	2	0.1
3C	Balance	10	-	4	0.1
3D	Balance	10	-	2	0.2
4A	Balance	10	5	1	0.1
4B	Balance	10	5	2	0.1
4C	Balance	10	5	4	0.1
4D	Balance	10	5	2	0.2

CONCLUSIONS

The weldability and microstructure of Fe-Cr-Al weld overlays deposited onto carbon steel substrates was investigated. Work has also been initiated for improving the weldability of Fe-Cr-Al overlays through TiC additions. Results acquired to date show that cracking susceptibility is a strong function of the aluminum and chromium content of weld overlay. Additions of chromium to Fe-Al weld overlays will decrease the amount of aluminum that can be accommodated in the overlay before cracking begins to occur. The hydrogen cracking susceptibility of the Fe-Cr-Al welds can not be linked exclusively to the formation of the inherently brittle intermetallic compounds (Fe_3Al and FeAl). The presence of $(Cr,Fe)_xC_y$ and $(Fe,Al)_3C$ carbides significantly affected the cracking behavior of the welds, as high amounts of these carbides prevented hydrogen cracking in samples containing the intermetallic compounds. Additions of Ti and C to Fe-Cr-Al alloys leads to the formation of a microstructure with an α/TiC eutectic type constituent in an α matrix. The amount of α/TiC constituent is expected to increase with increasing Ti, C, Al, and Cr.

ACKNOWLEDGEMENTS

The authors gratefully acknowledge financial support of this research by the Fossil Energy Advanced Research and Technology Development Materials program, U.S. Department of Energy, under contract DE-AC05-96OR22464 with U.T. Battelle. The authors also gratefully acknowledge useful technical discussions with Dr. Peter Tortorelli from Oak Ridge National Laboratory.

REFERENCES

1. J. R. Regina, J. N. DuPont, and A. R. Marder, Gaseous Corrosion Resistance of Fe-Al Based Alloys Containing Cr Additions. Part I – Kinetic Results. *Accepted for Publication - Mat. Sci. and Eng. , A* (2004).
2. J. R. Regina, J. N. DuPont, and A. R. Marder, Corrosion Behavior of Fe-Al-Cr Alloys in Sulfur- and Oxygen-Rich Environments in the Presence of Pyrite. *Corrosion* **60**, 501-509 (2004).
3. S. W. Banovic, J. N. DuPont, P. F. Tortorelli, and A. R. Marder, The role of aluminum on the weldability and sulfidation behavior of iron-aluminum cladding. *Weld. Res. (Miami)* **78**, 23S-30S (1999).
4. M.G. Mendiratta, S.K. Ehlers, D.K. Chatterjee, and H.A. Lipsitt, Tensile flow and fracture behavior of DO3 iron-25 at% aluminum and iron-31at% aluminum alloys, Metallurgical and Materials Transactions A, 18A, (1987, pp. 283-291.
5. I. Maroef, D. L. Olson, M. Eberthart, and G. R. Edwards, Hydrogen trapping in ferritic steel weld metal. *International Materials Reviews* **47**, 191-223 (2002).
6. J. Regina, J.N. DuPont, and A.R. Marder, The Effect of Chromium on the Weldability and Microstructure of FeCrAl Weld Claddings, accepted for publication in *Welding Journal*.
7. J.N. DuPont, Mathematical Modeling of Solidification Paths in Ternary Alloys: Limiting Cases of Solute Redistribution, *Metallurgical and Materials Transactions A*, Vol 37A, June, 2006, pp. 1937-1947.
8. T.W. Clyne and W. Kurz, *Metallurgical Transactions A,* 1981; 12A: p. 965

SYNTHESIS AND OXIDATION PERFORMANCE OF AL-ENRICHED γ+γ' COATINGS ON NI-BASED SUPERALLOYS VIA SECONDARY ALUMINIZING

Y. Zhang and J. P. Stacy
Department of Mechanical Engineering, Box 5014
Tennessee Technological University, Cookeville, TN 38505-0001
E-mail: yzhang@tntech.edu; Tel.: (931) 372-3265; Fax: (931) 372-6345

B. A. Pint and J. A. Haynes
Metals and Ceramics Division
Oak Ridge National Laboratory, Oak Ridge, TN 37831-6156
E-mail: pintb@ornl.gov; Tel.: (865) 576-2897; Fax: (865) 241-0215

B.T. Hazel, B.A. Nagaraj
GE Aircraft Engines, Cincinnati, OH 45215-6301

ABSTRACT

"Simple" Pt-enriched γ+γ' coatings (16-19 at.% Al) were fabricated on René 142 and single-crystal N5 Ni-based superalloys by electroplating a thin layer of Pt followed by a diffusion treatment in vacuum at 1150-1175°C. By introducing a secondary short-term aluminizing step via pack cementation with NaCl activator, "enriched" γ+γ' coatings were achieved with an increased Al content (~22 at.% Al). The changes in composition profiles between the "simple" and "enriched" γ+γ' coatings were discussed. Incorporation of reactive elements, such as Hf, into the γ+γ' coating during the aluminizing process also was explored. The cyclic oxidation performance of the "enriched" γ+γ' coatings were evaluated at 1100 C.

INTRODUCTION

Thermal barrier coatings (TBCs) are widely used to reduce the operating temperature of the underlying superalloy hardware in gas turbines [1]. One of the industry-accepted bond coats for TBCs is the single-phase β-(Ni,Pt)Al coating [2]. Failure of TBCs is often associated with spallation of the Al_2O_3 scale along the scale-bond coat interface [1]. In service, the β-phase bond coats are susceptible to phase transformations as the Al content depletes from the β phase to more Ni-rich phases such as martensite or γ'-Ni_3Al [3,4]. The volume changes from these phase transformations contribute to rumpling during thermal cycling and affects the ability of the bond coat to maintain an adherent Al_2O_3 scale [5-7].

Studies by Gleeson et al. [8,9] indicate that Ni-20Al-20Pt+Hf cast alloys (at.%) with a γ+γ' microstructure and γ+γ'-based coatings consisting of mainly Ni-20Al-22Pt-7Co-7Cr-0.7Hf (at.%) formed adherent α-Al_2O_3 scales with significantly reduced rumpling during cyclic oxidation testing. Our previous work [10,11] focused on the oxidation performance of the "simple" γ+γ' coatings synthesized by electroplating the superalloy substrate with ~7 μm of Pt followed by a diffusion treatment [12-14]. For superalloys that contained 13 at.% Al, the Al content in the resulting coating was 16-19 at.% [11]. As compared to bare alloys, improved oxidation resistance was observed for the "simple" γ+γ' coatings on directionally-solidified (DS) René 142 and single-crystal René N5 alloys. However, the overall scale adherence was inferior to the β-(Ni,Pt)Al coatings [11].

The objective of this study was to develop a better understanding of the processing parameters for fabricating the γ+γ' coatings with increased Al levels of ~22 at.% Al (hereafter referred to as "enriched"

γ+γ' coatings). This was achieved by introducing a short-term pack aluminizing process after the "simple" γ+γ' coating application. The effects of different activators in the pack powders and the pack-specimen arrangement were investigated. Preliminary oxidation tests were conducted with the emphasis on comparing the oxidation behavior of the "enriched" and "simple" γ+γ' coatings, as well as the β-(Ni,Pt)Al coating.

EXPERIMENTAL PROCEDURE

DS René 142 and single-crystal low-sulfur (1 ppma S) Y-free René N5 superalloys were used as substrates. The chemical composition of René 142 is Ni-13.4Al-7.7Cr-11.9Co-2.1Ta-1.6W-0.9Mo-0.9Re, in at.%. The composition of N5 is Ni-13.5Al-8.1Cr-7.5Co-2.1Ta-1.7W-0.9Mo-1.0Re-0.07Hf, in at.%. Superalloy specimens (16.5 mm in diameter x 1.5 mm) were electroplated with ~7 μm Pt, followed by a diffusion anneal at 1175°C to form the "simple" γ+γ' coating [10,11].

A subsequent pack aluminizing process was used to produce the "enriched" γ+γ' bond coatings. Secondary processing was conducted in a tube furnace at 1050°C for 30 min with flowing Ar+5%H_2 gas. The packs consisted of 2% activator, 10% (Cr-15 wt.% Al) binary masteralloy (99.5%, -100 mesh), balance inert Al_2O_3 (99.5%, 100-200 mesh) filler powder (all pack compositions are given in wt.%). Two activators, NH_4Cl (99.999%, -10 mesh) and NaCl (99.995%, -30 mesh), were used in this study. Hf-doped γ+γ' coatings were fabricated by adding 2 wt.% of HfO_2 (99.95%, -325 mesh) to the pack powder mixture, replacing some of the Al_2O_3. As shown in Fig. 1, the substrate was surrounded by porous Al_2O_3 foam (85% open porosity) to avoid direct contact with the powders and thus eliminate embedment of powder particles in the coating [15]. The Al_2O_3 foam was cut into 1 and 2 mm thick discs; a small ring section was cut and placed around the specimen.

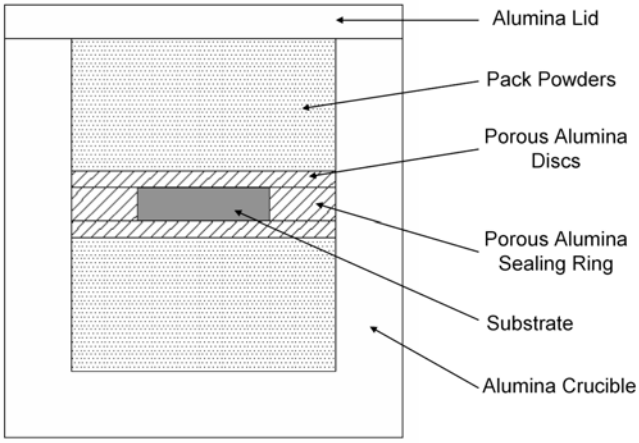

Fig. 1. Schematic of pack cementation arrangements with porous alumina discs.

Cyclic oxidation tests with cycles of 1 h at temperature and 10 min out of the furnace were performed on the coated specimens at 1100°C in dry O_2. The phase constitution of the coatings was determined by X-ray diffraction (XRD). Specimens were characterized using a scanning electron microscope (SEM) equipped with energy dispersive spectroscopy (EDS). Composition profiles through the coatings were measured by electron probe microanalysis (EPMA) using pure metal standards.

RESULTS AND DISCUSSION

For the specimens that were aluminized in a pack of $2NH_4Cl$-10(Cr-15Al)-$88Al_2O_3$ with 1 mm thick discs, the Al concentration at the coating surface was ~46 at%, as measured by EDS. Clearly, β phase

rather than γ+γ' was formed on the coating surface. When 2 mm discs were used, the increased distance between the specimen and pack powder resulted in a slight decrease in the surface Al level, to ~40 at.%.

A dramatic decrease in the surface Al content was observed when NaCl was used as the activator instead of NH_4Cl, while maintaining the 2 mm disc setup. The coating formed in a pack of 2NaCl-10(Cr-15Al)-88Al_2O_3 showed ~24 at. % Al at the surface measured by EDS, which was confirmed to be ~27 at.% by EPMA. This result clearly demonstrated the effect of activator on the Al deposition. As pointed out in the literature [16], the stability of NH_4X-activated (X=Cl, Br, or I) packs is considerably lower than that of NaX-activated packs. As a result, higher deposition rates can be expected with NH_4Cl during the early stages of the coating cycle. To illustrate the difference in partial pressures of aluminum chlorides between packs of 2NH_4Cl-10(Cr-15Al)-88Al_2O_3 and 2NaCl-10(Cr-15Al)-88Al_2O_3, thermodynamic calculations were conducted in the temperature range of 800-1050ºC using commercial software HSC 5.0 [17]. Figure 2 shows the plots of the partial pressures of AlCl and $AlCl_2$, which are considered to be responsible for Al deposition [18]. The P_{AlCl} and P_{AlCl2} generated in the NH_4Cl-activated pack at 800ºC were even higher than that from the NaCl pack at 1050ºC. For the present aluminizing process, the heating and cooling time between 800 and 1050ºC was ~35 min. When NH_4Cl activator was used, Al deposition occurred not only during the 30 min holding at 1050°C, but also during part of the heating and cooling process [11]. The thermodynamic results also provide an explanation for the formation of the thin layer of b phase on the coating surface in the previous study [11] when the aluminizing was carried out in a pack of 2NH_4Cl-10(Cr-15Al)-88Al_2O_3 without any holding time at 1050°C.

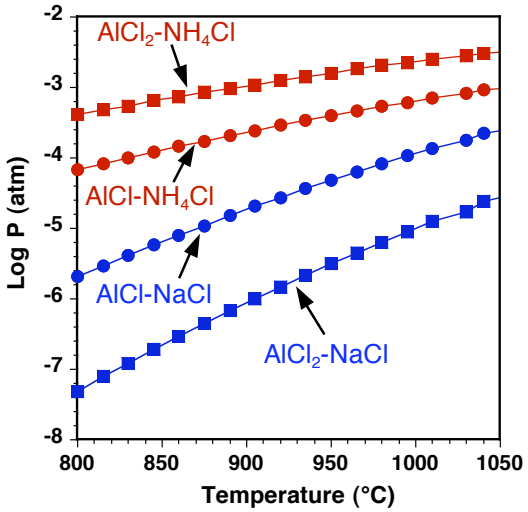

Fig. 2. Partial pressures of main aluminum halide species in packs of 2NH_4Cl-10(Cr-15Al)-88Al_2O_3 and 2NaCl-10(Cr-15Al)-88Al_2O_3 at 800-1050 C.

Figure 3 shows the XRD patterns of the "simple" and "enriched" γ+γ' coatings. Even though the two samples exhibited very similar diffraction patterns, according to the Ni-Al-Pt phase diagram [8], 27 at.% Al at the coating surface implied that the surface layer of the "enriched" coating was γ'. This was further confirmed by the backscattered-electron image of the coating cross section, Fig. 4a, where a continuous layer of light-contrast γ' phase was present near the coating surface. In addition, voids were found near the interface between the coating and substrate, as shown in Fig. 4a. The cause of the void formation is still unclear. Although Kirkendall voids could form if the diffusion fluxes of Al, Ni and Pt across the interface were not balanced, no such voids were shown on the cross-section of a diffusion couple of Ni-22Al-30Pt (at.%) and CMSX-4 superalloy [19]. Hydrogen evolution during the Pt electroplating process could not be completely excluded [20], as more voids had been noticed in the resulting coatings if the original Pt layer was deposited at a higher plating rate using an increased current density.

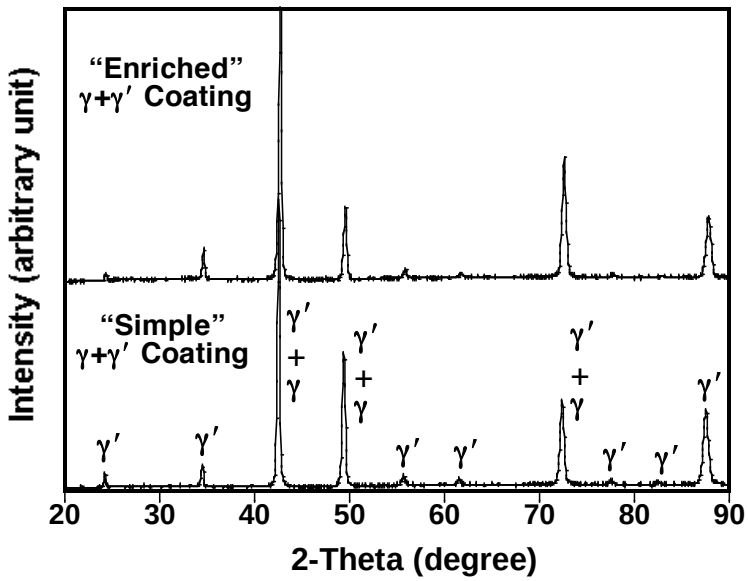

Fig. 3. Comparison of XRD patterns of the "enriched" and "simple" γ+γ' coatings.

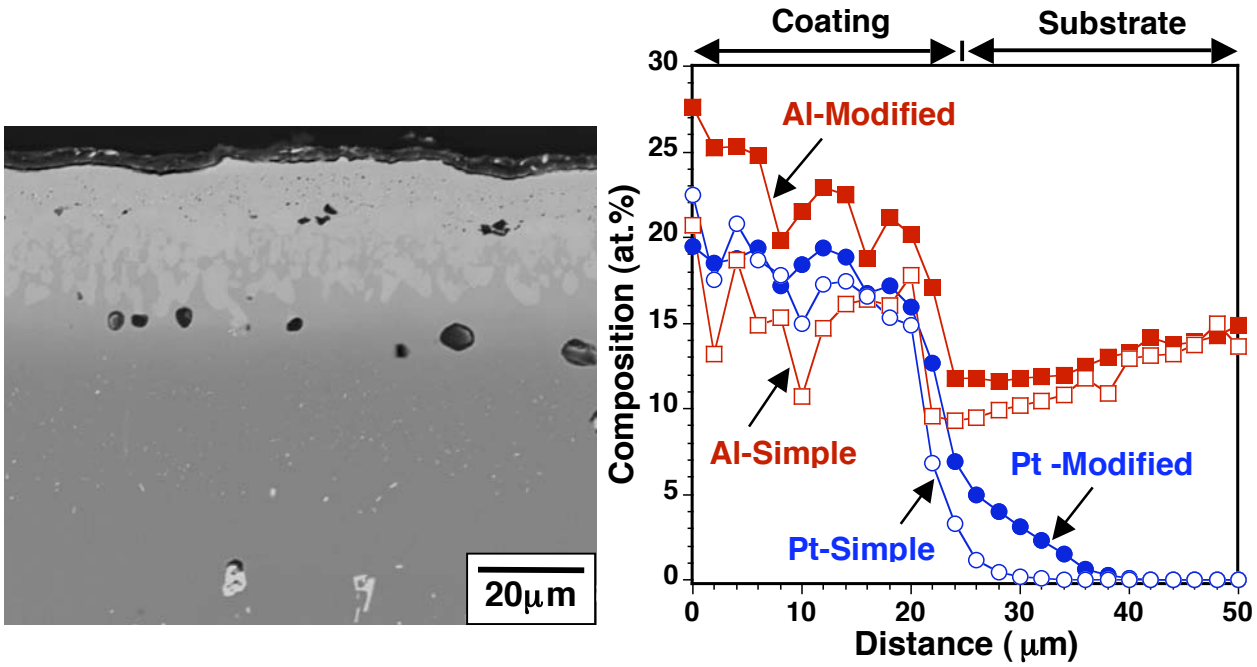

(a) (b)

Fig. 4. (a) Back-scattered electron image of cross section of the "enriched" γ+γ' coating on a René 142 alloy, and (b) EPMA composition profiles of the Al and Pt in "simple" and "enriched" γ+γ' coatings.

A comparison of the EPMA composition profiles for Al and Pt in the "enriched" and "simple" γ+γ' coatings is presented in Fig. 4b. The overall coating thickness of both coatings was ~26 μm. While no significant change in the Pt content was found, the average Al content in the "enriched" γ+γ' coating was increased from 16.3 to 22.7 at.%. The average concentrations of alloying elements in both coatings are given in Table 1. The Cr and Co contents were lower in the "enriched" coating. A slight increase in Ta, from 1.6 to 2.2 at.% (3.9 to 5.0 wt.%), was noticed in the "enriched" coating, whereas Re and W

decreased from 0.8 to 0.5 at.% (2.2 to 1.1 wt.%) and 1.4 to 0.9 at.% (3.5 to 2.1 wt.%), respectively. The Mo level was too low for a meaningful comparison. The changes in the amounts of the alloying elements in the "enriched" γ+γ' coating, compared to the "simple" γ+γ' coating, could be attributed to the relative amount of the γ and γ' phases in the two coatings, as well as the partitioning behavior of these alloying elements between the two phases. Elements such as Cr, Co, and Re tend to concentrate in the g phase, while Ta preferentially partitions to the γ' phase [21]. W and Mo can act as γ or γ' formers, depending upon their concentration. With the increased Al content in the "enriched" coating, γ' became the primary phase, leading to the lower average concentrations of Cr, Co, W, Mo, and Re and higher Ta in the coating.

Table I. Comparison of average concentrations of alloying elements in "simple" and "enriched" γ+γ' coatings (in at.%).

Element	"Simple" γ+γ' Coating	"Enriched" γ+γ' Coating
Al	16.3	22.7
Pt	18.1	18.2
Cr	6.8	3.1
Co	8.6	6.8
Ta	1.6	2.2
Re	0.8	0.5
W	1.4	0.9
Mo	—	—

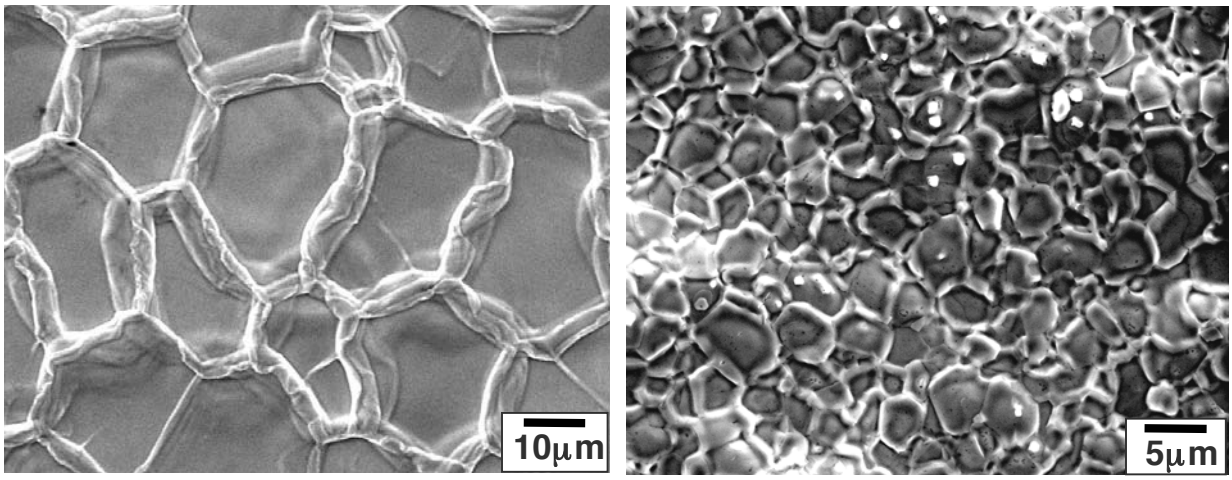

(a) (b)

Fig. 5. SEM secondary-electron images of surface morphologies of (a) "enriched" γ+γ' coating and (b) "enriched" γ+γ' coating.

It is noteworthy that the surface morphology of the "enriched" γ+γ' coating (more accurately, the grain size of the γ' surface layer) differed from the standard single-phase β-(Ni,Pt)Al coating. For a typical

(Ni,Pt)Al coating synthesized by chemical vapor deposition (CVD) (6h at 1100ºC) [22], the coating consisted of large aluminide grains of ~50-100 μm, Fig. 5a. The "enriched" γ+γ' coating, however, exhibited much smaller grains in the range of ~3 to 5 μm, Fig. 5b. Note that the starting "simple" γ+γ' coating had even smaller grains, < 3 μm, and the 30-min pack aluminizing led to the grain growth. A lateral growth of the β-NiAl coating grains has been reported during short-term CVD aluminizing experiments [23], where relatively rapid growth was observed during the early stages of aluminizing (for up to 45 minutes), and it then slowed down considerably. However, the mechanism for the coating grain growth observed for the "enriched" γ+γ' coating appeared different from the β coating. For the present "enriched" coating, the Al flux at the coating surface facilitated the γ' grain to grow at the expense of the γ grains via grain boundary movement. Another observation worth mentioning is that the secondary aluminizing process for obtaining the γ+γ' coating with a final Al content of ~22-26 at.% only introduced a very small amount of Al, with a weight gain of ~0.2 mg/cm^2. Higher weight gains were an indication of the formation of the β phase in the coating, which again suggests that to maintain the γ+γ' phase constitution in the coating the Al activity needs to remain at a very low level.

Table II summarizes the correlation between the specific weight gain of the specimens during aluminization, coating phase constitution, surface Al, and coating thickness for different pack aluminizing conditions. It is worth mentioning that the secondary aluminizing process for obtaining the γ+γ' coating with ~22-26 at.% Al only introduced a very small amount of Al, with a weight gain of ~0.2 mg/cm^2. If the weight gain was ≥ 0.7 mg/cm^2, it was difficult to prevent the formation of the β phase in the coating. Samples with weight gains above 5 mg/cm^2 were found to consist of single β phase. The specific weight gain can therefore be used as one quick examination to find out whether a γ+γ' 2-phase coating is obtained.

Table II. Correlation of specific weight gain, phase constitution, surface Al concentration, and coating thickness for different pack aluminizing conditions.

Pack Condition (Temperature: 1050°C)	Specific Weight Gain (mg/cm^2)	Phase Constitution	Surface Al (at.%)	Coating Thickness (μm)
30 min, 2NaCl-10(Cr-15Al)-88Al_2O_3, 2.0 mm Al_2O_3 discs	0.2	γ+γ'	26	30
0 min, 2NH_4Cl-10(Cr-15Al)-88Al_2O_3, no discs [11]	0.7	β / γ+γ'	50	4 / 25
120 min, 2NH_4Cl-25(Cr-15Al)-73Al_2O_3, no discs	5.0	β	N/A	40

Incorporation of Hf in the "enriched" γ+γ' coatings was carried out in a pack of 2NaCl-10(Cr-15Al)-2HfO_2-86Al_2O_3 using the same arrangement shown in Fig. 1. The surface grain structure of the Hf-doped coating was nearly identical as the coating without Hf. XRD analysis also indicated the same γ+γ' phase constitution, with no Hf-rich phases detected. More in-depth characterization using special techniques such as glow discharge mass spectroscopy is needed to determine the Hf level in the coating.

Two N5 samples coated with "enriched" γ+γ' coatings with and without Hf incorporation are currently undergoing cyclic oxidation testing, together with a "simple" γ+γ' coating specimen. A CVD β-(Ni,Pt)Al coating on N5 also was included for comparison. Figure 6 shows the mass change data of the four coating specimens after 400, 1h cycles at 1100°C. As observed previously [11], the β coating showed the lowest mass gain. The "simple" and "enriched" γ+γ' coatings displayed similar mass gains after 400

cycles, where the "enriched" coating without Hf somehow registered slightly lower mass gain. The oxide scale remained adherent on three γ+γ' coating specimens, except some localized spallation on the "simple" γ+γ' coating, Fig. 7. The "enriched" γ+γ' coating with Hf showed a slightly more uniform scale. As shown in Figs. 7c and 7d, the oxide scale has some degree of ridge-like structure on the "enriched" γ+γ' coatings, though not as evident as for typical β-NiAl [24,25]. The oxidation test will continue and longer exposures are expected to differentiate the oxidation performance of these coatings.

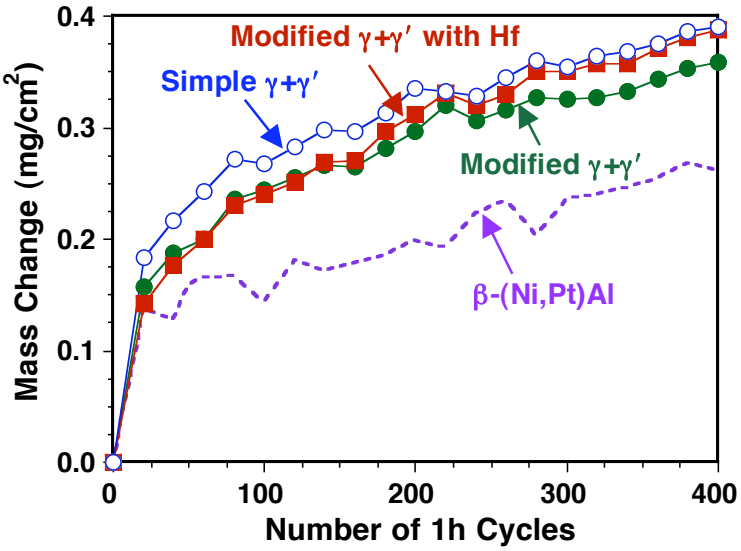

Fig. 6. Specific specimen mass change plots for the "simple" γ+γ' coating, "enriched γ+γ' coating with and without Hf incorporation, and β-(Ni,Pt)Al coating during 1h cyclic oxidation testing at 1100°C.

SUMMARY

"Simple" γ+γ' coatings with 16-19 at.% Al were synthesized by electroplating ~7μm of Pt on superalloy substrates, followed by a diffusion treatment at 1175°C. Experiments were conducted to increase the Al content to ~22 at.% Al in the γ+γ' coating by a secondary pack aluminizing process. During initial efforts, a high rate of Al deposition resulted in the formation of β phase at the coating surface. Modifications to the pack cementation process included the variation in the specimen-pack arrangement and, more importantly, the change of activator from NH_4Cl to more stable NaCl. These changes led to the formation of "enriched" γ+γ' coatings with an Al content of 27 at.% at the coating surface and an average of 22 at.% Al in the coating. Some concentration differences in alloying elements such as Cr, Co, Ta, Re, and W were observed in the "enriched" coating as compared to the "simple" γ+γ' coating, as a result of the different partitioning behaviors of these elements between the γ and γ' phases. Initial oxidation testing at 1100°C showed a more adherent oxide scale on the "modified" γ+γ' coatings.

ACKNOWLEDGMENTS

The authors would like to acknowledge K.M. Cooley, G.W. Garner, and L.R. Walker at Oak Ridge National Laboratory (ORNL) and L.R. Liu at Tennessee Technological University (TTU) for assisting with the experimental work, and I.G. Wright and P.F. Tortorelli at ORNL for reviewing the manuscript. The research is sponsored by the U.S. Department of Energy, Fossil Energy Advanced Materials Research Program, under contract DE-AC05-00OR22725 with UT-Battelle LLC and subcontract 4000032193 with TTU and the SHaRE User Facility by the Division of Materials Sciences and

Technology. Also, this material is based upon work supported by the National Science Foundation-GOALI Program under Grant No. 0504566.

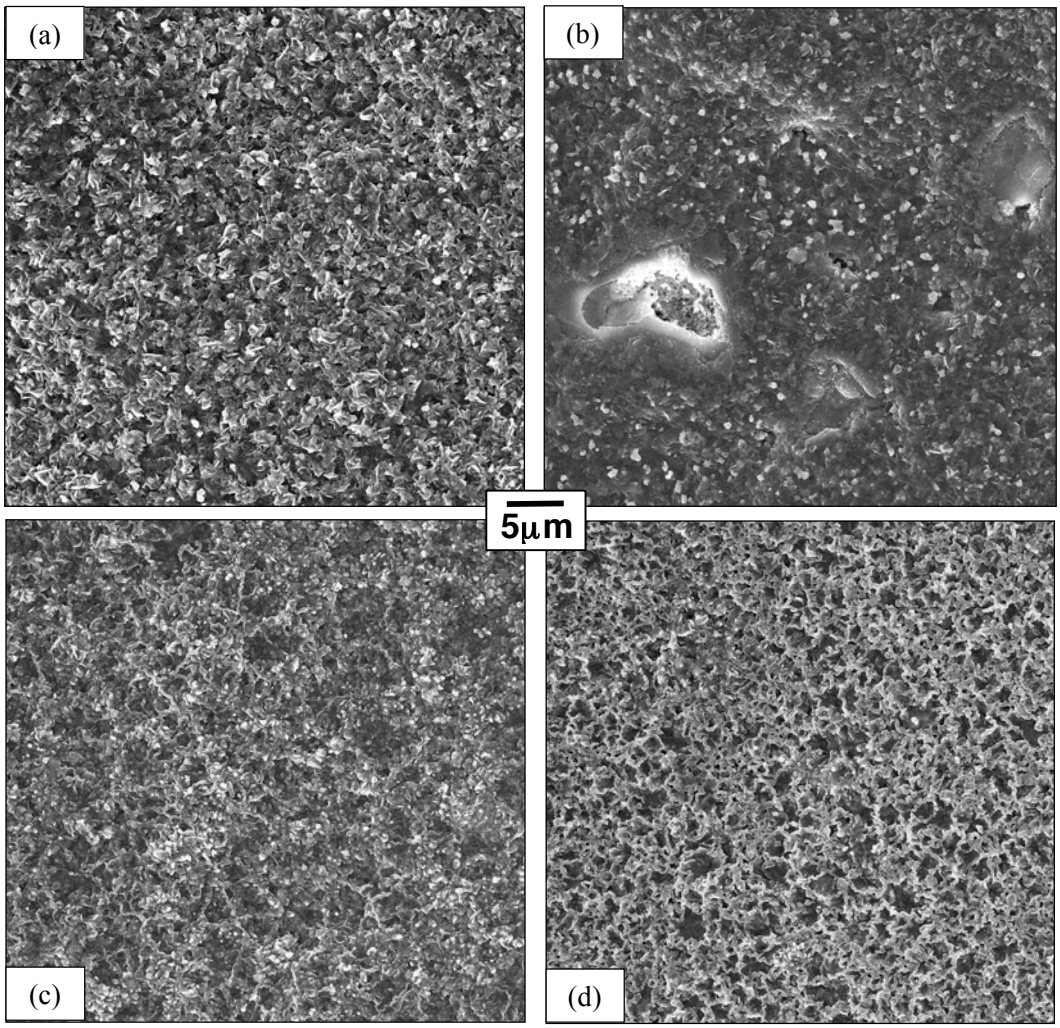

Fig. 7. Secondary-electron images of the surfaces of coated low-S René N5 alloys after 400 1h cycles at 1100 C: (a) and (b) "simple" γ+γ' coating, (c) "enriched" γ+γ' coating, and (d) Hf-doped "enriched" γ+γ' coating.

REFERENCES

1. G.W. Goward, Surf. Coat. Technol. 108-108 (1998) 73.
2. B.M. Warnes, D.C. Punola, Surf. Coat. Technol. 94-95 (1997) 1.
3. Y. Zhang, J.A. Haynes, B.A. Pint, I.G. Wright, W.Y. Lee, Surf. Coat. Technol. 163-164 (2003) 19.
4. M.W. Chen, R.T. Ott, T.C. Hufnagel, P.K. Wright, K.J. Hemker, Surf. Coat. Technol. 163-164 (2003) 25.
5. V.K. Tolpygo, D.R. Clarke, Acta Mater. 48 (2000) 3283.

6. D.R. Mumm, A.G. Evans, L.T. Spitsberg, Acta Mater. 49 (2001) 2329.
7. B.A. Pint, S.A. Speakman, C.J. Rawn, Y. Zhang, JOM (Jan 2006) 47.
8. T. Izumi and B. Gleeson, Mater. Sci. Forum 522-523 (2006) 221.
9. V. Deodeshmukh, N. Mu, B. Li, B. Gleeson, Surf. Coat. Technol. 201 (2006) 3836.
10. Y. Zhang, B.A. Pint, J.A. Haynes, I.G. Wright, Surf. Coat. Technol. 200 (2005) 1259.
11. Y. Zhang, D.A. Ballard, J.P. Stacy, B.A. Pint, J.A. Hyanes, Surf. Coat. Technol. 201 (2006) 3857.
12. B.A. Nagaraj, W.B. Connor, R.W. Jendrix, D.J. Wortman, L.W. Plemmons, US Patent No. 5,427,866, 1995.
13. D.S. Rickerby, S.R. Bell, R.G. Wing, US Patent No. 5,667,663, 1997.
14. O.A. Adesanya, K. Bouhanek, F.H. Stott, P. Skeldon, D.G. Lees, G.C. Wood, Mater. Sci. Forum 369-372 (2001) 639.
15. R. Bianco, R.A. Rapp, J. Electrochem. Soc. 140 (1993) 1181.
16. S.R. Levine, R.M. Caves, J. Elctrochem. Soc. 121 (1974) 105.
17. HSC Chemistry 5.0 for Windows- Chemical Reaction and Equilibrium Software with Extensive Thermochemical Database, Outokumpu Research Oy, Pori, Finland.
18. Z.D. Xiang, J.S. Burnell-Gray, and P.K. Datta, J. Mater. Sci. 36 (2001) 5673.
19. S. Hayashi, W. Wang, D.J. Sordelet, and B. Gleeson, Metall. Trans., 36A (2005) 1769.
20. R.C. Sanwald, Metallography, 4 (1971) 503.
21. C.C. Jia, K. Ishida, T. Nishizawa, Metall. Mater. Trans., 25A (1994) 473.
22. Y. Zhang, W.Y. Lee, J.A. Haynes, I.G. Wright, B.A. Pint, K.M. Cooley, and P.K. Liaw, Metall. Mater. Trans., 30A (1999) 2679.
23. G.Y. Kim, W.Y. Lee, J.A. Haynes, and T.R. Watkins, Metall. Trans., 32A (2001) 615.
24. J. Doychak, J.L. Smialek, T.E. Mitchell, Metall. Trans., 20A (1989) 499.
25. B.A. Pint, M. Treska, L.W. Hobbs, Oxid. Met., 47 (1997) 1.

PROTECTION SYSTEMS: CORROSION RESISTANT COATINGS

Beth L. Armstrong
Oak Ridge National Laboratory
1 Bethel Valley Road, P.O. Box 2008, Oak Ridge, TN 37831-6063
Email: armstrongbl@ornl.gov; Telephone: (865) 241-5862; Fax: (865) 574-6918

Kevin M. Cooley
Oak Ridge National Laboratory
1 Bethel Valley Road, P.O. Box 2008, Oak Ridge, TN 37831-6063
Email: cooleykm@ornl.gov; Telephone: (865) 574-4559; Fax: (865) 574-6918

ABSTRACT

Material loss caused by exposure to the severe operating environments in gasifiers (slagging and non-slagging), industrial waste incinerators, and other advanced fossil or biomass-fueled power systems results in reduced service life and reliability, as well as increased operating costs. This project aims to improve performance of materials by combining intelligent design with colloid science and coating technology to develop cost-effective materials and processes for optimum performance and maximum service life in their specific fossil environment. Lower cost methods and novel approaches of applying coatings to metals are being explored to meet more near-term goals. Thus, the development of novel coatings utilizing low-cost aqueous processing methods such as dip coating is being pursued. Colloidal processing of metallic particles in aqueous suspension offers an economic route for forming uniform, metallic coatings on complex-shaped components via a simple process. The issues of adhesion, uniformity and processing parameters on resulting material phases, the effective corrosion resistance in specified fossil environments, and the mechanical properties at use temperatures will be the technical challenges that must be addressed in order to prove feasibility for metallic-based systems. A review of the ORNL dip coating process for application of coatings onto ferritic martensitic alloys will be discussed.

INTRODUCTION

Advanced fossil energy processes have hostile environments with temperatures as high as 1550°C and atmospheres that contain water vapor, sulfur, nitrogen, trace heavy metals, molten slag and alkali salts. Ceramic and metallic material systems can potentially play important roles in the harsh fossil environments. The metal systems of interest are ferritic martensitic steels to address corrosion issues in superheaters, boilers, heat exchangers, turbines, and Ni-based super alloys to address corrosion issues in ultrasupercritical systems.

Coatings for both ceramic and metallic systems have been long utilized for protection purposes in many industries. Some applications include paint (architectural, automotive, marine), environmental barriers for micro turbines and other distributed energy systems, and thermal barriers for fossil and distributed energy systems. There are many techniques available to fabricate layers (coatings) of varying thicknesses. Some of these include plasma vapor deposition (PVD), electron beam – plasma vapor deposition (EB-PVD), chemical vapor deposition (CVD), pack cementation, and slurry or dip coating (1-7). With the exception of pack cementation and slurry coating, these processes are typically costly, line of sight techniques which do not lend themselves to coating large, three dimensional parts (i.e. nonconformal surfaces). Pack cementation is very effective for non-complex stoichiometric coating material systems while slurry coating can handle a wider variety of material systems.

In metallic systems, one advantage of a coating is that the substrate alloy can be optimized for properties other than corrosion resistance (i.e. ductility, formability, creep strength, etc) (8-9). The technical challenge is that the physical, chemical, and mechanical differences between the substrate and the coating can lead to detrimental interactions, which can limit lifetime. Interdiffusion between coating and substrate can result in the formation of brittle intermetallic phases or the loss of protective scale-forming elements. For example, in thermal barrier coatings

(TBC)/superalloy systems, a major problem is the loss of Al from the bond coat to the substrate superalloy over time at temperature, which ultimately contributes to an inability to maintain Al_2O_3 growth and subsequent coating failure (6, 10). Thus, the design of the protective coatings in consideration of the substrate has received increased attention in recent years. For example, recent work by Gleeson et al has identified Ni-Al-Pt bond coat compositions for which Al diffuses from the substrate superalloy into the coating, helping to maintain a reservoir of Al for Al_2O_3 formation by the coating, rather than loss of Al from the coating alloy to the substrate. Typically, these Al coatings are applied after annealing of the metal and require further post heat treatment processing to convert the Al to Al_2O_3. This step can degrade physical properties of the metal while adding additional processing time and expense to the process. A slurry coating process may allow changes to current processing steps by either limiting the processing temperatures that the coating/metal interface sees (slurry coating is a room temperature process) and/or by reducing steps (i.e., combining the coating and metal annealing process into one). If a less expensive, non-line of sight process can be utilized to deposit a metallic coating or a film that will react to form the appropriate metal or ceramic phase directly, control of the metal's physical properties can be maintained or optimized while minimizing processing time and/or expense. This has been demonstrated recently by Agüero who has used aluminide slurries to coat ferritic martensitic steels (7).

Colloidal processing offers a low cost alternative approach for producing uniform coatings on complex-shaped components via a simple dip coating process (i.e., the ORNL slurry coating process) (4-5). Control of the rheological behavior of the suspension by tailoring interparticle (or surface) forces is paramount to achieve a high quality defect free coating. In aqueous-based suspensions long-range attractive van der Waals forces must be balanced by repulsive forces to tailor the desired degree of suspension stability. Typically, ionizable polymeric dispersants, or polyelectrolytes, are used to modify the surface of particles to impart repulsive electrosteric forces (11-12).

This year the work on the development of concentrated aqueous suspensions comprised of aluminum particles was evaluated. This effort focused on applying Al coatings to ferritic, martensitic alloys (Fe-9Cr-1Mo, T91) using a dip or slurry coating process. The coatings were heat treated at varying temperatures to determine the robustness of the processing conditions (which will enable alternative coating windows in the alloying process).

EXPERIMENTAL PROCEDURE

Aluminum, (H10, Valimet Inc., Stockton, CA) was used as the metal powder in this study. The aluminum powder had an average particle size of ~ 13.19 μm and surface area of 0.4475 m^2/g, determined using dynamic light scattering (Horiba, Inc., Kyoto, Japan) and B.E.T. (Autosorb-1, Quantachrome Instruments, Boynton Beach, FL), respectively. Polyacrylic acid (PAA, 450kg/mol, Aldrich Chemicals, Milwaukee, WI), an anionic polyelectrolyte, was used as the dispersant and PL001 (Polymer Innovations, Inc., Vista, CA) as the rheological modifier for the Al system. Water purity was measured using inductively coupled plasma mass spectroscopy (ICPMS, X Series 2, Thermo Fisher Scientific, Inc., Waltham, MA). The standards (QCS26, High Purity Standards, Charleston, SC) and the nitric acid matrix (Ultrex Pure., J.T. Baker, Phillipsburg, NJ) were used to calibrate the ICPMS. Contact angle was measured using the Sessile drop technique. A droplet of Al slurry was dropped onto the surface of commercial ferritic (Fe-9Cr-1Mo, T91) substrates, and the wetting angle was calculated using Rhino (McNeel North America, Seattle, WA).

Zeta potential measurements were carried out on the Al particles in dilute aqueous suspension using capillary electrophoresis (Zetasizer 3000HS, Malvern Instruments Ltd., Worcestershire, UK). Dilute suspensions (10^{-3} vol% solids) were prepared by adding the appropriate amount of powder to aqueous, KNO_3 solutions (0.001 *M*) of varying pH ranging from 2 to 11. The solutions were adjusted to the appropriate pH using nitric acid or ammonium hydroxide.

Rheological measurements were carried out on concentrated aluminum suspensions using a controlled-stress rheometer (Rheometric Scientific SR5, TA Instruments, New Castle, DE) fitted with a concentric cylinder. Concentrated aluminum suspensions (5 vol% solids) were formulated by mixing an appropriate amount of aluminum powder into aqueous solutions (pH 7) of varying PAA concentration. A solvent trap was used to minimize the evaporation of water. In this way, variations in sample handling were minimized to ensure

reproducibility of the data. Stress viscometry measurements were carried out by logarithmically ramping an applied shear stress from 0.025 to 200 Pa. A delay time of 60 s between consecutive data acquisition events was used in this study.

Commercial T91 (Fe-9.3at.%Cr-0.56Mo-0.46Mn-0.26V-0.55Si-0.15Ni-0.46C-0.22N-0.005S) was machined into test specimens. T91 substrates that were 11.9 mm x 19.1 mm x 1.7 mm in size were dipped into the aluminum suspensions of varying Al concentration at a fixed PAA concentration (1.15 mg/m^2). All of the coated substrates were dried under ambient conditions and sintered at varying temperatures in an argon atmosphere. Sintered samples were examined by scanning electron microscopy (SEM) and by electron probe microanalysis (EPMA) using wavelength dispersive x-ray analysis.

RESULTS AND DISCUSSION

ZETA POTENTIAL

Zeta potential measurements were carried out on dilute aluminum and alumina suspensions (10^{-3} vol% solids in deionized water) of varying pH and the results are shown in Fig. 1. The isoelectric point (IEP) of aluminum was initially observed at pH 3. However, the aluminum particle surface underwent charge reversal after pH 5, and a sharp increase in zeta potential to 10.9 mV occurred. This phenomenon may indicate the formation of a passive hydroxide layer on the surface of the aluminum particles. This theory is reinforced by comparing the zeta potential curve of an aluminum oxide (Al_2O_3) powder (AKP 30, Sumitomo, Japan). The zeta potential of the Al_2O_3 closely matches the behavior seen in the Al powder at higher pH's. The net positive surface potential at pH 9 of the Al powder indicates that an anionic polyelectrolyte (e.g., the PAA dispersant) that is fully (negatively) charged at these pH conditions will strongly adsorb to the surface of the particles. The adsorbed PAA, in turn, should promote dispersion of the particles. Based on our findings, all of the rheological studies were completed with PAA as the dispersant.

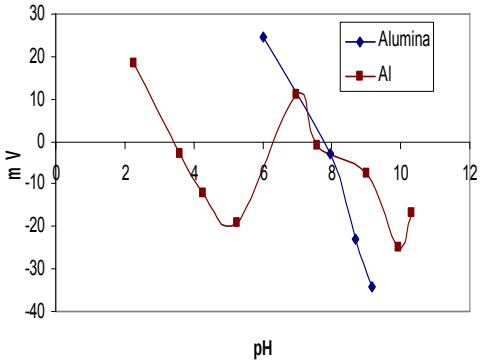

Fig. 1. Zeta potential as a function of pH for dilute aluminum and alumina suspensions (10^{-3} vol% solids).

RHEOLOGICAL BEHAVIOR

Previously work demonstrated that ceramic gels with slightly shear-thinning flow behavior were identified as the optimum rheological conditions for coating dense, ceramic substrates with the ceramic suspensions (4-5). The same behavior was maintained in the Al slurries in this study to achieve the desired uniform coating surfaces remained constant. Previous work also demonstrated that the effect of small amounts of contamination from the organic processing aids and the water purity affected the slurry flow behavior and ultimately the gel structure and resulting coating microstructure. In the silicate-based oxide material systems evaluated previously, a gel structure would form in the resulting coating in the presence of minor amounts of contaminates, such as barium, strontium lanthanum, copper, zinc and lead. Thus, water purity was tested in order to eliminate this as a variable. Finally, the effect of contamination from two separate water sources was evaluated in this study.

Water for all slurries was obtained from two sources; a deionized water purifier (E-Pure, Barnstead) and a steam operated distiller system (Barnstead). It was assumed that the distilled water would contain less contamination than the deionized water (DI). As seen in Table 1, the level of contamination in the distilled water (Dist) source was actually higher. The amount of contamination although low (in the parts per billion) may be enough to cause gelation, wetting or viscosity in slurries with materials sensitive to hydrolysis and gelation, such as doped silicates or alumina. Since the aluminum powder being used in this study appears to have an alumina or aluminum hydroxide surface as seen from the zeta potential curves discussed previously, the water source of the slurry will remain an issue until further analysis can be completed.

Table 1. ICPMS Analysis of Deionized and Distilled Water Sources.

Isotope	Deionized Water (ppb)	Distilled Water (ppb)
Na	2	4
Al	< 2	48
K	2.8	4
Mn	< 2	53.2
Fe	< 2	.91
Ni	< 2	130
Cu	< 2	85.7
Zn	9	550
Sr	20	.09
Ba	1.2	1.2
Pb	.44	545

Rheological measurements were carried out on the Al suspensions of varying solids concentration in both deionized (DI) and distilled (Dist) water as shown by the plot of apparent viscosity as a function of applied shear stress in Fig. 2. The PAA concentration was fixed at 1.15 mg PAA/m^2 Al. As anticipated, apparent viscosity increased with increasing Al concentration and the effect of the purity of the water source was not evident. Newtonian behavior was observed at 1 vol% solids, but slight shear thinning behavior was observed at solids loadings of 3 and 5 vol%, respectively. Due to the low solids concentration at the 1 vol % condition, Newtonian flow is not unexpected.

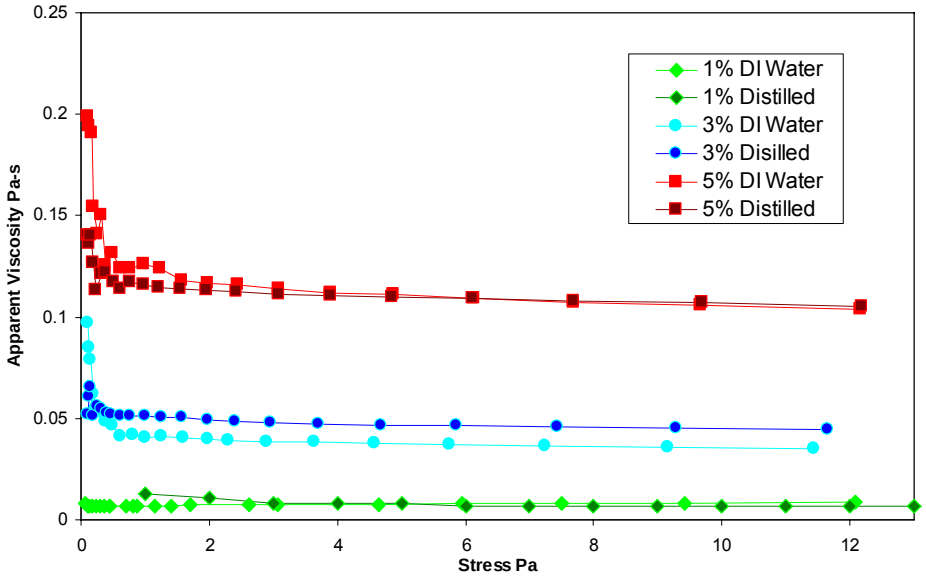

Fig. 2. Apparent viscosity as a function of shear stress for aluminum suspension of varying Al concentration.

COATING FORMATION

The effect of contamination from the deionized and the distilled water sources was not evident in the flow behavior. Consequently, the contact angle was measured using the Sessile drop technique to evaluate the effective wetting of the Al slurries as a function of solids loading and water source on the surface of the ferritic substrates. The effect of the water purity was much more evident in the Sessile drop studies. The distilled water based slurries had higher

contact angles or reduced wetting than the equivalent solids loading slurry made with deionized water as shown in Table 2. If gelation is occurring as a function of the added contamination, reduced wetting behavior would be anticipated. The contact angle also increased with increasing Al solids loading relative to the water source. This is also anticipated due to the relative increase in viscosity from the increased solids. An image of a representative Al slurry droplet on a T91 substrate is shown in Figure 3.

Figure 3. Representative Al slurry droplet on a T91 substrate.

Slurry (%Al)	Contact Angle
1% Š DI H_2O	25.21
1% Š Dist H_2O	41.52
5% Š DI H_2O	33.91
5% Š Dist H_2O	57.39

Table 2. Contact angle as a function of water source and Al solids loading.

For effective coating behavior, the balance of shear thinning behavior to maintain uniform coating thickness as well as low contact angles to improve wetting is critical. To physically determine the balance between rheology and wetting, substrates must be slurry coated, the substrate and the coating sintered, and the resulting coating microstructure (thickness, uniformity, and Al diffusion) characterized as a function of the densification properties (temperature and time). A baseline slurry was selected for all dipping and densification studies based on water purity, wetting and the rheology data. The Al slurry with the highest solids loading demonstrating shear thinning behavior and having the lowest contact angle was selected. Thus, T91 substrates were dipped into Al suspensions made with deionized water (5 vol% solids), and the resulting coating are displayed in Fig. 4. Adequate coating coverage was attained.

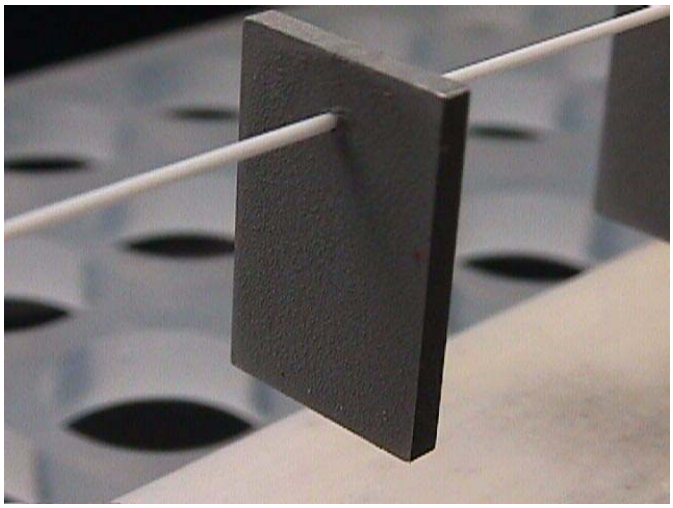

Figure 4. As-dipped Al coated T91 substrate.

SINTERING BEHAVIOR

All densification studies were carried out on T91 substrates dipped into Al suspension made with deionized water at 5 vol% Al solids loading. Sintering temperatures were selected based on typical ferritic steel processing conditions of 750°C and 1050°C. Coated substrates were sintered at these temperatures in Ar for two hours. After sintering at

750°C for 2 hours, a non-uniform layer of Al "islands" or nodules were visible across the surface of the substrates. The thickness of each of Al islands varied, however the average thickness was ~ 30 μm, as shown in Figure 5. Increasing the sintering temperature to 1050 °C yielded a uniform layer of Al-rich T91, with columnar grains (Figure 6) across the substrate with a maximum interdiffusion distance of Al up to 120 μm. It is not certain at this time why the formation of Al islands occurred, how the non-uniform islands diffuse so uniformly across the substrate at an increased temperature, or why the columnar grains form. These early results at 1050°C are encouraging however since the concentration of Al at the surface is ~9 atomic % (Figures 7 and 8). Figure 7 is a scanning electron micrograph of the area mapped using EPMA. Figure 8 shows the Al content as a function of depth into the T91 substrate for the Al coatings sintered at 1050°C. Pint et al. has reported that a minimum concentration of Al (~3.5 at%) is necessary to improve coating lifetimes (13). Further iterations are necessary to increase the concentration of the Al in the substrate and develop an understanding of how processing variables control Al diffusion concentration and depth.

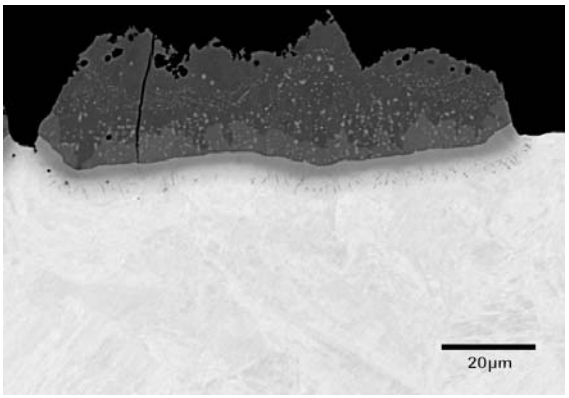

Figure 5. Scanning electron micrograph of Al coating on T91substrate after heat treatment to 750°C for 2 hours in an argon environment.

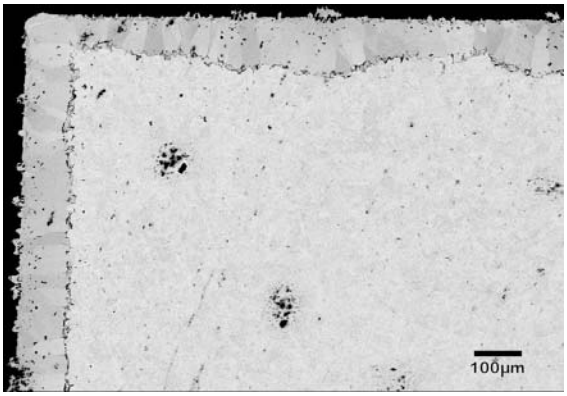

Figure 6. Scanning electron micrograph of Al coating on T91substrate after heat treatment to 1050°C for 2 hours in an argon environment.

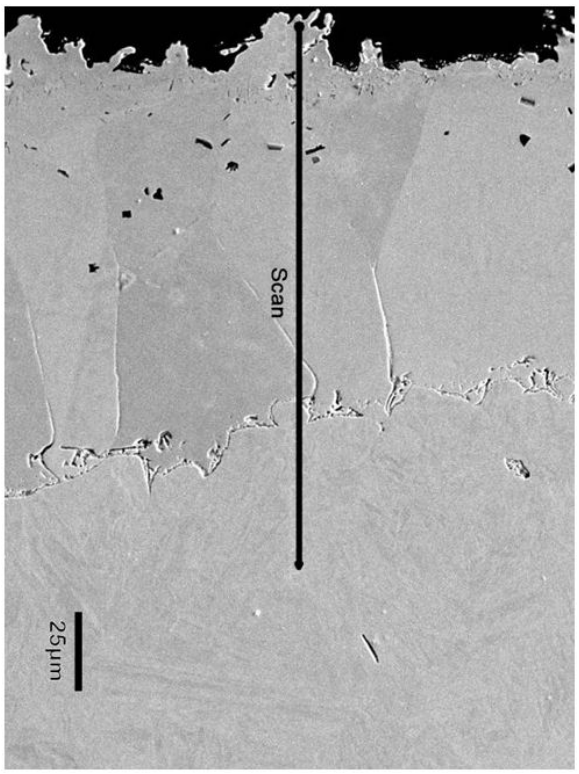

Figure 7. Scanning electron micrograph of EPMA scanned area for coating sintered at 1050°C for 2 hours in Ar.

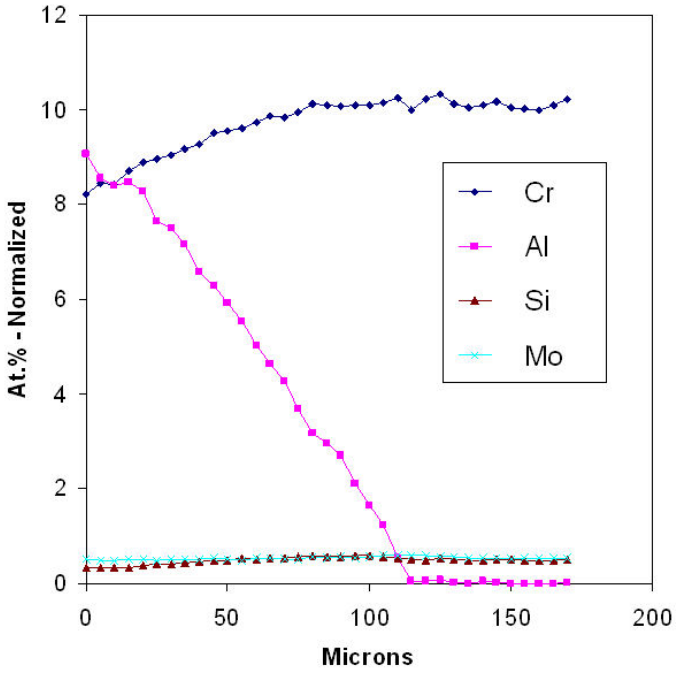

Figure 8. Al content by EPMA as a function of depth for coating sintered at 1050°C for 2 hours in Ar.

CONCLUSIONS

The ORNL slurry coating approach is a low-cost method to deposit protective layers on ferritic, martensitic steels for use in fossil energy applications. The surface of aluminum particles in aqueous suspension was characterized using zeta potential measurements. A polyelectrolyte dispersant was identified to modify the rheological behavior of aluminum suspensions. Wetting behavior of the aluminum slurries was altered by Al solids loadings and contamination from the water source. Sintering conditions were varied to examine their influence on coating quality and Al interdiffusion. Efforts are underway to optimize the properties of the slurry system and characterize the resulting corrosion properties.

ACKNOWLEDGMENTS

The authors would like to thank L. Walker at Oak Ridge National Laboratory for his assistance on the SEM and EPMA. B. Pint provided helpful comments and guidance on this research. B. Pint, E. Payzant, and T. Besmann provided helpful comments on this manuscript. The coating research was sponsored by the U.S. Department of Energy, Office of Fossil Energy Advanced Research Materials Program under Work Breakdown Structure Element ORNL-1(B) under work breakdown element 3FEAA075. The Oak Ridge National Laboratory is operated by UT–Battelle LLC for the U.S. Department of Energy under contract DE-AC05-00OR22725.

REFERENCES

1. Haynes, J.A., Lance, M. , Cooley, K., Ferber, M., Lowden, R., Stinton, D., *J. Am. Ceram. Soc*., **83** [3], 657-659 (2000).
2. Spitsber, I., Mumm, D., Evans, A.G., *Materials Science and Engineering A*, **394**, 176-191 (2005).
3. Strangman, T., *Thin Solid Films*, **127**, 93-105 (1985).
4. Armstrong, B., Kirby, G., Cooley, K., *Proceedings of The 29th International Technical Conference on Coal Utilization & Fuel Systems*, Clearwater, FL (2004).
5. Kirby, G., Cooley, K., and Armstrong, B., *Proceedings of GT2005 ASME Turbo Expo 2005: Power for Land, Sea, and Air*, Reno-Tahoe, NV (2005).
6. Opila, E., *J. Am. Ceram. Soc*., **86** [8], 1238 (2003).
7. Agüero, A., Muelas, R., Pastor, A., Osgerby, S., Surface & Coatings Technology 200, 1219-1224 (2005).
8. M.P. Brady, P.F. Tortorelli, K.L. More, E.A Payzant, B.L. Armstrong, H.T. Lin, M.J. Lance, F. Huang, and M.L Weaver, *Materials and Corrosion,* **56**, 748-755 (2005).
9. Brady M. P., Armstrong B. L., Lin H-T., et al., *Scripta Materialia,* **52** (5): 393-397 (2005).
10. Gleeson, B., Wang, W., Hayashi, S., Sordelet, D., *Materials Science Forum*, **461-464,** 213-222 (2004).
11. Cesarano, J. and Aksay, I., *J. Am. Ceram. Soc.*, **71** (4) 250-55 (1988).
12. Cesarano, J. and Aksay, I., *J. Am. Ceram. Soc.*, **71** (12) 1062-67 (1988).
13. Pint, B., Zhang, Y., Dryepondt, S., Walker, L., and Wright, I., Presentation at the 21st Annual Fossil Energy Materials Conference, Knoxville, TN, (2007).

MICROSTRUCTURE AND PROPERTIES OF HVOF-SPRAYED PROTECTIVE COATINGS

Richard Wright
Idaho National Laboratory
PO Box 1625, MS 2218 Idaho Falls, ID 83415
Richard.Wright@INL.gov, (208) 526-6127

Joel Simpson
Idaho National Laboratory
PO Box 1625, MS 2218 Idaho Falls, ID 83415
Joel.Simpson@INL.gov (209) 526-9797

ABSTRACT

Coatings of iron based aluminides have been deposited on steel substrates using the high velocity oxygen-fuel method (HVOF). The coatings are highly dense, contain relatively low fraction of oxides and have compressive residual stress in the as-deposited condition. While the microstructures are stable during corrosion testing in either oxidizing or simulated combustion gas environments the state of stress in the coating and the bonding to the substrate can change significantly as a result of corrosion or thermal cycling and this potentially leads to coating failure. Mechanical properties of free standing HVOF processed specimens have been characterized and compared to material that remained attached to substrates to separately determine the influence of microstructure evolution and constraint due to residual stress arising from the coating-substrate interaction on the cracking of coatings. A series of thermal cycling tests is being developed and the influence on corrosion resistance and mechanical properties will be determined.

INTRODUCTION

Alloys based on intermetallic compositions are being developed for advanced fossil fired power plants due to their potential to operate at higher temperature and resistance to environmental effects. Properties of these materials have shown considerable improvement after nearly two decades of development, however, they continue to face a number of challenges with respect to ductility and high temperature strength.[1-4] One approach to take advantage of the environmental resistance of these materials while minimizing their limitations is to create coatings on more conventional structural materials.

Coatings can be applied by a variety of methods, including weld-overlay, reaction synthesis, physical vapor deposition and thermal spray processes.[5-14] Thermal spray processing has the advantage of being able to deposit materials with widely varying melting points from power precursors. It is only recently, however, that processes like plasma spraying and high-velocity oxygen fuel (HVOF) thermal spray deposition have begun to move from an Edisonian approach to more science based process design and control. It is becoming increasing common to control the properties of metallic and intermetallic coatings through measurement and control of the properties (size, temperature and velocity) of droplets in-flight from the spray torch during coating deposition. Through systematic control of the particle velocity and temperature it is possible to largely control the state of residual stress in the coating and the density and macrostructure.[15]

The environmental resistance of coatings can be different from bulk materials due to chemical alteration of the powder during coating deposition giving rise to areas of alloy depletion and oxide inclusions,

porosity, and micro-cracking of the coating. In addition to environmental effects, the performance of the coating can also be influenced by residual stress, the nature of the bond between the coating and substrate, and the potential for poor bonding between layers in thick coatings built up through multiple spray passes. Stresses between the coating and substrate can be the result of thermal expansion mismatch between the coating and substrate during the high temperature excursion associated with coating deposition, or as a result of repeated thermal cycling representative of service conditions.[15]

Laboratory testing of coating durability is problematic because of the difficulty with replicating service conditions. In addition, durability is not an intrinsic property of the coating or substrate that can be unambiguously measured. Coating durability can be separated in a general way into components relating to bonding to the substrate and cracking of the coating. The bonding is typically measured in the as-deposited condition or after simulated service conditions using a simple pull test as described in ASTM C 633. The resistance of the interface to cracking can be determined using modified fracture mechanics methods, however, this type of testing has not been widely applied due to difficulty in performing the tests and the fact that results are difficult to apply in design.[16]

Resistance to cracking that might arise due to tensile loading is relatively straightforward to measure by loading coating-substrate couples until cracking is noted. The load at which cracking occurs can be determined using acoustic emission or visual means during testing or by post-mortem metallographic analysis. The fracture properties measured in this type of test are for the coating-substrate couple and not necessarily intrinsic to the coating material itself. Although this type of laboratory testing can be of value for scaling relative coating performance, determining cracking behavior due to service conditions is much more difficult since it can involve creep, cyclic behavior, or environmentally assisted failure mechanisms.

This paper reports on development of performance tests for HVOF sprayed intermetallic coatings. Testing focused on iron aluminide compositions sprayed onto substrates with differing thermal expansion coefficients. Thermal spray parameters were varied to alter the residual stress in the as-deposited coatings and the influences of test geometry and thickness of the coating on the propensity toward cracking were characterized.

EXPERIMENTAL METHODS

As reported previously, Fe_3Al coatings for coating fracture strain testing were prepared on stainless steel substrates using the HVOF process with kerosene and oxygen as the combustion gasses.[17,18] Two different particle velocities, 560 and 620 m/s were used and coating thickness was varied from 50 to 410μm. The microstructure of as-deposited coatings was characterized using metallographic examination of polished and etched cross-sections of the coating.

The room temperature cracking behavior of coatings was measured by tensile testing coated substrates. The substrates were rectangular dog-bone type specimens with coating material applied to the reduced section. Substrate strain to failure was previously reported for 500 μm specimens of Fe_3Al on several different substrate materials. Cracking of the coating was monitored by two acoustic emission sensors attached to the substrate in the grip section at both ends of the specimen. The experimental set-up is shown schematically in Figure 1 and Figure 2.

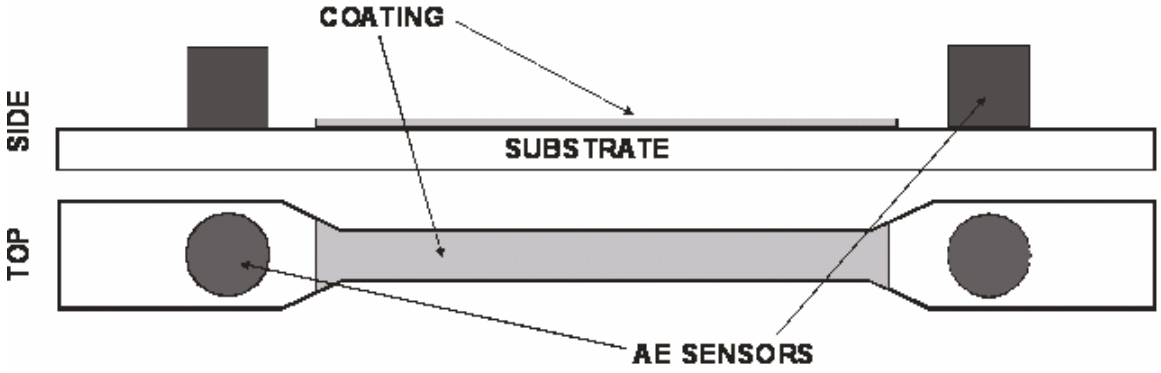

Figure 1. Schematic illustration of the test configuration for determining coating cracking strain.

The acoustic emission sensors were used to indicate a major cracking event in the sample. Visual examination was used during tests and in post-mortem examination. For the thickest coatings cracking was always clearly indicated by high-energy acoustic events. For less-thick coatings visual examination indicated a high density of microcracks or minor spallation of the coating could occur without clear high-energy acoustic events being recorded.

RESULTS AND DISCUSSION

The microstructure of coatings deposited with particle velocities of 570 and 630 m/s are shown in Figure 3a and b, respectively. In both cases the coating is fully dense and appears to be well bonded to the substrate. Some fraction of particles is unmelted in both coatings as indicated by hemispherical features that are flat on the impact side of the particle (i.e., the side of the particle that is oriented toward the substrate). The coatings illustrated in figure 3 were deposited under nominally identical conditions except for the particle velocity, the coating formed using the higher velocity particles was considerably less thick. It has been shown previously that higher velocity particles tend to fragment to a greater degree upon impact with the substrate and a significant volume of the fragmented material rebounds from the substrate and is not incorporated into the coating. This results in reduced deposition efficiency; the ratio of material that is incorporated into the coating compared to the amount that is feed through the torch is reduced with higher particle velocity. Thus, to form coating with equivalent total thickness a larger number of coating passes was necessary with higher velocity particles.

Photographs of the coating surface after tensile loading to a strain resulting in coating failure are shown in Figure 4 for Fe_3Al coatings with three different thicknesses, 50, 130 and 410 μm. The 410 μm thick coatings displayed single large cracks at failure, similar to those reported previously for coatings 500 μm in thickness. Very thin coatings, 50 μm in thickness, exhibited no significant cracking. It can be noted in Figure 4, however, that there are patches along the edge that are much brighter than the surrounding coating material. These bright features are regions where small amounts of coating have spalled from the coating with fracture parallel to the coating-substrate interface.

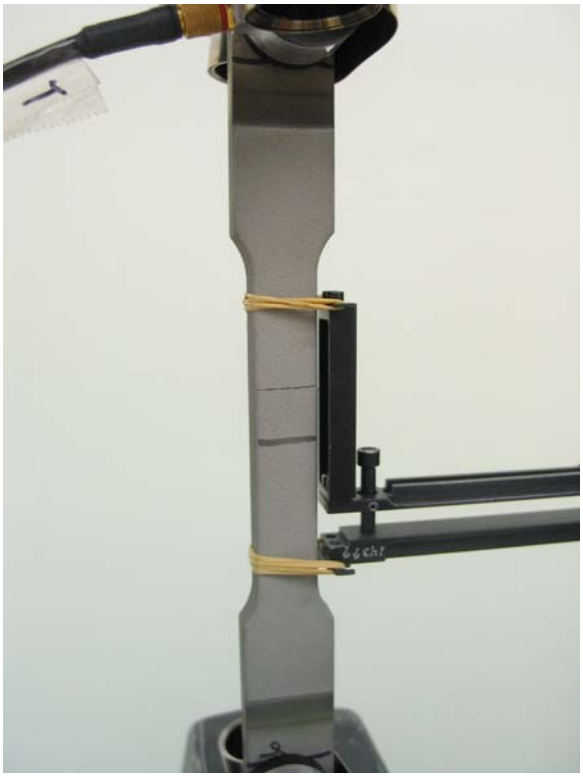

Figure 2. Photograph of a strain to failure test with the acoustic emission apparatus and clip gage attached to measure attached. This 500 μm thick Fe_3Al coating failed with a single major through-thickness crack.

Through-thickness cracking is life limiting since it will allow the corrosive environment access to the coating-substrate interface. For protective coatings that are prone to cracking during thermal cycling as a result of accumulated strain due to thermal expansion mismatch this observation suggests that thin coatings will provide greater service life. For general corrosion, however, it is evident that a thick coating will provide a greater corrosion allowance during service. It is well known that the HVOF coating process results in coatings that have significant compressive residual stress in the as-deposited condition. This compressive stress is a result of peening from high velocity particle impact during deposition. While the compressive deposition stresses might be expected to mitigate service induced stresses from thermal cycling, the Fe_3Al coatings have sufficiently low yield strength at expected service conditions that the initial stress is relieved during the first thermal cycle above about 700°C.

It is evident from Figure 4 that the spallation in thin coatings and microcracking in moderately thick coatings are initiated at the edge of the dog-bone tensile specimens. The influence of edge effects on laboratory measurement of strain to failure is difficult to quantify. It seems likely that strain to failure measured with this type of specimen is reduced compared to expected service conditions on large sections or tubular geometry. A laboratory test is being developed to eliminate the influence of edge effects and to allow rapid thermal cycling. Round bar substrate specimens have been obtained and Fe_3Al coatings will be deposited on the cylindrical reduced gage section for testing. Thermal cycling will be accomplished with induction heating with the specimen clamped in a heat sink so that the thermal cycle can be varied from times a short as a few hundred seconds. This test configuration is shown schematically in Figure 5. Based on the tests to date, visual inspection will be used to determine the strain to failure in these round bar tests as it appears to be the preferred method to identify microcracks.

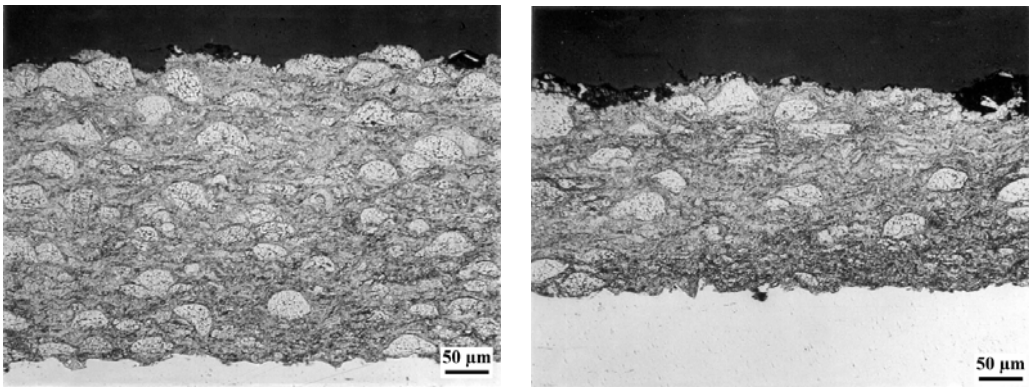

(a) (b)

Figure 3. Microstructure of Fe_3Al coatings produced using HVOF with particle velocity of (a) 570 and (b) 630 m/s.

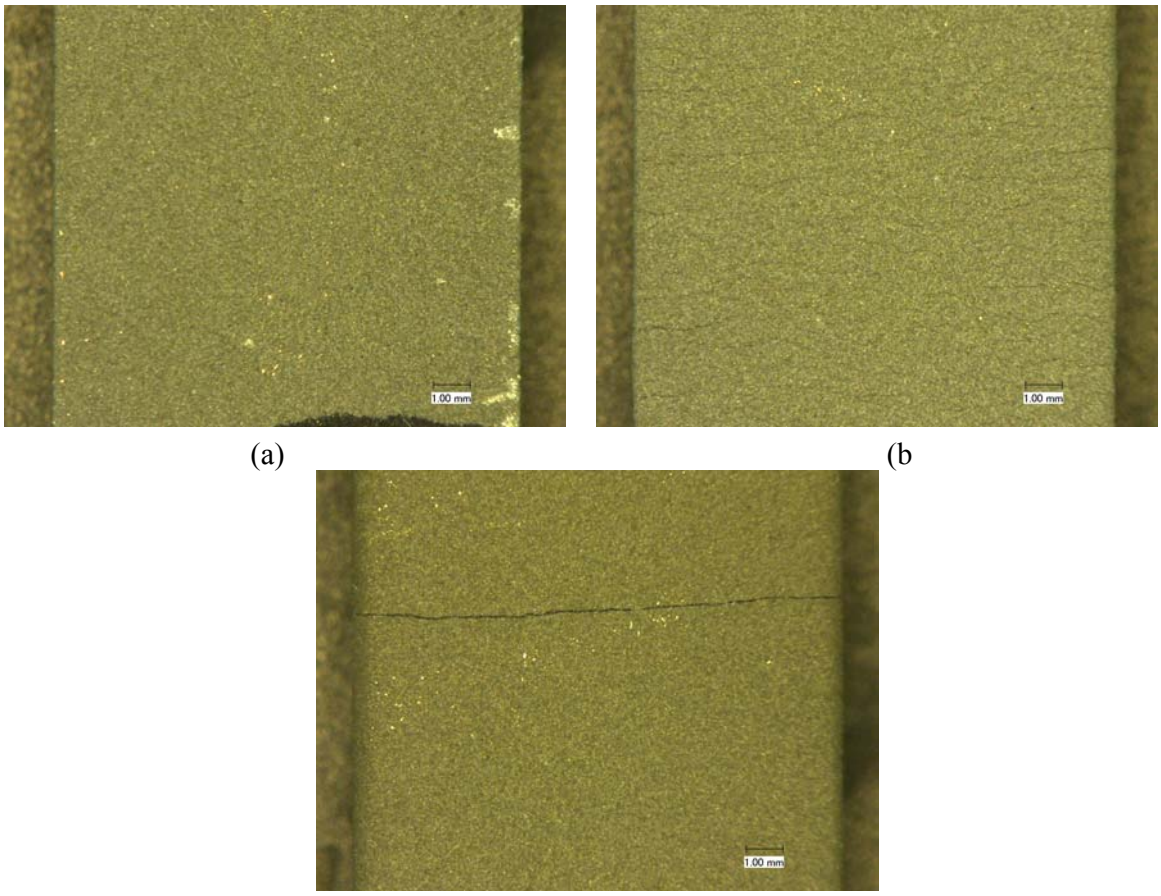

(a) (b

(c)

Figure 4. Macrographs of the surface of coatings strained to failure in tension; (a) 50 µm, (b) 130 µm and (c) 410 µm in thickness.

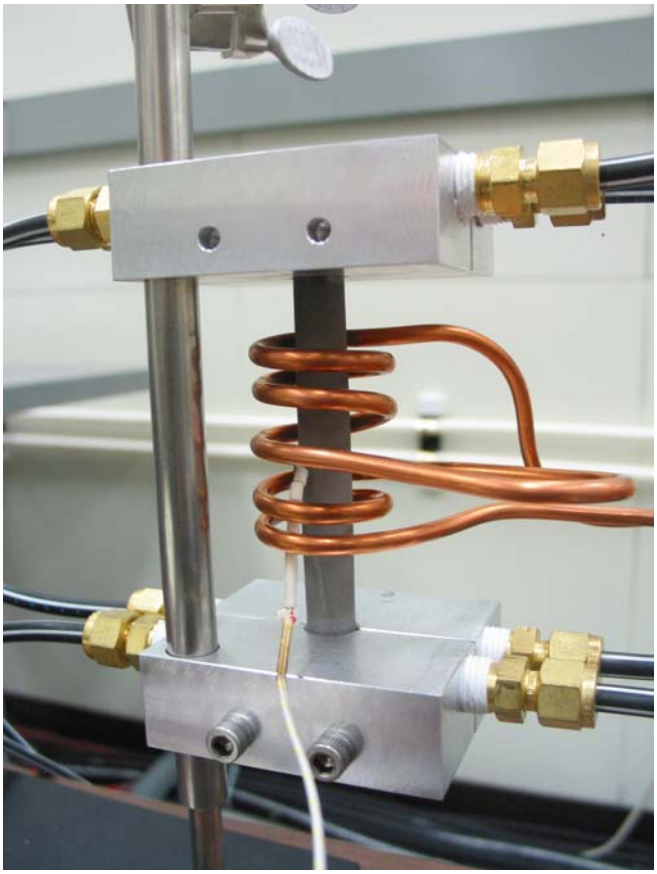

Figure 5. Induction heated round bar geometry for performance testing of coating cracking in simulated service without the influence of edge cracking.

CONCLUSIONS

Fully dense and adherent Fe_3Al coatings have been produced using the HVOF process. Methods to characterize the performance of coatings under expected service conditions are being developed. Tensile testing of coatings on flat dog-bone type specimens has shown that 50 μm thick coatings show a small amount of coating spallation, while 410 μm coatings fail as a result of one major through-thickness crack. Coatings with intermediate thickness show a high density of microcracks. While this type of test may be suitable for screening coating behavior, cracks are initiated at the edge of the specimen. Behavior from the flat specimen geometry may not be a reasonable approximation of behavior expected under service conditions where large panels or tubular geometry will prevail. A round bar type of specimen capable of being rapidly thermally cycled using induction heating is being developed to address this issue.

REFERENCES

1. C. T. Liu, E. P. George, P. J. Maziasz and J. H. Schneibel: *Mater. Sci. Eng. A*, 1998, vol. A 258, pp. 84-98.
2. Ian Baker and P. R. Monroe: *Int. Mater. Rev*., 1997, vol. 42, pp. 181-205.
3. J. R. Knibloe, R. N. Wright, V. K. Sikka, R. H. Baldwin and C. R. Howell, *Mater. Sci. Eng A*, vol. A153, p. 382-90, 1992.
4. J. R. Knibloe, R. N. Wright and V. K. Sikka, *J. Mater. Sci.*, vol. 28, p. 2040-2048, 1993.
5. B. H. Rabin and R. N. Wright, *Metall. Trans.*, vol. 22A, p. 277-287, 1991.
6. B. H. Rabin and R. N. Wright, *Metall. Trans.*, vol. 23A, p. 35-44, 1992.
7. T. C. Totemeier, R. N. Wright and W. D. Swank: *J. Thermal Spray Technol.*, 2002, vol. 11, pp. 400-08.
8. T. C. Totemeier, R. N. Wright and W. D. Swank: *Metall. Mater. Trans. A*, 2003, vol. 34A, pp. 2223-31.
9. T. C. Totemeier, R. N. Wright and W. D. Swank: *Intermetallics*, 2004, vol. 12, pp. 1335-44.
10. D. K. McDonald and E. S. Robitz: *Coal Ash Corrosion Resistant Materials Testing Program – Evaluation of the Second Section Removed in August 2003, in 4th International Conference on Advances in Materials Technology for Fossil Power Plants*, 2004, Hilton Head, SC, EPRI.
11. C. K. Lin and C. C. Berndt: *J. Thermal Spray Technol*., 1994, vol. 3, pp. 75-104.
12. T. W. Cline and S. C. Gill: *J. Thermal Spray Technol*., 1996, vol. 5, pp. 401-18.
13. J. R. Regina, J. N. DuPont and A. R. Marder: *Corrosion*, 2004, vol. 60, pp. 501-09.
14. B. S. Covino, et al. : *Corrosion Behavior of an HVOF-Sprayed Fe_3Al Coating in a High-Temperature Oxidizing/Sulfidizing Environment, in 4th International Conference on Advances in Materials Technology for Fossil Power Plants*, 2004, Hilton Head, SC, EPRI.
15. T. C. Totemeier and J. K. Wright: *Surf. Coat. Technol*., 2006, vol. 200, pp. 3955-3962.
16. Y. C. Tsui and T. W. Cline: *Thin Solid Films*, 1997, vol. 306, pp. 23-33.
17. T. C. Totemeier, R. N. Wright and W. D. Swank: in *17th Annual Conference on Fossil Energy Materials*, National Energy Technology Laboratory, Pittsburgh, PA, 2003, available at www.netl.doe.gov.
18. T. C. Totemeier and R. N. Wright; in *18th Annual Conference on Fossil Energy Materials*, National Energy Technology Laboratory, Pittsburgh, PA, 2004, available at www.netl.doe.gov.

DEVELOPMENT OF NONDESTRUCTIVE EVALUATION METHODS FOR CERAMIC COATINGS

J. G. Sun
Argonne National Laboratory, Nuclear Engineering Division
9700 S. Cass Ave., Argonne, IL 60439
E-mail: sun@anl.gov; Telephone (630)252-5169; FAX (630)252-2785

ABSTRACT

Nondestructive evaluation (NDE) methods are being developed at Argonne National Laboratory for thermal barrier coatings (TBCs) applied to components in the hot-gas path of advanced high-efficiency and low-emission gas turbines, including syn-gas fired turbines. TBCs are typically applied by electron beam–physical vapor deposition and air plasma spraying on metallic vanes, blades, and combustor liners to allow for increased temperature capabilities of these hot gas-path components. As TBCs become "prime reliant," it becomes important to know their conditions to assure the reliability of these components. Six imaging NDE methods were developed/identified for TBC characterization. These NDE methods can be used to assess the reliability of new coating processes, identify defective components that could cause unscheduled outages, monitor degradation rates during engine service, and provide data for reaching rational decisions on replace/repair/re-use of components.

INTRODUCTION

Advances in thermal barrier coatings (TBCs), applied by two deposition methods, electron beam–physical vapor deposition (EB-PVD) and air plasma spraying (APS), are allowing higher temperatures in the hot-gas path of gas turbines, including syn-gas fired turbines.[1-3] However, as TBCs become "prime reliant" to the performance and reliability of the engine components such as vanes, blades, and combustor liners, it becomes important to know their condition after coating application and at scheduled or unscheduled outages.

Work at Argonne National Laboratory (ANL) is underway to develop NDE methods for TBCs. TBC failure normally starts from initiation of small cracks at the TBC topcoat/bond coat interface. These cracks then grow and link together to form delaminations which eventually cause TBC spallation. Effort at ANL has been focused on optical NDE methods including laser backscatter to detect TBC pre-spall and delamination[4] and optical coherence tomography to measure TBC thickness.[5] Optical NDE methods take advantage of the fact that TBCs are optically translucent. As a result, surfaces within and below the TBC can be examined using appropriate optical wavelengths. These methods are mainly used for semi-transparent EB-PVD and thin APS TBCs because of the limited optical penetration depth.

Effort at ANL in last year was also directed to develop thermal-imaging methods that are not limited to TBC thickness. Because large thermal-conductivity disparities exist between the TBC topcoat, the metallic substrate, and the air that fills TBC cracks when they present, thermal imaging is sensitive to detect TBC degradation (cracks and delaminations) because it involves

nondestructive measurement of TBC thermal properties. Two thermal imaging methods were developed. One is a multilayer thermal-imaging processing method that can simultaneously determine the 2D TBC thickness, conductivity, and optical absorptance distributions.[6,7] This method directly accounts for the TBC translucency that has been a major problem for thermal-imaging application to TBCs. The other is a thermal tomography method which can directly image the 3D distribution of thermal effusivity in a TBC material system.[8]

NDE METHODS FOR TBC CHARACTERIZATION AND IMAGING

Although many NDE methods have been proposed for characterizing TBCs, few were capable or practical to image TBC condition on entire component surface. Because TBC degradation likely starts at locations with abnormal properties due to poor processing or sever service condition, imaging NDE methods, instead of spot-check methods, are especially valuable for monitoring TBC degradation and for predicting TBC lifetime. ANL has developed and identified six imaging NDE methods for TBCs. Four are optical methods: (1) cross-polarization laser backscatter developed by ANL; (2) mid-infrared-wavelength reflectance (MIRR) developed by NASA;[9] (3) optical coherence tomography (OCT);[10] and (4) cross-polarization confocal microscopy developed by ANL.[11] The other two are thermal imaging methods both were developed by ANL as described earlier: (5) multilayer thermal imaging and (6) 3D thermal tomography. Within these six methods, three are capable for 2D imaging [(1), (2), and (5)] and three for 3D imaging [(3), (4), and (6)]. ANL has developed four of these methods and has experience in using the other two methods (OCT and MIRR). All methods are being evaluated at ANL to determine their capability/limitation for quantitative characterization and life prediction for TBCs. In the following, these methods are briefly described and additional research needs to be carried out are identified.

Cross-Polarization Laser Backscatter

When a polarized laser beam is incident on a translucent material such as a TBC, the total backscattered light consists of surface reflection and subsurface backscatter. However, the surface reflection typically has no change in its polarization state while the subsurface scatter has a significant change. Based on this principle, ANL developed the cross-polarization backscatter detection method to selectively measure only the subsurface backscatter from translucent materials, while filtering out the strong surface reflection.[12] The method has been used to investigate TBCs, specifically for health monitoring during isothermal heat-treatment testing, and preliminary results for pre-spall prediction were determined for EB-PVD and APS TBCs.[4,5,13] This method will be further studied to establish the quantitative correlation between backscatter intensity and TBC degradation (cracking) near the topcoat/bond-coat interface and as functions of TBC thickness. In addition, because optical penetration depth increases with wavelength, detection sensitivity at longer wavelengths (in near-infrared range) will be examined.

Mid-Infrared Reflectance (MIRR)

Mid-infrared reflectance (MIRR) imaging was developed specifically for health monitoring of TBCs by Eldridge at NASA.[9] Because optical penetration for TBCs is at maximum in mid-infrared wavelengths (3-5 μm), MIRR may have higher sensitivity to detect TBC degradation near the topcoat/bond-cot interface. In this method, a steady-state infrared light source is used to

illuminate the TBC surface and the total reflection, including those from the TBC surface, TBC volume, and cracks near topcoat/bond coat interface, is imaged by an infrared camera in the 3-5 μm band pass. Correlations have been established between progression of delamination cracks, which is related to pre-spall condition, and the MIRR data. Because this method is simple and the instrumentation is available at ANL, it will be investigated for detecting delaminations and predicting pre-spall condition for relatively thick APS TBCs, and for comparison with other NDE methods.

Optical Coherence Tomography (OCT)

OCT is a 3D method originally developed for imaging biological materials.[10] It is based on the Michelson interferometer between a reference and a detection beam to differentiate the reflection from different depths of a translucent material. Using a low-coherence diode laser, an average OCT system can achieve a spatial resolution of 5–15 μm. This method was explored at ANL because the cross-sectional scanning images from this method allow for a direct measurement of the thickness of ceramic coatings, including most environmental barrier coatings (EBCs) and TBCs. For these coatings, thickness uniformity is an important parameter because temperature drop across the coating is dependent upon the thickness, especially if the thermal conductivity is uniform.[14] Details of the experimental setup for the ANL system and preliminary results for EBCs and TBCs have been presented previously.[5] This method will be further studied to determine its detection depth and spatial resolution when imaging the microstructure and cracking within TBCs.

Cross-Polarization Confocal Microscopy

Cross-polarization confocal microscopy is a new 3D imaging method developed by ANL.[11] It combines two well-established optical methods, the cross-polarization backscatter detection and the scanning confocal microscopy, and can achieve 3D subsurface imaging with sub-micron spatial resolutions, which is about one order of magnitude smaller than other optical technologies. Similar to OCT, this method could be used to directly image the TBC thickness but with better spatial resolution. A schematic diagram of the system is shown in Fig. 1. Preliminary tests indicated that, with a moderate 40X objective lens at an optical wavelength of 633 nm, the system has an axial (depth) resolution of ~2 μm and a lateral resolution of ~0.6 μm. Figure 2 shows a typical cross-sectional scan image of the subsurface of a silicon-nitride specimen with two surface opening cracks induced by indentations at different loads;[15] this is the first known result of a direct image of such fine cracks. The crack extension in the subsurface is clear visible up to ~40 μm. This method will be evaluated for imaging TBC microstructure and cracking during the next year.

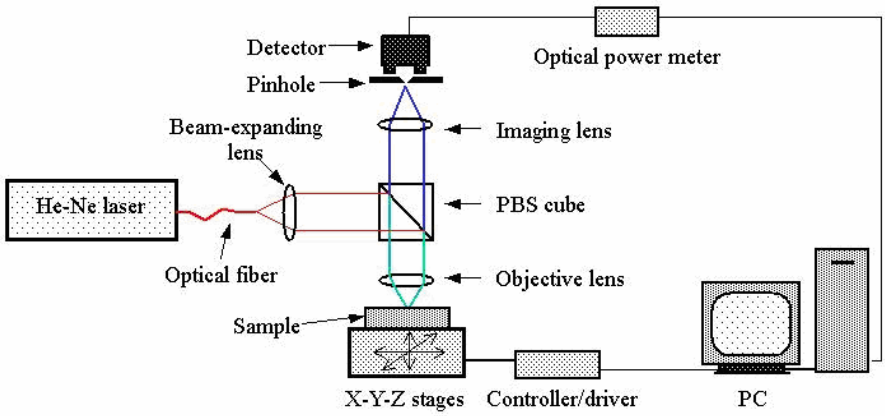

Fig. 1. Illustration of cross-polarization confocal microscopy system.

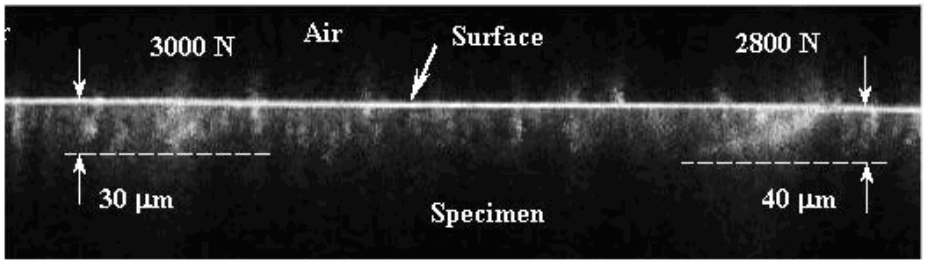

Fig. 2. Cross-sectional confocal-scan image showing cracks in a silicon-nitride ceramic subsurface.

Multilayer Thermal Imaging

In a three-layer TBC system consisting of a ceramic topcoat, a bond coat, and a metallic substrate, a large disparity in thermal conductivity exists between the topcoat and the substrate and, when the topcoat is delaminated with air filling the gap, between the topcoat and the air. For TBC system characterization, flash thermal imaging is effective because it involves nondestructive measurement of thermal properties. Based on pulsed thermal-imaging data, a new multilayer processing method was developed recently by ANL for simultaneously imaging the TBC thickness, conductivity, and optical absorptance.[6,7]

Figure 3 shows a schematic diagram of a one-sided pulsed-thermal-imaging setup. After a pulsed thermal energy is applied onto the sample surface, the temperature decay on the surface is continuously monitored by an infrared camera. The premise is that the heat transfer from the surface (or surface temperature/time response) is affected by internal material structures and properties.[16] In the new multilayer method, a TBC is modeled by a multilayer material system and the 1D heat-transfer equation under the pulsed thermal-imaging process is solved by numerical simulation. The numerical formulation also incorporates finite heat absorption depth effect due to the TBC translucency. The numerical solutions (of surface temperature decay) are then fitted with the experimental data by least-square minimization to determine unknown parameters in the multilayer material system. Multiple parameters in one or several layers can be determined simultaneously. For a TBC system, the most important parameters are the thickness, thermal conductivity, and absorption coefficient of the TBC in the first layer. This data fitting process is automated for all pixels within the thermal images and the final results are presented as images of TBC thickness, conductivity, and absorption coefficient.[6]

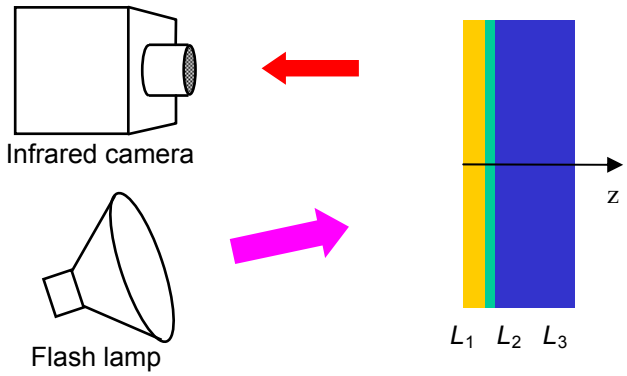

Fig. 3. Schematic of pulsed thermal imaging of a 3-layer material system.

Pulsed thermal imaging test was conducted for an as-processed APS TBC specimen shown in Fig. 4a. It consists of a nickel-based substrate of 2.5 mm thick and a TBC layer with its surface being divided into 4 sections having nominal thicknesses 0.33, 0.62, 0.95, and 1.2 mm. Because this TBC specimen is as-processed, its thermal conductivity and optical absorption coefficient are expected to be uniform. A typical thermal image is shown in Fig. 4b. Figure 5 shows surface-temperature slopes for the 4 thickness sections of this TBC specimen. Comparison of experimental data (Fig. 5a) with theoretical results (Fig. 5b), obtained using approximate material properties, clearly indicates the difference of TBC thickness in these 4 sections.

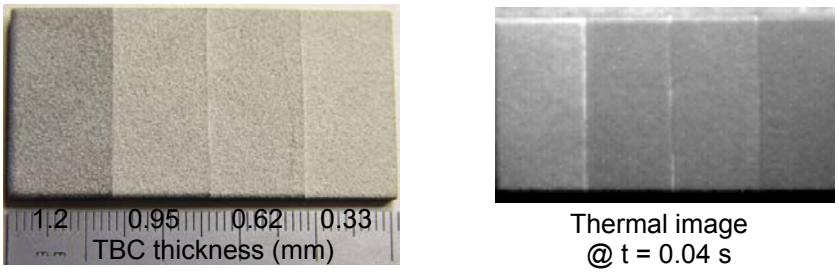

(a) (b)

Fig. 4. (a) Photograph and (b) thermal image of a TBC specimen with 4 sections of thicknesses.

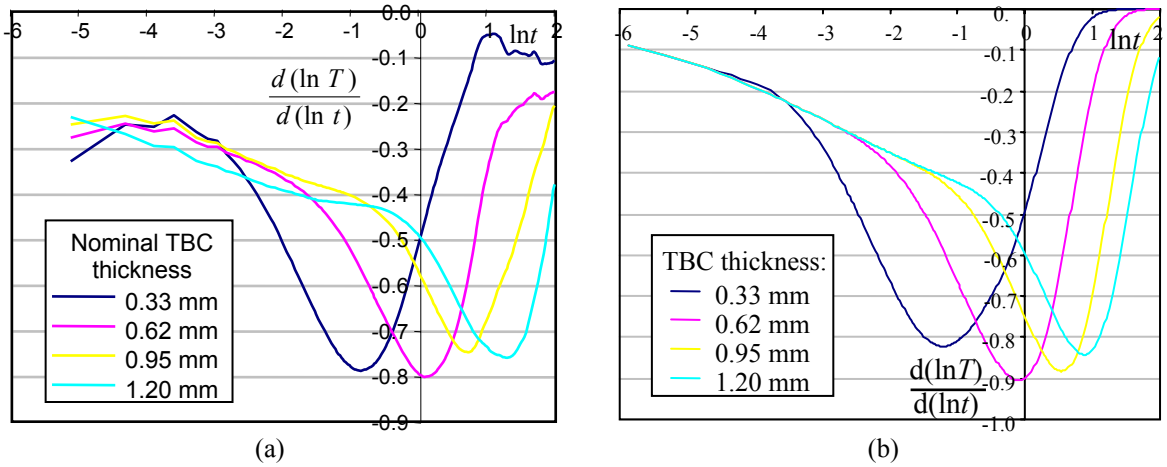

Fig. 5. (a) Measured and (b) predicted surface-temperature-slope data for TBCs of different thicknesses.

Thermal Tomography

All current thermal-imaging methods can only generate 2D images of different material parameters (including the multilayer method described above). A thermal tomography method, which for the first time can construct 3D images of the entire volume of a test specimen, has been developed recently at ANL.[8] This method directly converts the pulsed thermal-imaging data into a 3D thermal effusivity data that can be viewed/sliced in any plane direction (similar to 3D data from x-ray CT); where thermal effusivity is an intrinsic material thermal property. This method can be directly used for imaging inhomogeneous and multilayer materials without prior knowledge of the material structure and can resolve all flaws, large or small, within the specimen volume; all are new capabilities not achievable by current methods. Thermal tomography has been evaluated for imaging delaminations in both EB-PVD and APS TBCs. Figure 6 shows a plane and a cross-section thermal effusivity image for a 0.3mm thick APS TBC specimen; delaminations (showing with darker grayscales) of various size and severity are detected in both images. In the cross-section image, the thickness of the topcoat and the substrate is also imaged. This method will be further investigated next year for determination of various properties of the TBC layer.

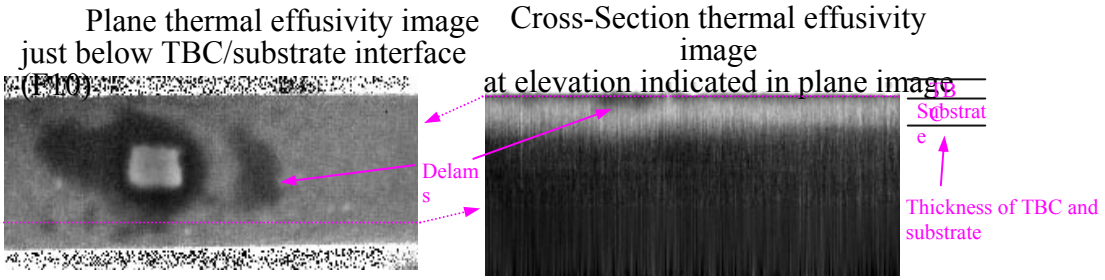

Fig. 6. Typical plane and cross-section thermal effusivity images constructed by thermal tomography method for a 0.3mm thick APS TBC specimen

CONCLUSION

Six NDE methods have been identified to be capable for characterization and imaging of various TBC parameters. Four methods are based on optical principles: (1) cross-polarization laser backscatter, (2) mid-infrared-wavelength reflectance (MIRR), (3) optical coherence tomography (OCT), and (4) cross-polarization confocal microscopy; and two on thermal imaging: (5) multilayer thermal imaging and (6) 3D thermal tomography. Within these methods, three can perform 2D imaging [(1), (2), and (5)] and three for 3D imaging [(3), (4), and (6)]. ANL has developed four of these methods [(1), (4)-(6)] and has experience in using the other two methods (OCT and MIRR). These methods have already been developed with various levels of maturity and have been preliminarily evaluated at ANL for TBC characterization. Effort in next year will be focused on quantitative determination of TBC parameters and on application for TBC life prediction.

REFERENCES

1. North Atlantic Treaty Organization, "Thermal Barrier Coatings," Advisory Group for Aerospace Research and Development Report, AGARD-R-823, Neuilly-Sur-Seine, France, April 1998.
2. US National Research Council, National Materials Advisory Board, "Coatings for High Temperature Structural Materials," National Academy Press, Washington, DC, 1996.
3. US National Aeronautics and Space Administration, "Thermal Barrier Coating Workshop," NASA Conference Publication 3312, 1995.
4. W.A. Ellingson, S. Naday, R. Visher, and C. Deemer, "Development of Nondestructive Evaluation Technology for High Temperature Ceramic Coatings," Proc. 19th Annual Conference on Fossil Energy Materials, Knoxville, TN, May 11-13, 2005.
5. W.A. Ellingson, S. Naday, R. Visher, R. Lipanovich, L. Gast and C. Deemer, "Development of Nondestructive Evaluation Technology for Ceramic Coatings," Proc. 20th Annual Conference on Fossil Energy Materials, Knoxville, TN, June 12-14, 2006.
6. J.G. Sun, "Method for Analyzing Multi-Layer Materials from One-Sided Pulsed Thermal Imaging," Argonne National Laboratory Invention Report, US patent pending, 2006.
7. J.G. Sun, "Thermal Imaging Characterization of Thermal Barrier Coatings," paper presented at the American Ceramic Society's 31st International Cocoa Beach Conference & Exposition on Advanced Ceramics & Composites, Daytona Beach, FL, Jan. 21-26, 2007.
8. J.G. Sun, "Method for Thermal Tomography of Thermal Effusivity from Pulsed Thermal Imaging," Argonne National Laboratory Invention Report, US patent pending, 2006.
9. J.I. Eldridge, C.M. Spuckler, and R.E. Martin, "Monitoring Delamination Progression in Thermal Barrier Coatings by Mid-Infrared Reflectance Imaging," Int. J. Appl. Ceram. Technol., Vol. 3, pp. 94-104, 2006.
10. B.E. Bouma and G.J. Tearney, Handbook of Optical Coherence Tomography, Marcel Dekker, New York (2002).
11. J.G. Sun, "Device and Nondestructive Method to Determine Subsurface Micro-structure in Dense Materials," US Patent No. 7,042,556, issued May 9, 2006.
12. J.G. Sun, W.A. Ellingson, J.S. Steckenrider, and S. Ahuja, "Application of Optical Scattering Methods to Detect Damage in Ceramics," in Machining of Ceramics and

Composites, Part IV: Chapter 19, Eds. S. Jahanmir, M. Ramulu, and P. Koshy, Marcel Dekker, New York, pp. 669-699, 1999.
13. W.A. Ellingson, R.J. Visher, R.S. Lipanovich, and C.M. Deemer, "Optical NDT Methods for Ceramic Thermal Barrier Coatings," Materials Evaluation, Vol. 64, No. 1, pp 45-51, 2006.
14. P. Bengtsson and J. Wingren, “Segmentation Cracks in Plasma Sprayed Thick Thermal Barrier Coatings,” in. Proc. Gas Turbine Materials Technology, eds. P.J. Maziasz, I.G. Wright, W.J. Brindley, J. Stringer, and C. O’Brien, pp. 92-101 (1998). Published by ASM International, Materials Park, OH.
15. W.K. Lu, Z.J. Pei, and J.G. Sun, "Subsurface Damage Measurement in Silicon Wafers with Cross-Polarization Confocal Microscopy," Int. J. Nanomanufacturing, Vol. 1, pp. 272-282, 2006.
16. J.G. Sun, “Analysis of Pulsed Thermography Methods for Defect Depth Prediction,” J. Heat Transfer, Vol. 128, pp. 329-338, 2006.

SESSION 4

FUNCTIONAL MATERIALS

RESULTS FROM A SIDEWALL PANEL FIELD TRIAL OF A SPALL RESISTANT REFRACTORY MATERIAL DEVELOPED AT NETL FOR SLAGGING GASIFIERS

James Bennett
U.S. Department of Energy, NETL, 1450 Queen Ave., SW, Albany, OR 97321
E-mail: james.bennett@netl.doe.gov; Telephone: (541) 967-5983; Fax: (541) 967-5845

Art Petty, Kyei-Sing Kwong, Cindy Powell, Hugh Thomas, Rick Krabbe
U.S. Department of Energy, NETL, 1450 Queen Ave., SW, Albany, OR 97321

ABSTRACT

High pressure, high temperature gasification has been commercially used since the 1950's to produce syngas (CO and H_2) for power and chemicals. As a technology, gasification has begun to experience rapid growth because of its high efficiency, fuel flexibility, and low environmental emissions. Gasification is also a leading technology under consideration for the production of hydrogen for fuel cells in a hydrogen based economy and for advanced power generation systems such as FutureGen. Entrained bed slagging gasifiers are one type of containment vessel in the gasification process currently used by industry, but suffer from downtime due to refractory liner failure, which contributes to an on-line availability lower than the 90 plus percent desired by industry. Slagging gasifiers operate at temperatures between 1250-1575^{o}C, at pressures of up to 7 MPa, and typically utilize two types of carbon feedstock - coal and petcoke, or combinations of them. These gasifiers are lined with high chrome oxide refractories that fail primarily by slag corrosion/dissolution and/or spalling through slag penetration/interaction. NETL developed and laboratory tested a high chrome oxide phosphate containing refractory material, patented it (US Patent # 6,815,386), and worked with Harbison-Walker Refractories Co. to commercially produce and field test the material. Field test results in the sidewall panel of commercial gasifiers will be discussed. In these tests, the newly developed material showed significant improvements in performance over conventionally used liner materials.

INTRODUCTION

Gasification of carbon containing materials for the production of CO and H_2 (called syngas) has become an important aspect of process generation, feedstock for chemical production, and an environmentally acceptable way of processing low-value wastes from industries such as petroleum refinement. It is a leading candidate for the production of H_2 in a hydrogen based economy that would include fuel cells; and is considered a critical component of advanced power generation technologies such as Integrated Gasification Combined Cycle (IGCC) power production or in the U.S. DOE's near Zero Emissions Advanced Fossil Fuel Power Plants. The gasification process is as follows: $C + H_2O + O_2 \rightarrow H_2 + CO + CO_2 + H_2S$ + minority gases + by products. The primary carbon feedstock materials used in gasification are coal and petroleum coke, or combinations of them.

Air cooled slagging gasifiers are among the leading technologies used to process these materials, with an example shown in Figure 1. This type gasifier operates in a reducing environment (oxygen partial pressures about 10^{-9}), at temperatures as high as 1575^{o}C, and at pressures that can range up to 7 MPa. A typical slagging gasifier is lined with high chrome oxide refractory materials to protect it from the severe service environment of gasification. The refractory may contain up to 95 pct chrome oxide, and typically

last no more than 2 years, with high wear areas failing within 3 months. Refractory failure is typically by slag corrosion/dissolution of the refractory or by slag penetration of the refractory, followed by spalling. Slag originates from impurities (ash) in the carbon feedstock that liquefy during gasification, and are often high in oxides of Si, Fe, Al, and Ca. They may also contain elevated levels of K, Na, Mg, Ni, and V; depending on the carbon source (Ni and V tends to originate from petcoke). Slag impacts and can severely limit refractory service life.

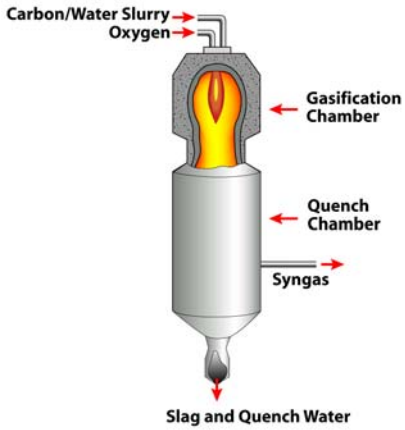

Figure 1 – Typical air cooled slagging gasifier.

Gasifier operators have identified refractory service life as a key barrier to widespread commercialization of gasification technology. Failure of the refractory lining is expensive, both in terms of material replacement costs (as high as $1,000,000) and in lost production (due to gasifier shutdown). Downtimes can range from 5-14 days for lining repair. Users desire a gasifier availability of 85-95 pct for utility applications and more than 95 pct in applications such as chemical feedstock production, with service life of at least 3 years. Failure to meet these goals has impacted the utilization of gasification technology.

Although refractory liner life is a key roadblock to this technology, only a limited number of research studies have been published recently on the failure of refractories used for slagging gasifiers[1-4]. Operating conditions that effect refractory service life include material throughput, temperature, and oxygen partial pressure. During gasification, ash liquefies at the high temperatures to form slag, which flows down the interior of the gasification chamber, interacting with and infiltrating the high chrome oxide refractory liners. This interaction leads to failure of the refractory. The high chrome oxide refractory materials currently used in gasifiers and listed in Table 1 evolved from research in the 1970-1980's funded by U.S. DOE, EPRI, and private industry[1]; and indicated a minimum of 75 pct Cr_2O_3[3] was necessary to provide the best chemical resistance to gasifier slag corrosion.

Table 1 – Chemical composition of two high chrome oxide refractories commonly used in air cooled slagging gasifiers

Property	Brick Type	
	A	B
Chem. (wt %)* - Cr_2O_3	90.1	87
- Al_2O_3	9.3	3.0
- ZrO_2	NL	6.5
Bulk Density (g/cc)**	4.27	4.07
Porosity (pct)**	14.8	16.5
CCS (MPa)**	66.5	66.9

* Data from manufacturer's technical publication NL = Not listed
** Data from laboratory measurements

In this study, post-mortem examination, of refractory bricks that were in service in slagging gasifiers was used to determine interactions between elements in the slag with Cr_2O_3 and Al_2O_3 in the refractory. These interactions were used to identify and understand phase and microstructural changes that occur in service, and were the basis for developing an improved high chrome oxide refractory material. Emphasis was placed on microstructural changes that occur at the refractory hot face leading to refractory failure. An evaluation is made in this study of the NETL developed and patented phosphate containing high chrome oxide material, and its performance in field trials.

EXPERIMENTAL PROCEDURE/RESULTS AND DISCUSSION

POST MORTEM ANALYSIS OF CONVENTIONAL REFRACTORY MATERIALS

In cooperation with gasifier users and refractory manufacturers, NETL conducted post-mortem analyses of refractories removed from commercial gasifiers to determine causes of failure and service life issues needing research focus. Results are presented in Figure 2.

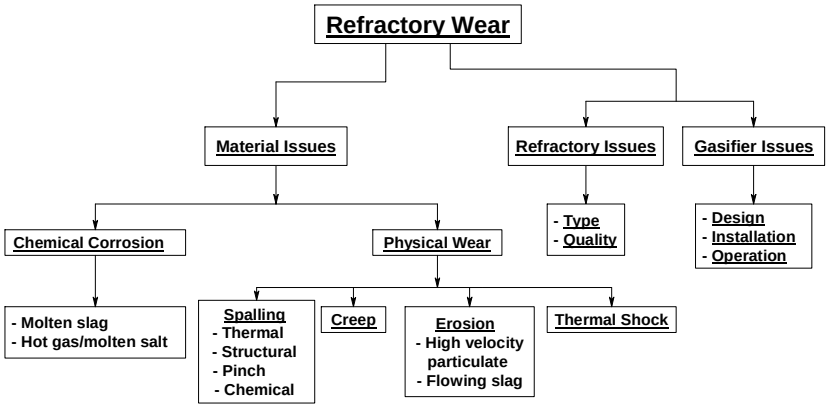

Figure 2 - Cause of failure in slagging gasifiers identified through post-mortem analysis in hot face refractory liners.

Two primary causes of refractory failure were determined from post-mortem studies, refractory corrosion and spalling. Figure 3 shows the hot face refractory lining located on the sidewall of a gasifier, with widespread surface corrosion and spalling circled (Figure 3a); and with the cross section (interior) of a brick showing deep slag penetration (Figure 3b) and a void associated with spalling in progress (indicated by the arrow on Figure 3b).

PHOSPHATE CONTAINING HIGH CHROME OXIDE DEVELOPMENT

Spalling occurs most in specific gasifier locations, such as the sidewalls, and is caused by: 1) slag penetration within the refractory pores and the resulting material property differences between the penetrated versus un-penetrated areas; and 2) by thermal cycling of the gasifier. Spalling leads to the removal of surface material in thicknesses up to 25 mm, and is a cycle that repeats itself, resulting in premature refractory failure and gasifier shutdown. Laboratory exposure to gasifier slag under simulated gasifier conditions of a number of oxide/non oxide refractory materials, combined with thermodynamic

studies, confirmed the outstanding chemical resistance of chromium oxide. For this reason, the focus of this NETL research was to improve the spalling resistance by limiting slag penetration in high chrome oxide refractories. An evaluation of materials to limit slag penetration was conducted using approximate 50 mm cubes in a static cup test of the porous refractory structures indicated phosphate additions dramatically decreased slag penetration. A 25 mm hole was drilled in the center of samples to a depth of approximately 35 mm, and filled with a granulated gasifier slag. Testing was conducted from 1500-1600°C in an Ar environment to approximate the reducing conditions of a slagging gasifier. Figure 4 shows the results of initial cup tests and changes in slag penetration resistance with phosphate additions at 1600°C. Phosphate additions to the chrome oxide refractory were also found to decrease internal cracking, which is visible in the refractory material in Figure 4 (see Figure 4a and 4b, without and with phosphate treatment).

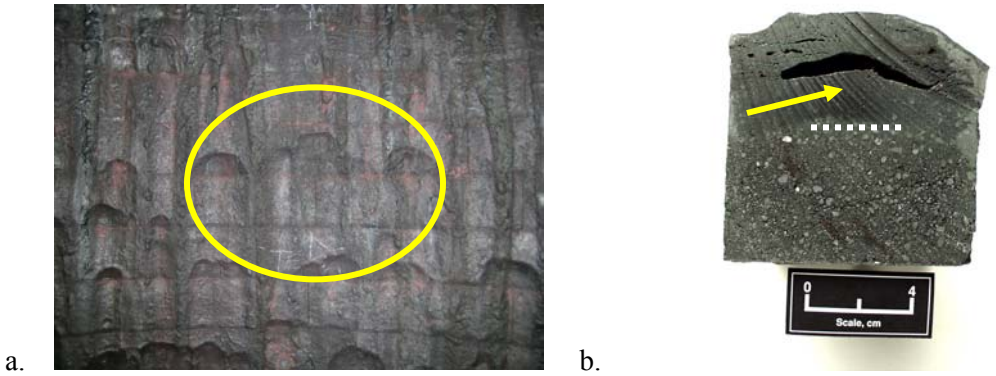

Figure 3 – Causes of refractory failure in a slagging gasifier. a) Gasifier sidewall with spalling [section circled] and corrosive wear [over the refractory liner surface]. b) Cross section of refractory with a spalling void [see arrow] and deep slag penetration [dashed line].

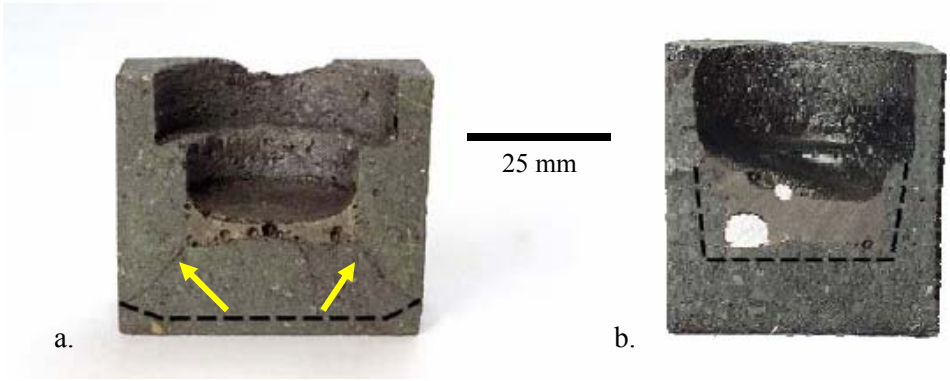

Figure 4 – Cup test results of gasifier slag penetration in high chrome oxide refractories without (a) and with (b) phosphate additions after sample exposure at 1600°C for one hour in an Ar atmosphere. Dashed line indicates slag penetration, arrows internal cracking.

Because the cup test is isothermal, and uses a static rather than a dynamic slag environment, further material evaluation and refinement in a flowing slag with a thermal gradient across the brick was conducted in the rotary slag test[5]. Information from the cup test was used as a tool to eliminate materials that did not have promise, while rotary slag testing was used to rank materials based on slag penetration and wear. Full sized brick (22.9 cm by 11.4 cm by 7.6 cm) of the phosphate compositions were fabricated at ANH Refractories Company (Harbison-Walker Refractories Company) of Pittsburgh, PA, for rotary slag testing, which was conducted at 1675°C. Data on the refined phosphate containing NETL

and commercial brick compositions is listed in Table 2, and indicates improved slag penetration resistance, improved thermal shock resistance, and comparable slag corrosive wear resistance in the NETL developed refractory versus commercially used liner materials. All other physical properties in the NETL developed material were comparable to, or better than, commercial materials. The improved performance of the phosphate containing high chrome oxide material led NETL to apply for, and be granted, a patent on this material (US Patent # 6,815,386).

Table 2 – Chemical and physical properties of Commercial (Com) and NETL developed high chrome oxide refractories

BRICK TYPE:	Com A	Com B	NETL
Chemistry			
(Wt %) - Cr_2O_3	95.1	87	92.0
Al_2O_3	4.3	3.0	4.7
ZrO_2	NL	6.5	NL
P_2O_5	NL	NL	3.3

	Com A	Com B	NETL
Bulk Density (g/cc)	4.27	4.07	4.20
Apparent Porosity (%)	14.8	16.5	12.7
CCS (MPa)	65.5	66.9	63.1
Reheat expansion *[1]	+0.64	-0.08	+0.11
*Creep deformation** [2]	+0.18	-1.98	- 0.24
Rotary slag *[3]			
– % area change	+ 5.2	+5.8	+0.6
– mm penetration	5.2	4.8	1.8

NL = Not Listed

*[1]= 1550ºC, 50 hr hold
*[2] = 1550ºC, 50 psi, 50 hr hold
*[3] = 1667ºC, 5 hrs of slag feed, 2 ½ rpm

FIELD TRIALS OF PHOSPHATE CONTAINING HIGH CHROME OXIDE REFRACTORY

Because the NETL developed refractory showed comparable-to-superior physical properties to commercial materials, the decision was made for commercial field testing in air cooled slagging gasifiers. Testing targeted the lower cone/throat areas (high corrosive wear, low-to-no spalling) and the sidewall areas (high corrosive wear/high-to-low spalling wear) in two types of gasifies. Test materials were commercially manufactured, with installation and material performance documented. A summary of field trials and their status is shown in Table 3, with material testing and evaluation still on-going. The duration of the test was determined by issues unrelated to the test material performance.

Table 3 – Summary of gasifier field trials on NETL developed, phosphate containing high chrome oxide refractory

Gasifier Type, Feedstock	Test Sample Location	Days Testing*	Field Trial Status	Test Results
Type A, coal	Lower Cone	17	Completed	Run prematurely ended – inconclusive testing
Type A, coal	Lower Cone	82	Completed	Comparable or slightly better corrosion resistance
Type A, coal	Sidewall	237	Completed	Superior spalling, comparable or slightly better corrosion
Type A, coal/petcoke	Slope	275 +	Underway	Visual – comparable corrosion, unknown spalling
Type A, coal/petcoke	Throat	275 +	Underway	Visual – comparable corrosion, unknown spalling
Type B, petcoke	Unknown	300 +	Completed	Evaluation underway

*Test duration was determined by issues unrelated to test material performance.

Preliminary physical data from field trials indicates the phosphate containing high chrome oxide refractory has superior performance in preventing surface spalling, and has slag resistance equaling, or slightly better than, conventional high chrome oxide refractories. Laboratory examination of these materials following field trial has indicated possible mechanisms by which phosphate additions improve high chrome oxide performance in a gasifier. They are as follows: 1) phosphate additions decrease porosity, contributing to a decrease in slag penetration; 2) phosphates promote the formation of a dense Cr_2O_3-FeO spinel solid solution layer at the refractory/slag interface that inhibits slag penetration; 3) phosphate additions promote the formation of an immiscible $Ca_3(PO_4)_2$ phase in the slag, increasing slag viscosity and decreasing slag corrosivity; and 4) phosphates promote the formation of lower melting bond phases that aid in thermal shock resistance.

The sidewall test panel dramatically demonstrates the influence of phosphate additions on high chrome oxide material performance, as shown in Figure 5. The 24 brick test panel area, faintly outlined in Figure 5a, had no spalling and appeared to have a protective effect on the refractories above it, whereas severe spalling occurred below the test panel. A direct comparison of the remaining thickness of brick removed from the gasifier in Figures 5b (conventional refractory with no phosphate additions outside the test panel) and 5c (phosphate containing refractory within the test panel) illustrates the improved performance of the phosphate containing refractories, which had no internal cracking and were much thicker than conventional refractories, indicating longer potential service life.

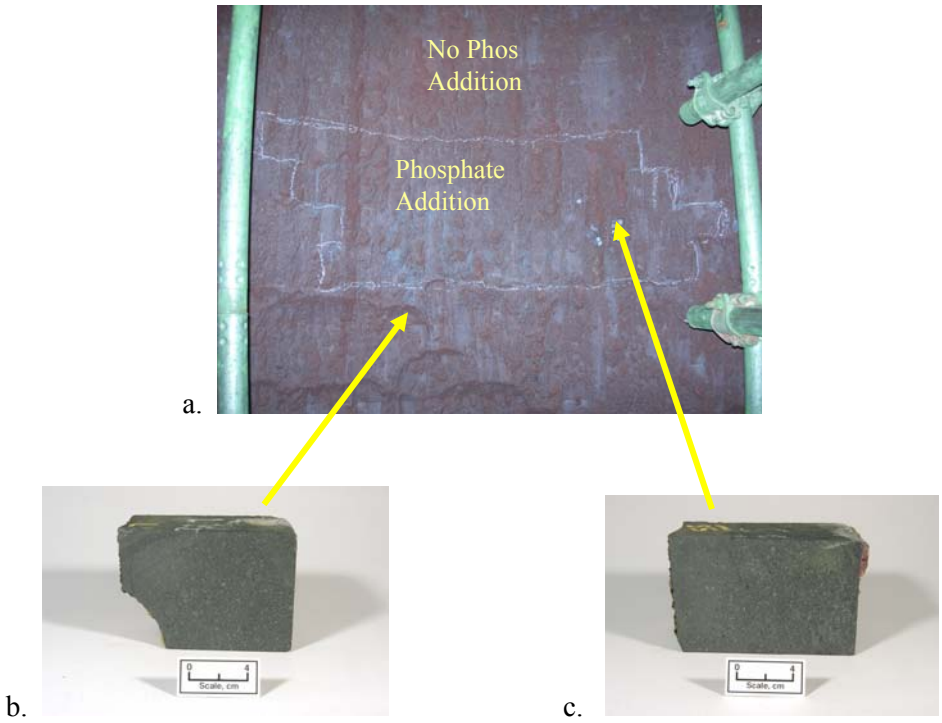

Figure 5 - Sidewall test panel (24 brick circled in white) after 237 days of service in an air cooled coal slagging gasifier environment. a) Test panel prior to removal. Note spalling below the test panel. b) Cross section of traditional refractory below the test panel. Brick had no phosphate additions. c) Cross section of phosphate containing refractory. Note refractory is thicker and has no internal cracking or surface spalling.

Spalling and internal cracking of the conventional versus the improved refractory in the test panel is shown in Figure 6, which shows the cross section (from the hot face to the cold face) of the phosphate containing test panel brick and surrounding conventional refractory. Internal cracking leading to spalling was observed in all conventional high chrome oxide materials shown, in addition to the irregular surface resulting from spalling in many brick. Conventional refractory materials below the test panel were observed to be much thinner and contained internal cracks, both evidence of spalling. Conventional refractory materials above the test panel contained only the internal cracks. The test panel materials containing the phosphate additions showed no evidence of internal cracks or spalling.

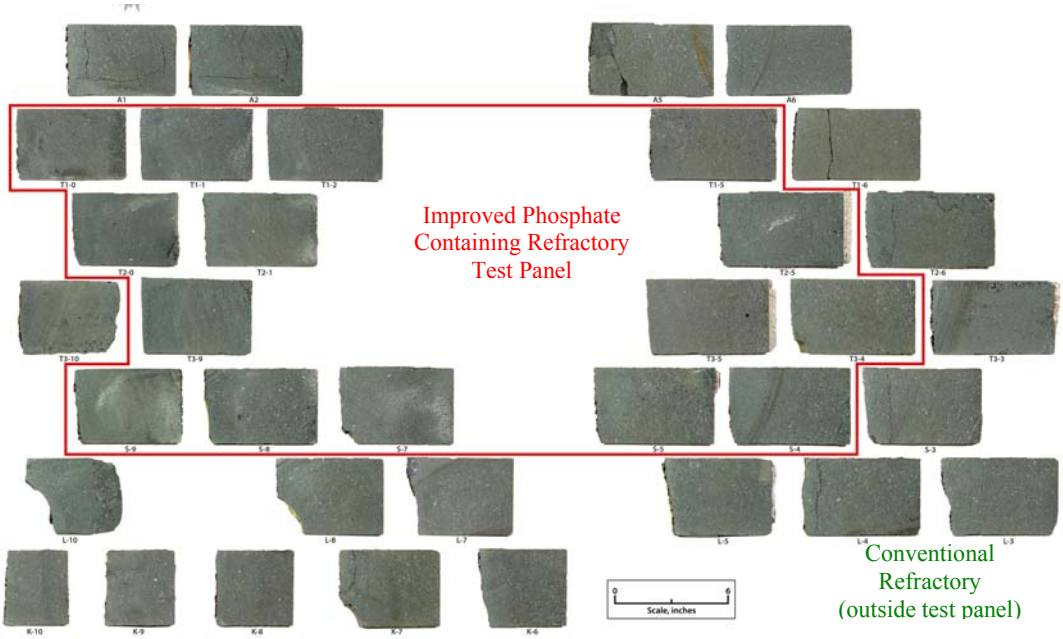

Figure 6 – Cross section of refractory materials in sidewall test panel. Test panel is composed of phosphate containing high chrome oxide refractory (surrounded by red) versus conventional high chrome oxide refractory materials. Brick are cut in half going from the hot face (on the left) to the cold face of the test refractory materials. The conventional refractory materials are thinner and have internal cracks or have spalled versus the phosphate refractory materials.

In gasifier zones where spalling is the major refractory wear mechanism, the results of filed trials indicate that the phosphate containing high chrome oxide refractory can result in improved service life of 50 pct or greater than conventional refractories, based on the remaining thickness of test materials. This would increase refractory service file from 2 to 3 years, for example. The observed improvements in performance has resulted in Harbison-Walker Refractories Company signing a licensing agreement with NETL to manufacture and market the novel refractory composition, which is being produced under the product name of Aurex® 95P.

CONCLUSIONS

The mechanisms of failure in high chrome oxide refractory materials removed from slagging gasifiers were evaluated through post mortem analysis. The major failure causes were corrosion and/or spalling of the refractory hot face surface. NETL targeted the reduction or elimination of spalling in the refractory

materials as a way to reduce wear, and developed a phosphate composition with improved spalling resistance through laboratory research. In cooperation with Harbison-Walker Refractories Company, full size brick of this refractory composition were produced and installed in commercial gasifiers for field trails. Testing was conducted in two different types of gasifiers; and used coal, petcoke, or combinations of them as carbon feedstock. Test materials were evaluated in a number of gasifier locations, with the most comprehensive study conducted on a sidewall for 237 days. Results indicated the phosphate containing refractory had at least a 50 pct improvement in service life over conventional materials in this sidewall application (where spalling was the primary wear mechanism) based on an estimation of remaining refractory material. The improved refractory material has been licensed to Harbison-Walker Refractory Company for commercial production.

REFERENCES

1. Bennett, J.P., K.S. Kwong, C. Powell, H. Thomas, and R. Krabbe; "An Analysis of the Causes of Failure in High Chrome Oxide Refractory Materials from Slagging Gasifiers"; UNITECR "05; Nov. 8-11, 2005; Orlando, FL; Cer. Trans.; v. 180; J.D. Smith, ed.; pp 935-939.
2. Bennett, J.P., K.S. Kwong, A.V. Petty, C. Powell, H. Thomas, D. Prior, and M. Schnake; "Field Trial Results of an Improved Material for Slagging Gasifiers"; 23nd Ann. Int. Pitts. Coal Conf.; Sept. 25-27, 2006; Pittsburgh, PA; CD-ROM, ISBN 1-890977-23-3, 9 pp.
3. W.T. Bakker, "Refractories for Present and Future Electric Power Plants," Key Engineering Materials, Trans Tech Publications, (1993), Vol. 88, pp. 41-70.
4. Z. Guo; "Refractories for Gasifiers"; Am. Cer. Soc. Bull.; June 2004; on line at www.ceramicbulletin.org; p. 9101-9108.
5. Cobble, J.R. and L.Y. Sadler III, A Laboratory Test to Evaluate the Resistance of Refractories to Molten Slags, USBM RI 8468, 1980, 13 pp.

THERMOCHEMICAL MODELING OF REFRACTORY CORROSION IN SLAGGING COAL GASIFIERS IN SUPPORT OF DEVELOPMENT OF IMPROVED REFRACTORY MATERIAL

Theodore Besmann
Oak Ridge National Laboratory, Oak Ridge, TN 37831
E-mail: besmanntm@ornl.gov; Telephone: (865) 574-6852; Fax: (865) 574-6918

Arthur Petty, Kyei-Sing Kwong, James Bennett, Cynthia Powell
U. S. Department of Energy, NETL, 1450 Queen Ave., SW, Albany, OR 097321
E-mail: Arthur.Petty@netl.doe.gov; Telephone: (541) 967-5825; Fax: (541) 967-5845

ABSTRACT

Slagging coal gasifiers suffer from significant attack by the coal slag on the refractory liner. To better understand the corrosive attack on the refractory the interactions were thermochemically simulated. The slag is observed to penetrate the refractory, which complicates modeling the phase behavior of the slag-penetrated interior of the refractory. To address this issue a simple strategy was adopted such that step-wise changes in composition with decreasing slag content were assumed to account for the compositional changes as slag penetrates the refractory, at least partially through its thickness. The thermochemical equilibrium calculations following this strategy typically yielded three solution phases as well as the stoichiometric crystalline phases $AlPO_4$ and $Ca_3(PO_4)_2$ depending on composition/penetration. In addition, under some conditions a slag liquid miscibility gap exists such that two slag liquids co-exist.

INTRODUCTION

Coal gasification offers one of the most versatile and clean ways to convert coal into electricity, hydrogen, and other valuable energy products. The first coal gasification electric power plants are now operating commercially in the United States and in other nations, and it is predicted that coal gasification will be at the heart of future generations of clean coal technology plants for several decades into the future. For example, at the core of the U.S. Department of Energy's FutureGen prototype power plant will be an advanced coal gasifier.

Rather than burning coal directly, gasification uses partial oxidation in the presence of steam at high temperatures and pressures to react coal to CO, hydrogen, and minority hydrocarbon gases and byproducts. Thus a gasifier differs from a combustor in that the amount of air or oxygen available inside the gasifier is carefully controlled so that only a relatively small portion of the fuel burns completely.

The mineral content of the coal is liberated in the partial combustion process and this byproduct must be eliminated from the gasifier through removal from the bottom. The most common type of gasifier is a slagging gasifier where the temperatures in the gasifier exceed the melting point of the minerals in the coal and thus melt, forming a slag. Such gasifiers can operate at temperatures up to1650°C in a reducing environment governed by the gasification process. These conditions require the use of ceramic refractories as liners to protect the combustion chamber walls from the high temperatures and contact with the corrosive slag. Currently, during combustion molten oxide slag flows along the surface of the liner and reacts with the refractory hot-face often causing relatively rapid failure.[1] Most refractories also possess significant porosity, and the slag is typically observed to infiltrate some distance into the refractory. Ex situ work in the early 1980's showed improved corrosion resistance for chromia-magnesia

and chromia-alumina spinel refractories where increasing chromia content yielded better performance.[2-4] A new series of high chromia-alumina sesquioxide refractories developed at the U. S. Department of Energy National Energy Technology Laboratory in Albany, Oregon has shown significant improvement in behavior in gasifier environments.[5] Examination of refractories after significant service life in a gasifier and from laboratory 24-hour slag-refractory cup tests have shown that during operation, the molten slag (i) dissolved the refractory, (ii) reacted with the sesquioxide to produce spinel, and (iii) penetrated into the 85% dense bodies.

Little is known about the progression of slag-refractory interactions, including the chemical thermodynamics of the reactions, the thermochemical and phase behavior or the liquid, and the nature of the resulting complex phases that form. Zhang and Lee[6] have creatively described use of phase equilibria for comprehending refractory corrosion. Hirata, et al[7] have developed an empirical relation for the corrosion rate in these systems. And Jak, et al[8] have coupled experimental and thermodynamic modeling to provide a basis for obtaining a thermochemical understanding. This background sets the stage for performing thermochemical calculations that simulate corrosive attack of refractories in slagging gasifiers.

CALCULATIONAL BASIS

Thermochemical Equilibrium Calculations

The basic data were obtained from the 1996 version of the SGTE Pure Substance Database[9] that accompanies the FactSage[10] thermochemical software package used to perform the thermochemical calculations. The slag liquid as well as spinel and sesquioxide solid solution phases are important in the system equilibria, and therefore models of these needed to be included in the calculations of phases considered. These are available for use with FactSage and are based on assessments and optimizations reported in the literature.[11-17]

Materials

The composition of the refractory was adopted from the Harbison-Walker AUREX® 95P which was developed based work with U. S. Department of Energy National Energy Technology Laboratory in Albany, Oregon 92 wt% chromia, 4.7wt% alumina, and 3.3wt% phosphate (P_2O_5).[18] The slag composition was based on a simplified Pittsburgh No. 8 coal:[19]

Component	Wt%
SiO_2	47
Al_2O_3	25
Fe_2O_3	17
CaO	6
MgO	1
Na_2O	1
TiO_2	1
K_2O	2

Conditions

Temperature - 1450°C
Total pressure – 68 bar
Oxygen partial pressure (fixed) – 10^{-8} bar
No other gaseous species present
No carbon present

CALCULATIONAL RESULTS

Thermochemical equilibrium calculations were performed using the FactSage computational software package.[10] Initial calculations were performed to determine the phases in solely the slag and the refractory under the conditions described above. Equilibrium states were then calculated for the combined slag and refractory, with compositions modified to simulate infiltration of slag into the refractory.

Slag

The equilibrium slag phase composition was computed at both an operating temperature of 1450°C and low temperature of 300°C. At 1450°C the slag phases were simply 7.6wt% $KAlSi_2O_6$ (leucite) with the remainder a single slag liquid. The slag composition under equilibrium conditions at 300°C consists of

Phase	**Wt.%**
Al_2SiO_5 andalusite	22.69
SiO_2 low quartz	18.98
Al_2O_3-Fe_2O_3 corundum	17.49
$CaAl_2Si_2O_8$ anorthite	13.95
$KAlSi_3O_8$ K-feldspar	11.00
$Na_2Ca_3Si_6O_{16}$	9.63
$Mg_4Al_{10}Si_2O_{23}$ sapphirene	5.30
TiO_2 rutile	0.98

Refractory

At 1450°C the refractory composition under equilibrium conditions is computed to consist of a sesquioxide (corundum) phase plus 5.7 wt% of aluminum phosphate ($AlPO_4$). At 300°C the FactSage database yields two sesquioxide phases that result from a solid-solid miscibility gap in the Al_2O_3-Cr_2O_3 system that is computed to form, together with 5.7 wt% of aluminum phosphate. Besmann, et al[20] in modeling this system indicates the miscibility gap will not extend to such a high chromia content. Recalculating the system without a miscibility gap yields a single sesquioxide phase plus the 5.7 wt% aluminum phosphate.

Refractory-Slag Equilibria

In order to simulate the interaction with slag at the refractory surface it was assumed that a 50 wt% mixture of refractory and slag equilibrated at 1450°C. As noted above, the slag is observed to penetrate the refractory, which complicates modeling the phase behavior. To address this issue a simple strategy similar to that of Lee, et al[21] was adopted that accounted for compositional changes as slag infiltrates the refractory at least partially through its thickness. It was assumed that any non-liquid (crystalline) phases that result from an equilibrium calculation of a slag-refractory composition, for example a 50 wt% refractory-slag mixture, would precipitate and not be carried into the interior of the refractory. This would engender a compositional change in the slag liquid, and a new composition would then be utilized to interact with the refractory simulating interactions at some depth. With a starting basis of the computed 50 wt% slag and refractory phase compositions, it was then assumed that 40 wt% of the new slag composition would react with 60 wt% of refractory, thus also simulating a decrease in the amount of slag present as it penetrates the refractory. This strategy was repeated in 10 wt% increments to 10 wt% slag-90 wt % refractory. The relatively high thermal conductivity of chromia allowed the assumption that temperature was constant at 1450°C.

The thermochemical equilibrium calculations following the above strategy typically yielded three solution phases as well as the stoichiometric crystalline phases $AlPO_4$ and $Ca_3(PO_4)_2$, depending on

composition/penetration. In addition, under some conditions there would be a slag liquid miscibility gap and two slag liquids could co-exist. Figure 1 is a plot of the total mass of each phase at equilibrium using a 100 g basis for each calculation (the two slag liquids are combined). The effect of removing the precipitating phases as the slag penetrates the refractory can be seen in the decreasing spinel content, which no longer forms at a slag percentage below a point between 20 and 30 wt%.

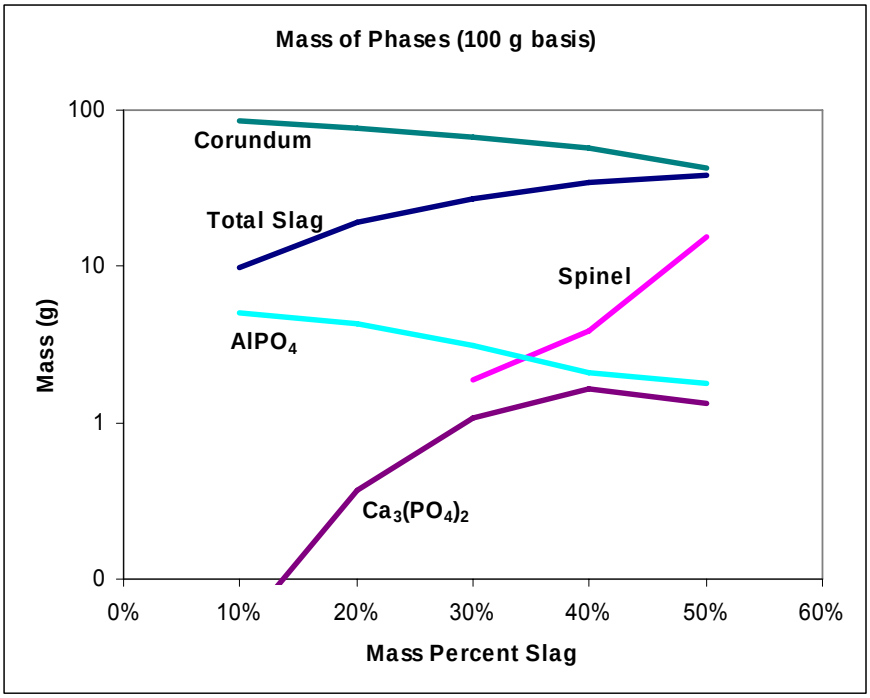

Figure 1. Mass of each phase in the equilibrated slag-refractory system under simulated conditions for penetration of the slag by the refractory (decreasing mass percent slag).

Figure 2 indicates the metal content within the slag (with the metals all present as oxides) as mass fraction versus the input mass percent slag in the simulated penetration of slag into the refractory. While most elements varied somewhat, iron in particular experienced a sharp decrease with decreasing slag content simulating slag penetration of the refractory. The small concentration of chromium in the slag behaves similarly. These are the result of iron and chromium having significant concentrations in the spinel, and as the spinel is seen to precipitate in each subsequent calculation and removed from the next calculation, quantities of these components are thus removed from the equilibria.

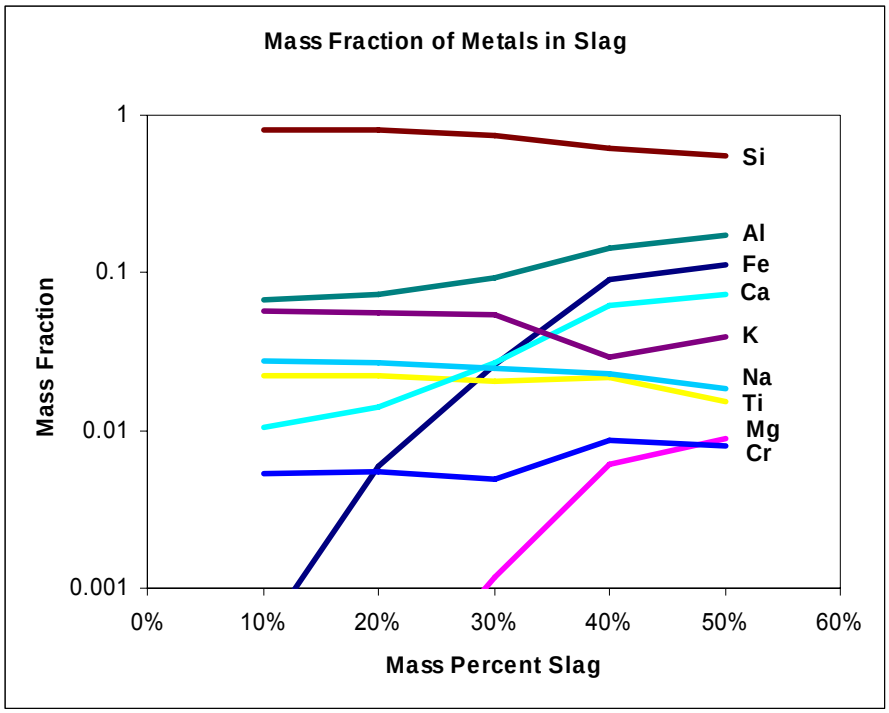

Figure 2. Mass fraction of metal as oxides in the slag phase under simulated penetration of the refractory (decreasing mass percent slag).

The metal oxide content of the spinel phase is seen in Fig. 3. The phase is no longer present at low slag contents, i.e., when the slag has significantly penetrated the refractory, so the plot extends only to 30 wt% slag. This is the effect of constituents, namely iron, precipitating in the spinel phase near the refractory surface. The iron and chrome oxide major components are relatively constant, with the minor constituents of aluminum and magnesium oxides decreasing and increasing in the phase, respectively, with slag penetration.

The sesquioxide (corundum) phase which makes up the bulk of the refractory is, of course, largely chromia. From Figure 4 it can be seen, however, that the phase picks up iron oxide from the slag, which does decrease in content further into the refractory as less is available from the slag. Alumina also appears to decrease as the slag penetrates the refractory as less is available from the slag, having been lost in precipitation of the spinel as well as due to the smaller amount of slag that is present in the calculation.

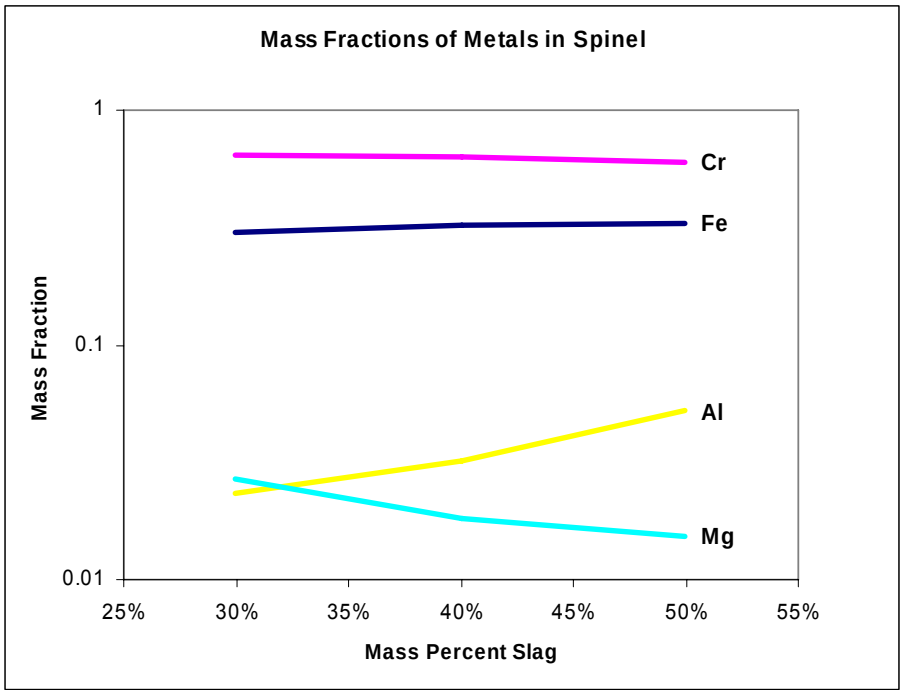

Figure 3. Mass fraction of metal as oxides in the spinel phase under simulated penetration of the refractory (decreasing mass percent slag).

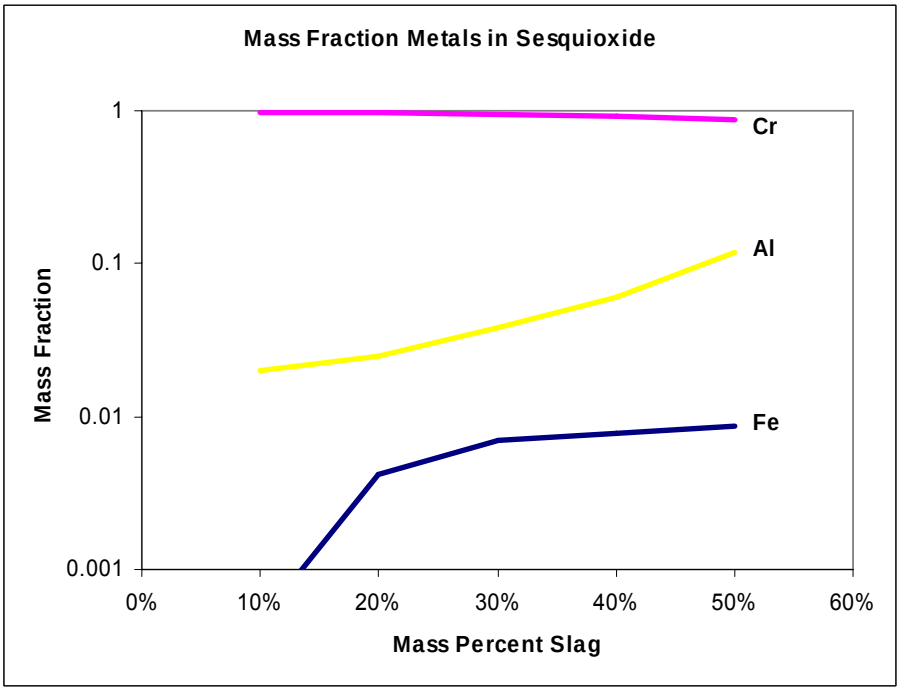

Figure 4. Mass fraction of metal as oxides in the sesquioxide (refractory) phase under simulated penetration of the refractory (decreasing mass percent slag).

LOW TEMPERATURE PHASE ASSEMBLAGES

The calculations described above at 1450°C were repeated at 300°C to simulate the slag-refractory system where the slag has penetrated the refractory to some depth and the system has now been allowed to equilibrate at low temperature. The solution phases present under these circumstances were the spinel and sesquioxide, although the spinel was not present except at high slag concentrations. Several stoichiometric phases are at equilibrium in the system under these conditions, and they are represented in Figure 5.

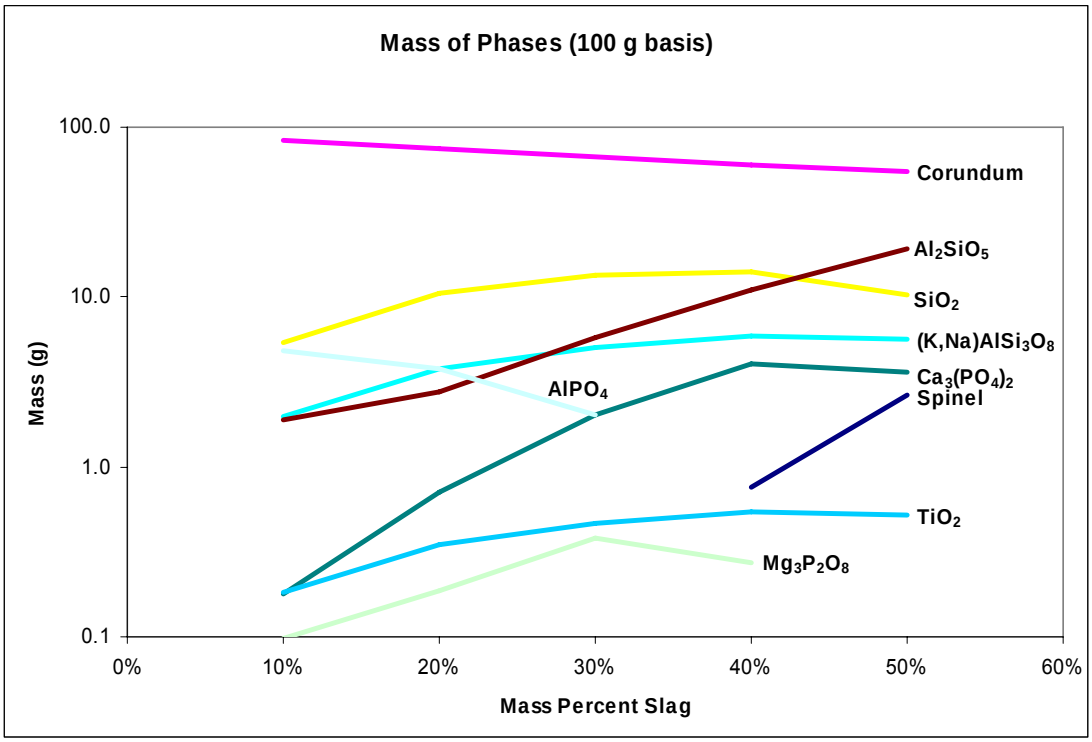

Figure 5. Low temperature (300°C) mass of each phase in the equilibrated slag-refractory system under simulated conditions for penetration of the slag by the refractory (decreasing mass percent slag)

To try to quantify attack of the refractory by the slag the equilibrium mass of the refractory constituent phases sesquioxide and aluminum phosphate at each condition of slag penetration was compared to the equilibrium mass of the constituents with no slag present. That ratio is plotted in Figure 6. From the results it appears that the sesquioxide phase is consumed to some extent by the slag near the refractory surface, but sesquioxide can also slightly gain in mass at some depth of penetration. The aluminum phosphate phase, however, loses almost 40% of its mass near the surface, which decreases to essentially no loss in the simulation when only 10% is slag. The loss of the phosphate phase, should it be an intergranular phase in the refractory, may be the controlling mechanism in refractory failure by direct slag attack.

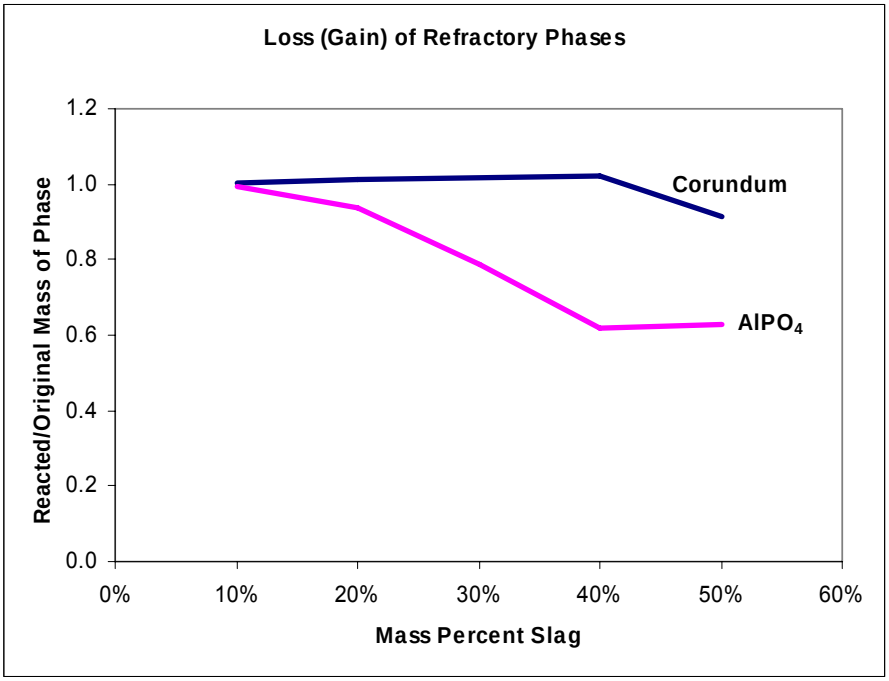

Figure 6. Mass ratio of reacted to original refractory phases sesquioxide (corundum) and aluminum phosphate under simulated penetration of the refractory (decreasing mass percent slag).

CONCLUSIONS

The thermochemical data and solution models for the constituents of a representative slag and high-chrome refractory were used in calculations to represent attack of the refractory by the slag. Penetration of the slag into the refractory was simulated by sequential calculations where precipitated phases are removed from the calculations between each step. The phases present, and the content of the solutions indicate significant compositional changes, and in particular loss of iron from the slag through the formation of a spinel phase and to a much lesser extent inclusion in the refractory sesquioxide phase. Attack of the aluminum phosphate phase in the refractory is indicated by the thermochemical calculations, and may be a controlling mechanism in refractory failure.

ACKNOWLEDGMENTS

Research was sponsored by the Office of Fossil Energy, National Energy Technology Laboratory, U.S. Department of Energy, under contract number DE-AC05-00OR22725 with UT-Battelle, LLC.

REFERENCES

1. C. R. Kennedy, “The Corrosion Of Refractories In Contact With Siliceous Mineral Residues At High-Temperatures,” Pure And Applied Chemistry 54 (7): 1335-1348 (1982).
2. J. Rawers, L. Iverson, and K. Collins, “Initial stages of coal slag interaction with high chromia sesquioxide refractories,” Journal of Materials Science, 37, pp. 531-538 (2002).

3. A. Muan, “Equilibrium relations in systems containing chromium oxide, with a bearing on refractory corrosion in slagging coal gasifiers,” High Temperatures – High Pressures, Vol. 14, pp. 653-660, (1982).
4. Z. Guo, “Refractories for Gasifiers,” American Ceramic Society Bulletin, pp. 9101-9107, (2004).
5. J. P. Bennett and K. S. Kwong, “Refractory Liner Materials Used in Slagging Gasifiers,” Refractories Applications and News, Vol. 9, no. 5, pp. 20-25, Sept./Oct. 2004.
6. S. Zhang and W. E. Lee, “Use of phase diagrams in studies of refractories corrosion,” International Materials Reviews, Vol. 45, No 2, pp. 41-84, (2000).
7. T. Hirata, T. Morimoto, S. Ohta, and N. Uchida, “Improvement of the corrosion resistance of alumina-chromia ceramic materials in molten slag,” Journal of the European Ceramic Society, 23, pp. 2089-2096 (2002).
8. E. Jak, S. Degterov, B. Zhao, A. D. Pelton, and P. C. Hayes, “Coupled Experimental and Thermodynamic Modeling Studies for Metallurgical Smelting and Coal Combustion Slag Systems,” Mettallurgical and Materials Transactions B, Vol. 31B, pp. 621-630 (2000).
9. SGTE Pure Substance Database, 1996 Version, Scientific Group Thermodata Europe, (1996).
10. C. W. Bale, P. Chartrand, S. A. Degterov, G. Eriksson, K. Hack, R. Ben Mahfoud, J. Melançon, A. D. Pelton, and S. Petersen, CALPHAD, 26, 190 (2002).
11. G. Eriksson and A.D. Pelton, "Critical Evaluation and Optimization of the Thermodynamic Properties and Phase Diagrams of the CaO-Al_2O_3, Al_2O_3-SiO_2 and CaO-Al_2O_3-SiO_2 Systems," Metall. Trans., 24B, pp. 807-816 (1993).
12. S. Decterov and A. D. Pelton, “Critical Evaluation and Optimization of the Thermodynamic Properties and Phase Diagrams of the CrO-Cr_2O_3, CrO-Cr2O_3-A1$_2O_3$ and CrO-Cr20$_3$-CaO Systems,” J. Phase Equilibria, 17, pp. 476-487 (1996).
13. S. Decterov and A. D. Pelton, "Thermodynamic Calculation of Gas/Slag/Refractory Equilibria in Coal Gasification in Corrosion of Materials by Molten Glass," Amer. Ceram. Soc., pp. 91-103 (1996).
14. S. A. Decterov, I.-H. Jung, and A. D. Pelton, "Thermodynamic Modeling of the FeO-Fe_2O_3-MgO-SiO_2 System", J. Am. Ceramic Soc., 85, pp. 2903-2910 (2002).
15. S A. Decterov, I.-H. Jung, E. Jak, Y.-B. Kang, P. Hayes, and A. D. Pelton, "Thermodynamic Modeling of the Al_2O_3-CaO-CoO-CrO-Cr_2O_3-FeO-Fe_2O_3-MgO-MnO-NiO_2-SiO_2-S System and Applications in Ferrous Process Metallurgy,” Proc. VII Int'l. Conference on Molten Slags, Fluxes and Salts, South African Inst. Mining & Metallurgy,” Johannesburg, SA, pp. 839-849 (2004).
16. E. Jak, S. Decterov, P. C. Hayes and A. D. Pelton, "Thermodynamic Modelling of the System Al_2O_3-SiO_2-CaO-FeO-Fe_2O_3 to Predict the Flux Requirements for Coal Ash Slags," Fuel, 77, pp. 77-84 (1997).
17. Jak, S. Decterov, A.D. Pelton, J. Happ, and P.C. Hayes, "Thermodynamic Modelling of the System Al_2O_3-SiO_2-CaO-FeO-Fe_2O_3 to Characterise Coal Ash Slags", Impact of Mineral Impurities in Solid Fuel Combustion'97, Ed. R.P. Gupta, T.F. Wall and L. Baxter, Kluwer Academic/Plenum, NY, pp. 723-733 (1999).
18. J. P. Bennett, K. S. Kwong, A.V. Petty, C. Powell, H. Thomas, D. Prior, and M. Schnake; “Field Trial Results of an Improved Refractory Material for Slagging Gasifiers,” Proceedings of the 23nd Annual International Pittsburgh Coal Conference, Sept. 25-27, 2006; Pittsburgh, PA, session 31, paper 31-3.
19. M. S. Oh, D. D. Brooker, E. F. de Paz, J. J. Brady, and T. R. Decker, “Effect of crystalline phase formation on coal slag viscosity,” Fuel Processing Technology, 44, pp. 191-199, (1995).
20. T. M. Besmann, N. S. Kulkarni, and K. E. Spear, “Thermochemical Analysis and Modeling of the Al_2O_3–Cr_2O_3, Cr_2O_3–SiO_2, and Al_2O_3–Cr_2O_3–SiO_2 Systems Relevant to Refractories,” J. Am. Ceram. Soc., 89 [2] pp. 638–644 (2006).
21. W. E. Lee, B. B. Argent, and S. Zhang, “Complex Phase Equilibria in Refractories Design and Use,” J. Am. Ceram. Soc., 85 [12] pp. 2911-2918 (2002).

A POROUS IRON ALUMINIDE MEMBRANE FOR HYDROGEN SEPARATION

Stephen N. Paglieri
Los Alamos National Laboratory; P.O. Box 1663, MS-C927; Los Alamos, NM 87545
E-mail: steve.paglieri@lanl.gov; Telephone: (505) 667-0652; Fax: (505) 665-1226

Robert L. Terpstra
Ames Laboratory, 222 Metals Development Building, Rm. 109, Ames, IA 50011
E-mail: terpstra@ameslab.gov; Telephone: (515) 294-5747; Fax: (515) 294-8727

Iver E. Anderson
Ames Laboratory, 222 Metals Development Building, Ames, IA 50011-3020
E-mail: andersoni@ameslab.gov, Telephone: (515) 294-9791; Fax: (515) 294-8727

ABSTRACT

Porous membranes were fabricated from Fe-16Al-2Cr (wt.%) microparticles ≤ 3-μm diameter. Membrane surface morphology was characterized using optical profilometry. A slurry of Fe-16Al-2Cr particles was applied onto porous stainless steel supports (40-μm particle cut off grade) and sintered at 975°C for 1 h. The membrane had high hydrogen and argon permeability during testing at temperatures up to 600°C, but the gas permselectivities were characteristic of Knudsen diffusion. After heat treatment at 800ºC for 24 h in UHP argon, X-ray photoelectron spectroscopy (XPS) showed that the porous iron aluminide membrane was covered with a layer of alumina that should serve as an effective barrier to metallic interdiffusion between the porous support and a thin palladium film on its surface.

INTRODUCTION

Ultra-pure hydrogen can be conveniently produced using metal membranes. Palladium alloy membranes are frequently used to purify hydrogen for compound semiconductor manufacturing, and in laboratories. It is also advantageous to use membranes reactors to perform chemical reactions more efficiently[1]. Unfortunately, the high cost of palladium prevents metal membrane technology from replacing large-scale hydrogen purification methods such as pressure swing adsorption. Filters for hot gas cleanup have been fabricated using iron-aluminide particles that resist oxidation and degradation by gaseous impurities commonly present in coal gas[2]. Extruding the molten metal through a nozzle and shearing the stream with high-velocity gas such as helium produces microparticles with a narrow size distribution[2]. Alloys with extra aluminum such as Fe-16Al-2Cr can form a thermally grown aluminum oxide layer on the surface that protects the metal from further degradation. An advantage of thermally grown layers compared to coatings is more uniform surface coverage with fewer defects. For example, chrome-containing alloys have been shown to form a continuous nitride layer at 1373 K that resists leaching in the acidic environment of a proton exchange membrane fuel cell (PEMFC)[3].

Porous metal as a palladium membrane support has the advantages of similar coefficient of thermal expansion to palladium, increased strength compared to porous ceramic or glass, and the potential to more easily seal into a module[4]. Porous metal tubes and sheet are commercially available in poresizes as small as 0.1 μm particle retention. However, the as-received surface roughness and poresize is too great to successfully deposit a thin (< 10 μm), pinhole-free palladium or palladium alloy film[5]. The deposition of a palladium film without defects depends on the ability to span all of the pores in the support membrane[6]. Therefore, the critical qualities of a palladium membrane support are low surface roughness and small poresize[7]. Metallic atoms

from stainless steel such as chromium are also known to diffuse through into palladium and cause a decrease in membrane permeability. Metallic interdiffusion that occurs between palladium and porous stainless steel at temperatures ≥ 450°C has been reduced by thin layers of oxide, nitride, or refractory metal[5; 8-12]. Of course, membrane stability then depends on the stability of the intermediate layer. The ability to operate at higher temperatures will improve efficiency and enable more flexibility in membrane applications.

EXPERIMENTAL

The iron-aluminide microparticles were prepared by a high-velocity gas jet extrusion method described in detail elsewhere[2]. The Fe-16Al-2Cr particles were nominally ≤ 3 μm. A slurry of particles was prepared and applied to a porous stainless steel (Mott Metallurgical) frit that was press fit into the ends of a 0.95 cm ID Inconel tube that had been drilled out to form a lip inside. A 1 mm gap was left between the porous frit and the end of the tube for the microparticle slurry. The top of the particle film was smoothed off evenly with a razor blade and the membrane was fired in a vacuum furnace at 975°C for 1 h. Single gas hydrogen and argon permeation tests were performed using a flow-through system. Retentate pressure was controlled using a back-pressure regulator and permeate flowrate was measured using a calibrated flowmeter. Overall system control and datalogging was carried out using National Instruments Labview software and Fieldpoint modules. XPS was performed in a Kratos Axis-Ultra surface analysis system. Optical profilometry was performed using a WYKO NT2000 Profiler that uses vertical scanning interferometry.

RESULTS AND DISCUSSION

MEMBRANE PERFORMANCE

Permeation measurements were conducted on the composite membrane consisting of porous stainless steel (nominal 40 μm poresize) coated with a layer of the 3-μm particles. The flowrate versus pressure drop through the composite membrane is shown in Figure 1. From SEM micrographs of cross sections of a similarly prepared membrane, the layer consisting of the 3 μm Fe-16Al-2Cr particles was ~0.1-mm thick. The effective surface area of the membrane was 0.625 cm^2.

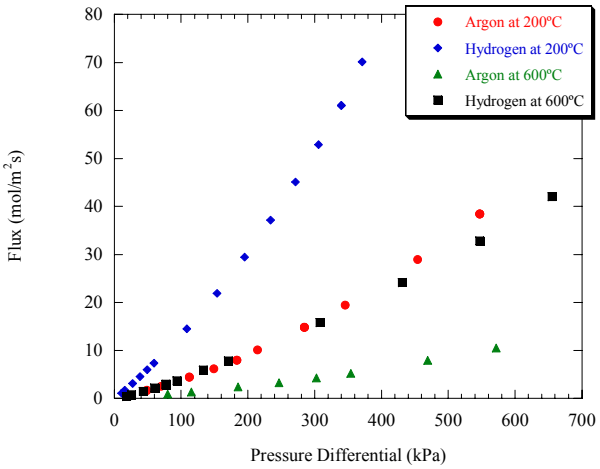

Figure 1: H_2 and Ar flowrates through a 0.625 cm^2, porous Fe-16Al-2Cr (3-μm particle) membrane at 200 and 600ºC and ΔP = 0-656 kPa

For Knudsen flow, where the interaction of gaseous atoms or molecules with the pore wall becomes more prevalent because of the small poresize, the separation factor is determined by the inverse ratio of square root of molecular weights of the gases [13]:

$$\alpha_{Knudsen} = \sqrt{\frac{MW_{Ar}}{MW_{H_2}}} = 4.45$$

The ideal gas permselectivities ($\alpha_{H2/Ar}$) calculated from the data in Figure 1 were between 2.7 and 3.1. Therefore, the gas permeation mechanism through the porous membrane had contributions from both Knudsen and viscous flow.

MEMBRANE CHARACTERIZATION

After heat treatment at 800ºC for 24 h in UHP Ar, the surface of the Fe-16Al-2Cr membrane was analyzed using AES (Table 1). As shown in Table 1, aluminum, oxygen, some iron and chrome, and significant amounts of carbon and nitrogen were detected. The surface consists mostly of alumina. These results are in agreement with similar XPS analysis conducted at Ames Laboratory. Carbon is a commonly seen contaminant, and some of the carbon present is undoubtedly a result of air exposure.

Table 1. Results of XPS analysis of Fe-16Al-2Cr surface, heat-treated at 800°C for 24 h in UHP Ar.

Element	Atomic %
carbon	25
nitrogen	6
oxygen	29
aluminum	36
chrome	1
iron	3

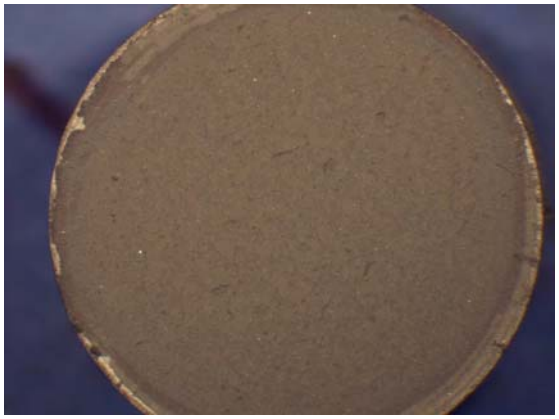

(a)

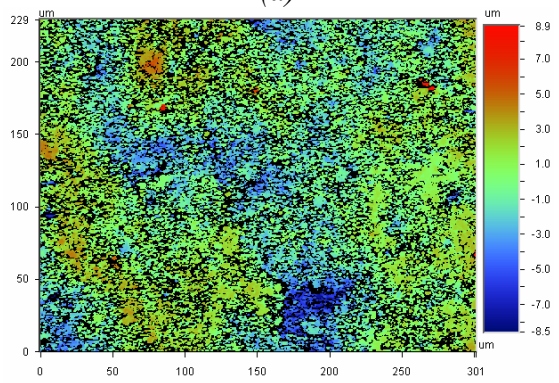

(b)

Figure 2. (a) surface of Fe-16Al-2Cr membrane. (b) optical profilometry of membrane surface (R_a = 1.51 μm)

When depositing a palladium film onto a porous membrane support, low surface roughness of the substrate is essential for depositing a thin, defect-free film. Optical profilometry of surface of the iron aluminide membrane gave a root mean square roughness, R_a = 1.51 μm, as shown in Figure 2.

CONCLUSIONS

Porous membranes fabricated from Fe-16Al-2Cr (wt.%) particles ≤ 3-μm diameter were characterized for hydrogen and argon permeability, surface chemistry, and surface structure. The membrane was tested up to 600°C and had high hydrogen and argon permeability, but the gas permselectivities were indicative of Knudsen diffusion. XPS showed that the membrane was covered with a thin layer of alumina that could serve as an effective barrier to metallic interdiffusion for a thin palladium film deposited onto the surface. The membrane also had a low surface roughness, R_a = 1.51 μm, determined by optical profilometry.

ACKNOWLEDGEMENTS

This work was funded by the U.S. DOE, Office of Fossil Energy (Advanced Research Materials program). Thanks to Dr. Thomas J. Venhaus for XPS work and Dr. Hain Oona, Ben Roybal, and Hailey M. Murdock for experimental assistance.

REFERENCES

1. V.M. Gryaznov, "Metal containing membranes for the production of ultrapure hydrogen and the recovery of hydrogen isotopes," *Sep. Purif. Meth.*, 29(2) (2000), 171-187.
2. I.E. Anderson, and R.L. Terpstra, "Progress toward gas atomization processing with increased uniformity and control," *Mater. Sci. and Eng. A*, 326 (2002), 101-109.
3. M.P. Brady, K. Weisbrod, I. Paulauskas, R.A. Buchanan, K.L. More, H. Wang, M. Wilson, F. Garzon, and L.R. Walker, "Preferential thermal nitridation to form pin-hole free Cr-nitrides to protect proton exchange membrane fuel cell metallic bipolar plates," *Scr. Metall.*, 50(7) (2004), 1017-1022.
4. J. Shu, B.P.A. Grandjean, E. Ghali, and S. Kaliaguine, "Simultaneous deposition of Pd and Ag on porous stainless steel by electroless plating," *J. Membr. Sci.*, 77 (1993), 181-195.
5. P.P. Mardilovich, Y. She, Y.H. Ma, and M.-H. Rei, "Defect-Free Palladium Membranes on Porous Stainless-Steel Support," *AIChE J.*, 44(2) (1998), 310-322.
6. Z. Shi, S. Wu, and J.A. Szpunar, "Bridge Model of Nanoparticles Deposited on Pores Area of the Substrate During a Membrane Fabrication," *Appl. Phys. Lett.*, 87 (2005).
7. F. Roa, J.D. Way, R.L. McCormick, and S.N. Paglieri, "Preparation and characterization of Pd-Cu composite membranes for hydrogen separation," *Chem. Eng. J.*, 93(1) (2003), 11-22.
8. K.S. Rothenberger, A.V. Cugini, B.H. Howard, R.P. Killmeyer, M.V. Ciocco, B.D. Morreale, R.M. Enick, F. Bustamante, I.P. Mardilovich, and Y.H. Ma, "High pressure hydrogen permeance of porous stainless steel coated with a thin palladium film via electroless plating," *J. Membr. Sci.*, 244 (2004), 55-68.
9. C. Su, T. Jin, K. Kuraoka, Y. Matsumura, and T. Yazawa, " Thin Palladium Film Supported on SiO_2- Modified Porous Stainless Steel for a High-Hydrogen-Flux Membrane," *Ind. Eng. Chem. Res.*, 44 (2005), 3053-3058.
10. J. Shu, A. Adnot, B.P.A. Grandjean, and S. Kaliaguine, "Structurally Stable Composite Pd-Ag Alloy Membranes: Introduction of a Diffusion Barrier," *Thin Solid Films*, 286(1-2) (1996), 72-79.
11. S.E. Nam, and K.H. Lee, "Preparation and Characterization of Palladium Alloy Composite Membranes with a Diffusion Barrier for Hydrogen Separation," *Ind. Eng. Chem. Res.*, 44 (2005), 100-105.
12. G. Gao, Y. Li, J.Y.S. Lin, and B. Zhang, "Characterization of zirconia modified porous stainless steel supports for Pd membranes," *J. Porous Mater.*, 13 (2006), 419-426.
13. M. Mulder. (1991). *Basic Principles of Membrane Technology*, Kluwer Academic Publishers, Dordrecht, The Netherlands.

ADVANCES IN BRAZING:
HIGH TEMPERATURE BRAZING OF MONOLITHIC 430 TO POROUS 430L STAINLESS STEEL FOR HYDROGEN SEPARATION APPLICATIONS

V. Malave,[*] A. Meier,[*] and K. S. Weil[**]

[*]Inamori School of Engineering at Alfred University, 2 Pine St, Alfred, NY 14802, USA
[**]Pacific Northwest National Laboratory, 902 Battelle Blvd, P.O. Box 999, Richland, WA 99352

ABSTRACT

The feasibility of high-temperature vacuum brazing of monolithic 430 to porous 430L SS for hydrogen separation applications has been investigated. Nickel (Ni) braze interlayers are prone to form secondary phases that affect joint strength, and porous substrates have the potential to further diminish the joint mechanical performance. The mechanical strength, braze microstructure, and phase chemistry were evaluated for three different Ni-Cr based filler alloys (Si-B, Si, and B-containing type). Brazing using a Ni-Cr-Si alloy resulted in extremely low braze strengths due to brittle phases formed along the joint centerlines in a Si-rich matrix which assisted crack nucleation and propagation during solidification. Higher joint strengths were obtained using a Ni-Cr-B alloy but the strength was limited by significant braze alloy infiltration into the porous body resulting in unwanted secondary phase formation. High-quality joints were achieved using a Ni-Cr-Si-B braze alloy regardless of the intermetallic compounds formed during brazing.

INTRODUCTION

The development of porous inorganic membranes for high-temperature hydrogen separation (from natural gas) is currently being investigated by the Oak Ridge National Laboratory (ORNL) and Pacific Northwest National Laboratory (PNNL) for coal gasification applications [1]. For this purpose, a system that serves to filter hydrogen and contains a joint between a monolithic tube with a porous section has been proposed. A schematic of this system for high-temperature hydrogen separation from natural gas is illustrated in Figure 1. The porous substrate has a 430L stainless steel support structure with a thickness greater than 400 μm (and a pore size ranging between 0.5 to 50.0 μm). The adjoining braze must provide a hermetic seal to ensure that H_2 extraction is efficient. In this application, the natural gas from which hydrogen would be extracted has been heated in the previous water gas shift reaction to temperatures ranging between 700 and 800ºC.

Ni-based filler metals have been successfully used for brazing ferritic stainless steels and a review of potential nickel based brazing alloys for this application has been performed by Malave [2]. Nickel-chromium-based (Ni-Cr) have been used as filler metals in joining iron-chromium alloys. However, the high concentrations of metalloid elements (i.e. silicon (Si) and boron (B)) and phosphorous (P) that act as melting-temperature depressant elements also form intermetallic compounds with chromium (Cr) and nickel (Ni) [3-5]. These phases are extremely hard and very brittle. They commonly agglomerate along the centerline of the joint, thereby decreasing the load-carrying capacity of the brazed joint. This brittle phase formation is a function of braze alloy chemistry, brazing time, brazing temperature, and joint thickness [3,5,6] so careful braze process control is necessary to obtain optimal joint strength.

Brazing of porous metals further complicates the brazing process. When porous materials are brazed, the filler metal alloy tends to flow by capillary action into the porous material depleting joint of braze material which can in turn result in weak braze joints [7]. Efforts have been made to produce reliable brazed joints in porous bodies, including methods that introduce additional materials into the structure. Several of the methods to produce reliable brazed joints in porous bodies have been reviewed by Malave [2].

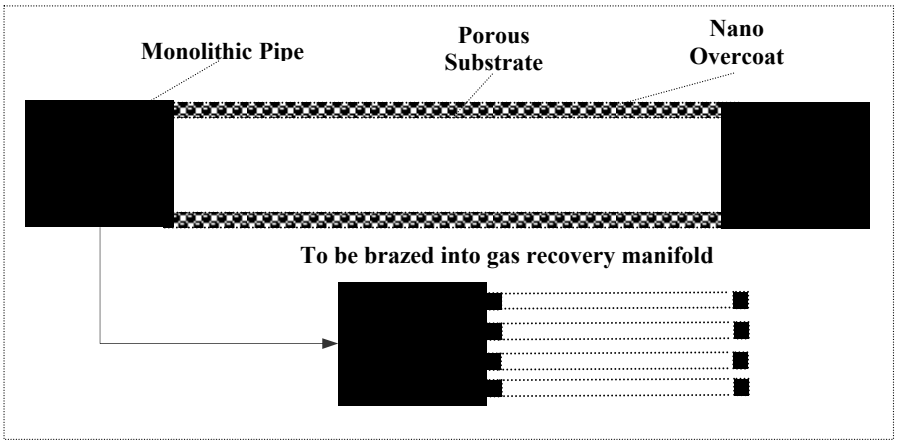

Figure 1 Schematic of system for brazing monolithic pipe to porous membrane for hydrogen separation applications.

EXPERIMENTAL

The feasibility of joining SS 430/porous-430L (monolithic-to-porous forms) has been carried out by means of the investigation of this material's brazing behavior with two different joint-types: a) a monolithic-to-monolithic joint (SS 430) and b) a monolithic-to-porous joint (SS 430/porous-430L), with the latter sandwiched between monolithic sections.

Materials

The base metal used for all monolithic brazing, joint characterization, and mechanical property studies was cold-rolled commercial grade 430 SS plates with a thickness of 4.8 mm. The nominal chemical composition for this alloy is Fe with 16.00-18.00 Cr, 1.00 Si, 1.00Mn, 0.12 C, 0.04 P, and 0.03 S (wt.%) [8]. The mechanical properties of the as-received cold rolled and annealed 430 SS samples were determined via tensile tests. The UTS for the annealed samples was between 330 and 366 MPa. Since the brazing temperatures in this investigation exceeded the 430 SS annealing temperature, the minimum strength obtained from the annealed tensile tests was used as a baseline.

The base metal was porous 430L SS fabricated by the Oak Ridge National Laboratories (ORNL, TN). The as-received material was tube-shaped and approximately 55.0 mm-length x 11.5 mm-OD x 0.7 mm-thickness. The as-received porous tubes were cut and flattened for brazing purposes. Chemical quantification from an EDX analysis of the as-received porous-430L tubes yielded the following chemistry: 73.7 Fe, 17.8 Cr, 2.4 Si, 5.4 O, and 0.7 C (wt%). Using mercury porosimetry, it was determined that the porous tubes exhibited a pore-volume of 0.0375 ml/g which is equivalent to approximately 29% porosity. Three Ni-based braze alloys, produced by Wall Colmonoy, Co. (Madison Heights, MI), were selected: 1) Nicrobraz L.M.® (BNi-2), a Ni-Cr-Si-B alloy , 2) Nicrobraz 30® (BNi-5), a Ni-Cr-Si alloy, and 3) Nicrobraz 150®, a commercial grade Ni-Cr-B alloy. The braze alloys were supplied in transfer-tape form, containing a controlled quantity of braze metal approximately 127 μm thick. The chemical compositions and brazing ranges for these braze alloys are given in Table 1.

Brazing Procedure

Prior to the brazing operations, the joining surfaces of the SS 430 specimens were ground to produce the desired surface finish (either a 15-μm or 1 μm polished surface). After grinding, the base metals (430 and porous 430L) were ultrasonically cleaned using acetone and then rapidly dried with hot air. Subsequently, the porous 430L substrates were baked at 100°C for about 30 minutes. The Ni-based transfer tapes were then placed on the ground and cleaned parent metals' surfaces. A porous metal layer was placed between them for the monolithic/porous sandwich configuration samples. Figure 2 shows a schematic of the butt joint-type specimen used for the monolithic-to-porous sandwich joint configuration. The specimens were vertically positioned in a graphite fixture and held in place using alumina wedges in order to maintain joint alignment and to avoid direct contact between the

SS plate surfaces and the graphite fixture. The following thermal cycle was performed under a vacuum of approximately 10^{-1}-10^{-2} Pa (10^{-4}-10^{-5} torr):

1. Heat to 950ºC at a rate of 20ºC per minute.
2. Hold at 950ºC for 1.2 ks (20 minutes).
3. Heat to desired brazing temperature at 20ºC/minute.
4. Hold at the brazing temperature for the desired time.
5. Cool to 800ºC at 1ºC/minute.
6. Cool to room temperature at 8ºC/minute.

Table 1 Composition and Brazing Temperature Range of Braze Alloys [9]

Ni-Based Braze Alloy AWS BNi-Series	Chemical Composition, wt.%						Melting Temperature (°C)		Brazing Temperature (°C)
	Cr	Fe	Si	C[a]	B[a]	Ni	Solidus	Liquidus	
BNi-2 Nicrobraz L.M.	7.0	3.0	4.5	0.06	3.10	Bal	970	1000	1010-1175
BNi-5 Nicrobraz 30	19.0	-	10.2	0.06	0.03	Bal	1080	1135	1150-1205
Commercial Nicrobraz 150	15.0	-	-	0.06	3.50	Bal	1055	1055	1065-1205

a. Maximum values

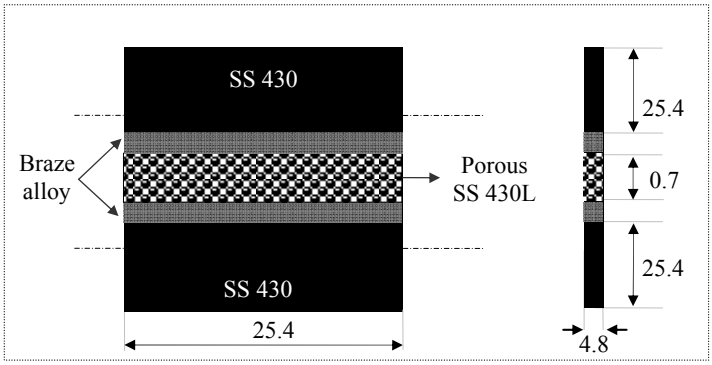

Figure 2 Schematic of SS 430/porous-430L brazed joint sandwich configuration (dimensions in mm).

Experimental Parameters

Testing was divided into three phases. The first phase was an evaluation of the effect of hold time, braze alloy, and joint thickness. For the second and third phases, additional variables were added for the most promising braze alloys from the first phase in an effort to determine the optimum brazing conditions for these systems. A total of 42 test conditions were evaluated. The overall brazing variables were:

- Joint thickness: 127, 254, and 381 μm.
- Isothermal hold: 0.6, 1.8, and 3.6 ks.
- Type of brazed joints: monolithic-to-monolithic components (SS 430) and monolithic-to-porous components (SS 430/porous-430L).
- Ni-Cr-based braze alloy: Si-B, Si, and B-type (as previously specified in Table 1).

- Brazing temperature: 1040, 1175 and 1205ºC.
- Monolithic surface finish: 1 μm and 15 μm.

Characterization

After the brazing operation, sections of the brazed samples were machined for joint strength testing. Uniaxial tensile tests were performed at room temperature using an Instron-mechanical testing frame with Series IX Automated software. Testing was performed at a constant displacement rate of 2 mm/min. The brazed specimens had a gage length of approximately 25 mm. A cross-section of each brazed joint was mounted in a phenolic mold and successively down to a final 1 μm finish with diamond paste. The microstructure of the joints was revealed by etching with Villellas reagent for about 20 seconds. The samples were then coated with gold-palladium (Au-Pd) for SEM and EPMA characterization. Braze cross-sections were examined using a Polyvar Met optical microscope. Optical observations were supported by further characterization using an environmental SEM (model: FEI Quanta 200F). Additional investigations were performed to determine joint quality and microstructural evolution (including intermetallic compound formation). An EPMA (model: JEOL JXA-8200 WD/ED) was employed to achieve accurate quantitative and qualitative (through compositional x-ray maps) local chemical composition of brazed joints by means of a wavelength-dispersive spectrometer (WDS). Analysis of B was performed in the Ni interlayer and in the segregation products of the joints obtained, having approximately 10% and 2% of quantitative estimate error, respectively [10]. The capabilities of this analysis technique and its experimental accuracy are discussed in greater detail elsewhere [2].

RESULTS AND DISCUSSION

Brazed Joint Tensile Strengths

A summary of the experimentally determined monolithic and monolithic-to-porous brazed-joint maximum strengths is presented in Table 2 (blank entries indicate that no brazed joint was fabricated under the specified brazing conditions). The minimum values and the individual test results are reported elsewhere [2]. The tensile test results corresponding to the different monolithic-to-porous SS 430/porous-430L workpieces brazed for 1.8 ks are also summarized in Figure 3.

For the Ni-Cr-Si-B braze alloy, joint strengths (316 to 380 MPa) on the order of the annealed SS base metal UTS were obtained for the SS 430/porous-430L joints brazed at 1175ºC for 1.8 ks. The presence of the porous substrate did not adversely effect the joint strength (the SS 430 joint strength ranged between 287 and 322 MPa under the same brazing conditions). The SS braze strength decreased when joined under the same brazing conditions for either 0.6 ks (303 to 308 MPa) or 3.6 ks (242 to 249 MPa). The brazing temperature was another factor that determined the joint strength. A detrimental effect on the joint mechanical strength (28 to 53 MPa) occurred when the temperature was decreased to 1040ºC, particularly when thick-interlayer joints were brazed. Thus, the maximum strength was directly proportional to maximum brazing temperature of the braze alloy regardless the joint thickness. For brazes fabricated at 1175ºC for 1.8 ks with a 254 μm thick-interlayer; the use of a monolithic surface polished to 1 μm resulted in an increased joint strength (366 MPa) relative to the 15 μm surface. The 381 μm (extra-thick) interlayer joint exhibited the highest strength obtained in this study (380 MPa).

For the Ni-Cr-Si braze alloy, extremely weak SS 430/porous-430L joints (10 to 125 MPa) were obtained when joining under all brazing conditions studied. The presence of the porous substrate in the sandwich configuration resulted in a decrease in strength relative to the brazed monolithic SS components (e.g. 241 versus 29 MPa for SS 430 and SS 430/porous-430L brazes respectively when joined with a 127 μm-thick interlayers at 1205ºC for 3.6 ks). Increasing the brazing temperature resulted in a decrease in strength for the SS 430/porous-430L joints (e.g. 29 versus 241 MPa respectively when raising the brazing temperature from 1175 to 1205ºC for 3.6 ks).

For the Ni-Cr-B braze alloys, intermediate to relatively high joint strengths were obtained for the SS 430 (156 to 279 MPa) and SS 430/porous-430L (157 to 224 MPa) joints under the different brazing conditions evaluated. The SS 430 joints exhibited slightly higher strength than the SS 430/porous-430L joints. Increasing the brazing temperature did not result in a significant strength improvement in the SS 430 and SS 430/porous-430L joints.

Table 2 Monolithic SS 430- and Monolithic-to-Porous SS 430/Porous-430L Brazed Joint Maximum Tensile Strengths (All Strengths in MPa)

Braze Alloy (Condition)	Hold Time=0.6 ks		Hold Time=1.8 ks		Hold Time=3.6 ks	
	SS 430	SS 430/ Porous-430L	SS 430	SS 430/ Porous-430L	SS 430	SS 430/ Porous-430L
Ni-Cr-Si-B alloy (Joints brazed at 1175ºC using 15-µm grit SiC polished monolithic surface)						
Thin-interlayer joint (a)	300	303	308	329	238	242
Thick-interlayer joint (b)	320	308	287	327	347	249
Extra-thick-interlayer joint (c)	-	-	-	380	-	-
Ni-Cr-Si-B alloy (Joints brazed at 1040ºC using 15-µm grit SiC polished monolithic surface)						
Thin-interlayer joint	-	-	53	229	-	-
Thick-interlayer joint	-	-	28	40	-	-
Ni-Cr-Si-B alloy (Joints brazed at 1175ºC using 1-µm diamond polished monolithic surface)						
Thin-interlayer joint	-	-	289	316	-	-
Thick-interlayer joint	-	-	322	365	-	-
Ni-Cr-Si alloy (Joints brazed at 1175ºC using 15-µm grit SiC polished monolithic surface)						
Thin-interlayer joint	-	-	164	82	178	125
Thick-interlayer joint	-	-	50	19	177	35
Ni-Cr-Si alloy (Joints brazed at 1205ºC using 15-µm grit SiC polished monolithic surface)						
Thin-interlayer joint	-	-	-	-	241	29
Thick-interlayer joint	-	-	-	-	-	-
Ni-Cr-B alloy (Joints brazed at 1175ºC using 15-µm grit SiC polished monolithic surface)						
Thin-interlayer joint	-	-	239	184	156	194
Thick-interlayer joint	-	-	279	191	206	157
Ni-Cr-B alloy (Joints brazed at 1205ºC using 15-µm grit SiC polished monolithic surface)						
Thin-interlayer joint	-	-	227	224	-	-
Thick-interlayer joint	-	-	269	198	-	-

(a) Thin interlayer=127 µm. (b) Thick interlayer=254 µm. (c) Extra-thick interlayer=381 µm.

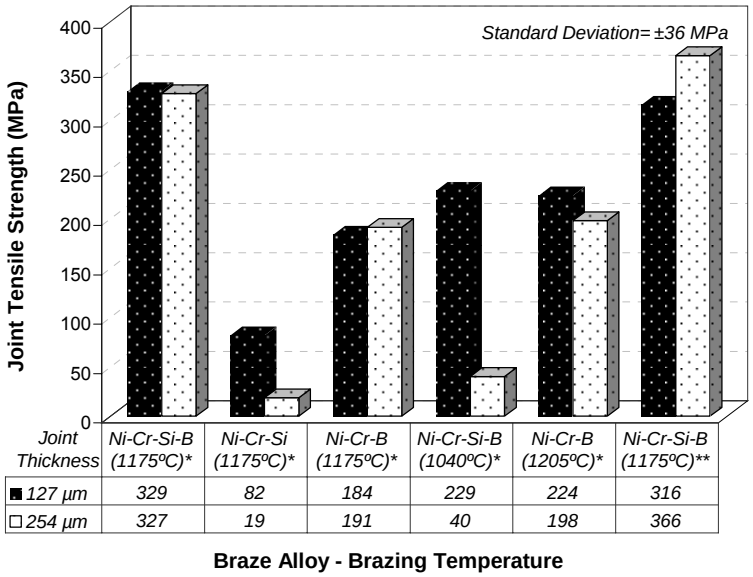

Figure 3 Tensile strength of monolithic-to-porous, SS 430/porous-430L, joints brazed for 1.8ks. (*) 15-µm grit SiC polished surface. (**) 1-µm diamond polished surface.

SS 430/Porous-430L Brazed Joint Microstructure and Chemical Composition

The braze microstructural development for the brazed alloys was relatively complicated. Each of the brazing parameters evaluated in this work influenced the nature of the secondary phases formed. In the systems studied, there was an interchange of elements between the Ni-based braze alloy and the monolithic 430- and porous 430L base metals. While the Ni interlayer was increasing in Fe and Cr composition by dissolution and infiltration from the SS components, the filler-metal elements were entering the base metals (Si and/or B when applicable, and to some extent Ni and Cr) during the brazing process. This resulted in a dilution of the Ni-interlayer alloy. Typical microstructures are presented and the major features are described in order to introduce the complexity of these microstructures.

The EPMA compositional x-ray maps used for the quantitative analysis of the bond Ni-interlayer and secondary-phase products are archived elsewhere [2]. Basically, these x-ray maps were used to analyze the Fe, Cr, Ni, Si, B, and C present in the bond region to qualitatively estimate: a) the bond elemental distribution and b) the chemical composition of the different joint zones (dissolution, base metal outside of the braze affected zone, infiltration, Ni-based solid solution, and segregation-products formation zones). Only the major results are presented and discussed. The emphasis of the chemical analysis is on the secondary phases as they were identified as the major factor in determining the strength of the joints.

(1) ***Ni-Cr-Si-B Braze Alloy (BNi-2):*** A typical microstructure for a Ni-Cr-Si-B braze alloys is shown in Figure 4. The typical structures exhibited by the brazes joined with Ni-Cr-Si-B alloy, can be divided morphologically into seven segments [2]. It is postulated that the flow of the braze alloy into the SS base metals was stopped during the joining operation, forming well-defined dissolution and infiltration zones in the joints brazed at 1175ºC. Good fillets were formed from the brazing operation, demonstrating adequate wetting when brazing at 1175ºC for 1.8 ks. In these joints, it was observed that: a) reduced zones of brittle structures formed only at some outer edges of the joints, b) shrinkage voids formed through intermetallic compounds at outer edges, and c) porosity formed in the central zone of the fillet surfaces and dissolution zones, as shown in Figure 4. Based on the EPMA analysis, a large number of intermetallic compounds (borides: Cr_xB_y and/or $Fe_xCr_yB_z$ and silicides: Ni_xSi_y, and $Ni_xCr_ySi_z$) formed in the braze layer during solidification. The degree of dissolution varied from 81 to 151 μm in the central segment of the joint. Meanwhile, the maximum degree of infiltration in the central segment of the joint varied from 109 to 192 μm. High-quality joints were obtained when brazing at 1175ºC for 1.8 ks regardless of the different secondary phases formed in the braze region during solidification. In this respect, neither the formation of borides nor the capillary flow of the braze material into the porous substrate affected the joint strength. This is an unexpected result since the formation of brittle phases has been stated in previous reports to have a detrimental effect on the joint strength [3,4,11].

The joints having thick interlayers exhibited large zones of intermetallic compound formation. These zones were generally concentrated in the outer section of the joints for the brazing temperature as illustrated in Figure 5. The secondary phase formation increased with brazing time and these hard phases were highly concentrated in the joint central region, as shown in Figure 6a. The EPMA results indicate that the joint strength was not affected by the segregation products formed during the brazing process with the exception of: a) Ni_xB_y-rich structures (possible compounds: Ni_3B and/or Ni_2B), [12] and b) clusters of Si and/or B segregation products (the latter formed along the bond centerline) [13,14]. The joint brazed with a 1-μm diamond polished monolithic surface produced a sound, nearly intermetallic-compound free, and outer edge-voidless joint (Figure 6.b). For these brazes, the Cr depletion from the base metal into the Ni solid solution was also reduced which could be related to the high boron content remaining in the Ni-Cr-Si-B braze alloy (0.53 wt.%).

(2) Ni-Cr-Si Braze Alloy (BNi-5): A typical microstructure for the Ni-Cr-S braze alloys is shown in Figure 7. Six different segments were identified in the joints [2]. Extremely weak joints were obtained for this alloy system. In these brazes, it was observed that: a) large zones of brittle structures formed along the joint centerline causing crack nucleation and propagation from the bond outer-to-central region during solidification (as shown in Figure 7); b) porosity formed along the Ni interlayer; and c) non-uniform dissolution zones formed. The bond interlayer consisted of Ni-Cr-Si-Fe solid solution and segregation products distributed along the braze centerline. The secondary phases consisted of Cr-rich, Ni_xSi_y, and $Ni_xCr_ySi_z$. It is proposed that the latter two compounds assisted the section cracking due to thermal stresses developed during solidification and that the Cr_xSi_y compounds probably did not severely affect the joint integrity. It is also hypothesized that the high Si content in the braze solid solution was the major factor that weakened the braze (as the Si content in the solid solution increased, the joint strength decreased). The

degree of dissolution ranged from 35 to 79 µm. and the highest strengths exhibited by the joints brazed with the Ni-Cr-Si braze alloys were related to the minimum penetration depth of the braze material. The degree of infiltration into the porous substrates was difficult to estimate since in most brazes there was a complete infiltration of Ni and Cr from the braze alloy into the porous 430L occurred.

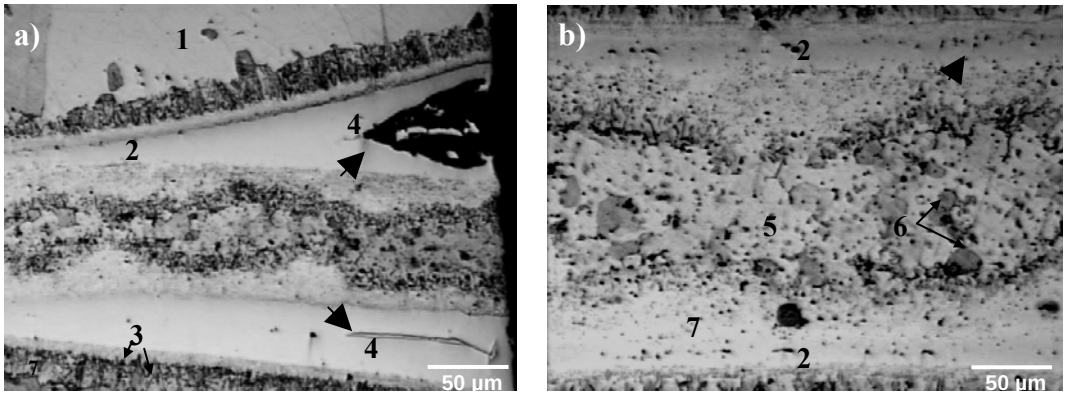

Figure 4 Typical microstructure of the SS 430/porous-430L joint brazed at 1175ºC for 1.8 ks with a 127 µm-thick Ni-Cr-Si-B interlayer (optical micrographs): a) joint outer section: arrow indicates Cr_xB_y segregation products and voids formed through them and b) joint central segment: arrow indicates porosity in the interlayer.

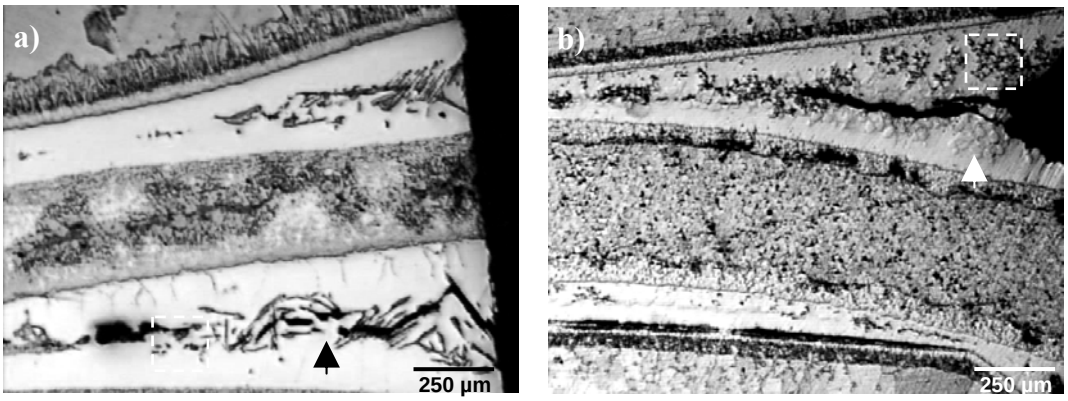

Figure 5 Typical microstructure of SS 430/porous-430L joints outer edge brazed with a 254 µm-thick Ni-Cr-Si-B interlayer (optical micrographs): a) 1175ºC for 1.8 ks: arrow indicates platelike Cr_xB_y precipitates and outlined square encloses B-rich phases and b) 1040ºC for 1.8 ks: arrow indicates globular Si-rich phases and outlined square encloses Cr_xB_y.

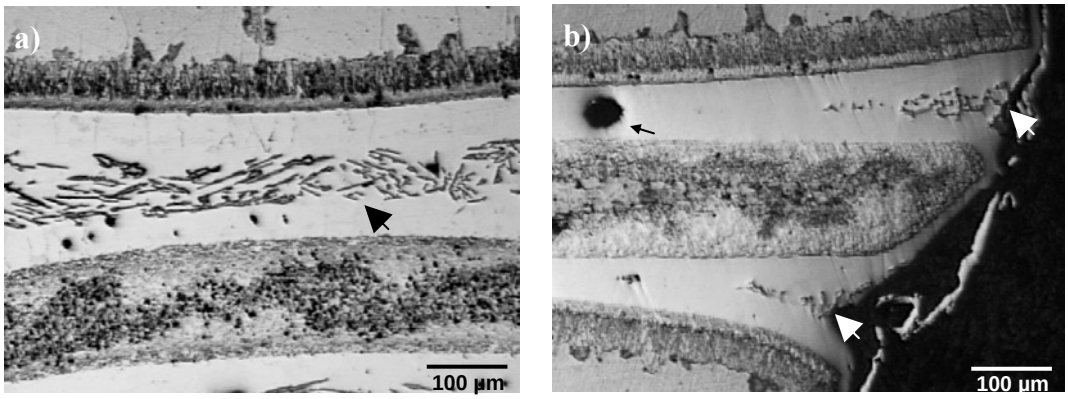

Figure 6 Typical microstructure of SS 430/porous-430L joints brazed with a 254 µm-thick Ni-Cr-Si-B interlayer at: a) 1175ºC for 3.6 ks: arrow indicates platelike segregation products along central joint and b) 1175ºC for 1.8 ks with 1-µm diamond polished SS surface: arrows indicate a few needles-shaped segregation products in the joint outer edge, slender arrow points to void formation (optical micrographs).

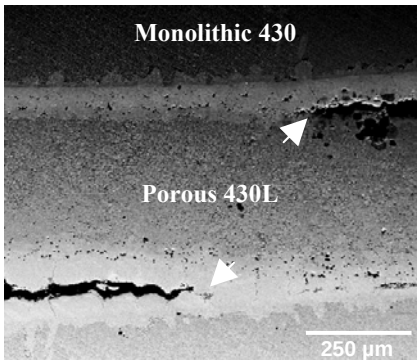

Figure 7 Typical microstructure of SS 430/porous-430L joint central region brazed with a 127 µm-thick Ni-Cr-Si interlayer at 1175ºC for 1.8 ks: arrows indicate crack propagation through Ni_xSi_y or $Ni_xCr_ySi_z$ secondary phases (SEM/BSE image).

(3) Ni-Cr-B Braze Alloy (NB 150): A typical microstructure for the Ni-Cr-B braze alloys is shown in Figure 8. The corresponding typical microstructure for a thicker interlayer and a longer hold time is shown in Figure 9. The typical microstructure of these joints was characterized by: a) void formation and void coalescence at the joint side edges subsequent to secondary phase precipitation (as shown in Figure 8); b) large infiltration of the porous substrate (as shown in Figure 8); c) distortion in the porous substrate that assisted the formation of detrimental thick sections in the bond, causing secondary phases to form (as illustrated in Figure 8b); d) cracking through intermetallic compounds during solidification (as shown in Figure 9); and e) porosity formed along the interlayer. Moderate-to-complete infiltration in the porous body was exhibited by the brazes under the different brazing scenarios evaluated. It is hypothesized that the braze alloy did not stop flowing into SS porous substrate and therefore boron remained in the liquid braze alloy when isothermal solidification began. Intermediate to relatively high joint strengths were obtained under the different brazing conditions evaluated in this investigation. It is suggested that aggressive infiltration caused distortion in the porous substrate, which assisted the formation of unusual thick sections in the bond, where secondary phases formed. The secondary phases formed in the bond region (complex compounds, Cr_xB_y, $Fe_xCr_yB_z$, and $Ni_xCr_yB_z$) did not exhibit a significant correlation with the joint strength. The minimum

strength (157 MPa) was obtained for the braze exhibiting the formation of $Ni_xCr_yB_z$. Platelike Cr_xB_y phases were found to be similar to those formed in the Ni-Cr-Si-B-interlayer joints. The degree of dissolution of the SS base metal in the joint central region varied from 107 to 143 µm. All of the Ni-Cr-B-interlayer-brazes analyzed in this study exhibited large poorly-defined infiltration zones in the porous substrates.

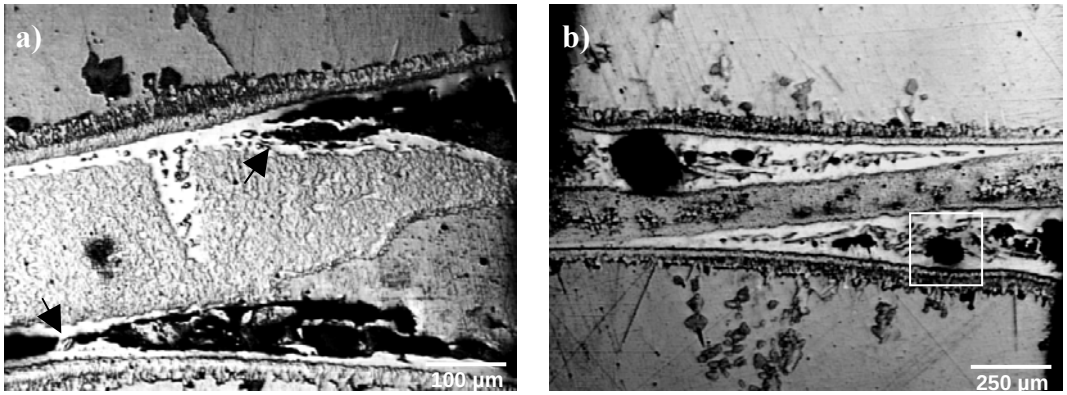

Figure 8 Typical microstructure of SS 430/porous-430L joints brazed with Ni-Cr-B interlayers at: a) 1175ºC for 1.8 ks with a 127 µm-thick interlayer exhibiting complete infiltration and voids at joint outer edges: arrow indicates complex intermetallic compounds; b) 1205ºC for 1.8 ks with a 254 µm-thick interlayer exhibiting detrimental thick bond's sections and porous substrate distortion: outlined square indicates voids formed within borides matrix (optical micrographs).

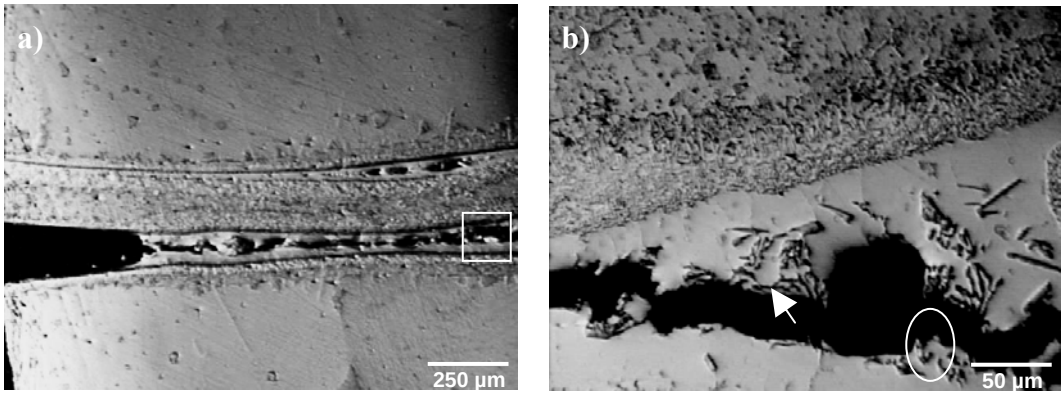

Figure 9 Typical microstructure of SS 430/porous-430L joints brazed at 1175ºC for 3.6 ks with a 254 µm-thick Ni-Cr-B interlayer (optical micrographs): a) braze exhibiting cracking along interlayer centerline during solidification and b) outlined square indicates cracking through secondary phases: arrow points to $Ni_xCr_yB_z$ compound and area outlined by oval indicates Cr_xB_y compounds.

CONCLUSIONS

Joint strengths on the order of the ultimate tensile strength of annealed 430 SS demonstrate the feasibility of brazing monolithic SS 430 to SS porous-430L. The highest quality joints were obtained when brazing with a Ni-Cr-Si-B braze alloy (BNi-2) at 1175ºC for 1.8 ks specifically for the 254 µm-thick interlayer joints with SS surfaces polished to 1 µm. It is postulated that the latter variable assisted in the formation of nearly free segregation-formation and

outer-edge voids. For thick-interlayer brazes, this brazing condition prevented excess Cr depletion from the monolithic base metal to the braze alloy. Conversely, the SS 430/porous-430L joints brazed with the Ni-Cr-Si interlayers were the weakest joints in this study exhibiting extremely low strengths (19 to 125 MPa) under the different brazing conditions evaluated in this study. This weakness was particularly apparent when brazed with thick interlayers. Intermediate to relatively high strength (157 to 224 MPa) was exhibited by the SS 430/porous-430L brazes joined using the Ni-Cr-B braze alloy under the different brazing variables examined. Generally, the low-strength joints exhibited large unbrazed zones and the formation of detrimental secondary phases that provided sites where cracks originated and/or propagated.

ACKNOWLEDGEMENTS

The authors would like to thank Mr. Gerald Wynick, Dr. Herbert Giesche, Mr. James Thiebaud, and Mr. Stephen Galle at Alfred University for their technical assistance. The authors would also like to thank Drs. Brian Bischoff and Rod Judkins of ORNL for providing the porous stainless steel substrates. This work was supported by the U.S. Department of Energy, Office of Fossil Energy, Advanced Research and Technology Development Program. The Pacific Northwest National Laboratory (PNNL) is operated by Battelle Memorial Institute for the United states Department of Energy (U.S. DOE) under Contract DE-AC06-76RLO 1830.

REFERENCES

[1] Dr. Brian Bischoff, Oak Ridge National Laboratory (ORNL), Oak Ridge, TN, December, 2006, Private Communication.

[2] V. Malave, High Temperature Brazing of Monolithic 430 to Porous-430L Stainless Steel for Hydrogen Separation Applications, MS Thesis, Inamori School of Engineering at Alfred University, 2006.

[3] A. Sakamoto, Optimizing Processing Variables in High-Temperature Brazing with Nickel-Based Filler Metals, *Weld. J*, Vol 68, No 3, 1989, p 63-71.

[4] R. Johnson, TETIG Diagrams – A New Way to Optimise the Design Parameters and Heat Treatment of Joints Made in High Temperature Brazing Alloys, *Metall. Mater. Technol.*, Vol 14, No 12, 1989, p 559-565

[5] X.W. Wu, R.S. Chandel, H.P. Seow, and H. Li, Wide Clearance Brazing of Stainless Steel to Nickel-Based Superalloy, *J. Mater. Process Technol.*, Vol **113** No 1-3, 2001, p 215-221.

[6] E. Lugscheider and K.D. Partz, High Temperature Brazing of Stainless Steel with Nickel-Base Filler Metals BNi-2, BNi-5, and BNi-7, *Weld. J.,*Vol 62, No 2, 1983, p 160.s-164.s.

[7] L.J. Whims and D.A. Bales, United Technologies Corporation, *Materials Brazing*, U.S. Pat. No 5155326, 1990.

[8] D. Benjamin and C.W. Kirkpatrick, *Properties and Selection, Stainless Steels, Tool Materials, and Special Purpose Metals*, American Society for Metals, Metals Park, OH, 1980, p 5, 34-35, 195, 198.

[9] *NICROBRAZ Technical Data Sheet*, The Wall Colmonoy Corporation, Madison Heights, MI.

[10] G. Wynick, Alfred University, Alfred, NY, October, 2006, Private Communication.

[11] R. Johnson, The Use of TETIG Diagrams in High Temperature Brazing, *Weld. J.*, Vol 60, No 10, 1981, p 185.s-193.s.

[12] R. Johnson, Microstructural Aspects of Brazing Ferritic Steel with Two Ni-S-B Braze Filler Metals, *Weld. J.*, Vol 57, No 4, 1978, p 93.s-102.s .

[13] T. Tokunaga, K. Nishio, H. Ohtani, and M. Hasebe, Thermodynamic Assessment of the Ni-Si System by Incorporating Ab Initio Energetic Calculations into the CALPHAD Approach, *CALPHAD*, Vol 27, No 2, 2003, p 161-168.

[14] B. Grushko and B.Z. Weiss, Structure of Vacuum Brazed BNi-5 Joint of Inconel 718, *Metall. Trans. A*., Vol 15A, No 4, 1984, p 609-620.

GAS SENSORS FOR FOSSIL ENERGY APPLICATIONS

Timothy R. Armstrong
Oak Ridge National Laboratory, 1 Bethel Valley Road, Oak Ridge, TN 37831
E-mail: armstrongt@ornl.gov, Telephone: (865) 574-7996; Fax: (865) 241-0112

David L. West
Oak Ridge National Laboratory, 1 Bethel Valley Road, Oak Ridge, TN 37831
E-mail: westdl@ornl.gov, Telephone: (865) 576-2264; Fax: (865) 574-4357

Fred C. Montgomery
Oak Ridge National Laboratory, 1 Bethel Valley Road, Oak Ridge, TN 37831
E-mail: montgomeryfc@ornl.gov, Telephone: (865) 576-8808; Fax: (865) 576-3894

ABSTRACT

Recent advances in SO_x sensor development at The Oak Ridge National Laboratory have demonstrated that a simple, single material, electrochemical sensor can measure SO_2 concentration between 1 and 100 ppm at temperatures between 600 and 900°C. This new solid state sensor operates much like a mixed potential sensor and has been optimized to have no baseline drift, an issue that has plagued many solid state sensors. In our mixed potential sensor the difference in catalytic response between two different electrode materials provides a "differential electrode equilibria" (mixed potential sensor) to selectively measure SO_2. ORNL has developed a novel electrode design and configuration has led to the elimination of the baseline drift. Recent work has demonstrated that interferents such as CO, NO_2, and NO do not alter the sensor output. Future work will focus on the contribution of steam and oxygen to the sensor signal.

INTRODUCTION

Sulfur dioxide (SO_2) is produced by the combustion of sulfur-containing fuels such as coal. Although most of the SO_2 thus produced can be captured with limestone (or other techniques) good environmental stewardship demands that combustion exhausts be monitored for the release of this gas. It is important that SO_2 release be minimized because this compound will form sulfuric acid (H_2SO_4, the principal component of acid rain) when mixed with the O_2 and H_2O naturally present in the earth's environment as shown in Fig. 1.

Currently most SO_2 monitoring is done using ultraviolet (UV) fluorescence, a technique that offers excellent precision and selectivity but requires complex and expensive instrumentation. It also requires the gas to be cooled to near room temperature, thus introducing potential difficulties with condensation [1]. Hence attention has been focused on electrochemical sensors owing to their ease of fabrication, high sensitivity, rapid response, online monitoring and the feasibility for miniaturization [2,3]. In the last 5 years numerous approaches [4-20] to measure SO_2 concentrations in gas streams have been investigated. Most of these approaches have issues

limiting their development and deployment as functional SO_x sensors and none have resulted in a viable sensor.

In this research our objective is to develop compact and inexpensive SO_2 sensors that can operate at high temperatures (~700–900°C). Development of such a sensor would offer three advantages:

1. The need to cool the exhaust gas would be eliminated.
2. Operation closer to the combustion zone would be enabled.
3. The cost of the sensor would be reduced.

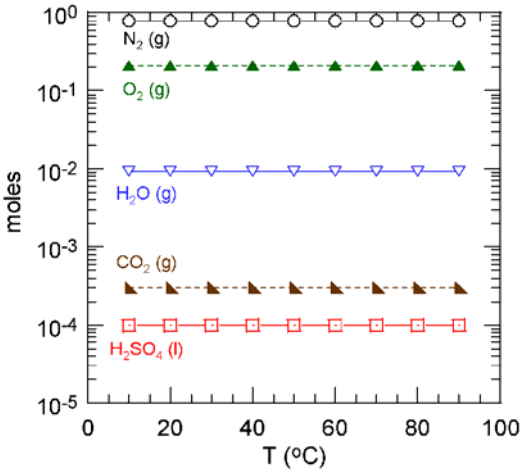

Figure 1: Predicted equilibrium species in a mixture of (in mol) 0.79 N_2, 0.21 O_2, 0.01 H_2O, and 1 x 10^{-4} SO_2. The sulfur is all present as sulfuric acid (H_2SO_4).

EXPERIMENTAL APPROACH

The most successful examples of compact and inexpensive sensors that operate at high temperature are the "lambda" O_2 and pumping-type NO_x sensors developed for transportation applications. Therefore our development efforts have been centered on similar materials and techniques for the detection of SO_2. In particular, we are developing SO_2 sensors that are based on yttria-stabilized zirconia ($Zr_{1-x}Y_xO_{2-2x}$ where x=0.16), an oxygen-ion conducting solid electrolyte that offers excellent stability at high temperature.

In FY 06 it was found that YSZ-based sensing elements with a reasonably simple geometry offered excellent response to SO_2 but addition of steam to the gas stream (as would be encountered in actual operation) led to unstable and non-reproducible behavior. The baseline drift and the effect of interferents such as hydrocarbons and carbon monoxide also needed to be characterized (and subsequently minimized). Therefore, at the onset of FY 07 our objectives were threefold in nature:

1. Develop alternative materials and/or operating conditions that enable stability in the presence of steam.
2. Characterize/minimize the baseline drift.
3. Characterize/minimize the response to interferents.

RESULTS AND DISCUSSION

Two steps were taken in order to improve the stability of the sensor elements in steam: One of the electrode materials was changed from a Mg-modified lanthanum chromite to a Sr-modified lanthanum manganite, and the operating temperature of the sensing element was increased from 750 to 800 °C. This resulted in the performance shown in Fig. 2. There it can be seen that water vapor does have a small effect on the sensor response to SO_2, but the presence of H_2O no longer affects the baseline as was the case previously.

"Drift" is often a problem with gas sensors and, as mentioned above, the drift behavior of these developmental SO_2 sensing elements was not well characterized at the beginning of FY 2007. Experiments early in the fiscal year showed that zero drift occurred in these sensors, as illustrated in Fig. 3. Two strategies have been employed to combat this drift, with the first being the introduction of a third electrode. As Fig. 4 shows, using this electrode as a "reference" reduces the drift significantly. We believe the reduced drift is a result of less net electromigration at the measuring electrodes (no current is passed through the reference electrode). The second strategy, a much more recent development than the first, is to adopt a sensing modality that does not involve application of an electrical stimulus to the sensing element. This modality has shown excellent response to SO_2 with minimal drift at about 600 ^oC and will be investigated further in the future if funding continues on this project.

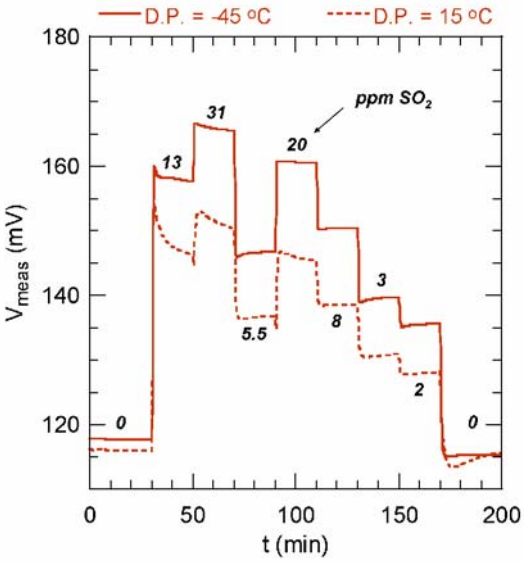

Figure 2: Sensing performance in "dry" (-45 ^oC dew point) and "wet" (15 ^oC dew point) gas. Data collected at 800 ^oC with 7 vol% O_2, balance N_2.

Since these sensing elements are designed to be operated in combustion exhausts, cross-sensitivity to interfering gases such as carbon monoxide and dioxide is a concern. To characterize this behavior, the sensing element of Fig. 4 was subjected to various interferents. The resulting data is shown in Fig. 5, and it can be seen there that the response to interferents is relatively small compared to the response to SO_2. (For example, referring to Fig. 5, 300 ppm of propylene (C_3H_6) induces about a 5% change in V_{meas}.) From Fig. 4, an order of magnitude smaller amount of SO_2 (~10 ppm) induces about a 5% change in V_{meas}. Therefore we consider these sensing elements to display minimal cross-sensitivity.

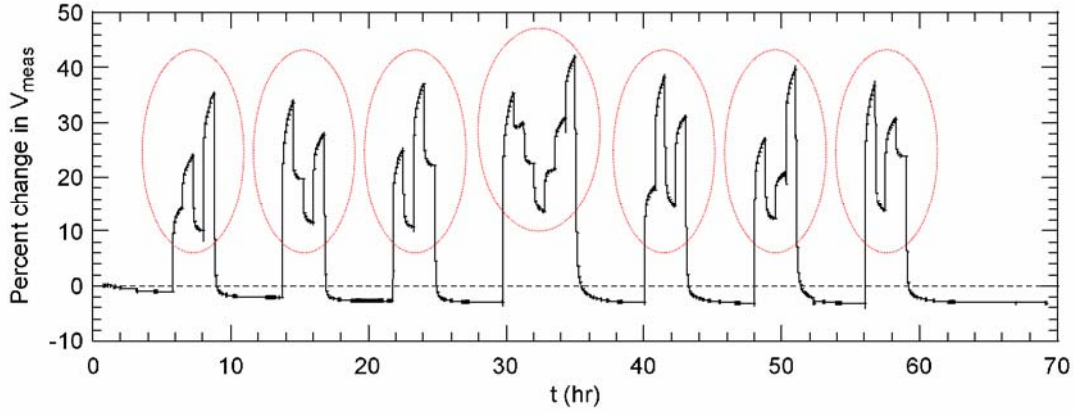

Figure 3: Drift of sensor response with a 2-electrode element configuration. The input SO_2 concentration was varied (in random order) between 2, 5.5, 13, and 31 ppm in the circled regions. T_{oper} = 900 ^oC with 7 vol% O_2, 1.2 vol% H_2O (~10 ^oC dew point), balance N_2.

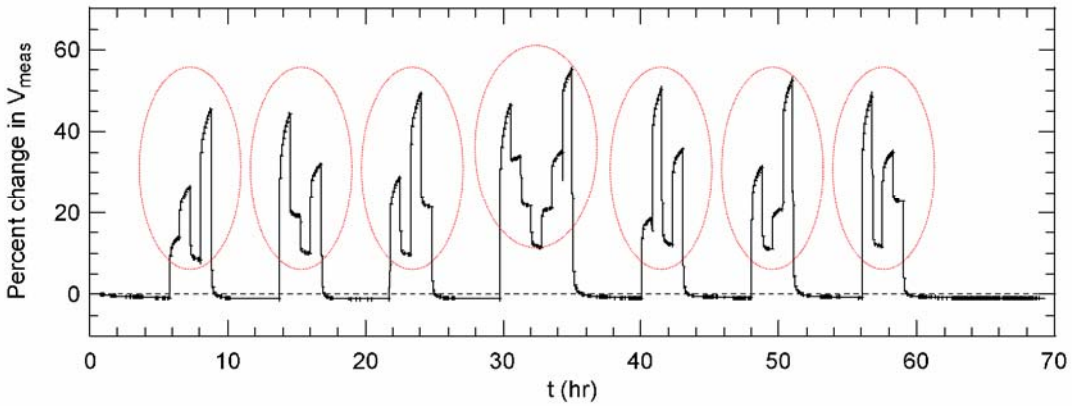

Figure 4: Drift of sensor response with a 3-electrode element configuration. The test regimen was identical to that used for the data in Fig. 3 above.

CONCLUSIONS AND PLANNED FUTURE WORK

We have been successful in developing compact SO_2 sensing elements that are capable of operation at elevated temperature (~800–900 ^oC). The response to SO_2 is strong and readily measurable for SO_2 levels in the 10 ppm range and the effects of potential interferents such as carbon monoxide are comparatively small.

The future work we have planned on this project (contingent on further funding) includes testing at higher steam levels, further studies of long-term stability, and incorporation of the sensing elements into prototype "off the shelf" sensors. We will also explore the different sensing modality mentioned above in the discussion of baseline drift.

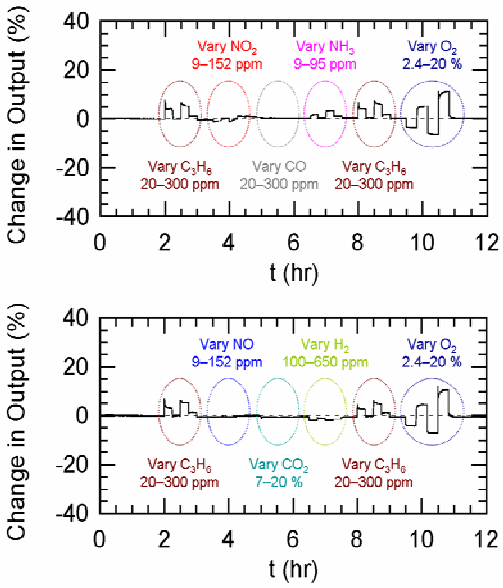

Figure 5: Response to various interfering gases. T_{oper} = 900 ^oC with 7 vol% O_2 (except where indicated), balance N_2.

ACKNOWLEDGEMENTS

The authors would like to thank B. Armstrong for assistance in sample preparation. Research sponsored by the Department of Energy's Fossil Energy Program. Oak Ridge National Laboratory (ORNL) is managed by UT-Battelle, LLC for the U. S. Department of Energy under Contract No. DE-AC05-00OR22725.

REFERENCES

1. J. Svitel, M. Stredansky, A. Pizzariello, S. Miertus, Electroanalysis 10 591-596 (1998).
2. U. Bilitewski and A. P. F. Turner Biosensors for environmental monitoring Harwood Academic Publishers, the Netherlands 2000.
3. K. S. Alber, J. A. Cox, P. J. Kulesza Electroanalysis 9 97-102 (1997).
4. L. Wang and R. V. Kumar, J. Electroanalytical Chemistry, **543** 190-114) (2003).
5. R. Moos, F. Rettig, A. Hurland, and C. Plog, Sensors and Actuators B, **93** 43-50 (2003).
6. C. Imawan, H. Steffes, F. Solzbacher, and E. Obermeier, Sensors and Actuators B, **78** 119-125 (2001).
7. R. Angelucci, A. Poggi, L. Dori, G. C. Cardinali, A. Parisini, A. tagliani, M. Mariasaldi, F. Cavani, Sensors and Actuators B, **74** 95-99 (1999).
8. 5. S. Suganuma, M. Watanabe, T. Kobayashi, S. Wakabayashi, Solid State Ionics, **126** 175-179 (1999).
9. J. L. Solis, V. Latto, Sensors and Actuators B, **48** 322-327 (1998).
10. D. R. Shankaran, and N. Uehera, and T. Kato, Sensors and Actuators B, **87** 442-447 (2002).
11. Sasaki, H. Tsuchiya,, M. Nishioka, M. Sadakata, and T. Okubu, Sensors and Actuators B, **86** 26-33 (2002).
12. D. Morris and R. G. Egdell, J. Mat. Chem., 11 3207-3210 (2001).
13. B. Min and S. Choi, Sensors and Actuators B, 93 209-213 (2003).
14. H. Li, and Q. Wang, J. Xu, W. Zhang, and L. Jin, Sensors and Actuators B, **87** 18-24 (2002).
15. R. Knake, P. Jacquinot, and P. C. Hauser, Analyst, **127** 114-118 (2002).
16. G. M. Kale, L. Wang, and Y. R. Hong, Solid State Ionics, **161** 15-163 (2003).
17. W. E. Hodgson, D. Pletcher, and S. Sotiropoulos, Sensors and Actuators B, **50** 181-185 (1998).
18. F. Berger, M. Fromm, A. Chambaudet, and R. Planade, Sensors and Actuators B, **45** 175-181 (1997).
19. M. Gautheir, A. Chamberland, A. Belanger, and M. Poirier, J. Electrochem. Soc. **124** 1584 (1977).
20. W. L. Worrell, and Q. Liu, J. Electrochem. Soc., **168** 355 (1984).

SESSION 5

BREAKTHROUGH CONCEPTS

NANOPRECIPITATES IN STEELS

Joachim H. Schneibel
Oak Ridge National Laboratory, P.O. Box 2008, Oak Ridge, TN 37831
E-mail: schneibeljh@ornl.gov; Telephone: (865) 576-4644; Fax: (865) 574-7659

Zhao Ping Lu*
Oak Ridge National Laboratory, P.O. Box 2008, Oak Ridge, TN 37831
E-mail: luzp@ornl.gov; Telephone: (865) 576-7196; Fax: (865) 574-7659

Sang Hoon Shim
Oak Ridge National Laboratory, P.O. Box 2008, Oak Ridge, TN 37831
E-mail: shims@ornl.gov; Telephone: (865) 576-7245; Fax: (865) 576-5413

ABSTRACT

The creep strength of ferritic steels is improved by high number densities of nano-scale dispersoids, such as in the oxide dispersion strengthened steels MA956, MA957, and PM2000. The oxide dispersoids in these steels contain Y and Al or Y and Ti. They can be as small as a few nanometers in size. Processing of such steels is traditionally carried out by mechanical alloying of a mixture of elemental or pre-alloyed powders together with Y_2O_3 powder. However, mechanical alloying is an energy-intensive process which is not readily scaled up. The goal of the present research is to identify alternative, more attractive ways of producing ultrafine strengthening dispersoids in steels. Internal oxidation, in which reactive elements contained in a metallic matrix are selectively oxidized may be one such way. Initial internal oxidation experiments were carried out with Fe-Ti-Y solid solution alloys and Fe-Ti-Y intermetallics. In one approach, the oxygen partial pressure was controlled with a mixture of Fe and Fe_2O_3 powders. In another approach, Fe-Ti-Y powders were mixed with an appropriate amount of Fe_2O_3 powder and annealed in vacuum in order to induce a displacement reaction. The size of the precipitates could be reduced by lowering the temperature at which the internal oxidation anneal occurred. With appropriate heat treatments, precipitates as small as 10 nm could be produced. The current work thus shows that internal oxidation has the potential to produce strengthening ultrafine dispersoids in steels.

INTRODUCTION

Based on a minimum rupture life of 100,000 hours at an applied stress of 100 MPa, the creep strength of ferritic steels used in coal-fired power plants is limited to a temperature of about 620°C [1]. At higher temperatures, the creep life of ferritic steels decreases precipitously. For example, increasing the temperature from 600 to 650°C reduces the creep life of the alloy HCM12A (Fe-11Cr-0.4Mo-2W-0.2V-0.05Nb-0.02Al-0.06N-0.1C, wt%) by a factor of 100 [2]. Higher service temperatures may be obtained with austenitic stainless steels (approximately 690°C) or nickel-base alloys (720°C and above) [1].

Oxide dispersion strengthened (ODS) steels produced by mechanical alloying followed by hot extrusion are creep- and oxidation-resistant at temperatures well in excess of the maximum temperatures possible for conventional alloys [3]. Klueh et al. showed that the high-temperature creep strength of ODS steels can

*Present address: State Key Laboratory for Advanced Metals and Materials, University of Science and Technology Beijing, E-mail: luzp@skl.ustb.edu.cn; Telephone: +86-10-82375387

substantially exceed that of a 9Cr ferritic steel [4]. Ferritic ODS steels contain high number densities of extremely small and stable dispersoids. Kim et al. [5] showed that Ti additions were critical for obtaining nanoclusters with sizes of a few nm in a Fe-12Cr-3W-0.4Ti-0.25Y_2O_3, wt% ("12YWT") ODS steel. Miller et al.'s [6] recent atom probe tomography of a 12YWT ODS steel showed titanium-, yttrium- and oxygen-enriched particles with diameters on the order of 2-3 nm and number densities on the order of $2\times10^{24}/m^3$. Annealing for 24 hour at 1300°C increased the particle diameters only by a factor of 3 indicating a high thermal stability. It does therefore not come as a surprise that ODS steels are considered for power plant parts such as heat exchanger pipes.

Although ODS steels have high creep strengths, several issues limit their widespread use [3]. The first issue is joining. ODS steels cannot be joined by fusion welding as this destroys the very microstructure giving them their unique properties. Less conventional joining techniques such as plasma-assisted pulsed diffusion bonding and transient liquid phase bonding have recently shown promise [3]. The second issue is the anisotropy in the mechanical properties of these materials. The third issue, which may be the most important, is their high production cost. High cost and the ensuing lack of market penetration are a major reason why Plansee GmbH Lechbruck, Germany, is discontinuing its PM2000 alloy.

Ferritic ODS alloys are fabricated by powder-metallurgical (PM) processing involving mechanical alloying of precursor metal or alloy powders with Y_2O_3 powder, followed by consolidation via hot extrusion. The mechanical alloying, which is carried out in a high-energy ball mill, is required to create a uniform dispersion of nanoscale dispersoids. This PM approach is a rather expensive process which is, in addition, difficult to scale up.

Arguably, the most widely used ODS alloy is GlidCop© copper*, which consists of a matrix of pure copper containing an ultrafine dispersion of Al_2O_3 particles ranging in size from 3 to 12 nm with an interparticle spacing of 30 to 100 nm and a particle density of 10^{22} to 10^{23} m^{-3} [7]. Interestingly, GlidCop© copper is not fabricated by mechanical alloying, but by internal oxidation of Cu-Al precursor powders. This suggests that it is worth exploring an internal oxidation route for the processing of ferritic steels. Compared with mechanical alloying, internal oxidation methods are likely to be more economical.

In the present work, preliminary results on the internal oxidation of Fe-Ti-Y solid solution alloys and intermetallics will be presented. While it is by no means clear at this time whether an internal oxidation route is a realistic alternative to the mechanical alloying of ferritic steels with Y_2O_3 powder we will show that it can produce nanoscale dispersoids with sizes as small as 10 nm.

*Formerly produced by SCM Metal Products, Inc., now produced by North American Höganäs High Alloys LLC.

EXPERIMENTAL PROCEDURE

Fe-Ti-Y alloys and intermetallics were arc-cast from elemental precursor materials in a partial pressure of argon, followed by annealing for 24 hours at 1000 or 1100°C in vacuum. Two approaches were employed for the internal oxidation of the Y and Ti to Y_2O_3, TiO_2, or $Ti_2Y_2O_7$. In one approach, the alloys were ground into powder, mixed with an amount of Fe_2O_3 sufficient to oxidize all the Ti and Y, cold compacted, and annealed in vacuum. The purpose of the vacuum anneal was to carry out the displacement reaction between the Fe_2O_3 and the Ti and Y to form (Ti,Y) oxides. In the second approach, coupons of the alloys were ground to a 600 grit SiC finish and encapsulated in an evacuated quartz tube containing a mixture of 0.5 g Fe and 0.5 g Fe_2O_3 ("Rhines pack"). The powder was placed in one end of the tube and separated from the alloy coupon by a constriction and a quartz wool barrier. The quartz tube was then placed in a furnace in order to accomplish the internal oxidation with the partial pressure defined by the Fe-Fe_2O_3 mixture which caused oxidation of the Ti and Y, but not the Fe.

The internally oxidized specimens were examined by optical and scanning electron microscopy (SEM) in the secondary electron (SE) and the backscattered electron (BSE) modes, as well as by X-ray diffraction. Internally oxidized coupons were ground and polished at a glancing angle with respect to the surface in order to increase the width of the internally oxidized zone from ~20-50 μm to ~1 mm. Hardness measurements were performed with a Nanoindenter XP (MTS Nano Instruments, Oak Ridge, TN) using a Berkovic tip. An indentation depth of 100 nm was chosen resulting in an edge length of the triangular impressions of approximately 750 nm. The hardness values were calculated from individual load-depth data using the standard Oliver-Pharr method [8].

EXPERIMENTAL RESULTS AND DISCUSSION

SOLID SOLUTION ALLOYS

An arc-cast alloy with the composition Fe-0.8Ti-0.4Y (at%) was annealed for 24 hours at 1000°C in vacuum, filed into powder, mixed with 2.1 wt% Fe_2O_3 powder, cold-pressed, and annealed for 24 h at 1000°C in vacuum. Figure 1 shows the (Ti,Y) oxide dispersoids present after the displacement reaction. The larger dispersoids have a diameter on the order of 1 μm, but smaller dispersoids with diameters on the order of 100 nm are also observed.

Not surprisingly, lower annealing temperatures resulted in smaller oxide particles. Figure 2 shows the oxide particles formed in Fe-0.8Ti-0.4Y after annealing for 4 days at 800°C with an Fe-Fe_2O_3 powder mixture. Annealing of a similar alloy at 700°C produces even smaller particles with diameters on the order of 50 nm (note that the scale markers in Figs. 2 and 3 are different).

In order to produce creep-resistant ODS alloys from Fe-based solid solution alloys, even finer dispersoids will have to be created by lowering the temperature of the internal oxidation anneals. The thermal stability of such small dispersoids is not known at this time. Also, it is not clear whether the Cr or Al needed for oxidation protection can be introduced directly as alloying elements, or whether they have to be added at a later stage during the powder processing.

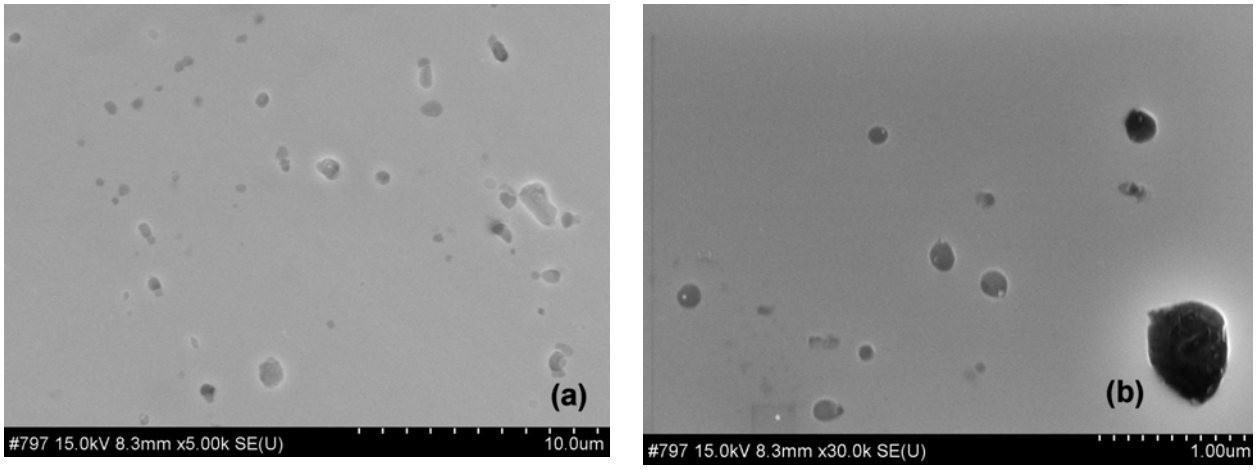

Fig. 1. SEM micrographs of Fe-0.8Ti-0.4Y (at%) after internal oxidation with Fe_2O_3 for 24 hours at 1000°C at (a) 5,000× and (b) 30,000× magnification.

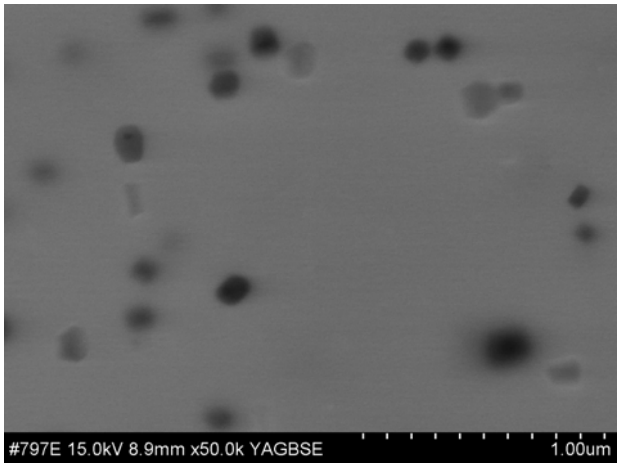

Fig. 2. Oxide particles in Fe-0.8Ti-0.4Y (at%) after internal oxidation for 4 days at 800°C.

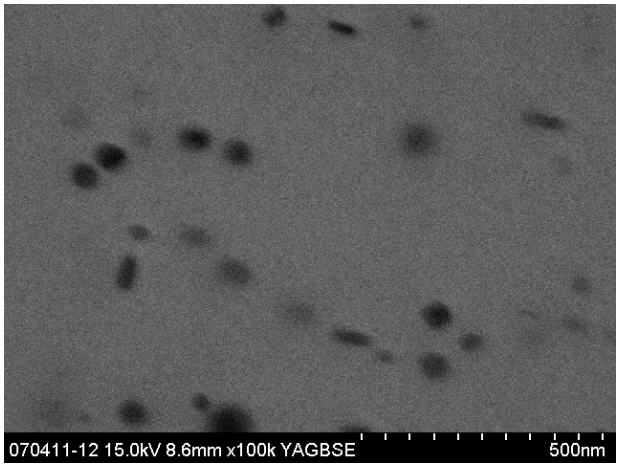

Fig. 3. Oxide particles in Fe-0.42Ti-0.18Y (at%) after internal oxidation for 6 days at 700°C.

INTERMETALLIC ALLOYS

An intermetallic ingot with the composition $Fe_{17}Y_2$ (Fe-10.5Y, at%) was ground into -325 mesh powder (<45 μm), blended with Fe_2O_3 powder to produce a 87.6 wt% $Fe_{17}Y_2$ – 12.4 wt% Fe_2O_3 mixture, and annealed for 1 day at 1000°C in vacuum. Figure 4 shows large (1 μm) particles, but much smaller particles are also visible.

Similarly, an ingot of $Fe_{11}Ti_1Y_1$ (Fe-7.7Ti-7.7Y, at%) was ground into -325 mesh powder, blended with Fe_2O_3 powder to produce a 81.8 wt% $Fe_{11}Ti_1Y_1$ – 18.2 wt% Fe_2O_3 mixture, and vacuum-annealed for 1 day at 1000°C. Fig. 5 shows the oxide particles which were identified to be $Y_2Ti_2O_7$ and Y_2O_3 by powder X-ray diffraction, see Fig. 6.

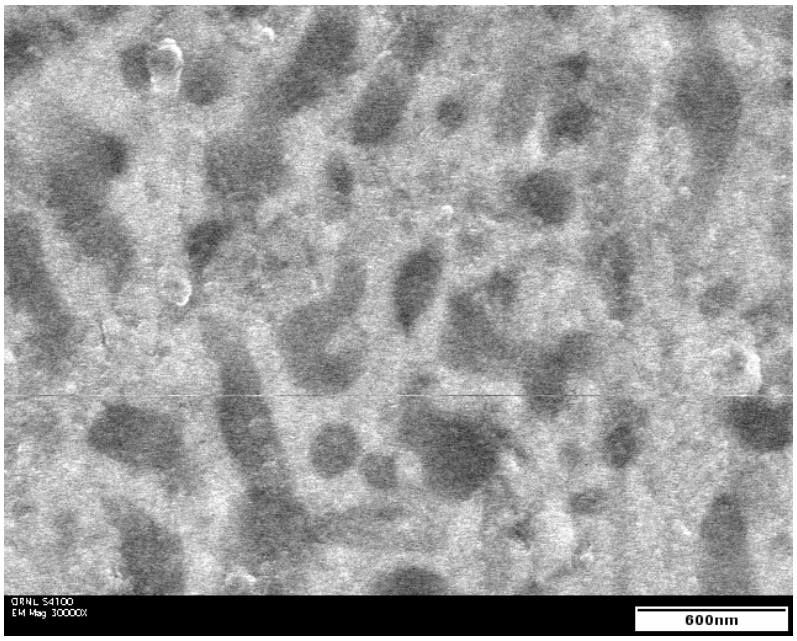

Fig. 5. SEM-BSE image of $Y_2Ti_2O_7$ and Y_2O_3 particles in $Fe_{11}Y_1Ti_1$ internally oxidized for 1 day at 1000°C

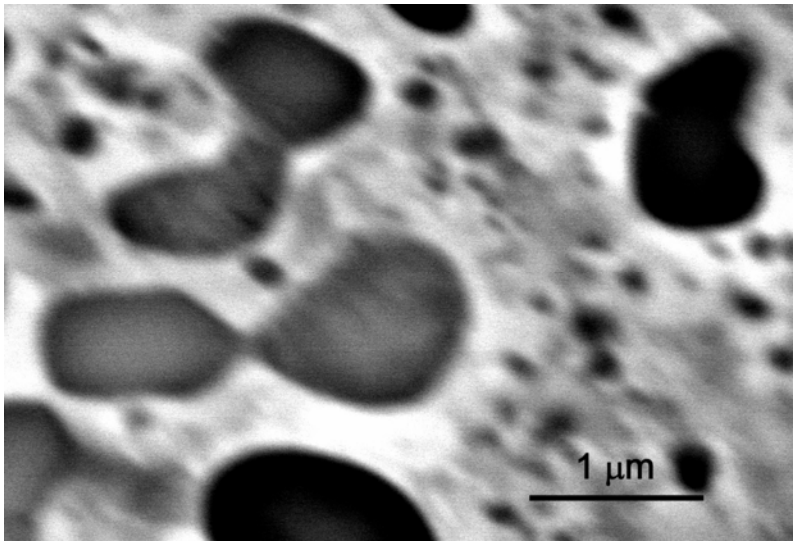

Fig. 4. SEM-BSE image of Y_2O_3 particles in $Fe_{17}Y_2$ internally oxidized for 1 day at 1000°C.

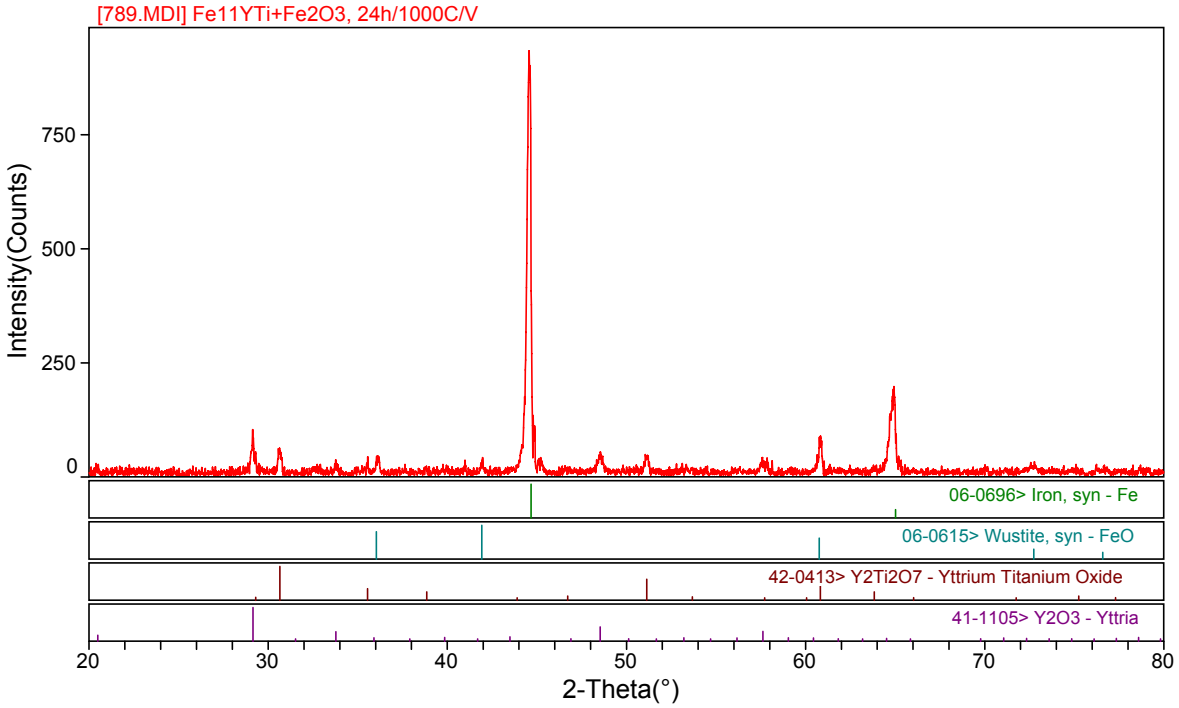

Fig. 6. Powder X-ray diffraction pattern of $Fe_{11}Y_1Ti_1$ after internal oxidation for 1 day at 1000°C.

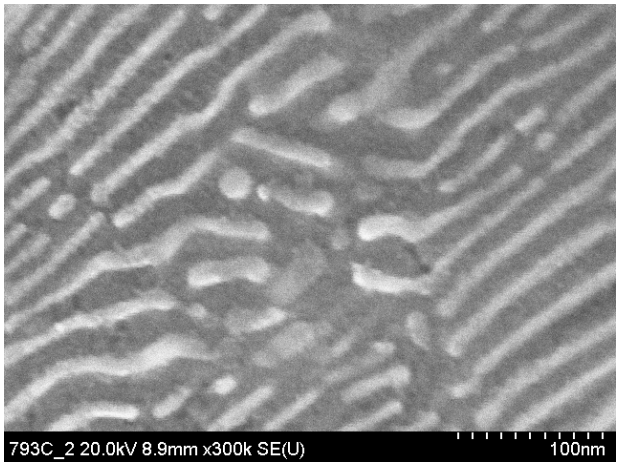

Fig. 7. Y_2O_3 lamellae (bright) produced by internal oxidation of $Fe_{17}Y_2$ with a Fe-Fe_2O_3 powder mixture for 3 days at 700°C.

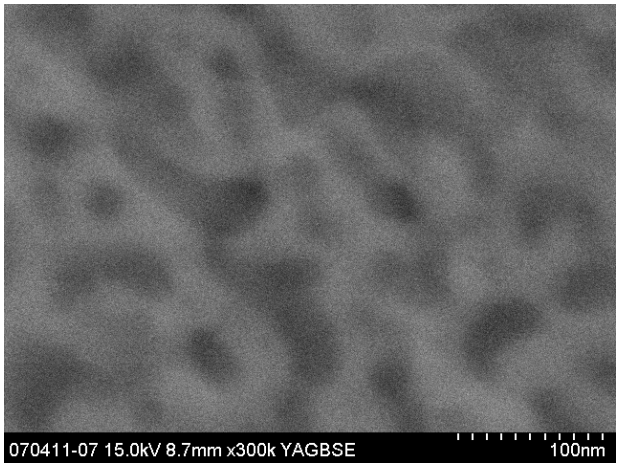

Fig. 8. Oxide particles (dark) produced by internal oxidation of Fe-6.5Ti-6.5Y (at%) with a Fe-Fe_2O_3 mixture for 3 days at 700°C.

Similar to the solid solution alloys, internal oxidation at reduced temperatures produces much finer oxide particles or lamellae as illustrated in Figs. 7 and 8.

Figure 9 shows hardness measurements for Fe-6.5Ti-6.5Y (at%) coupons which were internally oxidized with Fe-Fe_2O_3 for 3 days at 700°C and at 600°C, respectively. The figures show the hardness values of the internally oxidized layers and of the intermetallic, with an in-between transition zone. Since the stoichiometric composition of the intermetallic is $Fe_{11}Y_1Ti_1$ (Fe-7.7Ti-7.7Y, at%), the coupons contained the much softer Fe-Ti-Y solid solution as a second phase. Therefore, a fraction of the hardness measurements indicates soft material – the Fe-Ti-Y solid solution. This is the reason for the large scatter in Fig. 9. The hardness of the internally oxidized $Fe_{11}Y_1Ti_1$ phase itself is given by the upper bound of the hardness measurements in Fig. 9. The unoxidized $Fe_{11}Y_1Ti_1$ intermetallic is very hard – its hardness is on the order of 12-14 GPa. Internal oxidation for 3 days at 700°C produces oxide particles with sizes on the order of 20 nm (see Fig. 8). The corresponding hardness is on the order of 9 GPa [Fig. 9(a)]. Annealing for 3 days at 600°C is expected to result in a smaller particle size and thus higher hardness. Consistent with this, the maximum hardness of the internally oxidized zone in Fig. 9(b) is, with a value of approximately 11 GPa, distinctly higher than that produced by annealing at 700°C.While extremely fine oxide dispersoids or lamellae can be produced by internal oxidation of Fe-Ti-Y intermetallics, there are several issues that need to be addressed. First, since the high volume fractions of dispersoids are likely to degrade ductility and fracture toughness, ways to reduce this volume fraction need to be found. Second, it is not clear how and at what point the Cr or Al required for oxidation protection should be introduced. Third, the thermal stability of the dispersoids needs to be examined.

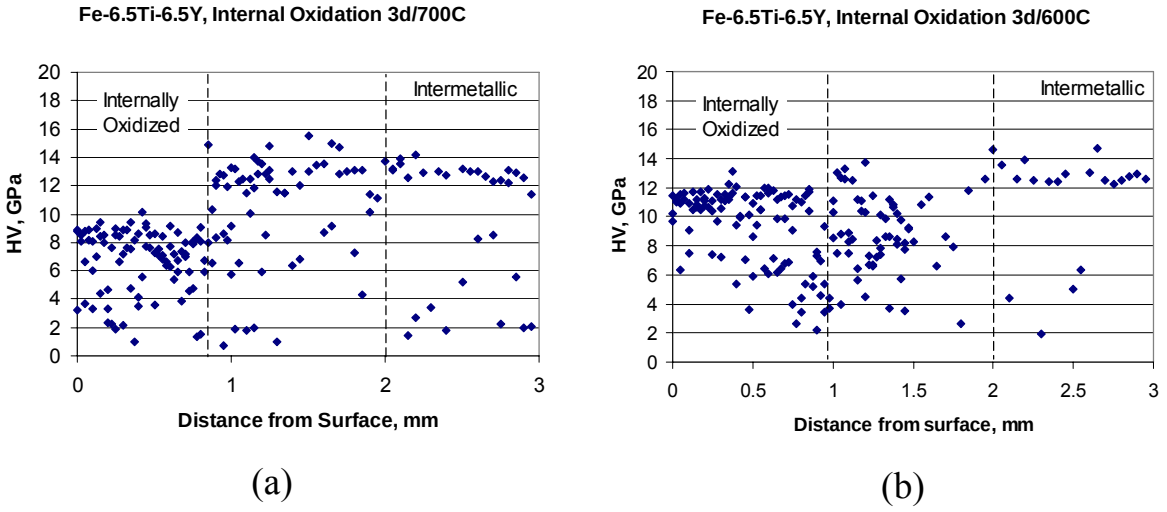

Figure 9. Hardness of Fe-6.5Ti-6.5Y after internal oxidation for 3 days at (a) 700°C and (b) 600°C. The actual thickness values of the internally oxidized layers were on the order of 20-50 μm.

Miller et al. have shown that the clusters in ODS steels are substoichiometric oxides with a composition roughly based on $(Ti_{1-x}Y_x)_1O_1$ [6]. Fu et al. [9] have performed calculations showing that vacancies are required to stabilize the clusters. These vacancies are presumably generated by the mechanical alloying. While it is unrealistic to expect high vacancy concentrations during internal oxidation anneals, it is interesting to note that Fe-Ti-Y intermetallics may contain substantial concentrations of structural vacancies. Revel et al. [10] claim that the Ti atoms in $Fe_{8.6}Ti_{1.1}Y$ are restricted to a single type of crystallographic site, but only half of this type of site is occupied by Ti. This suggests a vacancy defect structure. It is tempting to speculate that these vacancies might be exploited to stabilize the ultra-fine dispersoids formed during internal oxidation.

SUMMARY AND CONCLUSIONS

Internal oxidation experiments were carried out with Fe-Ti-Y solid solution alloys and Fe-Ti-Y intermetallics. With appropriate heat treatments, oxide particles as small as 10 nm could be produced. This shows that internal oxidation has the potential to produce ultrafine dispersoids. However, a number of issues still remain. First, the thermal stability of the dispersoids needs to be examined. Second, ways to introduce Cr or Al into the alloys have to be found. Third, while not only Fe-Ti-Y solid solutions, but also Fe-Ti-Y intermetallics are of interest, it remains to be seen whether the high volume fraction of dispersoids formed during internal oxidation of Fe-Ti-Y intermetallics can be sufficiently diluted to result in alloys with adequate fracture toughness and ductility.

ACKNOWLEDGEMENTS

This work was sponsored by the Office of Fossil Energy, Advanced Research Materials (ARM) Program, U.S. Department of Energy, under contract DE-AC05-00OR22725 with Oak Ridge National Laboratory managed by UT-Battelle, LLC. A portion of this research was conducted at the SHaRE User Facility, which is sponsored by the Office of Basic Energy Sciences, Division of Scientific User Facilities, U.S. Department of Energy.

REFERENCES

1. J. P. Shingledecker and I. G. Wright, Proceedings of the 8th Liege Conference on Materials for Advanced Power Engineering 2006, Forschungszentrum Jülich GmbH, Germany, 2006, pp. 107-120.
2. B. Nath, E. Metcalfe, and J. Hald, in "Microstructural Development and Stability in High Chromium Ferritic Power Plant Steels," A. Strang and D. J. Gooch, eds., The Institute of Materials, London, England, 1997, pp. 123-143.
3. I. G. Wright, N. S. Bornstein, E. Dyadko, and S. Dryepondt, in "Proceedings of the twentieth Annual Conference on Fossil Energy Materials," R. R. Judkins, ed., Oak Ridge National Laboratory Report ORNL/4741, Oak Ridge, TN, 2006, pp. 30-38.
4. R. L. Klueh, J. P. Shingledecker, R. W. Swindeman, and D. T. Hoelzer, J. Nuclear Materials 341 (2005) 103-114.
5. I.-S. Kim, B.-Y. Choi, C.-Y. Kang, T. Okuda, P. J. Maziasz, and K. Miyahara, ISIJ International 43 (2003) 1640-1646.
6. M. K. Miller, D. T. Hoelzer, E. A. Kenik, and K. F. Russell, Intermetallics 13 (2005) 387-392.
7. T. S. Srivatsan, N. Narendra and J. D. Troxell, Materials & Design 21[3] (2000) 191-198.
8. W. C. Oliver and G. M. Pharr, J. Mater. Res. 7 [6] (1992) 1564-1583.
9. C. L. Fu, M. Miller, M. Krcmar, D. Hoelzer, and C. T. Liu, TMS2007 136th Annual Meeting & Exhibition, February 25-March 1, 2007, Orlando, FL, USA, Abstract in Final Program, p. 27.
10. R. Revel, E. Tomey, J. L. Soubeyroux, and D. Fruchart, J. Alloys and Compounds 202 (1993) 57-61.

MECHANISMS OF IMPURITY EFFECT AND DUCTILITY ENHANCEMENT OF MO AND CR ALLOYS

N. Ma[1], B.R. Cooper [1], C.-Y. Feng[2], and B. S.-J. Kang[2]
[1]Physics Department
[2]Mechanical and Aerospace Engineering Department
West Virginia University
Morgantown, WV 26506

ABSTRACT

The objective of this research is to understand and minimize the impurity effect for room-temperature ductility improvement of Mo- and Cr-based alloys by the inclusion of suitable metal oxide dispersions. Mo- and Cr-based alloys are brittle at room temperature due to oxygen and nitrogen embrittlement, respectively. Past research showed that suitable amount of MgO or $MgAl_2O_4$ dispersion can improve the room temperature tensile ductility of Cr or Mo alloys. However, the experimental results showed inconsistent room-temperature ductility behavior with alloys under similar composition and processing conditions. The purpose of this research is (i) to identify the mechanisms responsible for the impurity embrittling and to tailor ductility enhancement based on fundamental atomistic electronic structure analysis, which will guide the selection of suitable nano-sized metal oxides to be incorporated in the Mo or Cr alloys to achieve the desirable room-temperature ductility, and (ii) to further develop a micro-indentation technique suitable for in-situ mechanical property measurement and ductile/brittle evaluation.

On the first research task, using *ab-initio* FP-LMTO techniques, we investigate the electronic structures of Mo and Cr, with possible embrittling impurities (nitrogen or oxygen) and with or without MgO layers. The corresponding electronic structures and chemical bonds near the surface boundaries are calculated. Based on these results and by extending the Rice's criterion, we propose several hypotheses to explain the mechanism of impurity effect and ductility enhancement of Mo and Cr alloys. In addition, we developed *ab-initio* database for more efficient tight-binding schemes. Such schemes are suitable to study some of the dynamic effects, such as impurity gettering and defects transport, that are pertinent to the ductility enhancement mechanism. We also conduct large scale simulations (10^4-10^5 atoms) for the purpose of understanding the qualitative effect of varying the dispersion particle sizes.

On the second research task, we have further developed and refined a micro-indentation technique suitable for in-situ material mechanical properties and ductility/brittle evaluation of small-size sample alloys. Theoretical background, experimental verification, and some preliminary test results are presented.

INTRODUCTION

Due to their ultra-high working temperature (>1000^{o}C) and excellent oxidation and corrosion resistance, a number of Cr and Mo based alloys are being developed as the next generation structural

materials for fossil energy applications. However, a severe drawback with these material systems is the limited room-temperature ductility. It has been known that certain species of trace elements, including nitrogen (N) and oxygen (O), can cause embrittlement of Cr and Mo alloys, respectively. For example, the ductile-to-brittle transition temperature (DBTT) of pure Cr (with less than 0.0001 atomic pct of N) is within the ambient temperature range, while that of unalloyed recrystallized Cr with commercial purity is approximately 150^{o}C in tension [1]. There have been numerous studies concerning improving the ductility of Cr- and Mo-based alloys at ambient temperature. In order to stabilize or remove the interstitial impurities, scavenging elements, such as tungsten, molybdenum, and rhenium were alloyed with Cr resulting in increased ductility [2]. Another route was demonstrated by Brady *et.al*. [3] that suitable amount of MgO dispersion improves the room temperature tensile ductility of Cr by 10-20%. Based on microstructural analysis with TEM imaging techniques, they found the oxide dispersions attracted the detrimental agents (notably N and S) to precipitate near the oxide-metal interface. Therefore, detrimental impurity management mechanism (i.e., by preventing the detrimental impurities from segregating to the Cr grain boundaries) has been invoked to explain the ductility enhancement. Interestingly, similar microstructures were discovered in their later experiments using La_2O_3, TiO_2 and Y_2O_3 as dispersions, but none displayed any ductility enhancement. This indicates that other factors, perhaps hiding at deeper levels below the microstructures, are contributing to the Cr's ductility enhancement.

This research contains two research tasks: (i) to conduct atomistic computational modeling and simulations on the study of impurity embrittlement and metal oxides ductility enhancement mechanism in Mo and Cr alloys, and (ii) to continue the development of a micro-indentation technique suitable for in-situ material mechanical property measurement and ductile/brittle characterization of the various small-size Mo and Cr alloys studied in this
research project.

TASK 1: ATOMISTIC MODELING AND SIMULATION

The classic theory of Griffith [1, 4] demonstrates that brittle fracture will occur when the hosting material can stably sustain an atomically sharp crack in the lattice without breakdown by dislocation generation. Therefore, the characteristic failure mode of a material depends on the relative easiness of creating new surfaces compared with forming and emitting dislocations. Based on this theory, Rice [5] proposed a criterion to quantitatively measure the tendency of a material to be brittle or ductile in terms of the ratio of the energies for surface and dislocation formation. In practice, however, this criterion has limited applications because a system's total energies can be affected by many other non-relevant factors, which makes it difficult to obtain the relevant energetics for the ideal cleavage and stacking fault configurations, due to the lack of *ab-initio* knowledge of the rich variety of interactions among the imperfections within the system, including impurities, dislocations, cracks, and grain boundaries at quite different length scales. At the basic fundamental level, the mechanisms responsible for the impurity and addictive effects are still largely unknown.

In this work, we attempt to extend the Rice's criterion and proposed several hypotheses that enable us to conveniently study the impurity effect on material ductility. These new hypotheses are based on the

properties of the valence electrons that participate in forming chemical bonds between atoms in solids. The knowledge of the valence electrons will then translate into that of the chemical bonds, and hence their ductile or brittle mechanical properties through Rice's criterion. Comparing to the energetics approach, the one based on electronic structure analysis will provide a more comprehensive understanding of the mechanisms from a deeper level, yet it involves standard techniques that are readily available with many electronic structure software packages. These hypotheses not only help us to understand the material's mechanic properties from a deeper and more fundamental level, but also serve as a basis to guide the selection of suitable nano-size metal oxides to be incorporated in the Mo or Cr alloys to achieve the desirable room-temperature ductility and to form the strategy for a systematic approach to enhance the material's properties for better performance.

In the following sections, we shall first present these hypotheses starting from the Rice's criterion, followed by our results of electronic structure analysis on Cr- and Mo-based alloy systems, where we will explain in detail about the impurity embrittlement and the observed ductility enhancement with the inclusion of MgO spinel, as demonstrated in Brady's experiments [3]. We conclude with discussions and a brief future work plan.

The Extensions Of Rice's Criterion

In transitional metal such as Cr and Mo, atoms are bonded by sharing their valence electrons. The Rice criterion suggests that if it costs less energy to assume a stacking fault configuration than to break the bonds, the material would be ductile. The stacking fault state creates layers of misaligned atoms, in which the chemical bonds between layers need to be stretched and distorted. To make this configuration energetically more favorable than the cleavage (bonds broken state), we anticipate that the electrons making up these bonds need to be delocalized and mobile so that they can easily follow the misaligned ions and refill the voids to preserve the bonds. To assess the mobility of the valence electrons near the Fermi level, we analyzed the following electronic properties:

(a) Electronic Charge Distribution (Real Space Distribution)

A more globally shared (delocalized) electron state is easier to reshape and adapt to the ionic displacement (like the stacking faults) than a localized state. In a Full potential linear muffin-tin orbital (FP-LMTO) calculation, the electronic charge is partitioned into muffin-tin (MT) spheres and interstitial areas. Charge in interstitial area is considered as being shared by ions, which contributes to ductile chemical bonds. Charge in the MT spheres may still be considered delocalized and beneficial to ductility if it is uniformly shared by many different MT spheres. To distinguish between localized and delocalized charge in the latter case, we calculate the variance of its population distribution among all MT spheres, and the smaller variance indicate better sharing. The results of this analysis are provided in Section 2.2.1. The extent of localization for a given electronic state may also be measured by entropy, defined as $S = \exp (- \Sigma n_i \log n_i)$, where n_i is the partition of the charge on the ith atomic site. States with larger entropy are more mixed in space, and therefore more delocalized. This method is used in our larger scale molecular dynamic simulations in Section 2.2.4.

(b)Density of States (Energy Space Distribution)

The Density of States (DOS) provides another measure of mobility across the Fermi level. Due to

Pauli's exclusive principle, most of electrons are frozen in the low lying energy levels, while a small population of electrons immediately below the Fermi level may be excited into the empty orbitals (conduction bands) above the Fermi level. Electronic states in conduction bands are generally more delocalized and mobile. Therefore, the shape of DOS near the Fermi level can provide useful information for the characterization of chemical bonds and their mechanical properties. The results of this analysis are shown in Section 2.2.2.

(c) Angluar Momentum Projected Population (Angular Momentum Space Distribution)

Chemical bonds formed by ***s*** electrons tend to be more flexible than those formed by ***d*** electrons. This is because the distribution of ***s*** electron has rotational symmetry, and the unstable stacking fault configuration may be assumed with the rotation and stretch of the bonds which costs little energy. In this case, the bonds are metallic and ductile. In contrast, chemical bonds formed by ***d*** electrons are strongly angular dependent. Any changes in the preferred bonding direction result in large energy penalty. Therefore the characteristics of the chemical bonds are more covalent-like, and brittle. By comparing the population of occupied angular channels, we may predict the ductile/brittle properties of the materials. The results of this analysis are shown in Section 2.2.3.

TASK I: RESULTS AND DISCUSSION

As shown in Figure 1, to study the mechanisms of the impurity and addictives effects, we considered the following two model systems; (a) 1 x 1 x 3 Cr/Mo supercell containing one nitrogen/oxygen impurity at the center (Figure 1a), and (b) 1 x 1 x 3 Cr/Mo supercell interfaced with 6 stacks of MgO layers, with nitrogen/ oxygen impurities near the interface (Figure 1b)

Between these models, system (a) represents the impurity embrittled metal, while system (b) represents the ductility enhancement due to the inclusion of MgO. FP-LMTO techniques [6], which accurately treat the muffin-tin's interstitial region, have been used to calculate the electronic structures for the above systems. A three-kappa linked base is used to expand the muffin-tin tail functions. The energies for these bases are set to be -0.9, 0.3, and 1.2, respectively. Iterations are repeated until a convergence of 10^{-5} rydberg is achieved, after which the electronic charge density and DOS are obtained and analyzed.

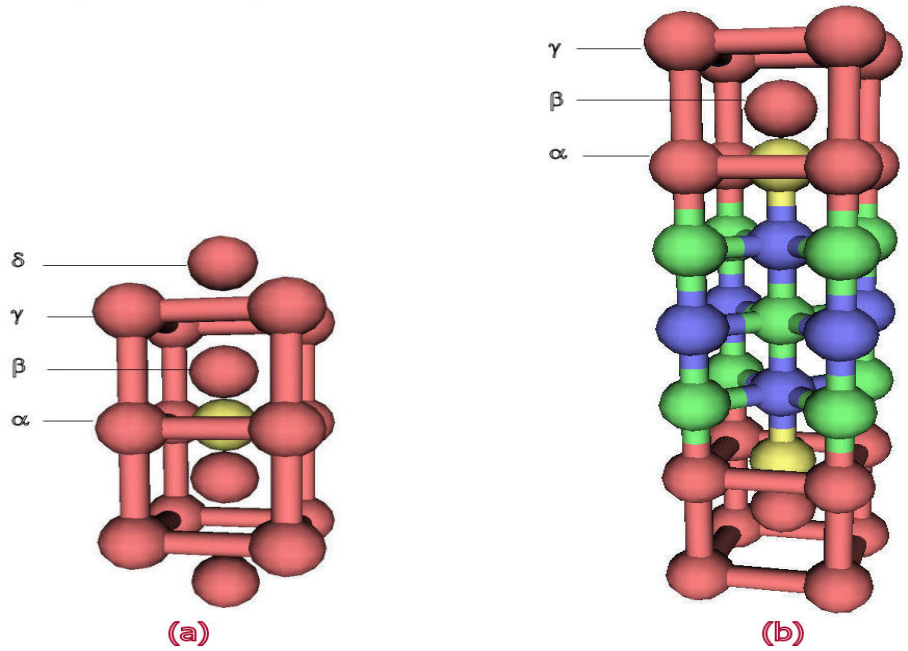

Figure 1. The schemes of the simulated systems: (a) a 1x1x3 Cr or Mo supercell (redspheres) containing a nitrogen or oxygen impurity (yellow sphere) at the center; (b) a 1x1x3 Cr or Mo supercell (top and bottom parts) interfaced with 6 stacks (figure only show 3 for simplicity) of MgO layers (center part, Mg and O atoms are represented by blue and green spheres, respectively), with two nitrogen or oxygen impurities (yellow spheres) near the interface.

Electronic Charge Distribution

The charge distribution of a given electronic state gives one some idea about how localized or delocalized an electron is. As discussed in Section 2.1, the distribution of a delocalized electron is easy to deform so as to preserve the chemical bonds should ions be misaligned. Therefore delocalized electrons contribute to the system's ductility. In FP-LMTO calculations, the charge distribution is conveniently partitioned into interstitial regions and muffin-tin spheres.

Table 1. The overall proportion of interstitial charge in Cr alloys.

	System (a)	System (b)
Proportion of interstitial charge	14%	16%

Table 2. The overall proportion of interstitial charge in Mo alloys.

	System (a)	System (b)
Proportion of interstitial charge	27%	35%

The Interstitial charge is shared by ions in system. Thus, they contribute the most to the ductile bonds. Tables 1 and 2 give the overall proportion of interstitial charge for electronic states within 0.1Ryd.

across the Fermi level. In both tables, the impurity embrittled system has lower proportion of charge in the interstitial than the ductility enhanced system.

The muffin-tin (MT) charge is distributed among the different MT spheres. Compared to the interstitial charge, it is more localized to ions. However, if a given electronic state has a uniform distribution among the MTs, it is still considered as being shared, and helps to "glue" the system together. Tables 3 and 4 show the average variance of MT charge distribution for electronic states within 0.1Ryd. across the Fermi level. In both tables, the system (b), with MgO layers, has lower variance, indicating the charge is shared more uniformly among the muffin-tins. This is in consistent with the system's ductile behavior. Therefore, we conclude that the delocalized and uniformly distributed electrons tend to form ductile bonds that resist to cleavage.

Table 3. The average variance of MT charge distribution in Cr alloys.

	System (a)	System (b)
average σ^2	0.0139	0.0124

Table 4. The average variance of MT charge distribution in Mo alloys.

	System (a)	System (b)
average σ^2	0.0120	0.0039

Density Of States (DOS)

In Figure 2 and Figure 3 we present the results of DOS calculations for the Cr and Mo alloys systems, respectively. Both figures show enhanced DOS for Cr/Mo atoms near the impurity. A very distinctive feature is that the majority of DOS curves cross the Fermi line at their minima in system (a) while those crosses at maxima in system (b). Due to Pauli's exclusion principle, the electrons will first occupy the levels below the Fermi line and leave those above Fermi line mostly unoccupied. The states corresponding to the unoccupied levels are less crowded and usually more mobile. As mentioned in Section 2.1, the mobile electrons are easy to deform and are beneficial to the ductility property. Thus, for systems with larger DOS at Fermi level (whose DOS crosses Fermi line at maxima), electrons will be easier to cross the Fermi line and assume such a mobile state, and consequently the system is ductile, and vice versa. This further explains the impurity embrittlement and ductility enhancement effects.

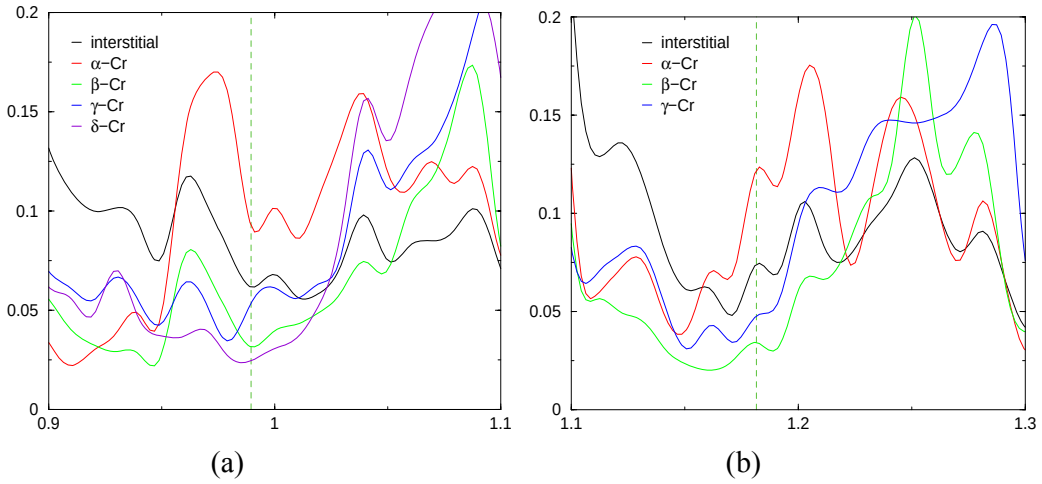

Figure 2: The DOS for Cr alloys.

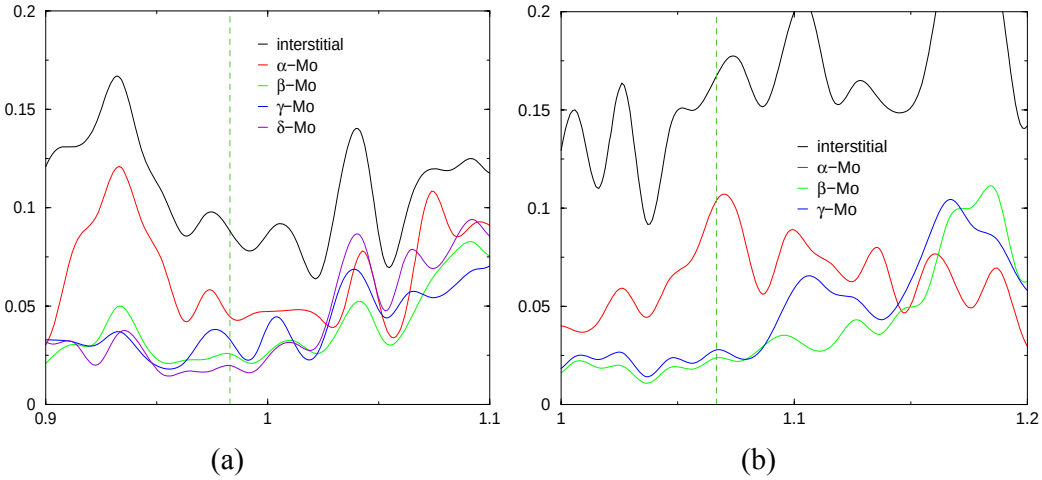

Figure 3. The DOS for Mo alloys

.

Angular Momentum Projected Population

The total charge population in both ***4s*** and ***3d*** angular momentum channels is determined for Cr in brittle and ductile systems, and the results are tabulated in Table 5. Comparing the columns, we find that both ***s*** and ***d*** channel charge population is increased due to the inclusion of MgO. Evidentially, the bond strength is enhanced. In addition, the increase of population in ***s*** channel is more prominent, and the ***s*** to ***d*** population ratio is also increased from 5.8% to 6.7%. Electrons in ***s*** angular momentum channel are isotropic in space. Correspondingly, bonds formed by ***s***-electrons behave more like metallic bonds. On the other hand, bonds formed by ***d***-electrons have strong directional preferences, which behave more like covalent bonds. The fact that metallic bonds render ductility and covalent bonds cause brittleness can be understood through Rice's criterion. In systems where metallic bonds dominant, the uniformly shared electrons are more tolerant with stacking faults; whereas in covalent materials, dislocation flow usually means breaking and reconnecting bonds with significant higher energy barrier. Assuming an equal energy cost to create

new surfaces by cleavage, the Rice ratio (γ_{us}/γ_0) is then higher in metallic systems than in covalent systems. Therefore, the ratio of ***s*** and ***d*** channel population is an indicative of whether the material shall display brittle or ductile behavior. By changing the balance of ***s*** and ***d*** channel charge population, MgO helps to improve Cr's mechanic properties.

Table 5. Calculated charge population in s and d channels (Cr alloy).

	System (a)	System (b)
s-channel	1.306	1.596
d-channel	22.503	23.738
Ratio ***s***/***d*** (%)	5.8%	6.7%

Molecular Dynamics Simulations

Using an *ab-initio* tight-binding electronic package called FIREBALL^{TM} [7], we were able to extend the simulated system to a much larger scale, and carry out the molecular dynamics simulations to watch the system's evolution with time. FIREBALL^{TM} is based on the density functional theory (DFT), and thus has the inherited accuracy comparable to other *ab-initio* methods. However, the computing time is significantly reduced because the Hamiltonian matrix elements have been expanded into one-, two-, and three-center integrals that are pre-computed into database for later interpolation. The many-body exchange-correlation potential and energy are treated similarly using a combined multi-center expansion [8] and linearization approximation approach. This scheme makes FIREBALL^{TM} particularly efficient and capable of simulating larger scale systems such as nanostructures and DNAs.

Molecular dynamics simulations are carried out for Cr and Mo systems with the inclusion of MgO or spinel phase. In each of the systems, an impurity atom (N for Cr and O for Mo) is initially placed within the metal matrix. We then let the system freely involve at constant temperature (set as 600^{o}K), and watch the dynamics of the impurity atom. Figure 4 shows the initial and final configurations of Cr/MgO system after 1000 simulation steps (~1ps). The nitrogen impurity (marked as the orange sphere) was seen to gradually diffuse from the metal matrix to the metal/metal-oxide interfacial boundaries. This result is consistent with Brady's experiments, where they found the MgO tends to cause precipitations of N near the interface rather than actual getter of N as proposed by Schruggs who originally discovered the ductility enhancement effect [3]. Similar results have been found in the Cr/spinel system. In contrast, the Mo/MgO and Mo/spinel systems do not exhibit any oxygen diffusion. Therefore, alternative explanations of the observed ductility enhancement may be needed. Schneibel [9] has argued that grain size control among other issues is more important in affecting the mechanical properties for Mo-based systems. On the other hand, the inclusion of some other metal oxides is found to have impurity precipitation effects in Cr-based alloys however without any ductility improvement. This suggests the complexity of the problem, and necessary further investigations that are currently in progress.

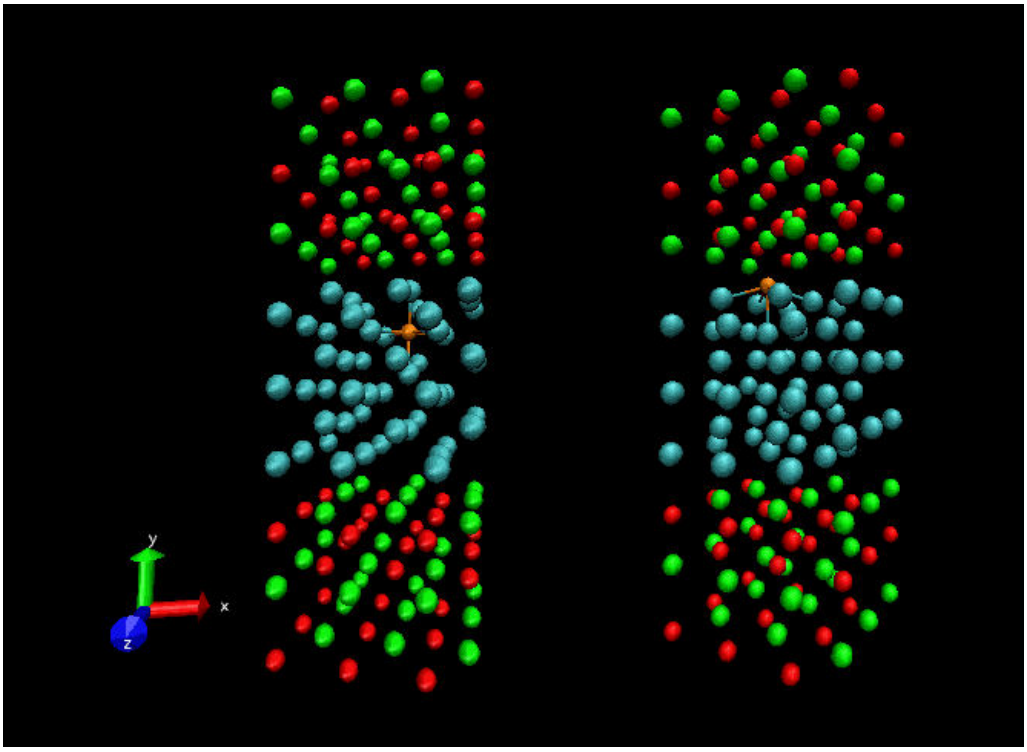

Figure 4: The diffusion of N in Cr/MgO system. Blue, green, red, and orange spheres represent, respectively, the Cr, Mg, O, and N species. The temperature is 600°K. Shown on the left is the initial system configuration, where the nitrogen impurity is placed inside the Cr matrix. The final system configuration after 1000 simulation steps (1ps) is shown on the right. The diffusion length is about 0.2 nm.

To understand how the position of impurity may affect the system's mechanic properties, we carried out the electronic structure analysis on both the initial and final configurations as shown in Figure 4. DOS and entropy have been computed for each electronic state near the Fermi level, and are presented in Figure 5. As explained in Section 2.1, DOS measures the mobility of the electrons while entropy depicts the overall spreading of charge in space. The total number of states within +/-1eV of the Fermi level is found to be 73 in the initial state and 76 in the final state. The average entropy for these states is 81.4 in the initial state and 83.9 in the final state, respectively. Evidentially, the diffusion of nitrogen atom indeed promotes both the mobility and uniform space distribution of the charge within the system. According to our criteria, the ductility should increase in the final state. This explains the ductility enhancement effects observed in Brady's experiments.

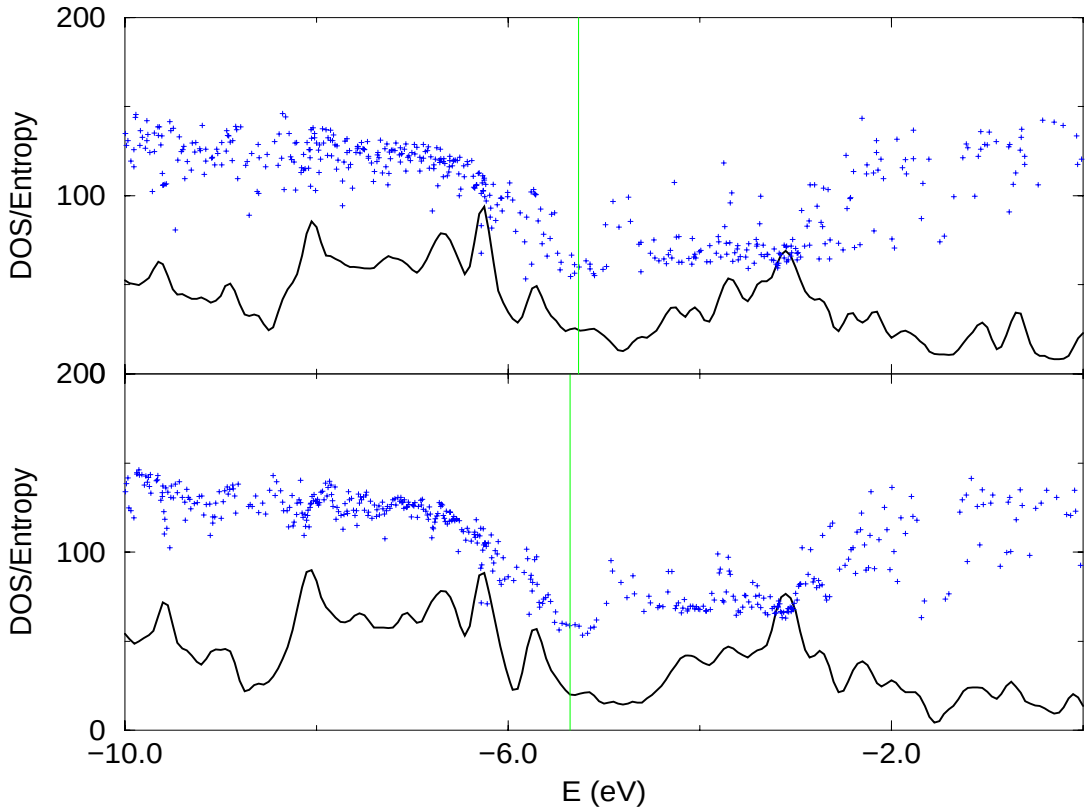

Figure 5. The computed density of state (black solid line) and entropy (blue pluses) plots for the initial (upper panel) and final (lower panel) configurations in Figure 4. The green vertical line represents the Fermi surface.

TASK I: CONCLUSIONS

Through atomistic modeling using FP-LMTO techniques, we obtained and compared the electronic structures of selected Cr/Mo systems containing N/O impurities and/or MgO layers. Several microscopic criteria have been identified to connect with material's ductile/brittle property. These include the extent of delocalization of the electronic state, the shape of the DOS curves near the Fermi level, and the angular momentum projected population. These criteria are shown to be in consistency with the Rice's criterion based on energetic arguments. Based on these criteria, we explained the impurity embrittlement and ductility enhancement effects due to N/O and MgO. These criteria are then used in larger scale (nano-scale) simulations to study other metal oxide dispersions as well as their size effects.

In-Situ Material Mechanical Property Measurement and Ductile/Brittle Characterization

In new alloys development using vacuum hot-pressed process such as the Mo and Cr alloys, many sample alloys are developed and needed to be tested for mechanical property evaluation. Current practice requires to prepare test specimen (with sufficient specimen size) in order to conduct tensile test to obtain the material Young's modulus and stress/strain curve. It would be advantageous to

develop a suitable material testing technique that is capable of obtaining mechanical properties and ductile/brittle evaluation on small-size (i.e. mm-size, such as 6 mm diameter and 6 mm long) sample alloys, this will greatly facilitate new alloys development. In this research task, a simple micro-indentation technique is developed to meet this goal.

Background

In material nano- and micro-indentation research, among all the indentation parameters, load-depth relation and unloading characteristics have been studied extensively either experimentally or numerically to elucidate the relevant mechanical behavior or properties. For example, it is well accepted to use the initial unloading stiffness of the load-depth curve to determine the material's Young's modulus [10-14]. This approach can be traced back to Sneddon's [10] classical elastic indentation solutions which describe the general relationship among the load, displacement and contact area for any punch that can be treated as a solid of revolution of a smooth function. In the 1970s, Bulychev and co-workers [11] defined the initial unloading slope and reduced modulus, thus providing a theoretically sound methodology for determining the Young's modulus. This method is applicable to both spherical and pyramidal indenters. Using instrumented indentations, Doerner and Nix [12] further investigated the unloading characteristics. In 1992, Oliver and Pharr [13] showed that Bulychev's technique can be applied to any indenter that can be described as a body of revolution of a smooth function.

In the indentation research for Young's modulus measurement, the contact area and initial unloading stiffness are the key parameters to be determined. However, in most cases, direct measurement of the contact area is not applicable or not possible. Typically, the unloading stiffness is used to estimate the contact area through some iterative algorithm [14-16]. Furthermore, high-precision displacement sensors are needed in order to accurately obtain load-depth curve and the unloading stiffness data [11-13]. As for the direct measurement of contact area, Kleesattel [17] designed a special apparatus for direct measurement of the contact region through a spherical sapphire indenter while conducting indentation tests, but the scanning method yields only one line of the contact region, and real-time access of the indented surface is not possible. By applying a special lighting technique, Frank [18] developed a transpyramidal indentation viewing system. It was also implemented by Sakaia et al [19] using a similar technique. Recently, with the support from the DOE/NETL Advanced Research Materials (ARM) Program, we have developed a Transparent Indenter Measurement (TIM) technique [20-23]. By integrating a Twyman-Green type interferometer into the spherical transparent indenter head, the TIM system can directly measure the indentation-induced out-of-plane deformation as well as the indented surface. It was found that by using the difference of out-of-plane deformation, Young's modulus can be evaluated without unloading stiffness measurement. Recently, a similar TIM approach was also done by Miyajima and Sakia [24] using sapphire spherical indenters on Aluminum and Zirconium oxide materials.

In this research, based on the experience learned from the research and development of the TIM technique, we have further developed a simple multiple partial unloading micro-indentation method for material's Young's modulus measurement. Experimental validation tests of several metallic alloys and related theoretical discussions are presented.

Multiple Partial Unloading Micro-Indentation Experimental Setup

Figure 6 shows the schematic of a simple indentation system. As shown, a spherical indenter assembly is attached to one end of the load cell, which is then attached to a PZT actuator. The PZT actuator serves as both loading apparatus and displacement sensing device. For the research work done in this paper, 1.5 mm diameter spherical indenters made of tungsten were used.

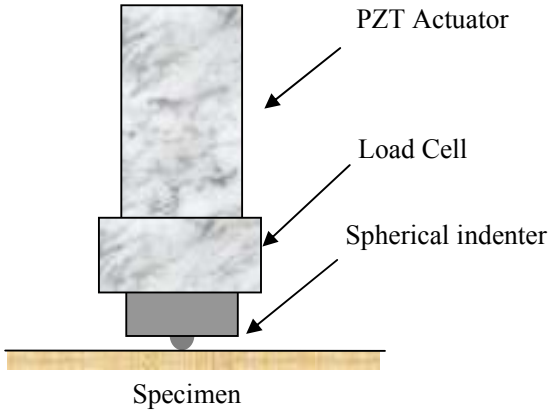

Figure 6. Load-displacement sensing indentation system.

A schematic load-displacement curve from the aforementioned experimental setup is shown in Figure 7. The PZT actuator provides the overall indentation depth (h) measurement, which includes both the indentation penetration depth and system deformation, i.e.,

$$h = h_i + h_s \qquad (1)$$

where h_i is the indentation penetration depth and h_s is the loading system deformation.

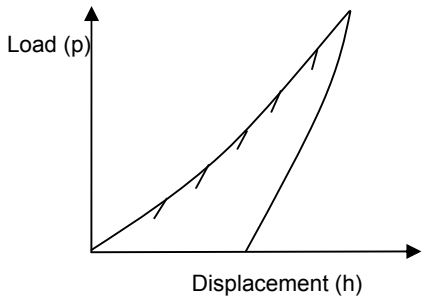

Figure 7. One indentation test with multiple partial unloadings.

At every unloading step (Figure 7), the unloading compliance is,

$$\frac{dh}{dp} = \frac{dh_i}{dp} + \frac{dh_s}{dp} = \frac{dh_i}{dp} + C_s \qquad (2)$$

where C_s is the system compliance, which can be assumed to be a constant for a given system and within a given loading range.

Following the theoretical analysis of indentation [10-11, 14], the unloading compliance of a spherical indentation test can be expressed in terms of the indentation load, i.e.,

$$\frac{dh_i}{dp} = C \times \frac{1}{p^{1/3}} \qquad (3)$$

where $C = \left(6RE_r^2\right)^{-1/3}$, R is the radius of the indenter, and E_r is the reduced modulus, defined by $\frac{1}{E_r} = \frac{1-v_i^2}{E_i} + \frac{1-v_0^2}{E_0}$. E_i is the Young's modulus and v_i is the Poisson's ration of the test specimen, and subscript 0 denotes the indenter's mechanical properties. Substitute Equation (3) into Equation (2),

$$\frac{dh}{dp} = C \times \frac{1}{p^{1/3}} + C_s \qquad (4)$$

Equation (4) shows that $\frac{dh}{dp}$ and $\frac{1}{p^{1/3}}$ has a linear relationship if C_s remains constant within a given loading range, and thus measurement of slope C provides an alternative method for material Young's modulus measurement. It should be noted that, after obtaining the Young's modulus, other mechanical properties, such as hardness, stress-strain curve can also be determined [15].

For mechanical property measurement using instrumented nano/micro indentation technique, the effect of the system compliance is always a concern and this is why in-situ high precision and sometimes sophisticated displacement sensor is often used to remedy this problem. In this research, a rather simple approach is proposed to try to alleviate this problem by making the assumption that within a selected loading range (of an indentation test where data are collected for mechanical property evaluation) the system compliance is constant (i.e. load versus load-line system displacement is linear within the loading range). It should be noted that, experimentally, it is difficult to conduct direct measurement of the system compliance and thus prove the validity of this assumption. However, we noticed the investigation work of Oliver and Pharr [13] on system compliance measurement. Their approach is similar to what described in this paper, the difference is that instead of calculating the Young's modulus as proposed in this paper, it was used for system compliance determination.

In practice, Equation (4) also provides a convenient guideline to justify the validity of the proposed methodology, i.e., if the system compliance changes during the indentation loads, the linear relationship as depicted in Equation (4) can not be maintained.

EXPERIMENTAL INVESTIGATION

Test Procedure

Based on the aforementioned multiple partial unloading technique, a LabVIEW™ software tool is developed to conduct the indentation tests. The program will first detect the contact position between the indenter and the sample within a given load threshold (~0.1N), then it will conduct the multiple partial unloading indentation test using pre-defined parameters, such as the velocity of the indenter, the penetration depth and the unloading magnitude. After the completion of the indentation test, the program will process the data to determine the material Young's modulus from the slope measurement. For the results shown in this paper, all tests were conducted with six or ten loading/partial unloading steps, and each partial unloading displacement was either 0.5μm or 1μm, nominally.

Materials

To verify the feasibility of this technique, indentation tests were carried out on Al 7075-T6 and Inconel 783. The published Young's modulus values for Al 7075-T6 and Inconel 783 are 71.7GPa and 177.3 GPa, respectively [25, 26]. The Inconel 783 alloy had standard heat treatment (1120°C/1hr/AC + 845°C/8hrs/AC + 720°C/8hrs 50°C/hr 620°C/8hrs/AC). The Young's modulus of the sapphire indenter is 340GPa with Poisson's ratio equal to 0.29. Preliminary tests were then carried out on several research alloys, as listed in Table 6. As shown in Table 6, in addition to the ORNL alloys, three batches of Mo alloys were prepared at WVU using a sonication process. TiO_2 (~5 nm) and Mo (~65 nm) were taken as 5g and 95g respectively according to their weight percent ratio. Similarly 5g of MgO(~50 nm size) and 95g of Mo (~ 65 nm) were taken for the other composite. Then we followed the following procedure for assuring uniform mixing of the components. Mo was dissolved in ethyl alcohol and sonicated for 10 minutes in presence of Ar. Then TiO_2 was mixed slowly to the Mo solution with continuous sonication. The total mixture was sonicated for 1 hour in Ar atmosphere. The mixture was kept at room temperature for 1 day to remove ethanol. Finally it was dried in vacuum. In the same way we prepared the $(MgAl_2O_4)_{0.05}(Mo)_{0.95}$ composite (~35 nm particle size of $MgAl_2O_4$). The dried powder samples were kept in Ar-filled glove box and packed in presence of Ar. These are the as-prepared sample powders which were sent to Dr. J.H. Schneibel at ORNL for vacuum hot-pressed casting.

Table 6. Materials Matrix

(Alloys received from M.P. Brady and J. H. Schneibel, ORNL)
#678, Mo-3.4wt%$MgAl_2O_4$: 1800°C/4hr/3ksi/Vacuum, Mo powder 2-8μm, $MgAl_2O_4$, 1-5μm
#696, Mo-3.0wt%$MgAl_2O_4$: 1800°C/1hr/3ksi/Vacuum, Mo powder 2-8μm, $MgAl_2O_4$, 1-5μm
#695, Mo only : 1800°C/1hr/3ksi/Vacuum, Mo powder 2-8μm
#697, Mo-6.0wt%$MgAl_2O_4$: 1800°C/1hr/3ksi/Vacuum, Mo powder 2-8μm, $MgAl_2O_4$, 1-5μm
#698, Mo-3wt%MgO : 1800°C/1hr/3ksi/Vacuum, Mo powder 2-8μm, MgO, 1-5μm
Cast Re-(26-30) Cr wt% nominal: 1800°C/1hr/3ksi/Vacuum
(Powder mix prepared at WVU and sent to J.H. Schneibel for vacuum hot-pressed)
WVU-1, Mo-5.0wt%$MgAl_2O_4$: 1800°C/0.5hr/3ksi/Vacuum
WVU-2, Mo-5wt%MgO : 1800ºC/1.0hr/3ksi/Vacuum
WVU-3, Mo-5.0wt%TiO_2 : 1700°C/0.5hr/3ksi/Vacuum

TASK II RESULTS

Al 7075-T6

Several indentation tests were carried out on the Al 7075-T6 alloy. Figure 8(a) shows the typical indentation load and displacement data, in which ten partial unloading/reloading were introduced. Based on the unloading line data, compliances at each unloading step were calculated. They were then further processed according to the algorithm discussed in the multiple partial unloading procedure. Figure 8(b) shows data analysis results based on Equation (4). The processed data show the existence of a linear relationship within most of the applied indentation loading range. Using the linear unloading line, Young's modulus was calculated by applying Equation (4) and assuming a Poisson ratio of 0.3. An average value of 67.2 GPa was obtained. The experimental data obtained are in good agreement with the book value of 71.7 GPa.

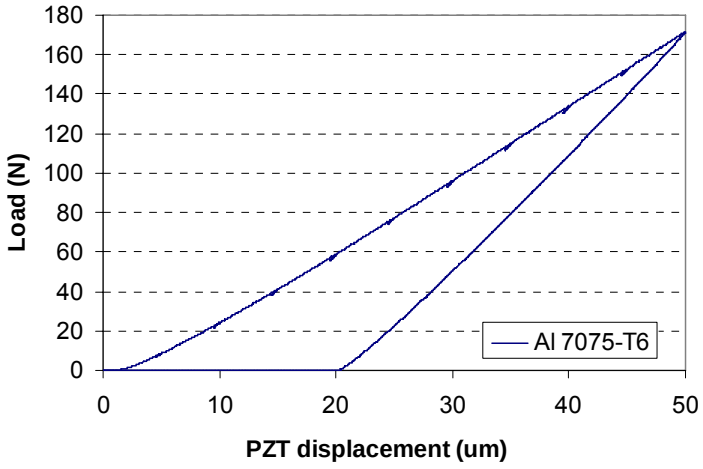

(a) Load-displacement curve with multiple-partial unloadings

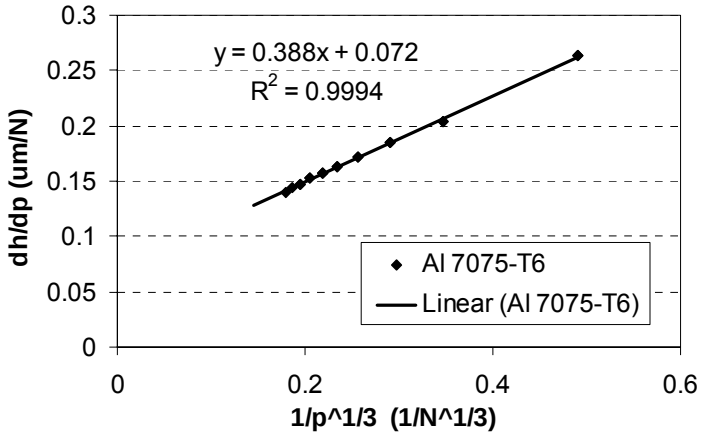

(b) Linear relationship

Figure 8. Experimental results for Al 7075-T6 alloy.

Inconel 783

Figure 9 shows the typical indentation test results for Inconel 783. In Figure 9(a), there were ten partial unloading displacements of 0.5 μm each. Based on the linear unloading line data, compliances at each unloading step were calculated and then further processed according to the multiple partial unloading technique. Similar to the Al 7075-T6 test, a linear relationship is observed within most of indentation loads, as show in Figure 9(b). However, the data starts to deviate from the linear relationship at higher indentation loads, indicating the breakdown of the constant system compliance assumption, as discussed earlier. Again, using only the linear part in Figure 9(b), and based on Equation (4), Young's modulus values were calculated. An average value of 168.4 GPa is obtained and agreed well with the book value of 177.3 GPa.

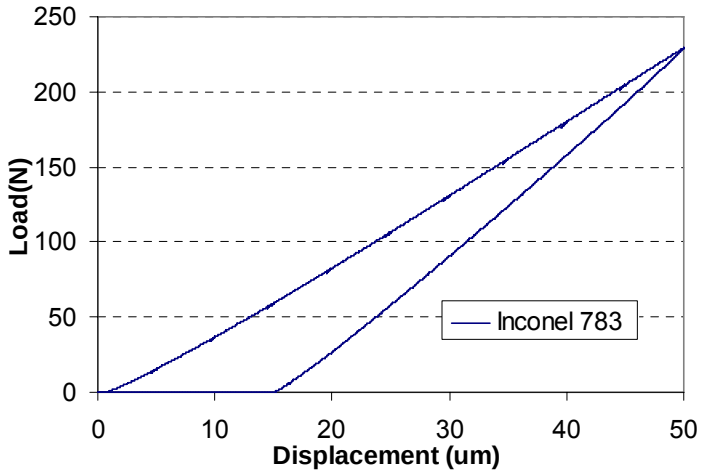

(a) Load-displacement curve with multiple-partial unloadings

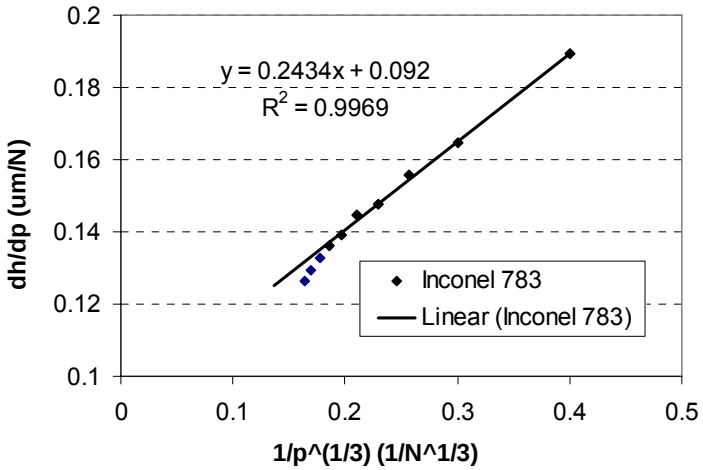

(b) Linear relationship

Figure 9. Experimental results for Inconel 783 alloy.

Mo and Cr Alloys

Micro-indentation tests were carried out on several research alloys as listed in Table 6. The results were presented in Figure 10, Figure 11, and Table 7. As for ductile/brittle evaluation of these alloys, relatively larger indentation loads (400 Nto 2000 N) were applied to the samples. The higher indentation load is to have a sufficient elastic rebounding (after indentation unloading) that may cause cracking at the region just outside the perimeter line of the indentation contact zone, if the material is brittle. Preliminary results show that for the ORNL alloys, alloy #678 is the only alloy with sufficient room-temperature ductility while other alloys are brittle as evidenced with indentation-induced cracking, as shown in Figure 12. The results are in consistent with the research work of ref. 3 and ref. 9. As for the WVU alloys, preliminary results show that only WVU-3 has some degree of room-temperature ductility and the metal oxide dispersion is not uniform especially for WVU-1 and WVU-2, as shown in Figures 13 to 15. The non-uniform oxide dispersion may be due to the fact that the prepared powder mix was exposed in air for about 60 to 80 seconds when pouring the powder mix to the crucible for vacuum hot-pressed casting. Further research is planned to process the alloys without exposing the powder mix to air during the vacuum hot-pressed procedure.

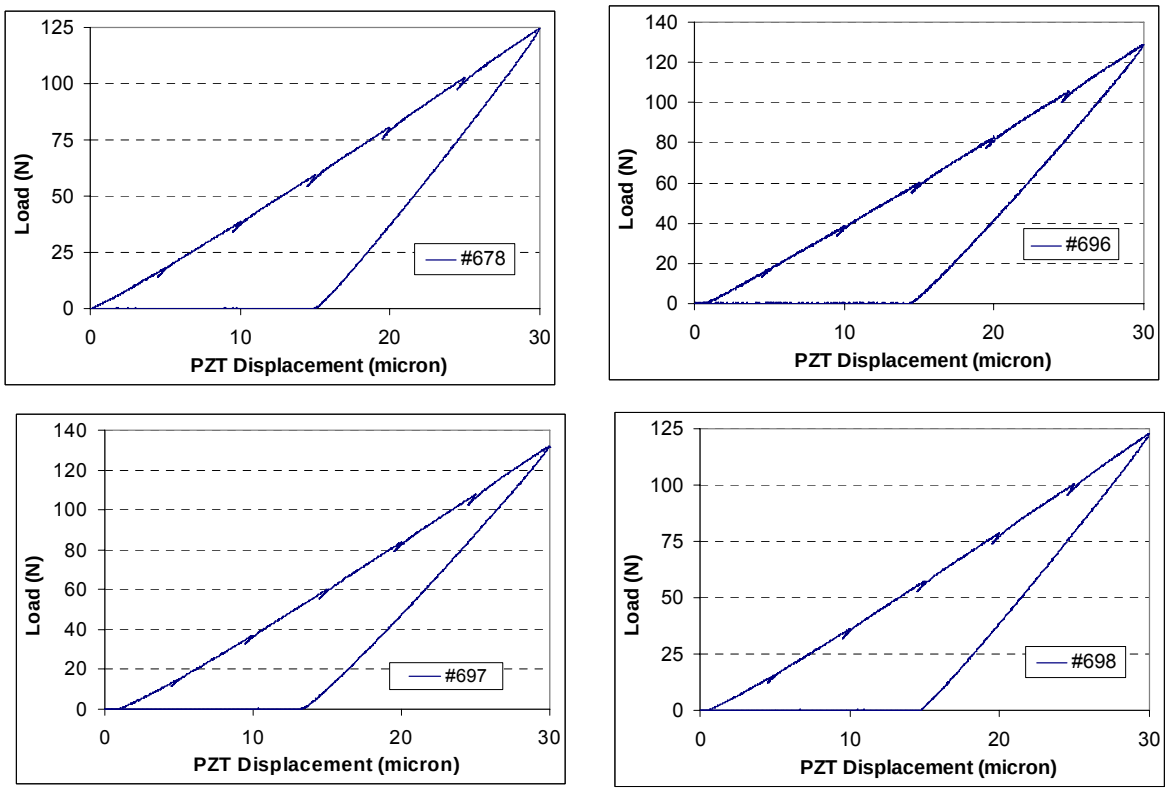

Figure 10. Typical load-displacement curve, ORNL Mo alloys, #678, #696, #697, #698.

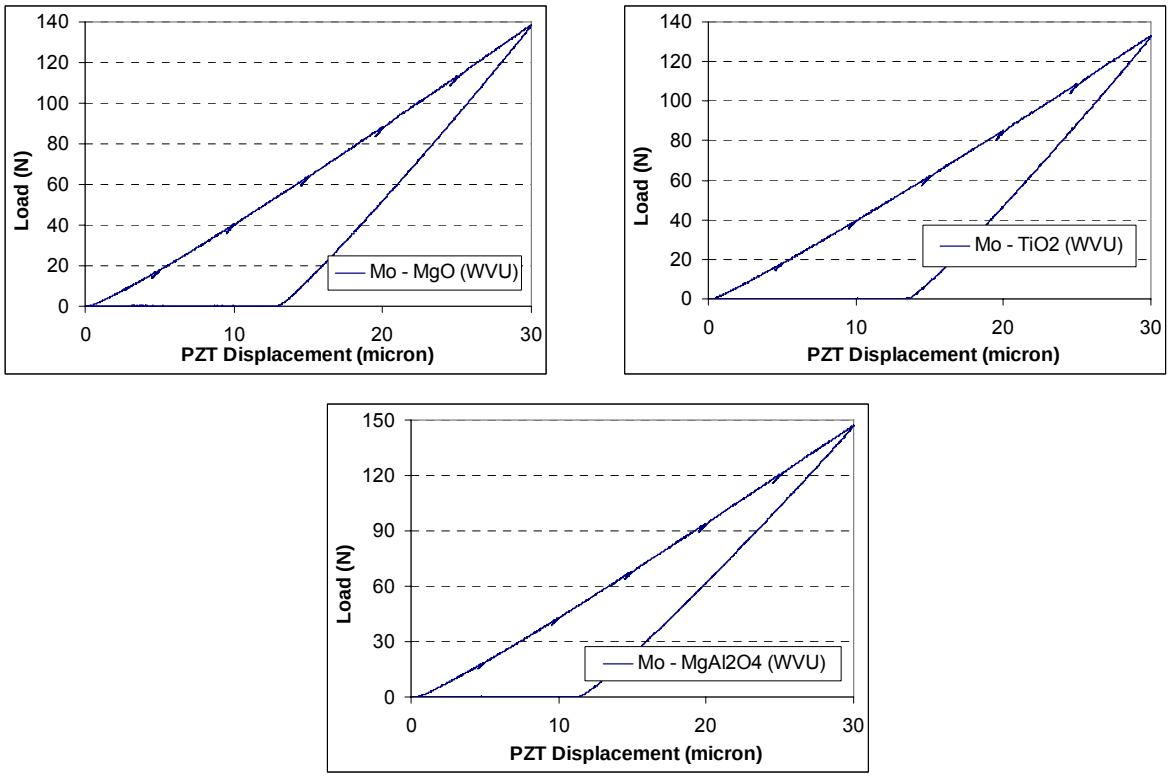

Figure 11. Typical load-displacement curve, WVU Mo-MgO, Mo-$MgAl_2O_4$, Mo-TiO_2 alloys.

Table 7. Summary - Young's Modulus Measurement

Material	Young's modulus (GPa)
Cast Re-(26-30) Cr wt%	234
#678, Mo-3.4wt%$MgAl_2O_4$	229
#696, Mo-3.0wt%$MgAl_2O_4$	200
#697, Mo-6.0wt%$MgAl_2O_4$	192 (from tensile test : 189)
#698, Mo-3wt%MgO	211
WVU-1, Mo-MgO	254
WVU-2, Mo-TiO_2	226
WVU-3, Mo-$MgAl_2O_4$	202

(Averaged value from five indentation tests, typical)

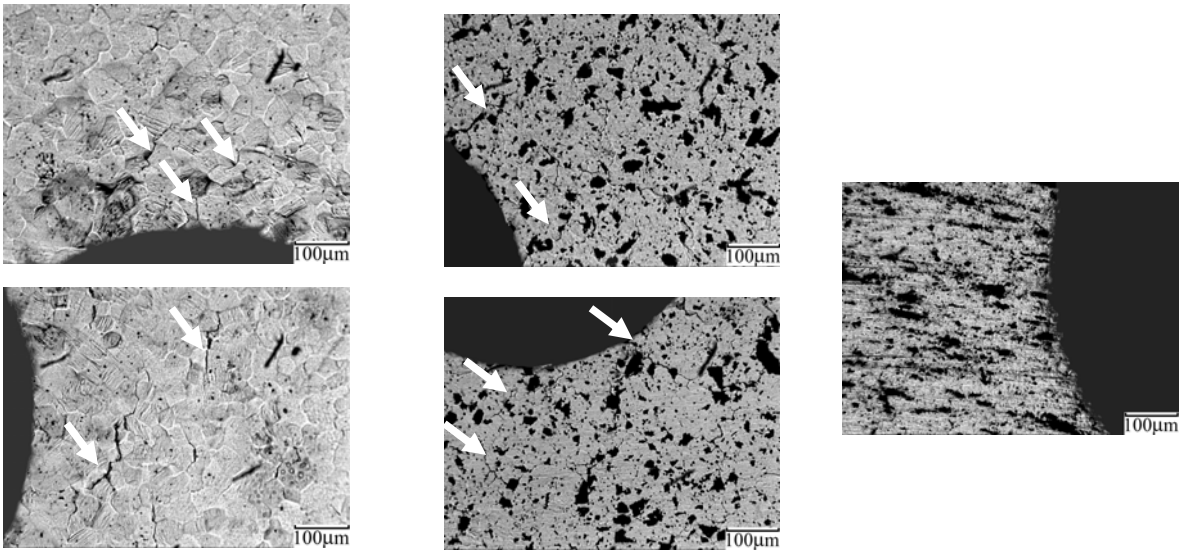

#695, brittle, indentation load 1500N, cracks are observed

#697, brittle, indentation load 1000N, cracks are observed

#678, Ductile, indentation 2000N, no cracks were observed

Figure 12. Material surface condition evaluation, ORNL Mo alloys.

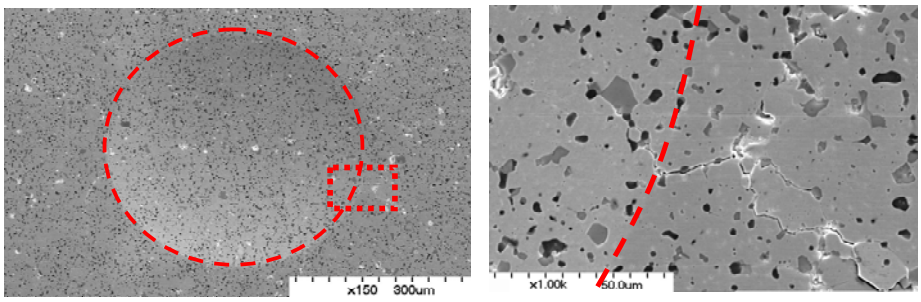

Figure 13 Ductile/brittle characterization using spherical micro-indentation Mo-MgO (WVU-1), 400N indentation, cracking.

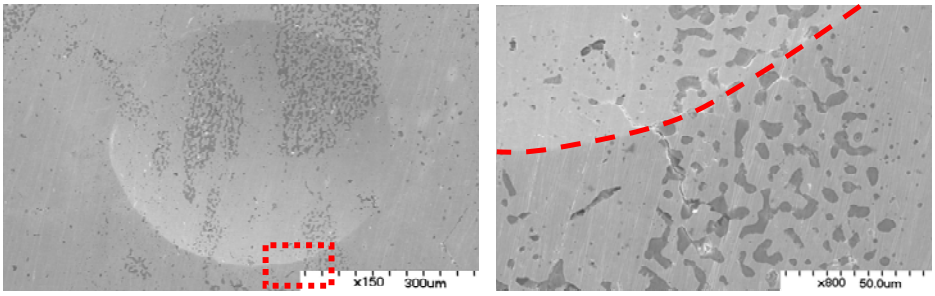

Figure 14 Ductile/brittle characterization using spherical micro-indentation Mo-TiO_2 (WVU-2), 400N indentation, cracking.

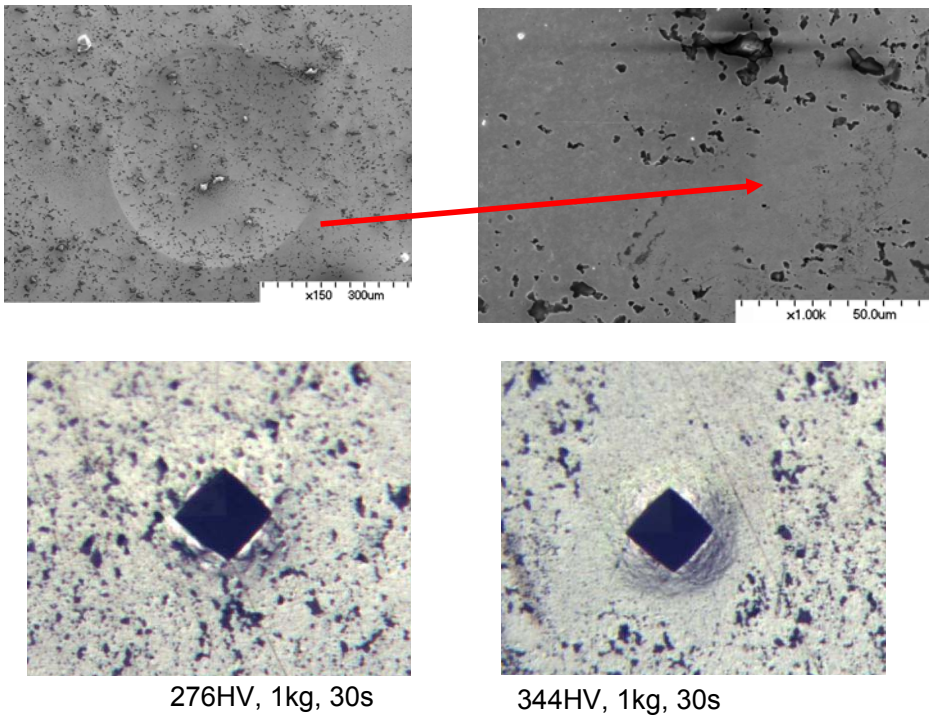

Figure 15 Ductile/brittle characterization using spherical micro-indentation
Mo- $MgAl_2O_4$ (WVU-3), 400N indentation, no cracking.
Vickers hardness tests show plastic flow at the matrix region.

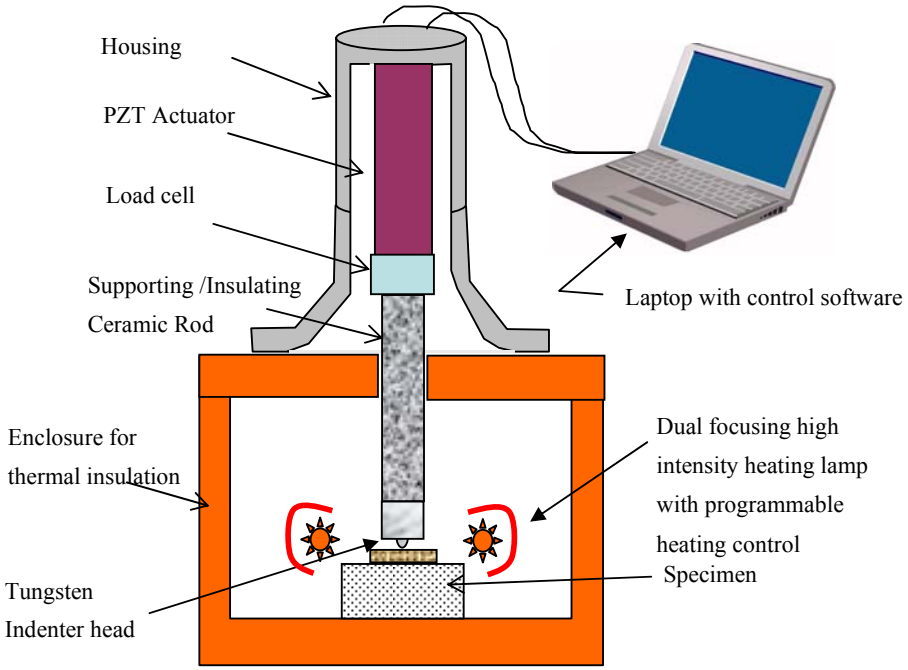

Figure 16. High temperature indentation using multi-partial unloading technique.

TASK II CONCLUSION

We present a simple multiple partial unloading micro-indentation testing method for in-situ surface material Young's modulus measurement and ductile/brittle evaluation on small-size alloys. Test results of two metallic alloys, (Al 7075-T6, and Inconel 783) show the validity of this technique. The proposed micro-indentation method does not require the use of sophisticated displacement sensor for indentation depth measuremet and has the potential for the development of a portable micro-indentaiton instrument for on-site, in-situ component inspection and surface mechanical property evaluation. It can be configured for high temperature indentation test as schematically shown in Figure 16, which is under preparation with preliminary high temperature indentation tests planned for this project.

ACKNOWLEDGMENT

The work is sponsored by DOE Office of Fossil Energy, Advanced Research Materials (ARM) Program, under contract DE-AC05-00OR22725 managed by UT-Battelle, LLC. The research is also supported by DOE/NETL University Coal Research (UCR) Program under contract DE-FG26-05NT42526.

REFERENCE

1. W.D. Klopp, NASA TM X-1867, September (1969).
2. Y.F. Gu, H. Harada, Y.Ro, and T. Kobayashi, Metal. & Mater. Trans. A 36A, 577-582, (2005).
3. M.P. Brady, I.M. Anderson, M.L. Weaver, H.M. Meyer, L.R. Walker, M.K. Miller, D.J. Larson, I.G. Wright, V.K. Sikka, A. Rar, G.M. Pharr, J.R. Keiser, C.A. Walls, Mater. Sci. & Eng. A358, 243-254, (2003)
4. A.A. Griffith, Trans. First Intl. Cong. Appl. Mech. Delft, 55-63, (1924)
5. J.R. Rice, J. of the Mech. & Phys. of Sol. (UK), 40, 239-271, (1992)
6. D.L. Price and B.R. Cooper, Phys. Rev. B 39, 4945-4957, (1989); D.L. Price, J.M. Wills and B.R. Cooper, ibid. 46, 11368-11375, (1992).
7. J.P. Lewis, K.R. Glaesemann, G.A. Voth, J. Fritsch, A.A. Demkov, J. Ortega, and O.F. Sankey, Phys. Rev. B 64, 195103, (2001).
8. A. P. Horsfield, Phys. Rev. B 56, 6594-6602, (1997).
9. J.H. Schneibel, Metal. & Mater. Trans. A 34A, 25, (2003).
10. Ian N. Sneddon, "The relation between load and penetration in the axisymmetric boussinesq problem for a punch of arbitrary profile," Int. J. Engng Sci, Vol. 3, pp. 47-57, (1965).
11. S.I. Bulychev, V. P. Alekhin, M. Kh. Shorshorov, A. P. Ternovskii and G. D. Shnyrev, "Determining Young's modulus from the indentor penetration diagram," Industrial laboratory, Vol.41, No.9, pp. 1409-1412, Sep. (1975).
12. M. F. Doerner, W. D. Nix, "A method for interpreting the data from depth-sensing indentation instruments," J. Mater. Res. 1(4), pp. 601-609, Jul/Aug, (1986).
13. W. C. Oliver; G. M. Pharr, An improved technique for determining hardness and elastic modulus using load and displacement sensing indentation experiments, JOURNAL OF MATERIALS RESEARCH, 7 (6), pp.1564-1583 June, (1992).
14. K. L. Johnson, Contact Mechanics, Cambridge Univeristy Press, (1985).

15. B. Taljat, T. Zacharia, “New analytical procedure to determine stress-strain curve from spherical indentation data,” Int. J. Solids structures, Vol. 35, No. 33, pp. 4411-4426, (1998).
16. F. M. Haggag, “Field Indentation Microprobe for structural integraity evaluation,” U.S. Patent No. 4,852,397, August 1, (1989).
17. Claus Kleesattel, “Method and apparatus for the measurement of hardness testing indentations,” Patent No. 4,277,174, July 7, (1981).
18. Stefan Frank, “Transpyramidal indentation viewing - new possibilities for mobile hardness testing,” 15th World Conference on Non-Destructive Testing, Rome, October, (2000).
19. M. Sakaia and N. Hakiri, T. Miyajima, “Instrumented indentation microscope: A powerful tool for the mechanical characterization in microscales,” J. Mater. Res., Vol. 21, No. 9, pp. 2298-2303, Sep., (2006).
20. C. Feng, B. S. Kang, “A transparent indenter measurement method for mechanical property evaluation,” Experimental Mechanics, pp. 91-103, 46, (1), Feb., (2006).
21. C. Feng, B. Kang, “Young’s modulus measurement using a simplified transparent indenter measurement technique,” Experimental Mechanics, to be published.
22. B. S.-J. Kang, C.-Y. Feng, A. Manivannan, N. Ma, and B.R. Cooper, “In-situ mechanical property measurement and influence of impurity elements on grain boundary strength of Cr and Mo alloys,” 19th Annual Conference on Fossil Energy Materials, May 9-11, (2005).
23. B. S.-J. Kang, N. Ma, C.-Y. Feng, and B.R Copper, “In-situ mechanical property measurement and study of impurity embrittlement and metal oxides ductility enhancement mechanism in chromium alloys based on electronic structure analysis,” 20th Annual Conf. on Fossil Energy Materials, June 12-14, (2006).
24. T. MIYAJIMA and M. Sakaia, “Optical indentation microscopy – a new family of instrumented indentation testing,” Philosophical Magazine, Vol. 86, Nos. 33–35, pp. 5729-5737, Dec. (2006).
25. IN783 mechanical properties, **http://www.specialmetals.com**
26. Al 7075-T6 mechanical properties, **http://www.matweb.com**

ADVANCED PROCESSING OF METALLIC POWDERS FOR FOSSIL ENERGY APPLICATIONS

Iver E. Anderson
222 Metals Development, Ames Lab. (USDOE), Iowa State University, Ames, IA 50011
E-mail: andersoni@ameslab.gov; Telephone: (515) 294-9719; Fax: (515) 294-8727

Robert L. Terpstra
109 Metals Development, Ames Lab. (USDOE), Iowa State University, Ames, IA 50011
E-mail: terpstra@ameslab.gov; Telephone: (515) 294-5747; Fax: (515) 294-8727

Joel R. Rieken
223 Metals Development, Mater. Sci. & Eng., Iowa State University, Ames, IA 50011
E-mail: jrieken@iastate.edu; Telephone: (515) 294-1602; Fax: (515) 294-8727

Stephen N. Paglieri
Los Alamos National Laboratory; P.O. Box 1663, MS-C927; Los Alamos, NM 87545
E-mail: steve.paglieri@lanl.gov; Telephone: (505) 667-0652; Fax: (505) 665-1226

ABSTRACT

This project seeks to develop innovative methods and to enhance process control of metal powder production by gas atomization methods to benefit the implementation of several emerging Fossil Energy technologies that utilize metal powders of specific size ranges and types, which are not efficiently produced by industrial powder processing. Current improvements in high efficiency gas atomization nozzles were directed toward maximizing powder yields in special size classes, e.g., ultrafine (dia. < 10 μm) powders to eliminate a major barrier to the use of new concepts for fabrication of hydrogen membranes, for example. In the present work, a new Pd thin film membrane support concept was developed that used coarse (40 μm porosity) stainless steel frit to support a thin (75 μm) primary membrane support, made from dia. < 3μm atomized powder of Fe-16Al-2Cr (wt.%). The membrane support surface, with 0.1-0.5 μm porosity, was sintered at AL and a finished membrane achieved encouraging hydrogen separation performance at LANL. Further sintering process modifications successfully suppressed densification cracking and most sintered surface irregularities, as revealed by SEM on surfaces and cross-sections. Auger electron spectroscopy (AES) with depth profiling analyzed as-sintered and modified surfaces to determine suitability as an inter-diffusion barrier with the Pd-X film. Results of further hydrogen separation work were reported by LANL in a companion paper. The approach of gas atomization with reactive gas (Ar + 5%O2) for making powders of Fe-Cr (e.g., 410SS) with Y additions was explored further with reactive gas injection (downstream of the breakup zone). The intent is to form an oxide dispersion strengthened (ODS) microstructure upon full consolidation as a viable alternative to mechanical alloying. SEM analysis helped compare as-consolidated Fe-12.5Cr-1Y to a heat-treated microstructure and revealed continued dissolution of Cr_2O_3 at the prior particle boundaries. This is consistent with the desired Y_2O_3 exchange reaction that can strengthen interparticle bonding and promote an ODS microstructure. Hot stage X-ray diffraction tracked the transformations during annealing. TEM analysis of as-HIP samples identified yittria dispersoids of 10-100nm dia. and showed dislocation pinning. Samples were provided to ORNL for additional consolidation testing and characterization.

INTRODUCTION

The introduction of new types of powder alloys to the commercial marketplace is significantly impeded by the uncertainty of powder size distribution control, i.e., the difficulty of "tuning" an atomization process to accommodate increased production in a size range not normally accessed. For example, specific powder size classes are often obtained by extensive size classification of a typical powder yield with its characteristic powder size distribution, using sieves and pneumatic separators to produce the desired fraction. Especially for complex alloy compositions without additional markets and with strict impurity limits, e.g., alloy powders for fossil energy applications, this conventional practice is quite costly, because of the losses and (possible) contamination from extensive particle size classification operations and the need to inventory or to scrap the remaining powder that is not desired. A better approach is to gain improved control of the energy transfer process involved with liquid metal disintegration by supersonic gas flows to generate liquid droplets of the desired size range (predominantly) in the atomization spray, which will solidify to powders of the proper size for a specific application[1].

The enhanced production of ultra-fine powders of high temperature alloys with dia. ≤ 10 μm was chosen for an initial objective of this research thrust involving improved powder processing for various fossil energy applications. In one important type of application for these special powders, a hydrogen purifying membrane that uses an interstitial separation concept involving rapid atomic diffusion through certain metal lattice structures (e.g., Pt, Pd, V) requires a porous metallic surface with very low surface roughness as a support for effective physical vapor deposition of the continuous metal film[2]. The preferred pore size of the metallic support surface is very small, in the range of 0.1-0.5 μm, to help achieve the desired low surface roughness. To produce controlled porosity of this size range requires ultra-fine powders of high temperature alloys such as Fe-16Al-2Cr (wt.%) with dia. < 5 μm. An additional benefit of this alloy choice is the ability to grow (upon annealing in UHP Ar) an alumina scale[3] of sufficient thickness to inhibit interdiffusion, especially of Cr and Fe that can otherwise degrade the hydrogen transport rate of the Pd[4]. Another type of hydrogen membrane application, e.g., in a coal-fired IGCC system, uses a physical separation concept with a porous metallic cylinder of an oxidation resistant alloy, e.g., Fe-Cr, as a support for a ceramic membrane with nano-metric pores (5-20 nm) that preferentially pass hydrogen and reject larger gas atoms and molecules, e.g., CO, CO_2, NO_x, and SO_x(5). The pore size that has been found most beneficial for the support cylinder is 1-2 μm, requiring powders of about 10μm diameter. For further advances into elevated temperatures for this type of membrane, it is also desirable to utilize a type of powder for the structural membrane support that resists creep and continued sintering and pore closure to well above 1000C. Preliminary experiments at ORNL indicated that a novel type of oxide dispersion-strengthened (ODS) stainless steel powder made from Fe-Cr-Y by a reactive gas atomization process at Ames Lab is suitable for this type of application. Such special high temperature alloy powders in ultrafine sizes (dia. < 10μm) are either extremely expensive, of insufficient quality, or unavailable commercially.

Previous work on the support structures for hydrogen purification membranes had attempted to fabricate a freestanding thin wafer form of a porous substrate surface from dia. < 3μm powders of Fe-16Al-2Cr (wt.%) powders[6]. These studies achieved a sufficient sintered state in this wafer

structure to exhibit the proper degree of low surface roughness and open porosity[6]. However, a cracking problem related to sintering shrinkage was encountered with the porous wafers, even when supported on a loose bed of high purity alumina particles during sintering. These problems with mechanical integrity made it difficult to deposit a continuous Pd film and to test the full membrane for hydrogen permeation. Thus, advancement of this work demanded a new fabrication procedure for the Pd membrane porous support layer.

A novel processing technique for Initial experiments on generation of a novel type of oxide dispersion-strengthened (ODS) stainless steel powder made from Fe-Cr-Y by a reactive gas atomization process had succeeded in producing only small quantities of powder due to premature termination of the melt stream flow. Promising results were achieved for this powder as a precursor for simplified production of ODS ferritic stainless steel alloys with isotropic microstructure, compared to the conventional mechanical alloying approach that results in anisotropic mechanical properties[7]. These results and the need for porous supports for ceramic membranes encouraged further development of the in situ gas phase reaction process to enable fully successful atomization runs to be completed. Diagnosis of the previous problem indicated that a high local melt viscosity increase from excess oxygen dissolution at the melt pouring orifice due to a close-coupled nozzle recirculation effect[1], which may have lead to premature "freeze-off" of the melt stream. Thus, new efforts were initiated to inject the reactive gas mixture at a location downstream of the atomization nozzle, but where the atomized particles were still hot enough to experience excess surface oxidation. In addition, further characterization of the HIP consolidated microstructure of these special powders was performed to gather more evidence of Y_2O_3 dispersoid formation. Heat treatment effects were also explored by high temperature X-ray diffraction of loose powders and by SEM analysis of consolidated microstructures.

EXPERIMENTAL PROCEDURE

Powders of an iron aluminide alloy, Fe-16Al-2Cr (wt.%), were produced with a high-pressure gas atomization (HPGA) system[1] to use in the current sintering experiments to make porous membrane support surfaces. Briefly, the full atomization vessel was evacuated to less than 100 mtorr before backfilling with a full atmosphere of Ar gas to begin melting of the elemental alloy components (99.99%, commercial high purity) in sufficient quantity to make an initial charge weight of 12 kg. The molten alloy was poured at 1700˚C and atomized with Ar gas at a supply pressure of 5.5 MPa into a fine droplet spray that cooled during free-fall in the spray chamber and solidified into powder, which was collected from the powder containers[1]. The powder yield was blended and pre-screened at 106μm (ASTM 140 mesh) to eliminate a small amount of atomization debris (splats and irregular agglomerates). A full set of ASTM screens with opening sizes below 140 mesh and down to 635 mesh (20μm) were used to obtain an estimate of the particle size distribution[1]. A portion of the < 20μm dia. powder was pneumatically classified (AccuCut, Donaldson, Inc.) to < 3μm dia. for the sintering experiments. Analysis of the cracking problems during sintering of the free-standing porous wafers lead to development of a new approach that uses a secondary support frit underneath the membrane support, as shown in Fig. 1, to add some mechanical interlocking and structural stiffness.

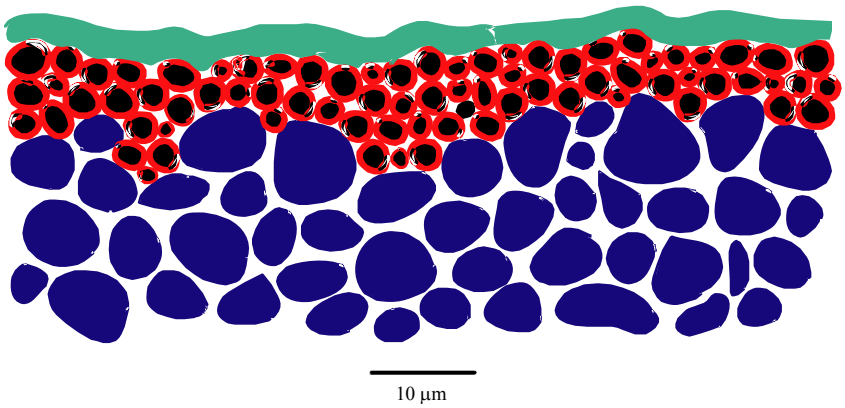

Figure 1. Schematic of a revised approach for more robust support of a Pd interstitial hydrogen separation membrane.

To implement this approach, a sample configuration was designed that included a 9.6 mm O.D. x 6.4 mm I.D. x 2 cm length alloy (Inconel 625) tube that was counter-bored to accept a 316L stainless steel frit (40 µm avg. pore size) that was press fit from one end (into the enlarged bore). The exterior surface of the frit was set into the end face (either flat or chamfered) of the tube by about 75 µm to provide a recessed mold cavity for slurry "casting" of the ultra-fine powder of Fe-16Al-2Cr. In this slurry casting operation, the < 3 µm dia. powder was blended with methanol and poured onto the recessed mold cavity, followed by immediate "striking-off" of the surface with a planar (razor) blade to produce a reasonably flat powder surface. Evaporation of the residual methanol was performed at ambient temperature in air, until the surface appeared dry. Each sample was vacuum (10^{-6} torr) sintered at 975C for times of 1-4 hours, based on previous work[6]. Optical microscopy and SEM of the sintered surface and a mounted and polished cross-section (unetched) of each sample provided initial characterization of the sintering results. Auger electron spectroscopy with depth profiling allowed measurement of the (Al) oxide film thickness in the as-sintered condition and after post-sintering heat treatment (in UHP Ar atmosphere at 800C for 24h) for controlled oxide growth.

New efforts to produce an externally oxidized precursor powder for ODS microstructures utilized 4kg of an Fe-12.5Cr-1.0Y (wt.%) alloy that was atomized in an HPGA system at a pouring temperature of 1700C with UHP Ar gas at a supply pressure of 6.9 MPa with a 45-30-029 HPGA nozzle[8]. A reactive gas mixture, Ar + 5%O_2, was injected (vertically down) through a 20 cm dia. "halo" nozzle at a location 20 cm downstream of the atomization nozzle to interact with the particle spray that was expanding conically during freefall in the spray chamber, as shown in Fig. 2. The resulting powder was collected from the collection cans and chamber and was blended and pre-screened at 106µm (ASTM 140 mesh) to eliminate a small amount of atomization debris (splats and irregular agglomerates). The resulting sub-106 µm powder was screened at 45 µm to generate < 45 µm powder samples for bulk oxygen analysis (by dissolved gas fusion, LECO unit) and for chemical analysis by ICP-AES by a vendor (NSL Analytical Labs). The balance of the powder was screened at 53 and 20 µm to prepare samples for sintering and hot isostatic pressing (HIP) experiments, similar to the previous work[9], to examine consolidation processing options.

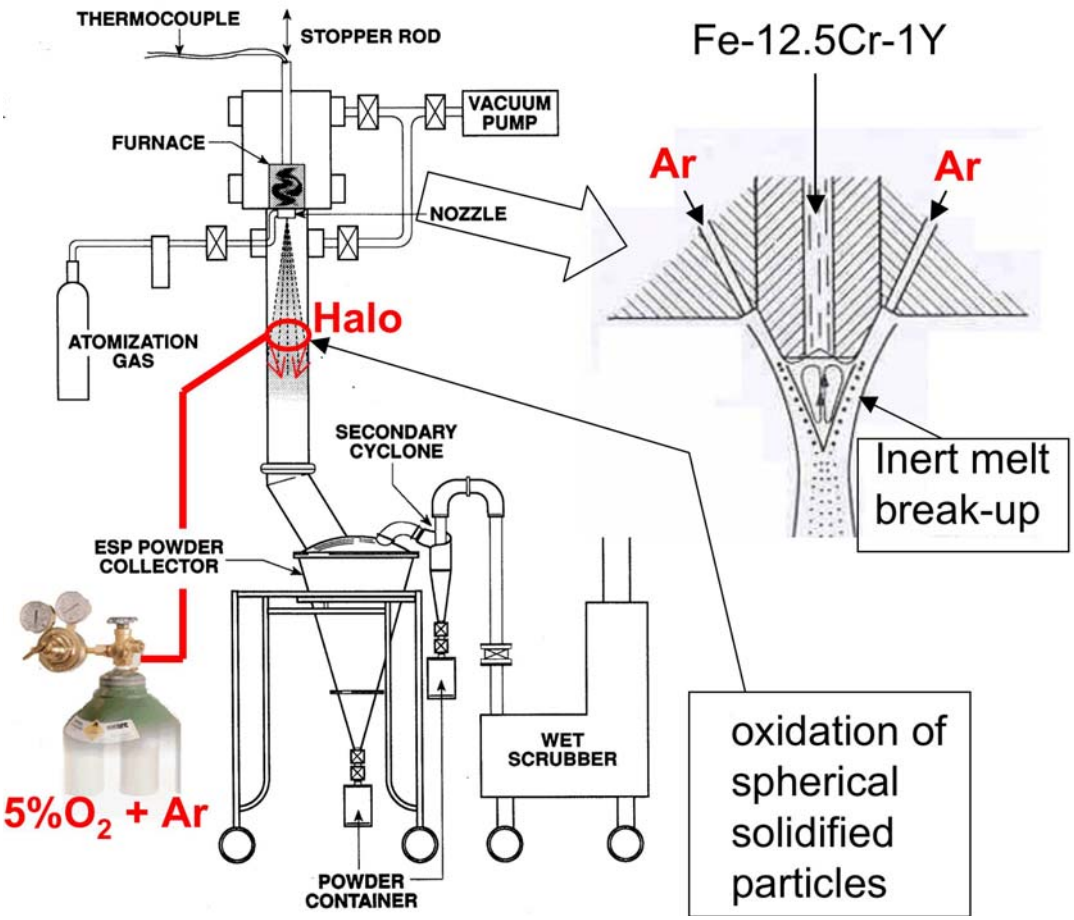

Figure 2. Schematic of downstream halo approach to injection of a reactive gas mixture (Ar + 5%O_2) into the HPGA system at a distance of 20 cm below the atomization nozzle (shown in the inset sketch) that was supplied with UHP Ar gas.

In addition, further characterization of as-atomized powder from a previous experiment[8] was performed to characterize the heat treatment response of loose powder (< 20 μm dia.) that exhibited 2 wt.% oxygen content. Heat treatment effects were explored by preliminary measurements using high temperature (800 to 1200C in 50C increments) X-ray diffraction (Cu K-α radiation) of loose powders in a continuously pumped (sensor not working) vacuum atmosphere using a PANalytical X-Pert Pro diffraction system. Further characterization of HIP consolidated microstructures from previous experiments was performed to gather more evidence of decomposition of the Cr_2O_3 phase on prior particle boundaries by SEM analysis of the microstructures, using quantitative image analysis methods (ImagePro software).

RESULTS AND DISCUSSION

The initial test of the new approach for fabrication of the Pd membrane support produced a fairly promising result, but the surface still exhibited several significant types of defects. The sample configuration started with a flat surface on the projecting end of the tube and the sintering parameters were 4 h at 975C. Analysis of optical microstructures (given in Fig. 3) and SEM

observations indicated that the powder sintering time (4 h) was too long, leading to excess sintering shrinkage stress that promotes centerline and rim cracking. It is useful to note that the stress state generated in middle and at interface with tube interior wall was probably tensile.

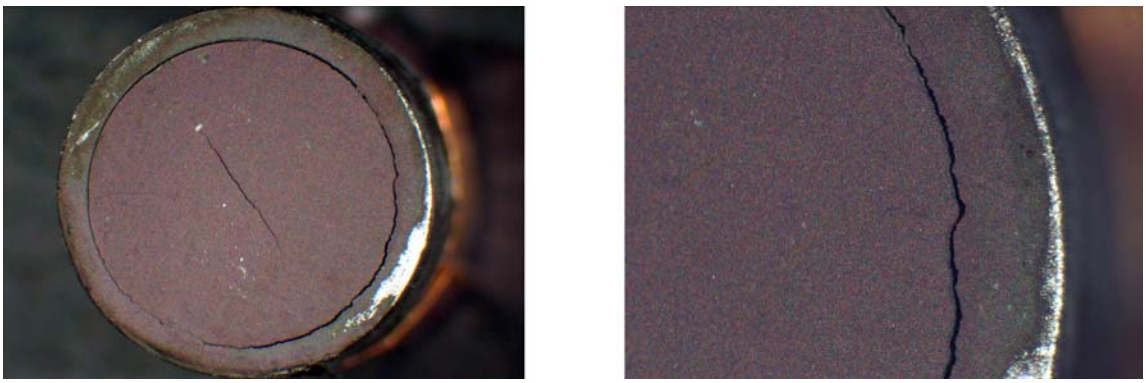

a) b)

Figure 3. Optical micrographs of two views of the initial sintering experiment, showing a) a significant centerline crack and a clear circumferential crack that extended around the interface with the interior of the tube, and b) a higher magnification of a region of the circumferential crack.

A second experiment was conducted with the same sample configuration, but using a shorter sintering time of 1 h. As Fig. 4 shows, the shorter sintering time was effective apparently at reduction of sintering shrinkage and tensile stresses, sufficient to eliminate the centerline cracking. Unfortunately, evidence of circumferential cracking persisted, leading to the need for a sample configuration change to accommodate the remaining tensile stresses that must have been too high for the thin (75 μm) sintered layer.

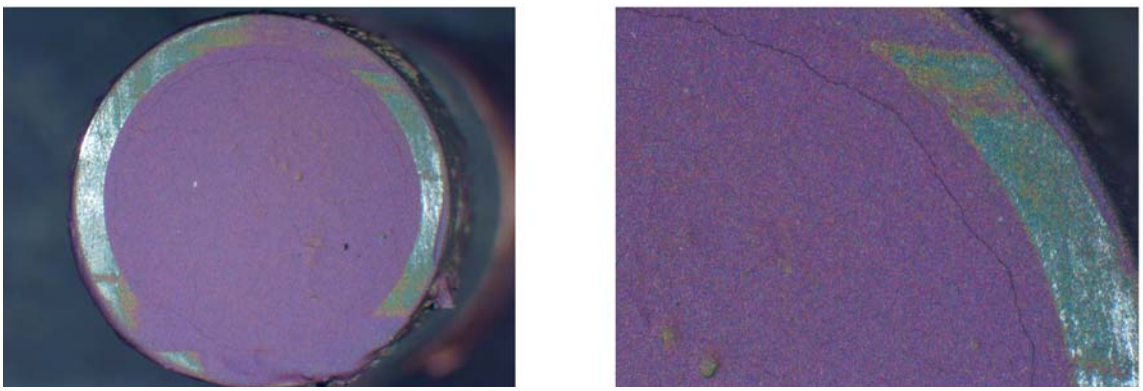

a) b)

Figure 4. Optical micrographs of two views of the second sintering experiment, showing a) no centerline cracking and a very minor circumferential crack in one region, slightly inward of the interior interface of the tube, and b) a higher magnification of a region of the minor circumferential crack.

One idea for changing the design of the sample configuration involved the cutting of a 3 degree (from horizontal) chamfer in the flat end of the tube (see Fig. 5a) to allow the radial sintering shrinkage to be accommodated by sliding along the chamfered surface without building tensile stresses in the thin layer. The optical micrograph in Fig 5b reveals that this configuration was successful at eliminating the last evidence of circumferential cracking. Also, the SEM

micrograph in Fig 5c shows that the sliding mechanism worked as intended, where a short length of separation appeared along the lower region of the chamfer. However, the majority of this inclined surface was sealed well and this new design feature of the tube seemed to help maintain the full layer in a crack-free condition.

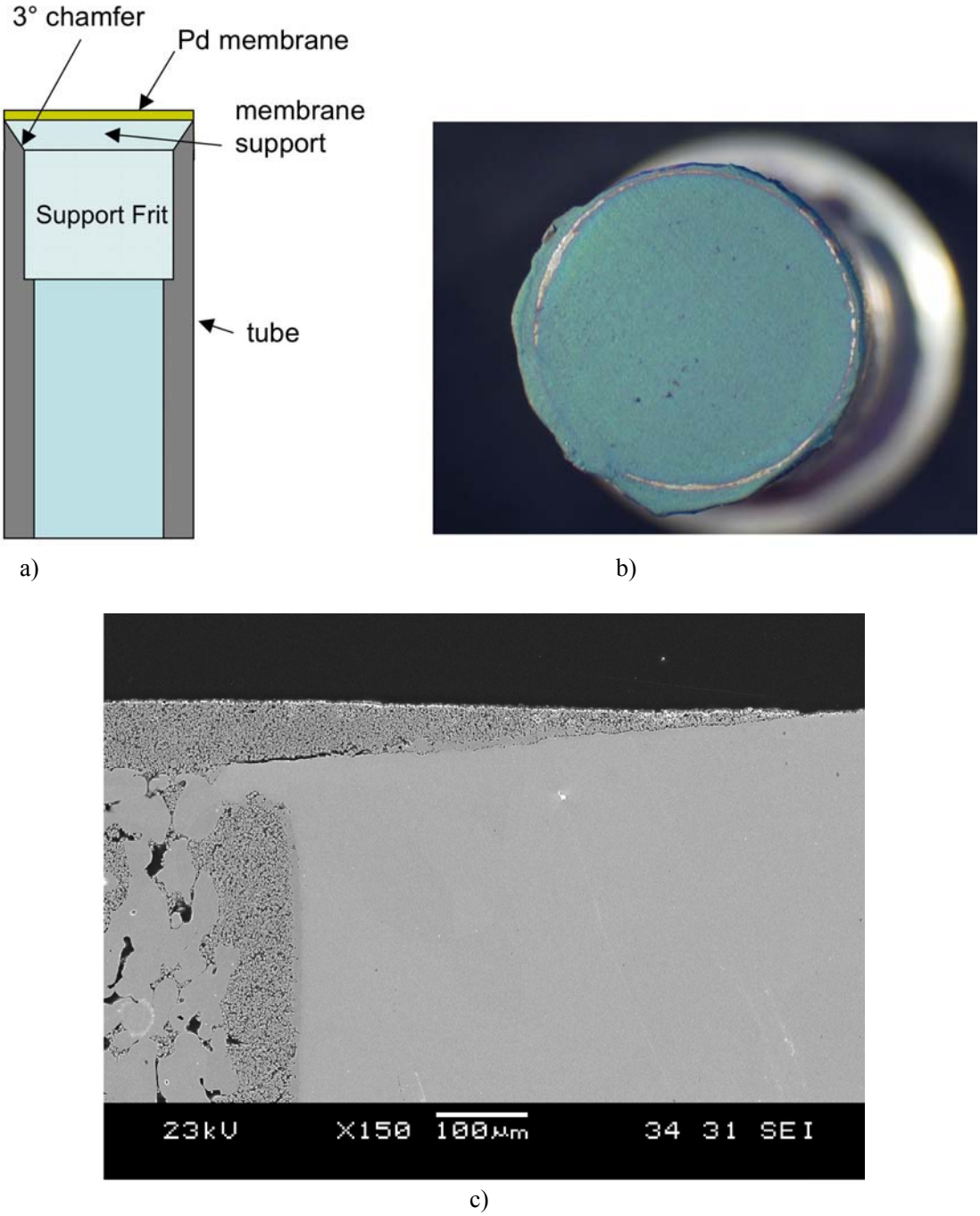

a) b)

c)

Figure 5. Collection of illustrations to show, a) the chamfered tube configuration (not to scale) with labels on the important features, b) an optical micrograph of the sintered surface (uncracked) of the membrane support layer, and c) a cross-section SEM micrograph of the chamfered region of the membrane support, showing the true angle and the degree of integrity maintained by the sintered layer in the tube interface region.

Closer examination of the sintered surface shown in Fig. 5b with the SEM revealed other types of defects (see Fig. 6a). The most significant defect from the standpoint of subsequent PVD deposition of a Pd thin film appeared to be the type of "sink hole" pit/depression shown in Fig. 6a and, in more detail, in Fig. 6b. It is unlikely that a Pd film could bridge this type of gap, which could produce a "pinhole" defect in the resulting membrane film, an unacceptable condition for high purity hydrogen separation. Thus, the source of these sinkholes needed to be found to enable an approach to be developed to eliminate them from the membrane support. Fortunately, SEM cross-sections (see Figs. 6c and 6d) were able to reveal the general sinkhole source, namely excessive penetration of the ultrafine powders down into the large (40μm) frit porosity. Apparently, the methanol carrier fluid assisted powder flow (during slurry application) down into the relatively wide pores (see Fig. 6d) of the stainless steel frit that was selected for this experiment. Following analysis of additional experimental results, it was concluded that the future sample configuration should substitute a stainless steel frit with a significantly finer average pore size, where probably about 10 μm would be ideal.

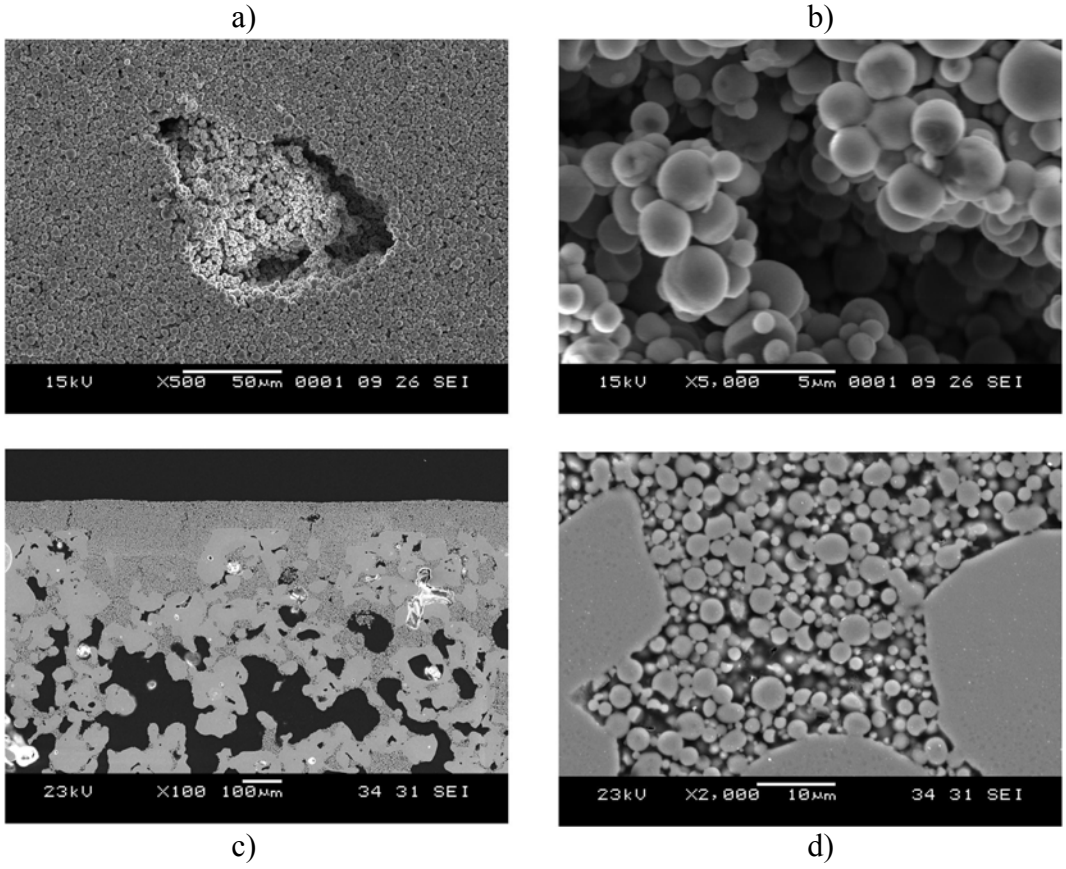

Figure 6. Assembly of SEM micrographs showing, a) a sinkhole type of sintering defect in the membrane support surface of Fig. 5, b) higher magnification of the defect, showing the depth and span of the hole, c) cross-section of the sintered membrane support, revealing the excessive penetration depth of the < 3 μm powder, and d) a higher magnification of the passage between pores in the frit that enabled such flow.

Another important feature of the porous membrane support system that required development was a method to apply a diffusion barrier coating to the exposed surface of the membrane

support, at the interface where the Pd thin film will be deposited. As mentioned in the introduction, the Fe-16Al-2Cr alloy is known to be capable of forming an alumina scale, following a controlled oxidation annealing treatment, i.e., 800C in a UHP Ar atmosphere for 24h (3). The surface of a membrane support sample was examined before this treatment by Auger electron spectroscopy with depth profiling, as shown in Fig. 7a, and the results indicated an Al oxide film thickness of about 5-7 nm. Re-examination of the sample surface after the oxidation anneal revealed an alumina film thickness of about 10-12 nm, as indicated in Fig. 7b, approximately double the as-sintered thickness. While experimental verification of the barrier film coating effectiveness at suppressing interdiffusion into a Pd film remains to be performed, the ability to grow a significant alumina scale on the surface appears promising for this objective.

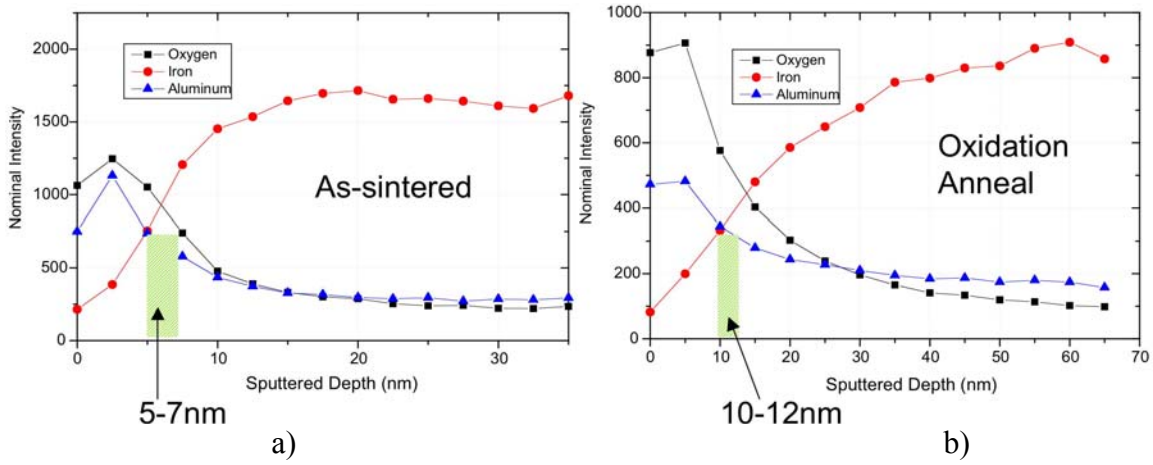

Figure 7. Summary of results of Auger electron spectroscopy at a series of depth profiling increments for, a) the as-sintered surface of a Fe-16Al-2Cr porous membrane support and, b) the same surface after an oxidation anneal.

Previous experiments that produced an externally oxidized precursor powder for ODS microstructures utilized an Fe-12.5Cr-1.0Y (wt.%) alloy that was subject to an in situ gas phase reaction with Ar + 5%O_2 atomization gas[10]. To solve the problem with premature melt stream freeze-off from excess oxygen dissolution at the melt pouring orifice, new efforts involved the use of UHP Ar atomization gas combined with injection of the reactive Ar + 5%O_2 gas at a location 20 cm downstream of the atomization nozzle. This combination was intended to permit uninterrupted (low oxygen) atomization processing, but to provide reactive gas during freefall of the atomized particles at a location where they would still retain sufficient heat to promote excess surface oxidation. The exterior surfaces of the powder from the current atomization experiment (see Fig. 8b) appeared to be less rumpled, with more visible evidence of the underlying solidification structure of each atomized particle than the previous powders in Fig. 8a. Also, the current powders appeared to be more uniformly spherical, consistent with a less dominant surface oxide. The difference in surface appearance and shape of the atomized powders also was consistent with the measurements of bulk oxygen content, where the current powders had a bulk oxygen content of 800 ppmw (0.08 wt.%), compared to the previous powders with 2.0 wt.% oxygen[8]. Both of these measurements were for < 45 μm dia. powders.

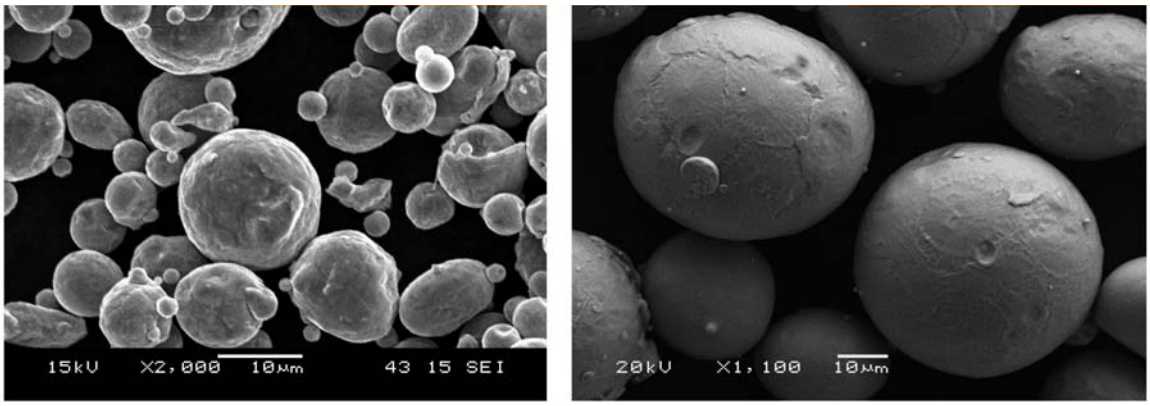

a) b)

Figure 8. SEM micrographs of as-atomized Fe-12.5Cr-1Y powders that were produced with a) reactive atomization gas (Ar + 5%O_2), and b) inert (Ar) atomization gas with a downstream reactive gas (Ar + 5%O_2) injection.

The reactive gas atomized Fe-12.5Cr-1Y powder from the previous experiments was coated with a significant layer (1-3 µm thick) of Cr_2O_3 oxide, as demonstrated in cross-section micrographs (see Fig. 9). The SEM micrograph in Fig. 9 also illustrates that the oxide coating, or "shell," had a tendency to spall from each particle during the powder handling involved with sieving (20-53 µm size fraction shown) and metallographic mounting. Cross-sections of the current Fe-12.5Cr-1Y powder did not reveal any apparent oxide coating, but surface analysis by Auger electron and X-ray photoelectron spectroscopy is planned to characterize the powder surfaces after downstream gas reaction processing.

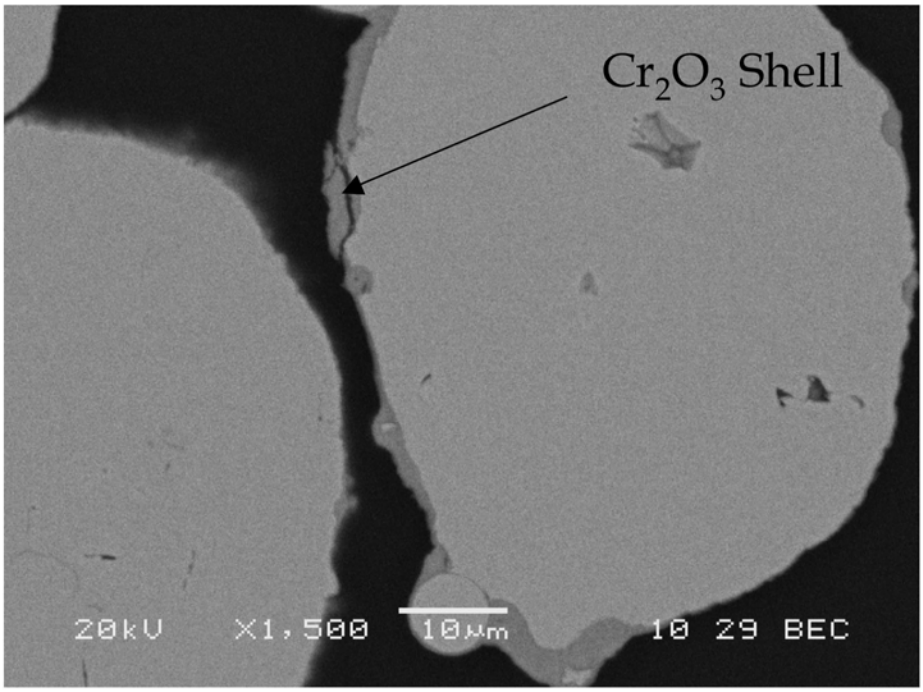

Figure 9. SEM cross-section micrograph of 20-53 µm powder from a previous reactive atomization experiment with evidence of spalling of the Cr oxide surface coating.

Further characterization of HIP consolidated Fe-12.5Cr-1Y powder from a previous reactive gas atomization experiment also focused on gathering quantitative evidence of the exchange reaction between the Cr_2O_3 trapped at the prior particle boundaries (ppb) and the Y content dissolved in the Fe-rich matrix phase. For the as-consolidated sample shown in Fig. 10a, the HIP conditions were 303 MPa at 1300C for 2h, which produced a fully dense microstructure that showed signs (spherodization and discontinuous layers) of initial dissolution of the Cr_2O_3 phase at the ppb, presumably releasing oxygen that can transport and react with dissolved Y in the matrix. Quantitative metallographic analysis revealed 7.3%, of the dark Cr_2O_3 phase in the as-HIP condition, compared with 5.7% after a further vacuum annealing treatment of 1300C for 2h (see Fig. 10b), showing evidence for additional progress of the intended oxide exchange reaction.

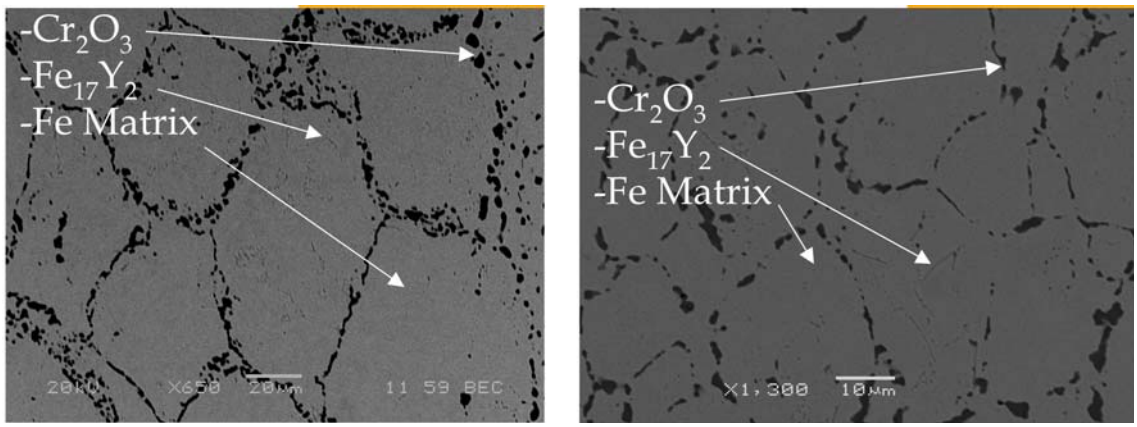

a) b)

Figure 10. SEM micrographs in backscattered electron contrast of HIP consolidated microstructures made from reactive gas atomized Fe-12.5Cr-1Y powders from a previous experiment, showing, a) the as-HIP microstructure and, b) a consolidated sample after further annealing at 1300C for 2h.

New TEM results (see Fig. 11) were successful at EDS identification of numerous examples of Y oxide and Y-Cr-O dispersoids from 10-100 nm in diameter in the as-HIP microstructure made from Fe-12.5Cr-1Y powders of a previous reactive gas atomization experiment. The semi-quantitative identification of the dispersoid compositions and size agree with other observations of microstructures from similar ODS alloys (without Ti) made by mechanical alloying methods[11]. While the intention of the alloy design was to generate a ferritic Fe-Cr matrix that could be heat treated in either austentic or ferritic phase fields, preliminary results from high temperature X-ray diffraction analysis of < 20 µm dia. powder from a previous reactive gas atomization experiment showed some unexpected phase transformation behavior[9]. The first phase transformation occurs in the temperature range of 850-950C, where α-iron apparently transformed to an FCC iron oxide (FeO), termed wustite[9]. Upon further heating, a second transformation takes place in the temperature range of 1150-1200C, where FCC-FeO transforms to FCC γ-iron[9]. While these results are intriguing, the uncertain vacuum atmosphere in the high temperature (malfunctioning vacuum sensor) diffractometer makes it necessary to repeat and extend these measurements after repairs are completed. New bulk measurements of the crystal structure transformations as a function of temperature also are planned on the high intensity X-ray system of the Advance Photon Source at ANL to provide further verification. In addition, diffusion couple experiments have been initiated recently to investigate atomic transport kinetics and spatial distribution as a function of temperature for oxygen, Y, and Cr

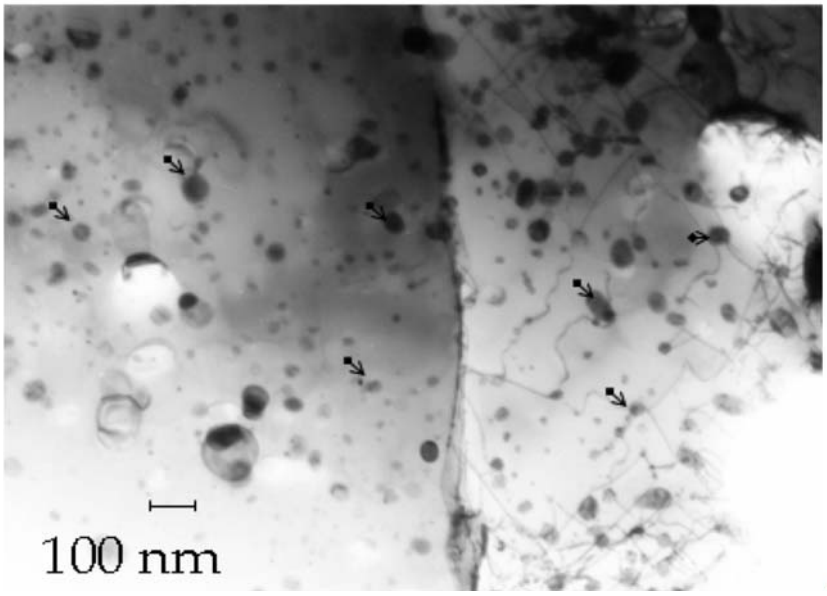

Figure 11. TEM bright field micrograph showing a significant population of spherical dispersoids in the as-HIP microstructure of a Fe-12.5Cr-1Y alloy, where small arrows mark the location of particles that were examined by EDS for approximate composition.

CONCLUSIONS

A new sample configuration and modified sintering conditions were successful at producing a near-optimum porous membrane support surface from < 3μm spherical gas atomized Fe-16Al-2Cr (wt.%) powders. A chamfered edge was needed for the support tube needed to prevent rim cracking. The results indicated that to achieve an optimum membrane support surface, a secondary support frit with reduced pore size is needed to eliminate the remaining defects in the membrane support. Tests of the completed (with Pd thin film) hydrogen separation membrane system are needed to verify the effectiveness of an increased oxide diffusion barrier film at suppressing Fe and Cr diffusion into Pd. A novel processing technique for precursor powder involving gas atomization and in situ oxidation shows promise for simplified production of ODS ferritic stainless steel alloys with isotropic microstructure, compared to the current mechanical alloying approach that results in anisotropic mechanical properties. Atomization parameters have been demonstrated to control the concentration of oxygen (from 2 wt.% to 800 ppmw) introduced into the alloy system during in-situ oxidation of the precursor powder. Hot isostatic pressing of such powder was shown by SEM and TEM results to produce a desirable ODS microstructure. Preliminary heat treating experiments have proven the ability to manipulate the formation of the secondary strengthening dispersoid phase, suggesting that a heat treatment temperature of 1300C (similar to MA processing) is useful for oxide dispersion development. An effective heat treatment schedule is being formulated using high temperature in-situ x-ray diffraction and new diffusion couple experiments to control the final ODS microstructure. Mechanical property measurements also are planned for this ongoing work.

ACKNOWLEDGEMENTS

The authors would like to acknowledge the Ames Laboratory Materials Preparation Center and staff for their efforts in supporting this study. This paper is also dedicated to the memory of our co-author, Bob Terpstra, who passed away before the completion of this manuscript. Support from DOE-FE (ARM program) through Ames lab contract no. DE-AC02-07CH11358 is gratefully acknowledged.

REFERENCES

1. I. E. Anderson, R. L. Terpstra, J.A. Cronin, and R. S. Figliola, "Verification of Melt Property and Closed Wake Effects on Controlled Close-Coupled Gas Atomization Processes," in *Advances in Powder Metallurgy & Particulate Materials-2006*, compiled by W.R. Gasbarre and J.W. von Arx, Metal Powder Industries Federation, Princeton, NJ, 2006, part 2, pp. 1-16.

2. S. Paglieri, in Conference Proceedings of 19th Annual Conference on Fossil Energy Materials, 2005, available at the USDOE website: www.netl.doe.gov.

3. P. Tortorelli, et al., in *Proceedings of the 5th International Conference on Hot Gas Filtration*, NETL, Morgantown, WV, 2002, web publication.

4. H. Klette et al. *Membrane Technology,* **5** (2005) p. 7.

5. B. Bishoff, et al., in Conference Proceedings of 17th Annual Conference on Fossil Energy Materials, 2003, available at the USDOE website: www.netl.doe.gov.

6. R.L. Terpstra and I.E. Anderson, "Development of Thin Macro-Porous Metallic Support Structures for Hydrogen Separation Membranes," in *Advances in Powder Metallurgy & Particulate Materials-2005*, compiled by C. Ruas and T.A. Tomlin (Metal Powder Industries Federation, Princeton, NJ, 2005), Part 9, pp. 149-160.

7. J.S. Benjamin, "Mechanical Alloying," *Scientific Am*., **234**, no. 5 (1976) pp. 40-48.

8. R. L. Terpstra, I. E. Anderson, F. Laabs, and J. R. Rieken, "Simplified Powder Processing of Oxide Dispersion Stainless Steel," in *Advances in Powder Metallurgy & Particulate Materials-2006*, compiled by W.R. Gasbarre and J.W. von Arx, Metal Powder Industries Federation, Princeton, NJ, 2006, part 9, pp. 1-14.

9. J. Rieken, I.E. Anderson, R. L. Terpstra, and F. Laabs, "Gas Atomized Oxide Dispersion Strengthened Ferritic Stainless Steel," in *Advanced Metallic Composites and Alloys for High Performance Applications*, A. Pandey, ed., TMS-Minerals, Metals, and Materials Soc., Warrendale, PA, 2007, pp. 21-32.

10. I.E. Anderson, B.K. Lograsso, and T.W. Ellis, “Gas Atomization Synthesis of Refractory or Intermetallic Compounds and Supersaturated Solid Solutions,” U S. Patent No. 5,368,657, November 29, 1994.

11. M.K. Miller, D.T. Hoelzer, E.A. Kenik, and K.F. Russell, “Stability of Ferritic MA/ODS Alloys at High Temperatures,” *Intermetallics*, **13** (2005) p. 387.

MICROSTRUCTURES OF THE HOT-DEFORMED Ti-Al-Nb-W-B ALLOYS

Lan Huang
Department of Materials Science and Engineering, The University of Tennessee, Knoxville, TN 37996-2200
E-mail: lhuang2@utk.edu; Telephone: (865) 974-0645; Fax: (865) 974-4115

P. K. Liaw
Department of Materials Science and Engineering, The University of Tennessee, Knoxville, TN 37996-2200
E-mail: liaw@utkux.utcc.utk.edu; Telephone: (865) 974-6356;
Fax: (865) 974-4115

C. T. Liu
Oak Ridge National Laboratory, Oak Ridge, TN 37831-6115
E-mail: liuct@ornl.gov; Telephone: (865) 574-4449; Fax: (865) 574-7659

ABSTRACT

A large ingot produced through the magnetic-flotation-melting method with the composition of Ti-45Al-7Nb-0.15B-0.4W, in atomic percent, tends to have a larger grain size (~ 110 μm) and a larger amount of the β-phase in the alloy compared with the small drop-casted specimens, which have a fine grain size of ~ 50 μm, after the HIPping and homogenization treatment.[1] In order to reduce the amount of the β-phase, heat treatments have been conducted. Additional deformation techniques, such as hot forging, have been chosen to refine the grain size of the alloy. The microstructual evolution of the TiAl-based alloy after hot forging and related heat treatments has been investigated. Mechanical properties of the alloy after the deformation and heat treatments have been studied. A duplex structure, obtained after hot-deformation and heat-treatments, has a refined grain size and enhanced room-temperature ductility and yield strength.

Keywords: TiAl alloys; heat treatment; hot forging

INTRODUCTION

The TiAl-based intermetallics have great application potentials in the aviation and automobile industry for their excellent high-temperature properties, such as the good oxidation resistance and high strength. Thus, the TiAl-based intermetallics have attracted the interests of many materials researchers and have been in the front field of materials-science studies for all times.[2-5] But the TiAl alloys have encountered many difficulties for large-scaled applications in the industry because of their low toughness, and especially their low ductility at ambient temperature. The TiAl-based alloy can be manufactured by the casting or powder metallurgy. The powder-metallurgy technique has been extensively studied, and some achievements have

been applied in the industry.[6-10] Since the melting point of the TiAl alloy is high, and its chemical activity is very strong at elevated temperatures, the alloy is very easy to be oxidized. Thus, the TiAl-alloy powder with less oxygen is very difficult to produce. Hence, the use of the powder-metallurgy technique in the TiAl alloy is limited. The procedure of casting is relatively simple, and its cost is relatively low, so that it has been widely used in producing the TiAl alloy. But the grain size of the alloy produced by this technique is quite large, which severely impacts the mechanical properties of the alloy. The refinement of the grain size in this TiAl-based alloy is necessary in order to improve the mechanical properties. One of the refining methods is to add elements into the TiAl alloy.[11-13] Cyclic heat treatment can also refine the grain size of the alloy.[14-17] Another effective way to refine the grain size is through mechanical processing. Based on a reasonable choice of the alloy system, a grain size of 60 μm, in the as-cast condition, has been obtained through the magnetic-floatation-melting method in the present work. Since the TiAl alloy is very brittle at room temperature, it is very difficult to be cold worked for the grain refinement. One effective way to refine the grain size of the TiAl-based alloy is through hot working.[18-22] Since the TiAl alloy remains quite brittle at elevated temperatures, it needs to be coated while hot deformation takes place. With the coating, the alloy can be iso-pressed during the hot deformation at elevated temperatures, this step counteracts with the tensile strength induced during forging, which improves the efficiency of hot working.[23] The relationship among the hot working, microstructures, and mechanical properties of the TiAl-based alloy can be studied, and the TiAl-based alloy with an enhanced mechanical property can be obtained.

EXPERIMENTAL PROCEDURES

The Ti-45Al-7Nb-0.15B-0.4W (at.%, atomic percent) ingot of 15kg was produced by the magnetic-floatation-melting method, using a German magnetic floatation cold crucible furnace. High-purity Nb, W, and B powders, Ti particles (99.6% purity), and Al pieces (99.99% purity), were uniformly placed in the copper crucible for magnetic floatation melting. The large ingot sample is levitated and melted in the middle of the magnetic field created by the induction coils. Small samples, 10 mm in diameter (d) and 10 mm in length (l), were spark-eroded from the large ingot for hot-simulation experiments. The small samples were canned in the carbon steel, and then hot-pressed on the Gleeble1500 hot simulator for the hot-simulation experiments. The hot-compression temperatures range from $1{,}050^0$C to $1{,}230^0$C, with a deformation of 50%, at a strain rate of 0.02 s^{-1}. The optimal hot-deformation temperature of the TiAl alloy is between $1{,}180^0$C - $1{,}200^0$C. Hot deformation had been conducted to the TiAl-based alloy after the hot-simulation experiments. The TiAl alloy had been hot deformed twice, first at $1{,}180^0$C, with a deformation of 60%, and a strain rate of 0.02 s^{-1}; and, then, at $1{,}180^0$C, with a deformation of 50%, and a strain rate of 0.02 s^{-1}. After the first hot-deformation procedure, the samples had been heat treated at $1{,}220^0$C. A second hot-deformation process had been conduced on the TiAl-based following the heat treatment. After the second deformation procedure of the TiAl-based alloys, heat treatments had been performed on the alloys in order to obtain different kinds of microstructures. For more detailed structure and composition analyses, the JSM-5600LV scanning-electron microscopy (SEM) was used, with an acceleration voltage of 20 KV.

EXPERIMENTAL RESULTS

1. Hot simulation of the TiAl-based alloys.

The TiAl-based alloy samples were canned in the carbon steel for hot-simulation experiments. As shown in Fig. 1(a), at a compression temperature of $1{,}050^0$C, the TiAl-based alloy showed no deformation while the can had deformed. At a temperature of $1{,}100^0$C, the TiAl-based alloy started to deform. As the temperature became higher, at $1{,}180^0$C, the alloy deformed at a relatively larger strain without any cracks initiated at its cross section. While the hot-compression temperature reached $1{,}230^0$C, as indicated in Fig. 1(b), the can had deformed severely, and cracks had been initiated in the cross section of the TiAl-based alloy.

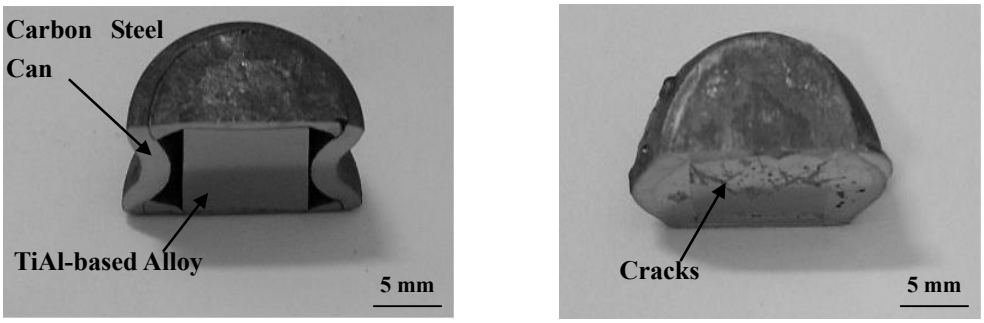

(a) $1{,}050^0$C (b) $1{,}230^0$C

Fig. 1 Canned Ti-45Al-7Nb-0.15B-0.4W alloy after the hot compression at (a) $1{,}050^0$C and (b) $1{,}230^0$C

2. Microstructures of the alloy after the first forging and heat treatment.

The microstructure of the as-cast Ti-45Al-7Nb-0.15B-0.4W alloy, after the hot-isostatic pressing (HIPping) at $1{,}250^0$C / 4 h / 150 MPa and homogenization treated at $1{,}250^0$C / 16 h, is composed of a near-fully lamellar structure. A significant amount of the β phase, mainly distributing along the lamellar grain boundaries, can be observed in the alloy, as shown in Fig. 2. The average grain size of the alloy is 110 μm. After the first forging process at $1{,}180^0$C, with a deformation of 60%, at a strain rate of 0.02 s^{-1}, the grains in the alloy have been deformed. The β phase remains in the alloy after this deformation, Fig. 3. A heat treatment has been conducted on the hot-deformed alloy at $1{,}220^0$C / 4h / air cool. The un-deformed grains, surrounded by recrystallized small grains, can rotate and deform easily in the second deformation process.

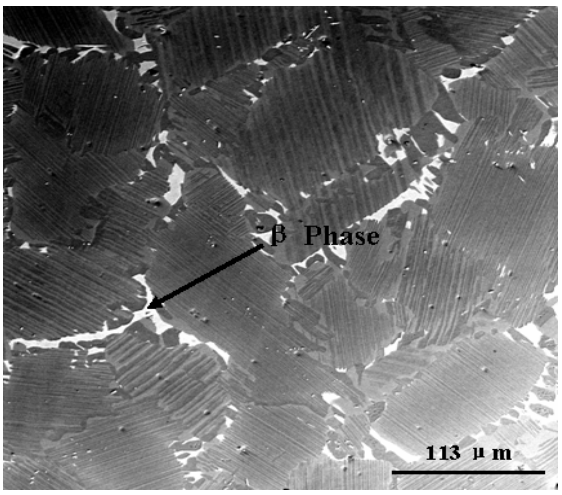

Fig. 2 Microstructure of the Ti-45Al-7Nb-0.15B-0.4W alloy after the HIPping and homogenization treatment

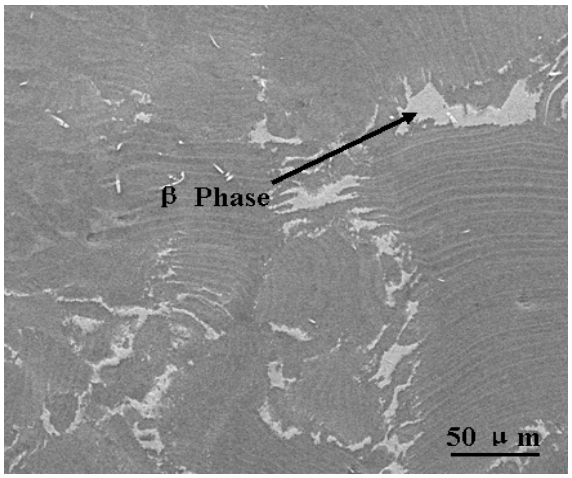

Fig. 3 Microstructure of the as-forged Ti-45Al-7Nb-0.15B-0.4W alloy

3. Microstructures of the alloy after second-forging and heat treatments.

After the heat treatment, a second hot-deformation process at a temperature of 1,180^{0}C, with a deformation of 50%, and at a strain rate of 0.02 s^{-1}, has been conducted on the alloy. Compared to the first deformation process, the grains in the alloy have been thoroughly deformed after the second deformation process, the remaining β phase can still be observed in the alloy, Fig. 4. Different heat treatments have been performed to the hot-deformed alloy. As shown in Fig. 5, after heat treating the alloy at 1,260^{0}C / 5h / furnace cool (FC), a duplex structure can be obtained. The microstructure of the alloy is composed of the lamellar structure and the primary γ phase. No β phase has been observed after this heat treatment. The average grain size of the alloy is approximately 20 μm. After heat-treating the hot-deformed alloy at 1,250^{0}C, 5h + 1,295^{0}C, 10 min., FC, a fully-lamellar structure with an average grain size of 100 μm can be obtained. No β phase has been observed in the alloy after this heat treatment.

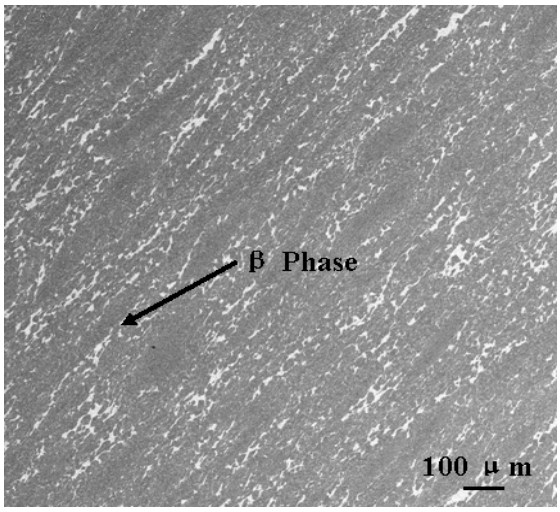

Fig. 4 Microstructure of the as-forged-II Ti-45Al-7Nb-0.15B-0.4W alloy

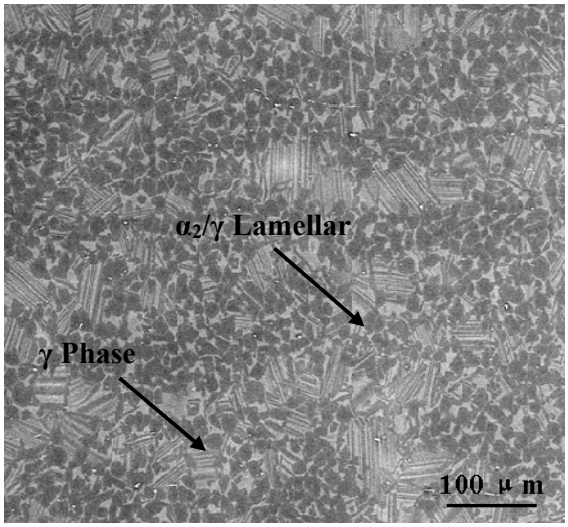

Fig. 5 Microstructure of the deformed Ti-45Al-7Nb-0.15B-0.4W alloy heat treated at $1{,}260^0$C / 5h / furnace cool (FC)

4. Tensile properties of the hot-forged TiAl-based alloys.

For the as-cast TiAl-based alloy, the ductility is nearly 0, and the yield strength is also low. Tensile tests have been conducted on the hot-deformed alloy, heat treated at $1{,}260^0$C / 5h / furnace cool (FC), with the duplex structure. The ductility of the alloy can reach 2.0%, and the yield strength of the alloy is 710 MPa. For the hot-deformed alloy, heat treated at $1{,}250^0$C / 5h + $1{,}295^0$C / 10 min. / FC, with the fully-lamellar structure, the ductility of the alloy is 1.4%, and the yield strength of the alloy is 530 MPa.

DISCUSSIONS

1. Microstructure of the as-cast large TiAl-based alloy.

The large as-cast Ti-45Al-7Nb-0.15B-0.4W alloy, produced through the magnetic-flotation-melting method, is composed of an equiaxed structure with an average grain size of 60 μm. After the HIPping and homogenization treatment, the average grain size grows to 110 μm. The microstructure of the alloy is composed of a near-fully lamellar structure and residual β phase. Compared with the same composition produced through drop casting, with a much smaller ingot size, the average grain size of the alloy is approximately 50 μm, after the HIPping and homogenization treatment. The microstructure of the small drop-cast alloy is a duplex structure, composed of a lamellar structure and the primary γ phase. No β phase was found under this condition. The difference in the microstructural features of the alloys is mainly due to the size of the ingot, which greatly affects the cooling rate of the TiAl-based alloy. When the small ingot produced through arc-melting is cooled down rapidly, the as-cast microstructure of the sample is composed of a non-equilibrium structure, and there is no microsegregation in the alloy. Thus, after the HIPping and homogenization treatment at a temperature of $1{,}250^0$C in the α + γ phase range, the microstructure of the alloy reaches an equilibrium condition, and there is no β phase observed in the alloy. For the large ingot produced through the magnetic-flotation-melting method, the cooling rate is suppressed due to the large ingot size, 110 mm in diameter (d) and 300 mm in length (l). Hence, the high-temperature remaining β phase can be observed in the as-cast condition. After the HIPping and homogenization treatment at $1{,}250^0$C, the kinetic energy for the atomic diffusion is not sufficient to reach an equilibrium condition. Therefore, the β phase remains in the alloy. In order to reduce the amount of the β phase, and refine the grain size of the large ingot, hot deformation has been conducted.

2. Effects of hot simulation on the TiAl-based alloy.

Below the temperature of $1{,}050^0$C, the force resistance for deformation is large in the TiAl-based alloy, the canned TiAl-based alloy cannot be hot deformed, Fig. 1(a). At a temperature of $1{,}100^0$C, the force resistance for the deformation of the TiAl-based alloy starts to decrease, the canned alloy can be hotly deformed at a temperature equal to or higher than $1{,}100^0$C. At the temperatures of $1{,}100^0$C, and $1{,}180^0$C, the TiAl-based alloy had deformed without any cracks initiated at its cross section, the deformation amounts of the canned TiAl alloy along the compressing direction are 30% and 50%, respectively. Thus, the TiAl-based alloy can be hot-compressed by the minimum force to obtain enough deformation in this temperature range. While hot-compressed at $1{,}230^0$C, cracks had been initiated in the cross section of the TiAl-based alloy. The can had been largely deformed, and its strength decreased, resulting in losing its protection for the TiAl-based alloy, as shown in Fig. 1(b). This trend shows that when using the carbon steel as canning materials for the TiAl alloy, the hot-deformation temperature should not exceed $1{,}230^0$C. Since cracks could initiate and propagate easily in the alloy, which could lead to the failure in the hot deformation of the TiAl alloys. An optimal temperature range has been chosen according to which the capsule was strong enough to support the hot deformation of the samples without any cracking initiating in the specimens in this temperature range. Therefore, for the carbon-steel-canned

TiAl-based alloy, the temperature range for hot deformation is $1{,}180^0$C – $1{,}200^0$C, and the optimal temperature is $1{,}180^0$C.

3. Effects of hot-forging and heat-treating on the large TiAl-based alloy.

The Ti-45Al-7Nb-0.15B-0.4W alloy produced through the magnetic-flotation-melting method was first hot deformed with a deformation of 60% at $1{,}180^0$C. After this deformation process, the grains in the alloy have been deformed, and the β phase still remained in the deformed alloy. Heat treatments have been conducted on the hot-deformed alloy in order to benefit the rotation of the un-deformed grains in the second deformation process. Small grains recrystallized in the alloy after heat treating at $1{,}220^0$C / 4 h / air cool. The average grain size did not grow larger under this heat treatment. As the annealing time exceeds 4 hours at $1{,}220^0$C, the grain size tends to grow larger in the alloy. The recrystallization of small grains in the alloy after the heat treatment causes the un-deformed grains in the alloy to rotate and deform easily in the second deformation process.

The second hot deformation at $1{,}180^0$C, with a deformation of 50%, was conducted. The alloy has been severely deformed. The β phase still remains in the deformed alloy. In order to reduce the amount of the β phase, different heat treatments have been conducted. When heat treating the TiAl-based alloy above the eutectoid temperature (T_e, approximately $1{,}175^0$C), and under the α-phase transus temperature, T_α ($1{,}290 \pm 5^0$C), a duplex structure can be obtained. Above T_e, as the heating temperature increases, the volume fraction of the γ phase tends to decrease as the amount of the α phase increases. The grain size also generally increases as the heat-treating temperature increases in this range. After the hot-deformation process, the amount of the β phase can be reduced as the heat-treating temperature is hold still at a certain temperature range, such as $1{,}260^0$C, 6h, FC. Since through the hot deformation, the kinetic energy has been stored in the deformed grains, the microsegregation in the alloy can be eliminated due to the fast atomic diffusion, when heat treating the alloy in the α + γ, two-phase temperature range. Thus, when heat treating the deformed alloy at $1{,}260^0$C / 5h / FC, a duplex structure with a fine grain size of ~ 20 μm, with no β phase, can be obtained, Fig. 5. If the heat-treating temperature is increased to $1{,}270^0$C, the grain size tends to grow larger, the amount of the γ phase decreases, and the microstructure tends to turn into a fully-lamellar structure. As the heat-treating temperature increases to T_α, a fully-lamellar structure can be obtained. In order to control the grain growth, the heat-treating time cannot exceed 5 hours. A fast cool is required so as to restrain the growth of the primary γ phase, and to obtain a fully-lamellar structure. Hence, when heat treating the hot-forged alloy at $1{,}250^0$C / 5 h + $1{,}295^0$C / 10 min., FC, a fully-lamellar structure with a grain size of 100 μm, with no β phase, can be obtained.

4. Effects of hot-forging on mechanical properties of the TiAl-based alloys.

The tensile elongation of the TiAl-based alloys at room temperature is strongly dependent on the colony size, showing an increased ductility with decreasing the colony size. The strength at room and elevated temperatures is sensitive to the interlamellar spacing, exhibiting an increased strength with decreasing the interlamellar spacing.[24-25] For TiAl-based alloys, the fully-lamellar (FL) structure, composed of α_2/γ lamellae, has a low tensile ductility at room

temperature but higher fracture strength than the other microstructures. On the other hand, the duplex (DP) structure, composed of the lamellar colony and primary γ phase, tends to have a good room-temperature tensile ductility but low fracture strength.[24] The as-cast large ingot specimen after the HIPping and homogenization treatment, with a near fully-lamellar structure and an average grain size of 110 μm, exhibits both low yield strengths and room-temperature tensile ductilities. After the hot-forging process, a duplex structure with a fine grain size of ~ 20 μm can be obtained. The ductility of the alloy with the duplex structure has been increased to 2.0%, and the yield strength of the alloy has been increased to 710 MPa. With other additional heat treatment at $1{,}250^0$C / 5h + $1{,}295^0$C / 10 min. / FC after the hot deformation, a fully-lamellar structure with an average grain size of ~ 100 μm can be obtained. The ductility of the alloy is 1.4%, and the yield strength is 530 MPa. As in comparison to other hot-forged and heat-treated TiAl-based alloys in previous reported work, Ti-48Al-2Cr-2Nb-1B and Ti-44Al-8Nb-1B,[27] with grain sizes varying from 70 ~ 110 μm, the highest yield strength was 670 MPa, and the best ductility was 1.9%, the Ti-45Al-7Nb-0.15B-0.4W alloy with a duplex structure, obtained after the hot deformation and consequent heat treatments, tends to have a smaller grain size and exhibits better tensile ductility and yield strength.

CONCLUSIONS

1. A large sample produced through the magnetic-flotation-melting method with the composition of Ti-45Al-7Nb-0.15B-0.4W has an equiaxed structure with an average grain size of 60 μm in the as-cast condition. After the HIPping and homogenization treatment at $1{,}250^0$C, the average grain size of the alloy increases to 110 μm. The microstructure is composed of a near-fully lamellar structure, with a significant amount of the β phase dispersed along the grain boundaries.
2. Hot forging and subsequent heat treatments are effective ways to refine the grain size and reduce the amount of the β phase in the alloy. The optimal hot-deformation temperature for the Ti-45Al-7Nb-0.15B-0.4W alloy is between $1{,}180^0$C – $1{,}200^0$C.
3. A duplex structure with a fine grain size of ~ 20 μm, and no β phase, can be obtained after hot-forging and heat-treating the alloy at $1{,}260^0$C / 5h / FC. A fully-lamellar structure with a grain size of 100 μm, with no β phase, can be obtained after hot-forging and heat-treating the alloy at $1{,}250^0$C, 5h + $1{,}295^0$C, 10 min., FC.
4. Both the tensile ductility and the yield strength of the alloy can be increased in the TiAl-based alloy with a duplex structure, after the hot forging and heat treatment.

ACKNOWLEDGEMENTS

The present research is sponsored by the Fossil Energy Materials Program, with Dr. R. Judkins, Dr. J. Zollar, and Dr. I. Wright as program managers, under the contact number of 11X-SP173V, and the National Science Foundation Combined Research-Curriculum Development (CRCD) Program, with Ms. Mary Poats as the contract monitor, under the contract number of EEC-0203415.

REFERENCE

[1] L. Huang, P. K. Liaw, C. T. Liu, "Microstructural Control of Ti-Al-Nb-W-B Alloys," Metallurgical and Materials Transactions A, 2007, ISSN:1543-1940 (Online).

[2] S. Zghal, M. Thomas, A. Couret, "Structural Transformations Activated During the Formation of the Lamellar Microstructure of TiAl Alloys," Intermetallics, 2005, 13(9):1008-1013.

[3] M. Yoshihara, Y.-W Kim, "Oxidation Behavior of Gamma Alloys Designed for High Temperature Applications," Intermetallics, 2005, 13(9):952-958.

[4] A. M. Hodge, L. M. Hsiung, T. G. Nieh, "Creep of Nearly Lamellar TiAl Alloy Containing W," Scripta Materialia, 2004, 51(5):411-415.

[5] Z. W. Huang, "Inhomogeneous Microstructure in Highly Alloyed Cast TiAl-based Alloys, Caused by Microsegregation," Scripta Materialia, 2005, 52(10):1021-1025.

[6] L. M. Hsiung, T. G. Nieh, "Microstructures and Properties of Powder Metallurgy TiAl Alloys," Materials Science and Engineering A, 2004, 364(1-2):1-10.

[7] R. Gerling, R. Leitgeb, F. P. Schimansky, "Porosity and Argon Concentration in Gas Atomized γ-TiAl Powder and Hot Isostatically Pressed Compacts," Materials Science and Engineering, 1998, 252(2):239-247.

[8] J. Beddoes, L. Zhao, P. Au, "The Brittle-Ductile Transition in HIP Consolidated Near γ-TiAl + W and TiAl + Cr Powder Alloys," Materials Science and Engineering A, 1995, 192-193:324-332.

[9] H. Hashimoto, T. Abe, Z. M. Sun, "Nitrogen-Induced Powder Formation of Titanium Aluminides During Mechanical Alloying," Intermetallics, 2000, 8(7):721-728.

[10] R. Gerling, A. Bartels, H. Clemens, "Structural Characterization and Tensile Properties of a High Niobium Containing Gamma TiAl Sheet Obtained by Powder Metallurgical Processing," Intermetallics, 2004, 12(3):275-280.

[11] D. Hu, "Effect of Boron Addition on Tensile Ductility in Lamellar TiAl Alloys," Intermetallics, 2002, 10(9):851-858.

[12] T. T. Cheng, "The Mechanism of Grain Refinement in TiAl Alloys by Boron Addition-An Alternative Hypothesis," Intermetallics, 2000, 8(1):29-37.

[13] P. J. Maziasz, R. V. Ramanujan, C. T. Liu, "Effects of B and W Alloying Additions on the Formation and Stability of Lamellar Structures in two-phase γ-TiAl," Intermetallics, 1997, Vol. 5(2):83-95.

[14] J. Yang, J. N.Wang, Y. Wang, "Refining Grain Size of a TiAl Alloy by Cyclic Heat Treatment Through Discontinuous Coarsening," Intermetallics, 2003, Vol.11(9):971-974.

[15] J. N. Wang, J. Yang, Q. F. Xia, "Effect On the Grain Size Refinement of TiAl Alloys by Cyclic Heat Treatment," Materials Science and Engineering A, 2002, Vol.329-331:118-123.

[16] J. Yang, J. N. Wang, Y. Wang Y, "Control of the Homogeneity of the Lamellar Structure of a TiAl Alloy Refined by Heat Treatment," Intermetallics, 2001, Vol.9(5):369-372.

[17] W. J. Zhang, L. Francesconi, E. Evangelista, "A Novel Heat Treatment to Develop Very Fine Lamellar Structure in Cast Gamma-Base TiAl Alloys," Materials Letters, 1996, Vol.27(4-5):135-138.

[18] A. Bartels, H. Kestler, H. Clemens, "Deformation Behavior of Differently Processed γ-Titanium Aluminides," Materials Science and Engineering A, 2002, Vol.329-331:153-162.

[19] M. Nakamura, M. Nobuki, T. Tanabe, “Microstructure Control and High Temperature Properties of TiAl Base Alloys,” Intermetallics, 1998, Vol.6(7-8):637-641.
[20] F. Appel, M. Oehring, J. Paul, “Physical Aspects of Hot-Working Gamma-Based Titanium Aluminides,” Intermetallics, 2004, Vol.12 (7-9):791-802.
[21] L. H. Xu, X. J. Xu, J. P. Lin, “Effect of Canned Forging on Microstructure of High Nb-Containing TiAl Alloy,” Journal Materials Engineering, 2004(8):21-24.
[22] J. H. Zhang, B. Y. Huang, K. C. Zhou, “Pack Rolling of Ti-Al Based Alloy,” The Chinese Journal of Nonferrous Metals, 2001, 11 (6):1055-1058.
[23] Y. Liu, B. Y. Huang, K. C. Zhou, “Canned Forging Process of TiAl Based Alloy,” The Chinese Journal of Nonferrous Metals, 2000, Vol.10 (Suppl.1):6-9
[24] C. T. Liu, J. H. Schneibel, P. J. Maziasz, J. L. Wright, D. S. Easton, “Tensile Properties and Fracture Toughness of TiAl Alloys with Controlled Microstructures,” Intermetallics, 1996, 4:429-440.
[25] V. Recina and B. Karlsson, “Tensile Properties and Microstructure of Ti-48Al-2W-0.5Si γ-titanium Aluminide at Temperature between Room Temperature and 800°C,” Mater. Sci. Techno., 1999, 15(1):57-66.
[26] T. Cheng, “The Decomposition of the Beta Phase in Ti-44Al-8Nb and Ti-44Al-4Nb-4Zr-0.2Si Alloys,” Acta Metall Mater, 1998, 46(13):4801-4819.
[27] D. Hu, X. H. Wu, M. H. Loretto, “Advances in Optimization of mechanical properties in cast TiAl alloys,” Intermetallics, 2005(13):914-919.

MULTI-PHASE HIGH TEMPERATURE ALLOYS: EXPLORATION OF ALUMINA-FORMING, CREEP-RESISTANT AUSTENITIC STAINLESS STEELS

Michael P. Brady
Oak Ridge National Laboratory, Oak Ridge, TN 37831-6115
bradymp@ornl.gov; Tel: (865) 574-5153; FAX (865) 241-0215

Yukinori Yamamoto
Oak Ridge National Laboratory, Oak Ridge, TN 37831-6115
yamamotoy@ornl.gov; Tel: (865) 576-7095; FAX (865) 574-7659

Zhao Ping Lu
Oak Ridge National Laboratory, Oak Ridge, TN 37831-6115
luzp@ornl.gov; Tel: (865) 576-7196; FAX (865) 574-7659

Philip J. Maziasz
Oak Ridge National Laboratory, Oak Ridge, TN 37831-6115
maziaszpj@ornl.gov; Tel: (865) 574-5082; FAX (865) 574-7659

Michael L. Santella
Oak Ridge National Laboratory, Oak Ridge, TN 37831-6115
santellaml@ornl.gov; Tel: (865) 574-4805; FAX (865) 574-4928

Bruce A. Pint
Oak Ridge National Laboratory, Oak Ridge, TN 37831-6156
pintba@ornl.gov; Tel: (865) 576-2897; FAX (865) 241-0215

ABSTRACT

Work in 2007 focused on the development of a new class of heat-resistant austenitic stainless steel alloys which achieved a unique combination of high-temperature creep strength and excellent oxidation resistance via protective Al_2O_3 scale formation. Strengthening is achieved via the formation of stable nano NbC carbides with/without Fe_2Nb and related intermetallic phase dispersions, with controlled levels of Al to enable Al_2O_3 scale formation in both air and air + water vapor environments up to ~800-900^{o}C. The developed alloys exhibit comparable creep resistance to that of the best commercial heat-resistant austenitic stainless steels, and the protective Al_2O_3 scale formation provides oxidation resistance superior to that of advanced Cr_2O_3-forming heat-resistant austenitic alloys. Preliminary screening also indicated that the developed Al-modified alloys were amenable to welding.

INTRODUCTION

The efficiency of boiler/steam turbine power plants is a strong function of steam temperature and pressure [1]. Consequently, it is attractive to operate at higher temperatures and pressures to increase energy efficiency. However, under such conditions, high-temperature creep strength is a major issue for hot components in advanced fossil energy conversion and combustion systems. For example, current goals for advanced fossil energy power plants call for ferritic steels capable of operation above 600°C, and austenitic steels capable of operation at greater than 700°C. Components of interest range from superheater tubes to industrial gas turbine components. A key need is the concurrent development of strength and oxidation resistance.

Conventional heat-resistant stainless steels rely on Cr_2O_3 scales for protection from high-temperature oxidation. However, the oxidation resistance of Cr_2O_3-forming alloys in the presence of aggressive species such as water vapor, carbon, sulfur, etc. is compromised [2], inhibiting increases in operating temperature to achieve improved efficiencies. Alumina scales grow at a slower rate than Cr_2O_3, offer superior thermodynamic stability, and thus provide protection to higher temperatures than Cr_2O_3 in many aggressive, industrially-relevant environments [2]. Modification of the creep-resistant, austenitic face-centered cubic (fcc) form of Fe to form Al_2O_3 protective oxide scales has the potential to solve these problems, and permit higher operating temperatures in water vapor and other aggressive environments. A fundamental problem is that Al stabilizes the weaker body centered cubic (bcc) form of Fe, such that levels of Al typically added to achieve alumina scale formation result in bcc phase formation, and a loss of creep resistance at service temperature.

We recently reported the development of a creep-resistant, Al_2O_3-forming austenitic stainless steel, HTUPS 4 (high temperature ultrafine precipitate strengthened) [3]. The basis for achieving both Al_2O_3 scale formation and creep resistance in this alloy was a compositional modification to maintain a single-phase, face-centered cubic (fcc) matrix in the presence of the strong bcc-stabilizing effects of Al, and the avoidance of Ti and V microalloying additions. Additions of Ti and/or V have been used to aid formation of nano-MC (M = Nb, Ti, V, etc.) carbide dispersions to improve creep strength, but those additions also result in loss of the ability to form protective Al_2O_3 scales in these relatively low Al-containing alloys. The new alloy is based on Fe-20Ni-14Cr-2.5Al-0.95Nb weight percent, wt.%, with strengthening achieved via the formation and stability of nano-NbC carbides during creep.

DISCUSSION OF CURRENT ACTIVITIES

Efforts in 2007 focused on detailed characterization of the oxidation resistance and mechanical properties of the HTUPS 4 alloy. Systematic study of the effects of alloy additions on properties was also explored in order to provide a scientific basis for alloy optimization. This progress report is compiled from findings from this work, originally reported in references 3-5.

Low specific mass gains, consistent with the slow oxidation kinetics of protective Al_2O_3 scale formation, were observed for HTUPS 4 over the course of ten, 100-h cycles (1000 h total time at temperature) (Fig. 1a, after reference 3). By comparison, ~100 μm thick gas-turbine recuperator foils of NF709 (Fe-25Ni-20Cr wt.% base) and HR 120 (Fe-37Ni-25Cr wt.% base), state-of-the-

art Cr_2O_3-forming austenitic alloys, showed moderately higher specific mass gains. However, the mass change data reflects both the balance of oxygen uptake to form Cr_2O_3 and the mass loss from volatilization of the Cr_2O_3, such that the mass change curve under represented the actual rate of oxidation and Cr consumption. For example, at 800°C in air with 10% water vapor, NF709 foil suffers from volatility-driven Cr_2O_3 scale breakdown and extensive Fe-oxide nodule formation after only 5000-7000 h of exposure, depending on foil thickness [6-8]. Even at 700°C in air with 10% water vapor, NF709 alloy foil exhibits the onset of Fe-oxide nodule formation after ~10,000 h [6-8]. The higher Ni-containing alloys such as HR 120 show longer lifetimes in water-vapor containing environments due to healing of the Fe-oxide nodule formation by NiO [6, 8]. However, the high Ni levels also significantly increase alloy cost. The available data indicate that Al_2O_3 scale forming alloys are not adversely affected in air with water vapor at these temperatures, due to the high stability of Al_2O_3 in water vapor [8-9].

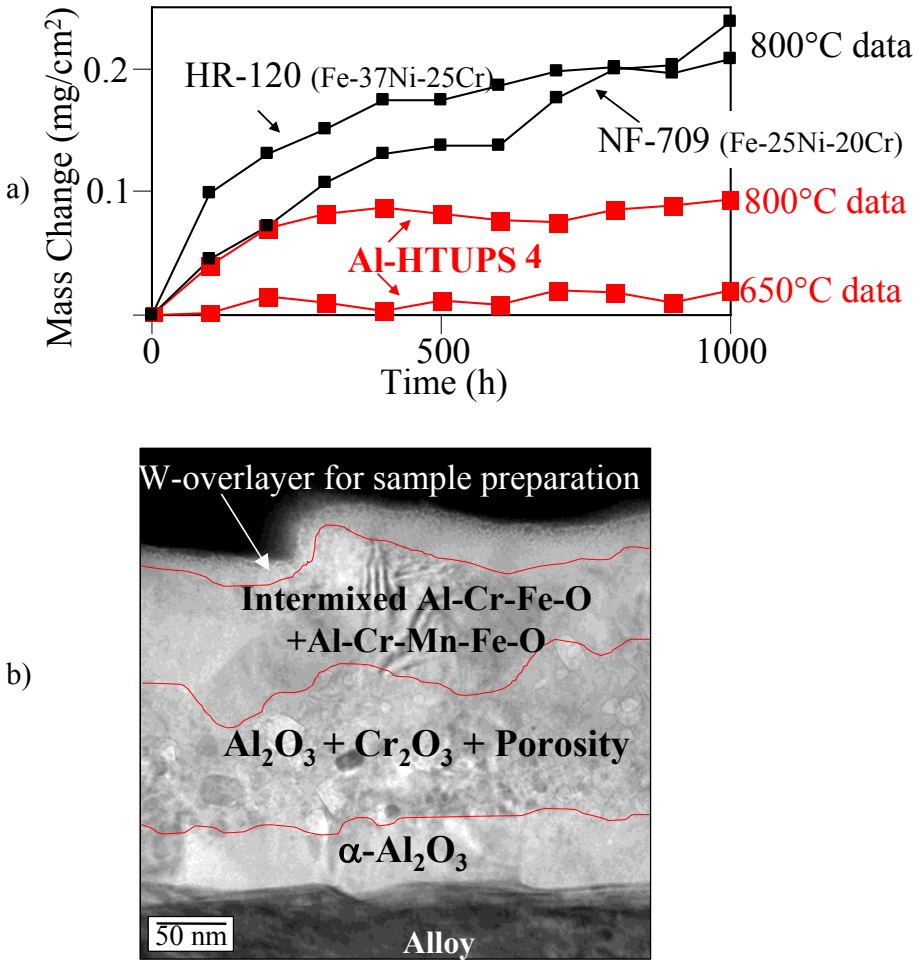

Fig.1- a) Oxidation kinetics in air with 10% water vapor (10-100 h cycles) (NF709 and HR 120 data from references 6,7), b) TEM bright field cross-section of scale formed on HTUPS 4 after 1000 h at 800°C in air with 10% water vapor. Oxidation data and micrograph from reference 3.

A bright field transmission electron microscopy (TEM) cross-sectional image of the scale formed on the HTUPS 4 alloy after 1000 h at 800°C in air with 10% water vapor is shown in Fig. 1b (the following description of scale microstructure is from reference 3). The scale consisted of a 40-50 nm inner region of columnar α-Al_2O_3 (diameter: 75-100 nm) adjacent to the alloy, and an overlying 60-100 nm thick, fine-grained (< 20 nm) intermixed layer of transition Al_2O_3 + Cr_2O_3 + porosity. In some scale regions, a 0.05-0.5 μm columnar-grained surface layer of intermixed Al-Cr-Fe-O + Al-Cr-Mn-Fe-O rich phase was also observed, as were occasional nodules 1-5 μm thick containing Nb-rich oxide regions. Auger electron spectroscopy profiling indicated that the oxide scale was Al-rich, with generally less than 10 at.% total combined of Cr, Fe, Si [3]. The observed oxide scale microstructure is consistent with the measured oxidation kinetics, which indicated relatively high mass gain during the first few hundred hours of exposure (when the mixed oxides were forming), followed by a transition to slow, protective oxidation kinetics when the α-Al_2O_3 layer developed.

Figure 2 shows creep rupture life data for HTUPS 4 relative to some commercially available heat-resistant alloys. The data indicate that HTUPS 4 exhibits creep resistance comparable to state-of-the-art austenitic stainless steels such as NF709, and approaches the range offered by the Ni-base alloy 617. In addition to the significant advantage of Al_2O_3 scale formation (both NF709 and 617 form Cr_2O_3 base scales), HTUPS 4 has Ni levels lower than NF709 and 617, and therefore has the potential to be lower cost. Figure 3 shows results of an initial weldability assessment of HTUPS 4 via a gas tungsten arc weld pass. No cracking is observed in or near the weld. Much more expansive welding studies will be needed before a definitive conclusion regarding the weldability of HTUPS 4 can be made; however, this initial finding is promising.

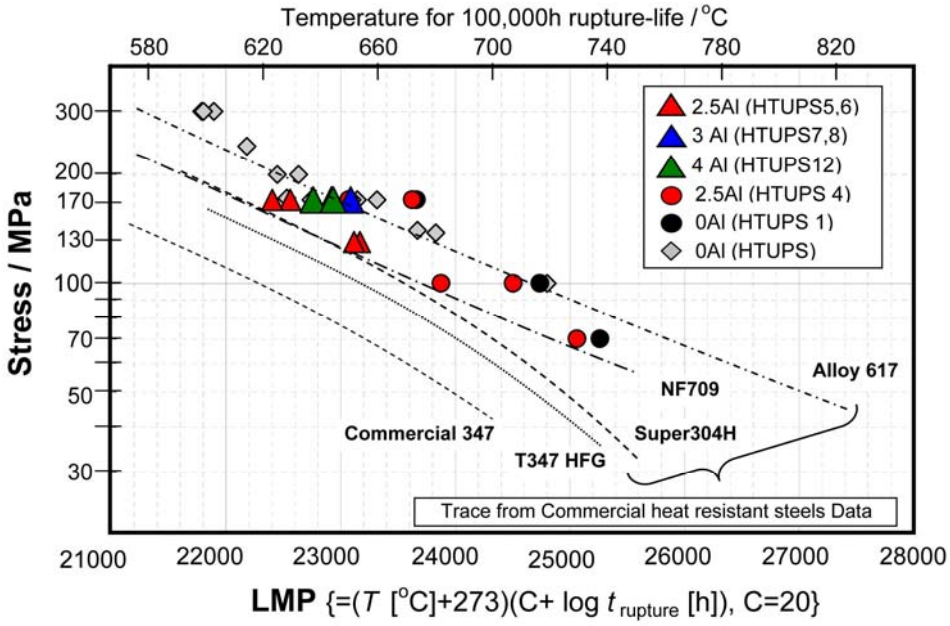

Fig. 2- Comparison of Larson Miller Parameter of the developed alloys in the present study with several commercial heat-resistant austenitic stainless steels and alloys. Figure modified from reference 3. Data for HTUPS 1 – 12 is for samples with 10% cold work.

One limitation of HTUPS 4 is that it requires cold work to aid nucleation of the nano NbC strengthening precipitates responsible for the excellent creep resistance. Exploration of the effects of Al, Nb, Ti, and V additions was therefore explored, with the ultimate goal of optimizing creep resistance and reducing or eliminating the need for cold work to obtain sufficient creep resistance.

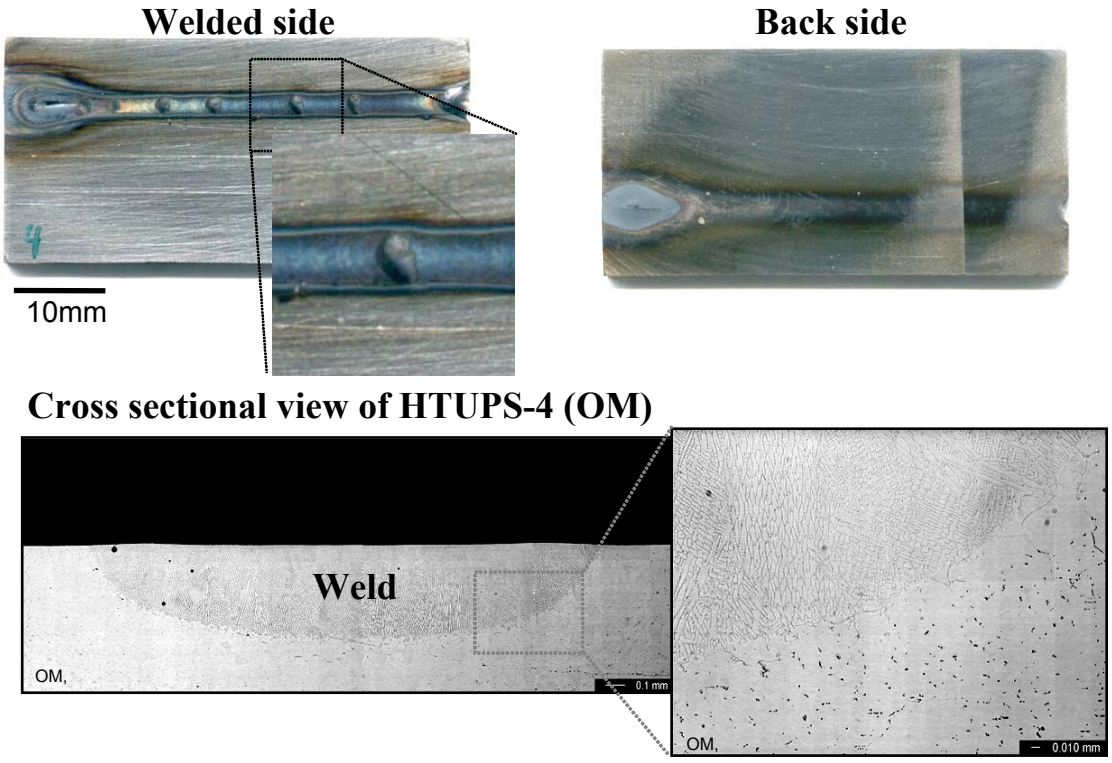

Fig. 3- Preliminary gas tungsten arc-weld screening of HTUPS 4 (OM = optical microscopy).

Fig. 4 shows short term oxidation behavior (from reference 4) for a Fe-21Ni-14Cr-2.5Al-1.7Nb wt.% base alloy with additions of Ti, V, and Ti + V, at the levels of 0.3Ti and 0.5V wt.% utilized in the original (Cr_2O_3-forming) HTUPS alloys, from which the Al_2O_3-forming HTUPS 4 alloy was derived [10]. Slow oxidation kinetics, consistent with Al_2O_3 scale formation, were initially observed for the base alloy, and for the alloys with individual additions of 0.3 Ti or 0.5V wt.%. However, the addition of both 0.3Ti and 0.5V resulted in a marked acceleration in oxidation kinetics, consistent with that observed in reference 3 for the development of the HTUPS 4 alloy. As shown in Fig. 5, the faster oxidation kinetics for the alloy with 0.3Ti and 0.5V were caused by the formation of an external Fe-Cr rich oxide scale, with internal oxidation of Al, rather than a continuous, external Al_2O_3 scale. These results suggest that small additions of Ti or V, individually, to improve creep resistance can be tolerated from an oxidation standpoint. For example, an Al_2O_3-forming austenitic alloy containing 0.2 wt.% V and strengthened by both nano MC carbides and Fe_2Nb Laves phase precipitates (alloy designation FNC 31 in the present work) resulted in a creep rupture life of over 800 h at 750°C and 100 MPa in air in the solution treated condition (no cold work). Subsequent cold work increased the creep rupture life to nearly

1800 h [5]. This alloy also exhibited mass gain kinetics consistent with Al_2O_3 scale formation at 800C in air and air with 10% water vapor [4].

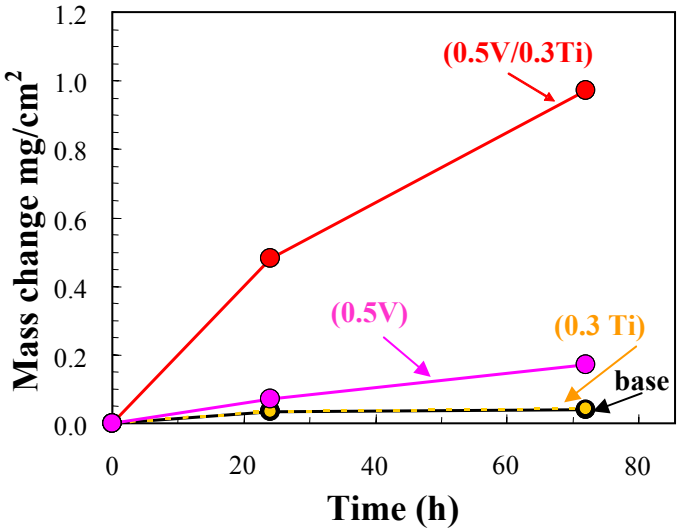

Fig. 4- Oxidation data at 800°C in air for Fe-21Ni-14Cr-2.5Al-1.7Nb wt.% base alloys with additions of Ti and/or V (after reference 4).

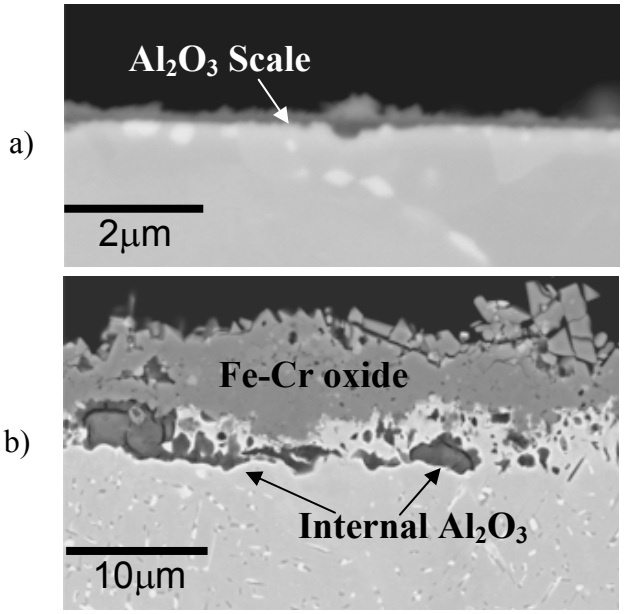

Fig. 5- Secondary electron mode cross-section images of a) 0.3 Ti alloy from Fig. 3 and b) 0.5V + 0.3Ti alloy from Fig. 3 after 72 h oxidation at 800°C (reference 4).

A series of Al_2O_3-forming austenitic alloys with Al contents from 2.5 - 4 wt.%, and Nb contents from 0.1 - 3 wt.%, incorporating small additions of Ti or V, were manufactured for exploration of creep and oxidation resistance (designated HTUPS 5-12, composition details currently proprietary). Initial creep results for some of these alloys are shown in Fig. 2. Creep resistance was generally comparable to, or only moderately lower, than HTUPS 4, indicating the potential viability of higher Al levels in these alloys.

Oxidation behavior was also explored for these alloys at 900°C in air (Fig. 6, microstructures from kinetic data presented in reference 4). HTUPS 4 does not exhibit exclusive, external Al_2O_3 scale formation at 900°C, and areas of internally oxidized Al were clearly observed. This indicates a loss of protective Al_2O_3 scale forming ability between 800 and 900°C for HTUPS 4. Only internal oxidation of Al and external Fe-Cr rich oxide formation were observed for HTUPS 8, which contains more Al than HTUPS 4 (3 vs 2.5 wt.% Al) but less Nb. Alumina scale formation was achieved at 900°C by either increasing Al content, HTUPS 12 with 4 wt.% Al, or increasing Nb content, FNC 31 (Fig. 6).

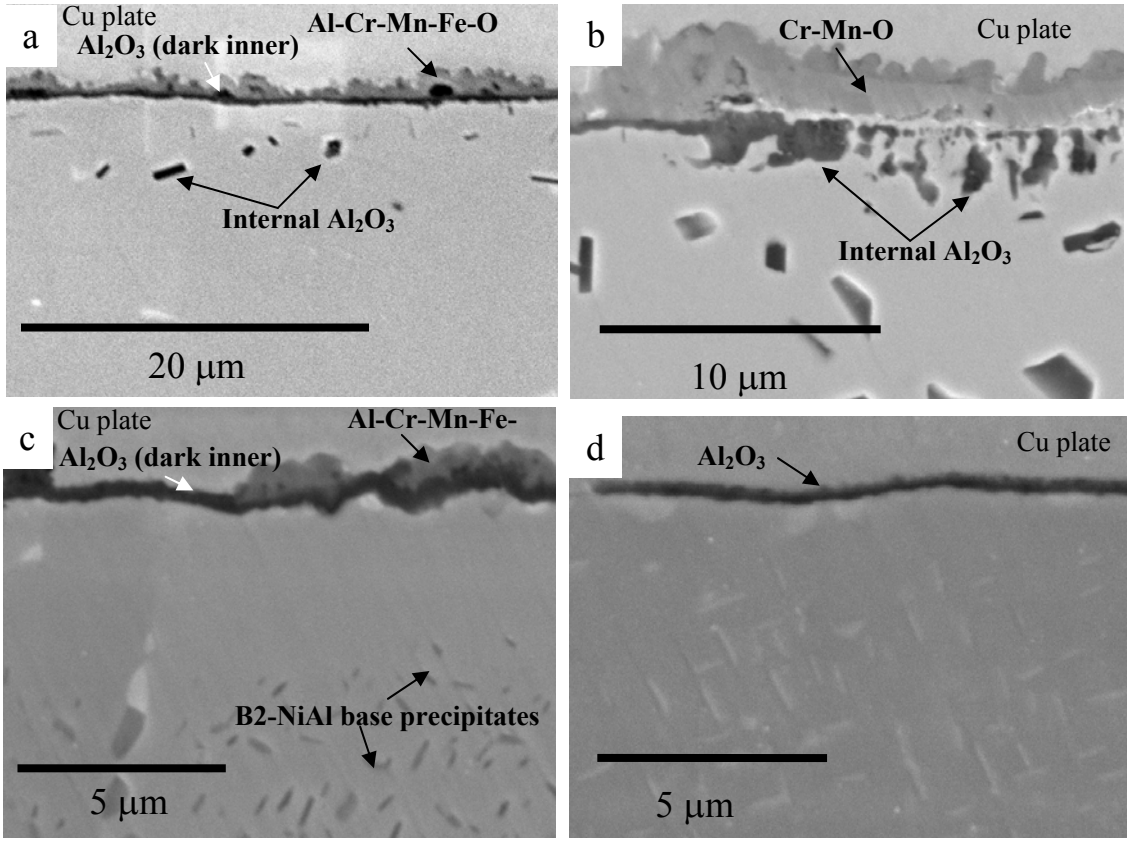

Fig. 6- SEM secondary electron image cross-sections of alloys oxidized for 100 h at 900°C in air. a) HTUPS 4 (2.5Al/0.95Nb); b) HTUPS 8 (3 Al/low Nb); c) HTUPS 12 (4 Al/low Nb); d) FNC 31 (2.5Al/high Nb). The Cu plate was used for sample preparation.

FUTURE WORK

The insights into balancing oxidation and creep resistance gained in this study hold the potential to modify a wide range of existing Fe-base alloy families to form protective Al_2O_3 scales, without loss of creep strength or increase in cost. We plan to explore the range of alloy types and composition threshold limits that this approach can be applied to. We are particularly interested in developing alloys with lower Ni contents to further reduce cost, and alloy modifications for increasing the upper temperature limit of Al_2O_3 scale formation for more demanding applications. Thus far, properties have only been demonstrated from small, laboratory scale arc-castings. The next step is to collaborate with interested alloy manufacturers to produce pilot-scale alloy heats by commercial methods, to provide a basis for scale up and transition to industrial use.

REFERENCES

1. R. Viswanathan and W. Bakker, *J. Mat. Eng. Perf.*, 10 (1), 81 (2001).
2. Kofstad, P., *High Temperature Corrosion*, (Elsevier, London, 1988).
3. Y. Yamamoto, M. P. Brady, Z. P. Lu, P. J. Maziasz, C.T. Liu, B.A. Pint, K.L. More, H.M. Meyer, and E.A. Payzant: Science, 316 (5823): 433-436 APR 20 2007
4. M.P. Brady, Y. Yamamoto, M.L. Santella, and B.A. Pint, Scripta Materialia, in press
5. Y. Yamamoto, M. P. Brady, Z. P. Lu, C. T. Liu, M. Takeyama, P. J. Maziasz, and B. A. Pint, Mater Trans, in press
6. B. A. Pint, *J. Eng. Gas Tur. Power-Trans. ASME*, **128**, 370 (2006)
7. D.J. Young and B.A. Pint, *Oxid. Met*., 66, 3/4, 137 (2006)
8. B. A. Pint, R. Peraldi, P. J. Maziasz, *Mat. Sci. Forum* 461-464, 815 (2004).
9. E. J. Opila, *Mat. Sci. Forum* 461-464, 765 (2004).
10. P. J. Maziasz, *JOM*, **41**, 14 (1989).

ACKNOWLEDGEMENTS

This research was sponsored by the U.S. Department of Energy, Fossil Energy Advanced Research Materials (ARM) Program. Oak Ridge National Laboratory is managed by U.T.-Battelle, LLC for the U.S. Department of Energy. The authors thank Joachim Schneibel and Joe Horton for reviewing this manuscript. Extensive discussions and technical input from John Shingledecker, and Ian Wright are also gratefully acknowledged.

APPENDIX 1

FINAL PROGRAM

PROGRAM FOR THE

21ST ANNUAL CONFERENCE ON FOSSIL ENERGY MATERIALS
KNOXVILLE MARRIOT, 500 E. HILL AVENUE (DOWNTOWN)
KNOXVILLE, TENNESSEE
APRIL 30-MAY 2, 2007

Monday, April 30th, 2007

12.00 noon Registration

1.00 pm Welcome and Introductory Remarks
Roddie Judkins, Oak Ridge National Laboratory

1.10 pm Brief Update on DOE's Advanced Research Materials Program
Robert Romanosky, U.S. Department of Energy, National Energy Technology Laboratory

Session 1 – NEW ALLOYS: PROPERTIES AND PERFORMANCE

1.25 pm Introduction/Chair
Roddie Judkins, Oak Ridge National Laboratory

1.30 pm Advanced Pressure Boundary Materials
Mike Santella, Oak Ridge National Laboratory

2.00 pm Corrosion Performance of Structural Alloys for Oxy-Fuel Combustion Systems
Ken Natesan, Argonne National Laboratory

2.30 pm Optimization of ODS-Fe_3Al and MA956 Alloys for Heat Exchanger Tubes
Bimal Kad, University of California at San Diego

3.00 pm Break

3.30 pm Applications for Dispersion-Strengthened Alloys in Thermal Power Systems
John Hurley, University of North Dakota, Energy and Environmental Research Center

4.00 pm Steam Turbine Materials and Corrosion
Gordon Holcomb, U.S. Department of Energy, National Energy Technology Laboratory

4.30 pm The Influence of a Cerium Surface Treatment on the Oxidation Behavior of Cr_2O_3-Forming Alloys
David Alman, U.S. Department of Energy, National Energy Technology Laboratory

5.00 pm Adjourn

Monday, April 30th, 2007

6.00-7.30 p.m. Networking and Poster Session

Session 2 – POSTERS

1. Development of Inorganic Membranes for Hydrogen Separation
   Brian Bischoff, Oak Ridge National Laboratory

2. Pilot Facility for the Production of Silicon Carbide Fibrils
   Richard Nixdorf, ReMaxCo Technologies, Inc.

3. Activated Carbon Composites for Air Separation
   Fred Baker, Oak Ridge National Laboratory

4. Wear Mechanisms of High Chrome Refractory Brick Removed from Commercial Gasifiers
   Arthur Petty, U.S. Department of Energy, National Energy Technology Laboratory

5. Enabling the Practical Application of Oxide Dispersion-Strengthened Ferritic Steels
   Ian Wright, Oak Ridge National Laboratory

6. Control of Defects and Microstructure in ODS Alloys
   Andy Jones, University of Liverpool

7. In-Plant Corrosion Probe Tests
   Gregg Stanko, Foster Wheeler Development Corporation

8. Concepts for Smart, Protective High-Temperature Coatings
   Peter Tortorelli, Oak Ridge National Laboratory

9. Optimizing Processing of Mo-Si-B Intermetallics Through Thermodynamic Assessment of the Mo-Si-B and Related Systems
   Matt Kramer, Ames Laboratory

Tuesday, May 1st, 2007

7.30 am Breakfast

Session 3 – COATINGS & PROTECTION OF MATERIALS

8.30 am Introduction/Chair
Patricia Rawls, U.S. Department of Energy, National Energy Technology Laboratory

8.35 am Long-Term Performance of Aluminide Coatings on Fe-Base Alloys
Bruce Pint, Oak Ridge National Laboratory

9.05 am Improving the Weldability of FeCrAl Weld Overlay Coatings
John Dupont, Lehigh University

9.35 am Synthesis and Oxidation Performance of Al-Modified $\gamma + \gamma^1$ Bond Coatings on Ni-Based Superalloys
Ying Zhang, Tennessee Technology University

10.05 am Break

10.30 am Protection Systems: Corrosion-Resistant Coatings
Beth Armstrong, Oak Ridge National Laboratory

11.00 am Microstructure and Properties of HVOF-Sprayed Protective Coatings
Richard Wright, Idaho National Engineering and Environmental Laboratory

11.30 pm Development of Nondestructive Evaluation Methods for Ceramic Coatings
Jiangang Sun, Argonne National Laboratory

12:00 pm Working Lunch, Presentation by Roddie R. Judkins, Director, ORNL Fossil Energy Program

Session 4 – FUNCTIONAL MATERIALS

1.55 pm Introduction/Chair, Cindy Powell
U.S. Department of Energy, National Energy Technology Laboratory

2.00 pm Results from a Sidewall Panel Field Trial of a Spall-Resistant Refractory Material Developed at NETL for Slagging Gasifiers
Cindy Powell, U.S. Department of Energy, National Energy Technology Laboratory

2.30 pm Thermochemical Modeling of Refractory Corrosion in Slagging Coal Gasifiers in Support of Development of Improved Refractory Material
Ted Besmann, Oak Ridge National Laboratory

3.00 pm A $PD_{60}CU_{40}$/Porous Iron Aluminide Membrane for Hydrogen Separation
Steve Paglieri, Los Alamos National Laboratory

3.30 pm Break

4.00 pm Sealing/Joining Technology for Gas Separation Membranes
Scott Weil, Pacific Northwest National Laboratory

4.30 pm Gas Sensors for Fossil Energy Applications
Tim Armstrong, Oak Ridge National Laboratory

5.00 pm Adjourn

Wednesday, May 2nd, 2007

7.30 am Breakfast

Session 5 – BREAKTHROUGH CONCEPTS

8.30 am Introduction/Chair
Ian Wright, Oak Ridge National Laboratory

8.35 am Nanoprecipitates in Steels
Joachim Schneibel, Oak Ridge National Laboratory

9.05 am Mechanisms of Impurity Effect and Ductility Enhancement of Mo and Cr Alloys
B. Kang/N. Ma, West Virginia University

9.35 am Advanced Processing Developments in Metallic Powders for Fossil Energy Applications
Iver Anderson, Ames Laboratory

10.05 am Break

10.30 am Microstructures of the Hot Deformed Ti-Al-Nb-W-Alloys
Peter Liaw, University of Tennessee

11.00 am Multiphase HT Alloys: Exploration of Alumina-Forming, Creep Resistant Austenitic Stainless Steels
Mike Brady, Oak Ridge National Laboratory

11.30 am Closing Remarks
Patricia Rawls
U.S. Department of Energy, National Energy Technology Laboratory
Roddie Judkins
Oak Ridge National Laboratory

11.45 pm Adjourn

APPENDIX 2

LIST OF ATTENDEES

EVENT PARTICIPANT LIST

21st Annual Conference on Fossil Energy Materials
April 30, 2007 - May 2, 2007

1. Derek Allen
   ALSTOM Power
   Cambridge Road
   Leicester, LEICS LE8 6LH
   Phone: 0047801775438
   Fax:
   E-mail: derek.allen@power.alstom.com

2. David Alman
   U.S. Department of Energy
   Albany Research Center
   1450 Queen Avenue, S.W.
   Albany, OR 97321
   Phone: 541/967-5885
   Fax: 541/996-5845
   E-mail: david.alman@netl.doe.gov

3. Mary Anne Alvin
   U.S. Department of Energy
   National Energy Technology Laboratory
   P.O. Box 10940, MS 58-202A
   Pittsburgh, PA 15236-0940
   Phone: 412/386-5498
   Fax: 412/386-4806
   E-mail: maryanne.alvin@netl.doe.gov

4. Iver Anderson
   Ames Laboratory
   Iowa State University
   222 Metals Development Bldg.
   Ames, IA 50011-3020
   Phone: 515/294-9791
   Fax: 515/294-8727
   E-mail: andersoni@ameslab.gov

5. Beth Armstrong
   Oak Ridge National Laboratory
   One Bethel Valley Road
   P.O. Box 2008, MS 6063
   Oak Ridge, TN 37831
   Phone: 865/241-5862
   Fax: 865/574-6918
   E-mail: armstrongbl@ornl.gov

6. Tim Armstrong
   Oak Ridge National Laboratory
   One Bethel Valley Road
   P.O. Box 2008, MS 6186
   Oak Ridge, TN 37830
   Phone: 865/574-7996
   Fax: 865/241-0112
   E-mail: armstrongt@ornl.gov

7. Douglas Arrell
   Siemens Power Generation
   4400 Alafaya Trail
   Orlando, FL 32765
   Phone: 407/736-7178
   Fax: 407/736-2334
   E-mail: Douglas.arrell@siemens.com

8. Fred Baker
   Oak Ridge National Laboratory
   One Bethel Valley Road
   P.O. Box 2008, MS 6087
   Oak Ridge, TN 37831
   Phone: 865/241-1127
   Fax: 865/576-8424
   E-mail: bakerfs@ornl.gov

EVENT PARTICIPANT LIST

21st Annual Conference on Fossil Energy Materials
April 30, 2007 - May 2, 2007

9. Theodore Besmann
Oak Ridge National Laboratory
One Bethel Valley Road
P.O. Box 2008, MS 6063
Oak Ridge, TN 37830
Phone: 865/574-6852
Fax: 865/574-6918
E-mail: besmanntm@ornl.gov

10. Brian Bischoff
Oak Ridge National Laboratory
One Bethel Valley Road
P.O. Box 2008, MS 6044
Oak Ridge, TN 37831-6205
Phone: 865/241-3172
Fax: 865/576-3502
E-mail: bischoffbl@ornl.gov

11. Charles Boohaker
Southern Company Services
600 North 18th Street
Mail Stop 14N-8195
Birmingham, AL 35203
Phone: 205/257-7537
Fax: 205/257-5367
E-mail: cgboohak@southernco.com

12. Mike Brady
Oak Ridge National Laboratory
One Bethel Valley Road
P.O. Box 2008, MS 6115
Oak Ridge, TN 37831-6115
Phone: 865/574-5153
Fax: 865/241-0215
E-mail: bradymp@ornl.gov

13. Eric Brosha
Los Alamos National Laboratory
PO Box 1663
MS D429
Los Alamos, NM 87545
Phone: 505/665-4008
Fax: 505/665-4292
E-mail: brosha@lanl.gov

14. Leslie Buchanan
Mitsui Babcock Energy Limited
Porterfield Road
Renfrew, Scotland PA4 8DJ
Phone: 44 (0) 1418853969
Fax: 44 (0) 1418853668
E-mail: lbuchanan@mitsuibabcock.com

15. Yen Chen
University of Wisconsin - Madison
743 ERB
1500 Engineering Drive
Madison, WI 53706
Phone: 608/890-1734
Fax: 608/263-7451
E-mail: chen2@wisc.edu

16. Regis Conrad
U.S. Department of Energy
Fossil Energy
19901 Germantown Road
Germantown, MD 20874
Phone: 301/903-2827
Fax:
E-mail: Regis.Conrad@hq.doe.gov

EVENT PARTICIPANT LIST

21st Annual Conference on Fossil Energy Materials
April 30, 2007 - May 2, 2007

17. Cristian Contescu
Oak Ridge National Laboratory
One Bethel Valley Road
P.O. Box 2008, MS 6087
Oak Ridge, TN 37831
Phone: 865/241-3318
Fax: 865/576-8424
E-mail: contescuci@ornl.gov

18. John Dupont
Lehigh University
5 E. Packer Avenue
Bethlehem, PA 18015
Phone: 610/758-3942
Fax: 610/758-4244
E-mail: jnd1@lehigh.edu

19. Tony Fry
National Physical Laboratory
Hampton Road
Teddington, Middlesex, TW110LW
Phone: 44 20 8943 6220
Fax: 44 20 8943 2989
E-mail: tony.fry@npl.co.uk

20. David Gandy
Electric Power Research Institute
1300 West WT Harris Boulevard
Charlotte, NC 28262
Phone: 704/595-2198
Fax: 704/595-2863
E-mail: davgandy@epri.com

21. Fred Glaser
U.S. Department of Energy
19901 Germantown Road
Germantown, MD 20874
Phone: 301/903-2676
Fax:
E-mail: fred.glaser@hq.doe.gov

22. Steve Halcomb
Tennessee Valley Authority
1101 Market Street
Chattanooga, TN 37402-2801
Phone: 423/751-4522
Fax: 423/751-6087
E-mail: smhalcomb@tva.gov

23. Lan Huang
University of Tennessee
Dept. of Materials Science and Engineering
Knoxville, TN 37996
Phone: 865/974-0645
Fax: 865/974-4115
E-mail: lhuang2@utk.edu

24. John Hurley
Energy & Environmental Research Center
15 N. 23rd Street
Grand Forks, ND 58203
Phone: 701/777-5000
Fax: 701/777-5181
E-mail: jhurley@undeerc.org

EVENT PARTICIPANT LIST

21st Annual Conference on Fossil Energy Materials
April 30, 2007 - May 2, 2007

25. Jeff Jensen
Caterpillar Inc.
P.O. Box 1875
TC-E 854
Peoria, IL 61656
Phone: 309/578-2969
Fax: 309/578-2953
E-mail: Jensen_Jeff_A@cat.com

26. Andy Jones
University of Liverpool
The Foresight Building
3 Brownlow Street
Liverpool, Merseyside L69 3GL
Phone: 44 151 794 8026
Fax: 44 151 794 8344
E-mail: andy.jones@liv.ac.uk

27. Chetwyn Jones
Cambridge International
207 Choptank Avenue
Cambridge, MD 21613
Phone: 410/228-3000 x1279
Fax:
E-mail: chet.jones@gmail.com

28. Roddie Judkins
Oak Ridge National Laboratory
One Bethel Valley Road
P.O. Box 2008, MS 6084
Oak Ridge, TN 37831-6084
Phone: 865/574-4572
Fax: 865/574-4357
E-mail: judkinsrr@ornl.gov

29. Bimal Kad
University of California-San Diego
409 University Center
La Jolla, CA 92093
Phone: 858/534-7059
Fax: 858/534-6373
E-mail: bkad@ucsd.edu

30. Bruce Kang
West Virginia University
Mechanical & Aerospace Engineering Dept.
353 ESB
Morgantown, WV 26506
Phone: 304/293-3111 x 2316
Fax: 304/293-6689
E-mail: bruce.kang@mail.wvu.edu

31. Bohumil Kazimierzak
Via-Cesty, s.r.o.
Oscadnica 1180
Oscadnica, Slovak Republic 023 01
Phone: 421414332621
Fax: 421414332623
E-mail: viacesty@viacesty.sk

32. Matt Kramer
Ames Laboratory
Iowa State University
37 Wilhelm Hall
Ames, IA 50011-3020
Phone: 515/294-0276
Fax: 515/294-4291
E-mail: mjkramer@ameslab.gov

EVENT PARTICIPANT LIST

21st Annual Conference on Fossil Energy Materials
April 30, 2007 - May 2, 2007

33. Peter Liaw
University of Tennessee
Department of Materials Science Engineering
434 Dougherty Hall
Knoxville, TN 37996
Phone: 865/974-5304
Fax: 865/974-4115
E-mail: rlc@utk.edu

34. Bob Lizewski
Praxair, Inc.
175 East Park Dr.
Tonawanda, NY 14150
Phone: 716/879-7128
Fax:
E-mail: bob_lizewski@praxair.com

35. Zhao-Ping Lu
Oak Ridge National Laboratory
One Bethel Valley Road
MS 6115
Oak Ridge, TN 37831
Phone: 865/576-7196
Fax: 865/574-7659
E-mail: luzp@ornl.gov

36. Ning Ma
West Virginia University
P.O. Box 6315
Morgantown, WV 26505
Phone: 304/906-9368
Fax:
E-mail: n_ma12@yahoo.com

37. David Mitchell
Siemens Power Generation, Inc.
4400 Alfaya Tr.
MC Q3-031
Orlando, FL 32826
Phone: 407/736-3909
Fax: 407/736-2334
E-mail: david.j.mitchell@siemens.com

38. Ken Natesan
Argonne National Laboratory
9700 South Cass Avenue
Building 212
Argonne, IL 60439
Phone: 630/252-5103
Fax: 630/252-8681
E-mail: natesan@anl.gov

39. Richard Nixdorf
ReMaxCo Technologies, Inc.
1010 Commerce Park Drive
Suite I
Oak Ridge, TN 37830
Phone: 865/482-7552
Fax: 865/482-7505
E-mail: nixdorfr@indceramicsolns.com

40. John Oakey
Cranfield University
Cranfield
Bedford, Bedfordshire MK43 0AL
Phone: 44/1234-754253
Fax: 44/1234-752413
E-mail: j.e.oakey@cranfield.ac.uk

EVENT PARTICIPANT LIST

21st Annual Conference on Fossil Energy Materials
April 30, 2007 - May 2, 2007

41. Steve Paglieri
Los Alamos National Laboratory
P.O. Box 1663
MS C927
Los Alamos, NM 87545
Phone: 505/667-0652
Fax: 505/665-1226
E-mail: steve.paglieri@lanl.gov

42. Bruce Pint
Oak Ridge National Laboratory
P.O. Box 2008
MS 6156
Oak Ridge, TN 37831-6156
Phone: 865/576-2897
Fax: 865/241-0215
E-mail: pintba@ornl.gov

43. Cynthia Powell
U.S. Department of Energy
National Energy Technology Laboratory
1450 Queen Avenue, SW
Albany, OR 97321
Phone: 541/967-5803
Fax: 541/967-5845
E-mail: cynthia.powell@netl.doe.gov

44. Mary Rawlins
U.S. Department of Energy
P.O. Box 2001
Oak Ridge, TN 37831
Phone: 865/576-4507
Fax:
E-mail: rawlinsmh@oro.doe.gov

45. Patricia Rawls
U.S. Department of Energy
National Energy Technology Laboratory
P.O. Box 10940
Pittsburgh, PA 15236-0940
Phone: 412/386-5882
Fax: 412/386-4775
E-mail: patricia.rawls@netl.doe.gov

46. Richard Read
U.S. Department of Energy
National Energy Technology Laboratory
P.O. Box 10940, MS 922-273C
Pittsburgh, PA 15236-0940
Phone: 412/386-5721
Fax: 412/386-5917
E-mail: read@netl.doe.gov

47. Robert Romanosky
U.S. Department of Energy
National Energy Technology Laboratory
P.O. Box 880, MS E02
Morgantown, WV 26507-0880
Phone: 304/285-4721
Fax: 304/285-4777
E-mail: rroman@netl.doe.gov

48. Andrew Rowe
RWE npower
Windmill Hill Business Park
Whitehill Way
Swindon, England SN5 6PB
Phone: 01793 893488
Fax: 01793 892288
E-mail: andrew.rowe@rwenpower.com

EVENT PARTICIPANT LIST

21st Annual Conference on Fossil Energy Materials

April 30, 2007 - May 2, 2007

49. Sanjay Sampath
Center for Thermal Spray Research
Department of Materials Science & Engineering
University of New York at Stony Brook
Stony Brook, NY 11794-2275
Phone: 631/632-9512
Fax: 631/632-7878
E-mail: sanjay.sampath@sunysb.edu

50. Domenic Santavicca
Penn State University
132 Research Building, East
University Park, PA 16802
Phone: 814/863-1863
Fax: 814/865-3389
E-mail: das8@psu.edu

51. Mike Santella
Oak Ridge National Laboratory
One Bethel Valley Road
P.O. Box 2008, MS 6096
Oak Ridge, TN 37831-6096
Phone: 865/574-4805
Fax: 865/574-4928
E-mail: santellaml@ornl.gov

52. Jeff Sarver
The Babcock & Wilcox Company
180 South Van Buren Avenue
Barberton, OH 44203
Phone: 330/860-6640
Fax: 330/860-6676
E-mail: jmsarver@babcock.com

53. Joachim Schneibel
Oak Ridge National Laboratory
P.O. Box 2008
MS 6115
Oak Ridge, TN 37831-6115
Phone: 865/576-4644
Fax: 865/574-7659
E-mail: schneibeljh@ornl.gov

54. John Shingledecker
Oak Ridge National Laboratory
One Bethel Valley Road
MS 6155
Oak Ridge, TN 37831-6155
Phone: 865/574-5108
Fax: 865/574-0641
E-mail: shingledecjp@ornl.gov

55. Nigel Simms
Cranfield University
Energy Technology Centre
Building 43A
Cranfield, Bedfordshire MK43 0AL
Phone: 44 1234 754754
Fax: 44 1234 754755
E-mail: n.j.simms@cranfield.ac.uk

56. David Stinton
Oak Ridge National Laboratory
P.O. Box 2008
Oak Ridge, TN 37831
Phone: 865/574-4556
Fax: 865/241-0411
E-mail: stintondp@ornl.gov

EVENT PARTICIPANT LIST

21st Annual Conference on Fossil Energy Materials
April 30, 2007 - May 2, 2007

57. Jiangang Sun
Argonne National Laboratory
9700 South Cass Avenue
Argonne, IL 60439
Phone: 630/252-5169
Fax: 630/252-2785
E-mail: sun@anl.gov

58. Peter Tortorelli
Oak Ridge National Laboratory
P.O. Box 2008
Oak Ridge, TN 37831-6156
Phone: 865/574-5119
Fax: 865/241-0215
E-mail: tortorellipf@ornl.gov

59. K. Scott Weil
Pacific Northwest National Laboratory
902 Battelle Boulevard
P.O. Box 999, MS K2-44
Richland, WA 99352
Phone: 509/375-6796
Fax: 509/375-2186
E-mail: scott.weil@pnl.gov

60. Jonathan Wells
RWE npower
Windmill Hill Business Park
Whitehill Way
Swindon, England SN5 6PB
Phone: 44 0 1793 89 2606
Fax: 44 0 1793 892 288
E-mail: jonathan.wells@rwenpower.com

61. Ian Wright
Oak Ridge National Laboratory
One Bethel Valley Road
Oak Ridge, TN 37831
Phone: 865/483-6687
Fax: 865/241-0215
E-mail: wrightig@ornl.gov

62. Richard Wright
Idaho National Laboratory
P.O. Box 1625
MS 2218
Idaho Falls, ID 83415
Phone: 208/526-6127
Fax: 208/526-4822
E-mail: Richard.Wright@inl.gov

63. Yukinori Yamamoto
Oak Ridge National Laboratory
One Bethel Valley Road
P.O. Box 2008, MS 6115
Oak Ridge, TN 37831
Phone: 865/576-7095
Fax: 865/576-6298
E-mail: yamamotoy@ornl.gov

64. Ying Zhang
Tennessee Technological University
115 West 10th Street
MS 5014
Cookeville, TN 38505
Phone: 931/372-3265
Fax: 931/372-6340
E-mail: yzhang@tntech.edu

EVENT PARTICIPANT LIST

21st Annual Conference on Fossil Energy Materials
April 30, 2007 - May 2, 2007

65. Jeff Zollar
Oak Ridge National Laboratory
P.O. Box 2008
MS 6084
Oak Ridge, TN 37831
Phone: 865/574-5135
Fax: 865/574-4357
E-mail: zollarja@ornl.gov

Participant Count: 65